Higgs Boson Physics beyond the Standard Model

By

Yun Jiang
B.S. (Zhejiang University) 2008
M.Sc. (National University of Singapore) 2011

Dissertation

Submitted in partial satisfaction of the requirements for the degree of

Doctor of Philosophy

in

Physics

in the

Office of Graduate Studies

of the

University of California

Davis

Approved:

_____
Chair, John F. Gunion

_____
Hsin-Chia Cheng

_____
John Terning

Committee in Charge

2015

In memory of fantastic growth during 5-year stay at Davis.

Dedicate to my first ten-year involvement in Physics.

"Theoretical research requires a high level of self-confidence and an unshakable belief that one can be strong enough to conquer the innumerable associated challenges."

— Yun Jiang

Contents

List of Figures

List of Tables

Yun Jiang

September 2015

Physics

ABSTRACT

Higgs Boson Physics beyond the Standard Model

The discovery of a new particle with mass of about 125 GeV was a real triumph of run-1 of the LHC. To date, the analysis of the full data collected clearly shows that its properties match very well those expected for the Higgs boson in the Standard Model (SM). However, the SM itself leaves many serious questions unsolved and cannot completely describe all the observed phenomena. Hence, it must be only a component of a more complete theory. Theories that go beyond the SM typically require an extended Higgs sector. Although stringently constrained by the LHC run-1 data, a non-minimal Higgs sector is theoretically very attractive and, if confirmed, would shine light on the mechanism of electroweak symmetry breaking.

Followed by a historical review of the birth of the Higgs boson, this volume supplies a brief introduction to SM Higgs boson physics and topical issues on Higgs searches at the LHC. An updated overview of the property analysis for the newly-discovered 125 GeV Higgs and other BSM Higgs bosons will be presented. We will also discuss its implications for various beyond-the-SM (BSM) Higgs models without and within the framework of supersymmetry.

The two-Higgs-doublet model (2HDM) is a very simple and appealing framework for such considerations. Either of the two CP-even Higgs bosons in the Type I and II 2HDM is able to provide a consistent description of the LHC Higgs signal. I will illustrate its status after LHC run-1 analysis and present the prediction for higher precision at the run-2. Given the very SM-like nature of this discovered particle, one often considers the decoupling limit in which the lightest one is the SM-like Higgs boson discovered at the LHC while others are very heavy. However, such a SM-like scalar Higgs boson can also be obtained in the alignment limit without the masses of other Higgs being large. In particular, I will address the seemingly extreme case in which there is a (pseudoscalar) Higgs light enough so that the SM-like state would have a rare decay mode. Finally, the results achieved in the case of alignment will be compared to those present in the decoupling

limit and the prospects for searching for non-SM Higgs bosons at future experiments will be discussed in detail.

In the framework of supersymmetry, the next-to-minimal supersymmetric SM (NMSSM) that has been widely studied is a most promising possibility because it allows for less fine-tuning. Following an analysis of the theoretical structure of this model, we first assessed the extent to which various semi-constrained NMSSM (scNMSSM) scenarios with one of the CP-even Higgs bosons, h_1 (the lightest) or h_2 (the second lightest), are able to describe the LHC signal as a SM-like Higgs. Meanwhile, if the h_1 and h_2 are approximately degenerate in mass then an enhancement of the $\gamma\gamma$ is very possible, although a SM-like level is also easily achieved. To experimentally probe the possibility of degeneracy, we developed diagnostic tools that could discriminate whether or not there are two (or more) Higgs bosons versus just one contributing to the LHC signals at 125 GeV. In addition, we considered the case where the h_1 provides a consistent description of the small LEP excess at 98 GeV whereas the h_2 possesses the primary features of the LHC Higgs-like signals at 125 GeV.

Beyond the SM, the Higgs sector and dark matter (DM) sector may be intimately connected. With protection by an extra discrete symmetry, a certain non-SM scalar scalar boson (Higgs partner) could be a possible DM candidate. As typical examples, we consider the lightest neutralino supersymmetric DM and the Higgs-portal scalar DM in the singlet extension of the two-Higgs-doublet model (2HDMS) together with presenting a decent description of the models. In both cases, implications for dark matter physics are discussed in various scenarios. Intriguingly, violating the isospin symmetry in the DM interaction with nucleons could result in a large suppression of the DM-nucleon cross section, approaching a level that is hardly reachable by many ambitious projects for DM direct detection. Given this dramatic change in the analysis of dark matter direct detection, I include an in-depth examination of this possibility in the generic Higgs-portal DM model.

ACKNOWLEDGMENTS

Let me take this good opportunityto thank those who have contributed to this thesis and make all possible ways available for my success of Ph.D. at U.C. Davis.

First and foremost acknowledgement is undoubtedly addressed to my advisor, Dr. John F. Gunion. He opened my horizon and led me into the fields of Higgs boson physics, dark matter and early Universe cosmology, which are the focus of interest in physics nowadays and the area leaving many puzzles to resolve. I greatly benefited from his patient supervision to proceed with research work smoothly and produce an outstanding publication record. He also offered me generous support to attend a large number of international schools/workshops/conferences to present our research work.This indeed enabled me to develop my presentation skill and also establish a significant global network within the community of my research area. More importantly, he always volunteers to nominate me for any high-level fellowship/award/prize for which I am qualified. And in the preparation for each application he is always making his all effort by means of strong recommendations and improving my writings, even correcting almost every typo, even a nonsignificant misusage of punctuation. Of course, he also made important contributions to this thesis. He provided essential suggestions on the structure of organization at the early stage and generously took the time to read through many versions of the draft and supply instructive comments.

The story between us began in Singapore in the winter of 2010. Just through a brief conversation, I was attracted by his easy-going personality and special working-style which perfectly matches mine. On the other hand, he was impressed with my fascination in particle physics and also great determination in the career development and thus decided to give me an offer even if my TOEFL score does not meet the minimal requirement for admission. From today's perspective, this is definitely an important offer which gave me hope when I was deeply frustrated and also shed light to my future. Recalling my growth at Davis, it has been a fantastic (or even one could say magic) five-years. During the course of Ph.D. completion, I have been significantly recognized by our HEP community

and have grown into a mature young researcher with a broad coverage of research topics.

In addition to his role as an advisor, he looks more like my grandpa to me. Many many happy and funny moments remain in my heart forever after. For instance, he asked me "Can I run in the campus?" when he just landed in Singapore after a long-distance flight. When I approached him to seek for the possibility of supervision at the end of my first-year, he assigned me a long list of questions. It is also clear in my memory that he taught me how to install the applications when I began using the Mactonish system and even helped me typing Shell and Linux commands step by step. (Well, now the situation is reverse. I become his teacher on any computer issues. That is really a funny thing.) In addition, I am deeply moved by his helping with my (first) grant application when it was already past midnight, at a time when he was suffering from severe pain. Of course, argument and debate also constitute one part of our story. We argued about my holiday leave, even there is such an occasion that I hold my objection for what he constructed when we submit the paper. Let us now just smile at these.

As a prestigious senior physicist, the way he treats students, the attitude and passion he puts toward research, and the solution he face the difficulties also greatly influence me and set up an example for my future academic career. Jack, I harbor great gratitude towards what all you have done for me in the last five years. Without you I would have never succeeded to make it this far. It is my biggest luck I could be your student and (hopefully) become the best graduate student throughout your more than 40-year teaching career. I will be your dream to the future.

Second, I am heartily thankful to my frequent (professor level) research collaborators, Dr. Sabine Kraml and Dr. Bohdan Grzadkowski. It is their patience, support and faith that led to success for our cooperation and made possible long-term collaboration. Without doubt, I enjoyed very much working with them. Their efficient work and competitive spirit promoted my growth and brought me a fruitful Ph.D. Besides, their strong recommendations played a decisive role for me in hunting an excellent postdoc position as well as receiving many other honors. Thanks are also due to my collaborator, Dr. Geneviève Bélanger, for her friendly teaching me the knowledge of dark matter and

her positive assessments which enabled me to receive invitations for several workshops. In short, they all provided assistance in numerous ways, ranging from academic consultations to various aspects of personal matters. I really feel so lucky that I could work with them at the beginning of my career.

Next I must acknowledge my special intellectual debt to a couple of my research collaborators throughout the world, including Dr. Béranger Dumont (French), Dr. Aleksandra Drozd (Polish), Dr. Aqeel Ahmed (Pakistan) and Jeremy Bernon (French), for both research collaboration and personal communication. Their smartness in physics and useful assistance in programming are essential factors in completing our projects. Special thanks to Ola for her bringing me the two-Higgs-doublet project and also to Aqeel for his welcoming me to join the extra-dimension project together with his patient teaching.

Meanwhile, I am also very grateful to many of the Chinese professors in our community such as Tao Han, T.C. Yuan, Jinmin Yang, Hongjian He, Tao Liu, Haijun Yang and Junjie Cao for useful physics discussions as well as friendly suggestions regarding my career development. In fact, the initial visits made possible by their generous financial support helped me to build my connections with high energy research in China. With their very positive evaluation, I had more and more frequent opportunities to become involved in Chinese physics activities, which significantly enhanced my recognition in the area of my research in China. Here I have to apologize that due to the space limit I cannot list the names of all those who provided me with support in the past.

In our particle theory group at Davis, there are three professors who provided comprehensive exposure to quantum field theory in a superb course, to whom I am indebted. Especially, I would like to thank Markus Luty for his passionate teaching, John Terning for his knowledgeability and Hsin-Chia Cheng for his accurate answers to my questions. Acknowledgement is also due to our experimental groups including Profs. Max Chertok, Emilijia Pantic and John Conway, who instructed me in high energy physics as well.

I am also grateful to all the faculty members and staff in our department for their considerable services. Among them, I would like to show my great gratitude to Onelia Yan and Angela Sharma. I guess they were almost driven mad by terrible financial and ad-

After over thirty years of waiting, in the summer of 2012 a new fundamental particle was discovered with mass equal to 125 GeV (1 GeV~1 proton mass) at the Large Hadron Collider (LHC). Since the discovery phase, extensive analyses using the run-1 data have been undertaken to characterize the properties of this particle with high precision, and to date have shown that this observed state is very close to the Higgs boson of the standard model (SM), that is responsible for the origin of mass for other particles in nature. Hence, the discovery of such a long-sought particle has put the final piece of the SM in place. To me, it was a privilege to witness this discovery, and the prospect of contributing to its understanding is very exciting.

As data comes in from the LHC, the relevant theoretical structures to explain the data need to be developed and verified. LHC data and its theoretical implications are thus the focus of the work in my Ph.D. program. I started my research in December 2011 when, coincidently, the first hint of observing a new particle was reported from the LHC. This enabled me to catch a golden discovery period in the area of Higgs research, and more luckily my diligent work brought me an impressive production in the first-year of my research. I have undertaken major efforts in the last three years to investigate the implications of LHC results for new physics that may exist beyond the SM, ranging from BSM Higgs physics to dark matter and cosmology, and to construct the nature of the underlying theory. To this end, it is necessary to use the latest results from the LHC experiments

and the cosmological observations to restrict the parameter space of existing models or build new effective models for physics at the TeV scale. My research concentrates on LHC phenomenology, especially that related to Higgs physics, supersymmetry and dark matter. Specifically, the phenomenology of the 125 GeV Higgs boson in the next-to-minimal supersymmetric SM (NMSSM) [1–5] and two-Higgs-doublet model (2HDM) [6–10] as well as scalar dark matter in the 2HDM plus singlet model [11] have constituted the primary parts of my work towards my Ph.D. degree and led to 14 co-authored publications, as a major contributor to all, with a total of over 500 citations.

The object of this volume is to present a review of the status of Higgs bosons physics and dark matter beyond the SM, topics which are the current focus of high energy physics, after the LHC run-1. This volume contains a concise but self-contained preliminary for the SM and LHC collider physics, covering most topics that are highly relevant to Higgs boson physics. Following this, I present an anatomy of the theoretical structures of the models and a well-organized phenomenological analysis for the BSM Higgs bosons in the NMSSM and 2HDM from my own publications (with essential modifications for confronting the full data analysis at LHC run-1). Theoretically, a non-SM Higgs boson could be a viable dark matter candidate when it is under the protection of an appropriate symmetry. This will be illustrated in terms of concrete models within or outside supersymmetry. Due to the length limit, the completed project regarding dark Higgs from warped extra dimensions [12] is not included.

As a good ending to my student age, I did my best to complete this thesis and promote it to a high quality in all ways available. This volume is definitely a useful reference to myself. I hope it will serve as a valuable resource to my colleagues and particularly to junior researchers working in the same area. In addition, it could also be nice learning material for graduate students who intend to do phenomenological research in this field.

Finally, it is my best wish that all of you will get benefit and fun in reading this material.

Yun Jiang
Davis, California

CHAPTER 1

Introduction: theoretical motivation for a Higgs boson

Back in 1964 [13–15], the theoretical physicists François Englert and Robert Brout, as well as Peter Higgs, suggested an explanation for the fact that most elementary particles – such as the electron – have a mass. This scenario predicted a new particle, which has been discovered at CERN (the European Organization for Nuclear Research) in 2012. This discovery led to the Physics Nobel Prize 2013.

1.1 Why is a Higgs boson needed in Nature?

Quantum field theory (QFT) is a theoretical framework for constructing quantum mechanical models of subatomic particles in particle physics. Treating particles as excited states of an underlying physical field, it has been enormously successful in describing the behavior of fundamental point particles and their interactions. Indeed, once the principles of relativity and quantum mechanics are invoked, QFT appears to be the only consistent framework for incorporating interacting fundamental point particles. If such a framework is to be predictive, then the properties of such fundamental particles are highly constrained—only spin 0, spin 1/2 and spin 1 are allowed [16]. It is remarkable that this

is precisely the spectrum of fundamental particles that have been observed in nature.

It is known that a gauge theory of self-interacting spin 1 particles naively appears to require that gauge bosons should be massless, since an explicit mass term for the gauge boson in the Lagrangian manifestly violates Yang-Mills gauge invariance. This is true for quantum electrodynamics (QED) and quantum chromodynamics (QCD) theories, where both photons and gluons are massless, it is however unacceptable for the gauge theory of weak interactions, since both the charged $(W^{\pm})$ and neutral (Z) gauge bosons are massive. In addition, an explicit fermion mass term which is the combination of a left-handed and right-handed fermion fields is also disallowed by the gauge invariance as left-handed fermions are electroweak doublets and right-handed fermions are electroweak singlets. A possible solution to this problem is to introduce a scalar boson which accounts for generating the mass of all known fundamental particles. The original idea was proposed in 1962 and the relativistic model was developed by three independent groups in 1964 [13–15]. Today it is simply named as the Higgs mechanism. The basic idea behind it and how the Higgs mechanism is implemented in the Standard Model (SM) will be reviewed.

Another motivation to postulate the existence of an elementary scalar particle arises from tree-level unitarity violation. Consider the theory of electroweak interactions without the attendant scalar sector. The amplitude for the scattering of longitudinally polarized gauge vector bosons, $V_L V_L \to V_L V_L$ (where $V_L = W_L$ or Z_L) at tree-level turns out to grow with the square of the center of mass energy [17, 18]. Such a result grossly violates unitarity at the scale $E \sim 4\pi m_W/g_W \simeq$ TeV and would be in violation of one of the sacred principles of quantum mechanics (which requires that the sum of probabilities can never exceed unity). This provides a hint for the presence of new physics below the TeV scale. With the help of the new scalar that couples to W^+W^- and ZZ with coupling strength gm_V^2/m_W, this tree-level unitarity violation can be mitigated. A similar inconsistency occurs in computing the scattering amplitude for the processes $V_L V_L \to f\bar{f}$, in particular into a pair of top quarks [19]. We will see in detail that these new interactions introduce an additional contribution to $V_L V_L \to V_L V_L$, which exactly cancels the bad high energy behavior of the scattering amplitude, and leaves a result that approaches a constant at

infinite energy.

A short story about the birth of Higgs in history [1]

The actual Higgs particle only features in Peter Higgs' second paper in 1964. The very clear prediction of the new particle in this paper is supposedly due to Yoichiro Nambu, the journal referee for the paper. The same mechanism of spontaneous symmetry breaking in high energy physics was, independently of and even slightly before Peter Higgs' papers, proposed by Francois Englert and Robert Brout. It is probably fair to assume that Robert Brout, had he not passed away in 2011, would have been the third Nobel Laureate in Physics, 2013. Still in 1964 the group of Gerald Guralnik, Carl Hagen, and Thomas Kibble published a more detailed and rigorous field theoretical study of the Higgs mechanism. In 1966 Peter Higgs wrote a third paper, in which he worked out many details of the Higgs mechanism and the Higgs boson, including scattering rates and decay widths. Still without linking the Higgs mechanism to the weak force, this can be considered the first phenomenological study of the Higgs boson.

1.2 Notations and terminology (if needed)

In this section we briefly survey our notations and abbreviations, together with indexing the terminology which is highly used in Higgs physics.

1.3 Scope and organization

This thesis originates from several publications and a number of talks given on LHC phenomenology, especially that related to the Higgs boson and to dark matter physics, during the completion of my Ph.D. degree. For the sake of concreteness and time limitation, I have to minimally cover the topics in the standard model (SM) and LHC physics. For the beginners who have little knowledge of quantum field theory, and especially for the ones who intend to work on phenomenology, I would recommend two modern-style textbooks, *Quantum Field Theory and Standard Model* written by Matthew Schwartz (2013) [21] and *The Standard Model and Beyond* written by Langacker (2007) [22], and a few excellent review notes such as Reina's TASI notes on *Higgs boson physics* [23, 24].

---

[1]This interesting historical story is borrowed from Tilman Plehn's lectures on LHC Physics [20].

Besides, *The Review of Particle Physics* published by the particle data group is the encyclopedia but quite bulky to the learners.

The main text is divided into three parts. The first two chapters constitute the first part containing some necessary preliminaries. Starting with the theoretical motivation for the Higgs boson, I review in Chapter 2 some topics related to the Higgs boson in the Standard model. Chapter 3 provides a self-contained introduction to Higgs boson physics at colliders and a succinct but up-to-date overview of Higgs searches at the LHC. Given the broad range studied in these fields, I will not come close to being exhaustively complete. This actually is not my intention. Instead, I would like to present the readers with some important background information that could prepare one to understand the discussions and explore the topical issues in Higgs physics. Part II is devoted to Higgs physics in the concrete models beyond the SM. Following a brief overview of the SM and possible implications for new physics after the Higgs discovery, I particularly consider the two-Higgs-doublet model (2HDM) and the next-to-minimal SM in Chapter 5 and Chapter 6, respectively. In both models, I will discuss the present status after the LHC run-I and study the prospects for searching for additional Higgs bosons at future colliders. A few particularly interesting scenarios on exotic Higgs bosons are also included. Moreover, Chapter 7 offers a diagnostic tool to distinguish whether or not the discovered Higgs signal actually arises from two Higgs bosons that are closely degenerate in mass. In Part III I will examine the connection from Higgs boson to dark matter. Specifically, a dedicated study on two possible candidates, the singlet Higgs-portal DM and the supersymmetric LSP neutralino DM, is addressed in Chapter 8, together with the role of isospin-violating effect in the dark matter direct detection analysis. In the end there follows a brief conclusion and outlook in Chapter 9.

Last, I would like to stress that the discussions in this thesis may be a little bit expanded, as compared to the journal articles, and will be the only resource to make the related details public. Also, the literature cited in the thesis sometimes is not meant to cite original. I also apologize that such subjects as the MSSM, extra dimension and inflation will not be covered in this thesis even though I have already worked on them and have

a related publication. This is partially because that covering these topics appropriately would at least double the length of the thesis.

PART I

Preliminaries: Standard Model

and LHC Higgs Physics

CHAPTER 2

SM Higgs boson physics

In this chapter I shall highlight the essence of the Higgs mechanism that accounts for the origin of mass and topics related to the Higgs boson in the standard model. The impact of various theoretical constraints on the mass of the Higgs boson will be also discussed. In the following, I will briefly review the various SM Higgs decay channels. For most of the readers, this chapter is in the nature of a review. [1]

2.1 Higgs boson in the standard model

In this section I will present a brief introduction to the mechanism of electroweak symmetry breaking. This allows us to set the stage and to fix the notation which will be used later on. For more elaborative discussion, I refer the reader to a standard textbook [22] or an excellent review [25].

---

[1]This chapter is primarily based on my lecture notes given at the PHY 250 special topics in Spring 2014 and most of the material presented in this chapter heavily relies on Reina's TASI 2011 notes [23, 24].

2.1.1 Spontaneous symmetry breaking

The underlying idea of the Higgs mechanism can be very easily illustrated by considering a classical abelian Yang-Mills theory which contains one vector field $A^\mu(x)$ and one complex scalar field $\phi(x)$. In this case, the full Yang-Mills Lagrangian is

$$\mathcal{L} = \mathcal{L}_A + \mathcal{L}_\phi \tag{2.1}$$

which is realized by adding to the Lagrangian

$$\mathcal{L}_A = -\frac{1}{4}F^{\mu\nu}F_{\mu\nu} \quad \text{with} \quad F^{\mu\nu} = (\partial^\mu A^\nu - \partial^\nu A^\mu) \ , \tag{2.2}$$

and the terms associated with the complex scalar field

$$\mathcal{L}_\phi = (D^\mu\phi)^* D_\mu\phi - V(\phi) \ , \tag{2.3}$$

where $D^\mu = \partial^\mu + igA^\mu$ and with a particular form of the potential $V(\phi)$,

$$V(\phi) = \mu^2\phi^*\phi + \lambda(\phi^*\phi)^2 \ , \tag{2.4}$$

in which λ must be positive for the scalar potential to be bounded from below. Obviously, this simply theory is invariant under the local phase transformation

$$\phi(x) \rightarrow e^{i\alpha(x)}\phi(x) \ , \ A^\mu(x) \rightarrow A^\mu(x) + \frac{1}{g}\partial^\mu\alpha(x) \ , \tag{2.5}$$

while a gauge field mass term (i.e., a term quadratic in the fields A^μ) would not be gauge invariant and cannot be added to $\mathcal{L}$ if the $U(1)$ gauge symmetry has to be preserved.

Nonetheless, the Lagrangian in Eq. (2.1) can still describe the physics of a massive gauge boson provided that the potential $V(\phi)$ in Eq. (2.4) has a minimum at which $\phi^*\phi \neq 0$. As seen in Eq. (2.4), the occurrence of a non trivial minimum, or, more precisely, of a non trivial degeneracy of minima critically depends on the sign of the μ^2 parameter in $V(\phi)$. For $\mu^2 > 0$ there is a unique minimum at $\phi^*\phi = 0$. The Lagrangian in Eq. (2.1) thus describes the physics of a massless vector boson (e.g. the photon in electrodynamics with $g = -e$) interacting with a massive charged scalar particle. On the other hand, for $\mu^2 < 0$ the potential develops a degeneracy of minima satisfying the equation

$$\phi^*\phi = -\frac{\mu^2}{2\lambda}. \tag{2.6}$$

It implies that something completely different takes place in this case. This can be revealed by choosing the ground state of the theory to be a particular ϕ among the many which satisfy the Eq. (2.6) of the minimum, and expand the potential in the vicinity of the chosen minimum. You will find that transforming the Lagrangian in such a way, the original gauge symmetry is now *hidden* or *spontaneously broken*, and new interesting features emerge. To be more specific, let us pick the following ϕ_0 minimum (along the direction of the real part of ϕ, as traditional)

$$\phi_0 = \left(-\frac{\mu^2}{2\lambda}\right)^{1/2} \equiv \frac{v}{\sqrt{2}} \tag{2.7}$$

(where v is called the vacuum expectation value (VEV) of the field ϕ) and shift the ϕ field accordingly:

$$\phi(x) = \phi_0 + \frac{1}{\sqrt{2}}\left(\phi_1(x) + i\phi_2(x)\right) \ . \tag{2.8}$$

More transparently, we parameterize the complex scalar field ϕ as:

$$\phi(x) = \frac{e^{i\frac{\chi(x)}{v}}}{\sqrt{2}}(v + \sigma(x)) \ \ \overset{U(1)}{\longrightarrow} \ \ \frac{1}{\sqrt{2}}(v + \sigma(x)) \ , \tag{2.9}$$

i.e. the χ degree of freedom can be *rotated away*, as indicated in Eq. (2.9), by enforcing the $U(1)$ gauge invariance of the original Lagrangian. With this gauge choice, known as the unitary gauge, the Lagrangian becomes:

$$\mathcal{L} = \mathcal{L}_A + \frac{g^2 v^2}{2} A^\mu A_\mu + \frac{1}{2}\left(\partial^\mu \sigma \partial_\mu \sigma + 2\mu^2 \sigma^2\right) + \dots \tag{2.10}$$

which unambiguously describes the dynamics of a massive vector boson A^μ with

$$m_A^2 = g^2 v^2 \tag{2.11}$$

and a massive real scalar field, generically called the *Higgs field* [2], of mass

$$m_\sigma^2 = -2\mu^2 = 2\lambda v^2 \tag{2.12}$$

It is interesting to note that the total counting of degrees of freedom (d.o.f.) before the original $U(1)$ symmetry is spontaneously broken and after the breaking has occurred is the same.

---

[2] To avoid the confusion I use σ rather than h or H to label the scalar field. The labels h or H are commonly employed for the SM Higgs field and will be largely used in the following context.

In essence, spontaneous breaking of a gauge theory by a non-zero VEV of a scalar field results in the disappearance of a Goldstone boson and its transformation into the longitudinal component of a massive gauge boson.

2.1.2 SM Higgs mechanism

The Standard Model refers, in fact, to $SU(3)_C \times SU(2)_L \times U(1)_Y$ gauge invariance when combined with the electroweak symmetry breaking mechanism. Very often, the electroweak sector of the theory is also referred to as the SM; in this review we will use this name for both options. The Higgs mechanism is implemented in the SM by introducing a complex scalar doublet Φ of $SU(2)$ with hypercharge $Y_\Phi = 1/2$,

$$\Phi = \begin{pmatrix} \phi^+ \\ \phi^0 \end{pmatrix} , \tag{2.13}$$

with Lagrangian

$$\mathcal{L}_\Phi = (D^\mu \Phi)^\dagger D_\mu \Phi - \mu^2 \Phi^\dagger \Phi - \lambda (\Phi^\dagger \Phi)^2 , \tag{2.14}$$

where the covariant derivative of Φ is defined as

$$D_\mu \Phi = (\partial_\mu - ig W_\mu^a \tau^a - ig' Y_\Phi B_\mu) \tag{2.15}$$

where $\tau^a = \sigma^a/2$ (for $a = 1, 2, 3$) are the $SU(2)$ Lie Algebra generators, proportional to the Pauli matrix σ^a. The SM gauge symmetry is spontaneously broken to a residual $U(1)_{em}$ symmetry when a particular VEV for Φ is chosen, e.g.:

$$\langle \Phi \rangle = \frac{1}{\sqrt{2}} \begin{pmatrix} 0 \\ v \end{pmatrix} \quad \text{with} \quad v = \left(\frac{-\mu^2}{\lambda} \right)^{1/2} \quad (\mu^2 < 0, \lambda > 0) . \tag{2.16}$$

Upon spontaneous symmetry breaking the kinetic term in Eq. (2.14) gives rise to the gauge boson mass terms. This can be seen explicitly below. Note that the content of the scalar sector becomes more transparent if one works in the unitary gauge and eliminates the unphysical degrees of freedom by virtue of gauge invariance. In analogy to what we wrote for the abelian case in Eq. (2.9), this amounts to parametrizing and rotating the $\phi(x)$ complex scalar field as follows:

$$\Phi(x) = \frac{e^{\frac{i}{v} \vec{\chi}(x) \cdot \vec{\tau}}}{\sqrt{2}} \begin{pmatrix} 0 \\ v + H(x) \end{pmatrix} \xrightarrow{SU(2)} \Phi(x) = \frac{1}{\sqrt{2}} \begin{pmatrix} 0 \\ v + H(x) \end{pmatrix} , \tag{2.17}$$

where v is given in Eq. (2.16). Under this expansion we then transform the kinetic term into:

$$(D^\mu \Phi)^\dagger D_\mu \Phi \longrightarrow \frac{1}{8}(0 \ v)\left(gW_\mu^a \sigma^a + g'B_\mu\right)\left(gW^{b\mu}\sigma^b + g'B^\mu\right)\begin{pmatrix} 0 \\ v \end{pmatrix} + \cdots$$

$$= \frac{1}{2}\frac{v^2}{4}\left[g^2(W_\mu^1)^2 + g^2(W_\mu^2)^2 + (-gW_\mu^3 + g'B_\mu)^2\right] + \cdots \tag{2.18}$$

At this step I intentionally omit the terms involving the scalar field H, which will be discussed later. Combining the A_μ^1 and A_μ^2 components linearly

$$W_\mu^\pm = \frac{1}{\sqrt{2}}(W_\mu^1 \mp iW_\mu^2) \tag{2.19}$$

one can recognize in Eq. (2.18) the mass terms for the charged gauge bosons $W_\mu^\pm$:

$$M_W = \frac{1}{2}gv \ , \tag{2.20}$$

Inversely, v is fixed in terms of the W boson mass M_W or the Fermi constant G_F determined from muon decay[3].

$$v = (\sqrt{2}G_F)^{-1/2} \simeq 246 \text{ GeV} \tag{2.21}$$

To correctly identify the mass terms, we perform an orthogonal rotation for the remaining two components W_μ^3 and B_μ.

$$\begin{pmatrix} W_\mu^3 \\ B_\mu \end{pmatrix} = \begin{pmatrix} \cos\theta_W & \sin\theta_W \\ -\sin\theta_W & \cos\theta_W \end{pmatrix}\begin{pmatrix} Z_\mu \\ A_\mu \end{pmatrix} \ , \tag{2.22}$$

where the Weinberg angle is given by $\tan\theta_W = g'/g$. The fact that the change of variables is a rotation ensures that the kinetic terms remain canonical when expressed in terms of A_μ and Z_μ. This leads to a neutral gauge boson Z_μ with mass

$$M_Z = \frac{1}{2}\sqrt{g^2 + g'^2}v \ , \tag{2.23}$$

---

[3]The strength of Fermi's interaction is given by the Fermi coupling constant G_F. The most precise experimental determination of the Fermi constant comes from measurements of the muon lifetime, which is inversely proportional to the square of G_F (when neglecting the muon mass against the mass of the W boson). Their connection roughly leads to the relation $G_F = \frac{\sqrt{2}}{8}\frac{g^2}{M_W^2}$.

and a massless corresponding photon field A_μ, that is the gauge boson of the residual $U(1)_{em}$ gauge symmetry. Thus, we have achieved (half of) our goal: by spontaneously breaking the symmetry $SU(2)_L \times U(1)_Y \rightarrow U(1)_Q$, three degrees of freedom, the $\chi^a(x)$ Goldstone bosons, have been absorbed by the $W^\pm$ and Z weak gauge bosons to form their longitudinal components and to get their masses. Since the $U(1)_Q$ symmetry is still unbroken, the photon which is its generator, remains massless as it should be. The masses for the $W^\pm$ and Z bosons are related by the Weinberg angle

$$M_W = M_Z \cos\theta_W \tag{2.24}$$

One can also identify the the electromagnetic gauge coupling from the term $A_\mu Q$, with $Q = T_3 + Y$ as the generator of $U(1)_{em}$ group.

$$e = \frac{gg'}{\sqrt{g^2 + g'^2}} \tag{2.25}$$

Next, we will examine the H-dependent terms omitted in Eq. (2.18). The terms linear in the gauge bosons $W_\mu^\pm$ and Z_μ define the coupling of the SM Higgs boson to the weak gauge fields:

Figure 2.1. Higgs couplings to the vector bosons. $(V = W, Z)$

This form of the Higgs couplings ensures the unitarity of the theory as will be seen later. Perhaps it has been noticed that the couplings of the Higgs boson to the gauge fields are proportional to their mass. Therefore H does not couple to the photon at tree level. It is important, however, to observe that some gauge couplings that are absent at tree level may be induced at higher order by loop corrections. Particularly relevant to the Higgs boson phenomenology present in this thesis are the couplings of the Higgs boson to a pair of photons, and to a photon and a Z boson, as well as the coupling to a pair

of gluons[4]. The analytical expressions for the one-loop induced $H\gamma\gamma$, $H\gamma Z$, and Hgg vertices are more involved and will be given in Section 2.3.

2.1.3 Yukawa interactions and fermion mass generation

As already mentioned, the SM gauge symmetry also forbids explicit mass terms for the fermionic degrees of freedom in the Lagrangian. The fermion mass terms must be generated via gauge invariant renormalizable Yukawa couplings to the scalar field Φ:

$$\mathcal{L}_{Yukawa} = -Y_u^{ij}\bar{Q}_L^i\Phi^c u_R^j - Y_d^{ij}\bar{Q}_L^i\Phi d_R^j - Y_e^{ij}\bar{L}_L^i\Phi l_R^j + h.c. \tag{2.26}$$

where $\Phi^c = -i\sigma^2\Phi^*$, and Y_f ($f = u, d, l$) are matrices of Yukawa coupling between the field Φ and the fermionic fields of the SM [5]. Q_L^i and L_L^i (where $i = 1, 2, 3$ is a generation index) represent left handed $SU(2)_L$ doublets of quarks and leptons, while u_R^i, d_R^i and l_R^i are the corresponding right handed singlets. When the scalar fields Φ acquires a non zero VEV through spontaneous symmetry breaking as displayed in Eq. (2.17), each fermionic degree of freedom coupled to Φ develops a mass term with mass parameter

$$m_f = Y_f\frac{v}{\sqrt{2}} \ , \tag{2.27}$$

where the process of diagonalization from the current eigenstates in Eq. (2.26) to the corresponding mass eigenstates is already realized, and Y_f are therefore the elements of the diagonalized Yukawa matrices corresponding to a given fermion. The Yukawa couplings of the f fermion to the Higgs boson y_f defined in Feynman rule (see Fig. 2.2) is proportional to Y_f:

$$y_f = Y_f/\sqrt{2} \tag{2.28}$$

Analogously, one obtains also the Higgs boson couplings to leptons.

Unlike the gauge bosons, the origin of fermion masses is somehow mysterious. As long as it is not better understood in some more general context beyond the Standard Model, the Yukawa couplings y_f represent free parameters of the SM Lagrangian. The

---

[4] Gluons are massless vector gauge bosons that mediate the strong interactions of quarks in quantum chromodynamics (QCD). Thus, they also belong to the SM when the strong interactions are included through the QCD Lagrangian. The full SM gauge symmetry is $SU(3)_C \times SU(2)_W \times U(1)_Y$.

[5] The matrices are supposed to be implicitly diagonalized in generation space at the price of a CKM matrix for the charged currents, so that $Y_f^{ij} = 0$ for $i \neq j$.
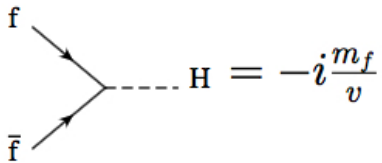
Figure 2.2. Higgs couplings to the fermions.

mechanism through which fermion masses are generated in the SM, although related to the mechanism of spontaneous symmetry breaking, requires therefore further assumptions and involves a larger degree of arbitrariness as compared to the gauge boson sector of the theory.

2.1.4 Higgs self-interactions

Let us now turn to the Higgs boson itself. Performing the field expansion and substituting into the scalar potential, Eq. (2.14), we can obtian the terms containing the real scalar field, the *Higgs boson H*, only:

$$\mathcal{L}_{\text{Higgs}} = \mu^2 H^2 - \lambda v H^3 - \frac{1}{4}\lambda H^4 \tag{2.29}$$

From this Lagrangian, one can reads the Higgs boson mass

$$m_H^2 = -2\mu^2 = 2\lambda v^2 \tag{2.30}$$

and the Feynman rules for the Higgs self-couplings (with the correct symmetry factor counting) are given by

$$g_{HHH} = i(3!)\,\lambda v = 3i\frac{m_H^2}{v} \; , \tag{2.31}$$

$$g_{HHHH} = i(4!)\frac{\lambda}{4} = 3i\frac{m_H^2}{v^2} \; . \tag{2.32}$$

Hence, the Higgs mass plays a crucial role in the dynamics of the Higgs sector. In particular, the heavier the Higgs mass the stronger the strength of the Higgs self-couplings. The observed Higgs mass of 126 GeV determines the parameter $\lambda \simeq 0.13$ and the quartic coupling $g_{HHHH} \simeq 0.77$, which implies that the Higgs dynamics is weakly coupled.

As far as the Higgs boson tree level couplings go, we observe that they are all expressed in terms of just two parameters, either λ and μ appearing in the scalar potential of $\mathcal{L}_{\text{Higgs}}$

(see Eq. (2.14)) or, equivalently, m_H and v, the Higgs boson mass and its VEV. Since $v \simeq 246\,\text{GeV}$ is measured in muon decay, the entire Higgs sector of the SM only depends on its mass m_H. This is certainly a very economical model, however, I would like to emphasize that the SM by introducing single Higgs doublet is just the simplest way to accomplish the electroweak symmetry breaking (EWSB) as the pattern $SU(2)_L \times U(1)_Y \to U(1)_{em}$. EWSB could be more intricate. Understanding the mechanism behind the EWSB is one of the most important objectives for Large Hadron Collider (LHC) program. If the newly discovered scalar at the LHC is to be interpreted as the Higgs boson of the SM, one should confirm that

$$g_{hVV}\, g_{hff} = \frac{m_V^2\, m_f}{v^2}\,, \qquad\qquad (2.33)$$

for all quarks and charged leptons f (in practice, $f = t, b, c$ and τ are the most relevant). In models of extended Higgs sectors, eq. (2.33) would be replaced by a unitarity sum rule in which the right-hand side of eq. (2.33) would be the result of summing over multiple Higgs states in the model [26].

2.2   Theoretical constraints on SM Higgs boson mass

We have known that the Higgs boson mass, m_h^{SM}, in principle, is a free parameter in the SM. However, several important constraints arising in the scalar sector link the mass of the Higgs boson to the energy scale where the validity of the SM is supposed to fail. Below that scale, the SM is the extremely successful effective field theory that emerges from the electroweak precision tests of the last decades. From this point of view, the Higgs sector of the SM contains actually two parameters, the Higgs mass m_H and the scale Λ from which new physics emerges.

In this section we will derive bounds on m_h^{SM} from theoretical considerations [27–35]. In particular we will concerntrate on issues of unitarity, triviality and vacuum stability. Experimental aspects of electroweak precision data [36–38] will be examined in the next section.
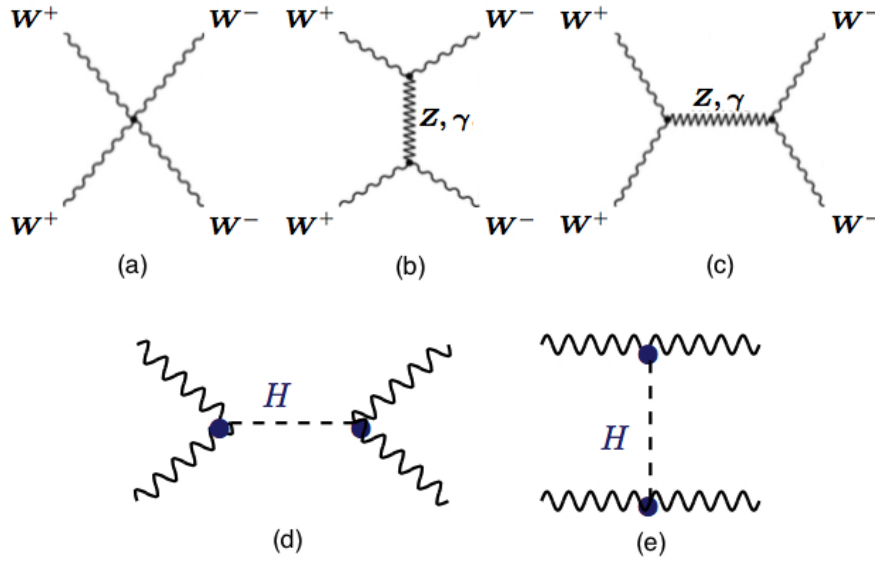
Figure 2.3. Feynman diagrams for the scattering of W bosons.

2.2.1 Tree-level unitarity

As mentioned in Section 1.1, the violation of unitarity could be alleviated when a scalar boson participates into the scattering process of longitudinal gauge bosons. Let us take as an example the scattering process $W_L + W_L \to W_L + W_L$ at high energy for a detailed discussion. The relevant Feynman diagrams are displayed in Fig. 2.3. In addition to the contact interaction, there are also additional diagrams involving the s- and t-channel exchanges of γ and Z bosons and the new scalar boson H. For each diagram the scattering amplitude takes the asymptotic form:

$$\mathcal{M}_i = A_i \frac{s^2}{v^4} + B_i \frac{s}{v^2} + C_i \tag{2.34}$$

where s is the square of center-of-mass energy and the coefficients A_i and B_i of the amplitude are summarized in Table 2.1. From the table, we see that the various contributions from gauge boson and Higgs exchange cancel at the order of $\mathcal{O}(s^2)$ and $\mathcal{O}(s)$. The cancellation of the $\mathcal{O}(s^2)$ contributions in Table 2.1 between the contact term and s- and t-channel gauge-boson exchange diagrams is guaranteed by gauge invariance.

After including the Higgs diagrams and summing all the contributions together, we

Table 2.1. The coefficients in the amplitude for the leading contributions to the scattering $W_L + W_L \to W_L + W_L$.

No.	diagram	A_i	B_i
a	$WWWW$ contact	$-3 + 6\cos\theta + \cos^2\theta$	$2(1 - 3\cos\theta)$
b	γ, Z t-channel	$3 - 2\cos\theta - \cos^2\theta$	$-\frac{3}{2}(1 - 5\cos\theta)$
c	γ, Z s-channel	$-4\cos\theta$	$-\cos\theta$
d	h s-channel	0	-1
e	h t-channel	0	$\frac{1}{2}(1 - \cos\theta)$

are left with a constant behavior for the amplitude. [6] In the high energy limit $s, m_H^2 \gg m_W^2, m_Z^2$, the total amplitude reads:

$$\mathcal{M}(W_L^+ W_L^- \to W_L^+ W_L^-) = -\frac{m_H^2}{v^2}\left(\frac{s}{s - m_H^2} + \frac{t}{t - m_H^2}\right) \quad . \tag{2.35}$$

On the other hand, using a partial wave decomposition, we can also write $\mathcal{M}$ as:

$$\mathcal{M} = 16\pi \sum_{l=0}^{\infty}(2l + 1)P_l(\cos\theta)a_l \quad , \tag{2.36}$$

where a_l is the spin l partial wave and $P_l(\cos\theta)$ are the Legendre polynomials. Applying the orthogonality of the $P_l(\cos\theta)$, one can, in turn, solve for the $J = 0$ partial wave the amplitude a_0 introduced above:

$$a_0 = \frac{1}{16\pi s}\int_{-s}^{0}\mathcal{M}\,dt = -\frac{m_H^2}{16\pi v^2}\left[2 + \frac{m_H^2}{s - m_H^2} - \frac{m_H^2}{s}\log\left(1 + \frac{s}{m_H^2}\right)\right] \quad . \tag{2.37}$$

In the high energy limit $(m_H^2 \ll s)$, a_0 reduces to:

$$a_0 \xrightarrow{m_H^2 \ll s} -\frac{m_H^2}{8\pi v^2} \quad , \tag{2.38}$$

---

[6] An alternative way to compute the scattering amplitudes is to use the Goldstone Equivalence theorem, valid in the high energy limit (i.e. for energies $s \gg M_V^2$), according to which for longitudinal gauge bosons can be expressed in terms of the scattering amplitudes for the corresponding Goldstone bosons, i.e.:

$$\mathcal{M}(W_L^+ W_L^- \to W_L^+ W_L^-) = \mathcal{M}(\omega^+ \omega^- \to \omega^+ \omega^-) + \mathcal{O}\left(M_W^2/s\right) \quad ,$$

where we have indicated by ω^i the Goldstone boson associated to the longitudinal component of the gauge boson V^i.

from which, the unitarity limit of $|\text{Re}\, a_0| < \frac{1}{2}$ derived from optical theorem imposes the Lee-Quigg-Thacker bound [17, 18] for the Higgs boson mass:

$$m_H < 870 \text{ GeV} \ . \tag{2.39}$$

Various upper bounds can be obtained from different longitudinal gauge boson scattering amplitudes. Among them the most stringent constraint comes from the coupled channel $W_L^+ W_L^- \to Z_L Z_L$.

Instead of solely considering pure scalar scattering, a systematic approach for the derivation of the tree-level unitarity constraints is to construct the full multi-state scattering matrix for all the physical scalar-scalar states (including possible states associated with longitudinal vector bosons) in the tree approximation at high enough energy (where the scattering is dominantly mediated by the direct quartic interactions), and then requiring its largest eigenvalue to be less than the upper limit. For example, the inclusion of the complete set of scattering channels (charged and neutral ones) into the analysis[7], leads more or less to a stronger unitarity constraint on the Higgs boson mass [19]

$$m_H < 710 \text{ GeV}. \tag{2.40}$$

The unitarity requirement tells us that if the Higgs boson mass is above the unitarity constraint then the SM becomes non-perturbative and some new physics should appear at some high scale to restore the unitarity of the theory. Demanding the tree-level scattering-matrix unitarity will constrain the scalar potential parameters (see examples of the two-Higgs doublet in Ref. [39] and its singlet extension in Ref. [11]). Of course, it may be difficult to determine the eigenvalues analytically if the dimension of the scattering matrix is too large. But, it is always numerically possible. There are also endless ramifications to this subject when dealing with models with an extended Higgs sector.

To justify the conclusion made in Section 1.1, let us consider again $W_L^+ W_L^- \to W_L^+ W_L^-$ scattering, assuming there were no Higgs boson. In the limit of $m_H^2 \gg s$, we see that:

$$a_0(W^+ W^- \to W^+ W^-) \simeq -\frac{s}{32\pi v^2} \ , \tag{2.41}$$

---

[7] This means that the full scattering matrix is constructed in the basis $(W_L^+ W_L^-, Z_L Z_L/\sqrt{2}, HH/\sqrt{2}, Z_L H, W_L^+ H, W_L^+ Z)$.
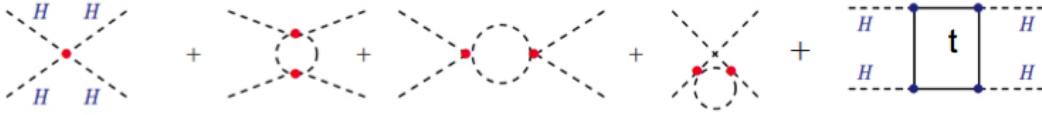
Figure 2.4. Typical Feynman diagrams for the tree level and one-loop Higgs self coupling.

from which the unitarity condition requires $\sqrt{s} \lesssim 1.8$ TeV.[8] This gives indications that new physics ought to be expected around 1-2 TeV, exactly in the range of energies that is being explored at the LHC Run 2.

2.2.2 Triviality and stability

In the preceding discussion, the quartic coupling λ of the Higgs potential that crucially determines the stability of the true vacuum is always treated as a positive constant. This is justified in the regime where λ is rather large. In fact, this parameter however varies because of quantum corrections, and even has the possibility of becoming negative at a certain high energy scale. As already known, the dependence of the λ on the energy scale Q is regulated by the renormalization group equation (RGE). In the SM the running of λ is governed by various interactions. In addition to the tree level contact interaction, the main contributions are induced from one-loop of the Higgs itself and of heavy fermions, as depicted in Fig 2.4.[9]

The one-loop RGE for the quartic coupling λ, including the lowest orders in all the relevant couplings, is given by:

$$32\pi^2 \frac{d\lambda}{dt} = 24\lambda^2 - (3g'^2 + 9g^2 - 24y_t^2)\lambda + \frac{3}{8}g'^4 + \frac{3}{4}g'^2 g^2 + \frac{9}{8}g^4 - 24y_t^4 + \cdots \quad (2.42)$$

where $t = \ln(Q^2/Q_0^2)$ is the logarithm of the ratio of the energy scale and some reference scale Q_0 squares, $y_t = m_t/v$ is the top-quark Yukawa coupling, and the dots indicate the presence of higher order terms that have been omitted.

We see that in the large λ limit the first term in Eq. (2.42) dominates. As a result,

---

[8] An even better bound emerges by considering the (properly normalized) isospin zero channel $1/\sqrt{6}(W_L^+ W_L^- + Z_L Z_L)$ and is $\sqrt{s} \lesssim 1.2$ TeV.

[9]Here we ignore the one-loop gauge boson diagram as it gives a small contribution at the order of $\mathcal{O}(g^8)$.

the quartic coupling λ grows and eventually becomes infinite. By dropping the remaining terms in Eq. (2.42), one can easily solve the evolution for λ:

$$\lambda(Q) = \frac{\lambda(v)}{1 - \frac{3}{4\pi^2}\lambda(v)\ln\left(\frac{Q^2}{v^2}\right)} \quad . \tag{2.43}$$

Here, the reference scale is set at the electroweak (EW) scale $Q_0 = v$ so that one can replace $\lambda(v)$ by m_H using the known relation $m_H^2 = 2\lambda(v)v^2$ at the EW scale. Apparently, the denominator of Eq. (2.43) vanishes at the energy

$$Q_{\mathrm{LP}} = v\,\exp\left(\frac{2\pi^2}{3\lambda}\right) = v\,\exp\left(\frac{4\pi^2 v^2}{3m_H^2}\right) \tag{2.44}$$

This point, at which $\lambda(Q)$ becomes infinite, is called Landau pole. One needs to have λ finite at all scales for which the theory is valid and thus one establishes the energy cut-off of the theory, $\Lambda \leq Q_{\mathrm{LP}}$. This condition places an explicit upper bound on m_H:

$$m_H^2 < \frac{8\pi^2 v^2}{3\log\left(\frac{\Lambda^2}{v^2}\right)} \quad , \tag{2.45}$$

Oppositely, when λ is small, the first term in Eq. (2.42) is no longer important, whereas the last term in Eq. (2.42) dominates and the evolution is primarily governed by the top loop diagram:

$$\lambda(Q) = \lambda(v) - \frac{3}{4\pi^2}y_t^2\log\left(\frac{Q^2}{v^2}\right) \quad . \tag{2.46}$$

To assure the stability of the vacuum state of the theory we need to require that $\lambda(Q) > 0$ always holds in the energy domain below the theory cut-off $Q < \Lambda$. The condition $\lambda(\Lambda) > 0$ gives a lower bound on m_H:

$$m_H^2 > \frac{3v^2}{2\pi^2}y_t^2\ln\left(\frac{\Lambda^2}{v^2}\right) \quad . \tag{2.47}$$

A more accurate evaluation, including higher order quantum correction in the scalar potential and using a 2-loop renormalization group improved effective potential, is shown in Fig. 2.5 (left) for a top quark mass $m_t = 175 \pm 6$ GeV and $\alpha_s(M_Z) = 0.118 \pm 0.002$. The upper and lower bands represents he triviality limit and stability bound, respectively. The region between the bands, gives the allowed range of m_H as a function of the scale of new physics Λ. The width of the bands corresponds to the various experimental and
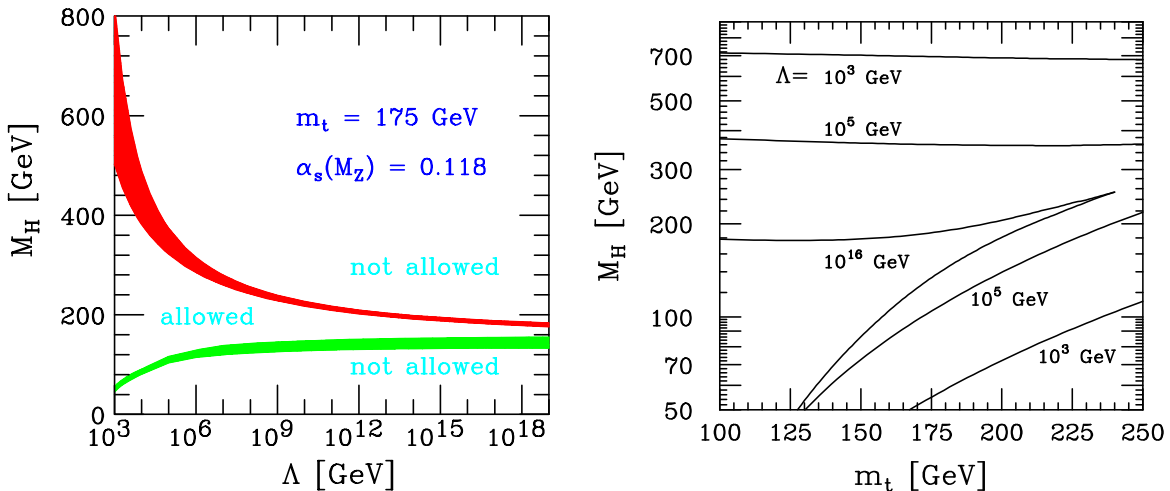
Figure 2.5. The triviality (upper) bound and the vacuum stability (lower) bound on the Higgs boson mass as a function of the new physics or cut–off scale Λ for a top quark mass $m_t = 175 \pm 6$ GeV (left) and in the (m_t, m_H) plane for various values Λ (right). In both plots $\alpha_s(M_Z) = 0.118 \pm 0.002$; the allowed region lies between the bands and the colored/shaded bands illustrate the impact of various uncertainties. Taken from Ref. [35] according to Ref. [25].

theoretical errors. As can be observed, if the new physics appears at the TeV scale, the Higgs boson mass is allowed to be in the range 50 GeV $\lesssim m_H \lesssim$ 800 GeV; while, requiring the SM to be valid up to the Grand Unification (GUT) scale, $\Lambda_{\text{GUT}} \sim 10^{16}$ GeV, the Higgs boson mass should lie in the range 130 GeV $\lesssim m_H \lesssim$ 180 GeV. Or we can alternatively illustrate the theoretical bounds (m_t, m_H) plane by varying the value of Λ, as shown in Fig. 2.5 (right). From this point of view, we see that the scale Λ at which the new physics should appear will depend on the precise value of the top quark mass. At present, the discovery of a SM-like Higgs of $m_H = 125$ GeV at the LHC [40] and the most recent measurement of the top-quark mass $m_t = 173.34$ GeV [41] appears to drive the potential unstable and invalidate the SM at a scale of order 10^{10} TeV. However, this is not exactly true if our world is standing on the edge of metastablity, in which the true EW vacuum is long lived as compared to the age of the universe. To be honest, the discussion on the stability of the EW vacuum is quite subtle. We will touch this issue and give a brief introduction in Chapter 4.

2.3 SM Higgs decay

Having derived in Section 2.1 the SM Higgs couplings to gauge bosons and fermions, we know that, at the tree level, the SM Higgs boson can decay into pairs of quarks and leptons, and into pairs of electroweak gauge bosons; while at one-loop it can also decay into two photons, two gluons, or a $Z\gamma$ pair. The predictions for the decay branching ratios for the SM Higgs are very important in the analysis of LHC data because they allow us to test the hypothesis that the discovered Higgs boson is the SM Higgs. All the masses of the SM particles ($W^{\pm}$, Z, the charged fermions, and the Higgs as of summer 2012) are now known. Therefore all the couplings of the Higgs boson relevant for Higgs collider phenomenology are uniquely predicted! This means that any deviation from these predictions in Higgs phenomenology would provide evidence of physics beyond the SM.

The aim of this section is to review the possible decays and present schematic expressions for the decay width. I will neither go into details in the calculations nor give a complete list of radiative corrections. As for radiative corrections, we close with a short comment on their general structure for Higgs decays and only discuss those aspects that can be useful as a general background. For a detailed review of QCD corrections in Higgs decays we refer the reader to Ref. [42]. Ref. [25] also contains an excellent summary of both QCD and EW radiative corrections to Higgs decays.

2.3.1 Fermionic decays

The tree level decay width for $H \to f\bar{f}$ ($f=q,l$, $q=$quark, $l=$lepton) reads:

$$\Gamma_0(H \to f\bar{f}) = N_c^f \frac{G_F m_H}{4\sqrt{2}\pi} m_f^2 \beta_f^3 \ , \tag{2.48}$$

where the color factor, $N_c^q = 3$ for quarks and $N_c^l = 1$ for leptons, accounts for the sum over the colors for final-state fermions; and $\beta_f = \sqrt{1 - \tau_f}$ with $\tau_f = 4m_f^2/M_H^2$. It shows that the fermionic decay grows linearly with m_H and is also proportional to the fermion mass m_f. As a result, the Higgs tends to decay into the heaviest kinematically-accessible fermions. The partial decay widths also exhibit a strong suppression near threshold, $\Gamma(H \to f\bar{f}) \sim \beta_f^3 \to 0$ for $m_H \simeq 2m_f$. This is typical for the decay of a Higgs particle
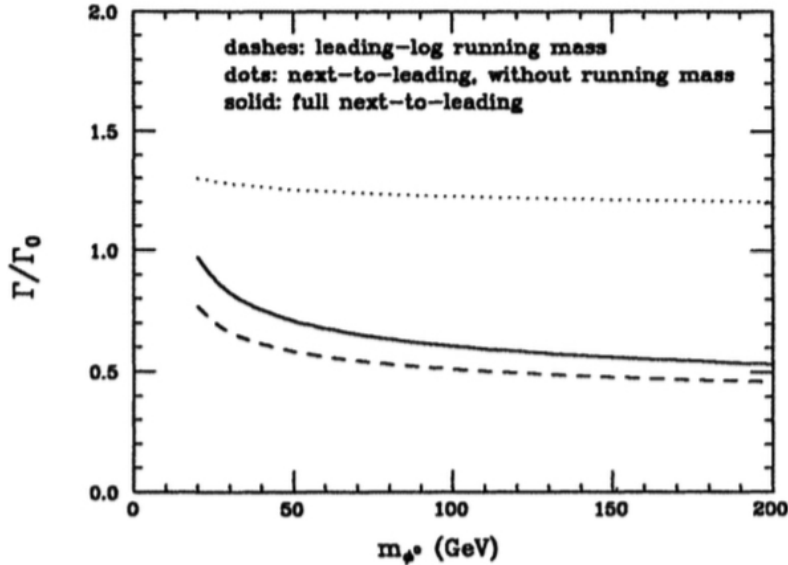
Figure 2.6. QCD corrections to the $H \to b\bar{b}$ decay width deriving from various sources. $m_b = 4.5$ GeV is taken and ϕ_0 represents the SM Higgs H in our notation. The notation of the curves can be found in Fig. 2.2 of Ref. [44]. *Source: taken from Ref. [44].*

with a scalar coupling eq. (2.28).[10]

In the decays into $q\bar{q}$, QCD corrections are significant and dominate over other radiative corrections, and therefore must be included. At the one–loop level, the generic Feynman diagrams for the corrections include gluon–exchange (which multiplies the Born term) and the emission of a gluon in the final state (whose interference with the virtual gluon exchange diagram must be added to the former). In the limit where m_H is much larger than the quark masses, $m_H \gg 2m_f$, one obtains for the next–to–leading order (NLO) decay width (the quark mass is kept only in the Yukawa coupling and in the leading logarithmic term) [45–50]

$$\Gamma_{\rm NLO}(H \to q\bar{q}) \simeq \frac{3G_\mu}{4\sqrt{2}\pi} m_H m_q^2 \left[1 + \frac{4}{3}\frac{\alpha_s}{\pi}\left(\frac{9}{4} + \frac{3}{2}\log\frac{m_q^2}{m_H^2}\right)\right] \tag{2.50}$$

As can be noticed, there is a large logarithmic $\log(m_q/m_H)$ contribution which, for very

---

[10] If the Higgs boson were a pseudoscalar A boson with couplings $y_f^A = \gamma^5 y_f^h$, for instance in the MSSM [43], the partial decay width would have been suppressed only by a factor β_f

$$N_c^f \frac{G_F m_H}{4\sqrt{2}\pi} m_f^2 \beta_f \tag{2.49}$$

light quarks, might render the partial decay width very small.[11] We can see this effect from Fig. 2.6 for the decay $H \to b\bar{b}$, which constitutes the largest decay branching ratio for the SM Higgs boson in the low mass region. In this figure we plot the decay width including the various sources at QCD NLO normalized to the tree level width as a function of Higgs mass m_H. Indeed, the net effect from both QCD higher-order corrections and running quark mass gives about 40% suppression ($K \equiv \Gamma/\Gamma_0 \simeq 0.6$) for a SM Higgs at 125 GeV. To date QCD corrections have been computed to an astounding N^{4}LO. For example, including the $\mathcal{O}(\alpha_S^2)$ [51, 52] and $\mathcal{O}(\alpha_S^3)$ [53, 54] corrections, the partial Higgs decay width into light quarks is modified to:

$$\Gamma(H \to q\bar{q})_{QCD} = \frac{3G_F m_H}{4\sqrt{2}\pi} \bar{m}_q^2(m_H)\beta_q^3 \left(1 + \Delta_{\mathrm{QCD}} + \Delta_t\right) \quad, \tag{2.51}$$

where Δ_t represents specifically QCD corrections involving a top-quark loop. Δ_{QCD} and Δ_t have been calculated up to three loops and are given by:

$$
\begin{aligned}
\Delta_{\mathrm{QCD}} &= 5.67\frac{\alpha_s(m_H)}{\pi} + (35.94 - 1.36N_F)\left(\frac{\alpha_s(m_H)}{\pi}\right)^2 + \\
&\quad (164.14 - 25.77N_F + 0.26N_F^2)\left(\frac{\alpha_s(m_H)}{\pi}\right)^3 \quad, \\
\Delta_t &= \left(\frac{\alpha_s(m_H)}{\pi}\right)^2\left[1.57 - \frac{2}{3}\ln\frac{m_H^2}{m_t^2} + \frac{1}{9}\ln^2\frac{\bar{m}_Q^2(m_H)}{m_H^2}\right] \quad,
\end{aligned}
\tag{2.52}
$$

where $\alpha_s(m_H)$ and $\bar{m}_Q(m_H)$ are the renormalized running QCD coupling and quark mass defined at the scale m_H in the $\overline{MS}$ scheme. N_F counts the number of light quark flavors that are present in the loops. We stress that using the $\overline{MS}$ running mass in the overall Yukawa coupling square of Eq. (2.51) is very important in Higgs decays, since it reabsorbs most of the QCD corrections, including large logarithms of the form $\ln(m_H^2/m_Q^2)$. The remaining uncertainty from uncalculated higher order QCD corrections is estimated to be only 0.1%.

As a final note, the electroweak corrections are negligible. They are known at next-to-leading order (NLO) and the numerical results were computed in Ref. [55].

---

[11] A possible negative decay width (which is definitely not a physical solution) can be avoided by replacing the quark mass m_q in Eq. (2.48) by the running mass $\overline{m}_q(m_H)$ at the scale of the Higgs mass in the modified minimal subtraction ($\overline{\mathrm{MS}}$) renormalization scheme, in which these large logarithms can be reabsorbed.

2.3.2 Bosonic decays

The tree level decay rate for $H \to VV$ $(V = W^\pm, Z)$ can be written as:

$$\Gamma(H \to VV) = \delta_V \frac{G_F m_H^3}{16\sqrt{2}\pi} \left(1 - \tau_V + \frac{3}{4}\tau_V^2\right) \beta_V \ , \tag{2.53}$$

where $\delta_W = 1$ and $\delta_Z = 1/2$ accounting for two identical Z bosons in the final state; and $\beta_V = \sqrt{1 - \tau_V}$ with $\tau_V = 4M_V^2/m_H^2$. The complicated dependence on the kinematic factor τ_V is due to the sum over the V polarization vectors. Note that the kinematic factor $\sqrt{1 - x_V}\left(1 - x_V + \frac{3}{4}x_V^2\right) \to 1$ when $m_H \gg 2M_W$. In contrast to the fermionic case, the VV decay grows with increasing Higgs mass as a form of m_H^3. This difference will significantly influence the pattern of SM Higgs decay as will be discussed later.
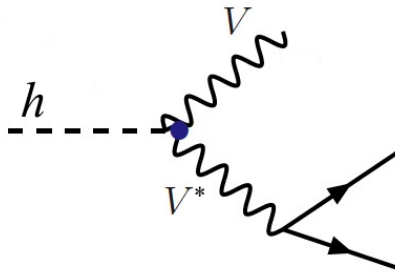
Figure 2.7. Three body offshell VV^* decay of the Higgs.

Of course, the expression in Eq. (2.53) is only valid for Higgs masses above the VV threshold. Below the W^+W^- and ZZ threshold, the SM Higgs boson can, however, decay via three (or four) body decays mediated by WW^* (W^*W^*) or ZZ^* (Z^*Z^*) intermediate states. This is a tedious calculation, but it has been done [12]. The example of three-body decay, in which the off-shell V^* decays into $f\bar{f}$ pair, is depicted in Fig. 2.7. As will be seen in Fig. 2.9 the off-shell decays $H \to WW^*$ and $H \to ZZ^*$ are relevant in the intermediate mass region around $m_H \simeq 160$ GeV, where they compete and overcome the $H \to b\bar{b}$ decay

---

[12] The current state-of-the-art theoretical predictions for SM Higgs decay to four fermions is implemented in a code called `PROPHECY4F`, which includes NLO QCD and NLO electroweak corrections to the full $4f$ final states with all interferences included. (For example, the processes $h \to W^*W^* \to \ell\nu\ell\nu$ and $h \to Z^*Z^* \to \ell\ell\nu\nu$ interfere with each other for same-flavor final state leptons. This interference is important when $m_h < 2M_W$ because the phase space overlap of the two processes becomes significant when the gauge bosons are forced off shell.)

mode. The decay rates for $H \to VV^* \to V f_i \bar{f}_j$ ($V = W^\pm, Z$), at the tree level, are given by:

$$\Gamma(H \to WW^*) = \frac{3g^4 m_H}{512\pi^3} F\left(\frac{M_W}{m_H}\right) \ , \tag{2.54}$$

$$\Gamma(H \to ZZ^*) = \frac{g^4 m_H}{2048(1 - s_W^2)^2 \pi^3} \left(7 - \frac{40}{3}s_W^2 + \frac{160}{9}s_W^4\right) F\left(\frac{M_Z}{m_H}\right) \ , \tag{2.55}$$

where $s_W \equiv \sin\theta_W$ and the function $F(x)$ is given by

$$
\begin{aligned}
F(x) = & -(1 - x^2)\left(\frac{47}{2}x^2 - \frac{13}{2} + \frac{1}{x^2}\right) - 3\left(1 - 6x^2 + 4x^4\right)\ln(x) \\
& + 3\frac{1 - 8x^2 + 20x^4}{\sqrt{4x^2 - 1}}\arccos\left(\frac{3x^2 - 1}{2x^3}\right) \ .
\end{aligned}
\tag{2.56}
$$

The remaining theoretical uncertainty from missing higher-order radiative corrections is estimated to be only $\sim 0.5\%$.

2.3.3 Loop-induced decays

In the absence of direct interactions, the $H\gamma\gamma$ and $H\gamma Z$ couplings are induced at one loop via both a fermion loop and a W-loop, while the Hgg coupling is only mediated by quark loops; the relevant diagrams are shown in Fig. 2.8. Despite their rareness, the loop-induced Higgs decays are very important [13].

h ----- (a) h ----- (b) h ----- (c)
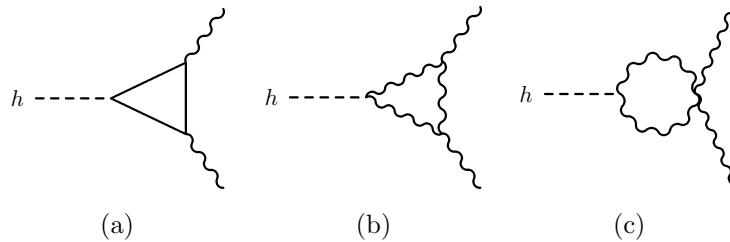
Figure 2.8. Schematic Feynman diagrams for $h \to \gamma\gamma$.

- *Decay into two photons*

The decay of the SM Higgs boson into two photons is mediated by W boson and heavy charged fermion loops. It is dominated by the W boson loop. The top quark loop

---

[13] We will see in the next chapter that $h \to \gamma\gamma$ was one of the two Higgs boson discovery channels. The promising prospects leading to the discovery at the hadron colliders were discussed for the first time in detail with some estimateof signal over background in the 1980s [56, 57].

contribution interferes destructively with the W loop contribution, reducing the partial width by roughly 30%. The bottom quark and tau lepton loops also contribute a small amount. At the lowest order the decay rate for $H \to \gamma\gamma$ takes the form:

$$\Gamma(H \to \gamma\gamma) = \frac{G_F \alpha^2 m_H^3}{128\sqrt{2}\pi^3} \left| \sum_f N_c^f Q_f^2 F_f^H(\tau_f) + F_W^H(\tau_W) \right|^2 , \tag{2.57}$$

where $N_c^f = 1, 3$ (for $f = l, q$ respectively), Q_f is the charge of the f fermion species, and the form factors F_f^H and F_W^H are given by:

$$\begin{aligned} F_f^H(\tau) &= 2\tau \left[1 + (1 - \tau) f(\tau) \right] , \\ F_W^H(\tau) &= -\left[2 + 3\tau + 3\tau(2 - \tau) f(\tau) \right] . \end{aligned} \tag{2.58}$$

where $\tau_f = 4m_f^2/m_H^2$ and the function $f(\tau)$ is defined as:

$$f(\tau) = \begin{cases} \arcsin^2 \frac{1}{\sqrt{\tau}} & \tau \geq 1 \\ -\frac{1}{4} \left[\ln \frac{1+\sqrt{1-\tau}}{1-\sqrt{1-\tau}} - i\pi \right]^2 & \tau < 1 , \end{cases} \tag{2.59}$$

The imaginary part in $f(\tau)$ for $m_h > 2m_i$ is a consequence of the particles in the loop being kinematically able to go on shell. When the particle in the loop is much heavier than the Higgs, $F_1 \to 7$ and $F_{1/2} \to -4/3$. This means that the fermion loop asymptotes to a constant at large m_f and can be understood as follows. The fermion triangle diagram generically goes like $1/m_f^2$ when the mass of the particle in the loop is large compared to any of the external invariant masses; however, this is multiplied by a factor of m_f/v from the Yukawa coupling and another factor of m_f from the fermion's helicity flip. Whereas, the contribution of light fermions (with masses $m_f \ll m_h$) to the amplitude falls like m_f^2/m_h^2 with decreasing fermion mass.

On the other hand, the W boson loop amplitude asymptotes to a constant for $m_h \gg M_W$. This limit can formally be obtained by taking $g \to 0$ while holding v and λ fixed. In that case a contribution from the charged Goldstone boson running in the loop survives, leading to a finite amplitude dependent on v and λ (recall that λ can be traded for m_h).

In analogy to the tree-level di-boson decay, the partial width $\Gamma(h \to \gamma\gamma)$ grows with increasing Higgs mass like m_H^3. This can be seen as a consequence of the effective-operator

description of the interaction, which is required to take the form $HF^{\mu\nu}F_{\mu\nu}$ in order to preserve electromagnetic gauge invariance. Expanding out the field strength tensors yields two factors of photon momentum in the amplitude.

Note that the QCD and electroweak corrections to $H \to \gamma\gamma$ decay width are each known to NLO, leaving a residual theoretical uncertainty of about 1%.

- *Decay into a photon plus a Z boson*

Similarly to the $\gamma\gamma$ case, this decay is built up by a dominant W boson loop and very small top quark loop. The decay rate for $H \to \gamma Z$ is given by:

$$\Gamma(H \to \gamma Z) = \frac{G_F^2 M_W^2 \alpha m_H^3}{64\pi^4} \left(1 - \frac{M_Z^2}{m_H^2}\right)^3 \left|\sum_f A_f^H(\tau_f, \lambda_f) + A_W^H(\tau_W, \lambda_W)\right|^2 , \qquad (2.60)$$

where $\tau_i = 4m_i^2/m_H^2$ and $\lambda_i = 4m_i^2/M_Z^2$ ($i = f, W$), and the form factors $A_f^H(\tau, \lambda)$ and $A_W^H(\tau, \lambda)$ are given by:

$$A_f^H(\tau, \lambda) = 2N_c^f \frac{Q_f(I_{3f} - 2Q_f \sin^2\theta_W)}{\cos\theta_W} [I_1(\tau, \lambda) - I_2(\tau, \lambda)] , \qquad (2.61)$$

$$A_W^H(\tau, \lambda) = \cos\theta_W \left\{ \left[\left(1 + \frac{2}{\tau}\right)\tan^2\theta_W - \left(5 + \frac{2}{\tau}\right)\right] I_1(\tau, \lambda) \right.$$
$$\left. + 4\left(3 - \tan^2\theta_W\right) I_2(\tau, \lambda) \right\} , \qquad (2.62)$$

where N_c^f and Q_f are defined after Eq. (2.57), and I_3^f is the weak isospin of the f fermion species. Moreover:

$$I_1(\tau, \lambda) = \frac{\tau\lambda}{2(\tau - \lambda)} + \frac{\tau^2\lambda^2}{2(\tau - \lambda)^2}[f(\tau) - f(\lambda)] + \frac{\tau^2\lambda}{(\tau - \lambda)^2}[g(\tau) - g(\lambda)] ,$$

$$I_2(\tau, \lambda) = -\frac{\tau\lambda}{2(\tau - \lambda)}[f(\tau) - f(\lambda)] , \qquad (2.63)$$

and

$$g(\tau) = \begin{cases} \sqrt{\tau - 1}\arcsin\frac{1}{\sqrt{\tau}} & \tau \geq 1 \\ \frac{\sqrt{1-\tau}}{2}\left[\ln\frac{1+\sqrt{1-\tau}}{1-\sqrt{1-\tau}} - i\pi\right] & \tau < 1 \end{cases} \qquad (2.64)$$

while $f(\tau)$ is defined in Eq. (2.59).

This process has been calculated at leading order only. For their explicit expression we refer the interested reader to the literature [25, 42]. As in the case of $H \to \gamma\gamma$, the QCD corrections are expected to be small, since they affect only the fermion loop contributions

which already give only a small contribution to the amplitude. The uncertainty due to the missing NLO electroweak corrections is estimated at about 5%.

Notice that, replacing the ZWW and vectorial $Zf\bar{f}$ couplings with the corresponding γWW and $\gamma f\bar{f}$ couplings and taking $M_Z \to 0$ in the kinematic factors λ_i, one obtains $A_W \to -F_1(\tau_W)$ and $A_f \to -N_{cf}Q_f^2 F_{1/2}(\tau_f)$; that is, the amplitudes reduce exactly to the $h \to \gamma\gamma$ case, up to an overall minus sign that was built into the definitions of A_W and A_f.

- *Decay into two gluons*

As far as $H \to gg$ is concerned, this decay is only mediated by fermion loops involving heavy quarks (corresponding to Fig. 2.8 (a)), with the main contribution coming from top quarks and a small contribution from bottom quarks at the few-percent level. At the one-loop leading order, the partial decay width reads

$$\Gamma(H \to gg) = \frac{G_F \alpha_s^2 m_H^3}{36\sqrt{2}\pi^3} \left| \frac{3}{4} \sum_q F_q^H(\tau_q) \right| \quad , \tag{2.65}$$

where $\tau_q = 4m_q^2/m_H^2$ and and the form factor $F_q^H(\tau)$ is given in Eq. (2.58) with $f(\tau)$ defined in Eq.(2.59).

The QCD corrections are known to N³LO, leading to about a 3% remaining scale uncertainty.[14] At NLO the expression for the corrected rate is remarkably simple

$$\Gamma(H \to gg(g), q\bar{q}g) = \Gamma_{\mathrm{LO}}(H \to gg) \left[1 + E(\tau_Q)\frac{\alpha_s^{(N_L)}}{\pi} \right] \quad , \tag{2.66}$$

where the correction factor in the large m_t limit, i.e. $m_H^2 \ll 4m_q^2$, is

$$E(\tau_Q) \longrightarrow \frac{95}{4} - \frac{7}{6}N_F + \frac{33 - 2N_F}{6}\log\left(\frac{\mu^2}{M_H^2}\right) \quad . \tag{2.67}$$

where μ is the renormalization point and defines the scale of α_s. When compared with the fully massive NLO calculation [58], the two calculations display an impressive 10%

---

[14]The "scale uncertainty" in QCD calculations is obtained by varying the renormalization scale by a factor of two in either direction about some chosen central value, and seeing how much the prediction changes as a consequence. Because the renormalization scale dependence is an artifact of truncating the perturbation series at a finite order, the dependence of the result on the renormalization scale provides an estimate of how big the higher-order terms have to be in order to cancel this dependence once they are included.

agreement, even in regions where the light Higgs approximation is not justified. This is actually due to the presence of large constant factors in the first order of QCD corrections. We also observe that the first order of QCD corrections has quite a large impact on the lowest order cross section, amounting to more than 50% of Γ_{LO} on average. This has been indeed the main reason to prompt for a NNLO QCD calculation of $\Gamma(H \to gg)$. The result, obtained in the heavy-top approximation, has shown that NNLO QCD corrections amount to only 20% of the NLO cross section, therefore pointing to a convergence of the $\Gamma(H \to gg)$ perturbative series. We will refer to this discussion when dealing with the $gg \to H$ production mode, since its cross section can be easily related to $\Gamma(H \to gg)$. The electroweak corrections are known at NLO, leading to about a 1% uncertainty from missing higher order corrections.

2.3.4 General properties of radiative corrections to Higgs decays

As has been seen, all Higgs boson decay rates are modified by both QCD and EW radiative corrections. First, QCD corrections are particularly important for $H \to q\bar{q}$ decays, where they mainly amount to a redefinition of the Yukawa coupling by shifting the mass parameter in it from the pole mass value to the running mass value, and also for $H \to gg$. Second, EW corrections can be further separated into: (i) corrections due to fermion loops, (ii) corrections due to the Higgs boson self-interaction, and (iii) other EW corrections. Both corrections of type (ii) and (iii) are in general very small except for large Higgs boson masses, i.e. for $m_H \gg M_W$. On the other hand, corrections of type (i) are very important over the entire Higgs mass range, and are particularly relevant for $m_H \ll 2m_t$, where the top-quark loop corrections play a leading role. Indeed, for $m_H \ll 2m_t$, the dominant corrections for both Higgs decays into fermions and gauge bosons come from the top-quark contribution to the renormalization of the Higgs wave function and vacuum expectation value.

2.3.5 SM Higgs branching ratio

With the partial width for all possible decays prepared, let us now assemble them together to obtain the total decay width. Consequentially, taking the ratio of the individual
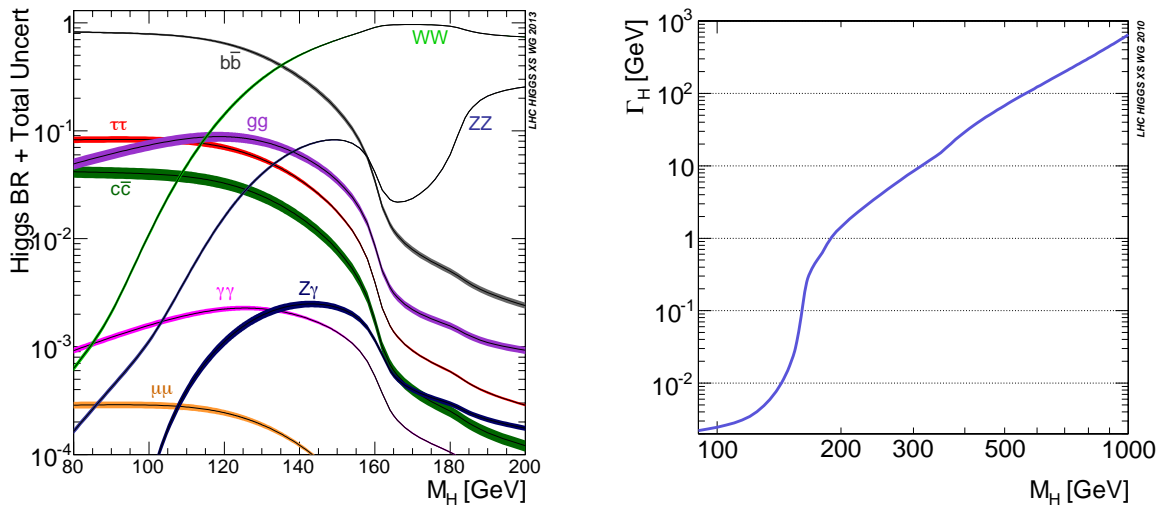
Figure 2.9. Left: The branching ratios for SM Higgs boson decay as a function of m_H. The central lines show the predictions, while the colored bands indicate the theoretical uncertainty. Right: SM Higgs total decay width as a function of m_H. *Source*: taken from Higgs Working Group [59].

decay to the total width for the Higgs yields to the decay branching ratio.

$$\mathrm{BR}(H \to XX) = \frac{\Gamma(H \to XX)}{\Gamma^H_{\mathrm{tot}}}, \tag{2.68}$$

where Γ^H_{tot} is the total width. It can also receive a contribution Γ_{new} from possible new non-SM decays. (For instance, the exotic decay into additional Higgs bosons in the two-Higgs-doublet models which will be studied in Chapter 5 and its supersymmetric version in Chapter 6.) If Γ_{new} comprises decays to invisible particles such as dark matter candidates (see examples in Chapter 8), it can be constrained through direct searches for invisibly-decaying Higgs events produced in VBF or WH or ZH associated production. This type of search has been completed and will be discussed in Section 3.3.4.

The left plot in Fig. 2.9 illustrates all the decay branching ratios of the SM Higgs boson as functions of its mass m_H. The curves represented are obtained by including all available QCD and electroweak (EW) radiative corrections. [15] The band for each curve is obtained by varying the parameters (the quark masses m_t and the strong coupling constant α_S) that enter both at tree level and in particular through loop corrections

---

[15]The computation for the relevant orders of QCD and EW corrections for Higgs decays has been thoroughly explored and the results are nowadays available in public codes like HDECAY [60].

within their uncertainties. The SM Higgs boson total width, i.e. the sum of all the partial widths $\Gamma(H \to XX)$, is represented in the right plot of Fig. 2.9.

It is remarkable to notice in Fig. 2.9 that a light SM Higgs boson ($m_H \leq 130 - 140$ GeV) behaves very differently from a heavy SM Higgs boson ($m_H \geq 130 - 140$ GeV). Indeed, a light SM Higgs boson mainly decays into a $b\bar{b}$ pair, followed hierarchically by all other pairs of lighter fermions. Loop-induced decays also play a role in this region. $H \to gg$ is dominant among them, and it is actually larger than many tree level decays. Unfortunately, this decay mode is almost useless, in particular at hadron colliders, because of background limitations. Among radiative decays, $H \to \gamma\gamma$ is tiny, but it is actually phenomenologically very important because the two photon signal can be seen over large hadronic backgrounds. On the other hand, for larger Higgs masses, the decays to W^+W^- and ZZ dominate. All decays into fermions or loop-induced decays are suppressed, except $H \to t\bar{t}$ for Higgs masses above the $t\bar{t}$ production threshold. In addition, there is an intermediate region, around $m_H \simeq 160$ GeV, i.e. below the W^+W^- and ZZ threshold, where the decays into WW^* and ZZ^* (when one of the two gauge bosons is off-shell) become important. These are indeed three-body decays of the Higgs boson that start to dominate over the $H \to b\bar{b}$ two-body decay mode when the large size of the HWW or HZZ couplings compensate for their phase space suppression[16].

Practically, the different analyses have different sensitivities to the presence of the SM Higgs boson. The $H \to \gamma\gamma$ and $H \to ZZ \to 4\ell$ (where $\ell = e, \mu$) channels play a special role because of their high sensitivity and excellent mass resolution of the reconstructed diphoton and four-lepton final states, respectively. The $H \to WW \to l\nu l\nu$ measurement has a high sensitivity due to large expected yields but relatively poor mass resolution because of the presence of neutrinos in the final state. The bb and $\tau\tau$ decay modes are beset by large background contributions and have relatively poor mass resolution, resulting in lower sensitivity compared to the other channels.

Finally, to give some phenomenological insight the branching ratios for a SM Higgs of 125 GeV are summarized in order of size in Table 2.2. All of the LHC measurements

---

[16]Actually, even four-body decays, corresponding to $H \to W^*W^*, Z^*Z^*$ may become important in the intermediate mass region and are indeed accounted for in Fig. 2.9 (left).

to date are roughly consistent with the SM predictions, within the current (large) uncertainties.

Table 2.2. Predicted decay branching ratios (BRs) for a 125 GeV SM Higgs boson, in order of size, from Ref. [61]. The last row is the predicted Higgs total width. Keep in mind that the relative uncertainties on the individual BR predictions are of order 3–10%.

Decay mode	BR	Notes (as of early 2014)
$b\bar{b}$	58%	Observed at about 2σ at CMS
WW^*	22%	Observed at 4σ
gg	8.6%	
$\tau\tau$	6.3%	Observed at 1–2 σ
$c\bar{c}$	2.9%	
ZZ^*	2.6%	Discovery mode (in $ZZ^* \to 4\mu$, $2\mu2e$, $4e$)
$\gamma\gamma$	0.23%	Discovery mode
$Z\gamma$	0.15%	
$\mu\mu$	0.022%	
Γ_{tot}	4.1 MeV	

Searching for Higgs boson(s) at the LHC

"By any measure, the Large Hadron Collider—the world's biggest experiment, is exceptional. It is a discovery machine!"

Searching for Higgs boson(s) is a challenging task but is definitely among the most important goals of the LHC program. It is mainly luminosity limited from the collider point of view. Since starting the running in 2010, the LHC has been accumulating an unprecedented amount of data and quickly passed all expectations in providing exclusion limits for the SM Higgs boson. Finally, in the summer of 2012, two experiment collaborations reported the observation of a new particle at the mass of 125 GeV. Subsequent precision studies of the properties of of this new particle are compatible with those expected for the SM Higgs boson. Meanwhile, other searches for probing BSM Higgs bosons are also under way.

The central subject of this chapter is Higgs boson physics at hadron colliders. Starting with the discussion on Higgs production at the LHC, we shall highlight the Higgs discovery, that is a historic moment in science, and also present the updated status of this new

particle (as of spring 2015) after the LHC Run 1, particularly including the combination analysis performed very recently. Apart from SM Higgs searches, for completeness we will also touch the BSM Higgs searches. But only the results that are highly relevant for the extended Higgs studies in Part II and Part III are collected. This is partially because giving an exhaustive list of Higgs searches and explaining the details about the colliders is impossible and also not the purpose of this thesis. Instead, my aim is to provide the minimal experimental background needed to understand the Higgs search from the theoretical point of view. For the readers who would like to learn Higgs statistics or the experimental techniques, there are many appropriate resources available.

3.1 Higgs collider phenomenology

Extracting the individual Higgs couplings from LHC data is a challenge because what is actually measured are the rates in individual production and decay channels. The event rate for the particular process $X \to H \to Y$ can be written as

$$\text{Rate}(X \to H \to Y) = \mathcal{L} \times \sigma(X \to H) \times \text{BR}(H \to Y) \propto \sigma_X \text{BR}_Y \tag{3.1}$$

where $\mathcal{L}$, in the unit of fb^{-1} or pb^{-1}, is the integrated luminosity accumulated at the collider, σ_X represents the production cross section, and the branching ratio can be computed as $\text{BR}(H \to Y) = \Gamma_Y/\Gamma_{\text{tot}}$ in the narrow-width approximation. In order to efficiently search for the SM Higgs boson at the LHC precise predictions for the production cross sections and the decay branching ratios are necessary. Essentially, both σ_X and Γ_Y depend on the couplings of Higgs through which it is produced and can decay, respectively.

As the second key ingredient in the analysis of Higgs data, the production cross sections can be computed by including the consideration of the parton distribution function (PDF) since the values of all the parameters that appear in the Higgs couplings are known. Along with the Higgs branching ratios discussed in Section 2.3.5, we thereby are able to predict the number of events for Higgs production via collisions of SM particles.

This section includes the discussion of possible Higgs production modes at the hadron colliders and particularly the favorable collider signatures for the Higgs search, and also the definition of signal strength, which is a very important parameter and has widely been
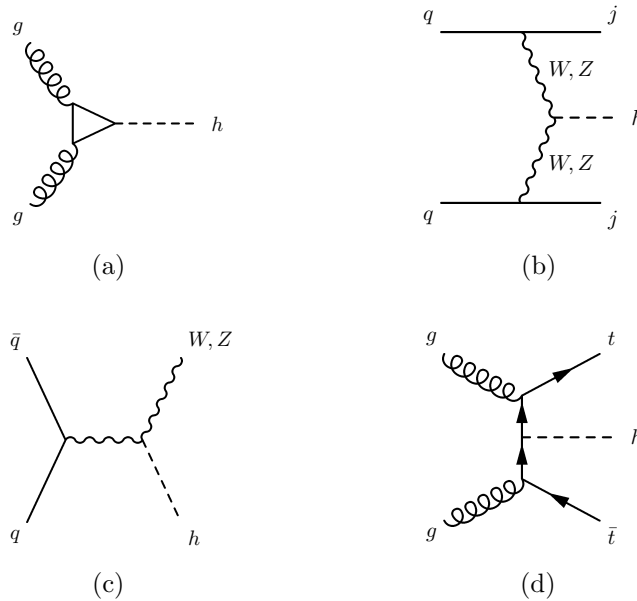
Figure 3.1. Feynman diagrams for the main Higgs production mechanisms at the LHC: (a) gluon fusion, (b) vector boson fusion, (c) Higgs-stralung, (d) ttH.

used by experimentalists to evaluate deviations with respect to the SM. As an aid to the reader, the theoretical calculation for the cross section of gluon fusion production will be briefly commented upon. More elaborate discussions can be found in [25, 58].

3.1.1 Higgs production at the LHC

At hadron colliders there are a number of mechanisms to produce the Higgs boson, some in association with other particles. Four main production modes are displayed in Fig. 3.1. The left plot in Fig. 3.2 shows the SM theory predictions for the main production cross sections in proton-proton (pp) collisions at $\sqrt{s} = 7$–8 TeV, where the colored bands indicate the theoretical uncertainties. Overall, Higgs boson production is dominated by the gluon fusion process $gg \rightarrow H$ (ggF), followed by the vector boson fusion process $qq' \rightarrow qq'H$ (VBF). Associated production with a W boson $q\bar{q}' \rightarrow WH(WH)$, a Z boson $q\bar{q}/gg \rightarrow ZH(ZH)$ or with a pair of top quarks $q\bar{q}/gg \rightarrow t\bar{t}H(ttH)$ are sizable as well. The WH and ZH production processes are collectively referred to as the VH process. In the following we shall individually address each one in sequence.

To visually compare the improvement for data collection from the 8 TeV Run 1 to the 14 TeV Run 2, I also present in Fig. 3.2 (right plot) the total cross section at the
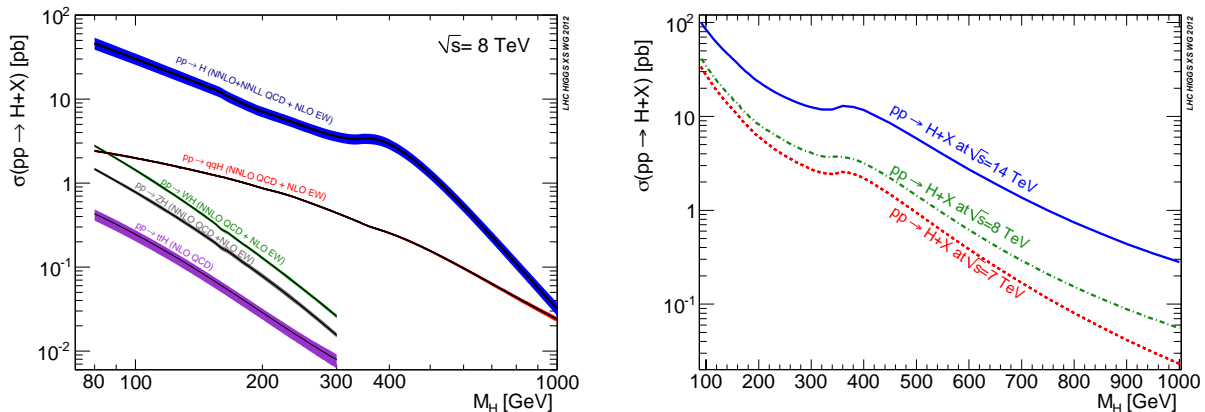
Figure 3.2. Left: Standard Model Higgs boson production cross sections at $\sqrt{s} = 8$ TeV. The central lines show the predictions, while the colored bands indicate the theoretical uncertainty. The transition for VBF at $m_H = 300$ GeV at 8 TeV is due to change from ZWA to complex-pole-scheme. Right hand plot shows the total cross sections for $\sqrt{s} = 7, 8, 14$ TeV. *Source*: taken from Higgs Working Group [59].

center-of-mass energy of $\sqrt{s} = 7, 8, 14$ TeV. For a Higgs boson mass of 125 GeV, the total production cross section is expected to be 17.5 pb at $\sqrt{s} = 7$ TeV and 22.3 pb at 8 TeV, and varies with the mass at a rate of about -1.6% per GeV. About one order enhancement in the total cross section from 8 TeV to 14 TeV leads to increased ability to isolate the background and achieve a high precision Higgs measurement at the more exciting Run 2.

- *Gluon fusion production*

As shown in Fig. 3.2 (left), the dominant Higgs production mode at the LHC is gluon fusion (abbreviated ggF), $gg \to H$ (see Fig. 3.1 (a)). In spite of being a loop-induced process, it is greatly enhanced by the top-quark loop and the large gg effective luminosity at gg center of mass energy. This process makes up about 85% of the total (inclusive) Higgs production cross section at the LHC. At leading order, the amplitude for $gg \to H$ is the same as that for the decay $H \to gg$, with the initial and final states swapped as we have commented in Section 2.3.3. (This amplitude must then be squared and integrated with the gluon parton densities.) Beyond leading order, however, the QCD corrections for gluon-fusion Higgs production are different from those for the $H \to gg$ decay, because of the presence of additional radiated jets in the final state, dramatically changing the kinematic structure. These QCD corrections are quite large, enhancing the gluon-fusion

Higgs production cross section by about a factor of two. As far as we know, a conservative estimate of uncertainties on the gluon fusion Higgs production cross section at the 7–8 TeV LHC are about $\pm 8\%$ from QCD scale uncertainty and $\pm 7\%$ from the uncertainty in the parton distribution functions. The Higgs discovery comes predominantly from this production mode.

For light- and intermediate-mass Higgs bosons, however, the very large cross section of this process has to compete against a very large hadronic background, since the Higgs boson mainly decays to $b\bar{b}$ pairs, and there is no other non-hadronic probe that can help to distinguish this mode from the overall hadronic activity in the detector. To beat down the background, one has to employ subleading Higgs decay modes, like $H \to \gamma\gamma$, and this dilutes the large cross section to some extent. For larger Higgs masses, above the ZZ threshold, on the other hand, gluon fusion together with $H \to ZZ$ produces a very distinctive signal, and makes this a "golden" mode for detection. For this reason, $gg \to H$ plays a fundamental role at the LHC over the entire Higgs-boson mass range, but is of very limited use at the Tevatron, where it can only be considered for Higgs boson masses very close to the upper reach of the machine ($m_H \simeq 200$ GeV).

- *Vector boson fusion production*

Vector boson fusion (VBF), $qq \to Hjj$, (see Fig. 3.1 (b)) at the LHC also has a fairly large cross section. It is about one tenth the size of that for gluon fusion. The process is distinctive experimentally because the two incoming quarks tend to be scattered by only a small angle, leading to two very energetic jets pointing close to the beam line in opposite halves of the detector (referred to as "forward jets" or "forward tagging jets"). This process thus becomes instrumental at the LHC (pp initial state) in both the low and intermediate mass regions because its characteristic final state configuration greatly helps to disentangle this signal from the hadronic background, using different Higgs decay channels. Moreover, it is interesting theoretically because it gives experimental access to the Higgs boson couplings to WW and ZZ in a production process.

- *Higgs-strahlung*

Another distinctive Higgs production process is associated production together with

a W or Z boson (see Fig. 3.1 (c)). The cross section for these two processes combined is about 60–70% as large as that for VBF. As for VBF, this process gives access to the Higgs boson coupling to WW or ZZ. Experimentally, the W or Z boson in the final state provides a useful handle to reduce background in searches for Higgs decays to $b\bar{b}$.

- *Top/bottom-quark associated production*

A challenging but important process is $t\bar{t}H$ associated production, in which the Higgs boson is radiated off a top-antitop quark pair (see Fig. 3.1 (d)). There are also contributions in which the Higgs boson is attached to the outgoing top quark or antiquark line, as well as contributions from $q\bar{q}$ or gg annihilation through an s-channel gluon. Even given enough statistics available at the LHC, very low production rate at 8 TeV and still very low at the 14 TeV (a mere 1% of the inclusive Higgs cross section at this higher energy) makes it very difficult to fully exploit the signature with $H \rightarrow b\bar{b}$ in the final state. Indeed, this channel has not been used for discovery but certainly has a great physics potential now that the properties of the discovered Higgs-like particle need to be thoroughly investigated. It offers the unique possibility of directly measuring one of its most important couplings, namely the coupling to top quarks. In turn, knowledge of the $Ht\bar{t}$ coupling from a direct (tree-level) process like $t\bar{t}H$ is essential in order to probe for contributions to the loop-induced Hgg coupling from non-SM particles in the loop.

On the other hand, the production of a SM Higgs boson with $b\bar{b}$ pairs is tiny, since the SM bottom-quark Yukawa coupling is suppressed by the bottom-quark mass. Therefore, the $b\bar{b}H, H \rightarrow b\bar{b}$ channel is the ideal candidate to provide evidence of new physics, in particular of extensions of the SM, like the two-Higgs-doublet models, where the bottom-quark Yukawa coupling to one or more Higgs bosons is enhanced by $\tan\beta$, see Table 5.4. Of course, this is a difficult channel to measure at the LHC because of the large hadronic background. It could, however, offer a striking signal of new physics if observed. The impact of the search using this channel on the extended Higgs model will be particularly discussed in Section 5.6.

In addition, there are two channels that are missing in Fig. 3.2 because of their small size in the SM, but which are indeed important to probe new physics if present. Contri-
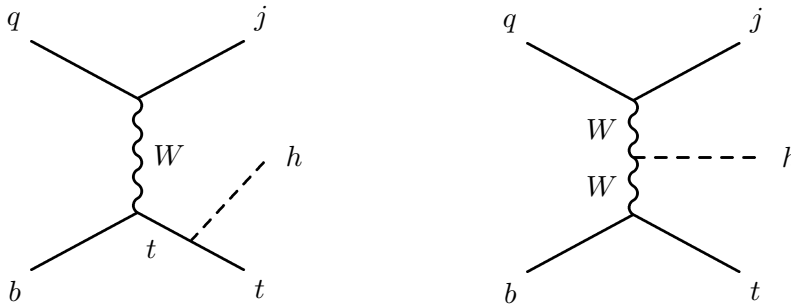
Figure 3.3. Feynman diagrams for single-top plus Higgs production.

butions are also expected from $b\bar{b} \to H(bbH)$ and the production in association with a single top quark (tH). The latter proceeds through either the $qb \to tHq'$ or $gb \to WtH$ process.

- *Single-top plus Higgs associated production*

A complementary (but even more experimentally challenging) process is single-top plus Higgs associated production. There are two Feynman diagrams (see Fig. 3.3) for this process, one in which the Higgs couples to the top quark and the other in which it couples to the W boson exchanged in the t-channel. In the SM, there happens to be a strong destructive interference between these two diagrams, resulting in a cross section that is probably too small to be measured at the LHC. However, it was pointed out recently [62] that this process provides an interesting test of the *relative sign* of the HWW and $Ht\bar{t}$ couplings, because a sign flip in one of the couplings relative to the SM would turn the destructive interference into constructive interference and make this cross section large enough to measure.

- *Double Higgs production*

One final process worth studying at the LHC is double Higgs production (Fig. 3.4). The value of this process is that it allows an experimental probe of the Higgs self-coupling through the hhh vertex. Nonetheless, it suffers from an extremely low cross section and thus is experimentally very tough. A recent study indicates that, in the final phase of LHC Run 2 (3000 fb^{-1} at each of two detectors at 14 TeV), one could get a $\pm 30\%$ measurement of the triple-Higgs coupling $\lambda_{HHH}^{\mathrm{SM}}$ [63].
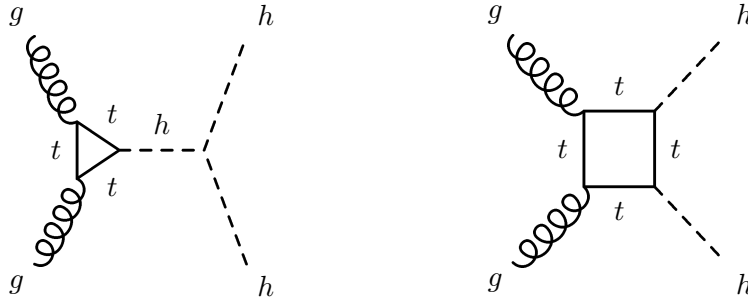
Figure 3.4. Sample Feynman diagrams for double Higgs production in hadron colli-
sions.

At present, the main production/decay channels relevant for current LHC data are gluon fusion (gg) and vector boson fusion (VBF) with Higgs decay to $\gamma\gamma$ or $ZZ^* \to 4\ell$. The LHC also probes W, Z+Higgs with Higgs decay to $b\bar{b}$, a channel for which Tevatron data is relevant, and $WW \to$ Higgs with Higgs$\to \tau^+\tau^-$. However, it is important to note that the different decay pattern of a light vs a heavy Higgs boson influences the role played, in each mass region, by different Higgs production processes at hadron and lepton colliders, as will be seen in Fig. 3.5. In particular, for the SM Higgs at 125 GeV the cross section values for the production modes and the values for the decay branching fractions, together with their uncertainties, are tabulated in Table 3.1.

Table 3.1. SM predictions of the Higgs boson production cross sections and decay branching ratios and their uncertainties for $m_H = 125.36$ GeV. The uncertainties on the cross sections are the quadratic sum of the uncertainties on the QCD scales, parton distribution functions and α_S. The uncertainty on the tH cross section is calculated following the procedure of Ref. [55]. *Source:* taken from Ref. [64].

Production process	Cross section (pb)		Decay channel	Branching ratio (%)
	$\sqrt{s} = 7$ TeV	$\sqrt{s} = 8$ TeV		
ggF	15.0 ± 1.6	19.2 ± 2.0	$H \to b\bar{b}$	57.1 ± 1.9
VBF	1.22 ± 0.03	1.57 ± 0.04	$H \to WW^*$	22.0 ± 0.9
WH	0.573 ± 0.016	0.698 ± 0.018	$H \to gg$	8.53 ± 0.85
ZH	0.332 ± 0.013	0.412 ± 0.013	$H \to \tau\tau$	6.26 ± 0.35
bbH	0.155 ± 0.021	0.202 ± 0.028	$H \to c\bar{c}$	2.88 ± 0.35
ttH	0.086 ± 0.009	0.128 ± 0.014	$H \to ZZ^*$	2.73 ± 0.11
tH	0.012 ± 0.001	0.018 ± 0.001	$H \to \gamma\gamma$	0.228 ± 0.011
			$H \to Z\gamma$	0.157 ± 0.014
Total	17.4 ± 1.6	22.3 ± 2.0	$H \to \mu\mu$	0.022 ± 0.001
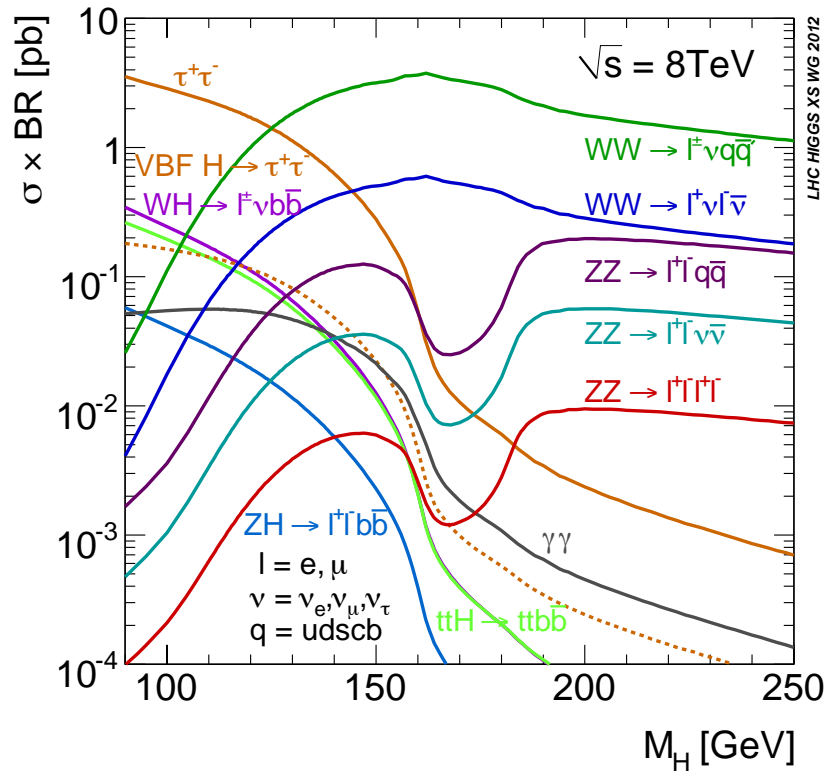
Figure 3.5. SM Higgs boson production cross section times branching ratio at $\sqrt{s} = 8$ TeV. For $H \to \tau\tau$ both inclusive (solid line) and VBF (dashed line) mode are plotted. *Source*: taken from Higgs Working Group [59].

3.1.2 Definition of signal strength

As seen in Eq. (3.1), the event rate R is proportional to the luminosity $\mathcal{L}$. To eliminate the disturbance coming from this hard technical parameter of the colliders, in the analysis experiments often normalize the event number for different production channels, X, and different decay modes, Y by taking the ratio to the prediction in the SM. This quantity is conventionally phrased in terms of "*signal strength*":

$$\mu_X(Y) \equiv \frac{\sigma(X)\mathrm{BR}(Y)}{\sigma_{\mathrm{SM}}(X)\mathrm{BR}_{\mathrm{SM}}(Y)}\,, \tag{3.2}$$

where the numerator and denominator are evaluated for the same Higgs mass. The production modes for the Higgs boson considered are ggF (gluon fusion, also denoted as gg), VBF (vector boson fusion), ttH (associated production with $t\bar{t}$) and VH (associated production with a vector boson). The relevant decay modes are those into

47
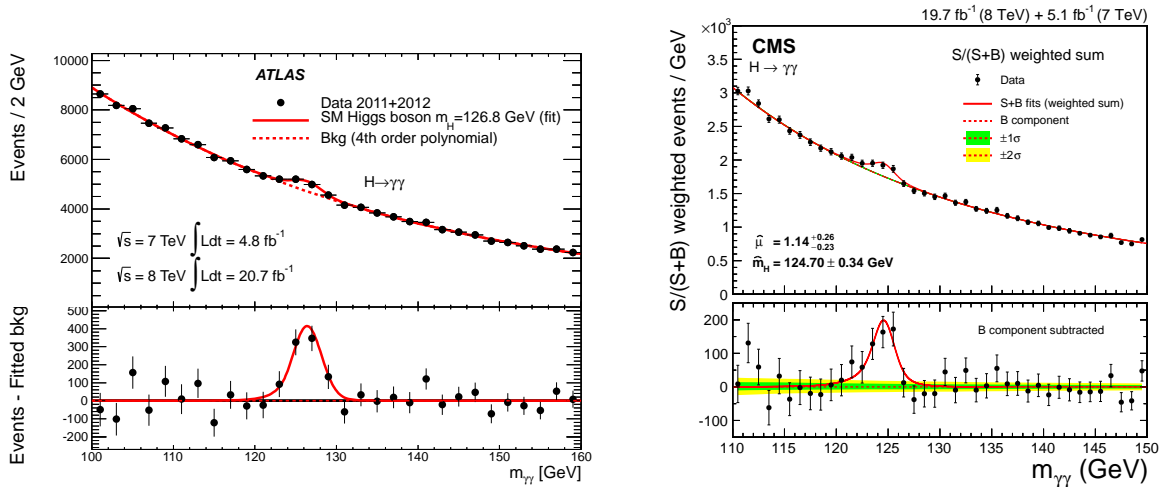
Figure 3.6. The diphoton invariant mass distribution from ATLAS (left) [65] and from CMS (right) [66]. The red lines represent the fitted background and signal. Both plots are generated from full Run 1 data analysis.

$Y = \gamma\gamma, VV, b\bar{b}$ and $\tau\tau$ (where $VV \equiv ZZ, WW$).

This signal-strength parameter is a measure of potential deviations from the SM prediction under the assumption that the Higgs boson production and decay kinematics do not change appreciably from the SM expectations. Calculations of the μ parameters in specific models will be described in the corresponding chapters.

3.2 New particle discovery and discovery channels

After over thirty years of waiting, in December of 2011 the ATLAS and CMS Collaborations at the LHC reported the first hint of observing a new particle and officially announced the discovery of a particle with Higgs boson-like properties and a mass of about 125 GeV with a 5σ signal in the summer of 2012 [67–69] . The confidence level of this signal reached 7σ (ATLAS) and 10σ (CMS) by the end of 2012. The discovery was primarily made through the analyses of two golden bosonic decay channels of the Higgs boson, $H \rightarrow \gamma\gamma$ (see Fig. 3.6) and $H \rightarrow ZZ^* \rightarrow \ell^+\ell^-\ell'^+\ell'^-$ (denoted $H \rightarrow ZZ \rightarrow 4\ell$ for simplicity) (see Fig. 3.7), where one or both of the Z bosons can be off-shell and where ℓ and ℓ' denote an electron or muon. The $H \rightarrow \gamma\gamma$ channel is characterized by a narrow resonant signal peak containing several hundred events per experiment above a large
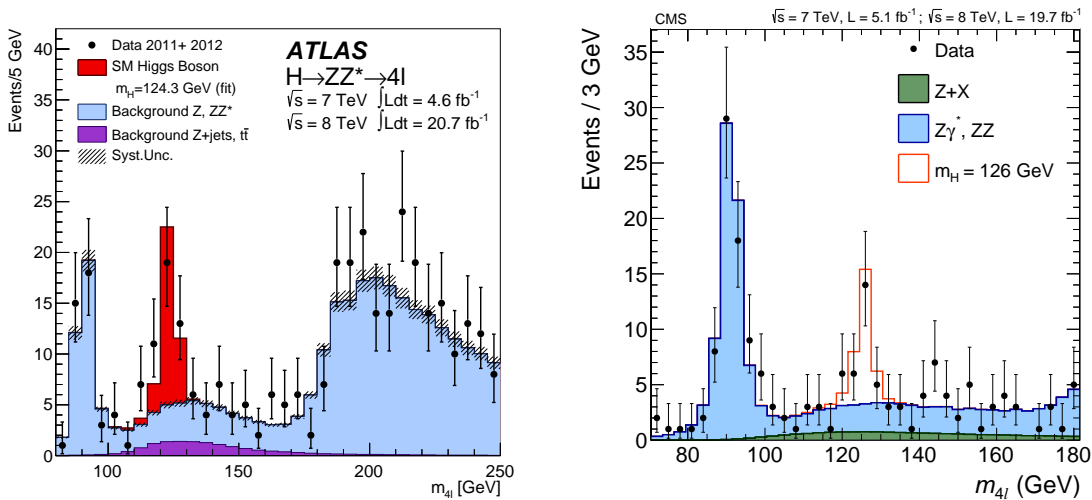
Figure 3.7. The four-lepton invariant mass distribution from ATLAS (left) [65] and from CMS (right) [71]. The red lines represent the fitted background and signal. Both plots are generated from full Run 1 data analysis.

falling continuum background. The overall signal-to-background ratio is a few percent. The $H \to ZZ \to 4\ell$ channel yields only a few tens of signal events per experiment, but has very little background, resulting in a signal-to-background ratio larger than 1.

Since then, a number of new measurements or updates of existing ones using the full samples of data collected in 2011 and 2012, commonly referred to as LHC Run 1, have been published by the experimental collaborations. The most significant changes, from the point of view of our analysis, were the long-awaited final results for the $\gamma\gamma$ decay mode from CMS [66] and from ATLAS [70] in the summer of 2014. The average rate in the $\gamma\gamma$ mode, that appeared to have a substantial enhancement before, is now converging to the SM level, although there is still considerable discrepancy between the two collaborations. In addition, there are also several other important new measurements or updates; for example uncertainties have been significantly reduced for the fermionic channels, particularly for $H \to b\bar{b}$ in $t\bar{t}H$ production. The results of ongoing analyses for this newly discovered particle as of spring 2015 will be summarized in the next section.

3.3 Precision study of the properties for the new discovered particle

Since the discovery phase, extensive analyses using the full Run 1 data set have been undertaken to characterize the properties of this particle such as its production cross sections and partial widths. To date, increasingly precise measurement shows that all observed properties of the new particle are very close, within the uncertainties, to those predicted for the Higgs boson of the SM. In this section I will review the current measurements of its properties, including its spin, parity, and coupling strengths to SM particles, as well as the upper bound on its invisible decay branching ratio.

3.3.1 Measurements of the mass

Having independently measured the mass of the discovered resonance m_H, the ATLAS and CMS Collaborations have started to combine the data sets to perform the analysis [40]. The combination is performed using only the $H \to \gamma\gamma$ and $H \to ZZ \to 4\ell$ decay channels, because these two channels offer the best mass resolution. The procedure for combining the Run 1 data sets of ATLAS and CMS is described in [40]. The resulting mass of the Higgs boson is determined to be

$$m_H = 125.09 \pm 0.24 \ \ \text{GeV}. \tag{3.3}$$

Figure 3.8 shows the negative log-likelihood ratio scans as a function of m_H, with all nuisance parameters profiled (solid curves), and with the nuisance parameters fixed to their best-fit values (dashed curves). The combined ATLAS and CMS results for m_H in the separate $H \to \gamma\gamma$ and $H \to ZZ \to 4\ell$ channels are presented in Fig. 3.8, along with a summary of the results from the individual channels.

Meanwhile, the correlation between the signal strength and the measured mass is also explored with 2D likelihood scans as functions of μ and m_H, as displayed in Fig. 3.9. There, the 68% confidence level (CL) regions are shown for each individual measurement, as well as for the combined result. In the analysis, the three signal strengths are assumed to be the same: $\mu_{gg\mathrm{F}+t\bar{t}H}^{\gamma\gamma} = \mu_{\mathrm{VBF}+VH}^{\gamma\gamma} = \mu^{4\ell} \equiv \mu$, and thus the ratios of the production cross sections times branching fractions are constrained to the SM predictions.
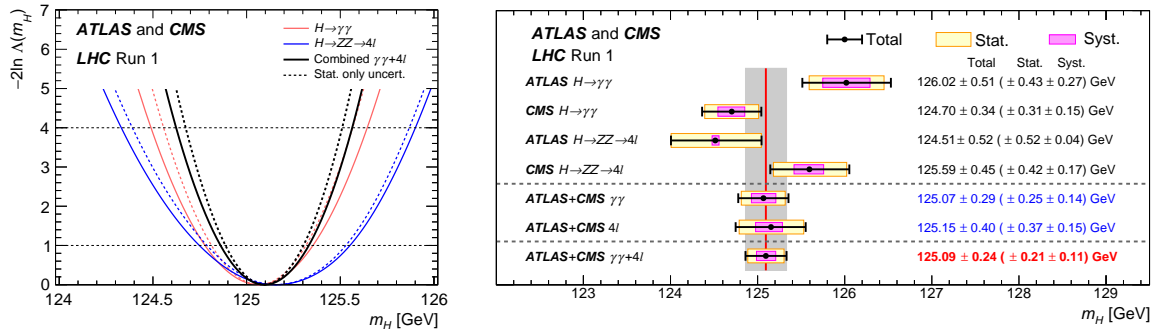
Figure 3.8. Determination of the mass for the discovered SM-like Higgs state by combining the ATLAS and CMS data sets from the $H \to \gamma\gamma$, $H \to ZZ \to 4\ell$ and combined channels. *Source:* taken from [40].
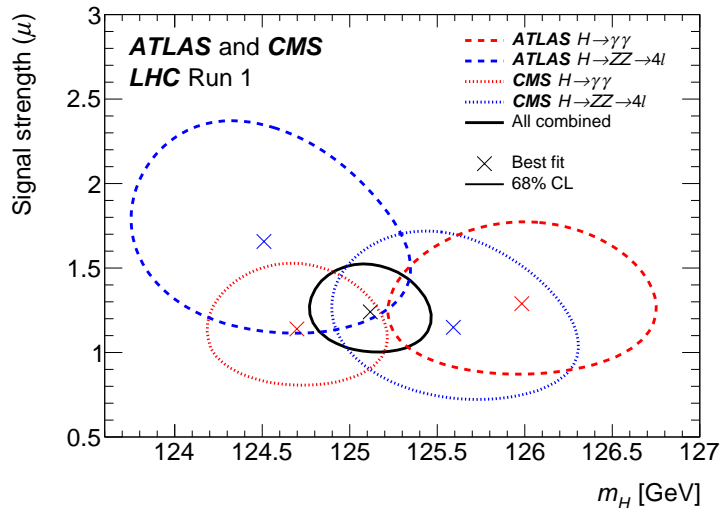
Figure 3.9. Correlation in the 2D plane of signal strength μ versus Higgs boson mass m_H for the ATLAS and CMS experiments. The 68% CL confidence regions of the individual measurements are shown by the dashed curves and of the overall combination by the solid curve. The markers indicate the respective best-fit values. *Source:* taken from [40].

3.3.2 Spin-parity properties

Another critical aspect is to determine the spin, parity, and charge conjugation quantum numbers J^{PC}. First of all, the Landau–Yang theorem forbids the direct decay of an on-shell spin-1 particle into a pair of photons [72, 73]. The spin-1 hypothesis is therefore strongly disfavoured by the observation of the $H \to \gamma\gamma$ decay.

The $J^P = 0^+$ and 0^- cases can be distinguished by angular and invariant mass distributions in $H \to ZZ \to 4\ell$, and also by the threshold behavior of VH. The 0^+ can
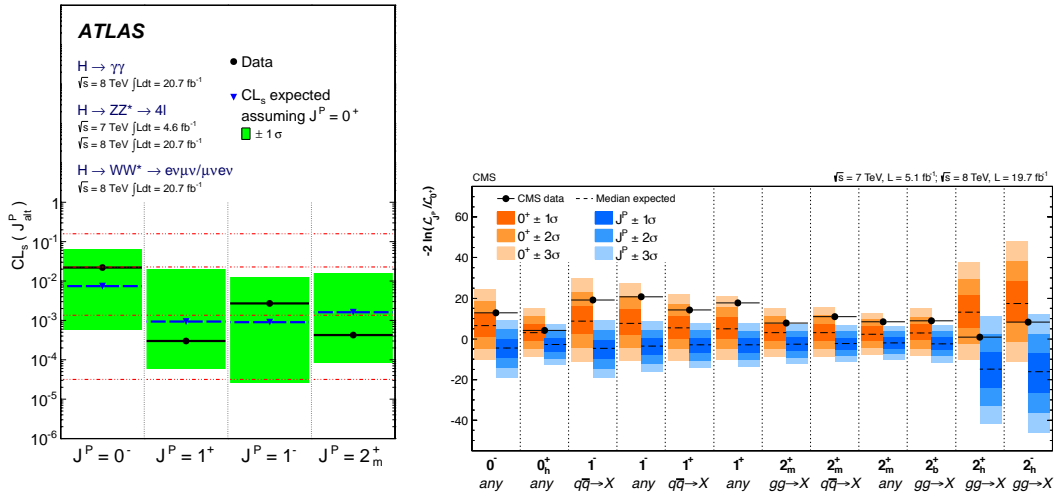
Figure 3.10. Summary of the spin-parity test for various alternative hypothesis with respect to the SM $J^P = 0^+$ from ATLAS [75] (left) and CMS [71] (right). The black point represents the observed value.

be distinguished from $1^{\pm}$ and 2^+ in ZZ^*, WW^*, and $\gamma\gamma$. To date, the SM spin–parity $J^P = 0^+$ hypothesis is compared with alternative hypotheses using the decay channel $H \rightarrow ZZ^*$, alone, at CMS [71, 74] while the ALTAS analysis uses Higgs boson decays $H \rightarrow \gamma\gamma$, $H \rightarrow ZZ^* \rightarrow 4\ell$ and $H \rightarrow WW^* \rightarrow \ell\nu\ell\nu$ (where ℓ denotes an electron or a muon), as well as the combination of these channels [75, 76]. The summary of these comparisons is presented in Fig. 3.10 for the two collaborations. It clearly indicates that the data are compatible with the Standard Model $J^P = 0^+$ quantum numbers for the Higgs boson. Most alternative hypotheses such as $J^P = 0^-$, 1^+, 1^-, 2^+ are now evidently excluded at $\gtrsim 98\%$ C.L.

3.3.3 Signal strengths measurements

As of spring 2015, CMS and ATLAS closed the chapter on Higgs measurements with the final harvest of results from the full Run 1 dataset. The combinations at AT-LAS [77] and CMS [78] have been comprehensive, taking as inputs the analyses of the $H \rightarrow \gamma\gamma, ZZ^*, WW^*, \tau\tau, b\bar{b}, \mu\mu$ and $Z\gamma$[1] Higgs boson decay modes, and the constraints on the ttH and off-shell Higgs boson production.

In the signal-strength discussion below, bbH is included in ggF, tH in ttH and $gg \rightarrow$

---

[1]$Z\gamma$ channel is only available at ATLAS.
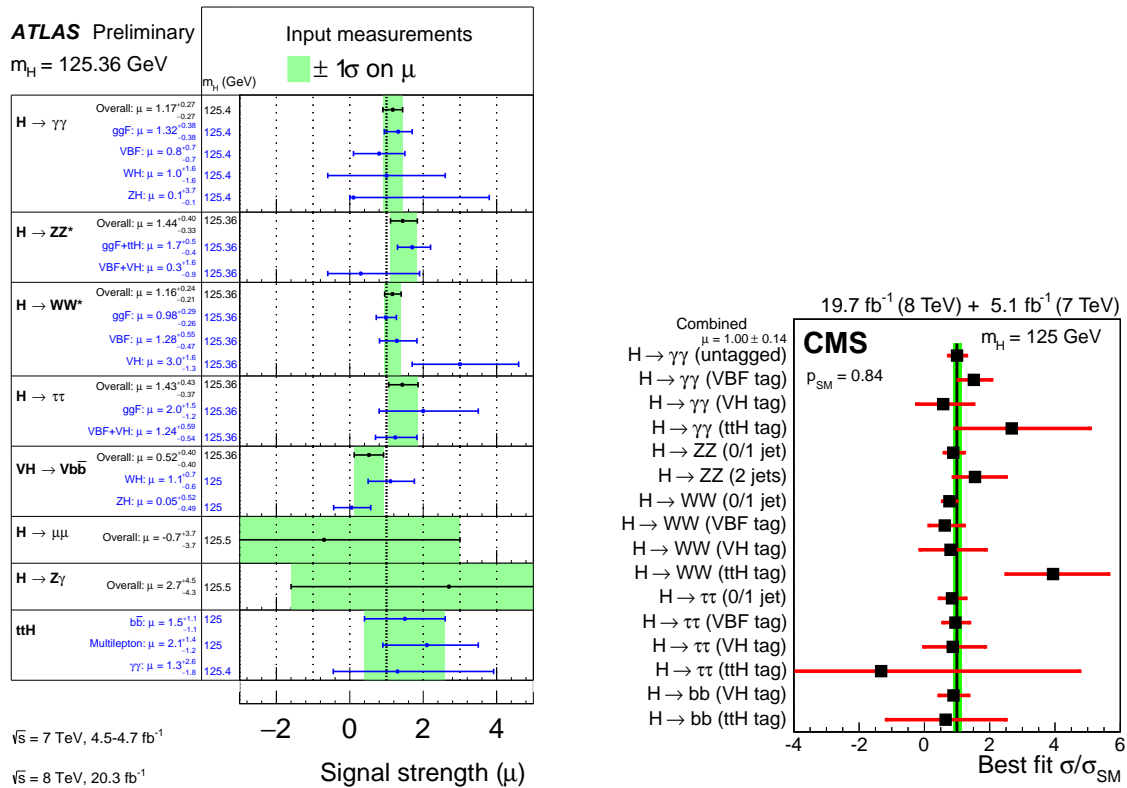
Figure 3.11. Summary of the signal-strength measurements from ATLAS [77] (left) and CMS [78] (right). The error bars represent $\pm 1\sigma$ total uncertainties, combining statistical and systematic contributions. In the left plot, the overall signal strength of each analysis (black) is the combined result of the measurements for different production processes (blue).

ZH in VH, unless noted otherwise. The ggF and bbH processes lead to similar event signatures and no attempt is made to separate them in the analyses. The ttH and tH events have similar topologies. The $gg \rightarrow ZH$ process leads to the same final state as the $q\bar{q} \rightarrow ZH$ process via VH production.

- *Individual production—decay*

We first present in Fig. 3.11 the results for signal-strength measurements of different production-decay processes (grouped by production tag at the CMS). These are used as inputs for grouping in the combined analysis that will be coming up in the following.

- *Grouped production—decay*

One step in going beyond a single signal strength modifier is to evaluate the signal strength in groups of channels from different analyses. Apparently, the groups chosen
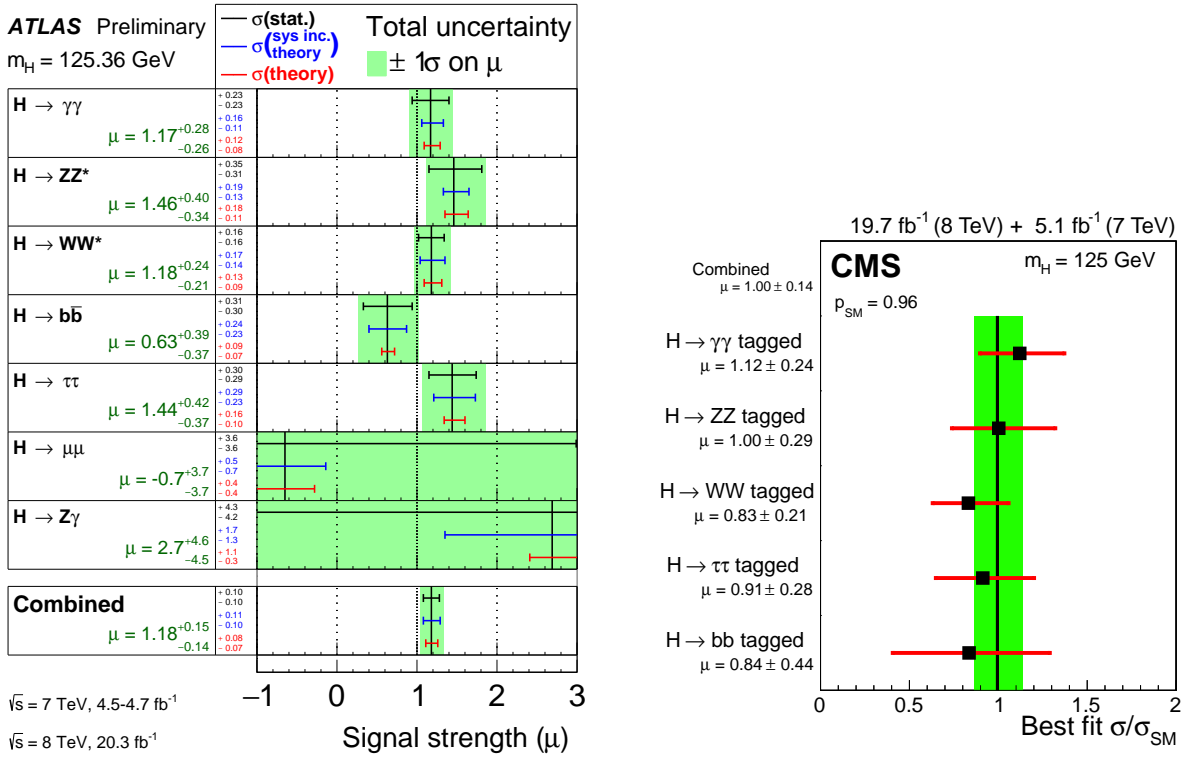
Figure 3.12. The best-fit signal strength for separate combinations grouped by predominant decay modes from ATLAS [77] (left) and CMS [78] (right). The horizontal bars indicate the ±1 standard deviation uncertainties for the individual combinations; while the overall $\sigma/\sigma_{\rm SM}$ uncertainties are shown by green shaded bands. The bars in the right plot include both statistical and systematic uncertainties.

reflect the different production tags, predominant decay modes, or both. Once the fits for each group are performed, a simultaneous fit to all groups is also performed to assess the compatibility of the results with the SM Higgs boson hypothesis.

The results for the independent combinations grouped by predominant decay mode and by production mode tag are illustrated in Fig. 3.12 and Fig. 3.13, respectively. In Fig 3.12 most of these results for ATLAS (left) and CMS (right) are similar to the separate measurements as shown in Fig. 3.11. A few noticeable changes can be attributed to the assignment of the Higgs boson yield of the ttH searches to appropriate Higgs boson decay channels. For example, the result of the ttH search in $H \to b\bar{b}$ is combined with that of the VH analysis of the $H \to b\bar{b}$ decay. This can also be understood from an excess for the ttH-tagged combination observed in Fig. 3.13, which is due to the enhancement in the ttH-tagged $H \to \gamma\gamma$ and H → leptons analyses as one can see in Fig. 3.11.
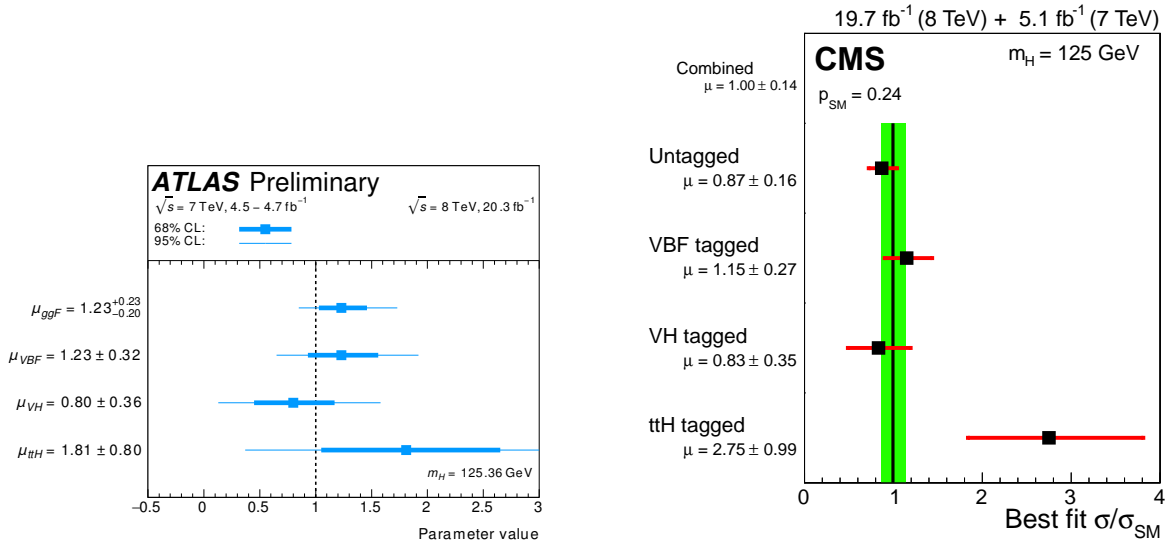
Figure 3.13. The best-fit signal strength for separate combinations grouped by tags targeting individual production mechanisms from the ATLAS [77] (left) and the CMS [78] (right). The horizontal bars indicate the ± 1 standard deviation uncertainties for the individual combinations; while the overall $\sigma/\sigma_{\rm SM}$ uncertainty are shown by green shaded bands. The bars in the right plot include both statistical and systematic uncertainties.

Last, we stress that these plots cannot be interpreted as compatibility tests for pure production mechanisms or decay modes due to the fact that the expected purities of the different tagged samples vary substantially.

- *Global signal strength*

Combing the ATLAS and CMS data sets as explained in Section 3.3.1, the signal strengths at the most recently measured value of m_H (see Eq. 3.3) are found to be $\mu^{\gamma\gamma}_{gg{\rm F}+t\bar{t}H} = 1.15^{+0.28}_{-0.25}$, $\mu^{\gamma\gamma}_{\rm VBF+VH} = 1.17^{+0.58}_{-0.53}$, and $\mu^{4\ell} = 1.40^{+0.30}_{-0.25}$. Assuming a common multiplier to all signal yields, they can be combined to result in a global, more precise measurement of the signal-strength parameter, providing the simplest test for consistency with the SM expectation. The combined overall best-fit signal strength μ (with $\mu^{\gamma\gamma}_{gg{\rm F}+t\bar{t}H} = \mu^{\gamma\gamma}_{\rm VBF+VH} = \mu^{4\ell} \equiv \mu$), relative to the SM expectation, is

$$\mu = 1.24^{+0.18}_{-0.16}. \tag{3.4}$$

and individually $\mu = 1.18^{+0.15}_{-0.14}$ for ATLAS [77] and $\mu = 1.0^{+0.14}_{-0.13}$ for CMS [78].

- *2D signal strength correlation*

The measurements of the signal strengths described above assume the SM predic-

tions for the relative contributions of different Higgs boson production processes and/or decay channels. Thus they may conceal differences between data and theoretical predictions. Therefore, in addition to the signal strengths of different decay channels, the signal strengths of different production modes are determined, exploiting the sensitivity offered by the use of event categories in the analyses of all channels.

The Higgs boson production processes can be categorised into two groups according to the Higgs boson couplings to fermions (ggF and ttH) or vector bosons (VBF and VH). Potential deviations from the SM can be tested with two signal-strength parameters $\mu^f_{\text{ggF}+ttH} \equiv (\mu^f_{\text{ggF}} = \mu^f_{ttH})$ and $\mu^f_{\text{VBF}+VH} \equiv (\mu^f_{\text{VBF}} = \mu^f_{VH})$ for each decay channel f. The 68% and 95% (not present in the right plot) CL two-dimensional contours of $\mu^f_{\text{ggF}+ttH}$ and $\mu^f_{\text{VBF}+VH}$ of the five main decay channels are shown in Fig. 3.14. The cutoff in the contours of the $H \to \gamma\gamma$ and $H \to ZZ^*$ decays appearing in the ALTAS analysis (see the left plot) is caused by the expected sum of signal and backgrounds yield in one of the contributing measurements going below zero in selected regions of the parameter space. Consistently, the SM expectation of $\mu^f_{\text{ggF}+ttH} = 1$ and $\mu^f_{\text{VBF}+VH} = 1$ is within the 68% CL contour of most of these measurements.

As has been seen above, it is apparent that the production and decays of the newly discovered particle are broadly consistent with the expectation for the SM Higgs. Of course, some models beyond the SM predict Higgs decays into invisible final states such as a dark matter particle or into other exotic light scalar states. The updated constraints on these scenarios will be mentioned below.

3.3.4 Higgs invisible decay

The search for invisible decays of the Higgs boson in the vector boson fusion production mode is carried out by both ATLAS [89] and CMS [90] using the full data sets collected in Run 1. Limits are set on the production cross section times invisible branching fraction, as a function of the Higgs boson mass. Neither collaboration has observed an excess in the data with respect to the expected background processes. Assuming standard model Higgs boson cross sections and acceptances, the 95% C.L. observed (expected) upper limit
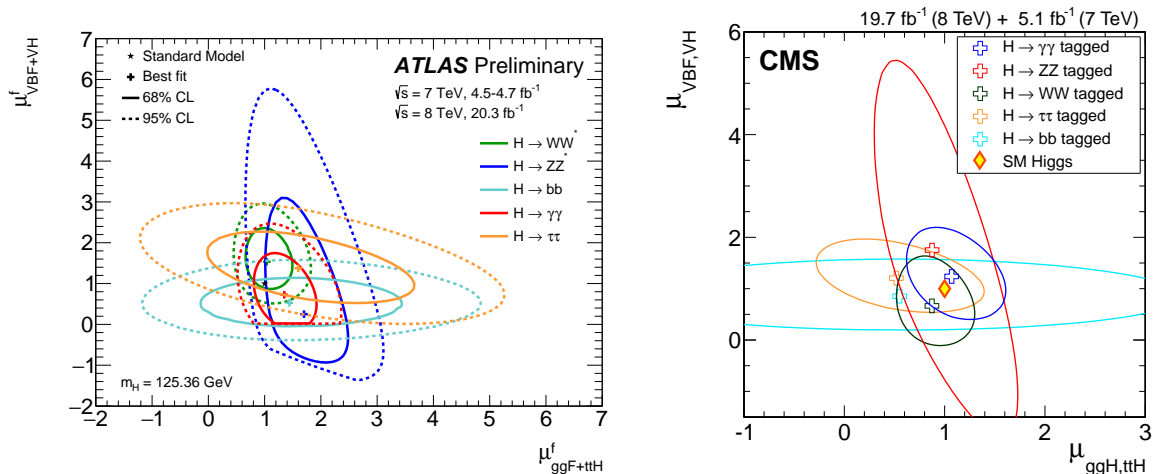
Figure 3.14. Correlation in the signal strength of the ggH and *ttH* and of the VBF and *VH* production mechanisms. The ALTAS resultis [77] shown in the left plot and the CMS [78] in the right. The best-fit values to the data (+) and the 68% (full) and 95% (dashed) CL contours are indicated, as well as the SM expectation marked. In the left plot, the sharp lower edges of the $H \to \gamma\gamma$ and $H \to ZZ^*$ contours are due to the small numbers of events in these channels and the requirement of a positive probability density function.

on the invisible branching fraction at $m_H = 125$ GeV is

$$\text{BR}(H \to \text{inv.}) < 0.29(0.35) \quad \text{(ATLAS)}, \tag{3.5}$$

and

$$\text{BR}(H \to \text{inv.}) < 0.57(0.40) \quad \text{(CMS)}. \tag{3.6}$$

This will place an important constraint on the models in which the Higgs, that is identified as the scalar discovered at the LHC, has decays into a non-SM state that is lighter than half of 125 GeV and that has a direct coupling to the Higgs. Such BSM states could be either exotic light Higgs bosons or Higgs dark matter. The impact on BSM model building will be exemplified in Section 5.7 and Chapter 8.

3.4   A brief overview for BSM Higgs searches

Following the discovery of the Higgs boson at the LHC, the search for new physics continues. Even though measuring the properties of this new particle is necessary in order to constrain the parameter space where new physics lies, at the same time, searches for additional Higgs bosons predicted by beyond the SM theories are also imperative and
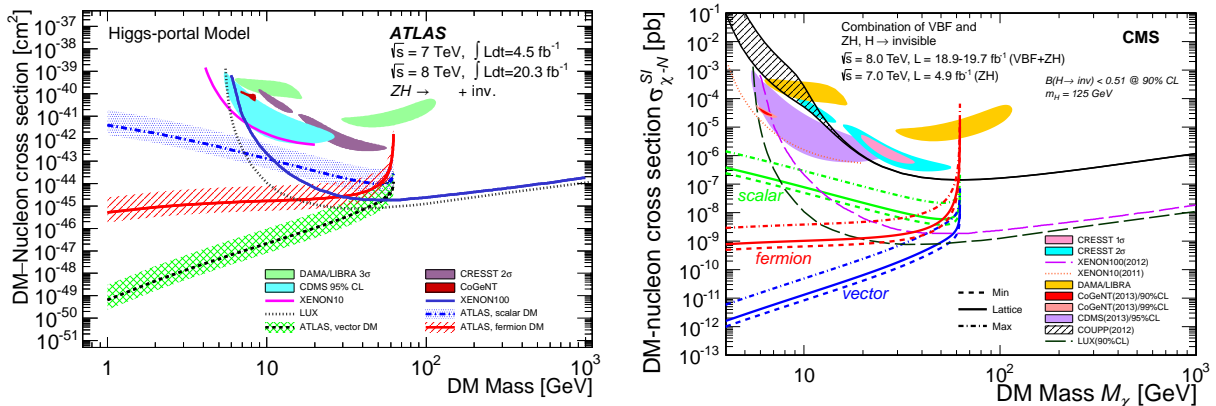
Figure 3.15. Upper limits on the spin-independent DM-nucleon cross section $\sigma^{\mathrm{SI}}_{\chi-\mathrm{N}}$ in Higgs-portal models, derived for $m_H = 125$ GeV and $\mathrm{BR}(H \to \mathrm{inv.}) < 0.51$. Limits are shown separately for scalar, vector and fermion DM. The solid lines represent the central value of the Higgs-nucleon coupling, which enters as a parameter, and is taken from a lattice calculation, while the dashed and dot-dashed lines represent lower and upper bounds on this parameter. Other experimental results are shown for comparison, from the CRESST [79], XENON10 [80], XENON100 [81], DAMA/LIBRA [82, 83], CoGeNT [84], CDMS II [85], COUPP [86], LUX [87] Collaborations. Favored regions for DAMA and CoGeNT are based on Ref. [88]. The results from the direct-search experiments do not depend on the assumptions of the Higgs-portal scenario. Cross-section limits and favored regions correspond to a 90% CL, unless stated otherwise in the legend.

even more exciting as it still remains possible that the discovered particle is part of an extended scalar sector, a scenario that is favoured by a number of theoretical arguments.

The aim of this section is to give a brief (but certainly incomplete) overview of the searches for new physics in the Higgs sector performed by ATLAS and CMS. The current status of the searches for additional scalar bosons as well as a possible pseudoscalar in the both low-mass (below 60 GeV) and high mass (above 200 GeV) regimes will be discussed. These include the model-independent and model dependent limits. For the latter case, the results are interpreted in the context of two-Higgs-doublets, MSSM and even NMSSM. Searches for the H and A are performed in the gluon-fusion and $b\bar{b}$ associated production processes, two high-rate production modes at the hadron collider as discussed in Section 3.1.1, and various decay channels. However, the emphasis in the following context is on searches in the channels $H \to ZZ$, $H, A \to \tau\tau, \gamma\gamma, t\bar{t}$ as well as the $H \to hh$ and $A \to Zh$ final states.
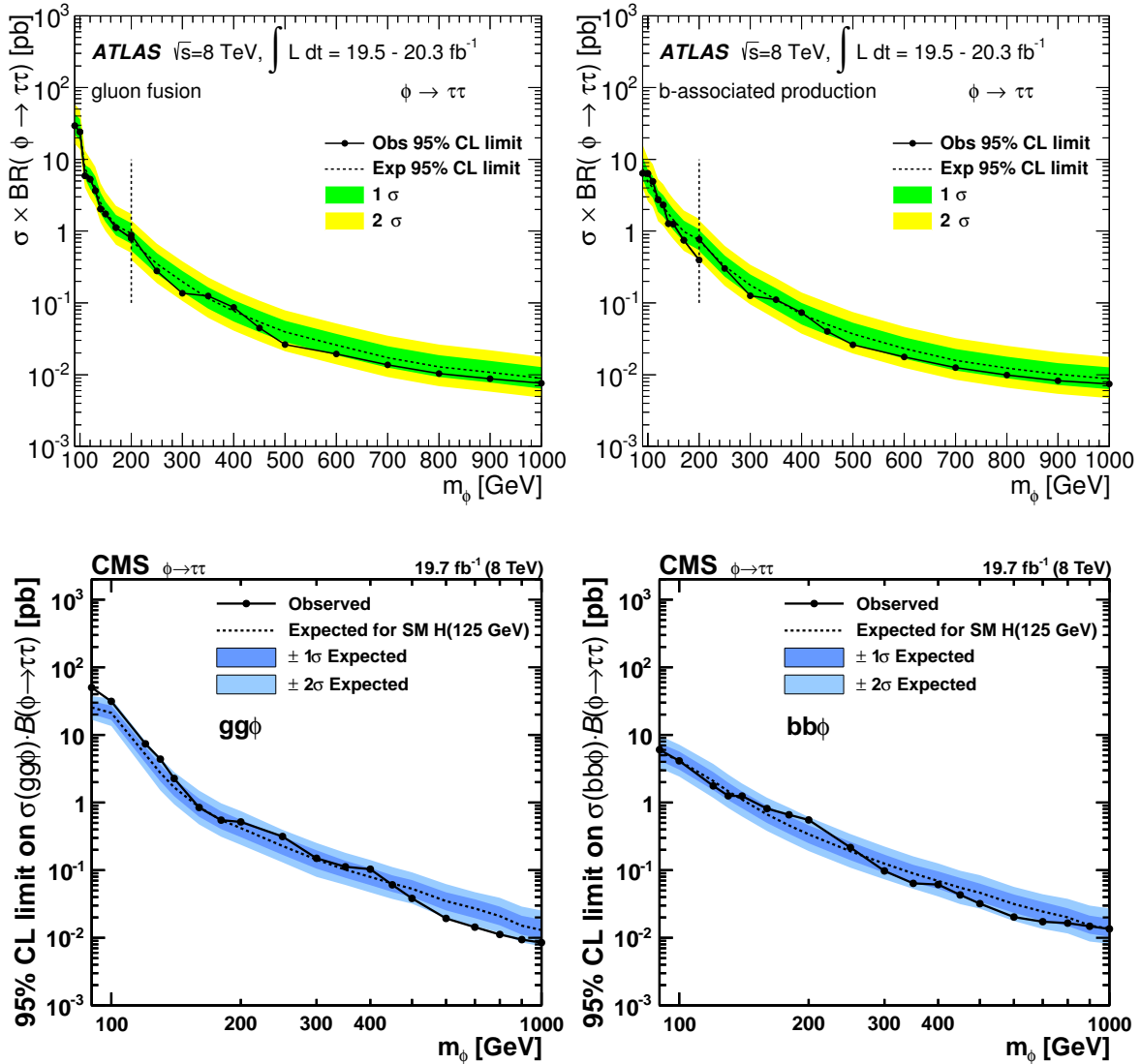
Figure 3.16. 95% CL upper limits on the cross section of a scalar boson ϕ produced via gluon fusion (left) and in association with b-quarks (right) times the branching fraction into τ pairs at 8 TeV center-of-mass energy as a function of m_ϕ, where ϕ denotes a generic Higgs-like state. Upper panel is from [91] (ATLAS) and lower is from [92] (CMS).

- *Search in the $H/A \to \tau\tau$ channel*

Most important are the limits for the $H/A \to \tau\tau$ decay channel from ATLAS [91] and CMS [92]. The current search for a neutral Higgs boson in this channel is constructed in the framework of the minimal supersymmetric extension of the SM (MSSM). The dominant neutral MSSM Higgs boson production mechanism is the gluon fusion process for small and moderate values of $\tan\beta$. At large values of $\tan\beta$, b-quark associated produc-

tion is the dominant contribution, due to the enhanced Higgs boson Yukawa coupling to b quarks. So far no excess of events has been observed in the tau-lepton-pair invariant mass spectrum, and the resulting exclusion limits based on the 8 TeV data are shown in Fig. 3.16. The present analyses are performed separately for the bbH ($b\bar{b}$ associated production of the Higgs) and ggF production modes.

- *Search in the $H \to ZZ^* \to 4\ell, 2\ell2\nu, 2\ell2\tau$ channels*

The latest model-independent limits come from the searches for $H \to ZZ$ from AT-LAS [93] and from CMS [71] and for $H \to ZZ^* \to 2\ell2\nu$ from CMS [94].

To search for a Higgs-like boson in addition to the one seen at 125 GeV, the mass distribution above $m_{4\ell} = 200$ GeV is analyzed at ATLAS. Upper limits are set on the production cross sections times branching ratio of $H \to ZZ^* \to 4\ell$ ($\ell = e, \mu$) as a function of m_H up to 1 TeV. For this analysis, the event classification into ggF-like, VBF-like and VH-like categories is employed. To allow for constraints on a new resonance which may have different production rates in the ggF and VBF modes, the upper limits at the 95% CL are estimated separately for the ggF and the combined VBF/VH production mechanisms, as illustrated in the left and right plots of Fig. 3.17 (upper panel), respectively. In addition, the analysis using the combined 7 TeV and 8 TeV data sets are also performed in the low mass region. The result is shown in the bottom plot of Fig. 3.17, where the 95% CL upper limit on the SM Higgs boson production cross section as a function of mH in the low mass region, divided by the expected SM Higgs boson cross section is drawn.

At CMS, the search for a heavy Higgs boson has been carried out in the $H \to ZZ^* \to 2\ell2\nu$ decay channel, where $\ell = e$ or μ. In analogy to ATLAS, the CMS search is also optimized separately for the vector boson fusion and the gluon fusion production processes. Up till now, no significant excess has been observed above the background expectation in the entire mass region. Figure 3.18 shows the results obtained from the shape-based analysis for a SM-like heavy Higgs boson using the 8 TeV dataset. In particularly, the VBF production component is shown separately after subtracting the gluon-gluon fusion signal contribution to this category. Besides the doublet extension, a re-interpretation of the results as a search for a Higgs singlet extension of the Standard Model is presented as well
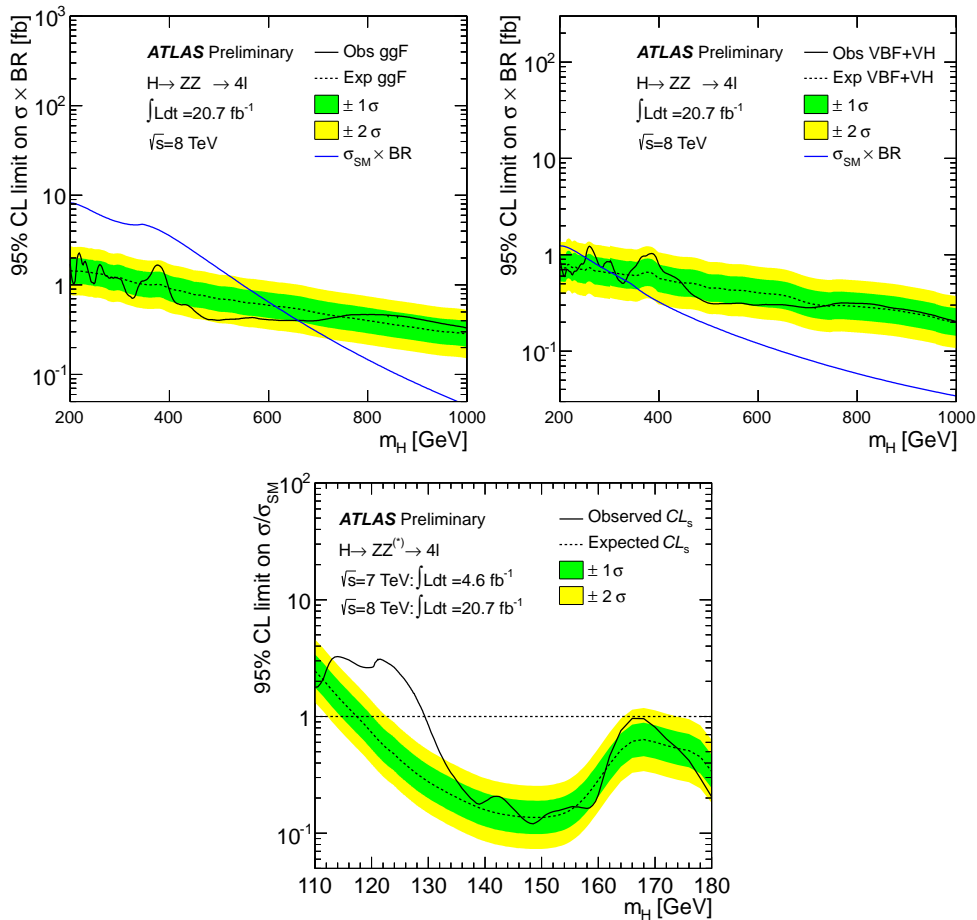
Figure 3.17. Upper panel: 95% CL upper limit on the production cross section times branching ratio of $H \to ZZ \to 4\ell$ ($\ell = e, \mu$) for an ggF (left) and VBF/VH (right) produced SM-like signal as a function of m_H. The blue solid curve represents the SM prediction. Lower panel: 95% CL upper limit on the SM Higgs boson production cross section as a function of m_H in the low mass region, divided by the expected SM Higgs boson cross section. *Source*: taken from [93].

in [94]. Additionally, the search at CMS also considers final states where both Z's decay to electron, muon, or tau lepton pairs. The upper limits obtained from the combination of the 4ℓ (where $\ell = e, \mu$) and $2\ell2\tau$ channels are shown in Fig. 3.18 (bottom). However, the limit is almost uniquely driven by the 4ℓ channels as can be seen from the result based on $H \to ZZ \to 2\ell2\tau$ only.

- *More exotic searches in the $H \to hh$ and $A \to Zh$ channels*

Last, perhaps the most interesting search channels are $H \to hh$ and $A \to Zh$. In general, decays $H \to hh$ and $A \to Zh$ of the heavy scalar and pseudo-scalar Higgs
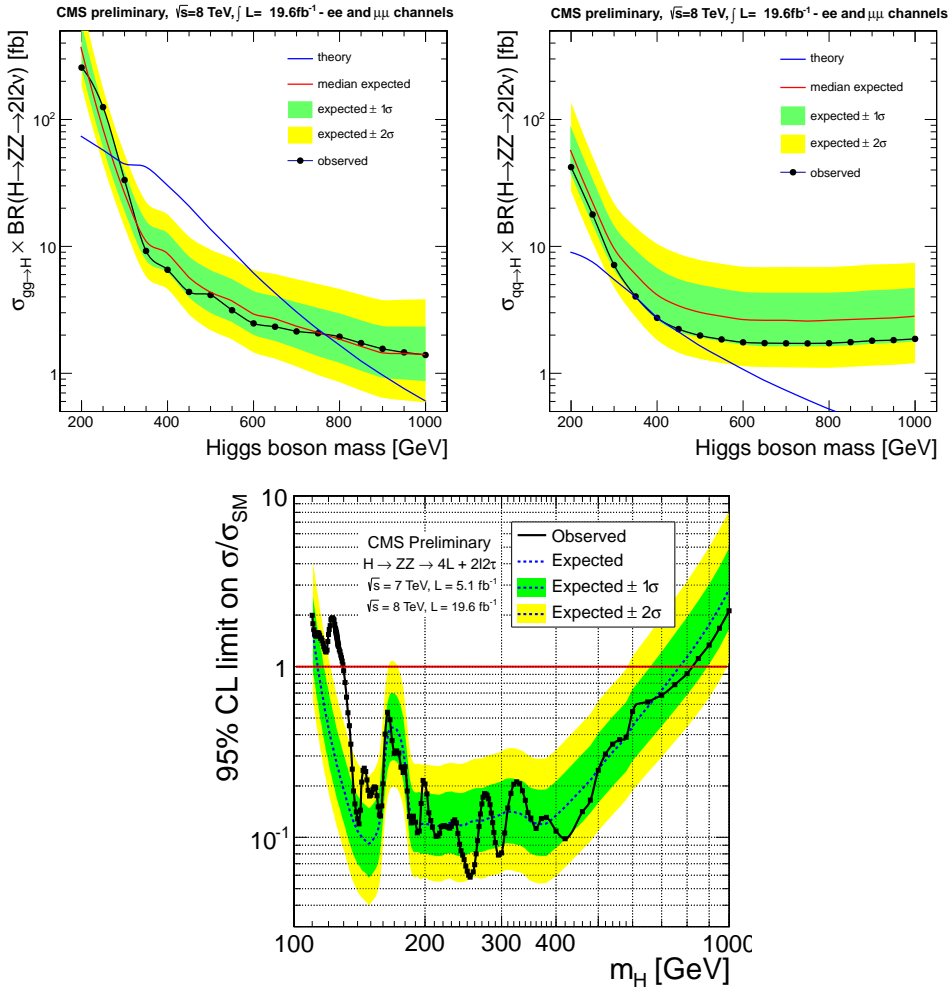
Figure 3.18. Upper panel: Upper limits at 95% CL on the gluon-gluon production cross section (left) and on the VBF production alone (right) of a SM-like Higgs boson as function of its mass. Taken from Ref. [94]. Lower panel: 95% CL upper limit on the ratio of the production cross section to the SM expectation. Taken from [71]

bosons, respectively, include the SM-like Higgs h in the final state and lead to events with isolated leptons and photons.

The search for $H \to hh$ is only available at CMS [95] and the 95% C.L. upper limits on $\sigma \times$ BR are shown in Fig. 3.19. In the analysis both observed multilepton events with diphoton candidates based on event kinematics are included.

At both ATLAS and CMS, the search for the pseudoscalar predicted by an extended Higgs sector is carried out in the decay chain of a heavy pseudoscalar Higgs boson A into a Z boson and a light Higgs boson h, which is assumed to be the recently discovered
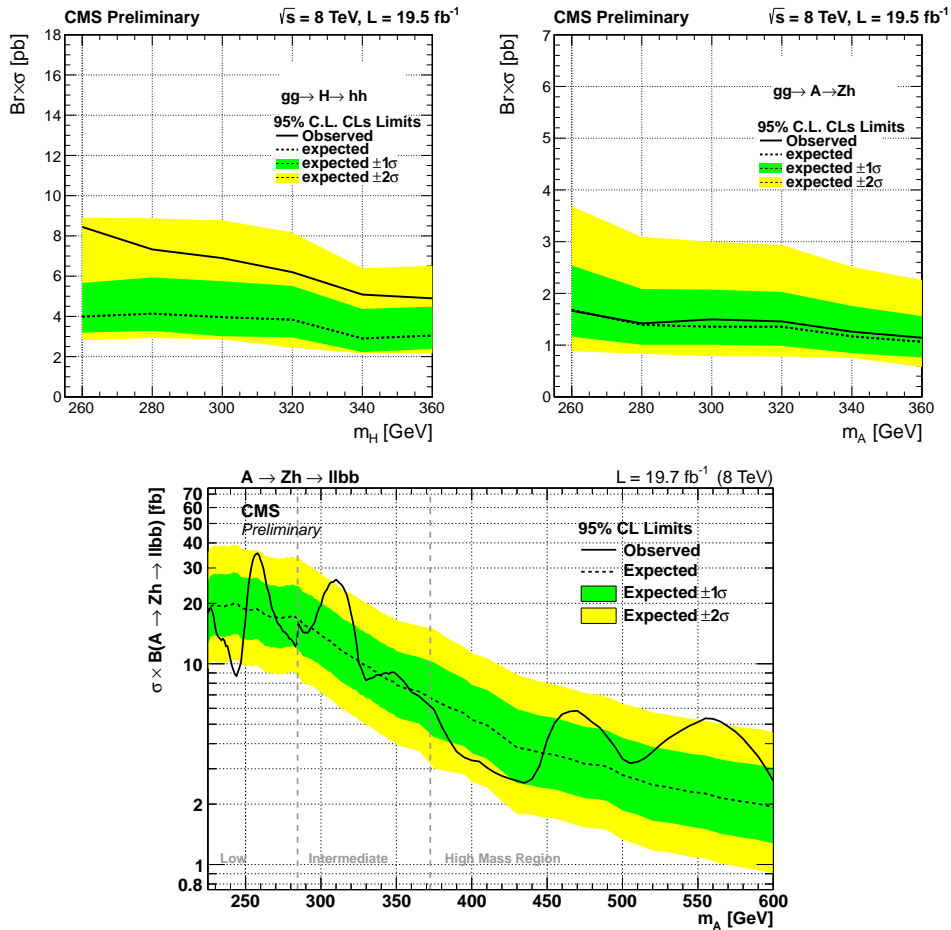
Figure 3.19. Upper from [95]: Upper limits at the 95 % CL for $H \rightarrow hh$ (left) and $A \rightarrow Zh$ (right) in terms of $\sigma \times$ BR. The analysis are based on multilepton and diphoton channels, and the diphoton channels help little in expected limits and up to one pb in the observed limit. BRs for h are assumed to have SM values. The mutual interferences between $H \rightarrow hh$ and $A \rightarrow Zh$ search channels are eliminated. Lower from [96]: The 95% CL upper limit on $\sigma \times$ BR$(A \rightarrow Zh \rightarrow \ell\ell b\bar{b})$ as a function of m_A in the narrow-width approximation.

SM-like Higgs boson with a 125 GeV mass. Decays of h to bb pairs with the Z boson decaying to electron or muon pairs are considered at both ATLAS [97] and CMS [95, 96], as well as $h \rightarrow bb$ decays with the Z boson decaying to neutrinos, that is, however, only taken into account by ATLAS [97].

Results are commonly presented in terms of $\sigma \times$ BR upper limits. Figure 3.19 (top-right) shows the signal probed with the multilepton and the diphoton channels, while the upper limits are set up in a broad mass region in Fig. 3.19 (bottom) in terms of
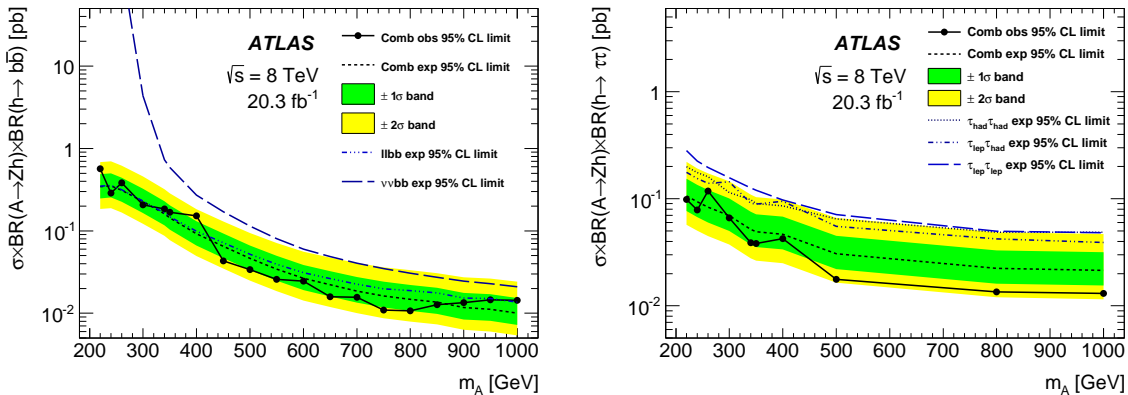
Figure 3.20. Upper limits at the 95% CL for the production cross section of a gluon-fusion-produced A boson times its branching ratio to Zh and branching ratio of h to bb (left) and $\tau\tau$ (right). *Source*: from [97].

$\sigma \times \mathrm{BR}(A \to Zh \to \ell\ell b\bar{b})$, considering the measured value for $\mathrm{BR}(Z \to \ell\ell)$ with $\ell = e, \mu$ and for a narrow A boson produced via the gluon-gluon fusion process. Notice that, while the narrow-width approximation is generally valid for $m_A < 2m_t$, the width of the A boson heavily depends on the model parameters for higher masses.

But beyond that, ATLAS additionally considers the search channel $A \to Zh \to \ell\ell\tau\tau$. In this case, three channels are considered, distinguished by the way the $\tau\tau$ pair decays: two τ leptons decaying hadronically, one leptonic and one hadronic decay and, finally, two leptonic decays. Fig. 3.20 shows the 95% CL limits on the production cross section times the branching ratio, $\sigma(gg \to A) \times \mathrm{BR}(A \to Zh) \times \mathrm{BR}(h \to bb/\tau\tau)$ for each individual subchannel. No evidence for the production of an A boson in these channels is found and the 95% C.L. upper limits derived for these two channels are 0.57-0.014 pb for bb and 0.098-0.013 pb for $\tau\tau$ in a range of $m_A = 220 - 1000$ GeV.

Besides the model-independent analysis, the results from ATLAS and CMS are combined and interpreted in the context of two-Higgs-doublet models.

Very recently we have heard that the search for a light pseudoscalar boson A in the mass region, 25-80 GeV, is being performed and the results will be made public very soon.

Finally, I have to apologize that the search for a charged Higgs, although definitely important, is not included as it will not have a significant impact on our model analysis because of the smallness of the charged Higgs production cross section. In some sense it

has unique physical potential. For instance, the existence of such a charged scalar would definitively imply that the minimal Higgs sector of the SM is insufficient and would thus provide an indication that the Higgs sector has to be extended.

PART II

Post-discovery BSM Higgs Physics

CHAPTER 4

Standard model after the Higgs discovery

The discovery at the LHC of a new particle with mass ~ 125 GeV and with properties compatible with those of the SM Higgs boson concludes decades of intense experimental and theoretical work to uncover the mechanism of electroweak symmetry breaking and mass generation. It has put the final piece of the SM in place and exhibits another – possibly the greatest ever – triumph of the SM, as not only does the SM predict the Higgs couplings to the SM fermions and bosons, but it also constrains the Higgs boson to be light compared to its unitarity bound of roughly the order of 1 TeV order as demonstrated in Section 2.2.

In view of this discovery, all fundamental parameters of the SM are known allowing, for the first time, to overconstrain the SM at the electroweak scale and evaluate its validity. In this chapter we shall review an update of the SM fit to electroweak precision data and present its consequences regarding the potential existence of new physics. The second part is devoted to addressing two important topical issues: the stability of the electroweak vacuum and the hierarchy problem. Both are crucial for motivating many of the ideas regarding physics beyond the SM. At the end, implications of updated Higgs

precision studies for new physics will be discussed.

4.1 Global electroweak fit

For a long time, global fits of the electroweak sector of the SM have been used to exploit measurements of electroweak precision observables at lepton colliders (LEP, SLC), together with measurements at hadron colliders (Tevatron, LHC), and accurate theoretical predictions at the multi-loop level, to constrain the free parameters of the SM, such as the Higgs and top masses. Today, all fundamental SM parameters entering these fits are experimentally determined, including information on the Higgs couplings, and the global fits are used as powerful tools to assess the validity of the theory and to constrain scenarios for new physics.

The main goal of this section is to quantify the compatibility of the mass of the discovered boson with the electroweak precision data and its impact on the indirect determination of the W boson mass, and the top quark mass. We only briefly review the most relevant aspects of the analysis and highlight recent changes, while providing the little background knowledge used in the analysis. A detailed description of the experimental data, the theoretical calculations, and the statistical framework can be found in the Gfitter Group publications [98, 99].

4.1.1 SM fit

Global fits of the SM have traditionally combined electroweak precision observables with accurate theoretical predictions to constrain the top quark and Higgs boson masses [98–102]. The discovery of a scalar boson at the LHC [67, 68], with mass m_H around 125 GeV, provides an impressive confirmation of the light Higgs prediction derived from these fits. To this end, the Gfitter Group [37, 38] performs a global fit assuming the new boson to be the SM Higgs boson and inserting the measured mass into the fit. The result is to overconstrain the electroweak sector of the SM. Key electroweak observables such as the W boson mass, M_W, and the effective weak mixing angle for charged and neutral leptons and light quarks, $\sin^2 \theta_{\text{eff}}^f$, can thus be predicted with a precision exceeding that of the direct measurements. These observables become sensitive probes of new physics [103]

limited in part by the accuracy of the theoretical calculations.

The input data to the fit consist of measurements at the Z pole[1] by the LEP and SLD collaborations [105], the world average values for the running quark masses [106], of M_W and Γ_W [106], and an up-to-date determination of the five-quark hadronic vacuum polarisation contribution to $\alpha(M_Z^2)$, $\alpha_{\mathrm{had}}^{(5)}(M_Z^2)$ [107]. For the mass of the top quark the latest average from the direct measurements by the LHC and Tevatron experiments [41] is adopted along with the additional 0.5 GeV theoretical uncertainty. The mass of the Higgs boson m_H is taken to be the average of the results by ATLAS [108] and CMS [109], 125.14 ± 0.24 GeV.

The result of the fit is summarized in Fig. 4.1. The bands in the left graph illustrate the comparison of the global fit results with the direct measurements in units of the measurement uncertainty. In general, the global fit to all the electroweak precision data and the measured Higgs mass achieve a pretty satisfactory consistency. Only a fraction of the contribution to the "incompatibility" stems from the W-boson mass, which agrees at the 1.3σ level with the fit prediction. The largest deviation between the best fit result and the data is introduced by the known tension between $A_{\mathrm{FB}}^{0,b}$ from LEP and A_ℓ from SLD, predicting respectively a larger (by 2.5σ) and smaller (by 1.9σ) Higgs mass. For comparison, the impact of including vs. not including the two-loop result for the Z partial widths and the $\mathcal{O}(\alpha_t\alpha_s^3)$ correction to M_W is also shown.

Another important consistency test of the SM is the simultaneous indirect determination of m_t and m_W, for which a scan of the C.L. profile of M_W versus m_t is shown in Fig. 4.1 (top-right) for the scenarios where the direct m_H measurement is included in the fit (blue) or not (grey). Clearly, both contours agree with the direct measurements (green bands and ellipse for two degrees of freedom). Thus, these results are compatible with, and exceed in precision, the direct measurements.

All in all, the knowledge of the Higgs mass dramatically improves the SM predictions of several key observables.

---

[1] Recently, full fermionic two-loop calculations have become available for the partial widths and branching ratios of the Z boson [104].
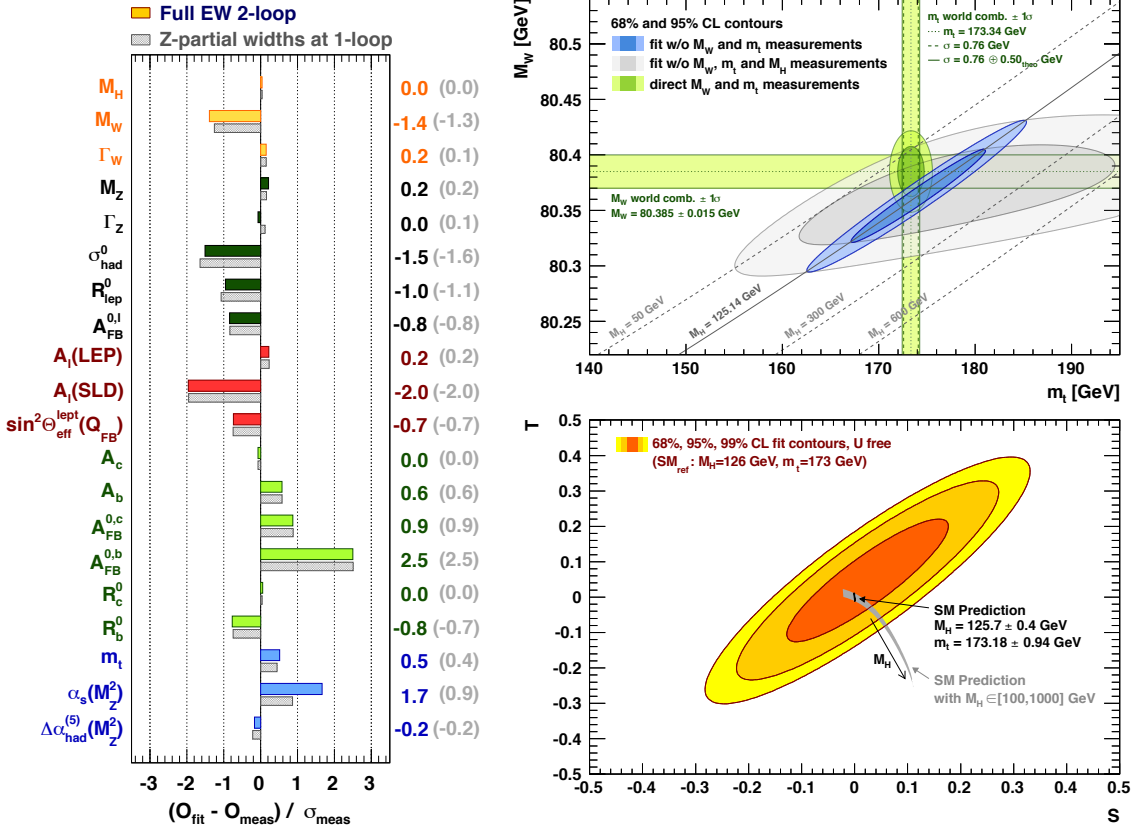
Figure 4.1. Left: Comparison of the fit results with the direct measurements in units of the experimental uncertainty. The colored, top bars from [38] include the two-loop calculations of the Z partial widths with the four-loop $\mathcal{O}(\alpha_t \alpha_s^3)$ correction to M_W, Top right: Contours at 68 and 95% C.L. obtained from scans of M_W versus m_t, for the fit including M_H (blue) and excluding M_H (grey), as compared to the direct measurements (vertical and horizontal green bands and ellipses). The theoretical uncertainty of 0.5 GeV is added to the direct top-mass measurement. In the figure, the corresponding direct measurements are excluded from the fit. Bottom right: Experimental constraints on the S and T parameters with respect to the SM reference ($M_H^{\mathrm{ref}} = 126$ GeV and $m_t^{\mathrm{ref}} = 173$ GeV). Shown are the 68%, 95% and 99% C.L. allowed regions, where the third parameter U is left unconstrained. The prediction in the SM is given by the black (gray) area when including (excluding) the new M_H measurements. *Source*: taken from Gfitter Group publications [37, 38].

4.1.2 S, T, U parameters

If the new physics scale is significantly higher than the electroweak scale, new physics effects from virtual particles in loops are expected to contribute predominantly through vacuum polarization corrections to the self-energies of the photon, Z boson, and W boson, and the mixing between the photon and the Z boson. These terms are traditionally

denoted oblique corrections, and are conveniently parametrised by a set of three measurable quantities, called S, T, U Peskin–Takeuchi parameters [110, 111], that parameterize potential new physics contributions to electroweak radiative corrections. The Peskin–Takeuchi parameters are defined so that they are all equal to zero at a reference point in the SM, with a particular value chosen for the measured Higgs boson mass. With this definition significantly non-zero S, T, U parameters represent an unambiguous indication of new physics.

Briefly speaking, the S and T parameters absorb possible new physics contributions to the neutral and to the difference between neutral and charged weak currents, respectively, and thus are both affected by varying the mass of the Higgs boson. As a result, the T parameter places a strong constraint on the mass correlations in an extended Higgs sector. In contrast, the U parameter is only sensitive to changes in the mass and width of the W boson. It tends not to be very useful in practice and is often set to zero, as the contributions to U from most new physics models are very small. This is essentially because U actually parameterizes the coefficient of a dimension-8 operator, while S and T can be represented as dimension-6 operators.

Constraints on the S, T, U parameters are extracted from a global fit to the high-precision electroweak data from particle collider experiments (mostly the Z pole LEP data) and atomic parity violation by calculating the difference of the oblique corrections as determined from the experimental data and the corrections obtained from a SM reference point (with fixed reference values of m_t and m_H).

The results of the study [38], choosing the SM reference as $m_H^{\text{ref}} = 125$ GeV and $m_t^{\text{ref}} = 173$ GeV, are

$$S = 0.05 \pm 0.11, \quad T = 0.09 \pm 0.13, \quad U = 0.01 \pm 0.11, \tag{4.1}$$

with correlation coefficients of $+0.90$ between S and T, -0.59 (-0.83) between S and U (T and U). The constraints at the 68%, 95% and 99% CL on S and T for an unconstrained U are shown in Fig. 4.1 (bottom right). For illustration also the SM prediction is shown. The m_H measurement reduces the allowed SM area from the grey sickle to the narrow black strip at about $S = T = 0$, which accounts for the propagation of the current

experimental uncertainties in m_H and m_t upon the SM prediction.

4.2 Electroweak vacuum

To be completed if needed.

4.3 Gauge hierarchy problem

One might argue the naive possibility is to assume that the SM remains valid even beyond scales at which it has been directly tested. There are a number of plausible reasons, particularly from the running of SM gauge coupling constants and the lifetime of the proton, to expect that a grand unified theory (GUT) could appear at a scale of 10^{14} GeV. Obviously, this GUT scale is much larger than the scale of weak interactions, which is approximately $v \sim 250$ GeV, and hence there is an energy desert all the way up a scale of 10^{14} GeV from the world of known SM particles. To physicists this scenario seems highly unlikely. On the other hand, this simplest hypothesis gives rise to a theoretical flaw: why is the Higgs boson so much lighter than the Planck mass (or a bit lower GUT scale)? This is one of the ways to define the "hierarchy problem" in the language of particle physics. One would expect that the large quantum contributions to the square of the Higgs boson mass would inevitably make the mass huge, comparable to the scale at which new physics appears, unless there is an incredible fine-tuning cancellation between the quadratic radiative corrections and the bare mass. This is actually the strongest evidence to convince ourselves that new physics should emerge at the TeV scale.

Suppose the SM has a cutoff Λ and unknown physics resides in the gauge couplings, Yukawa couplings and the Higgs potential. These parameters are derived from a more complete theory at a higher energy scale M. The energy scale of the SM or the mass of every ordinary particle in the standard model is proportional to the VEV of the Higgs field. This is not a new parameter, but is obtained by minimizing the Higgs potential.

$$V(H) = -m_H^2 H^2 + \lambda H^4 \tag{4.2}$$

in which m_H and λ represent the renormalized mass and couplings, respectively, that are actually measured. To make a prediction for the measured Higgs mass which is no
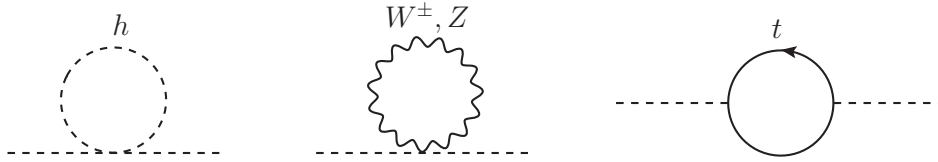
Figure 4.2. Quantum corrections to the SM Higgs boson

longer a free parameter after the discovery, we must calculate the corrections to the Higgs mass coming from the quadratically divergent diagrams, that are shown in Fig. 4.3. They include vacuum corrections to the Higgs mass from predominantly top quark loops, W and Z boson loops and from the Higgs itself. Regularizing them in a proper way and applying the renormalization scheme, one finds that the quantum corrections to the Higgs mass m_H^2 take the following form:

$$\underbrace{m_H^2}_{\sim \lambda v^2} = m_{\text{bare}}^2 + \underbrace{\frac{1}{16\pi^2}\lambda\Lambda^2 + \frac{1}{16\pi^2}g^2\Lambda^2 - \frac{3}{8\pi^2}y_t^2\Lambda^2}_{\text{quadratically-divergent radiative correction}} \tag{4.3}$$

The above expression indeed proves that the diagrams in Fig. 4.3 are all quadratically dependent on the cutoff. The potential of Eq. (4.2) gives $m_H = \sqrt{2\lambda}v$, which is approximately at the 10^2 GeV order of v for λ of order unity. On the other hand, suppose the SM is assumed to be an effective field theory with very heavy particles, for instance, some grand unified theory to replace the standard model at a scale of $\Lambda = 10^{14}$ GeV $\gg v$. Then the bare Higgs mass parameter would have to be finely tuned to 26 decimal places in order to cancel the complicated series thereby realizing a low energy scale and a small physical Higgs mass and the light masses of the known standard model particles. In addition, one would expect the fraction $m_{\text{bare}}^2/\Lambda^2$ to depend on the structure of the high energy scale theory and not that it is finely tuned to produce low energy scale physics. So it seems unnatural that a theory such as the standard model with an energy scale v has a more fundamental energy scale which is many orders of magnitude higher. This is known as the hierarchy problem. Physically, it arises from the fact that there are quadratically divergent loop contributions to the Higgs mass which drive the Higgs mass to unacceptably large values unless the tree level mass parameter is finely tuned to cancel the large quantum corrections.

Given this hierarchy problem one would expect that new physics should appear on an energy scale not too far away from that of the standard model. It is possible and instructive to make a rough estimate of the scale at which new physics may appear. At the LHC the 1-10 TeV energy scale will be probed directly for the first time. Thus an important question to answer is whether it is natural for the SM to be valid up to these scales (or if we can expect to discover new physics at the LHC). To make the argument, let us assume that the SM is valid up to a cut-off scale of $\Lambda = 10$ TeV. At even higher energies new physics takes over, which implies that we do not know how to compute loop diagrams with momenta larger than Λ, thus we will cut such loops off at Λ. This leads to a fine tuning of approximately one part in a hundred of the Higgs mass and thus of the electroweak scale that is sketched in Fig. 4.3. It is also important to note that the fine-tuning required is much greater as the cutoff Λ increases. Todays most powerful particle accelerators have probed up to energies of approximately 1 TeV. Taking Λ to be 1 TeV we find the most dangerous corrections of approximately $-(200 \text{ GeV})^2$ from the top loop, $(75 \text{ GeV})^2$ from weak gauge boson loops and $(45 \text{ GeV})^2$ from the Higgs self interaction diagram. Therefore, one can conclude that with a cut-off of 1 TeV no fine tuning is required, the SM with no new physics up to 1 TeV is perfectly natural. So we should not be surprised that we have not yet seen deviations from it at colliders. Finally, an estimate of the scale at which new physics should appear in order to avoid fine tuning of the electro-weak scale can be made by proposing a fine tuning of no more than 10 percent. This leads to a cut-off Λ of approximately 2 TeV. So it is to be expected that new particles exist and that these particles have masses of approximately 2 TeV.

In order for these particles to cancel the quadratic divergences caused by standard model corrections one might suggest that these new particles are related to the standard model particles by a symmetry. One popular and (partly) successful solution to the hierarchy problem is supersymmetry. In supersymmetric theories the quadratically divergent diagrams are cancelled by diagrams with superpartners running in the loops. Speaking colloquially, these cancellations occur because superpartners have opposite spin-statistics.

One proposed solution, popular amongst many physicists, is that one may solve the
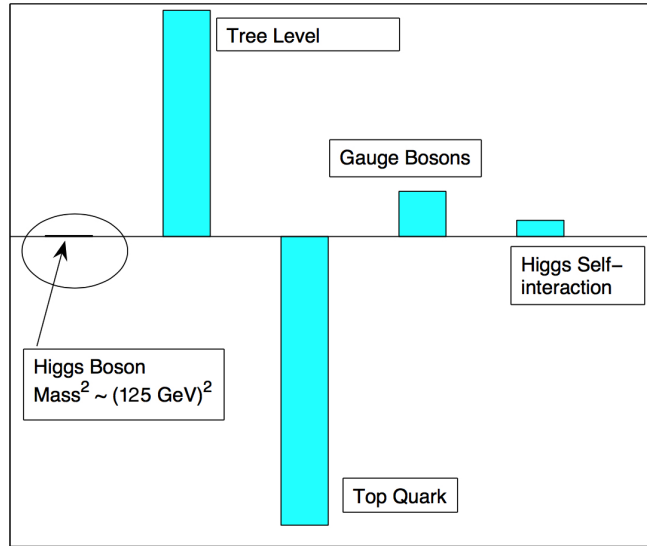
Figure 4.3. A graphical illustration of the fine tuning of the Higgs boson mass in a standard model with a cut-off of $\Lambda = 10$ TeV.

hierarchy problem via supersymmetry. Supersymmetry can explain how a tiny Higgs mass can be protected from quantum corrections. Supersymmetry removes the power-law divergences of the radiative corrections to the Higgs mass and solves the hierarchy problem as long as the supersymmetric particles are light enough. This still leaves open the μ problem, however. Currently the tenets of supersymmetry are being tested at the LHC, although no evidence has been found so far for supersymmetry.

Another sound solution is to introduce an extra dimension, which is first studied in the Randall-Sundrum (RS) model in which a single warped extra dimension is introduced to alternatively resolve the hierarchy problem of the SM. An interesting part of this is that the hierarchy problem is automatically solved. The main scale on the Planck brane would be the Planck scale. However, the change by 16 units causes the scales to change by 16 orders of magnitude. On the Planck brane, strings would be 10^{33} cm in size, but on the Tev brane they would be 10^{17} cm. In fact, this makes the mass scale for the Weak brane of order a TeV. Therefore, you no longer have the strange range of masses and energies.

4.4 Implications for new physics beyond the SM

The minimal version of the SM contains one complex Higgs doublet, resulting in one physical neutral CP-even Higgs boson after electroweak symmetry breaking (EWSB). Therefore, the discovery of the SM Higgs boson is a milestone in the quest to understand EWSB and has put the final piece of the SM in place. To date, fits of the Higgs couplings performed by ATLAS [77] and CMS [78] show no deviations from SM expectations. (A combined global fit of the Higgs couplings based on the run-1 results was performed by a collaboration of which I was a member in [112].) However, conceptually there is no reason why the Higgs sector should be minimal and the SM is not necessarily the ultimate theoretical structure responsible for EWSB.

Indeed, although the SM of electroweak interactions with the inclusion of a 125 GeV Higgs boson appears to describe physics extremely well down to the smallest distance scales yet probed and also does not lead to an unstable Universe where we live in, it leaves many serious questions (in addition to the hierarchy problem addressed in Section 4.3) unsolved and cannot completely describe all observed phenomena. For example one might wonder about neutrino masses, values of fundamental constants and couplings, the origin of families or the exact charge relations between various particles. An even greater question might be: what is the role of gravity in all this? For now it seems that only general relativity correctly describes the physics of gravity and perhaps string theory. Therefore, while the SM is a very good approximation to the full theory of elementary particles and forces at low energy scales, it is believed to be only a component of a more complete theory. At some energy it must give way to a more fundamental theory. This is perhaps a grand unified theory or string theory or something else (not yet considered).

Theories that go beyond the SM (for instance supersymmetry (SUSY) and Higgs-multiplet models) typically require an extended Higgs sector. Such a non-minimal Higgs sector, although stringently constrained by the LHC run-1 data, is theoretically very attractive and a manifestation of new physics. If confirmed, it would shine light on the mechanism of EWSB dynamics. Therefore, it is particularly interesting and relevant to study models with extended Higgs sectors, such as doublet and/or singlet extensions of the

SM. Meanwhile, it is important to assess all possibilities for other Higgs-like states that may have escaped detection at the run-1. Appealing models of our particular attention for such consideration in Part II are two-Higgs-doublet model (2HDM) and the next-to-supersymmetric SM (NMSSM). The former is an especially simple extension beyond the SM, while the latter has the least fine-tuning problem in the framework of SUSY.

In addition to likely representing a smoking gun for an extended Higgs sector, this discovery could also have far-reaching implications for our understanding of how Nature works at its most fundamental level, including connections with dark matter and other cosmological problems. In fact, apart from the big questions listed above, one of most outstanding failures of the SM is the lack of a candidate for dark matter (DM). As of today the constitution of DM remains unknown. However, there are various strong evidences for the existence of DM from cosmological and astrophysical observations. To account for these hints, there are many candidates which have been proposed for DM in a variety of BSM theories. With protection by an extra discrete symmetry, a certain non-SM scalar boson (Higgs partner) could be a possible DM candidate. In Part III we will provide two typical examples of DM for illustration, the lightest neutralino supersymmetric DM and the Higgs-portal scalar DM in the singlet extension of the two-Higgs-doublet model. Beyond the SM the Higgs sector and DM sector may be intimately connected. If so, detecting signs of an extended Higgs sector could shine light on still hidden elements of the DM sector, and vice versa. Thus, it is also of interest to explore the implications of recent developments in hunting for (additional) Higgs bosons and detecting DM in the context of a particularly simple model.

CHAPTER 5

BSM alternative I: two-Higgs-doublet model

Now that a new particle has been discovered at the LHC with properties close to those of the SM Higgs boson, it is clear that models with an extended Higgs sector will be significantly constrained by the data. In particular, it is worthwhile and important to assess in this context all possibilities for other Higgs-like states that may have escaped detection at run-1 of the LHC. Two-Higgs-doublet models are an especially simple and appealing framework for such considerations.

The study in this chapter is limited to the CP-conserving 2HDM of Type I and Type II. Following a brief overview of the model, I will present the Higgs potential in various parameterizations and derive the mass spectrum and couplings for Higgs bosons. Next, I provide an efficient strategy for scanning over the model parameters so as to perform a very comprehensive and complete analysis of the status of the CP-conserving 2HDMs of Type I and Type II. Very often I concentrate on both the case where the observed Higgs particle at the LHC is the lighter CP-even state h and that where it is the heavier CP-even state H.[1] To address this, an elaborate study on the specially important limit

---

[1]Given that the observed state clearly has ZZ, WW couplings that are not far from SM-like, it cannot be identified with the CP-odd pseudoscalar A which has no VV tree-level couplings.

called the alignment limit is included. In addition, implications for future experiments, including expectations regarding other lighter or heavier Higgs bosons will be discussed. In particular, we explore the possibilities for Higgs states with mass below about 60 GeV, *i.e.* less than half of the ~ 125 GeV mass of the observed SM-like Higgs boson. Finally, a novel case of degenerate scalar masses at ~ 125 GeV [2, 113] is sketched briefly.

5.1 General model description

Beyond the SM, the two-Higgs-doublet model (2HDM) provides one of the simplest structures for an extended Higgs sector. It employs a second Higgs doublet with the same hypercharge $Y = 1/2$ as that in the SM and provides more physical Higgs mass eigenstates. In particular, the Type II model is also realized in the minimal supersymmetric SM. This model has attracted a lot of attention recently. A large number of papers [114–123] performed fits of current data for the 125.5 GeV Higgs-like state (as per the status post Moriond 2013) within the context of 2HDMs, and investigated the consequent phenomenology of the other Higgs states present in the model. Among these papers, [115, 116, 118] consider 2HDMs with a conserved Z_2 symmetry, [120, 121, 124, 125] focus on the case of an aligned 2HDM, [119, 123] investigate the possibility of CP-violation in the Higgs sector, and [122] concentrates on the question of the triple-Higgs coupling. The general conditions for the alignment limit, in which the lightest CP-even Higgs boson of a 2HDM mimics the Standard Model Higgs, without decoupling the other scalars were studied in [126]. Previous studies of alignment without decoupling scenarios in the light of the LHC Higgs results were conducted in [124, 126, 127]. The specific case of additional light Higgs states in 2HDMs with mass below $\sim 125/2$ GeV was studied in [9]. Moreover, the prospects for future LHC running and/or for other future colliders in view of the current data were investigated in [124, 125, 128–130]. The possibility of CP violation in 2HDMs also implies an important link of such models to electroweak baryogenesis, a topic that was revisited recently in [131–134].

In this section, we review the theoretical structure of the two-Higgs doublet model. Comprehensive reviews of the model can also be found in, *e.g.*, [39, 44, 135]. In order

to avoid tree-level Higgs-mediated flavor changing neutral currents (FCNCs), we shall impose a Type-I or II structure on the Higgs-fermion interactions. This structure can be naturally implemented [136, 137] by imposing a discrete $\mathbb{Z}_2$ symmetry on the dimension-four terms of the Higgs Lagrangian. This discrete symmetry is softly-broken by mass terms that appear in the Higgs scalar potential. Nevertheless, the absence of tree-level Higgs-mediated FCNCs is maintained, and FCNC effects generated at one loop are all small enough to be consistent with phenomenological constraints over a significant fraction of the 2HDM parameter space [138–141].

Even with the imposition of the softly-broken discrete $\mathbb{Z}_2$ symmetry mentioned above, new CP-violating phenomena in the Higgs sector are still possible, either explicitly due to a physical complex phase that cannot be removed from the scalar potential parameters or spontaneously due to a CP-violating vacuum state. To simplify the analysis in this paper, we shall assume that these CP-violating effects are absent, in which case one can choose a basis of scalar doublet Higgs fields such that all scalar potential parameters and the two neutral Higgs field vacuum expectation values are simultaneously real. Moreover, we assume that only the neutral Higgs fields acquire non-zero vacuum expectation values, i.e. the scalar potential does not admit the possibility of stable charge-breaking minima [142, 143].

We first exhibit the Higgs scalar potential, the corresponding Higgs scalar spectrum and the Higgs-fermion interactions subject to the restrictions discussed above. Motivated by the Higgs data, we then examine the conditions that yield an approximately SM-like Higgs boson.

5.1.1 Higgs scalar sector potential

As will be seen, there are a number of different bases one can employ to specify the parameters of the Higgs sector. Each one has its own purposes and particular advantages despite the fact that some are less used. A full list of the available parameterizations, and their corresponding parameters, is given in Table 5.1. In the following we will discuss the form of the scalar potential and Higgs mass spectrum in the individual bases and also provide the conversion relation among the parameters used in different bases.

Table 5.1. Input parameters for the Higgs potential in different bases and parametrizations.

Type	Free parameters	Comment
General basis	$\lambda_1,\ \lambda_2,\ \lambda_3,\ \lambda_4,\ \lambda_5,\ \lambda_6,\ \lambda_7,\ m_{12}^2,\ \tan\beta$	General potential, Eq. (5.1)
HHG	$\Lambda_1,\ \Lambda_2,\ \Lambda_3,\ \Lambda_4,\ \Lambda_5,\ \Lambda_6,\ \tan\beta$	Z_2-symmetry only softly broken
Higgs basis	$\Lambda_1,\ \Lambda_2,\ \Lambda_3,\ \Lambda_4,\ \Lambda_5,\ \Lambda_6,\ \Lambda_7,\ m_{H^\pm}$	$\tan\beta = 0$
Physical basis	$m_h,\ m_H,\ m_A,\ m_{H^\pm},\ s_{\beta-\alpha},\ \lambda_6,\ \lambda_7,\ m_{12}^2,\ \tan\beta$	Physical masses

- *The general basis*

We first parametrize the scalar potential in the general basis, that is the most widely used parametrization when studying the theoretical structure of the 2HDM. Let Φ_1 and Φ_2 denote two complex $SU(2)_L$ doublet scalar fields with the same hypercharge $Y = 1/2$. The most general renormalizable scalar potential compatible with gauge invariance is

$$
\begin{aligned}
\mathcal{V} =\ & m_{11}^2 \Phi_1^\dagger \Phi_1 + m_{22}^2 \Phi_2^\dagger \Phi_2 - \left[m_{12}^2 \Phi_1^\dagger \Phi_2 + \text{h.c.} \right] \\
& + \frac{1}{2}\lambda_1 \left(\Phi_1^\dagger \Phi_1 \right)^2 + \frac{1}{2}\lambda_2 \left(\Phi_2^\dagger \Phi_2 \right)^2 + \lambda_3 \left(\Phi_1^\dagger \Phi_1 \right)\left(\Phi_2^\dagger \Phi_2 \right) + \lambda_4 \left(\Phi_1^\dagger \Phi_2 \right)\left(\Phi_2^\dagger \Phi_1 \right) \\
& + \left\{ \frac{1}{2}\lambda_5 \left(\Phi_1^\dagger \Phi_2 \right)^2 + \left[\lambda_6 \left(\Phi_1^\dagger \Phi_1 \right) + \lambda_7 \left(\Phi_2^\dagger \Phi_2 \right) \right]\left(\Phi_1^\dagger \Phi_2 \right) + \text{h.c.} \right\},
\end{aligned}
\tag{5.1}
$$

In general, m_{12}^2, λ_5, λ_6 and λ_7 can be complex. As earlier noted, in order to avoid tree-level Higgs-mediated FCNCs, we impose a discrete $\mathbb{Z}_2$ symmetry, $\Phi_1 \rightarrow +\Phi_1$ and $\Phi_2 \rightarrow -\Phi_2$ on the quartic terms of Eq. (5.1), which implies that $\lambda_6 = \lambda_7 = 0$. However, we allow a "soft" $\mathbb{Z}_2$ symmetry breaking so that $m_{12}^2 \neq 0$. [2] Furthermore, to avoid explicit $\mathcal{CP}$ violation in the Higgs sector, all λ_i and m_{12}^2 are assumed to be real.

The scalar fields will develop non-zero vacuum expectation values if the mass matrix m_{ij}^2 has at least one negative eigenvalue. We assume that the parameters of the scalar potential are chosen such that the minimum of the scalar potential respects the $U(1)_{em}$ gauge symmetry. Then, the scalar field vacuum expectations values are of the form

$$
\langle \Phi_1 \rangle = \frac{1}{\sqrt{2}} \begin{pmatrix} 0 \\ v_1 \end{pmatrix} \qquad \langle \Phi_2 \rangle = \frac{1}{\sqrt{2}} \begin{pmatrix} 0 \\ e^{i\xi} v_2 \end{pmatrix}.
\tag{5.2}
$$

---

[2] Unlike the Z_2 symmetric 2HDM which constrains $\tan\beta \lesssim 7$ [128], high $\tan\beta$ values are allowed when the Z_2 symmetry is softly broken.

For real parameters, the phase ξ could still be non-zero if the vacuum breaks $\mathcal{CP}$ spontaneously. We avoid parameter choices for which this happens and take $\xi = 0$. [3] In this case, the squared-mass parameters m_{11}^2 and m_{22}^2 can be eliminated by minimizing the scalar potential.

$$m_{11}^2 = m_{12}^2 t_\beta - \tfrac{1}{2}v^2 \left(\lambda_1 c_\beta^2 + \lambda_{345} s_\beta^2\right), \tag{5.3}$$

$$m_{22}^2 = m_{12}^2 t_\beta^{-1} - \tfrac{1}{2}v^2 \left(\lambda_2 s_\beta^2 + \lambda_{345} c_\beta^2\right), \tag{5.4}$$

where we have defined:

$$\lambda_{345} \equiv \lambda_3 + \lambda_4 + \lambda_5, \qquad t_\beta \equiv \tan\beta \equiv \frac{v_2}{v_1}, \tag{5.5}$$

where, by convention, $0 \leq \beta \leq \pi/2$ is chosen, and

$$v^2 \equiv v_1^2 + v_2^2 = \frac{4m_W^2}{g^2} = (246 \text{ GeV})^2. \tag{5.6}$$

Then, we expand the Φ_1 and Φ_2 fields w.r.t. their VEVs, respectively

$$\Phi_a = \begin{pmatrix} \phi_a^+ \\ (v_a + \rho_a + i\eta_a)/\sqrt{2} \end{pmatrix} \qquad a = 1, 2 \tag{5.7}$$

Of the original eight scalar degrees of freedom, three Goldstone bosons ($G^\pm$ and $G^0 = \eta_1 \cos\beta + \eta_2 \sin\beta$) are absorbed ("eaten") by the $W^\pm$ and Z, via electroweak symmetry breaking (EWSB), like what happens in the SM. The remaining five physical Higgs particles are: two CP-even scalars (h and H, with $m_h \leq m_H$), one CP-odd scalar (A) and a charged Higgs pair ($H^\pm$). The physical pseudoscalar state is

$$A = -\eta_1 \sin\beta + \eta_2 \cos\beta. \tag{5.8}$$

and the resulting squared-masses for the CP-odd and charged Higgs states are

$$m_A^2 = \overline{m}^2 - \lambda_5 v^2, \tag{5.9}$$

$$m_{H^\pm}^2 = m_A^2 + \tfrac{1}{2}v^2(\lambda_5 - \lambda_4), \tag{5.10}$$

---

[3]As noted in Appendix B of Ref. [39], if $|m_{12}^2| \geq \lambda_5|v_1||v_2|$, then the vacuum is CP-conserving and the vacuum expectation values v_1 and v_2 can be chosen to be non-negative without loss of generality.

where[4]

$$\overline{m}^2 \equiv \frac{2m_{12}^2}{s_{2\beta}} . \tag{5.11}$$

As for neutral CP-even states, ρ_1 and ρ_2 mix with each other according to the following squared-mass matrix:

$$\mathcal{M}^2 \equiv \begin{pmatrix} \lambda_1 v^2 c_\beta^2 + (m_A^2 + \lambda_5 v^2)s_\beta^2 & [\lambda_{345}v^2 - (m_A^2 + \lambda_5 v^2)]s_\beta c_\beta \\ [\lambda_{345}v^2 - (m_A^2 + \lambda_5 v^2)]s_\beta c_\beta & \lambda_2 v^2 s_\beta^2 + (m_A^2 + \lambda_5 v^2)c_\beta^2 \end{pmatrix} . \tag{5.12}$$

Rotating into the physical scalars (h, H):

$$\begin{pmatrix} h \\ H \end{pmatrix} = \begin{pmatrix} -\sin\alpha & \cos\alpha \\ \cos\alpha & \sin\alpha \end{pmatrix} \begin{pmatrix} \rho_1 \\ \rho_2 \end{pmatrix} \tag{5.13}$$

the masses and mixing angle α are found from the diagonalization process

$$\begin{pmatrix} m_H^2 & 0 \\ 0 & m_h^2 \end{pmatrix} = \begin{pmatrix} c_\alpha & s_\alpha \\ -s_\alpha & c_\alpha \end{pmatrix} \begin{pmatrix} \mathcal{M}_{11}^2 & \mathcal{M}_{12}^2 \\ \mathcal{M}_{12}^2 & \mathcal{M}_{22}^2 \end{pmatrix} \begin{pmatrix} c_\alpha & -s_\alpha \\ s_\alpha & c_\alpha \end{pmatrix}$$

$$= \begin{pmatrix} \mathcal{M}_{11}^2 c_\alpha^2 + 2\mathcal{M}_{12}^2 c_\alpha s_\alpha + \mathcal{M}_{22}^2 s_\alpha^2 & \mathcal{M}_{12}^2(c_\alpha^2 - s_\alpha^2) + (\mathcal{M}_{22}^2 - \mathcal{M}_{11}^2)s_\alpha c_\alpha \\ \mathcal{M}_{12}^2(c_\alpha^2 - s_\alpha^2) + (\mathcal{M}_{22}^2 - \mathcal{M}_{11}^2)s_\alpha c_\alpha & \mathcal{M}_{11}^2 s_\alpha^2 - 2\mathcal{M}_{12}^2 c_\alpha s_\alpha + \mathcal{M}_{22}^2 c_\alpha^2 \end{pmatrix} \tag{5.14}$$

Explicitly, the diagonal elements of the squared-masses matrix are given by [5]

$$m_{H,h}^2 = \tfrac{1}{2}\left[\mathcal{M}_{11}^2 + \mathcal{M}_{22}^2 \pm \Delta\right], \tag{5.16}$$

where $m_h \leq m_H$ and the non-negative quantity Δ is defined by

$$\Delta \equiv \sqrt{(\mathcal{M}_{11}^2 - \mathcal{M}_{22}^2)^2 + 4(\mathcal{M}_{12}^2)^2} . \tag{5.17}$$

---

[4]Here and in the following, we use the shorthand notation $c_\beta \equiv \cos\beta$, $s_\beta \equiv \sin\beta$, $c_\alpha \equiv \cos\alpha$, $s_\alpha \equiv \sin\alpha$, $c_{2\beta} \equiv \cos 2\beta$, $s_{2\beta} \equiv \cos 2\beta$, $\cos(\beta - \alpha) \equiv \cos(\beta - \alpha)$, $\sin(\beta - \alpha) \equiv \sin(\beta - \alpha)$, etc.

[5] This is the solution of

$$|\mathcal{M}_{12}^2| = \sqrt{(m_H^2 - \mathcal{M}_{11}^2)(\mathcal{M}_{11}^2 - m_h^2)} = \sqrt{(\mathcal{M}_{22}^2 - m_h^2)(\mathcal{M}_{11}^2 - m_h^2)} .$$

that is derived from the two conditions for which the mass matrix $\mathcal{M}$ is diagonal.

$$\text{Tr } \mathcal{M}^2 = m_H^2 + m_h^2, \qquad \det \mathcal{M}^2 = m_H^2 m_h^2 . \tag{5.15}$$

The mixing angle α, which is defined modulo π, is evaluated by setting the off-diagonal elements of the CP-even scalar squared-mass matrix Eq. (5.14) to zero. It is often convenient to restrict the range of the mixing angle to $|\alpha| \leq \frac{1}{2}\pi$.[6] In this case, c_α is non-negative and is given by

$$c_\alpha = \sqrt{\frac{\Delta + \mathcal{M}_{11}^2 - \mathcal{M}_{22}^2}{2\Delta}} = \sqrt{\frac{\mathcal{M}_{11}^2 - m_h^2}{m_H^2 - m_h^2}}, \tag{5.18}$$

and the sign of s_α is given by the sign of $\mathcal{M}_{12}^2$. Explicitly, we have

$$s_\alpha = \frac{\sqrt{2}\,\mathcal{M}_{12}^2}{\sqrt{\Delta(\Delta + \mathcal{M}_{11}^2 - \mathcal{M}_{22}^2)}} = \text{sgn}(\mathcal{M}_{12}^2)\sqrt{\frac{m_H^2 - \mathcal{M}_{11}^2}{m_H^2 - m_h^2}}. \tag{5.19}$$

In deriving Eqs. (5.18) and (5.19), we have assumed that $m_h \neq m_H$. The case of $m_h = m_H$ is singular; in this case, the angle α is undefined since any two linearly independent combinations of h and H can serve as the physical states. In the rest of this chapter except for Section 5.8, we shall not consider this mass-degenerate case further.

- *The HHG basis*

An alternative parametrization of the scalar potential is given in the Higgs Hunter's Guide (HHG) [44] and was originally introduced in [144]. This parametrization only allows for soft breaking of the Z_2 symmetry, equivalent to forcing $\lambda_6 = \lambda_7 = 0$ in the general potential. Although it explicitly exhibits the scalar potential minimum, the HHG parametrization obscures the decoupling limit.

In the HHG parametrization, the most general gauge invariant Higgs potential of the CP conserving 2HDMcompatible, subject to a discrete symmetry $\Phi_2 \to -\Phi_2$ that is only softly violated by dimension-two terms, is given by [44, 145, 146][7]

$$\begin{aligned} V = {} & \Lambda_1(|\Phi_1|^2 - V_1^2)^2 + \Lambda_2(|\Phi_2|^2 - V_2^2)^2 + \Lambda_3[(|\Phi_1|^2 - V_1^2) + (|\Phi_2|^2 - V_2^2)]^2 \\ & + \Lambda_4[|\Phi_1|^2|\Phi_2|^2 - |\Phi_1^\dagger \Phi_2|^2] + \Lambda_5[\text{Re}(\Phi_1^\dagger \Phi_2) - V_1 V_2]^2 + \Lambda_6[\text{Im}(\Phi_1^\dagger \Phi_2)]^2 \end{aligned} \tag{5.20}$$

where the Λ_i are real parameters. The VEVs of the two Higgs–doublet fields $V_{1,2}$ are related to the $v_{1,2}$ of eq. (5.2) by $V_{1,2} = v_{1,2}/\sqrt{2}$. The relations between the λ_i and Λ_i in

---

[6]Without loss of generality, one can assume that the mixing angle α varies between $-\pi/2$ and $\pi/2$. We choose our independent variables to be $\tan\beta$ and $\sin\alpha$, which are single valued in the allowed ranges.

[7] To distinguish the notation in the general basis, we employ the symbols V_i and Λ_i in the HHG basis.

the two bases can be found in Appendix A of [39].

$$\Lambda_1 = \tfrac{1}{2}\left[\lambda_1 - \lambda_{345} + 2m_{12}^2/(v^2 s_\beta c_\beta)\right],$$

$$\Lambda_2 = \tfrac{1}{2}\left[\lambda_2 - \lambda_{345} + 2m_{12}^2/(v^2 s_\beta c_\beta)\right],$$

$$\Lambda_3 = \tfrac{1}{2}\left[\lambda_{345} - 2m_{12}^2/(v^2 s_\beta c_\beta)\right],$$

$$\Lambda_4 = 2m_{12}^2/(v^2 s_\beta c_\beta) - \lambda_4 - \lambda_5,$$

$$\Lambda_5 = 2m_{12}^2/(v^2 s_\beta c_\beta),$$

$$\Lambda_6 = 2m_{12}^2/(v^2 s_\beta c_\beta) - 2\lambda_5, \tag{5.21}$$

where $\lambda_{345} \equiv \lambda_3 + \lambda_4 + \lambda_5$ and $v^2 s_\beta c_\beta = 2V_1 V_2$. Note that we have also assumed that the discrete symmetry $\Phi_2 \to -\Phi_2$ is only broken softly; an additional term, $\Lambda_7[\mathrm{Re}(\Phi_1^\dagger \Phi_2) - v_1 v_2]\mathrm{Im}(\Phi_1^\dagger \Phi_2)$, can be eliminated by redefining the phases of the scalar fields [147]. Using the same parameterization for the Higgs doublets as in Eq. (5.7), one obtains for the mass terms in the CP–even Higgs sector

$$(\rho_1, \rho_2) \begin{pmatrix} 4(\Lambda_1 + \Lambda_3)V_1^2 + \Lambda_5 V_2^2 & (4\Lambda_3 + \Lambda_5)V_1 V_2 \\ (4\Lambda_3 + \Lambda_5)V_1 V_2 & 4(\Lambda_2 + \Lambda_3)V_2^2 + \Lambda_5 V_1^2 \end{pmatrix} \begin{pmatrix} \rho_1 \\ \rho_2 \end{pmatrix} \tag{5.22}$$

while in the CP–odd and charged Higgs sectors, one has

$$\Lambda_6(\eta_1, \eta_2) \begin{pmatrix} V_2^2 & -V_1 V_2 \\ -V_1 V_2 & V_1^2 \end{pmatrix} \begin{pmatrix} \eta_1 \\ \eta_2 \end{pmatrix}, \quad \Lambda_4(\phi_1^-, \phi_2^-) \begin{pmatrix} V_2^2 & -V_1 V_2 \\ -V_1 V_2 & V_1^2 \end{pmatrix} \begin{pmatrix} \phi_1^+ \\ \phi_2^+ \end{pmatrix} \tag{5.23}$$

Diagonalizing the mass matrices and using Eq. (5.15) one obtains the physical masses of the Higgs bosons, which in the case of the pseudoscalar and charged Higgs bosons read

$$M_A^2 = \Lambda_6 V^2 \quad \text{and} \quad M_{H^\pm}^2 = \Lambda_4 V^2 \tag{5.24}$$

where $V^2 \equiv V_1^2 + V_2^2 = (174 \text{ GeV})^2$; the mixing angle α in the CP–even Higgs sector is obtained from the mass matrix using the relations given in Eqs. (5.18) and (5.19). Inverting these relations, one obtains the Λ's in terms of the Higgs masses, and the angles

α and β [44]

$$
\begin{aligned}
\Lambda_1 &= \frac{1}{4\cos^2\beta v^2}(\cos^2\alpha M_H^2 + \sin^2\alpha M_h^2) - \frac{\sin 2\alpha}{\sin 2\beta}\frac{M_H^2 - M_h^2}{4v^2} + \frac{\Lambda_5}{4}(1 - \frac{\sin^2\beta}{\cos^2\beta}) \,, \\
\Lambda_2 &= \frac{1}{4\sin^2\beta v^2}(\sin^2\alpha M_H^2 + \cos^2\alpha M_h^2) - \frac{\sin 2\alpha}{\sin 2\beta}\frac{M_H^2 - M_h^2}{4v^2} + \frac{\Lambda_5}{4}(1 - \frac{\cos^2\beta}{\sin^2\beta}) \,, \\
\Lambda_3 &= \frac{\sin 2\alpha}{\sin 2\beta}\frac{M_H^2 - M_h^2}{4v^2} - \frac{\Lambda_5}{4} \,, \quad \Lambda_4 = \frac{M_{H^\pm}^2}{v^2} \,, \quad \Lambda_6 = \frac{M_A^2}{v^2}
\end{aligned}
\tag{5.25}
$$

- *The physical basis.*

Another very useful basis is the physical basis. Inheriting the nature of its name, in the physical basis the Higgs masses are given as input together with the invariant $s_{\beta-\alpha}$.

Analogous to Eq. (5.25), we can solve for the scalar potential parameters $\lambda_1, \ldots, \lambda_5$ in the general basis in terms of the physical Higgs masses and the remaining m_{12}^2 variable. [8]

$$
\lambda_1 = \frac{m_H^2 c_\alpha^2 + m_h^2 s_\alpha^2 - m_{12}^2 t_\beta}{v^2 c_\beta^2} \,,
\tag{5.26}
$$

$$
\lambda_2 = \frac{m_H^2 s_\alpha^2 + m_h^2 c_\alpha^2 - m_{12}^2 t_\beta^{-1}}{v^2 s_\beta^2} \,,
\tag{5.27}
$$

$$
\lambda_3 = \frac{(m_H^2 - m_h^2)c_\alpha s_\alpha + 2m_{H^\pm}^2 s_\beta c_\beta - m_{12}^2}{v^2 s_\beta c_\beta}
\tag{5.28}
$$

$$
\lambda_4 = \frac{(m_A^2 - 2m_{H^\pm}^2)s_\beta c_\beta + m_{12}^2}{v^2 s_\beta c_\beta} \,,
\tag{5.29}
$$

$$
\lambda_5 = \frac{m_{12}^2 - m_A^2 s_\beta c_\beta}{v^2 s_\beta c_\beta} \,.
\tag{5.30}
$$

In addition, the minimization conditions of Eqs. (5.3) and (5.4) reduce to:

$$
m_{11}^2 = -\frac{1}{2c_\beta}\left(m_H^2 c_\alpha \cos(\beta - \alpha) - m_h^2 s_\alpha \sin(\beta - \alpha)\right) + m_{12}^2 t_\beta \,,
\tag{5.31}
$$

$$
m_{22}^2 = -\frac{1}{2s_\beta}\left(m_h^2 c_\alpha \sin(\beta - \alpha) + m_H^2 s_\alpha \cos(\beta - \alpha)\right) + m_{12}^2 t_\beta^{-1} \,.
\tag{5.32}
$$

Note that λ_6 and λ_7 do not appear when m_{11}^2 and m_{22}^2 are expressed entirely in terms of m_{12}^2 and physical Higgs masses.

The possibility of this conversion is entirely due to the simple structure of the Higgs sector in the 2HDM, in contrast to the more involved relations in the supersymmetric

---

[8]In the general with the presence of λ_6, λ_7, it is also possible to solve for any five of the scalar potential parameters λ_i in the general basis in terms of the physical Higgs masses and the remaining three undetermined variables [148–150]. It is convenient to solve for $\lambda_1, \ldots, \lambda_5$ in terms of λ_6, λ_7, m_{12}^2 and the Higgs masses [39].

models as will be clarified in Chapter 6. The parametrization is tremendously powerful for phenomenological studies as it gives us freedom to input given Higgs masses of particular interest. Of course, the remaining parameters in this parametrization are not more physical than in any general potential. Since λ_6, λ_7 (if present), and m_{12}^2 play a role in the Higgs self-interactions, their effects appear for instance in the loop-mediated decay $H \to \gamma\gamma$.

- *The Higgs basis*

The scalar potential given in Eq. (5.1) is expressed in the $\mathbb{Z}_2$-basis of scalar doublet fields in which the $\mathbb{Z}_2$ discrete symmetry of the quartic terms is manifest. To facilitate study of the decoupling limit, one employs the so-called Higgs basis [151, 152] in which the two Higgs-doublet fields are defined as:

$$H_1 = \begin{pmatrix} H_1^+ \\ H_1^0 \end{pmatrix} \equiv \Phi_1 c_\beta + \Phi_2 s_\beta \,, \qquad H_2 = \begin{pmatrix} H_2^+ \\ H_2^0 \end{pmatrix} \equiv -\Phi_1 s_\beta + \Phi_2 c_\beta \,, \qquad (5.33)$$

so that $\langle H_1^0 \rangle = v/\sqrt{2}$ and $\langle H_2^0 \rangle = 0$. The scalar doublet H_1 possesses SM tree-level couplings to all the SM particles. Therefore, if one of the CP-even neutral Higgs mass eigenstates is SM-like, then it must be approximately aligned with the real part of the neutral field H_1^0. Note however that the H_1^0 defined above is not a mass eigenstate.

The scalar potential, when expressed in terms of the doublet fields, H_1 and H_2, has the same form as Eq. (5.1),

$$
\begin{aligned}
\mathcal{V} \;=\; & Y_1 H_1^\dagger H_1 + Y_2 H_2^\dagger H_2 + Y_3 [H_1^\dagger H_2 + \text{h.c.}] \\
& + \tfrac{1}{2} Z_1 (H_1^\dagger H_1)^2 + \tfrac{1}{2} Z_2 (H_2^\dagger H_2)^2 + Z_3 (H_1^\dagger H_1)(H_2^\dagger H_2) + Z_4 (H_1^\dagger H_2)(H_2^\dagger H_1) \\
& + \left\{ \tfrac{1}{2} Z_5 (H_1^\dagger H_2)^2 + \left[Z_6 (H_1^\dagger H_1) + Z_7 (H_2^\dagger H_2) \right] H_1^\dagger H_2 + \text{h.c.} \right\} , \qquad (5.34)
\end{aligned}
$$

where the Y_i are real linear combinations of the m_{ij}^2 and the Z_i are real linear combinations

of the λ_i. In particular, since $\lambda_6 = \lambda_7 = 0$, we have [151][9]

$$Z_1 \equiv \lambda_1 c_\beta^4 + \lambda_2 s_\beta^4 + \tfrac{1}{2}\lambda_{345} s_{2\beta}^2 \,, \tag{5.35}$$

$$Z_2 \equiv \lambda_1 s_\beta^4 + \lambda_2 c_\beta^4 + \tfrac{1}{2}\lambda_{345} s_{2\beta}^2 \,, \tag{5.36}$$

$$Z_i \equiv \tfrac{1}{4} s_{2\beta}^2 [\lambda_1 + \lambda_2 - 2\lambda_{345}] + \lambda_i \,, \quad (\text{for } i = 3, 4 \text{ or } 5)\,, \tag{5.37}$$

$$Z_6 \equiv -\tfrac{1}{2} s_{2\beta} [\lambda_1 c_\beta^2 - \lambda_2 s_\beta^2 - \lambda_{345} c_{2\beta}] \,, \tag{5.38}$$

$$Z_7 \equiv -\tfrac{1}{2} s_{2\beta} [\lambda_1 s_\beta^2 - \lambda_2 c_\beta^2 + \lambda_{345} c_{2\beta}] \,. \tag{5.39}$$

Since there are five nonzero λ_i and seven nonzero Z_i, there must be two relations. The following two identities are satisfied if $\beta \neq 0, \tfrac{1}{4}\pi, \tfrac{1}{2}\pi$:[10]

$$Z_2 = Z_1 + 2(Z_6 + Z_7)\cot 2\beta \,, \tag{5.40}$$

$$Z_{345} = Z_1 + 2Z_6 \cot 2\beta - (Z_6 - Z_7)\tan 2\beta \,, \tag{5.41}$$

where $Z_{345} \equiv Z_3 + Z_4 + Z_5$. One can invert the expressions given in eqs. (5.35)–(5.39), subject to the relations given by Eqs. (5.40) and (5.41).

The squared mass parameters Y_i are given by

$$Y_1 = m_{11}^2 c_\beta^2 + m_{22}^2 s_\beta^2 - m_{12}^2 s_{2\beta} \,, \tag{5.42}$$

$$Y_2 = m_{11}^2 s_\beta^2 + m_{22}^2 c_\beta^2 + m_{12}^2 s_{2\beta} \,, \tag{5.43}$$

$$Y_3 = \tfrac{1}{2}(m_{22}^2 - m_{11}^2)s_{2\beta} - m_{12}^2 c_{2\beta} \,. \tag{5.44}$$

Y_1 and Y_3 are fixed by the scalar potential minimum conditions,

$$Y_1 = -\tfrac{1}{2}Z_1 v^2 \,, \qquad Y_3 = -\tfrac{1}{2}Z_6 v^2 \,. \tag{5.45}$$

Using Eqs. (5.11) and (5.45), we can express $\overline{m}^2$ in terms of Y_2, Z_1 and Z_6,

$$\overline{m}^2 = Y_2 + \tfrac{1}{2}Z_1 v^2 + Z_6 v^2 \cot 2\beta \,. \tag{5.46}$$

---

[9]To make contact with the notation of ref. [39], $\lambda \equiv Z_1$, $\lambda_V \equiv Z_2$, $\lambda_T \equiv Z_3 + Z_4 - Z_5$, $\lambda_F \equiv Z_5 - Z_4$, $\lambda_A \equiv Z_1 - Z_5$, $\hat{\lambda} \equiv -Z_6$ and $\lambda_U \equiv -Z_7$.

[10]For $\beta = 0, \tfrac{1}{2}\pi$, the $\mathbb{Z}_2$-basis and the Higgs basis coincide, in which case $Z_6 = Z_7 = 0$ and Z_1, Z_2, Z_{345} are independent quantities. For $\beta = \tfrac{1}{4}\pi$, the two relations are $Z_1 = Z_2$ and $Z_6 = Z_7$, and Z_{345} is an independent quantity.

The masses of $H^\pm$ and A are given by

$$m_{H^\pm}^2 = Y_2 + \tfrac{1}{2}Z_3 v^2 \,, \tag{5.47}$$

$$m_A^2 = Y_2 + \tfrac{1}{2}(Z_3 + Z_4 - Z_5)v^2 \,. \tag{5.48}$$

It is straightforward to compute the CP-even Higgs squared-mass matrix in the Higgs basis,

$$\mathcal{M}_H^2 = \begin{pmatrix} Z_1 v^2 & Z_6 v^2 \\ Z_6 v^2 & m_A^2 + Z_5 v^2 \end{pmatrix} \,. \tag{5.49}$$

The physical mass eigenstates are identified from Eqs. (5.13) and (5.33) as

$$H = (\sqrt{2}\mathrm{Re}\, H_1^0 - v)\cos(\beta - \alpha) - \sqrt{2}\mathrm{Re}\, H_2^0 \sin(\beta - \alpha) \,, \tag{5.50}$$

$$h = (\sqrt{2}\mathrm{Re}\, H_1^0 - v)\sin(\beta - \alpha) + \sqrt{2}\mathrm{Re}\, H_2^0 \cos(\beta - \alpha) \,. \tag{5.51}$$

Then, Eqs. (5.16) and (5.17) yield

$$m_{H,h}^2 = \tfrac{1}{2}\left[m_A^2 + (Z_1 + Z_5)v^2 \pm \Delta_H\right] \,, \tag{5.52}$$

where

$$\Delta_H \equiv \sqrt{\left[m_A^2 + (Z_5 - Z_1)v^2\right]^2 + 4Z_6^2 v^4} \,. \tag{5.53}$$

In addition, Eq. (5) yields

$$|Z_6|v^2 = \sqrt{\left(m_H^2 - Z_1 v^2\right)\left(Z_1 v^2 - m_h^2\right)} \,. \tag{5.54}$$

Comparing Eqs. (5.13) and (5.51), we identify the corresponding mixing angle by $\alpha - \beta$, which is defined modulo π. Diagonalizing the squared mass matrix, Eq. (5.49), it is straightforward to derive the following expressions:

$$Z_1 v^2 = m_h^2 s_{\beta-\alpha}^2 + m_H^2 c_{\beta-\alpha}^2 \,, \tag{5.55}$$

$$Z_6 v^2 = (m_h^2 - m_H^2)\sin(\beta - \alpha)\cos(\beta - \alpha) \,, \tag{5.56}$$

$$m_A^2 + Z_5 v^2 = m_H^2 s_{\beta-\alpha}^2 + m_h^2 c_{\beta-\alpha}^2 \,. \tag{5.57}$$

It follows that

$$m_h^2 = \left(Z_1 + Z_6 \frac{\cos(\beta - \alpha)}{\sin(\beta - \alpha)}\right) v^2 \,, \tag{5.58}$$

$$m_H^2 = m_A^2 + \left(Z_5 - Z_6 \frac{\cos(\beta - \alpha)}{\sin(\beta - \alpha)}\right) v^2 \,. \tag{5.59}$$

Note that Eq. (5.56) implies that[11]

$$Z_6 \sin(\beta - \alpha) \cos(\beta - \alpha) \leq 0 \,. \tag{5.60}$$

One can also derive expressions for $\cos(\beta - \alpha)$ and $\sin(\beta - \alpha)$ either directly from Eqs. (5.55) and (5.56) or by using Eqs. (5.18) and (5.19) with α replaced by $\alpha - \beta$. Using Eq. (5.60), the sign of the product $\sin(\beta-\alpha)\cos(\beta-\alpha)$ is fixed by the sign of Z_6. However, since $\beta - \alpha$ is defined only modulo π, we are free to choose a convention where either $\cos(\beta - \alpha)$ or $\sin(\beta - \alpha)$ is always non-negative.[12] In a convention where $\sin(\beta - \alpha)$ is non-negative (this is a convenient choice when the h is SM-like),

$$\cos(\beta - \alpha) = -\operatorname{sgn}(Z_6)\sqrt{\frac{Z_1 v^2 - m_h^2}{m_H^2 - m_h^2}} = \frac{-Z_6 v^2}{\sqrt{(m_H^2 - m_h^2)(m_H^2 - Z_1 v^2)}} \,, \tag{5.61}$$

where we have used Eq. (5.54) to obtain the second form for $\cos(\beta - \alpha)$ in Eq. (5.61).

Finally, we record the following useful formula that is easily obtained from Eq. (5.9),

$$\overline{m}^2 = m_A^2 + Z_5 v^2 + \tfrac{1}{2}(Z_6 - Z_7)v^2 \tan 2\beta \,. \tag{5.62}$$

Combining Eq. (5.62) with Eqs. (5.56) and (5.57) yields

$$Z_7 v^2 = (m_h^2 - m_H^2)\sin(\beta - \alpha)\cos(\beta - \alpha) + 2\cot 2\beta\left[m_H^2 s_{\beta-\alpha}^2 + m_h^2 c_{\beta-\alpha}^2 - \overline{m}^2\right]. \tag{5.63}$$

Using Eqs. (5.40) and (5.41), one can likewise obtain expressions for $Z_2 v^2$ and $Z_{345} v^2$ in terms of m_h^2, m_H^2, and $\overline{m}^2$. However, these expressions are not particularly illuminating, so we do not write them out explicitly here.

5.1.2 Higgs couplings

Having specified the Higgs potential, we can move on to determine the tree-level Higgs couplings in order to have a complete model.

We first highlight the coupling of the CP-even Higgs bosons to VV (where $V = W^\pm$ or Z), which is the most relevant coupling to the LHC physics. Denoting the SM Higgs boson by $h_{\rm SM}$, these couplings normalized to the $h_{\rm SM} VV$ coupling is given by

$$C_V^h = \sin(\beta - \alpha)\,, \qquad C_V^H = \cos(\beta - \alpha)\,. \tag{5.64}$$

---

[11]Once we establish a convention where $0 \leq \beta \leq \tfrac{1}{2}\pi$, the sign of Z_6 is physical.

[12]Such a convention, if adopted, would replace the convention employed in Eq. (5.18) in which c_α is taken to be non-negative.

As expected, if h is a SM-like Higgs boson then $C_V^h \simeq 1$ in the alignment limit, whereas if H is a SM-like Higgs boson then $C_V^H \simeq 1$ in the alignment limit.

More Higgs couplings to gauge bosons can be derived by following the spin–parity quantum number assignments [44]. In the absence of fermions, the CP–even H_i bosons [that is the linear combinations of $\mathrm{Re}(\phi_i)$] are $J^{PC} = 0^{++}$ states, while the CP–odd A_i particles [the linear combinations of $\mathrm{Im}(\phi_i)$] have $J^{PC} = 0^{+-}$, and both P and C symmetries are conserved[13]. The charged Higgs boson is a $J^C = 0^+$ state, while the Z and W bosons are mixtures of, respectively, $1^{--}/1^{++}$ and $1^-/1^+$ states. From these J^{PC} assignments, one can infer the general properties of the Higgs couplings to gauge bosons, including their existence or their absence at the tree–level and the possibility of inducing them by loops [153, 154]. A summary of possible tree–level and loop induced couplings among two Higgs bosons and one gauge boson as well as one Higgs boson and two gauge bosons is given in Table 5.2 [154]. CP is assumed to be conserved in the Higgs sector [also in the fermionic couplings] and only Higgs doublets and singlets are considered [the H^+W^-Z coupling can be present at the tree–level in higher extensions of the Higgs sector; see Refs. [155–157] for instance].

Next, we turn to specify the Yukawa sector and consider the Higgs boson couplings to fermions. The interaction of the Higgs bosons with fermions are model–dependent. The most general renormalizable Yukawa couplings of the two Higgs doublets to a single generation of up and down-type quarks and leptons (using third generation notation) is given by

$$
\begin{aligned}
-\mathcal{L}_{\mathrm{Yuk}} = {}& \mathcal{Y}_b^1 \bar{b}_R \Phi_1^{i*} Q_L^i + \mathcal{Y}_b^2 \bar{b}_R \Phi_2^{i*} Q_L^i + \mathcal{Y}_\tau^1 \bar{\tau}_R \Phi_1^{i*} L_L^i + \mathcal{Y}_\tau^2 \bar{\tau}_R \Phi_2^{i*} L_L^i \\
& + \epsilon_{ij} \left[\mathcal{Y}_t^1 \bar{t}_R Q_L^i \Phi_1^j + \mathcal{Y}_t^2 \bar{t}_R Q_L^i \Phi_2^j \right] + \mathrm{h.c.} \,,
\end{aligned}
\tag{5.65}
$$

where $\epsilon_{12} = -\epsilon_{21} = 1$, $\epsilon_{11} = \epsilon_{22} = 0$, $Q_L = (t_L \,, b_L)$ and $L_L = (\nu_L \,, e_L)$ are the doublet left handed quark and lepton fields and t_R, b_R and e_R are the singlet right-handed quark and lepton fields. However, if all terms in Eq. (5.65) are present, then tree-level Higgs-

---

[13]This is no longer the case when fermions are involved and, in this case, only CP–symmetry is approximately conserved. However, since in the Higgs–fermion Yukawa coupling the $f\bar{f}$ system has zero total angular momentum and thus has $C = +$ charge conjugation, the H_i and A_i states behave as scalar and pseudoscalar particles, respectively.

Table 5.2. The tree–level and loop induced Higgs couplings to one gauge boson and two gauge bosons in a general model with Higgs doublets where CP symmetry is assumed to be conserved in the Higgs and fermionic (except in the CKM matrix) sectors; Cc, CPc, $Q = 0$, $col = 0$ mean, respectively C, CP, charge and color conservation. *Source: borrowed from Ref. [158].*

HHV couplings			HVV couplings		
Coupling	Tree–level?	Loop?	Coupling	Tree–level?	Loop?
$H_i H_i Z, A_i A_i Z$	NO: Bose statistics		$H_i ZZ, H_i WW$	YES	–
$H_i H_i \gamma, A_i A_i \gamma$	NO (Bose statistics)		$H_i \gamma\gamma, H_i \gamma Z$	NO ($Q = 0$)	1–loop
$H_i H_j \gamma, A_i A_j \gamma$	NO ($Q{=}0$)	3–loop	$H_i gg$	NO (col=0)	1–loop
$H_i H_j Z, A_i A_j Z$	NO (CPc)	3–loop	$A_i ZZ, A_i WW$	NO (Cc)	1–loop
$H_i A_j \gamma^*$	NO ($Q = 0$)	1–loop	$A_i \gamma\gamma, A_i \gamma Z$	NO (Cc,$Q = 0$)	1–loop
$H_i A_j Z$	YES	–	$A_i gg$	NO (Cc, col= 0)	1–loop
$H^+ H^- Z(\gamma)$	YES	–	$H^+ W^- Z$	NO for doublets	1–loop
$H^+ W^- H_i(A_i)$	YES	–	$H^+ W^- \gamma$	NO (U(1)$_Q$–c)	1–loop

mediated FCNCs would be present, in conflict with experimental constraints. To avoid tree-level Higgs-mediated FCNCs, we extend the discrete $\mathbb{Z}_2$ symmetry to the Higgs-fermion Lagrangian. There are four possible choices for the transformation properties of the fermions with respect to $\mathbb{Z}_2$, which we exhibit in Table 5.3.

For simplicity, we shall assume that the pattern of the Higgs couplings to quarks and leptons is the same.[14] This leaves two possible options which are generally discussed for

---

[14]Otherwise it will induce the lepton-specific and flipped types of the 2HDM, see details in the review article [135].

Table 5.3. Four possible $\mathbb{Z}_2$ charge assignments that forbid tree-level Higgs-mediated FCNC effects in the 2HDM. [159].

	Φ_1	Φ_2	t_R	b_R	τ_R	t_L, b_L, ν_L, e_L
Type I	+	−	−	−	−	+
Type II	+	−	−	+	+	+
Type X (lepton specific)	+	−	−	−	+	+
Type Y (flipped)	+	−	−	+	−	+

the Higgs-fermion couplings [160]:

$$\text{Type I:} \quad \mathcal{Y}_t^1 = \mathcal{Y}_b^1 = \mathcal{Y}_\tau^1 = 0\,, \tag{5.66}$$

$$\text{Type II:} \quad \mathcal{Y}_t^1 = \mathcal{Y}_b^2 = \mathcal{Y}_\tau^2 = 0\,. \tag{5.67}$$

The Type I and Type II models are distinguished only by the pattern of their fermionic couplings. In Type II models [160, 161], the field Φ_2 generates the masses of isospin down–type fermions and Φ_1 the masses of up–type quarks and the couplings are just like in the MSSM [with again α being free]. In turn, in Type I models [160, 162], the field Φ_2 couples to both up– and down–type fermions. As a consequence, in the Type I model all fermions couple to just one of the Higgs doublets while in the Type II model up-type fermions couple to one of the Higgs doublet while down-type fermions couple to the other one.

After the EWSB, the Yukawa Lagrangian takes the form:

$$\mathcal{L}_{\text{Yukawa}} = - \sum_{f=u,d,\ell} \frac{m_f}{v} \left(C_F^h \overline{f} f h + C_F^H \overline{f} f H - i C_F^A \overline{f} \gamma_5 f A \right)$$
$$- \left\{ \frac{\sqrt{2} V_{ud}}{v} \, \overline{u} \left(m_u C_U^A \mathrm{P}_L + m_d C_D^A \mathrm{P}_R \right) d H^+ + \frac{\sqrt{2} m_\ell C_\ell^A}{v} \overline{\nu_L} \ell_R H^+ + \text{h.c.} \right\} \tag{5.68}$$

where $C_F^{\mathcal{H}}$ ($\mathcal{H} = h, H, A$) are the Higgs couplings to fermions normalized to their SM values ($F = U, D$ denotes the coupling to up- and down-type quark, respectively). Along with the Higgs bosons to vector bosons (C_V), the fermionic couplings C_F for various Higgs bosons are functions of α and β and given in Table 5.4. Also, the couplings of the

Table 5.4. Tree-level vector boson couplings C_V ($V = W, Z$) and fermionic couplings C_F normalized to their SM values for the two scalars h, H and the pseudoscalar A in Type I and Type II Two-Higgs-doublet models. The $H^\pm$ couplings to fermions follow that of A.

Higgs	Type I and II	Type I		Type II	
	VV	up quarks	down quarks & leptons	up quarks	down quarks & leptons
h	$\sin(\beta - \alpha)$	$\cos\alpha/\sin\beta$	$\cos\alpha/\sin\beta$	$\cos\alpha/\sin\beta$	$-\sin\alpha/\cos\beta$
H	$\cos(\beta - \alpha)$	$\sin\alpha/\sin\beta$	$\sin\alpha/\sin\beta$	$\sin\alpha/\sin\beta$	$\cos\alpha/\cos\beta$
A	0	$\cot\beta$	$-\cot\beta$	$\cot\beta$	$\tan\beta$

charged Higgs boson to fermions follow those of the CP–odd Higgs A, see *e.g.* [44] for details. We note that the range of α employed guarantees that the top quark Yukawa coupling is always positive in our convention. For the most part, in particular for the case of $m_h \sim 125.5$ GeV, one also finds that $\sin(\beta - \alpha) > 0$.

Finally, the couplings among Higgs bosons is worth discussing as well since it plays a crucial role in the Higgs self-interaction. In the general basis, one finds the following results among the neutral Higgs bosons [39]

$$
\begin{aligned}
g_{hAA} &= -v\left[\lambda_T \sin(\beta - \alpha) - \lambda_U \cos(\beta - \alpha)\right], & (5.69)\\
g_{HAA} &= -v\left[\lambda_T \cos(\beta - \alpha) + \lambda_U \sin(\beta - \alpha)\right], & (5.70)\\
g_{Hhh} &= 3v\Big[\lambda \cos(\beta - \alpha)\left(-\tfrac{2}{3} + s_{\beta-\alpha}^2\right) - \widehat{\lambda}\sin(\beta - \alpha)(1 - 3c_{\beta-\alpha}^2) \\
&\quad + (2\lambda_A - \lambda_T)\cos(\beta - \alpha)\left(\tfrac{1}{3} - s_{\beta-\alpha}^2\right) - \lambda_U c_{\beta-\alpha}^2 \sin(\beta - \alpha)\Big] & (5.71)
\end{aligned}
$$

where

$$
\begin{aligned}
\lambda_T &= \tfrac{1}{4}s_{2\beta}^2(\lambda_1 + \lambda_2) + \lambda_{345}(s_\beta^4 + c_\beta^4) - 2\lambda_5 - s_{2\beta}c_{2\beta}(\lambda_6 - \lambda_7), & (5.72)\\
\lambda_U &= \tfrac{1}{2}s_{2\beta}(s_\beta^2\lambda_1 - c_\beta^2\lambda_2 + c_{2\beta}\lambda_{345}) - \lambda_6 s_\beta s_{3\beta} - \lambda_7 c_\beta c_{3\beta}\,. & (5.73)
\end{aligned}
$$

while the CP–even Higgs boson couplings to $H^\pm$ bosons are, for instance, given by [146]

$$\lambda_{hH^+H^-} = \frac{M_h^2 - \lambda_5 v^2}{M_W^2} \cos(\beta + \alpha) + \frac{2M_{H^\pm}^2 - M_h^2}{2M_W^2} \sin 2\beta \sin(\beta - \alpha) , \quad (5.74)$$

$$\lambda_{HH^+H^-} = \frac{M_H^2 - \lambda_5 v^2}{M_W^2} \sin(\beta + \alpha) + \frac{2M_{H^\pm}^2 - M_H^2}{2M_W^2} \sin 2\beta \cos(\beta - \alpha) \quad (5.75)$$

Due to the limitation on the length of the thesis, I have just listed above the couplings that are relevant to the following discussion. For a complete list of triple and quartic couplings one could look up Refs. [39].

5.2   Setup of the analysis

In this section we provide some details regarding the parameter scans, the fitting of the signal strengths, and the incorporation of limits related to the Higgs bosons that are heavier than the 125.5 GeV state. In particular, we employ all the latest results for the signal strength measurements from LHC8, include a consistent treatment of feed down (FD) from the production of heavier Higgs states, and discuss the prospects for LHC14.

5.2.1   Input parameters and scan range

As in [6], we adopt a modified version of the code 2HDMC [163] for numerical calculations.[15] All relevant contributions to loop induced processes are taken into account, in particular those with heavy quarks (t, b and c), $W^\pm$ and $H^\pm$. The four types of parametrization discussed in Section 5.1.1 are implemented and available for inputting parameters in the 2HDMC program. We choose to use the "physical basis" in which the inputs are the physical Higgs masses $(m_h, m_H, m_A, m_{H^\pm})$, the vacuum expectation value ratio ($\tan \beta$), and the $\mathcal{CP}$-even Higgs mixing angle, α, supplemented by the $\mathbb{Z}_2$ soft-breaking paramter m_{12}^2. With the above inputs, $\lambda_{1,2,3,4,5}$ as well as m_{11}^2 and m_{22}^2 are determined, see Eqs. (5.26)-(5.30) and Eqs. (5.31) and (5.32).

---

[15]We have modified the subroutine in 2HDMC that calculates the Higgs boson decays to $\gamma\gamma$ and also the part of the code relevant for QCD corrections to the $q\bar{q}$ final state.

We scan over the following ranges:[16]

$$\alpha \in [-\pi/2, +\pi/2], \quad \tan\beta \in [0.5, 60], \quad m_{12}^2 \in [-(2 \text{ TeV})^2, (2 \text{ TeV})^2],$$
$$m_A \in [5 \text{ GeV}, 2 \text{ TeV}], \quad m_{H^\pm} \in [m^*, 2 \text{ TeV}], \tag{5.76}$$

where m^* is the lowest value of $m_{H^\pm}$ allowed by LEP direct production limits and B physics constraints. The LEP limits on the $H^\pm$ are satisfied by requiring $m_{H^\pm} \geq 90$ GeV, while the constraints from B physics place a lower bound on charged Higgs mass with respect to $\tan\beta$. Concretely, the lower bounds from B physics are shown as a function of $\tan\beta$ in Fig. 15 of [135] in the case of the Type II model (roughly $m^* \sim 300$ GeV in this case) and in Fig. 18 of [135] in the case of the Type I model. For the remaining physical Higgs masses, we consider

$$m_h \in [123 \text{ GeV}, 128 \text{ GeV}], \quad m_H \in]128 \text{ GeV}, 2 \text{ TeV}], \tag{5.77}$$

for the case that h is the observed state near 125.5 GeV, or

$$m_H \in [123 \text{ GeV}, 128 \text{ GeV}], \quad m_h \in [10 \text{ GeV}, 123 \text{ GeV}[, \tag{5.78}$$

for the case that H is the observed state near 125.5 GeV. The window of 125.5 ± 2.5 GeV is adopted to account for theoretical uncertainties. However, we do not consider the cases where the A and/or the other CP-even Higgs are close to 125.5 GeV and possibly contribute to the observed signal. Thus, for $m_h \sim 125.5$ GeV ($m_H \sim 125.5$ GeV) we require that m_H (m_h) and m_A not be within the $[123, 128]$ GeV window nor within a $m_h \pm 4$ GeV ($m_H \pm 4$ GeV) mass window where m_h (m_H) is the particular mass value generated within the $[123, 128]$ GeV range.

---

[16] A few useful comments are noted. First, the scan range of $|\alpha| \leq \pi/2$ implies that Yukawa couplings $C_U^h = C_D^h > 0$ for Type I, whereas for Type II $C_D^h < 0$ is possible when $\sin\alpha > 0$. Note that with this scanning range for α, $\sin(\beta - \alpha) < 0$ is in principle possible, but is excluded by LHC data in the case of $m_h = 125.5$ GeV. Thus, for both Type I and Type II models, C_V^h and C_U^h are always positive. Second, the upper and lower bounds on $\tan\beta$ are chosen to ensure that the bottom and top Yukawa couplings, respectively, lie within the perturbative region. A safe upper limit, as adopted here, is $\tan\beta \leq 60$. Last, the range m_{12}^2 chosen is too broad. To improve the scan efficiency one could take advantage of the correlation between m_{12}^2 and $\tan\beta$ as will be shown in Section 5.3. In addition, one could lower the upper bound on m_A, m_H and $m_{H^\pm}$ as the occurrence of heavy Higgs bosons is impossible in some scenarios. To better control the precision towards to the SM level for the 125 GeV Higgs, we alternatively use the free pair of parameters $(s_{\beta-\alpha}, \tan\beta)$ or $(c_{\beta-\alpha}, \tan\beta)$ instead of $(\sin\alpha, \tan\beta)$ in some scans, but this replacement requires a modification of the 2HDMC code.

Last, we should note that our scans were performed in a manner that provides adequate point density in all regions of the various plots and predictions of interest. This means that, besides very broad (usually flat) scans in the input parameters mentioned above, we also used scans designed to focus on "hard-to-reach" regions of parameter space of particular interest and importance.

5.2.2 preLHC constraints

The "preLHC constraints" includes both theoretical demands and experimental measurements. Theoretically, vacuum stability, unitarity and coupling-constant perturbativity (denoted jointly as SUP) are required to be satisfied. Regarding the experiment constraints, we consider electroweak precision measurement S, T, U, the direct searches at LEP and the exclusion limits from B physics. For this we closely follow the approach of [6].

The 2HDMC code implements precision electroweak constraints (denoted STU) [17] and limits coming from requiring vacuum stability, unitarity and coupling-constant perturbativity (denoted jointly as SUP). We note that it is sufficient to consider the SUP constraints at tree level as usually done in the literature. Evolution to higher energies would make these constraints, outlined below, stronger and would not be appropriate when considering the 2HDM as an effective low energy theory. In more detail, the vacuum stability condition requires that the scalar potential be positive in all directions in the limit of growing field strength [164]. Tree-level necessary and sufficient conditions for unitarity are formulated in terms of eigenvalues of the S-matrix in the manner specified in [165] for the most general 2HDM — the criterion is that the multi-channel Higgs scattering matrix must have a largest eigenvalue below the unitarity limit. Coupling constant perturbativity is defined as in 2HDMC by the requirement that all self-couplings among the Higgs-boson mass eigenstates be smaller than 4π. For the scenarios we consider, this becomes an important constraint on λ_1. In an earlier study [6] we also found that the SUP constraints are particularly crucial in limiting the level of enhancement of the $gg \to h \to \gamma\gamma$ channel.

---

[17]We adopt the $\pm 3\sigma$ uncertainty for STU data: $-0.3 < S < 0.33; -0.34 < T < 0.35; -0.25 < U < 0.41$.

For all our scans, we have supplemented the 2HDMC code by including the B/LEP constraints. For the LEP data we adopt upper limits on $\sigma(e^+e^- \to Z\,h/H)$ and $\sigma(e^+e^- \to A\,h/H)$ from [166] and [167], respectively, which thus essentially select the allowed parameter region in the (α, β) space. Regarding B physics, the constraints imposed are those from $\mathrm{BR}(B_s \to X_s\gamma)$, R_b, ΔM_{B_s}, ϵ_K, $\mathrm{BR}(B^+ \to \tau^+\nu_\tau)$ and $\mathrm{BR}(B^+ \to D\tau^+\nu_\tau)$. The most important implication of these results is to place a lower bound on $m_{H^\pm}$ as a function of $\tan\beta$.

We also computed the extra Higgs-sector contributions to the anomalous magnetic moment of the muon, $a_\mu = (g_\mu - 2)/2$. Since the experimentally measured value, $a_\mu = (1165920.80 \pm 0.63) \times 10^{-9}$ [106], differs by $\sim 3\sigma$ from its SM value it is important to check correlations involving $\delta a_\mu \equiv a_\mu - a_\mu^{SM}$. Given the B/LEP, STU and SUP constraints, it turns out that one-loop contributions to δa_μ within the 2HDM are small and negligible, and the leading contribution is that known as the Barr-Zee diagram [168] which emerges at the two-loop level. For completeness we include also sub-leading contributions, see [163]. Since the overall $\sim 3\sigma$ discrepancy between the experimental and theoretical SM values could still be due to fluctuations (the world average is based mainly on the E821 result [169] with uncertainties dominated by statistics) or underestimates of the theoretical uncertainties, we do not use the a_μ measurement as an experimental constraint on the models we discuss. Generally speaking, the 2HDM contribution to δa_μ is very small unless $\tan\beta$ is of order 100.

As a routine step, I encourage you to examine the results at the stage of imposing the preLHC constraints. Sometimes results with distinct features at this level provide guidance that enables one to narrow the windows scanned for some parameters. For educational purpose, we take two examples to show you how to improve the efficiency of the intensive scans.

First, as regards the possibilities for $\sin\alpha$, which determines the sign of C_D^h in Type II, there are important constraints from perturbativity of the quartic Higgs couplings (even in the case of the Type I model). Often the strongest constraint is associated with the λ_{AAAA} quartic coupling of four A Higgs bosons. Figure 5.1 shows the values of λ_{AAAA}
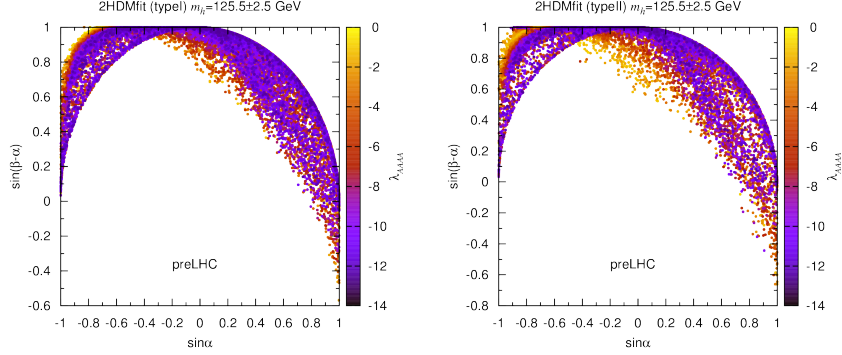
Figure 5.1. Values for the quartic coupling λ_{AAAA} for 2HDMs of Type I (left) and Type II (right) in the $\sin(\beta - \alpha)$ versus $\sin\alpha$ plane for $m_h \sim 125.5$ GeV shown as "temperature plots". For all points, the full set of preLHC constraints is satisfied, including all quartic couplings having absolute values below 4π.

that arise after the preLHC conditions listed in the Introduction are satisfied. From the figure we see that perturbativity of this quartic coupling creates a boundary of maximal $\sin(\beta-\alpha)$ values for $\sin\alpha > 0$ and of minimal $\sin(\beta-\alpha)$ values for $\sin\alpha \lesssim -0.3$. The other boundaries arise as a result of constraining other quartic couplings to their perturbative domain. Note in particular that in both Type I and Type II the maximal value of $\sin(\beta-\alpha)$ decreases as $\sin\alpha$ increases starting from $\sin\alpha \sim 0$, whereas $\sin(\beta - \alpha) \sim 1$ is possible for a broad range of $\sin\alpha < 0$ values. This will impact many phenomenological results. In particular, even though the $gg \to h$ fusion production rate is insensitive (not very sensitive) to the sign of $\sin\alpha$ for Type I (Type II), the $\gamma\gamma$ partial width is – as $\sin(\beta - \alpha)$ declines, the W-loop contribution to the $h\gamma\gamma$ coupling decreases, resulting in a decrease in BR($h \to \gamma\gamma$). Hence, the rate for $gg \to h \to \gamma\gamma$ quickly falls below the level acceptable for LHC precision Higgs results. This is also the case for $H \to WW^*$ originating from VBF or VH: while probed with poorer precision, the $\sin(\beta - \alpha)$ factor associated with the HVV vertex is present in both production and decay.

Another effective improvement is possible by constraining the mass range of heavy Higgs bosons. When a true decoupling limit is not applicable, for instance in the $H125$ scenario (will be discussed shortly), there is a maximum $m_{H^\pm}$ that can be achieved before perturbativity is violated, but this maximum applies for all parameter choices. To illustrate this, we present in Fig. 5.2 (upper row) "temperature" plots showing the quartic
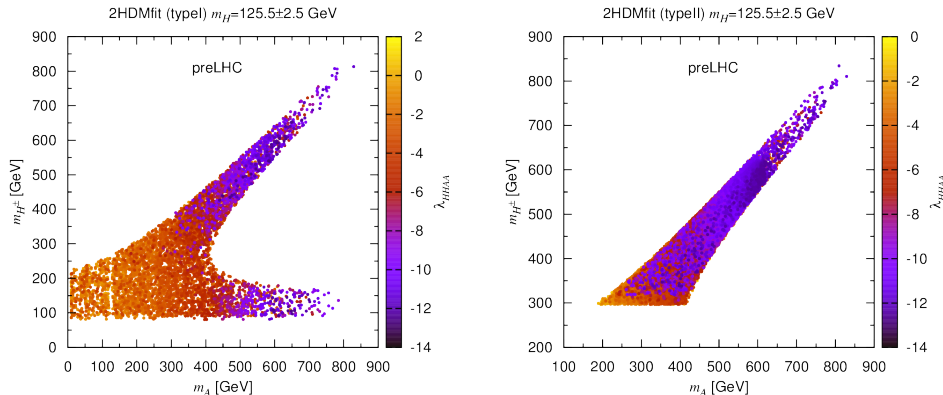
Figure 5.2. Scatterplots of λ_{HHAA} in the $m_{H^\pm}$ vs. m_A plane for the case of $m_H \sim$ 125.5 GeV. The values of λ_{HHAA} are color coded as indicated by the scales on the right of the plots. The full set of preLHC conditions is satisfied for all points shown.

coupling λ_{HHAA} in the plane of $m_{H^\pm}$ vs. m_A. λ_{HHAA} is one of a few quartic couplings that most frequently encounter the perturbativity bound. We see that λ_{HHAA} hits its perturbativity bound of $\sim 4\pi$ at about $m_A \sim m_{H^\pm} \sim 800$ GeV for both Type I and Type II. In the Type I case the perturbativity limit is also reached at low $m_{H^\pm}$ if m_A is as heavy as ~ 800 GeV. This wing of the $m_{H^\pm}$ vs. m_A plot is not present for Type II because of the lower bound of about 300 GeV on $m_{H^\pm}$ from B physics constraints.

5.2.3 Collider constraints at the LHC

Once the preLHC constraints have been applied, we check for consistency with the various signal strength measurements of the observed ~ 125.5 GeV Higgs boson at the LHC, including a consistent treatment of "feed down" from the production of heavier Higgs states. This job is the central piece of the analysis. In addition, we employ the most recent limits from searches for heavy Higgs-like states at the LHC, those are listed in Section 3.4, and require that the rates for channels involving heavier Higgs bosons all lie below the existing 95% confidence level (C.L.) limits.

In practice, for each scan point that passes the "preLHC" constraints explained above, we compute the Higgs signal strength μ (also "Higgs signal" for short or "Higgs rate" somewhere) defined in Eq. (3.2). Specifically, this μ is defined, for an individual 2HDM Higgs, denoted h_i (where $h_i = h, H, A$ are the choices), to be the ratio of the gg or WW-

fusion (VBF) induced Higgs cross section times the Higgs branching ratio to a given final state, X, relative to the corresponding value for the SM Higgs boson given by:

$$\mu_{gg}^{h_i}(X) \equiv (C_{gg}^{h_i})^2 \; \frac{\text{BR}(h_i \to X)}{\text{BR}(H_{\text{SM}} \to X)}, \quad \mu_{\text{VBF}}^{h_i}(X) \equiv (C_{WW}^{h_i})^2 \frac{\text{BR}(h_i \to X)}{\text{BR}(H_{\text{SM}} \to X)}, \tag{5.79}$$

where H_{SM} is the SM Higgs boson with $m_{H_{\text{SM}}} = m_{h_i}$ and $C_{gg}^{h_i}, C_{WW}^{h_i}$ are the ratios of the $gg \to h_i$, $WW \to h_i$ couplings (C_{WW}^A being zero at tree level) to those for the SM, respectively. Note that the corresponding ratio for $V^* \to V h_i$ ($V = W, Z$) with $h_i \to X$ is equal to $\mu_{\text{VBF}}^{h_i}(X)$, given that kinematic factors cancel out of all these ratios and that these ratios are computed in a self-consistent manner (that is, treating radiative corrections for the SM Higgs boson in the same manner as for the 2HDM Higgs bosons).

Technically, we actually computed the predictions for $\mu_{\text{ggF+ttH}}(Y)$ and $\mu_{\text{VBF+VH}}(Y)$ for the main decay modes Y ($\gamma\gamma, VV, b\bar{b},$ and $\tau\tau$) in terms of the reduced couplings C_U, C_D, and C_V, see Table 5.4. To this end, we also need the loop-induced $\gamma\gamma$ and gg couplings of the Higgs boson with mass around 125.5 GeV; for these we employ the full 1-loop amplitudes in `2HDMC` (including the contribution from the charged Higgs bosons in the $\gamma\gamma$ case), where SM contributions are scaled according to the values of C_U, C_D and C_V.

- *125 GeV Higgs signal fit*

The most important work is to impose the restrictions on the 2HDM parameter space from the measured Higgs signal, this important parameter is defined in Section 3.1.2. In practice, we employ the signal strength likelihoods in the $\mu_{\text{ggF+ttH}}$ versus $\mu_{\text{VBF+VH}}$ planes for each of the final states Y as determined in [170].[18] The $[\mu_{\text{ggF+ttH}}, \mu_{\text{VBF+VH}}]$ approach has been systematically adopted by the experimental collaborations. It has the advantage of taking into account correlations not accounted for when individual $X \to H \to Y$ channels are treated separately.

First, we follow the approach of [170] to combine the information provided by ATLAS, CMS and the Tevatron experiments on the $\gamma\gamma$, $ZZ^{(*)}$, $WW^{(*)}$, $b\bar{b}$ and $\tau\tau$ final states

---

[18]Combining VBF and VH is motivated in models where the couplings of the Higgs to WW and to ZZ are scaled equally, as is the case in any 2HDM because of custodial symmetry. Combining ggF and ttH is more a matter of convenience, partially motivated by the fact that the current LHC measurements do not probe ggF and ttH in any given final state at the same time: $H \to b\bar{b}$ is probed via ttH, not ggF, whereas all the other final states are probed quite precisely via ggF and with much poorer precision via ttH.

including the error correlations among the (VBF+VH) and (ggF+ttH) production modes. Concretely, we fit the likelihood from the 68% C.L. contour provided by the experiments for each decay mode Y in the $\mu_{\text{ggF+ttH}}(Y)$ versus $\mu_{\text{VBF+VH}}(Y)$ plane, using a Gaussian approximation. For each experiment, $-2 \log L_Y = \chi^2_Y$ can then be expressed as

$$
\begin{aligned}
\chi^2_Y &= (\boldsymbol{\mu}_Y - \hat{\boldsymbol{\mu}}_Y)^T \begin{pmatrix} \sigma^2_{\text{ggF},Y} & \rho_Y \sigma_{\text{ggF},Y} \sigma_{\text{VBF},Y} \\ \rho_Y \sigma_{\text{ggF},Y} \sigma_{\text{VBF},Y} & \sigma^2_{\text{VBF},Y} \end{pmatrix}^{-1} (\boldsymbol{\mu}_Y - \hat{\boldsymbol{\mu}}_Y) \qquad (5.80) \\
&= (\boldsymbol{\mu}_Y - \hat{\boldsymbol{\mu}}_Y)^T \begin{pmatrix} a_Y & b_Y \\ b_Y & c_Y \end{pmatrix} (\boldsymbol{\mu}_Y - \hat{\boldsymbol{\mu}}_Y) \\
&= a_Y (\mu_{\text{ggF},Y} - \hat{\mu}_{\text{ggF},Y})^2 + 2 b_Y (\mu_{\text{ggF},Y} - \hat{\mu}_{\text{ggF},Y})(\mu_{\text{VBF},Y} - \hat{\mu}_{\text{VBF},Y}) + c_Y (\mu_{\text{VBF},Y} - \hat{\mu}_{\text{VBF},Y})^2,
\end{aligned}
$$

where the indices ggF and VBF stand for (ggF+ttH) and (VBF+VH), respectively, and $\hat{\mu}_{\text{ggF},Y}$ and $\hat{\mu}_{\text{VBF},Y}$ denote the best-fit points obtained from the measurements [170]. The two-dimensional (2D) covariance matrix is explicitly shown in the first line of Eq. (5.80), with ρ_Y corresponding to the correlation between the measurements of (ggF+ttH) and (VBF+VH). From a digitized version of the 68% C.L. contour, it is possible to fit simultaneously the parameters a_Y, b_Y, c_Y, $\hat{\mu}_{\text{ggF},Y}$ and $\hat{\mu}_{\text{VBF},Y}$. A combination of ATLAS and CMS can then be made for each decay mode Y and expressed again in terms of a_Y, b_Y, c_Y, $\hat{\mu}_{\text{ggF},Y}$ and $\hat{\mu}_{\text{VBF},Y}$.

Next, we add up the individual χ^2_Y to obtain a "combined likelihood," which can be used in a simple, generic way to constrain nonstandard Higgs sectors and new contributions to the loop-induced processes, provided they have the same Lagrangian structure as the SM.

Finally, we demand that $\chi^2_Y < 6.18$ (for ATLAS and CMS combined) for each decay mode $Y = \gamma\gamma, VV (= WW, ZZ), b\bar{b}, \tau\tau$, which means that the Higgs rates for all channels fall within the 95% C.L. regions in the $[\mu_{\text{ggF+ttH}}, \mu_{\text{VBF+VH}}]$ plane, or in other words, such points are consistent at the 95.4% confidence level (CL) with the observed signal strengths for each decay mode Y.

- *Exclusion limits from other non-SM Higgs searches*

For very light A below 9.5 GeV, the limits from Upsilon decays [171] are important,

for which we follow the implementation in `NMSSMTools 4.6.0`. Moreover, we consider the limits from CMS on light pseudo scalars decaying into $\mu^+\mu^-$ [172] in the mass range $m_A = 5.5$–9 and 11.5–14 GeV, which are relevant in particular in Type II models.

As noted, it is also necessary to take into account LHC exclusion limits for Higgs bosons that are heavier than 125.5 GeV. In the case that the h is identified with the ~ 125.5 GeV state the relevant channels are $gg \to H \to 4\ell, 2\ell2\nu$, $gg \to H, A \to \tau\tau$ and $gg \to b\bar{b}H, b\bar{b}A \to b\bar{b}\tau\tau$ at the LHC. In the case that $m_H \sim 125.5$ GeV is assumed, the only LHC limits that apply are those on $gg \to A \to \tau\tau$ and $gg \to b\bar{b}A \to b\bar{b}\tau\tau$. Direct search limits on the $H^\pm$ at the LHC do not impact the parameter space once the B physics limits described below are imposed.

For $H/A \to \tau\tau$, we employ the recent CMS limits based on the 8 TeV data [92], which are presented separately for the bbH ($b\bar{b}$ associated production of the Higgs) and ggF production modes. In taking these limits into account, it will be important to note that in Type II models the coupling of the H and A to down-type fermions can be dramatically enhanced at large $\tan\beta$ compared to the SM expectation and that this enhancement will influence both bbH and ggF production. When m_A and m_H are within 15% of one another, which is the approximate resolution in the invariant mass of a pair of τ leptons, we will add their signals together.

Turning to $H \to ZZ$, we employ the latest ATLAS and CMS searches for heavy Higgs-like states in the $H \to ZZ \to 4\ell$ channel [71, 93] [19] and the CMS search in the $H \to ZZ \to 2\ell2\nu$ channel [94]. In the context of 2HDMs, there are two important considerations associated with using the limits as presented by the ATLAS and CMS collaborations. First, the VV couplings shown in Table 5.4 imply $(C_V^h)^2 + (C_V^H)^2 = 1$ for the coupling strengths relative to the SM Higgs. Thus, if the h is the 125.5 GeV state, the H will have a small coupling to W, Z due to the fact that the h must be very SM-like in order to describe the data at ~ 125.5 GeV, as shown, *e.g.*, in Fig. 10 of [170]. Thus, only ggF production is relevant for H. However, only ATLAS presents constraints

---

[19]Note that the CMS results on $H \to ZZ$ are presented after combination of the 4ℓ (where $\ell = e, \mu$) and $2\ell2\tau$ channels. However, the limit is almost uniquely driven by the 4ℓ channels as can be seen from the result based on $H \to ZZ \to 2\ell2\tau$ only, which is available as supplementary material on the TWiki page [173].

on a high mass Higgs arising purely from the ggF initial state with the full statistics at $7 + 8$ TeV, for $m_H > 200$ GeV [93]. All the other results, *i.e.* (*i*) ATLAS $H \to 4\ell$ for $m_H \in [130, 180]$ GeV, (*ii*) CMS $H \to 4\ell$ and (*iii*) CMS $H \to 2\ell 2\nu$ are implemented in our analysis under the assumption that the experimental search is fully inclusive. The limit is thus rescaled by a factor $\sigma^{\text{tot}}_{H_{\text{SM}}}/\sigma_{gg \to H_{\text{SM}}}$. Second, the width of the H in the 2HDM can be much smaller than the large SM Higgs widths assumed in the ATLAS and CMS analyses. We correct for the width difference by rescaling the observed limits on $\sigma \times \text{BR}$ by the factor $f = \sqrt{\frac{\Gamma_H^2 + (4 \text{ GeV})^2}{\Gamma_{H_{\text{SM}}}^2 + (4 \text{ GeV})^2}}$, where 4 GeV is the experimental resolution in the 4ℓ final state [174].

Finally, the limits derived from the pseudoscalar search $A \to Zh, h \to b\bar{b}$ from AT-LAS [97] and CMS [96] are imposed. (Limits from other searches, like for $A \to Z\gamma$ [175] or $hh \to b\bar{b}b\bar{b}$ [176], have no effect on the results; the very recent CMS limits on $A \to ZH$ and $H \to ZA$ [177] are not taken into account but will be commented upon in Section 5.6.) To evaluate all these constraints, production of the H and A via gluon-gluon fusion (ggF) and via associated production with a pair of bottom quarks (bbH,bbA) are computed at NNLO QCD[20] accuracy using `SusHi-1.3.0` [178], while the vector-boson fusion (VBF) mode for the H is computed at NLO with `VBFNLO-2.6.3` [179].

For convenience in the labeling, at this stage we define "postLHC8" points to be those which satisfy the preLHC constraints, the heavy Higgs limits and the Higgs fitting constraints.

- *Feed down of heavier Higgs to the 125 GeV Higgs*

There is a further issue arising from the fact that there are various ways in which the 125.5 GeV Higgs boson can be produced as a result of feed down from the production of heavier states. The reason to be concerned is that heavy Higgs bosons have a propensity for decaying to a vector boson plus a Higgs boson or to two Higgs bosons. Let us now address the issue of feed down specifically in two scenarios we consider in the following. For the h being the 125 GeV state, the most direct cases are $H \to hh$ and $A \to Zh$, but there are also chains like $H \to AA$ followed by $A \to Zh$ or $H \to H^+H^-$ with $H^\pm \to W^\pm h$

---

[20]The NNLO corrections for ggF are only computed for the top quark loop, as those for the bottom quark loop are very small.

and so forth. In contrast, the situation is quite simple in the case that the H is identified as the 125 GeV state, in which only the A can be heavy.[21] Given this possibility, the process $gg \to A \to ZH$ adds events to the ZH final state beyond those from $Z^* \to ZH$.[22] If such FD processes occur at a significant rate, the fit to the Higgs measurements using only direct h or H production processes may no longer be valid. These FD processes may be tested by a variety of means. For example, for the important FD sources of $A \to Zh$ and $H \to hh$, the final state mass can be reconstructed and m_A and m_H will be determined should the rates be significant; see the current limits from CMS in [95]. Then, data points lying within the relevant mass windows can be separated off. For the $H \to hh$ case, the decay products from the second h are visible for most h decays and events with this extra final state "activity" can be separated off. More complicated FD chains will have even more extra particles and constraints that will allow their separation.

For the present purpose, we will only consider the most important FD sources and associated ratios and quantitatively formulate the feed down.

$$\mu_{\mathrm{ggF}\mathbf{H}+bb\mathbf{H}}^{\mathrm{FD}} \equiv \frac{\sum_{\mathcal{H}} \left(\sigma_{\mathrm{ggF}\mathcal{H}} + \sigma_{bb\mathcal{H}}\right) P_{\mathrm{FD}}(\mathcal{H} \to \mathbf{H} + X)}{\sigma_{\mathrm{ggF}\mathbf{H}} + \sigma_{bb\mathbf{H}}}, \tag{5.81}$$

$$\mu_{Z\mathbf{H}}^{\mathrm{FD}} \equiv \frac{\sigma_{\mathrm{ggF}A}\mathrm{BR}(A \to Z\mathbf{H})}{\sigma_{Z\mathbf{H}}}, \tag{5.82}$$

where $\mathbf{H}$ is the 125.5 GeV states considered, and $\mathcal{H}$ represents the heavy Higgs H (if applicalbe), A and $H^\pm$ that can feed the 125.5 GeV signal. $P_{\mathrm{FD}}(\mathcal{H} \to \mathbf{H} + X)$ is the net branching ratio to produce one (or more) $\mathbf{H}$ in the $\mathcal{H}$ decay chains. Above, $\sigma_{\mathrm{ggF}\mathcal{H}}$ and $\sigma_{bb\mathcal{H}}$ refer to the cross sections for $gg \to \mathcal{H}$ and $bb\mathcal{H}$ associated production respectively. The expression of P_{FD} and the full formalism for the feed down calculations is given in Appendix A of [7].

We emphasize that the amount of FD is computed without accounting for any reduced efficiency for accepting such events into the 125.5 GeV signal as a result of the experimental cuts used to define the $gg \to h$, bbh or $Z^* \to Zh$ channels. In practice, it

---

[21]The feed down contribution of $H^\pm$ is also possible but negligible due to the small production cross section.

[22]The HAZ coupling is proportional to $\sin(\beta - \alpha)$, which the fits require to be $\lesssim 0.5$ in magnitude. What is important, however, is $\mathrm{BR}(A \to ZH) = \Gamma(A \to ZH)/\Gamma_{\mathrm{tot}}(A)$, which can still be large.

could be that the actual FD after the experimental cuts currently employed to define the various channels is considerably smaller than this maximally conservative estimate. The above-defined postLHC8 points for which the production rate from FD will not distort the fits to the 125.5 GeV resonance are called "FDOK".

In summary, all points that are retained obey the constraints from stability, unitarity and perturbativity (SUP), electroweak precision tests (STU), LEP searches, as well as the limits imposed by non-observation at the LHC of any Higgs bosons other than the SM-like one at 125 GeV. Regarding constraints from the Higgs signal strength measurements at 125 GeV, for each of the observed Higgs decay modes ($\gamma\gamma$, $WW^{(*)}$, $ZZ^{(*)}$, $b\bar{b}$, $\tau\bar{\tau}$) we require agreement at the 95% CL with the ATLAS+CMS combined signal strength ellipse in the (ggF+ttH) and (VBF+VH) plane, as explained in [7]. To facilitate the phenomenology analysis in the following context, we define the "postLHC8-FDOK" points to be those for which $\chi^2_Y < 6.18$ for each decay mode $Y = \gamma\gamma, VV (= WW, ZZ), b\bar{b}, \tau\tau$ and that in addition pass all other above-mentioned constraints, including being FDOK. Unless specifically indicated, we will mostly discuss these phenomenologically viable points that belong to this category throughout this chapter.

5.3 The status of 2HDM after LHC run-1

Since the Higgs boson discovery a large number of new measurements or updates of existing ones were published by the experimental collaborations. This is intensively described in Section 3.2. Most significant, from the point of view of our analysis of the 2HDMs, were the long-awaited final results for the $\gamma\gamma$ decay mode from CMS [66] in July and the update of the $\gamma\gamma$ results from ATLAS [70] at the end of August 2014. There were also several other important new measurements or updates; for example uncertainties have been significantly reduced for the fermionic channels, particularly for $H \to b\bar{b}$ in ttH production. All these new results were put together and analyzed in global coupling fits in [112].

One may ask what is the status of the 2HDM after full LHC run-1 data analysis and the implications in the 2HDM context of all these new (or updated) results on the signal

strengths of the $\sim$ 125.5 GeV Higgs boson. To address this important question, in the present section we revisit the analysis of [7], in which a comprehensive analysis of the status of Two-Higgs-Doublet Models (2HDMs) of Type I and Type II was performed. To this aim, we updated the constraints discussed in [7] using the latest LHC measurements of the $\sim$ 125.5 GeV Higgs signal as of Summer 2014 and performed scans of the 2HDM parameter space taking into account all relevant constraints which have been thoroughly discussed in the last section. We compare the results obtained using the combined 2013 and 2014 data to those obtained using just the 2013 data. The allowed parameter points using only the 2013 data were shown in [7] and are called "postLHC8(2013)-FDOK". In the plots to follow, we will identify the points that fit both the 2013 and the 2014 analyses as "postLHC8(2013 & 2014)-FDOK". For notations and conventions, we also refer to [7].

Motivated by the measurement of CP property for the discovered Higgs (see details in Section 3.3.2), we consider both the cases where the h or H is identified with the observed 125 GeV state — denoted $h125$ and $H125$, respectively, since they can have SM-like couplings as discussed in Section 5.1.2. Of course, the possibility of both h and H being very close to 125 in mass is also possible and will be addressed in Section 5.8. As a general structure, the discussion below involves the aspects of parameters, couplings and signal strength in each scenario.

- *h125 scenario*

Let us first focus on the case that the observed $\sim$ 125.5 GeV state is the h. To cover the case $m_h = 125.5 \pm 2.5$ GeV, we scan over m_H, m_A and $m_{H^\pm}$ as discussed earlier in Section 5.2.

Starting with the constraints on the model parameter space that originate from requiring that the signal strengths of the observed Higgs are matched at 95% C.L. in each final state. we show in Fig. 5.3 the points surviving all constraints in the $\cos(\beta - \alpha)$ versus $\tan\beta$ plane. The red points satisfy the Higgs signal constraints from both 2013 and 2014, while orange (blue) points pass only the 2014 (2013) Higgs constraints. Looking at the points that survive at the postLHC8-FDOK level, we observe that for $m_h \sim 125.5$ GeV in Type I models $|\cos(\beta - \alpha)|$ cannot be too large, especially if $\tan\beta \sim 1$. In the Type II
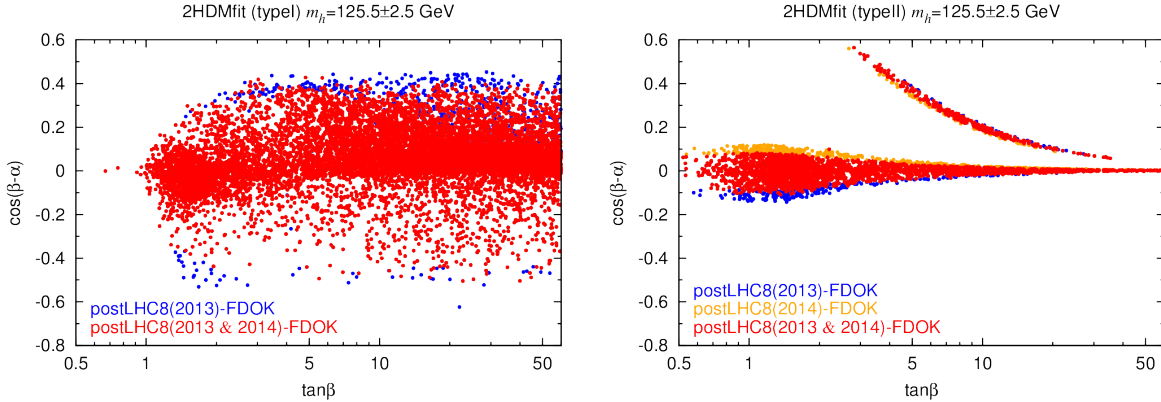
Figure 5.3. Constraints in the $\cos(\beta - \alpha)$ versus $\tan\beta$ plane for $m_h \sim 125.5$ GeV. Blue points are those which passed all constraints given the Higgs signal strengths as of Spring 2013 (*i.e.* the status considered in [7]), red points are those which remain valid when employing the Summer 2014 updates, and orange points are those newly allowed after the Summer 2014 updates. Note that the latter occur only in Type II but not in Type I models.

models, either $|\cos(\beta - \alpha)|$ can be quite close to 0 or it can fall in a second branch where fairly large positive $\cos(\beta - \alpha) \gtrsim 0.3$ is allowed if $\tan\beta \lesssim 7$. It turns out that this branch is associated with $\sin(\beta + \alpha) \approx 1$ and $\sin\alpha > 0$ [for which the b-quark Yukawa coupling has the opposite sign relative to the $\sin(\beta - \alpha) \to 1$ limit]. This "wrong-sign" Yukawa coupling, $C_D^h \sim -1$ is the focus of [180].

The change arising from 2014 data is rather small. In Type I, large values of $|\cos(\beta-\alpha)|$ get slightly more constrained, while in Type II there is a narrow strip around $\cos(\beta-\alpha) \approx -0.1$ and $\tan\beta \lesssim 2$ that is now excluded. On the other hand, in Type II slightly larger positive values of $\cos(\beta - \alpha)$ are allowed from the 2014 measurements. (Such orange points, which were not compatible with the 2013 results but are now allowed after the 2014 updates, occur only in Type II but not in Type I.) The banana-shaped branch spanning from $(\tan\beta, \cos(\beta - \alpha)) \approx (3, 0.6)$ to $(40, 0.1)$ is still present; this corresponds to the solution with a flipped sign for C_D. The reason for these slight changes lies mostly in the new combined signal strengths for the $\gamma\gamma$ decay mode: $\widehat{\mu}_{\text{ggF+ttH}}(\gamma\gamma) = 1.25 \pm 0.24$ and $\widehat{\mu}_{\text{VBF+VH}}(\gamma\gamma) = 1.09 \pm 0.46$ with a correlation of $\rho = -0.30$ [112], as compared to $\widehat{\mu}_{\text{ggF+ttH}}(\gamma\gamma) = 0.98 \pm 0.28$ and $\widehat{\mu}_{\text{VBF+VH}}(\gamma\gamma) = 1.72 \pm 0.59$ with a correlation of $\rho = -0.38$ in 2013 [170]. The result, after combining ATLAS and CMS data, is that the best-fit signal
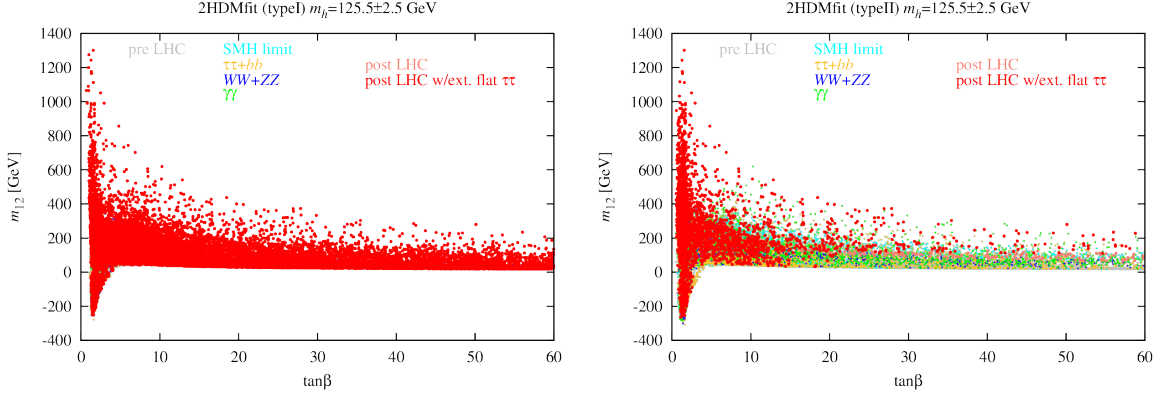
Figure 5.4. Constraints in the m_{12} versus $\tan\beta$ plane ($h125$)

strength in the ggF mode[23] has increased (although the new central value is consistent at the 1σ level with the 2013 results) while that in VBF+VH production has come down by a bit more than 1σ.

Next, we study the distribution of m_{12}^2, which softly breaks Z_2 symmetry. In the generic 2HDM m_{12}^2 can be nonzero, however, it is strongly correlated with $\tan\beta$, as shown in Fig. 5.4, due to the requirement of perturbativity, in particular for λ_1 and λ_2. For further exploration, we employ the expressions for λ_1 and λ_2 in terms of our input parameters, and for convenience, convert them to the ones in terms of the mass of one Higgs boson of order 125 GeV and the mass difference $\Delta m^2 \equiv m_H^2 - m_h^2$

$$\lambda_1 = \frac{m_h^2 + \Delta m^2 \cos^2\alpha - m_{12}^2 \tan\beta}{v^2 \cos^2\beta} = \frac{m_H^2 + \Delta m^2 \sin^2\alpha - m_{12}^2 \tan\beta}{v^2 \cos^2\beta} \tag{5.83}$$

The first two terms are always positive. For negative m_{12}^2, the last term in the above equation is a positive contribution; thus the bound on $\tan\beta$ becomes large as m_{12}^2 increases. When m_{12}^2 has a positive value, the last term switches to being negative and starts canceling with the first two terms, reaching full cancellation at a certain m_{12}^2 value, at which λ_1 approaches zero and very high $\tan\beta$ is allowed. After crossing this "zero" point, the last term makes an overwhelming contribution; as a result, the allowed $\tan\beta$ is restricted to smaller and smaller values as m_{12}^2 continues to increase. In the case of $m_h \sim 125.5$ GeV, the first two terms can be very large when H approaches the decoupling limit, so that

---

[23]In ttH production, uncertainties are still too large to have any impact.
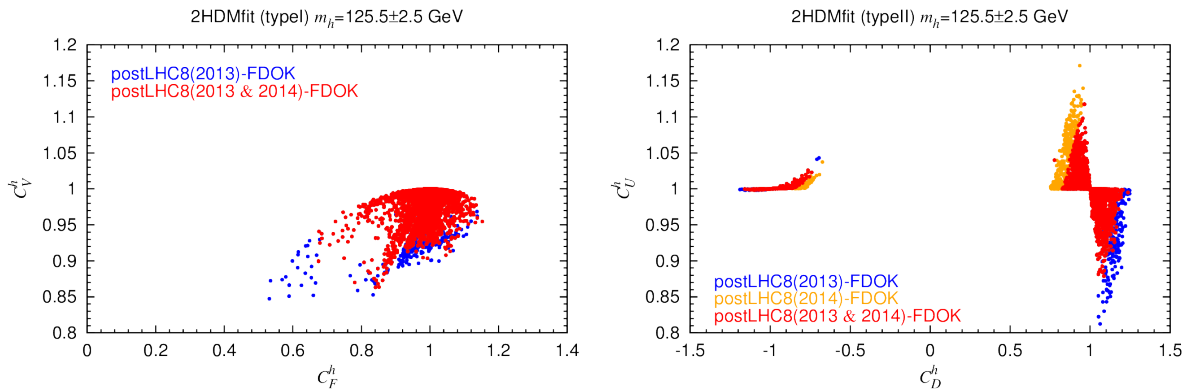
Figure 5.5. Reduced couplings C_V^h vs. C_F^h in Type I (left plot) and C_U^h vs. C_D^h in Type II (right plot) for $m_h \sim 125.5$ GeV scenarios.

m_{12}^2 starts from -250 GeV and ends up with a large positive value ~ 1300 GeV.[24]

Insight into the underlying couplings, C_V^h, C_U^h and C_D^h; C_V^h vs. C_F^h (Type I) and C_U^h vs. C_D^h (Type II); is provided by Fig. 5.5. There, we see that for both Type I and Type II, $C_V^h \sim +1$ is required for a decent fit to the Higgs data. Substantial suppression of the fermionic couplings is however possible in both models. In both cases, an enhanced $h \rightarrow \gamma\gamma$ rate can come from a suppression of C_D, which suppresses $\mathrm{BR}(h \rightarrow b\bar{b})$. In Type I, since $C_U = C_D \equiv C_F$, this goes hand-in-hand with a reduction of the hgg coupling; depending on which effect dominates, $\mu_{\mathrm{VBF}}^h(\gamma\gamma)$ can be enhanced, while $\mu_{gg}^h(\gamma\gamma)$ is suppressed (see Fig. 5.6). This does not occur in Type II, where enhancement/suppression of C_U and C_D is anti-correlated. In this case $C_D < 1$ leads to an enhancement and $C_D > 1$ to a suppression of both $\mu_{gg}^h(\gamma\gamma)$ and $\mu_{\mathrm{VBF}}^h(\gamma\gamma)$; since C_U works in the same direction, the effect can be more pronounced for $\mu_{gg}^h(\gamma\gamma)$ than for $\mu_{\mathrm{VBF}}^h(\gamma\gamma)$ (cf. the low-panel plot in Fig. 5.6). Further, $C_U^h \sim +1$ is needed in order to describe the observed $\gamma\gamma$ final state rates (*i.e.* a SM-like cancellation between the W and t loops contributing to the $h\gamma\gamma$ coupling is required). In Type I, $C_D^h = C_U^h$ and therefore both must also be close to $+1$. However, this is not required in the Type II models. In fact, the second branch apparent in Fig. 5.3 corresponds to the $C_D^h \sim -1$ region of the right-hand Type II plot of Fig. 5.5 — note that the magnitude, $|C_D^h| \sim 1$, is approximately fixed by the need for acceptable

---

[24]In contrast, m_{12}^2 starts from -350 GeV and ends up with a small positive value ~ 100 GeV in the $H125$ scenario.
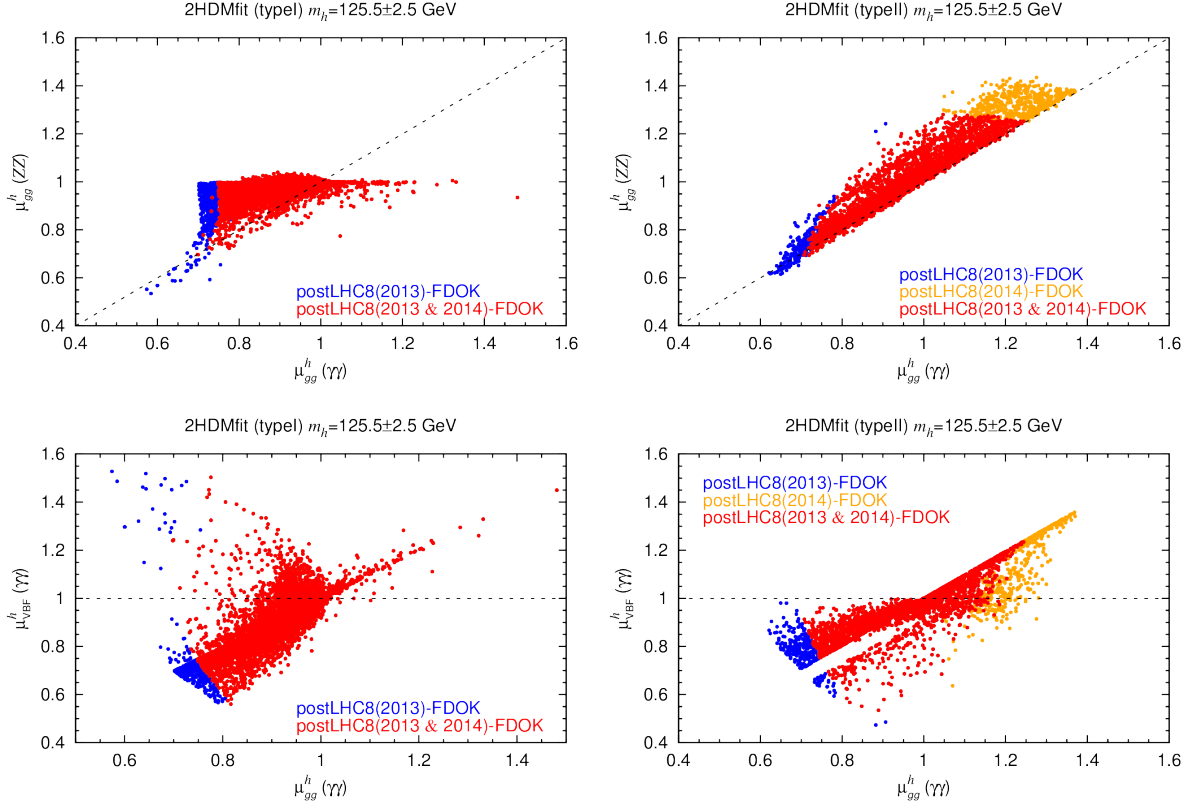
Figure 5.6. As in Fig. 5.3, but for $\mu_{gg}^h(ZZ)$ versus $\mu_{gg}^h(\gamma\gamma)$ (top row) and $\mu_{\mathrm{VBF}}^h(\gamma\gamma)$ versus $\mu_{gg}^h(\gamma\gamma)$ (bottom row).

fits to the $b\bar{b}$ and $\tau\tau$ final state rates.

To illuminate the precision with which individual channels are being fit, we show in Fig. 5.6 the signal strengths for $\mu_{gg}^h(ZZ)$ vs. $\mu_{gg}^h(\gamma\gamma)$ (upper row) as well as for $\mu_{\mathrm{VBF}}^h(\gamma\gamma)$ vs. $\mu_{gg}^h(\gamma\gamma)$ (lower row). From this figure, one sees explicitly that the low values of $\mu_{gg}^h(\gamma\gamma) \approx 0.6 - 0.7$ are no longer allowed. Moreover, while there has been no change in the maximum $\mu_{gg}^h(\gamma\gamma)$ obtainable in Type I, higher values up to about $\mu_{gg}^h(\gamma\gamma) \approx 1.4$ (vs. ~ 1.2 before) are attainable in Type II. The alert reader will have noticed that this upper limit is much lower than the 2σ range that should be allowed in principle. The limitation in fact comes from the $h \to VV (= WW, ZZ)$ decay mode in ggF production, for which we have $\widehat{\mu}_{\mathrm{ggF+ttH}}(VV) = 1.03 \pm 0.17$ from the 2014 measurements, and hence $\mu_{gg}^h(ZZ) < 1.37$ at 95.4% CL (as compared to $\widehat{\mu}_{\mathrm{ggF+ttH}}(VV) = 0.91 \pm 0.16$ in Spring 2013).

Other conclusions draw in the early analysis of [7] remain valid. As before, it is

apparent that requiring the μ values to lie within $\pm 10\%$ of unity would have a strong impact. Even $\pm 20\%$ measurements will remove many parameter choices. Note also that with sufficiently precise measurements of $\mu_{gg}^h(ZZ)$ and $\mu_{gg}^h(\gamma\gamma)$ there is a chance to distinguish Type I from Type II models; for most of the blue points if $\mu_{gg}^h(\gamma\gamma)$ is > 1, then $\mu_{gg}^h(ZZ)/\mu_{gg}^h(\gamma\gamma) < 1$ for Type I, whereas for Type II $\mu_{gg}^h(ZZ)/\mu_{gg}^h(\gamma\gamma) > 1$ always. Likewise, there are complementary correlations between the ggF and VBF modes, as illustrated for the $\gamma\gamma$ final state in the lower row of Fig. 5.6. In particular, if $\mu_{\mathrm{VBF}}^h(\gamma\gamma) > 1$, then $\mu_{gg}^h(\gamma\gamma) < 1$ is required in Type I, whereas just the opposite statement applies in Type II. In general, the cross correlations between different production×decay modes carry interesting information because of the dependences in particular of the hgg and $h\gamma\gamma$ couplings on C_U, C_V (and in Type II for large $\tan\beta$ also on C_D) and thus can be useful for distinguishing scenarios.

- *H125 scenario*

Let us now turn to the case that the observed SM-like Higgs near 125.5 GeV is the heavier CP-even state of the 2HDM, H. In this case, the lighter state, h, must have escaped LEP searches. However, we will see that a signal for the h could be hiding in the present data from the LHC and might be revealed in several focused analyses. The pseudoscalar A can be either lighter or heavier than the H. Since perturbativity for the quartic couplings prevents the A from being heavier than about 1 TeV, it can also give interesting signatures at LHC14.

Analogous to Fig. 5.3, we show in Fig. 5.7 the $m_H \sim 125.5$ GeV points in the $\sin(\beta-\alpha)$ versus $\tan\beta$ plane after all constraints have been applied. As before, we observe a slight narrowing of the allowed $\sin(\beta-\alpha)$ range, but no visible change in the $\tan\beta$ direction. It is interesting to note, however, that in Type I $m_H \sim 125.5$ GeV requires $\tan\beta \gtrsim 1$. It is also remarkable that, while in Type I $\sin(\beta-\alpha)$ can still vary from about -0.3 to 0.5 (corresponding to $C_V \gtrsim 0.87$), in Type II one is pretty much forced into the decoupling/alignment regime, the few points with sizable $\sin(\beta-\alpha)$ being quite rare and associated with the branch having a negative sign for C_D^H.

Correlations of signal strengths are illustrated in Fig. 5.8. Analogous arguments as for
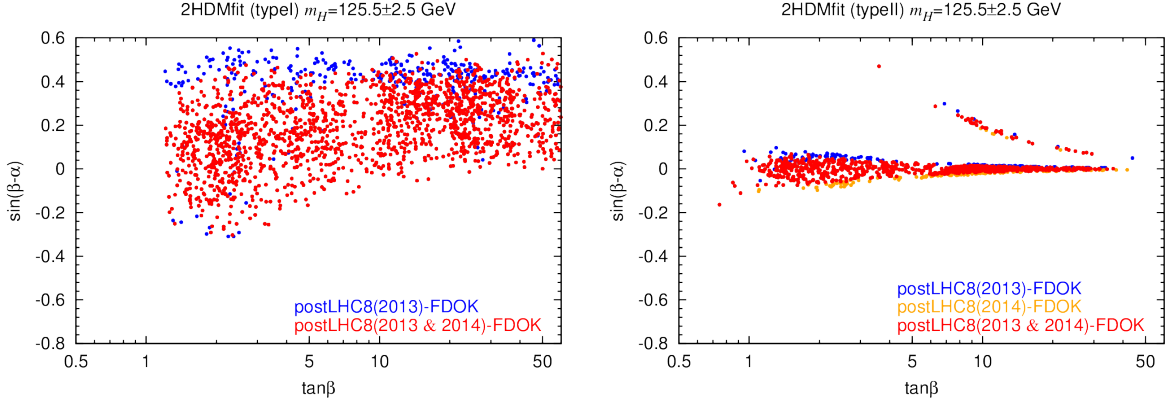
Figure 5.7. Constraints in the $\sin(\beta - \alpha)$ versus $\tan\beta$ plane for $m_H \sim 125.5$ GeV, comparing the current status as of Summer 2014 to that of Spring 2013.
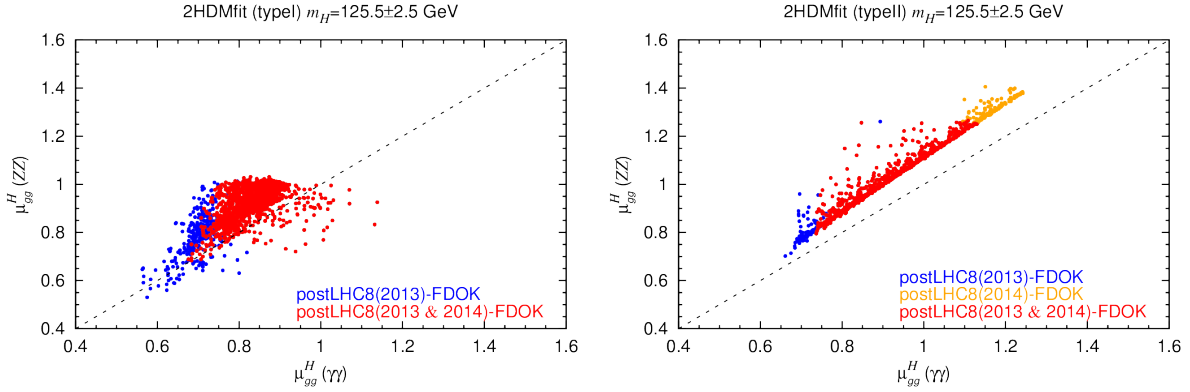
Figure 5.8. Correlations of signal strengths for $m_H \sim 125.5$ GeV scenarios.

the $m_h \sim 125.5$ GeV case apply. It is however worth noting that the direct correlation between $\mu_{gg}^H(\gamma\gamma)$, $\mu_{\mathrm{VBF}}^H(\gamma\gamma)$ and $\mu_{gg}^H(ZZ)$ in Type II is much stronger than for $m_h \sim$ 125.5 GeV. As above, additional Type II points occur with $\mu_{gg}^H(\gamma\gamma)$ and $\mu_{gg}^H(ZZ)$ values beyond those found in [7]. These would be removed if future measurements show that $\mu_{gg}^H(\gamma\gamma)$ ($\mu_{gg}^H(ZZ)$) is within 10% (20%) of unity. As was noted in [7], if $\leq \pm 5\%$ deviations from the SM are required for both the ZZ and $\gamma\gamma$ final states then the lower plots of Fig. 5.8 show that only a few points of the Type I model having $\mu_{gg}^H(\gamma\gamma) \gtrsim 0.95$ can survive and that *all* Type II points will be removed by this constraint.

116

5.4 Prediction for higher precision at the run-2

At this point, we turn to a consideration of what future measurements at LHC 13/14 or a linear collider might be most revealing. We will also observe that substantial FD is indeed possible in the full LHC run-1. However, the "danger" of FD contamination is likely to be reduced along with increased precision in the signal strength measurements at the run-2 . Implications for future experiments, including expectations regarding other lighter or heavier Higgs bosons, are given in the second section.

Let us first quantify the extent to which future higher precision measurements at the next LHC run might be able to restrict the model parameter space. Typical results for $h125$ and for $H125$ are illustrated in the top panel and bottom panel of Fig. 5.9, respectively. To make clear the impact of increased precision in the future, we will show points that survive if the observed values of $\mu_X^h(Y)$ *all* lie within $P\%$ of the SM prediction for the following channels (X, Y):[25]

$$(gg, \gamma\gamma),\ (gg, ZZ),\ (gg, \tau\tau),\ (\text{VBF}, \gamma\gamma),\ (\text{VBF}, ZZ),\ (\text{VBF}, \tau\tau) = (\text{VH}, bb),\ (\text{ttH}, bb)\,.$$
$$(5.84)$$

Here, we will consider $P = \pm 15\%$, $\pm 10\%$ and $\pm 5\%$. For this we use the shorthand notation SM$\pm 15\%$, SM$\pm 10\%$ and SM$\pm 5\%$, respectively.

Not unexpectedly, as increasingly precise agreement with the SM is imposed in the various channels, one is quickly pushed to small $|\cos(\beta - \alpha)|$ ($|\sin(\beta - \alpha)|$) for the $h125$ ($H125$) case, respectively, but $\tan\beta$ remains unrestricted.[26] Note that in the $h125$ case even SM$\pm 10\%$ on each of the individual μ's will have eliminated the "wrong-sign" down-quark Yukawa region (which corresponds to $\sin\alpha > 0$ or $C_D^h < 0$) of the Type II model. While the discussion for the $H125$ scenario is involved. In the case of Type I, consistency with the observed 125.5 GeV signal restricts $\sin(\beta - \alpha)$ less than was the case for $\cos(\beta - \alpha)$

---

[25]It is important to note that the $(\text{VBF}, \tau\tau) = (\text{VH}, bb)$ channels have exactly the same scaling factor in 2HDMs. We mention them together since they are experimentally very different channels and although individually they may not be measurable with a certain level of accuracy, in combination they should be able to determine the common μ to the specified accuracy.

[26]The value of $\tan\beta$ would be well-determined once the dark matter induced from this double-Higgs portal violates the isospin symmetry. The details of the model building and its consequences will be discussed in Chapter 8.
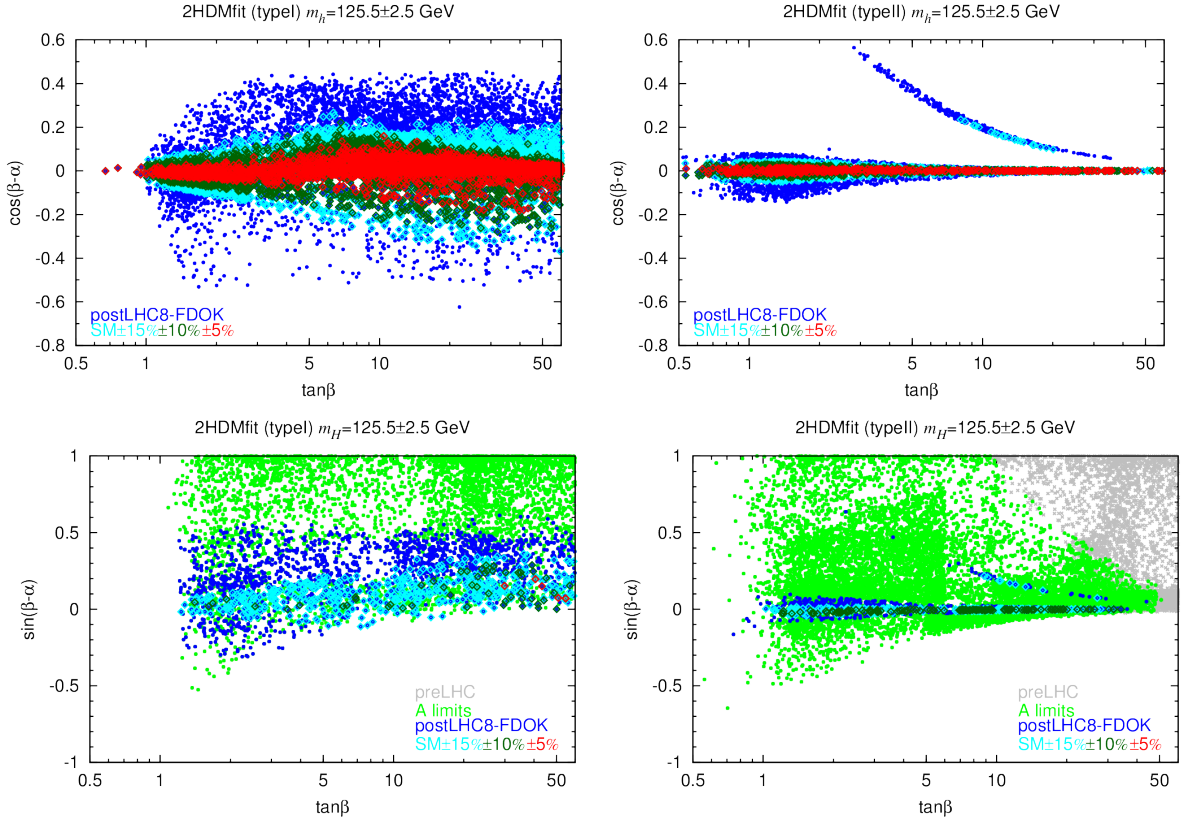
Figure 5.9. Constraints on the 2HDM of Type I and Type II in the $\cos(\beta - \alpha)$ vs. $\tan\beta$ plane for the $m_h \sim 125.5$ GeV scenario (top) and in the $\sin(\beta - \alpha)$ vs. $\tan\beta$ plane for the $m_H \sim 125.5$ GeV scenario (bottom), comparing current h or H fits (blue) to the case that the rates for all the channels listed in Eq. (5.84) are within $\pm 15\%$ (cyan), $\pm 10\%$ (green) or $\pm 5\%$ (red) of the SM Higgs prediction. The SM$\pm 15\%, \pm 10\%, \pm 5\%$ points *are* subjected to FDOK requirements. In the $m_H \sim 125.5$ GeV scenario we additionally show points that survive at the preLHC (grey), A-limits (green) for which, however, no FDOK requirements are imposed.

in the $m_h \sim 125.5$ GeV case. In contrast, for Type II the constraints on $\sin(\beta - \alpha)$ are similar in nature to the limits on $\cos(\beta - \alpha)$ in the case of the h. There is, however, an important difference. Namely, if $\pm 5\%$ agreement with the SM can be verified in all the channels listed in Eq. (5.84), then $m_H = 125.5$ GeV is eliminated in Type II but not in Type I. This can be traced to the fact that the charged-Higgs loop does not decouple at large $m_{H^\pm}$ and ends up suppressing the $H\gamma\gamma$ coupling and therefore the $\gamma\gamma$ final state rates. More details regarding the nondecoupling of the charged Higgs loop contribution to the $H\gamma\gamma$ coupling are presented in Appendix B of [7].

One quantity of particular interest for a SM-like h is the triple-Higgs coupling strength
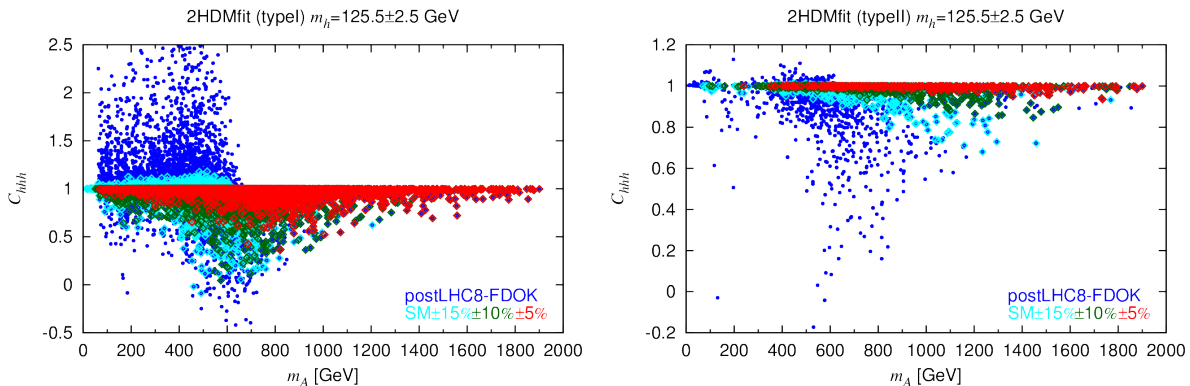
Figure 5.10. The postLHC8-FDOK points in the C_{hhh} vs. m_A plane for the $m_h \sim 125.5$ GeV scenario comparing current h fits to the case where future measurements show that the rates for all the channels listed in Eq. (5.84) are within $\pm 15\%, \pm 10\%, \pm 5\%$ of the SM Higgs prediction; FDOK is required in all cases. Color scheme is as for Fig. 5.9.

λ_{hhh}. We plot the current and possible future expectations in Fig. 5.10 for C_{hhh} (defined as the value of λ_{hhh} relative to the SM value). We observe that if the $\mu_X(Y)$ measurements were to have excursions from the SM predictions at the currently allowed 95% CL extreme, then measurement of a large deviation from $C_{hhh} = 1$ would be quite likely (also see [181]). For example, at the high-luminosity LHC14, with $L = 3000$ fb^{-1} one can measure λ_{hhh} to the 50% level [63], and given the limited constraints on the model implied by current Higgs data, deviations from $C_{hhh} = 1$ of this order, indeed up to 100% or more, are possible. However, if future LHC measurements imply increasingly smaller deviations from $\mu_X(Y) = 1$ in the various channels, then observing a deviation from $C_{hhh} = 1$ becomes increasingly difficult, even at the ILC. For example, from [63] we find that the predicted precision on λ_{hhh} for ILC1000 with $L = 500 - 1000$ fb^{-1} is of order 21% and for ILC1000 with $L = 1600 - 2500$ fb^{-1} it is of order 13%. At CLIC3000 with $L = 2000$ fb^{-1} the accuracy achievable would be about 10%.

Comparing to the deviations shown in Fig. 5.10, we see that in Type I a determination of $\mu_X(Y)$ rates at the level of SM$\pm 10\%$ still allows C_{hhh} as small as ~ 0, while SM$\pm 5\%$ allows C_{hhh} as small as 0.3, either of which will be observable for any of the listed machines and integrated L values. In contrast, for Type II, even SM$\pm 15\%$ would already imply that C_{hhh} must lie below 1. This agrees with the conclusion reached in [122] where it is stated
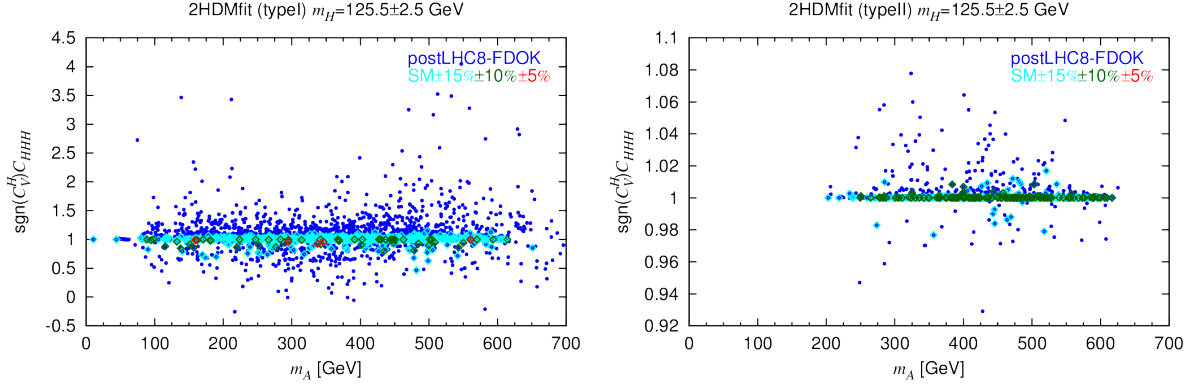
Figure 5.11. We display points in the $\text{sgn}(C_V^H)C_{HHH}$ vs. m_A plane for the $m_H \sim$ 125.5 GeV scenario comparing current H fits to the case where future measurements show that *all* channel rates are within $\pm15\%, \pm10\%, \pm5\%$ of the SM Higgs prediction; FDOK is required in all cases. Color scheme is as for Fig. 5.9, except that preLHC and A-limits points are not displayed.

that current 68% C.L. (1σ) limits (which are very close to our SM$\pm15\%$ constraint) imply $C_{hhh} \leq 1$ for Type II. We note further that the smallest C_{hhh} for SM$\pm10\%$ is ~ 0.9, while for SM$\pm5\%$ it is ~ 0.95. The former would require CLIC3000 while the latter would be beyond the reach of any of the above e^+e^- colliders. Thus, it is clear that future LHC Higgs data could have a very significant impact on the prospects for seeing an interesting deviation from $C_{hhh} = 1$ at ILC/CLIC. As an aside, we note from Fig. 5.10 that for Type II (but not Type I) models SM$\pm5\%$ is only possible for $m_A \gtrsim 250 - 300$ GeV depending on $\tan\beta$.

As in the case of $m_h \sim 125.5$ GeV, for $m_H \sim 125.5$ GeV it is interesting to assess the prospects for detecting a deviation in the triple-Higgs coupling as one goes from the current data set to H rates that are increasingly SM-like. In Fig. 5.11, we plot $\text{sgn}(C_V^H)C_{HHH}$, *i.e.* the ratio of the triple-Higgs coupling λ_{HHH} to the value it should have in the SM limit, as a function of m_A. (We include $\text{sgn}(C_V^H)$ because some of the points have $C_V^H < 0$ for our scanning procedure.) We observe that as the LHC signals become increasingly SM-like, the deviations of $\text{sgn}(C_V^H)C_{HHH}$ from unity are even more tightly limited than in the case of C_{hhh} for $m_h \sim 125.5$ GeV. Of course, we also see (again) that very few (no) points survive the SM$\pm5\%$ constraint in the case of Type I (Type II).

It is also interesting to examine the feed down effect which may invalidate the signal
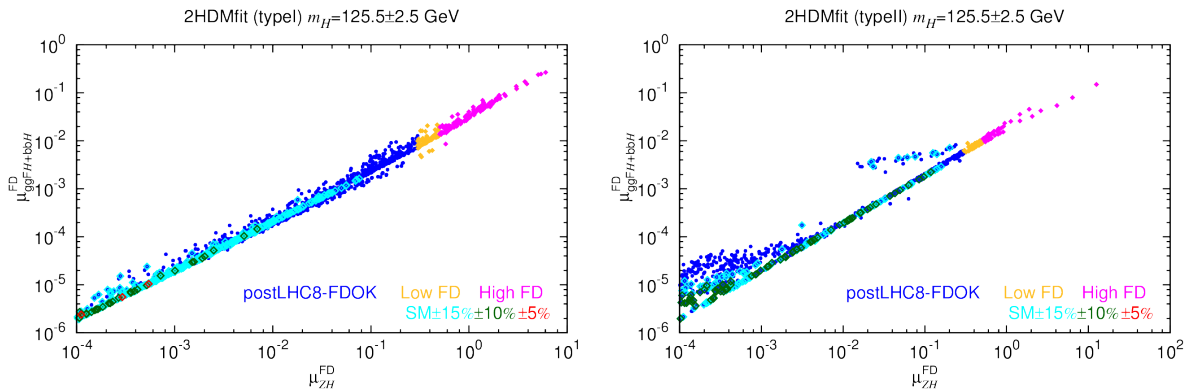
Figure 5.12. We plot $\mu^{\mathrm{FD}}_{\mathrm{ggF}H+\mathrm{bb}H}$ vs. μ^{FD}_{ZH} illustrating how high FD fractions can go for postLHC8 points for the $m_H \sim 125.5$ GeV scenarios. Also shown is how convergence of the H properties to SM-like values would limit the maximum possible feed downs. We display only points with $\mu^{\mathrm{FD}}_{ZH} \geq 10^{-4}$ — there are many points with much lower values.

fit for the 125 GeV state. To this aim, we exhibit in Fig. 5.12 a few features of μ^{FD}_{ZH} and $\mu^{\mathrm{FD}}_{\mathrm{ggF}H+\mathrm{bb}H}$ defined in Eqs. (5.81) and (5.82).[27] The two plots show the relative importance of μ^{FD}_{Zh} compared to $\mu^{\mathrm{FD}}_{\mathrm{ggF}h+\mathrm{bb}h}$. Clearly, the FD to the ZH final state from $A \to ZH$, μ^{FD}_{ZH} has the greatest potential for being large because of the large $gg \to A$ production rate in the numerator compared to the $Z^* \to ZH$ rate appearing in the denominator. In contrast, in $\mu^{\mathrm{FD}}_{\mathrm{ggF}H+\mathrm{bb}H}$ both numerator and denominator are ggF-dominated. More importantly, it also illustrates the fact that as the 125.5 GeV resonance is shown to be closer and closer to SM-like in all the various channels the maximum amount of FD that is possible is greatly reduced, becoming quite small for the SM±5% case. This means that increased precision in the signal strength measurements reduces the "danger" of FD contamination.

5.5 Decoupling and alignment in the 2HDM

In addition to performing an extensive analysis for the 2HDM by using the full LHC run-1 data sets, we are also specifically interested in a special limit of these models, namely the case in which one of the neutral Higgs mass eigenstates is approximately aligned with the direction of the scalar field vacuum expectation values. In this case, the coupling to gauge bosons of the Higgs boson observed at the LHC tends towards the SM

---

[27]For brevity we only display the plot for the $H125$ scenario. The conclusion drawn below also applied to the $h125$ case is qualitatively the same but less distinct.

limit, $C_V \to 1$.[28] This so-called *alignment limit* is most easily attained in the decoupling limit [39], where h is the SM-like state and all the other non-SM-like Higgs scalars of the model are heavy. However, the alignment limit of the 2HDM can also be achieved in a parameter regime in which one or more of the non-SM-like Higgs scalars are light (and in some cases very light). This region of *alignment without decoupling* is a primary focus of this section.

Considering experimental as well as theoretical uncertainties, the expected precision for coupling measurements at the LHC after collecting 300 fb^{-1} of data is about 4–6% for the coupling to gauge bosons, and of the level of 6–13% for the couplings to fermions [63]. The precision improves by roughly a factor of 2 for at the high-luminosity run of the LHC with 3000 fb^{-1}. At a future e^+e^- international linear collider (ILC) with $\sqrt{s} = 250$ GeV to 1 TeV, one may measure the couplings to fermions at the percent level, and the coupling to gauge bosons at the sub-percent level. A detailed discussion of the prospects of various future colliders can be found in [63].

We take this envisaged $\sim 1\%$ accuracy on C_V as the starting point for the numerical analysis of the alignment case. Concretely, we investigate the parameter spaces of the 2HDMs of Type I and Type II assuming that the observed 125 GeV state is the h, the lighter of the two CP-even Higgs bosons in these models, and imposing that $C_V^h > 0.99$ (note that $|C_V| \leq 1$ in any model whose Higgs sector consists of only doublets and/or singlets).

Taking into account all relevant theoretical and phenomenological constraints, including the signal strengths of the observed Higgs boson, as well as the most recent limits from the non-observation of any other Higgs-like states, we then analyse the phenomenological consequences of this scenario. In particular, we study the variations in the couplings to fermions and in the triple-Higgs couplings that are possible as a function of the amount of alignment when the other Higgs states are light, and contrast this to what happens in the decoupling regime. Moreover, we study the prospects to discover the additional Higgs

---

[28]We use the notation of coupling scale factors, or *reduced couplings*, employed in [112]: C_V ($V = W, Z$) for the coupling to gauge bosons, $C_{U,D}$ for the couplings to up-type and down-type fermions and $C_{\gamma,g}$ for the loop-induced couplings to photons and gluons.

states when they are light.

To study the decoupling/alignment limit in the best way, in this section we review the theoretical structure of the 2HDM in the Higgs basis, including, in particular, a comprehensive discussion of the couplings in the alignment regime. The results involving the parameter space, couplings and signal strength are presented for the case of $m_h = 125.5$ GeV only. Note that the decoupling limit does not apply to the $m_H = 125.5$ GeV case, as will be shortly discussed in Section 5.3.

5.5.1 Defining the alignment and SM-limit in the Higgs basis

As noted in Section 5.1.1, the Higgs basis field H_1 behaves precisely as the Standard Model Higgs boson. Thus, if one of the neutral CP-even Higgs mass eigenstates is approximately aligned with $\sqrt{2} \operatorname{Re} H_1^0 - v$, then its properties will approximately coincide with those of the SM Higgs boson. Thus, we shall define the *alignment limit* as the limit in which one of the two neutral CP-even Higgs mass eigenstates aligns with the direction of the scalar field vacuum expectation values. Defined in this way, it is clear that the alignment limit is independent of the choice of basis for the two Higgs doublet fields. Nevertheless, the alignment limit is most clearly exhibited in the Higgs basis. In light of Eqs. (5.50) and (5.51), the alignment limit corresponds either to the limit of $\cos(\beta - \alpha) \to 0$ if h is identified as the SM-like Higgs boson, or to the limit of $\sin(\beta - \alpha) \to 0$ if H is identified as the SM-like Higgs boson.

From Eq. (5.49), one can immediately derive the conditions that yield a SM-like Higgs boson. Since $\langle H_1^0 \rangle = v/\sqrt{2}$ and $\langle H_2^0 \rangle = 0$, the couplings of H_1 are precisely those of the Standard Model. Thus a SM-like Higgs boson exists if $\sqrt{2} \operatorname{Re} H_1^0 - v$ is an approximate mass eigenstate. That is, the mixing of H_1^0 and H_2^0 is subdominant, which implies that either $|Z_6| \ll 1$ and/or $m_A^2 + Z_5 v^2 \gg (Z_1 v^2), Z_6 v^2$. Moreover, if in addition $Z_1 v^2 < m_A^2 + Z_5 v^2$, then h is SM-like, whereas if $Z_1 v^2 > m_A^2 + Z_5 v^2$, then H is SM-like. In both cases, the squared-mass of the SM-like Higgs boson is approximately equal to $Z_1 v^2$.

Consider first the case of a SM-like h, with $m_h \approx 125$ GeV. In this case, $Z_1 v^2 < m_A^2 + Z_5 v^2$, $|\cos(\beta - \alpha)| \ll 1$, and $m_h^2 \approx Z_1 v^2$. It follows from Eq. (5.61) that the alignment limit can be achieved in two ways: (i) $Z_6 \to 0$ or (ii) $m_H \gg v$. The case of
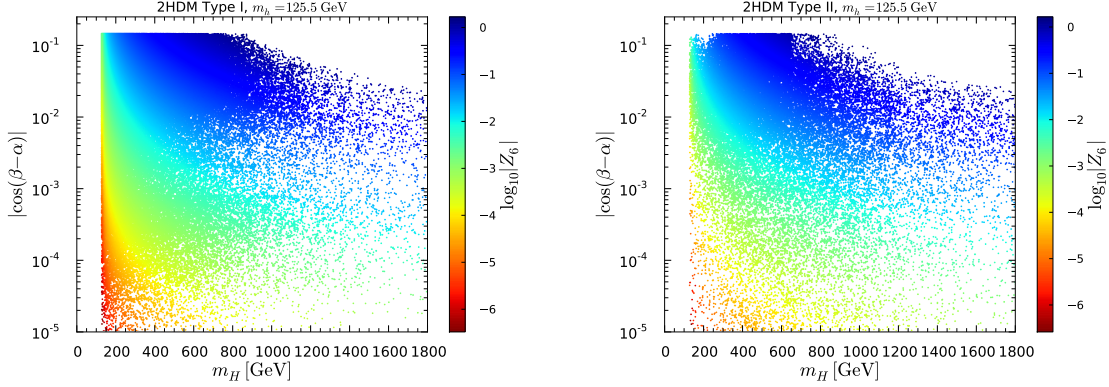
Figure 5.13. $|c_{\beta-\alpha}|$ versus m_H in Type I (left) and Type II (right) with $\log_{10}|Z_6|$ color code. Points are order form low to high $\log_{10}|Z_6|$ values.

$m_H \gg v$ (or equivalently $Y_2 \gg v$) is called the *decoupling limit* in the literature.[29] In this case, one finds that $m_H \sim m_A \sim m_{H^\pm}$, so one can integrate out the heavy scalar states below the scale of m_H. The effective Higgs theory below the scale m_H is a theory with one Higgs doublet and corresponds to the Higgs sector of the Standard Model. Thus not surprisingly, h is a SM-like Higgs boson. However, it is possible to achieve the alignment limit even if the masses of all scalar states are similar in magnitude in the limit of $Z_6 \to 0$. This is the case of *alignment without decoupling* and the main focus of this study. Finally, if both $|Z_6| \ll 1$ and $m_H \gg m_h$ are satisfied, the alignment is even more pronounced; when relevant we shall denote this case as the *double decoupling limit*.

Figure 5.13 shows the crucial relation between $|Z_6|$, $|c_{\beta-\alpha}|$ and m_H, illustrating the different ways alignment can occur with and without decoupling. As expected, $|Z_6|$ exhibits a clear dependence on the H–h mass difference, see Eq. (5.56), and steeply drops towards zero in the limit $|c_{\beta-\alpha}| \to 0$, *i.e.* when the h becomes purely SM-like. When m_H is of the order of 1 TeV, one needs to be extremely close to $s_{\beta-\alpha} = 1$ to have small $|Z_6|$, for instance $|Z_6| \approx 10^{-3}$ requires $|c_{\beta-\alpha}| \approx 6 \times 10^{-5}$ for $m_H = 1$ TeV, while for lighter H the departure of $s_{\beta-\alpha}$ from 1 can be more important, for instance the same $|Z_6| \approx 10^{-3}$ value requires $|c_{\beta-\alpha}| \approx 2 \times 10^{-3}$ for $m_H = 200$ GeV. It is in principle always possible to obtain

---

[29]More precisely, we are assuming that $m_H^2 \gg |Z_6|v^2$. Since Z_6 is a dimensionless coefficient in the Higgs basis scalar potential, we are implicitly assuming that Z_6 cannot get too large without spoiling perturbativity and/or unitarity. One might roughly expect $|Z_6| \lesssim 4\pi$, in which case $m_H \gg v$ provides a reasonable indication of the domain of the decoupling limit.

arbitrarily small values of $|Z_6|$ if one pushes $\sin(\beta - \alpha)$ arbitrarily close to 1. For the purpose of the numerical analysis, we limit ourselves to $|c_{\beta-\alpha}| \geq 10^{-5}$; we have checked that this captures well all features relevant for the $|c_{\beta-\alpha}| \to 0$ limit. Interestingly, as m_H becomes larger, we observe that the decoupling limit sets a stronger upper limit on $|c_{\beta-\alpha}|$ than the one set in the numerical scan ($|c_{\beta-\alpha}| \lesssim 0.14$). Observing a heavy $m_H \gtrsim 850$ GeV at the LHC would provide a better-than-1% indirect determination of the h-coupling to electroweak gauge bosons in the framework of these scenarios.

For completeness we note that in the case of a SM-like H we have $Z_1 v^2 > m_A^2 + Z_5 v^2$, $|\sin(\beta - \alpha)| \ll 1$ and $m_H^2 \approx Z_1 v^2$. Here, it is more convenient to employ a convention where $\cos(\beta - \alpha)$ is non-negative. One can then use eqs. (5.54), (5.60) and (5.61) to obtain an expression for $\sin(\beta - \alpha)$. In a convention where $\cos(\beta - \alpha)$ is non-negative,

$$\sin(\beta - \alpha) = -\,\mathrm{sgn}(Z_6)\sqrt{\frac{m_H^2 - Z_1 v^2}{m_H^2 - m_h^2}} = \frac{-Z_6 v^2}{\sqrt{(m_H^2 - m_h^2)(Z_1 v^2 - m_h^2)}}\,. \tag{5.85}$$

Taking $m_H \approx 125$ GeV, there is no decoupling limit as in the case of a SM-like h. However, the alignment limit without decoupling can be achieved in the limit of $Z_6 \to 0$.

5.5.2 Higgs couplings in the alignment limit

The next question to address is what variations in the couplings of the 125.5 GeV state are still possible in the limit of approximate alignment where $C_V^h \approx 1$. In the strict alignment limit, the fermion couplings to the SM-like Higgs boson should approach their Standard Model values. To see this explicitly, we note the identities,

$$\frac{\cos \alpha}{\sin \beta} = \sin(\beta - \alpha) + \cot \beta \cos(\beta - \alpha)\,, \tag{5.86}$$

$$-\frac{\sin \alpha}{\cos \beta} = \sin(\beta - \alpha) - \tan \beta \cos(\beta - \alpha)\,, \tag{5.87}$$

$$\frac{\sin \alpha}{\sin \beta} = \cos(\beta - \alpha) - \cot \beta \sin(\beta - \alpha)\,, \tag{5.88}$$

$$\frac{\cos \alpha}{\cos \beta} = \cos(\beta - \alpha) + \tan \beta \sin(\beta - \alpha)\,. \tag{5.89}$$

If h is the SM-like Higgs boson, then in the limit of $\cos(\beta - \alpha) \to 0$, the fermion couplings of h approach their Standard Model values. However, if $\tan \beta \gg 1$, then the alignment limit is realized in the Type-II Yukawa couplings to down-type fermions only if $|\cos(\beta -$

$\alpha)|\tan\beta \ll 1$. That is, if $|\cos(\beta-\alpha)| \ll 1$ but $|\cos(\beta-\alpha)|\tan\beta \sim \mathcal{O}(1)$, then the hVV couplings and the $ht\bar{t}$ couplings are SM-like whereas the $hb\bar{b}$ and $h\tau^+\tau^-$ couplings deviate from their Standard Model values. Thus the approach to the alignment limit is *delayed* when $\tan\beta \gg 1$. We denote this phenomenon as the *delayed alignment limit*. Similar considerations apply if $\cot\beta \gg 1$; however, this region of parameter space is disfavored as the corresponding $ht\bar{t}$ coupling quickly becomes non-perturbative if $\cot\beta$ is too large.

To illustrate this effect, we show in Fig. 5.14 the dependence of the reduced couplings to (up-type) fermions, see Table 5.4, $C_F^h \equiv C_U^h = C_D^h$ in Type I (C_U^h in Type II) on $|c_{\beta-\alpha}|$. The mass of the heavier scalar H is shown as a color code. We see that when m_H is light, for only 1% deviation from unity in C_V^h, C_U^h can deviate as much as about 10% (20%) from unity in Type I (Type II). Inverting the plotting order of m_H (not shown), it is interesting to note that these deviations are largest for $m_H \approx 700$–800 GeV while slightly more constrained for lighter m_H. On the other hand, in the decoupling limit the deviations in C_U^h are more constrained, with a maximum of 5% for $m_H \gtrsim 1.2$ TeV in both Type I and Type II. It is also interesting to observe how quickly alignment leads to SM-like couplings: for $|c_{\beta-\alpha}| \lesssim 10^{-2}$ the deviations in C_U^h are limited to just a few percent no matter the value of m_H.

The situation is quite different for the coupling to down-type fermions, C_D^h, in Type II, see Fig. 5.15. First of all, the possible deviations are larger than for C_U^h, with C_D^h ranging from about 0.70 to 1.15 even for $|c_{\beta-\alpha}| \sim 10^{-2}$. Indeed, this is an example of the delayed alignment limit discussed below Eq. (5.89); one needs $|c_{\beta-\alpha}|$ as low as about 3×10^{-4} to have C_D^h within 2% of unity. This drives the whole phenomenology of the scenario: as we will see, sizable deviations of C_D^h from 1 lead to possible large deviations in the signal strengths even for quite small $|c_{\beta-\alpha}|$. Inverting the plotting order of m_H (not shown), we note, however, that for any given $|\cos(\beta-\alpha)|$ of a few times 10^{-3} or smaller, C_D^h is limited to be closer to 1 when m_H is small than in the decoupling case with large m_H.

Moreover, $C_D^h = 1$ is not possible unless $|c_{\beta-\alpha}|$ is very small (again a few times 10^{-3} or smaller). In particular, large positive deviations of $C_D^h \gtrsim 1.12$ would indicate $m_H \lesssim 750$ GeV. On the contrary, C_D^h values which are substantially smaller than 1 can be
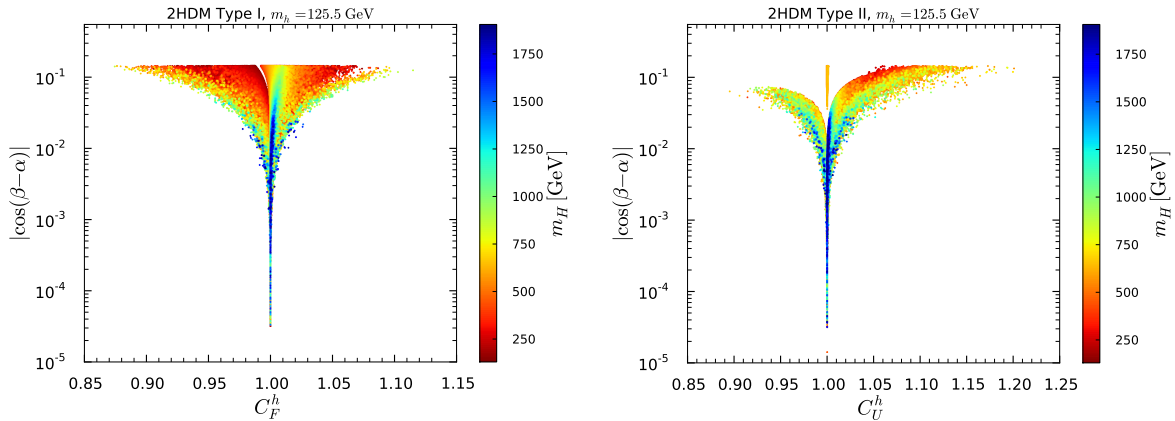
Figure 5.14. $|c_{\beta-\alpha}|$ versus C_F^h in Type I (left) and $|c_{\beta-\alpha}|$ versus C_U^h in Type II (right) with m_H color code. Points are ordered from low to high m_H. The points with $C_U^h \approx 1$ and $|\cos(\beta - \alpha)| > 0.03$ are the points for which $C_D^h \approx -1$, i.e. the opposite-sign Yukawa coupling points, see Fig. 5.15.
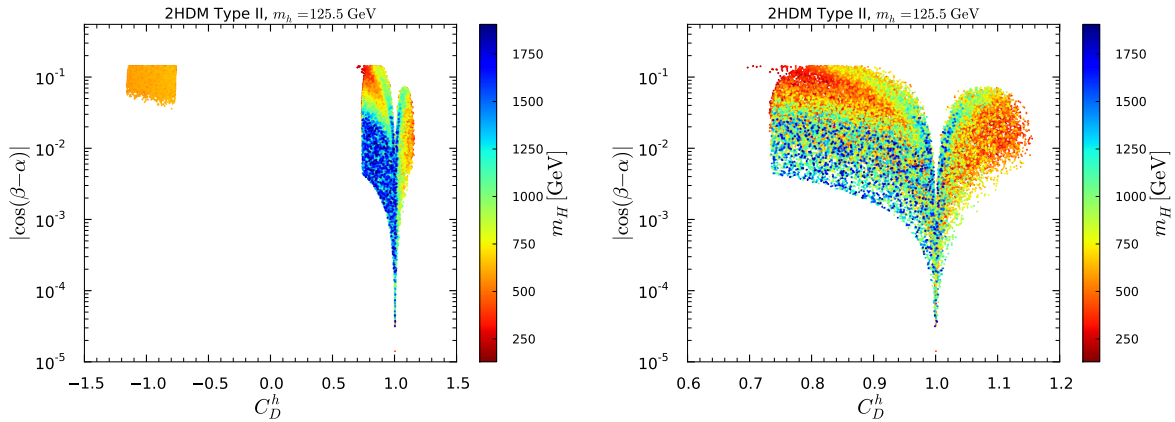
Figure 5.15. $|c_{\beta-\alpha}|$ versus C_D^h in Type II with m_H color code for the full C_D^h range (left) and zooming on the $C_D^h > 0$ region (right). Points are ordered from low to high m_H.

achieved in both the decoupling and non-decoupling regimes except for a small island of points located around $C_D^h \approx 0.8$ and $|c_{\beta-\alpha}| \approx 0.1$ that is achieved only for $m_H \lesssim 400$ GeV. Thus, a discovery of a light H state in association with a measured value of $C_D^h \sim 0.8$ would give an indirect way to probe sub-percent deviation of C_V^h in this Type II scenario.

Finally, for light m_H the sign of C_D^h relative to C_V^h and C_U^h can be opposite to the corresponding SM value. This is realized for not so small values of $|c_{\beta-\alpha}| \geq 0.035$, i.e. not in the deep alignment limit, for 230 GeV $\leq m_H \leq$ 665 GeV, $m_A \lesssim 650$ GeV and $0.08 \leq |Z_6| \leq 0.92$. For the points in this region, the up-type coupling is very close to

1, corresponding to the few isolated points observed in the right panel of Fig. 5.14. As discussed in [180], the eventual LHC run-2 precision will allow one to either confirm or eliminate the opposite-sign coupling possibility using precise signal rate measurements of the h in a few channels. Should the opposite-sign coupling be confirmed, one would expect to also see A signals (plus perhaps H signals) in the above mass range, thereby providing a confirmation of this scenario. (The cross sections for A and H signals will be discussed in Section 5.6.)

If H is the SM-like Higgs boson, then in the limit of $\sin(\beta - \alpha) \to 0$, the fermion couplings of H approach their Standard Model values. However, if $\tan \beta \gg 1$, then the alignment limit is realized in the Type-II couplings to down-type fermions only if $|\sin(\beta - \alpha)| \tan \beta \ll 1$. Thus, the delayed alignment limit also exists for Type-II Yukawa couplings. The $\cot \beta \gg 1$ region is disfavored since it leads to non-perturbative $Ht\bar{t}$ coupling as previously. Thus, only for Type-II down-type Yukawa couplings is the existence of the delayed alignment limit theoretically sound when either h or H is identified with the SM-like Higgs boson.

It is also useful to examine the trilinear Higgs self-couplings in the Higgs basis. Using the results of Ref. [39], the three-Higgs vertex Feynman rules (including the corresponding symmetry factor for identical particles but excluding an overall factor of i are given by:

$$g_{hAA} = -v\left[(Z_3 + Z_4 - Z_5)\sin(\beta - \alpha) + Z_7 \cos(\beta - \alpha)\right], \tag{5.90}$$

$$g_{HAA} = -v\left[(Z_3 + Z_4 - Z_5)\cos(\beta - \alpha) - Z_7 \sin(\beta - \alpha)\right], \tag{5.91}$$

$$g_{hHH} = -3v\left[Z_1 \sin(\beta - \alpha)c_{\beta-\alpha}^2 + Z_{345}\sin(\beta - \alpha)\left(\tfrac{1}{3} - c_{\beta-\alpha}^2\right)\right.$$
$$\left. + Z_6 \cos(\beta - \alpha)(1 - 3s_{\beta-\alpha}^2) + Z_7 s_{\beta-\alpha}^2 \cos(\beta - \alpha)\right], \tag{5.92}$$

$$g_{Hhh} = -3v\left[Z_1 \cos(\beta - \alpha)s_{\beta-\alpha}^2 + Z_{345}\cos(\beta - \alpha)\left(\tfrac{1}{3} - s_{\beta-\alpha}^2\right)\right.$$
$$\left. - Z_6 \sin(\beta - \alpha)(1 - 3c_{\beta-\alpha}^2) - Z_7 c_{\beta-\alpha}^2 \sin(\beta - \alpha)\right], \tag{5.93}$$

$$g_{hhh} = -3v\left[Z_1 s_{\beta-\alpha}^3 + Z_{345}\sin(\beta - \alpha)c_{\beta-\alpha}^2 + 3Z_6 \cos(\beta - \alpha)s_{\beta-\alpha}^2 + Z_7 c_{\beta-\alpha}^3\right], \tag{5.94}$$

$$g_{HHH} = -3v\left[Z_1 c_{\beta-\alpha}^3 + Z_{345}\cos(\beta - \alpha)s_{\beta-\alpha}^2 - 3Z_6 \sin(\beta - \alpha)c_{\beta-\alpha}^2 - Z_7 s_{\beta-\alpha}^3\right], \tag{5.95}$$

$$g_{hH^+H^-} = -v\left[Z_3 \sin(\beta - \alpha) + Z_7 \cos(\beta - \alpha)\right], \tag{5.96}$$

$$g_{HH^+H^-} = -v\left[Z_3 \cos(\beta - \alpha) - Z_7 \sin(\beta - \alpha)\right]. \tag{5.97}$$

The trilinear Higgs couplings expressed in terms of the physical Higgs masses are given in Appendix B of Ref. [10].

Consider the alignment limit, $\cos(\beta - \alpha) \to 0$, where h is SM-like. Then Eqs. (5.58) and (5.94) yield,[30]

$$g_{hhh} = g_{hhh}^{\rm SM}\left[1 + \frac{2Z_6}{Z_1}\cos(\beta - \alpha) + \left(\frac{Z_{345}}{Z_1} - \frac{2Z_6^2}{Z_1^2} - \frac{3}{2}\right)c_{\beta-\alpha}^2 + \mathcal{O}(c_{\beta-\alpha}^3)\right], \tag{5.98}$$

where the self-coupling of the SM Higgs boson is given by

$$g_{hhh}^{\rm SM} = -\frac{3m_h^2}{v}. \tag{5.99}$$

Note that in the alignment limit, $m_h^2 \approx Z_1 v^2$ [cf. Eq. (5.55)], which implies that $Z_1 \approx 0.26$.

It is convenient to make use of Eq. (5.61) [in a convention where $\sin(\beta - \alpha) \geq 0$] to write

$$\cos(\beta - \alpha) = -\eta Z_6, \tag{5.100}$$

where

$$\eta \equiv \frac{v^2}{\sqrt{(m_H^2 - m_h^2)(m_H^2 - Z_1 v^2)}} = \begin{cases} \mathcal{O}(1), & \text{for } m_H^2 \sim \mathcal{O}(v^2), \\ \mathcal{O}\left(\dfrac{v^2}{m_H^2}\right) \ll 1, & \text{in the decoupling limit.} \end{cases} \tag{5.101}$$

Inserting Eq. (5.100) in Eq. (5.98) yields

$$g_{hhh} = g_{hhh}^{\rm SM}\left\{1 + \left[(Z_{345} - \tfrac{3}{2}Z_1)\eta^2 - 2\eta\right]\frac{Z_6^2}{Z_1} + \mathcal{O}(\eta^3 Z_6^3) + \mathcal{O}(\eta^2 Z_6^4)\right\}. \tag{5.102}$$

In the decoupling limit (where $\eta \ll 1$),

$$g_{hhh} = g_{hhh}^{\rm SM}\left\{1 - \frac{2\eta Z_6^2}{Z_1} + \mathcal{O}(\eta^2 Z_6^2)\right\}. \tag{5.103}$$

---

[30]Eq. (5.98) is obtained in the convention where $\sin(\beta - \alpha)$ is non-negative, i.e. $\sin(\beta - \alpha)$ is close to 1.
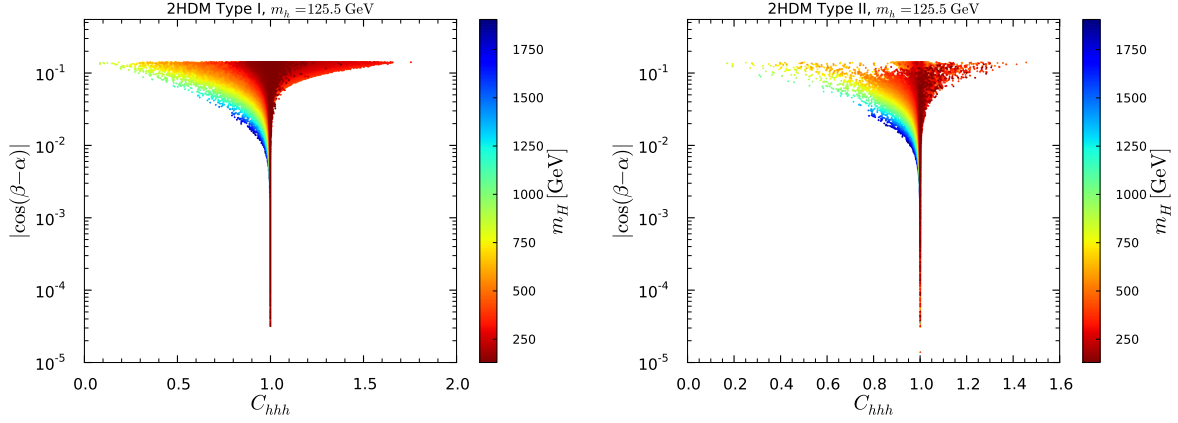
Figure 5.16. $|c_{\beta-\alpha}|$ versus the reduced triple Higgs coupling C_{hhh} in Type I (left) and Type II (right) with m_H color code. Points are ordered from high to low m_H values.

It follows that g_{hhh} is always suppressed with respect to the SM in the decoupling limit.[31] This behavior is confirmed in our numerical analysis. In contrast, in the alignment limit without decoupling, $|Z_6|$ is significantly smaller than 1 and $\eta \sim \mathcal{O}(1)$. It is now convenient to use Eq. (5.41) to eliminate Z_{345},

$$
g_{hhh} = g_{hhh}^{\text{SM}}\left\{1 + \left[\left(Z_7 \tan 2\beta - \tfrac{1}{2}Z_1\right)\eta^2 - 2\eta\right]\frac{Z_6^2}{Z_1} + (2\cot 2\beta - \tan 2\beta)\eta^2 \frac{Z_6^3}{Z_1} + \mathcal{O}(Z_6^3)\right\},
\tag{5.104}
$$

where the term above designated by $\mathcal{O}(Z_6^3)$ contains no potential enhancements in the limit of $s_{2\beta} \to 0$ or $c_{2\beta} \to 0$. Given that $\eta \sim \mathcal{O}(1)$ in the alignment limit without decoupling, the form of Eq. (5.104) suggests two ways in which g_{hhh} can be enhanced with respect to the SM. For example if $\tan\beta \sim 1$, then one must satisfy $(Z_7 - Z_6)\eta\tan 2\beta \gtrsim 2 + \tfrac{1}{2}Z_1\eta$. Alternatively, if $\tan\beta \gg 1$, then one must satisfy $Z_6\eta\cot 2\beta \gtrsim 1 + \tfrac{1}{4}Z_1\eta$ (the latter inequality requires $Z_6 < 0$, since $\cot 2\beta < 0$ when $\tfrac{1}{4}\pi < \beta < \tfrac{1}{2}\pi$). In both cases, $g_{hhh} > g_{hhh}^{\text{SM}}$ is possible even when $|Z_6|$ and $|Z_7|$ are significantly smaller than 1. Indeed, both of the above alternatives correspond to $Z_{345} \gg Z_1$ and $\eta Z_{345} \gg 1$ in Eq. (5.102).

While the exceedingly small deviations in C_V^h that we consider here will most likely not be directly accessible at the LHC, precision measurements of the other couplings together with a measurement of, or a limit on, $m_{H,A}$ can be used for consistency checks

---

[31]In the double decoupling limit where $\eta \ll 1$ *and* $|Z_6| \ll 1$, Eq. (5.103) shows that the deviation of g_{hhh} from the corresponding SM value is highly suppressed.

and for eventually pinning down the model. Of special interest in this context is also the triple Higgs coupling. The dependence of $C_{hhh} \equiv g_{hhh}/g_{hhh}^{\text{SM}}$ on $c_{\beta-\alpha}$ and m_H is shown in Fig. 5.16. It is quite striking that large values of $C_{hhh} > 1$ (up to $C_{hhh} \approx 1.7$ in Type I and up to $C_{hhh} \approx 1.5$ in Type II) can be achieved in the non-decoupling regime, roughly $m_H \lesssim 600$ GeV, for $|c_{\beta-\alpha}|$ values of the order of 0.1, whereas for heavier m_H, C_{hhh} is always suppressed as compared to its SM prediction. These features were explained in the discussion below Eq. (5.98).[32] Note also that for $m_H \sim 1$ TeV, C_{hhh} approaches the SM limit of 1 as $|\cos(\beta - \alpha)|$ decreases more slowly than is the case for lighter m_H; substantial deviations $C_{hhh} < 1$ are possible as long as $|c_{\beta-\alpha}|$ is roughly greater than a few times 10^{-2}. This comes from the $(2Z_6/Z_1)c_{\beta-\alpha}$ term in Eq. (5.98): since, in the convention where $\sin(\beta - \alpha) \geq 0$, $Z_6 c_{\beta-\alpha}$ is always negative, cf. Eq. (5.60), and since Z_6 can be sizable when $m_H \sim 1$ TeV, see Fig. 5.13, this can lead to a suppression as extreme as $C_{hhh} \approx 0.1$. (For $m_H \gg 1$ TeV the deviations are smaller in part because the possible range of $c_{\beta-\alpha}$ is limited as seen in Fig. 5.13.) For very light m_H, on the other hand, Z_6 is much smaller and hence the deviations with $C_{hhh} < 1$ are more limited. For $m_H \lesssim 250$ GeV we find $C_{hhh} \approx 0.80$–1.40 in Type I and $C_{hhh} \approx 0.90$–1.35 in Type II. This is at the limit of what can be measured, as the expected precision is about 50% at the high-luminosity options of the LHC and the ILC with 500 GeV, and about 10–20% at a 1–3 TeV e^+e^- linear collider with polarised beams [63].

As a second example, consider the hAA coupling given in Eq. (5.90). Using Eq. (5.41), we find that in the alignment limit,

$$
\begin{aligned}
g_{hAA} &= -\frac{1}{v}\left\{m_h^2 - 2Z_5 v^2 - (Z_6 - Z_7)v^2 \tan 2\beta + 2Z_6 v^2 \cot 2\beta + \mathcal{O}(\cos(\beta-\alpha))\right\} \\
&= -\frac{1}{v}\left\{m_h^2 - 2\lambda_5 v^2 + 2Z_6 v^2 \cot 2\beta + \mathcal{O}(\cos(\beta-\alpha))\right\},
\end{aligned}
\tag{5.105}
$$

A similar computation yields the Hhh coupling given in Eq. (5.93),

$$
g_{Hhh} = \frac{1}{v}\left\{3Z_6 v^2 - \left[m_h^2 - 4Z_6 v^2 \cot 2\beta + 2(Z_6 - Z_7)v^2 \tan 2\beta\right]\cos(\beta-\alpha) + \mathcal{O}(\cos(\beta-\alpha)^2)\right\}.
\tag{5.106}
$$

---

[32]This cannot be seen directly in Fig. 5.16, but we verified that points with $m_H > 630$ GeV never have $C_{hhh} > 1$.

In the alignment limit without decoupling, the $\mathcal{O}(1)$ terms in Eqs. (5.105) and (5.106) that are proportional to Z_6 should be regarded as terms of $\mathcal{O}(\cos(\beta - \alpha))$ (cf. Eqs. (5.100) and (5.101)). That is, the decoupling limit (with $Z_6 \sim \mathcal{O}(1)$) and the alignment limit without decoupling can be distinguished in the trilinear Higgs couplings. Indeed, the Hhh coupling is suppressed in the alignment limit without decoupling, whereas it can be of $\mathcal{O}(v)$ in the decoupling limit. All the other trilinear Higgs self-couplings can be analyzed in the alignment limit following the procedure outlined above.

Last but not least, it is noteworthy that

$$g_{hH^+H^-} = -v\left[Z_3 + \mathcal{O}(\cos(\beta - \alpha))\right], \tag{5.107}$$

approaches a finite nonzero value in the alignment limit, with or without decoupling. This is relevant for the analysis of the one-loop process $h \to \gamma\gamma$, which has a contribution that is mediated by a $H^\pm$ loop. In the decoupling limit, the charged Higgs loop amplitude is suppressed by a factor of $\mathcal{O}(v^2/m_{H^\pm}^2)$ relative to the $W^\pm$ and the top quark loop contributions. But, in the alignment limit without decoupling, the charged Higgs loop is parametrically of the same order as the corresponding SM loop contributions, thereby leading to a shift of the $h \to \gamma\gamma$ decay rate from its SM value. This is in stark contrast to the behavior of tree-level Higgs couplings, which approach their SM values in the alignment limit with or without decoupling. That is, the loop-corrected Higgs couplings to SM particles approach their SM values in the decoupling limit, but can yield deviations in the alignment limit without decoupling due to internal loops involving light non-SM-like Higgs states.

Consider next the case of a SM-like H. In the alignment limit, $\sin(\beta - \alpha) \to 0$,

$$m_h^2 = m_A^2 + Z_5 v^2 + \mathcal{O}(s_{\beta-\alpha}^2), \tag{5.108}$$

$$m_H^2 = Z_1 v^2 + \mathcal{O}(s_{\beta-\alpha}^2). \tag{5.109}$$

Using this result in Eq. (5.95) yields

$$g_{HHH} = g_{hhh}^{\mathrm{SM}}\left[1 + \mathcal{O}(s_{\beta-\alpha}^2)\right]. \tag{5.110}$$

Note that there is no decoupling limit in this case since by assumption $m_H \simeq 125$ GeV, so all Higgs squared-masses are of $\mathcal{O}(v^2)$. That is H is a SM-like Higgs in the alignment limit without decoupling. As in the first case of a SM-like h treated above, the deviation of g_{HHH} from the Standard Model value is quadratic in the small parameter, $\sin(\beta - \alpha)$. The analysis of the other trilinear Higgs self-couplings in the alignment limit is left as an exercise for the reader.

5.5.3 Natural alignment

Before concluding theoretical discussion, we examine a second theoretical distinction between the decoupling limit and alignment limit without decoupling. The SM Higgs sector is famously unnatural [182, 183]. In particular, a fine tuning of the Higgs sector squared-mass parameter is required in order to explain the observed value of the vacuum expectation value (vev), $v \approx 246$ GeV. The 2HDM generically requires two separate and independent fine tunings. In addition to identifying $v \approx 246$ GeV, which fixes the values of Y_1 and Y_3 in Eq. (5.45), one must also perform a second fine-tuning to fix the squared-mass parameter Y_2 to be of $\mathcal{O}(v^2)$. Thus, the regime of the decoupling limit (where $Y_2 \gg v^2$) is less fine-tuned than the general 2HDM, since the natural value for Y_2 is the ultraviolet cutoff of the theory beyond which new physics presumably enters. As long as the heavier Higgs scalars (whose squared masses are of order Y_2) are sufficiently massive, then h will be SM-like.[33]

In contrast, in the case of alignment without decoupling (or in the double decoupling limit), we have $|Z_6| \ll 1$, which is a finely-tuned region of the 2HDM parameter space (beyond the two tunings discussed above) unless we can demonstrate that $Z_6 = 0$ is a consequence of an enhanced symmetry of the theory. In the absence of Higgs–fermion Yukawa couplings, it is sufficient to consider the symmetry properties of the scalar potential. Note that we have already imposed a softly-broken $\mathbb{Z}_2$ symmetry, which yields $\lambda_6 = \lambda_7 = 0$ in the original basis. In addition, we observe that $Z_6 = Z_7 = 0$ [which also

---

[33]In general, $m_H^2 \gg |Z_6| v^2$ is sufficient to guarantee SM-like h couplings. However, in the 2HDM with Type-II Yukawa coupling and $\tan \beta > 1$, a SM-like h coupling to down-type quarks and leptons requires $m_H^2 \gg |Z_6| v^2 \tan \beta$, leading to the phenomenon of delayed decoupling [39, 180, 184] at large $\tan \beta$. This is a special case of delayed alignment introduced below Eq. (5.89).

implies that $Y_3 = 0$ in light of Eq. (5.45)] corresponds to an exact $\mathbb{Z}_2$ symmetry in the Higgs basis.

The conditions $Z_6 = Z_7 = 0$ can be implemented in three ways. If $s_{2\beta} = 0$, then only one of the two Higgs fields acquires a non-zero vev. This means that our original basis and the Higgs basis coincide (in a convention where H_1 denotes the Higgs field with the non-zero vev), in which case the original $\mathbb{Z}_2$ symmetry is unbroken. If $\lambda_6 = \lambda_7 = 0$ and $s_{2\beta}c_{2\beta} \neq 0$, then setting $Z_6 = Z_7 = 0$ in Eqs. (5.38) and (5.39) yields $\lambda_1 = \lambda_2 = \lambda_{345}$. Such a scalar potential exhibits a softly-broken CP3 symmetry, one of the three possible generalized CP symmetries that can be imposed on the 2HDM [185].[34] Finally, if the scalar potential exhibits an exact CP2 symmetry, or equivalently there is a basis in which the $\mathbb{Z}_2$ discrete symmetry ($\Phi_1 \to +\Phi_1$, $\Phi_2 \to -\Phi_2$) and a second $\mathbb{Z}_2$ interchange symmetry ($\Phi_1 \longleftrightarrow \Phi_2$) coexist [151, 185], then it follows that $\lambda_6 = \lambda_7 = 0$, $\lambda_1 = \lambda_2$ (with λ_5 real), $m_{11}^2 = m_{22}^2$ and $m_{12}^2 = 0$. In this case, Eqs. (5.3) and (5.4) yield $\tan\beta = 1$. [35] The latter can be maintained when the CP2 symmetry is softly broken such that $m_{12}^2 \neq 0$. Using Eqs. (5.38) and (5.39) then yields $Z_6 = Z_7 = 0$. Thus, in the absence of the Higgs-fermion Yukawa couplings, $Z_6 = 0$ is a consequence of an enhanced symmetry of the scalar potential, in which case the regime of alignment without decoupling and the double decoupling regime are both natural in the sense of 't Hooft [186].

5.5.4 Prediction for signal strengths in the alignment limit

In this section, we present the numerical results for the case that the lighter scalar h is the observed Higgs state at 125.5 GeV. In this case, $m_H \geq 129.5$ GeV, while the pseudoscalar A can in principle be heavier or lighter than h and/or H. As a general comment, many conclusions drawn in this particular study duplicate the ones discussed in Sec. 5.3. This is certainly not surprising as both the alignment and decoupling limits are covered in the general scan.

The variations in the couplings to fermions discussed above have direct consequences

---

[34]If $m_{12}^2 = 0$ in Eq. (5.1) in addition to $\lambda_6 = \lambda_7 = 0$, then the $\mathbb{Z}_2$ discrete symmetry ($\Phi_1 \to +\Phi_1$, $\Phi_2 \to -\Phi_2$) is exact. In this case, $Z_6 = Z_7 = 0$ implies that $\lambda_1 = \lambda_2 = \lambda_{345}$ *and* $m_{11}^2 = m_{22}^2$ [the latter via Eq. (5.44)], and corresponds to an *exact* CP3 symmetry of the scalar potential.

[35]Here we assume that $\lambda_1 \neq \lambda_{345}$; otherwise, the CP2 symmetry is promoted to the CP3 symmetry previously considered.

for the signal strengths of the SM-like Higgs boson. Since the results depend a lot on the fermion coupling structure, we examine this separately for Type I and Type II.

Putting everything together we find quite distinct correlations of signal strengths in both Type I and Type II that depend on whether the additional Higgs states are decoupled or not. This is illustrated in Fig. 5.17 for Type I and in Fig. 5.18 for Type II. In both figures, the panels on the left show the dependence on m_H while the panels on the right show the dependence on $|c_{\beta-\alpha}|$ for the non-decoupling regime with $m_H \leq 600$ GeV. We note that there are definite combinations of signal strengths that cannot be reached in the decoupling regime. A measurement of such values would be a very strong motivation to look for additional light Higgs states. In turn, when the masses of additional light Higgs states are measured, signal strength correlations as shown in Figs. 5.17 and 5.18 can help pin down the model. Furthermore, for $m_H \leq 600$ GeV even in the apparent alignment limit $|c_{\beta-\alpha}| \to 0$ there can be deviations in the signal strengths from unity that cannot be mimicked by decoupling.

Examples for Type I are the suppression of both $\mu_{gg}^h(\gamma\gamma)$ and $\mu_{gg}^h(ZZ^*)$, or the combination $\mu_{gg}^h(\gamma\gamma) > 1$ with $\mu_{gg}^h(ZZ^*) \approx 1$. The former case is also present in Type II for light m_H, while the latter does not occur at all in Type II. More concretely, in the decoupling regime of Type II, $\mu_{gg}^h(\gamma\gamma) \approx \mu_{gg}^h(ZZ^*)$, whereas for light m_H one can have $\mu_{gg}^h(\gamma\gamma) < \mu_{gg}^h(ZZ^*)$ even if $|\cos(\beta-\alpha)|$ is very small (comparing Fig 5.18, top row, left vs. right). Another example is the simultaneous suppression or enhancement of $\mu_{gg}^h(\gamma\gamma)$ and $\mu_{\text{VBF}}^h(\gamma\gamma)$ in Type I, that is not possible in the decoupling regime (cf. Fig 5.17, bottom left). In Type II, one can have a simultaneous enhancement, up to 1.45 of $\mu_{gg}^h(\gamma\gamma)$ and $\mu_{\text{VBF}}^h(\gamma\gamma)$ in the decoupling regime, but simultaneous suppression is limited to ~ 0.9–0.95 (cf. Fig 5.18, middle left); simultaneous suppression to a level of ~ 0.8 is however possible in the alignment limit for $m_H \lesssim 300$ GeV, i.e. well away from the decoupling regime. Precise enough signal strength measurements could therefore provide strong hints that we are in the alignment without decoupling regime of a 2HDM even if no additional Higgs states are discovered at that time.
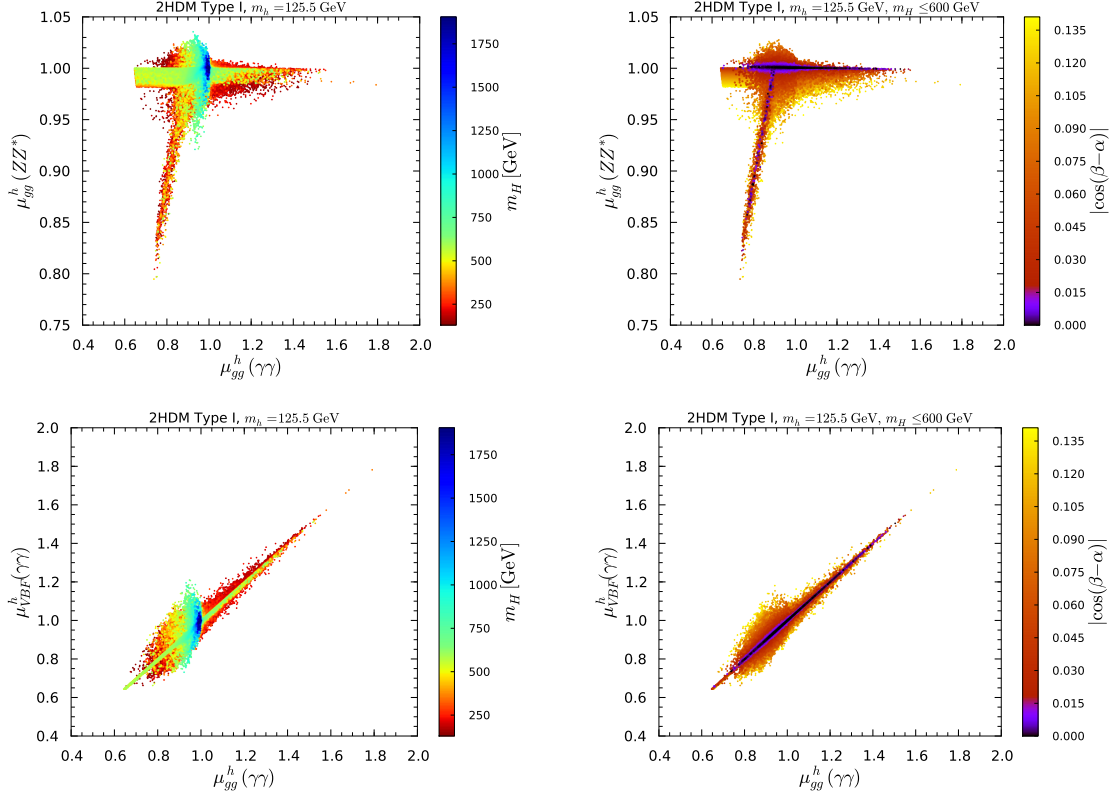
Figure 5.17. Correlations of signal strengths in Type I, on the left illustrating the dependence on m_H, on the right illustrating the dependence in $|c_{\beta-\alpha}|$. Points are ordered from low to high m_H values and high to low $|c_{\beta-\alpha}|$ values.

5.6 Search for other Higgs bosons at future colliders

Perhaps of greatest interest for the future are the constraints on the other Higgs bosons and resulting implications for their possible future discovery. To address this question, we show in Fig. 5.19 $m_{H^\pm}$ color-coded in the m_H versus m_A plane, with the ordering going from high (blue) to low (red) $m_{H^\pm}$ values. There is a strong interrelation among three Higgs masses, m_A, m_H and $m_{H^\pm}$, which arises from the constraints of the electroweak precision T parameter. Indeed, we see that in both Type I and Type II, if the scalar H is heavy and decoupled, the same is true for the pseudoscalar A and the charged Higgs $H^\pm$. Conversely, if the H is light, say below 600 GeV, also the A and $H^\pm$ must have masses below about 800 GeV. While the correlation of $m_{H^\pm}$ with m_H and m_A is somewhat different in Type I and Type II, in both models a light charged Higgs below 500–600 GeV requires that the H and A also be not too heavy, with mass below about

136

Figure 5.18. Correlations of signal strengths in Type II, on the left illustrating the dependence on m_H, on the right illustrating the dependence in $|c_{\beta-\alpha}|$. Points are ordered from low to high m_H values and high to low $|c_{\beta-\alpha}|$ values.

800 GeV. When inverting the plotting order of $m_{H^\pm}$ (not shown), we find that the charged Higgs mass also poses a lower limit on m_H and m_A: for $m_{H^\pm} \sim 1$ TeV, also $m_{H,A}$ are of that order. In turn, when m_H and m_A are in the non-decoupling regime, also $m_{H^\pm}$ cannot be much heavier. The range of m_A is also interesting. In principle m_A can be above or below $m_{h,H}$, and even $m_A < m_h/2$ is possible and consistent with the data [9]. However, once $m_{H^\pm}$ is fixed, the allowed range of m_A is limited (and vice versa). This is because that the perturbativity condition on λ_4 and λ_5 sets up both lower and upper bounds on m_A for a certain value of $m_{H^\pm}$. To see this, one can recall the relation between m_A and $m_{H^\pm}$ in Eq. (5.10). The same analysis applies to Type II models but with a lower bound on $m_{H^\pm}$ of about 300 GeV from B-physics constraints. As a result, the presence of simultaneously low m_A and m_H in Type II is eliminated. This is due to the fact that at low m_A the precision electroweak T parameter constraint would be violated if m_H differs
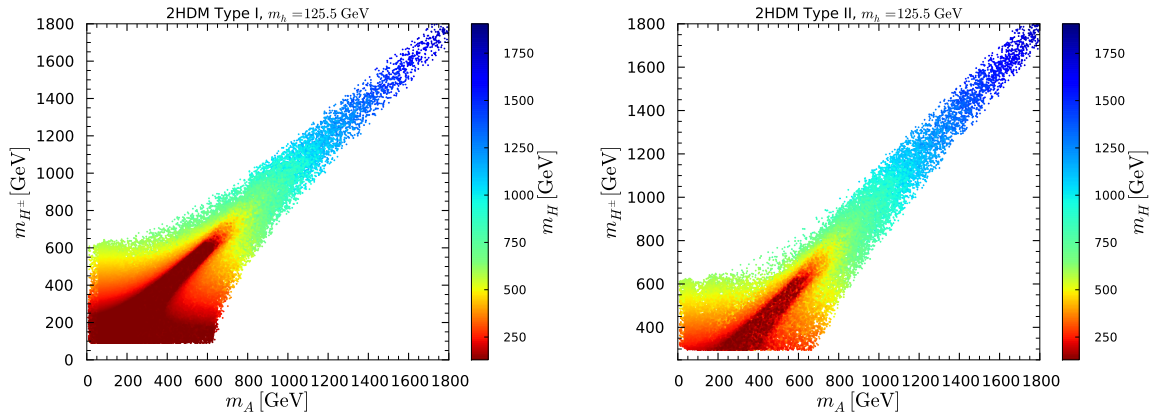
Figure 5.19. $m_{H^\pm}$ versus m_A in Type I (left) and Type II (right) with the color code indicating the value of m_H. Points are ordered from high to low m_H.

very much from $m_{H^\pm}$.[36]

We omit the plots for the $H125$ case as they have been displayed in Fig. 5.2. First of all, there is no decoupling limit for the $H125$ case with an upper bound of $m_{H^\pm} \sim m_A \lesssim$ 650 GeV and nondecoupling effects are inevitably of importance. The electroweak precision T parameter further shrinks the allowed region; as a result, there is more correlation between $m_{H^\pm}$ and m_A. If m_A is large then either $m_{H^\pm}$ is of similar size or it is between 100 GeV and 200 GeV. If m_A is small, $\lesssim$ 100 GeV, then $m_{H^\pm}$ will lie between 100 GeV and 200 GeV. Type II with $m_H \sim 125.5$ GeV is the most constrained case, with a strong $m_{H^\pm}$–m_A correlation. The additional bound of $m_{H^\pm} \sim 300$ GeV from B-physics results in $m_A \gtrsim 200$ GeV.

5.6.1 Main production modes

Following what is discussed above, it is important to consider implications of the current and future h fits for the heavier Higgs bosons. Hopefully, one will retain a significant possibility of detecting the heavier Higgs bosons even if the h is shown to be very SM-like. To assess the situation, we consider the two largest production modes at the LHC; these are gluon fusion, $gg \to X$, and associated production with a pair of b-quarks, $b\bar{b}X$, with $X = A, H$. To illustrate the comparison between these two production modes, we plot

---

[36]Very recently, the analysis of Misiak and collaborators [187] has improved the charged Higgs mass bound in the Type II 2HDM to $m_{H^\pm} \gtrsim 480$ GeV at 95% CL. We have not implemented this stricter bound in our scans.
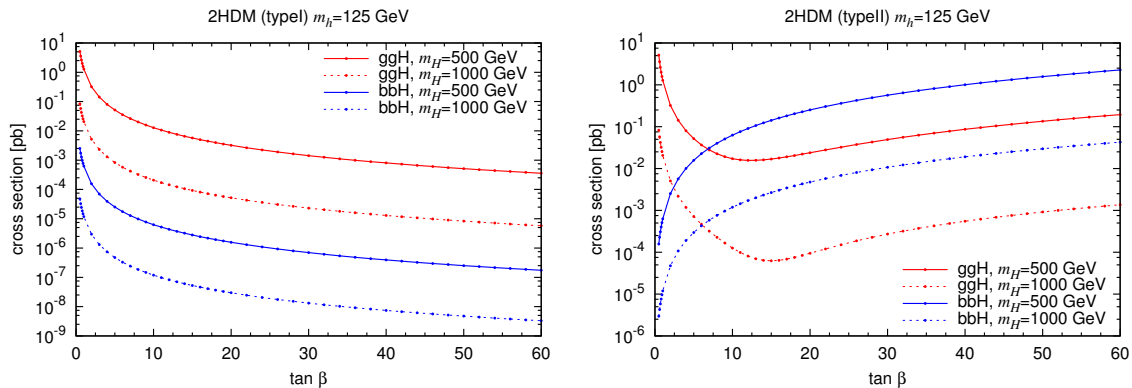
Figure 5.20. Cross sections (in pb) for $gg \to H$ and bbH production at $\sqrt{s} = 8$ TeV as a function of $\tan\beta$ for $m_H = 500$ GeV and 1 TeV. The results shown are for the SM limit of $\sin(\beta - \alpha) = 1$.

for two representative masses (500 GeV and 1 TeV) the two cross sections vs. $\tan\beta$ in Fig. 5.20 with α chosen so that $\sin(\beta - \alpha) = 1$. In the case of Type II, we observe that at low $\tan\beta$ it is $\sigma(gg \to H)$ that is biggest while at high $\tan\beta$ it is $\sigma(bbH)$ that is biggest by a factor of ~ 10 to 100.

The correlations of the $gg \to X$ and $b\bar{b}X$ cross sections at the 13 TeV LHC in the non-decoupling regime $m_H \leq 600$ GeV are shown in Fig. 5.21 for the Type I model and in Fig. 5.22 for the Type II model. We show the points that pass all present constraints (in beige) and highlight those that have a very SM-like 125 GeV Higgs state by constraining all the following signal strengths to be within 5% or 2% of their SM values, respectively, denoted as SM±5% (red) and SM±2% (dark red):

$$\mu^h_{gg}(\gamma\gamma), \ \mu^h_{gg}(ZZ^*), \ \mu^h_{gg}(\tau\tau), \ \mu^h_{VBF}(\gamma\gamma), \ \mu^h_{VBF}(ZZ^*), \ \mu^h_{VBF}(\tau\tau), \ \mu^h_{VH}(b\bar{b}), \ \mu^h_{t\bar{t}}(b\bar{b}) .$$
(5.111)

We start the discussion with production of A in Type I, shown in the left panel of Fig. 5.21. There is a strong correlation between the two production modes, gluon fusion and $b\bar{b}$ associated production, which stems from the fact that the relevant couplings are the same up to a sign: $C^A_U = -C^A_D = \cot\beta$. The larger spread in $\sigma(b\bar{b}A)$ observed for $\sigma(gg \to A) > 10^{-2}$ pb comes from the fact that for $m_A \lesssim 400$ GeV the $b\bar{b}A$ cross section grows faster with decreasing m_A than that of $gg \to A$. Therefore, along a line of fixed $\sigma(gg \to A)$ in the plot, a point with higher $\sigma(b\bar{b}A)$ has a smaller m_A. Note also that
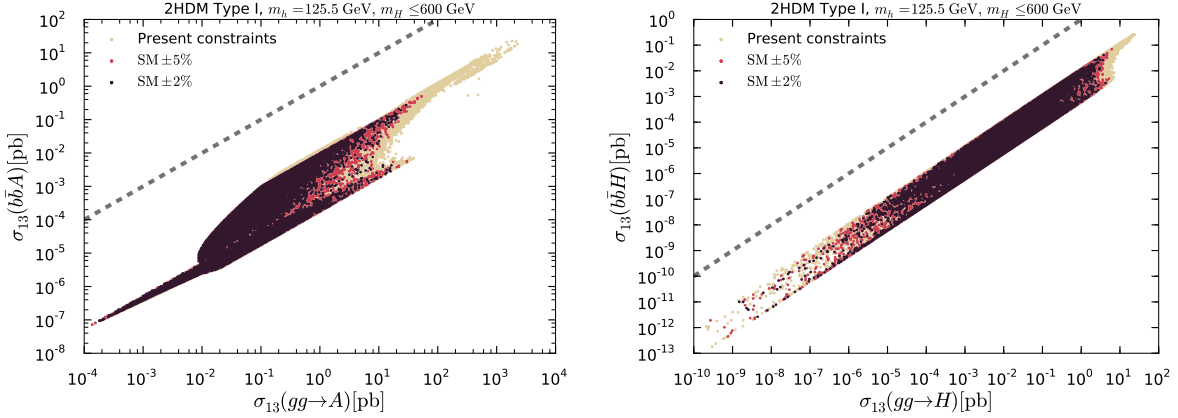
Figure 5.21. $\sigma(b\bar{b}X)$ versus $\sigma(gg \to X)$ for $X = A$ (left) and $X = H$ (right) in Type I at the 13 TeV LHC for points satisfying all present constraints (in beige) as well as points for which the signals strengths from Eq. (5.111) are within 5% and 2% of the SM predictions (in red and dark red, respectively). The dashed lines indicate $\sigma(b\bar{b}X) = \sigma(gg \to X)$.

there is an interference of the top and bottom loop diagrams in $gg \to A$ which changes sign depending on m_A. Overall, however, $\sigma(gg \to A)$ is always at least two orders of magnitude larger than $\sigma(b\bar{b}A)$.

The points with largest cross sections, $\sigma(b\bar{b}A) \approx 10$ pb and $\sigma(gg \to A) \approx 1000$ pb, correspond to the case $m_A < m_h/2$ which was studied in detail in [9]. One feature of this region is that $\mu_{gg}^h(\gamma\gamma)$ and $\mu_{gg}^h(ZZ^*, WW^*)$ always differ from each other by about 10%. Constraining all h signal strengths of Eq. (5.111) within 5% of unity therefore eliminates these points. Other points with high cross sections, but not in the very light pseudoscalar region, would also be eliminated by the SM±5% or SM±2% requirements. However, in this non-decoupling regime of $m_H \leq 600$ GeV, points with sizeable cross sections up to 0.2 pb for $\sigma(b\bar{b}A)$ and up to about 40 pb for $\sigma(gg \to A)$ still remain even at the SM±2% level. At this same SM±2% level, the smallest $\sigma(gg \to A)$ is about 0.1 fb.

Regarding production of the scalar H in Type I, shown in the right panel of Fig. 5.21, the correlation is even stronger between $\sigma(b\bar{b}H)$ and $\sigma(gg \to H)$ since both are driven by the same fermionic coupling $C_F^H = \sin\alpha/\sin\beta$. Note that, as in the A case, the gluon-fusion cross section is always larger than that for $b\bar{b}$ associated production. Sizable cross sections are still allowed under the SM±2% constraint, which implies that in the
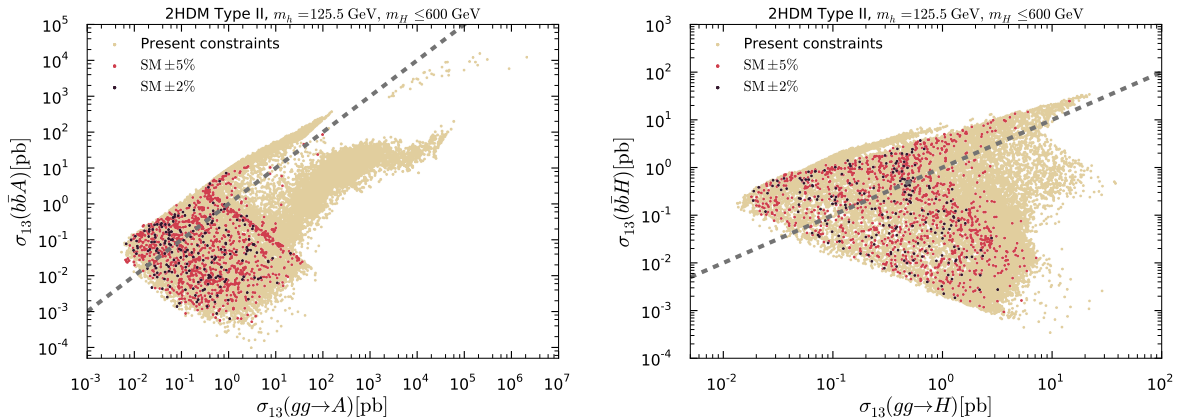
Figure 5.22. As Fig. 5.21 but for Type II.

non-decoupling regime there is a strong possibility of detecting a non-SM-like scalar state at the LHC. The structure of C_F^H is however such that the coupling can equally well be very much suppressed, leading to extremely small cross sections. We will come back to this below.

The corresponding results for Type II are presented in Fig. 5.22. In contrast to Type I, both $b\bar{b}$ associated production and gluon–gluon fusion modes for Type II are in principle important since either can be dominant in different regions of the parameter space. There is only modest correlation between the two production modes due to the more complex structure of the Type II fermionic couplings. For A production, one clearly sees the $m_A < m_h/2$ region as the detached scattered points with very large cross sections. As for Type I, these points disappear under the SM±5% constraint. Still, even for SM±2%, cross sections as large as $\sigma(b\bar{b}A) \approx 8$ pb and $\sigma(gg \to A) \approx 20$ pb can be achieved (although not simultaneously). For H production a similar picture emerges, with the cross sections however being a factor of a few smaller than for A production. The minimal cross sections in this $m_H < 600$ GeV non-decoupling regime for the A and H are correlated in a way that is very favorable for discovery during run-2 of the LHC. For example, if $\sigma(gg \to A)$ takes on its minimum SM±2% value of 10 fb then $\sigma(b\bar{b}A) \gtrsim 80$ fb, whereas if $\sigma(b\bar{b}A)$ takes on its minimal value of few×10^{-1} fb then $\sigma(gg \to A) \approx 10^3$ fb. These cross section levels imply that the A should be discoverable in at least one of the two production modes even in the extreme alignment limit.
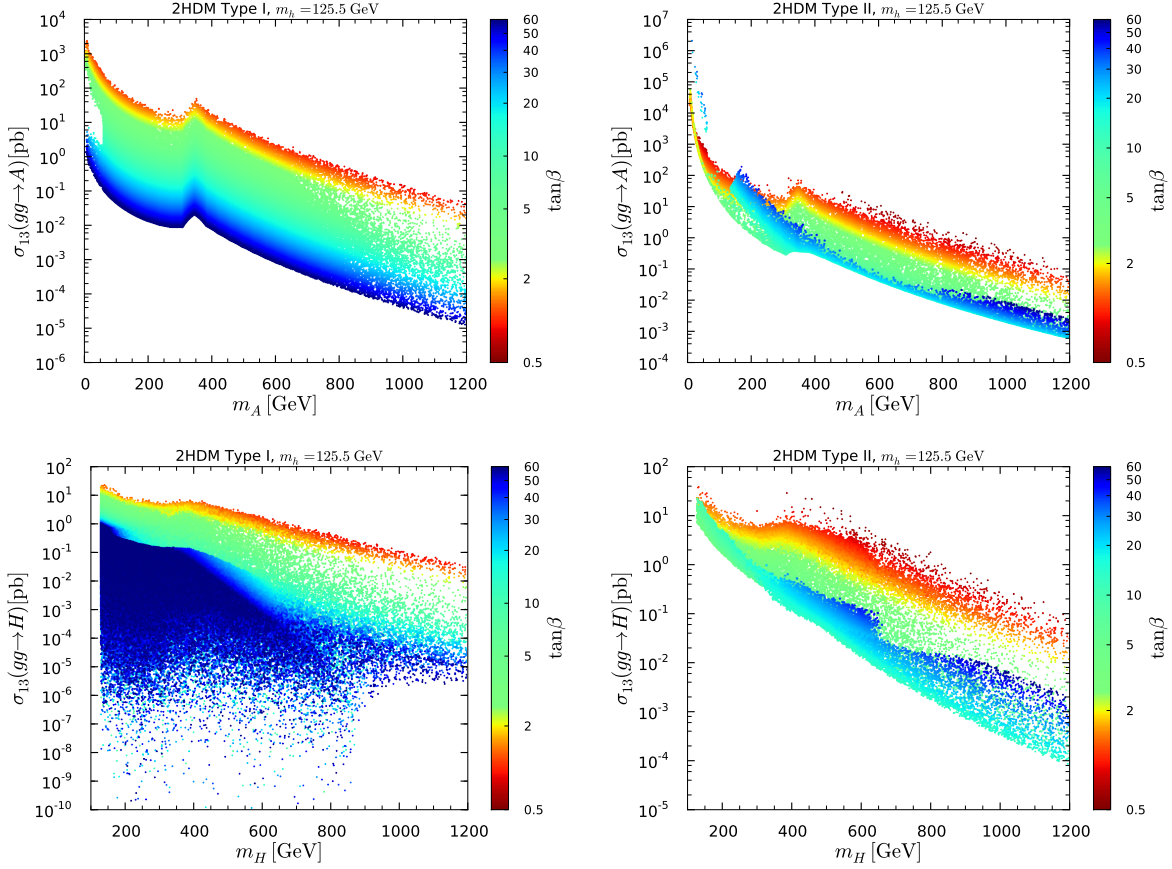
Figure 5.23. Cross sections in Type I (left) and Type II (right) for $gg \to X$ as functions of m_X for $X = A$ (upper row) and $X = H$ (lower row) with $\tan\beta$ color code. In all four plots, points are ordered from low to high $\tan\beta$.

Before considering specific decay channels of A and H, we present in Fig. 5.23 the gluon-fusion cross sections in Type I and Type II as functions of m_A and m_H at the 13 TeV LHC. Here, the color code shows the dependence on $\tan\beta$.[37] In Type I, the $gg \to A$ cross section is proportional to $\cot^2\beta$; this explains why it is larger (smaller) at lower (higher) $\tan\beta$. A cross section of 1 (0.1) fb is guaranteed for m_A as large as ~ 600 (850) GeV. On the other hand, the $gg \to H$ cross section in Type I is proportional to $(C_F^H)^2$ and can take on extremely small values for $m_H \lesssim 850$ GeV. The reason is that, in this region, the reachable values of $c_{\beta-\alpha}$ are high enough such that a cancellation between the two terms of $C_F^H = (s_{\beta-\alpha} - c_{\beta-\alpha}/t_\beta)$ occurs and leads to an almost vanishing coupling.

---

[37]To avoid a proliferation of plots, we choose to show here only the results for gluon fusion; all corresponding results for the $b\bar{b}$ cross section can be provided upon request.

In contrast, for $m_H \gtrsim 850$ GeV, this cancellation is not possible as the values of $c_{\beta-\alpha}$ are forced to be smaller as can be seen in Fig. 5.13. In Type II, the A production cross section can be very large in the very low m_A region as noted in [9] and any mass smaller than 1.1 (1.2) TeV gives a $gg \to A$ cross section larger than 1 (0.1) fb. For $gg \to H$, a cross section > 1 (0.1) fb is guaranteed up to $m_H \approx 850$ GeV (1.2 TeV). From these considerations the prospects for discovering the additional neutral states look promising should alignment without decoupling be realized.

5.6.2 H/A search in the specific channels

Let us now turn to specific signatures. There are many final states of potential interest. These include $H \to ZZ$, $H, A \to \tau\tau, \gamma\gamma, t\bar{t}$ as well as the $H \to hh$ and $A \to Zh$ final states.

- *Search in the standard modes*

With regard to the H/A limits coming from heavy Higgs bosons, we find that they have significant impact. In the case of Type I, the limits coming from $gg \to H, A \to \tau\tau$ are always stronger (even at high $\tan\beta$) than those coming from $gg \to b\bar{b}H, b\bar{b}A$ with $H, A \to \tau\tau$. This is because, in Type I models, all the fermionic couplings are the same and it is only a question of the $\tan\beta$-independent ratio of the $gg \to H, A$ cross section to the $gg \to b\bar{b}H, b\bar{b}A$ cross section. This ratio is always quite a bit larger than 1 (by typically a factor of at least 100) at any given mass. For Type II models, we note that the down-type coupling is enhanced by $\tan\beta$ and affects both production modes, in the $gg \to H, A$ case by enhancing the b-quark contribution to the one-loop coupling.

Results for $H \to ZZ$ at $\sqrt{s} = 14$ TeV are shown in Fig. 5.24. We observe that substantial $\sigma \times$ BR values (as high as ~ 1 pb at $m_H \sim 150$ GeV and ~ 1 fb at $m_H \sim 1$ TeV) are possible, but certainly not guaranteed. In the case of the Type II model, if the h is determined to have SM-like rates within $\pm 10\%$ or, especially, $\pm 5\%$ then the maximum possible $\sigma \times$ BR is substantially reduced and the minimum allowed m_H for $\pm 5\%$ is of order 200 GeV.

Results for $gg + bb \to H, A$ production in the $\tau\tau$ final state are displayed in Fig. 5.25 assuming $\sqrt{s} = 14$ TeV. Overall, the range of possible cross sections is quite large, with
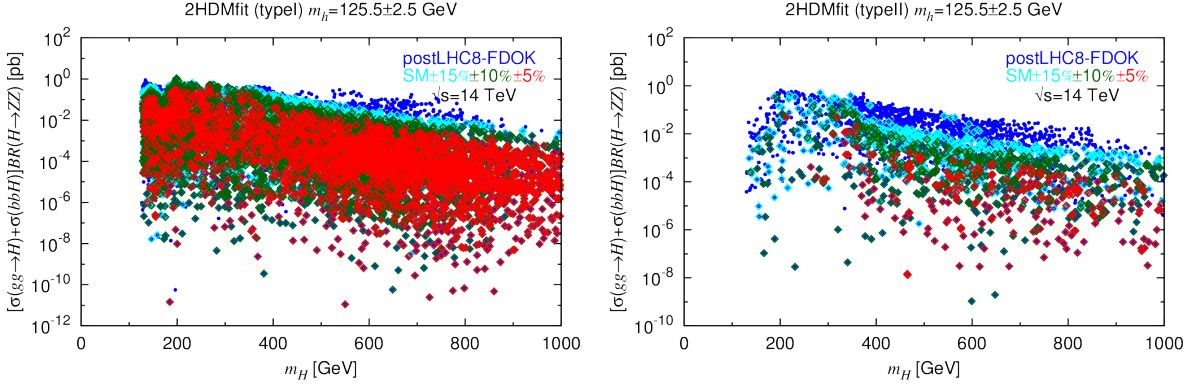
Figure 5.24. We plot $[\sigma(gg \to H) + \sigma(bbH)]\mathrm{BR}(H \to ZZ)$ as functions of m_H, for Type I (left) and Type II (right) 2HDMs. Only FDOK points are shown. Implications of various levels of precision for future h measurements are displayed. Color scheme is as for Fig. 5.9.

maximum values of order 1 to 10 pb and minimum values below 10^{-10} pb in the case of Type I (although this range is somewhat narrowed on average as the h is required to be more and more SM-like) and minimum values of order $10^{-4} - 10^{-5}$ pb in the case of Type II. It is worth noting that for lower values of m_H and m_A, $[\sigma(gg \to H) + \sigma(bbH)]\mathrm{BR}(H \to \tau\tau)$ and $[\sigma(gg \to A) + \sigma(bbA)]\mathrm{BR}(A \to \tau\tau)$ are typically quite substantial in the Type II case, but that few points survive below $m_H \sim 300$ GeV if the 125.5 GeV state rates lie within 5% of the SM Higgs predictions. We comment on one particular feature of the plots, namely the fact that the $t\bar{t}$ threshold is not apparent for Type II in the case of the A. This is a direct consequence of the fact that the LHC8 constraints include the limits from [92] on $gg \to A$ and bbA with $A \to \tau\tau$. The predicted 2HDM cross sections can significantly exceed these limits in the region below $2m_t$. Since these limits are included in obtaining the postLHC8 results the $t\bar{t}$ threshold that would otherwise be apparent is not present. Note that in the case of the H, the limits of [92] do not have a strong impact because the predicted values of $\sigma(gg \to H)\mathrm{BR}(H \to \tau\tau)$ are smaller due to the fact that $H \to ZZ$ decays are also present.

It is also interesting to consider the $\tan\beta$ dependence of the cross sections, indicated by a color code in Fig. 5.25. As expected from the fermionic couplings in Table 5.4, this dependence is opposite in Type I and Type II. Concretely, in Type I $[\sigma(gg \to H) + \sigma(bbH)]\mathrm{BR}(H \to \tau\tau)$ and $[\sigma(gg \to A) + \sigma(bbA)]\mathrm{BR}(A \to \tau\tau)$ increase as $\tan\beta$ gets
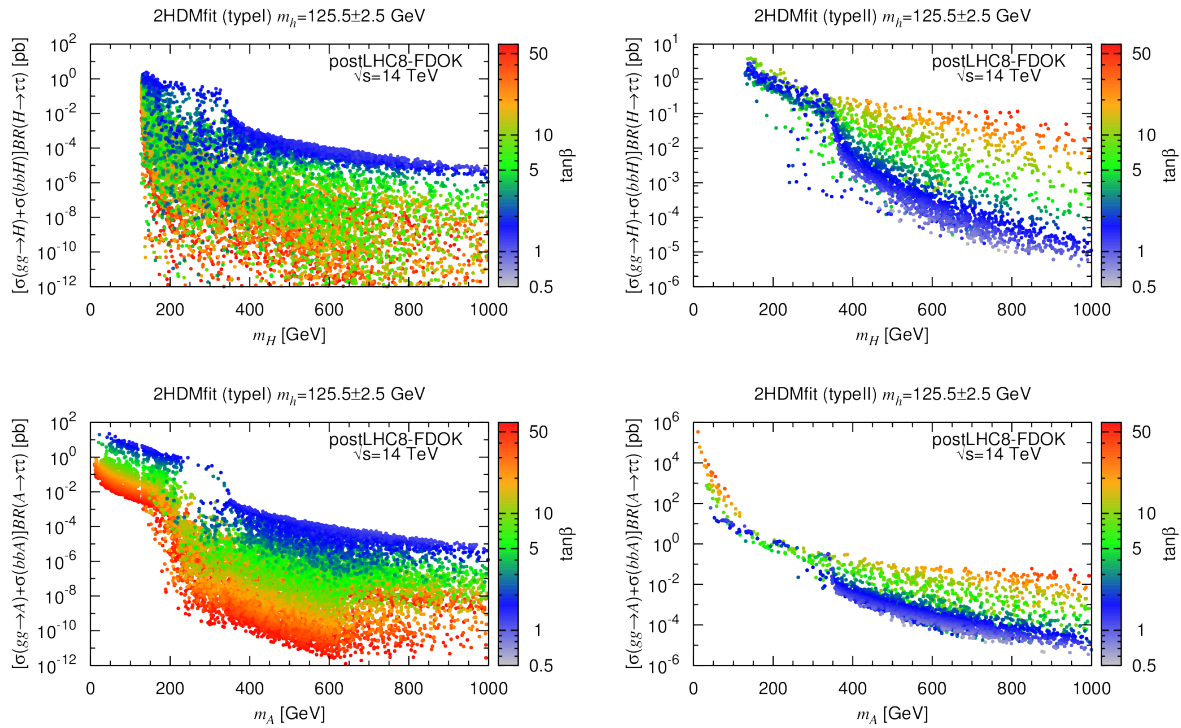
Figure 5.25. Scatter plots of $[\sigma(gg \to H) + \sigma(bbH)]\mathrm{BR}(H \to \tau\tau)$ and $[\sigma(gg \to A) + \sigma(bbA)]\mathrm{BR}(A \to \tau\tau)$, in pb, as functions of m_H (top row) and m_A (bottom row), respectively, for postLHC8-FDOK points with $m_h \sim 125.5$ GeV. The values of $\tan\beta$ are color-coded as indicated on the plots.

smaller, while in Type II larger cross sections are obtained for larger $\tan\beta$. Note also that in Type II the $t\bar{t}$ threshold is visible for small $\tan\beta \lesssim 3$ but not for larger values.

As an aside, we note that in both the H and A cases the $\mu\mu$ final state rates are obtained by simply multiplying by the relevant ratio of branching ratios, $\mathrm{BR}(H$ or $A \to \mu\mu)/\mathrm{BR}(H$ or $A \to \tau\tau)$, which is essentially independent of $\tan\beta$ in either Type I or Type II with a value of order 3.5×10^{-3}. Looking at Fig. 5.25, it would appear that prospects for detecting the H and A in the $\mu\mu$ final state are significant for m_A and m_H below the top threshold, especially in the case of $A \to \mu\mu$ in Type II when $m_A \lesssim 150$ GeV.

Of course, once m_A or m_H is above the $t\bar{t}$ threshold, the rates in the $t\bar{t}$ final state will be of great interest. These are shown in Fig. 5.26. Large $\sigma \times \mathrm{BR}$ values are certainly possible, but so also are very small values, although in the case of Type II the smallest values found at m_H or m_A of order 1 TeV is $\sim 10^{-4}$ pb. This latter might be detectable for full run-2 luminosity of $L = 300$ fb^{-1}, and is certainly of great interest for the high-luminosity run
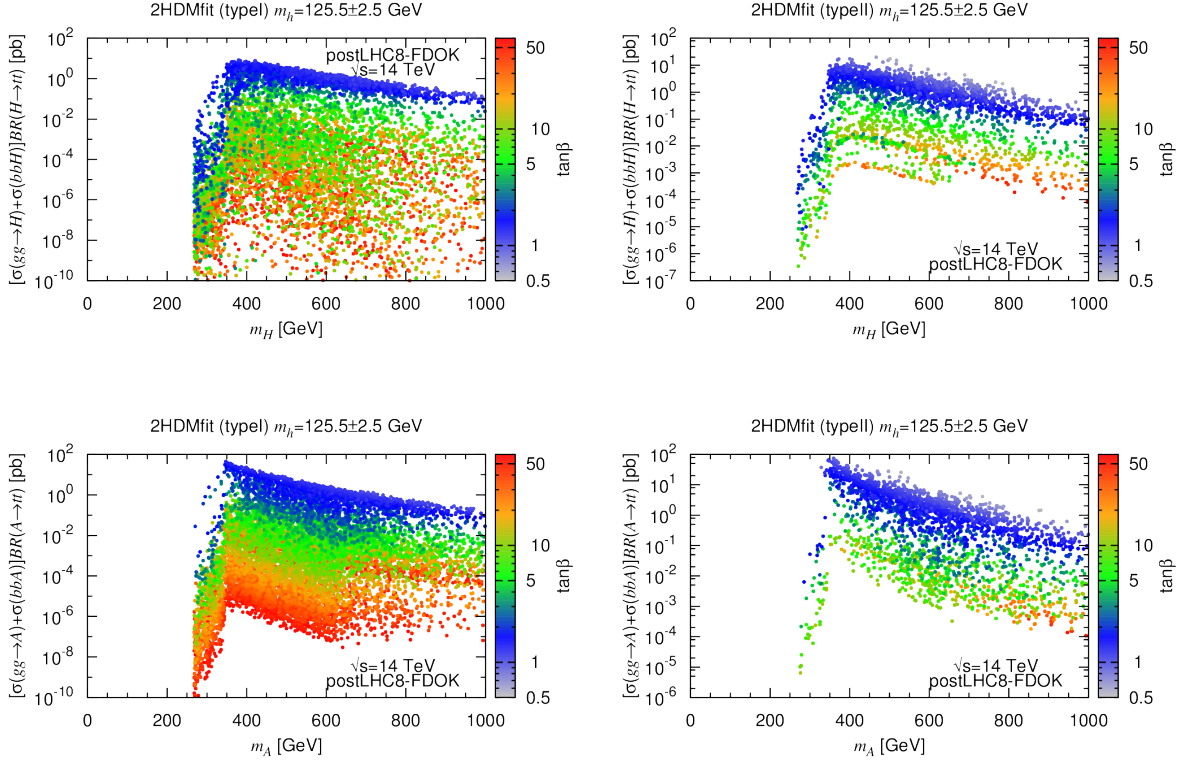
Figure 5.26. Scatter plots of $[\sigma(gg \to H) + \sigma(bbH)]\mathrm{BR}(H \to t\bar{t})$ as function of m_H (top row) and $[\sigma(gg \to A) + \sigma(bbA)]\mathrm{BR}(A \to t\bar{t})$ as function of m_A (bottom row) at $\sqrt{s} = 14$ TeV, for postLHC8-FDOK points with $m_h \sim 125.5$ GeV. The values of $\tan\beta$ are color coded as indicated by the scales on the right of the plots.

of the LHC which might accumulate $L = 3000$ fb^{-1}.

- *Search in the non-standard modes*

In the preceding plots, we have not displayed the impact of future h measurements that lie within SM±15%, SM±10% and SM±5%. In the case of Type I, agreement with the SM of ±10% or better implies that $m_A \lesssim 80$ GeV is excluded (whereas at the postLHC8 level very low m_A is allowed). This is apparent from examining the reach in m_A in Fig. 5.10. In the case of m_H, which already must lie above ~ 125.5 GeV for the $h125$ case, there is almost no impact as increasing agreement with the SM is required. For Type II, the impact is more varied. In the case of the A, as one moves through SM±15%, 10%, 5% fewer and fewer points are found at lower m_A, as can again be read from Fig. 5.10, but determining precise boundaries would require dedicated scanning. In the case of the H,
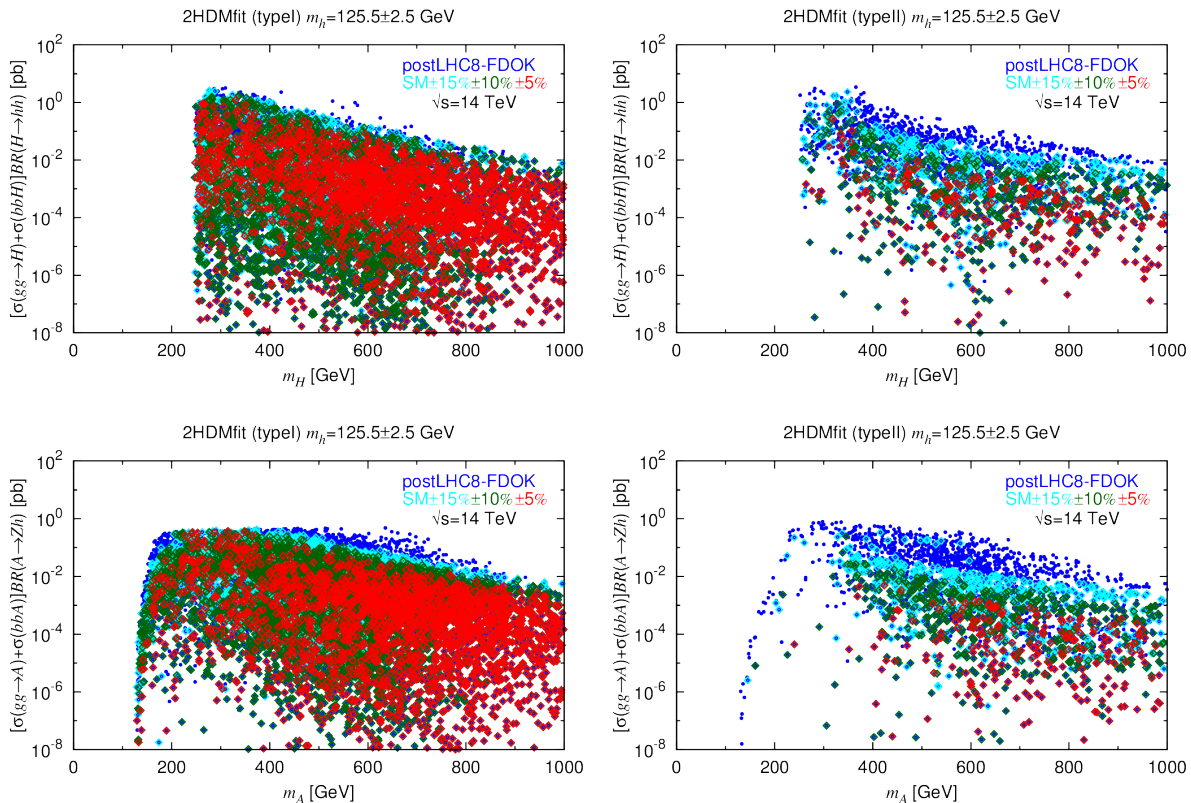
Figure 5.27. We plot $[\sigma(gg \to H) + \sigma(bbH)]\mathrm{BR}(H \to hh)$ and $[\sigma(gg \to A) + \sigma(bbA)]\mathrm{BR}(A \to Zh)$ as functions of m_H and m_A, respectively, for Type I (left) and Type II (right) 2HDMs. For this figure, only FDOK points are shown. Implications of various levels of precision for future h measurements are displayed. Color scheme as in Fig. 5.9. Values of $\sigma \times \mathrm{BR}$ below 10^{-8} are not plotted.

SM$\pm15\%$ and $\pm10\%$ do not restrict m_H beyond the postLHC8 range, but heavier m_H is preferred by SM$\pm5\%$.

Perhaps most interesting are the rates for $H \to hh$ and $A \to Zh$. In Fig. 5.27 we show results for the hh and Zh final states for $\sqrt{s} = 14$ TeV, indicating the impact of SM$\pm15\%$, $\pm10\%$, $\pm5\%$ requirements. We note that if the h measurements approach SM values, then this will limit only somewhat the maximum values achievable for the cross section in the hh and Zh final states in the case of Type I models — which means that there is a significant, although not large, probability of seeing the $H \to hh$ and $A \to Zh$ final states in gluon fusion and in associated production with b quarks. However, in the case of Type II models, increasingly SM-like h results imply much smaller cross sections than those shown (as allowed by current Higgs fitting for both hh and Zh final states).
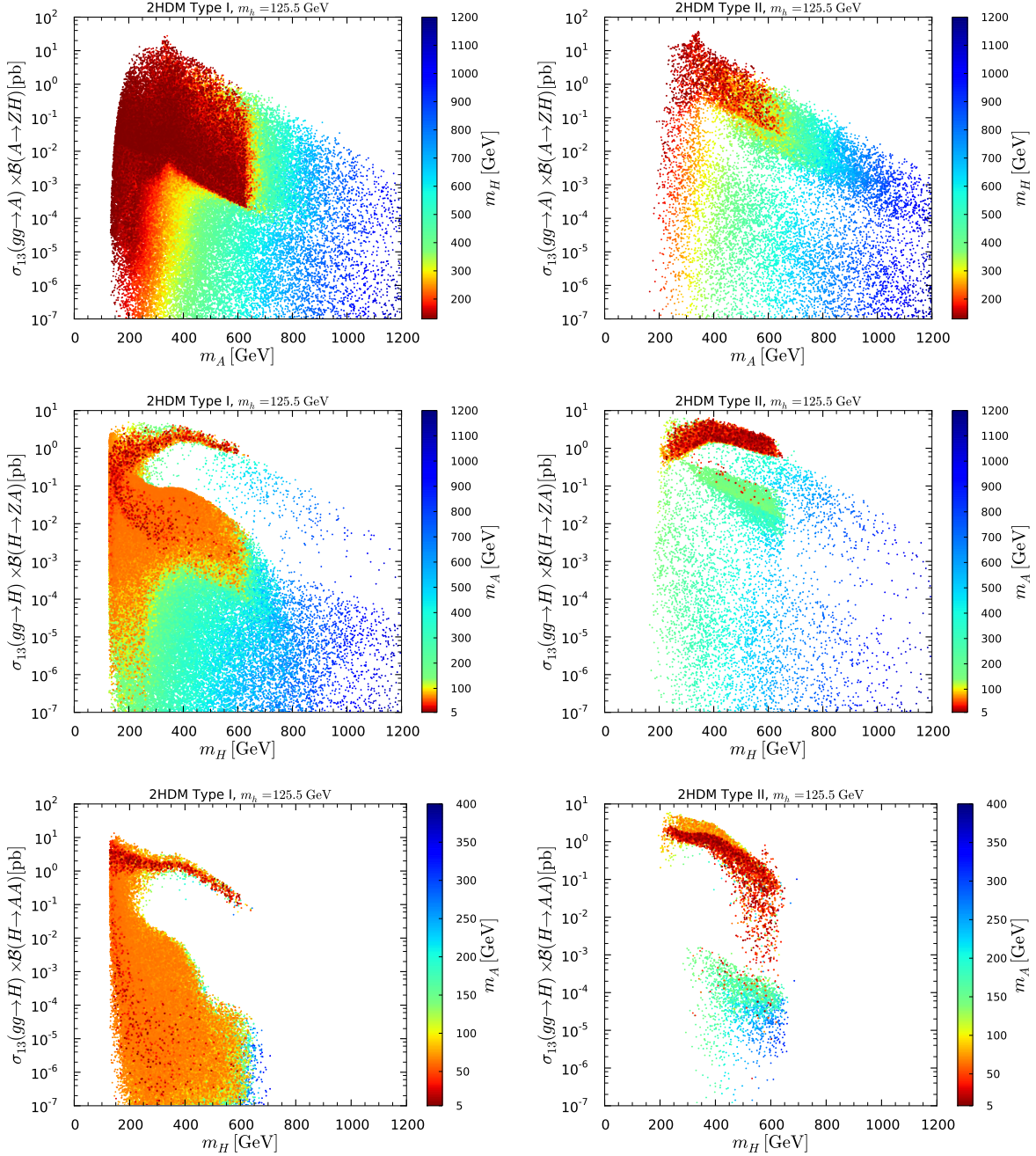
Figure 5.28. Cross sections times branching ratio in Type I (left) and in Type II (right) for Higgs-to-Higgs signatures, in the upper panel $gg \to A \to ZH$ with m_H color code, and in the middle and lower panels for $gg \to H \to ZA$ and $gg \to H \to AA$, respectively, with m_A color code. Points are ordered from high to low m_A or m_H.

Last but not least, if the mass splitting is large enough, $A \to ZH$, $H \to ZA$, and $H \to AA$ decays offer intriguing possibilities for discovering the extra non-SM-like neutral Higgs states in the regime of approximate alignment without decoupling. In Fig. 5.28,

the cross sections for $gg \to A \to ZH$, $gg \to H \to ZA$ and $gg \to H \to AA$ are exhibited. Large $gg \to A \to ZH$ cross sections are obtained for large $m_A - m_H$ splitting.[38] Looking back at Fig. 5.19 one sees that, in both Type I and Type II, the splitting can only be large for $m_A \lesssim 650$ GeV. This explains the preponderance of low m_H points with cross sections up to 20 pb for $m_A \lesssim 650$ GeV. However, $gg \to A \to ZH$ can also be heavily suppressed; since the AHZ coupling is proportional to $\sin(\beta - \alpha)$, this suppression is a purely kinematical effect.

Turning to the $H \to ZA$ and $H \to AA$ signatures, we observe a depleted area for $m_H > 300$ GeV and cross sections of the order of 0.1 pb. In this region, $\tan\beta = 2$–10 and Z_5 is small or negative leading to m_H, m_A masses for which the $H \to ZA$, AA decays are kinematically forbidden [cf. Eq. (5.59)]. In the region below, $\tan\beta > 10$ and Z_5 can be large enough to achieve $m_H > m_A + m_Z$ and/or $m_H > 2m_A$, but nevertheless the cross section is small because of the $\tan\beta$ dependence of $\sigma(gg \to H)$, see Fig. 5.23. The distinct branch with $gg \to H \to ZA$ and $gg \to H \to AA$ cross sections larger than about 1 pb, on the other hand, has $\tan\beta \lesssim 2$ and $\lambda_5 \approx 0$. Here, the term proportional to $\sin 2\beta$ in Eq. (5.37) gives a large enough $Z_5 > 0$ so that the $H \to ZA$ and/or $H \to AA$ decay is kinematically allowed. The small $\tan\beta$ leads to a large $gg \to H$ production cross section, see again Fig. 5.23. The CMS collaboration has very recently published a search for $A \to ZH$ and $H \to ZA$ [177]. For instance, for m_A (m_H) of about 200–600 GeV and very light H (A) below 100 GeV, the 95% CL limit on the relevant cross section is of the order of 30–50 fb in the $\ell\ell\tau\tau$ final state and 20–100 fb in the $\ell\ell b\bar{b}$ final state. Considering the branching ratios for $Z \to \ell\ell$ and $H \to \tau\tau, b\bar{b}$ ($A \to \tau\tau, b\bar{b}$), these limits just start to touch the highest cross sections in Fig. 5.28.

Finally, note that due to the kinematic constraint $m_H \geq 2m_A$ and the non trivial correlation between m_H and m_A observed in Fig. 5.19, the $H \to AA$ channel is only open for $m_H \lesssim 700$ GeV. In Type I the branch of points with cross sections ranging from about 10^{-1} pb to 10 pb is mainly populated by $m_A \leq 100$ GeV points with relatively low $\tan\beta \lesssim 10$. In Type II, points with low $m_A \lesssim 250$ GeV and $\tan\beta \lesssim 3$ are clearly

---

[38] A large splitting $m_A - m_H \approx v$ can be motivated by the possibility of a strong first order phase transition in 2HDMs [134].
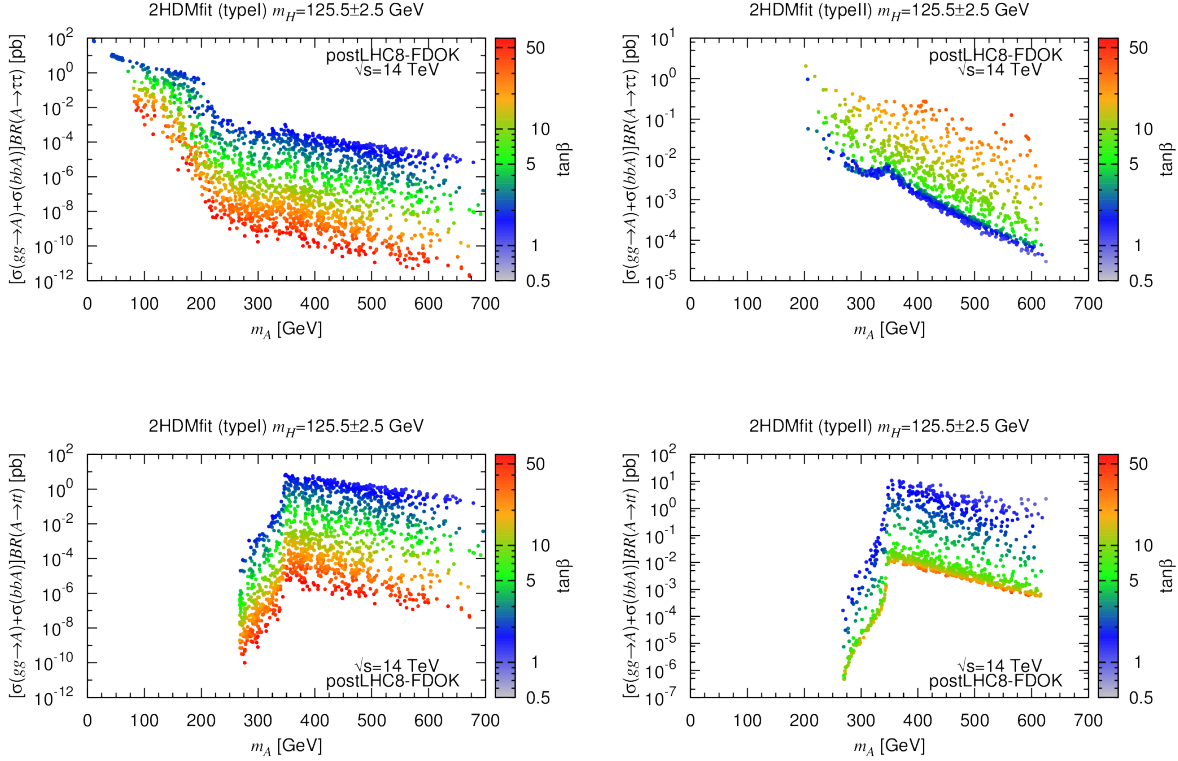
Figure 5.29. Rates (in pb) of pseudoscalar A production at $\sqrt{s} = 14$ TeV as a function of m_A for the $m_H \sim 125.5$ GeV scenarios, separated into different A decay modes: $A \to \gamma\gamma$ (top), $A \to \tau\tau$ (middle) and $A \to t\bar{t}$ (bottom). In each case, we sum over $gg \to A$ and $gg \to bbA$ production. The values of $\tan\beta$ are color-coded as indicated by the scale on the right of the plots.

separated from points with $m_A \gtrsim 150$ GeV and larger $\tan\beta \gtrsim 12$. This channel thus offers a complementary probe to the low m_A region discussed in [9].

- *Prediction for A cross sections in the H125 scenario*

Let us turn to the question of detecting the pseudoscalar A if the H is identified as the SM-like Higgs at 125 GeV. Figure 5.29 shows cross sections for pseudoscalar A production, concretely $[\sigma(gg \to A) + \sigma(bbA))] \times \mathrm{BR}(A \to \gamma\gamma)$ (top), $\times \mathrm{BR}(A \to \tau\tau)$ (middle) and $\times \mathrm{BR}(A \to t\bar{t})$ (bottom) at 14 TeV as a function of m_A.[39] Again, there is a large range of possible cross section values at any given m_A, with the $\tan\beta$ dependence, of course, being the same as for the $m_h \sim 125.5$ GeV case. As already observed in Fig. 5.2, the

---

[39]As commented in the last section, we plot the sum as this defines the inclusive production rate. Of course, separating $gg \to A$ and bbA production processes would eventually be possible.

possible range of m_A is limited when $m_H \sim 125.5$ GeV. In the case of Type II models, $m_A \lesssim 200$ GeV is eliminated due to the B-physics limit of $m_{H^\pm} \gtrsim 300$ GeV and the requirement of an acceptable T parameter (which limits the $A - H^\pm$ mass difference). In the case of Type I models, $m_A \lesssim 60$ GeV is possible but finding points with small enough $H \to AA$ to allow the H to have reasonably SM-like properties requires significant fine-tuning. For most m_A, the Type II maximal and minimal cross sections tend to be substantially (by a factor of > 1000) larger than for Type I. The lowest cross section values in Type I models are really very small at the largest allowed m_A values and would not allow the detection of the A boson. In contrast, in Type II models, even the very lowest cross section value of $\sim 5 \times 10^{-5}$ pb at $m_A \sim 630$ GeV would imply a handful of events for $L = 300$ fb^{-1}. The maximum Type II values imply a substantial number of events at all m_A, even at the largest masses, $m_A \sim 630$ GeV. (We remind the reader that 630 GeV is the upper limit allowed by perturbativity once the precision Higgs constraints, which limit $|\sin(\beta - \alpha)|$ to smaller values, have been included, cf. Fig. 5.2.)

As before, the rates for A production in the $\mu\mu$ final state are simply obtained by the $\tan\beta$-independent rescaling factor BR$(A \to \mu\mu)$/BR$(A \to \tau\tau) \sim 3.5 \times 10^{-3}$. For $m_A \lesssim 2m_t$, the cross section values near the upper limit obtained from such rescaling of the $\tau\tau$ final state rates shown in Fig. 5.29 are likely to be observable given the relatively narrow nature of the mass peak (typically of order a few GeV) and the excellent $\mu\mu$ invariant mass resolution.

5.6.3 Detecting a lighter Higgs h

Finally, let us next assess the feasibility for detecting the lighter h.

First of all, we see in Fig. 5.30 that a proper fit at the postLHC8 level is easily achieved if $m_h \gtrsim 60$ GeV, for which $H \to hh$ decays are kinematically forbidden. However, there is also a scattering of points for which small values of m_h are possible. Of course, finding points with $m_h \lesssim 60$ GeV for which BR$(H \to hh)$ is small enough to still allow the H rates in the various channels to fit the 125.5 GeV signal is highly nontrivial. It requires a delicate theoretical examination; the systematic technique will be discussed in detail in Section 5.7. A very "fine-tuned" scan is necessary to find these low-m_h points for which
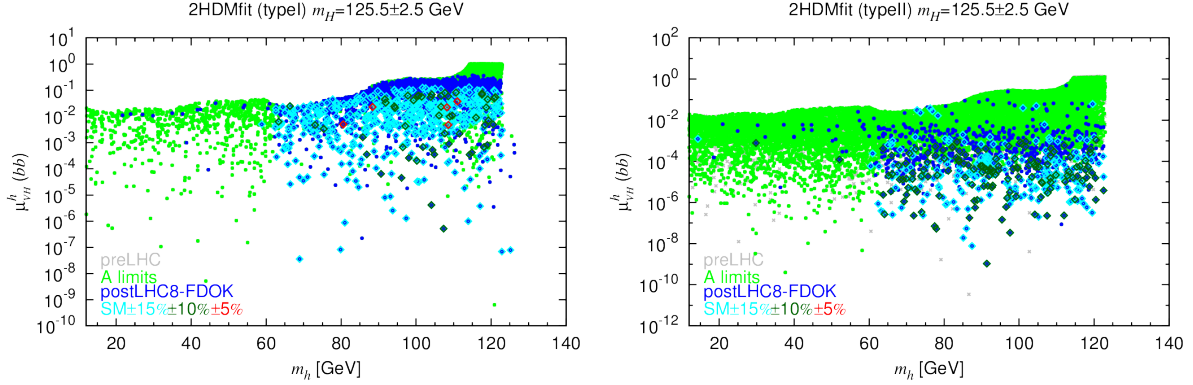
Figure 5.30. $\mu^h_{\rm VH}(b\bar{b})$, *i.e.* $V^* \to Vh$ associated production with $h \to b\bar{b}$ relative to the SM, as a function of m_h. Note that $\mu^h_{\rm VH}(bb)$ is actually independent of energy and that the ratio also applies to any situation where the subprocess of interest is $V^* \to Vh$, including the LEP $Z^* \to Zh$ process. There are no FDOK requirements imposed on the preLHC and A-limits points. The SM$\pm15\%, \pm10\%, \pm5\%$ points *are* subjected to FDOK requirements.

BR$(H \to hh)$ is small enough that the H signals fit the LHC data at an adequate level.

The most interesting modes for h detection may be $gg \to h \to \gamma\gamma$ and V^*h with $h \to b\bar{b}$. In the context of the current 8 TeV data, only the latter mode is of interest — expected signal strengths as a function of m_h are plotted in Fig. 5.30. While for many points the expected rates are obviously too small to have allowed detection of the h, there also exist postLHC8-FDOK points for which detection in the $Vh(b\bar{b})$ final state might be on the edge. We speculate that for the $Vh(b\bar{b})$ final state, a leptonic trigger on the V might still allow the predicted signal to emerge for the higher $\mu^h_{\rm VH}(b\bar{b})$ values.

As an aside, it is easily inferred from Fig. 5.30 that the postLHC8 and, even more so, the SM$\pm15\%, \pm10\%, \pm5\%$ requirements eliminate a large swath of the points that survive the A-limits constraint. It is also noteworthy that in the case of Type I all preLHC points automatically satisfy the A-limits requirement, whereas some preLHC (grey) points get excluded by the A limits in the case of Type II.

Considering Fig. 5.30, it is moreover interesting to ask whether the $\gtrsim 2\sigma$ LEP excess in the $Zb\bar{b}$ final state at $M_{b\bar{b}} \sim 98$ GeV could be explained by $m_h \sim 98$ GeV and $\mu^h_{\rm VH}(b\bar{b}) \sim 0.1 - 0.3$. We see that this is indeed possible in both the Type I and Type II models given current postLHC8 constraints on the H properties. Of course, the scatterplots suggest
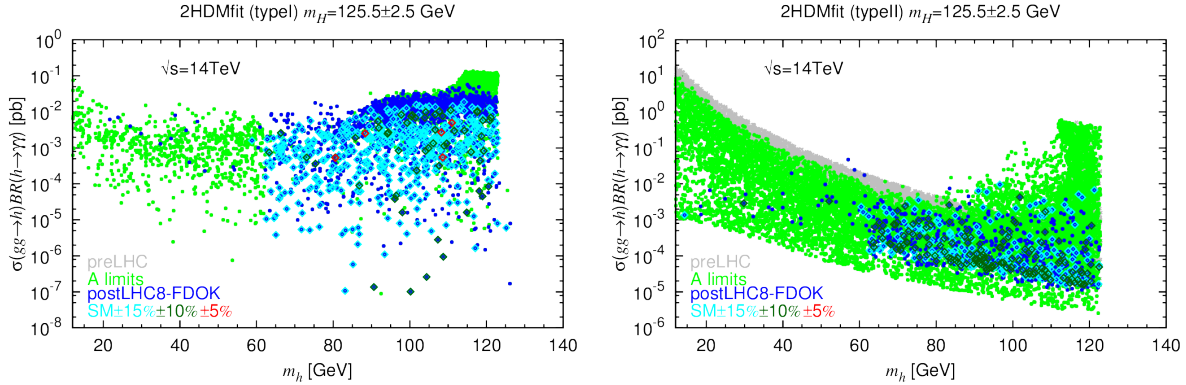
Figure 5.31. $\sigma(gg \to h)\mathrm{BR}(h \to \gamma\gamma)$ for $\sqrt{s} = 14$ TeV with postLHC8-FDOK constraints imposed as well as further limitations imposed by SM$\pm15\%, \pm10\%, \pm5\%$ constraints. There are no FDOK requirements imposed on the preLHC and A-limits points. The SM$\pm15\%, \pm10\%, \pm5\%$ points *are* subjected to FDOK requirements.

that this explanation is more fine-tuned in the Type II case. Furthermore, if the H rates are found to be within $\pm15\%$ of the SM rates, the value of $\mu^h_{\mathrm{VH}}(b\bar{b})$ is pushed well below the desired range in the case of Type II and is at a marginal level in the case of Type I. At the SM$\pm5\%$ level, the few surviving Type I points have $\mu^h_{\mathrm{VH}}(b\bar{b}) \lesssim 0.05$ (assuming that a more extensive scan would reveal red points with $m_h \sim 98$ GeV that would have a signal level comparable to those around 90 GeV and 108 GeV plotted), a value that is not very consistent with the LEP $\sim 2.3\sigma$ excess observed.

At 14 TeV, there is also potential for detecting the h in the $gg \to h \to \gamma\gamma$ mode, as shown in Fig. 5.31. Of course, while a significant event yield is possible for $L \geq 300$ fb^{-1}, the level of continuum irreducible and reducible backgrounds must be assessed and could prove too large for the blip at m_h to be observable.

Last but not least, an interesting question is whether the h, A (and $H^{\pm}$) could *all* escape detection for some parameter choices when $m_H \sim 125.5$ GeV. Given the upper limit discussed above of $m_A \lesssim 630$ GeV (after Higgs fitting constraints), a careful examination is required.

Consider first the A. In the case of Type I, Fig. 5.29 shows that for $m_A \in [200, 300]$ GeV (and most probably all the way out to the maximum allowed m_A) and large $\tan\beta$ the $\gamma\gamma, \tau\tau, t\bar{t}$ rates are all very small and would not allow discovery of the A even with $L = 3000$ fb^{-1}. In the case of Type II, the anticorrelation between the $\tau\tau$ and $t\bar{t}$ rates

as $\tan\beta$ is varied, together with the relatively substantial $\tau\tau$ rates for m_A below the $t\bar{t}$ threshold combine to guarantee that the A should be detectable with $L = 3000$ fb^{-1} in either the $\tau\tau$ or the $t\bar{t}$ mode, and perhaps in both.

As regards the h, it is first of all clear that if $|\sin(\beta - \alpha)|$ is very small (as certainly both allowed and preferred by Higgs fitting) then the $V^* \to Vh$ rates will be very tiny, as illustrated in Fig. 5.30 in the $m_h > 60$ GeV region for both Type I and Type II. The other potentially viable mode is $gg \to h \to \gamma\gamma$. However, Fig. 5.31 shows very small rates in this case as well for Type I. In contrast, the lowest cross sections in this channel in Type II are of order 10^{-5} pb, a level which might be accessible with $L = 3000$ fb^{-1}.

5.7 Light (pseudoscalar) Higgs boson study

As already discussed, one often considered limit of the 2HDM is the decoupling limit [39] in which $m_A, m_H, m_{H^\pm}$ are all large, in which case the h is very SM-like. A SM-like h or H can however also be obtained in the alignment limit without the masses of the other Higgs being large. In this section, we address the seemingly extreme case in which the h (H) is the SM-like 125 GeV state and the A (A and/or h) are lighter than 125 GeV, in particular light enough that the SM-like state can decay into them. Such decays generically have a large branching ratio (early references are [43], [188] and [44]) and would conflict with Higgs precision data unless the Higgs-to-Higgs-pair branching ratio is below about 0.1–0.3 [112], depending on the model.[40]

Only by tuning the model parameters so that the SM-like Higgs has very small coupling to a pair of lighter Higgs bosons can such a small branching ratio be achieved. Nonetheless, this is a parameter space window that cannot yet be excluded and that has many interesting special features, including rather large predicted cross sections for direct production of the light Higgs boson(s) — cross sections that might even be testable using the existing LHC 8 TeV data. The goal of this paper is to delineate these scenarios and their special properties.

We note that these scenarios are not achievable in the MSSM because of the strong

---

[40]A large survey of exotic Higgs decays is available in [189].

interrelations of the Higgs potential parameters required by supersymmetry; a light A is simply not consistent within the MSSM when the h has mass 125 GeV (unless the Higgs sector is CP-violating). MSSM scenarios in which the H has mass of 125 GeV and m_A, m_h are below m_H have been constructed [190], but those to date do not have $m_A, m_h < 125/2$ GeV. In the NMSSM, scenarios with a light a_1 and/or h_1 are possible in light of the current data [191–194] but are not the subject of this paper — they typically imply small cross sections for production of the light Higgs boson.[41] Other models in which the SM-like Higgs can decay to two lighter states include the 2HDM+singlet (S) models. In the latter, besides the $h \to AA$ decay it is also possible to have $h \to SS$ decay. If $m_S < 125$ GeV/2, the hSS coupling must be highly suppressed, just as the hAA coupling must be highly suppressed if $m_A < 125$ GeV/2, for a recent analysis see [11].

The key consideration for this study is the magnitude of the coupling of the SM-like Higgs to a pair of the other Higgs bosons, including the hAA, HAA and Hhh couplings, which are given in Eqs. (5.69), (5.70) and (5.71). A simple estimate is useful. In terms of g_{YXX}, where Y is the SM-like Higgs and X is the A for $Y = h$ and either the A or h for $Y = H$, one can define

$$R(XX) \equiv \frac{\Gamma(Y \to XX)}{\Gamma(Y \to bb)} \approx \frac{1}{12K} \left(\frac{g_{YXX} v}{m_Y m_b} \right)^2 \frac{\beta(m_X)}{\beta^3(m_b)} , \qquad (5.112)$$

where $\beta(m_X) = \sqrt{1 - 4m_X^2/m_Y^2}$ and the factor K accounts for QCD corrections and running quark mass. Taking $m_Y = 125$ GeV and assuming purely SM-like couplings for Y, the constraint $\mathrm{BR}(Y \to XX) = \Gamma(Y \to XX)/(\Gamma(Y \to XX) + \Gamma_{\mathrm{tot}}^{\mathrm{SM}}) \lesssim 0.3$ translates into $R(XX) \lesssim 0.7$, where we have used $\Gamma(Y \to bb) \approx 0.6 \, \Gamma_{\mathrm{tot}}^{\mathrm{SM}}$ as in the SM for simplicity. Using the SM-predicted value $K \approx 0.6$, we find that $|g_{YXX}| \lesssim 15$ GeV is required for $m_X = 62$ GeV, which goes down to $|g_{YXX}| \lesssim 5$ GeV for $m_X \simeq 10 - 40$ GeV. Such a small g_{YXX} is a very strong constraint — without parameter tuning $|g_{YXX}|$ is most naturally of the order of a TeV.

In the following, we consider $Y = h$ in Section 5.7.1 and $Y = H$ in Section 5.7.2. We begin each of these sections by discussing the special parameter choices required in order

---

[41]NMSSM scenarios with a light a_1 and/or h_1 that appears in the decay of a SM-like Higgs (*e.g.* $h_2 \to a_1 a_1$, where h_2 is SM-like) have a long history, the original paper being [195].

to avoid too large Higgs-to-Higgs-pair branching ratio(s) for the 125 GeV state and then proceed to the associated phenomenology.

5.7.1 Light pseudoscalar A in the $h125$ scenario

Using Eqs. (5.69), (5.72), (5.73) and the relationships of the λ_i to the physical Higgs masses and the Higgs mixing parameter, m_{12}^2, in the scalar potential (see [39]), one finds the following result for the hAA coupling:

$$g_{hAA} = \frac{1}{2v} \left[\left(2m_A^2 - m_h^2\right) \frac{\cos(\alpha - 3\beta)}{\sin 2\beta} + \left(8m_{12}^2 - \sin 2\beta \left(2m_A^2 + 3m_h^2\right)\right) \frac{\cos(\beta + \alpha)}{\sin^2 2\beta} \right]$$

$$(5.113)$$

Let us begin by taking the SM limit, $\sin(\beta - \alpha) = 1$, in the formula above:

$$g_{hAA} = -\frac{2m_A^2 + m_h^2 - 2\hat{m}_{12}^2}{v} \tag{5.114}$$

where $\hat{m}_{12}^2 = m_{12}^2 \sec\beta \csc\beta$ and m_{12}^2 can be positive or negative. Given that $|g_{hAA}|$ must be very small to have small BR($h \to AA$), we see that in this limit $m_h^2 \sim -2m_A^2 + 2\hat{m}_{12}^2$ is required.[42] While there is no symmetry that motivates this particular choice, it can certainly be satisfied for appropriately modest $\hat{m}_{12}^2$ and we find many allowed points of this nature.

The interrelations of the parameters in this region are illustrated in Fig. 5.32. The figure shows the combined impact of perturbativity and the requirement of small BR($h \to AA$). The large solid filled regions are those allowed by perturbativity for various different values of m_H (as indicated by the color code in the lower-left corner of the plot). The regions surrounded by dashed lines are those consistent with BR($h \to AA$) ≤ 0.3, with the central solid line corresponding to BR($h \to AA$) $= 0$ (or equivalently g_{hAA}=0), for the various m_A values coded as shown in the upper-right corner of the plot. We see that the higher the value of m_H, the smaller the $\tan\beta$ that is required by perturbativity. Imposing both perturbativity and BR($h \to AA$) ≤ 0.3 strongly constrains m_{12} within the allowed $\tan\beta$ range (note: $m_{12} \equiv \text{sgn}(m_{12}^2)\sqrt{|m_{12}^2|}$). Roughly, $m_{12} \approx 30 - 100$ GeV and $\tan\beta < 15$ are the interesting ranges to scan over for this solution.

---

[42]Without this cancellation, when the g_{hAA} coupling is large, one may still suppress the $h \to AA$ decay by minimizing its phase space; however, this is not the case of interest in this study.
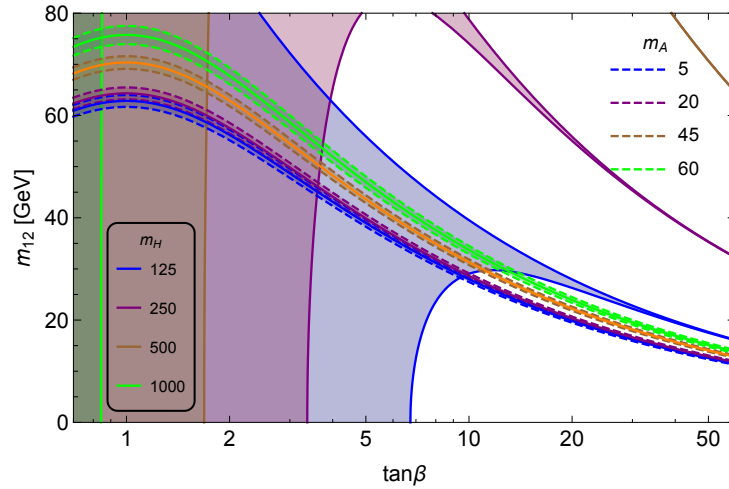
Figure 5.32. For $\sin(\beta - \alpha) = 1$, we show the regions of m_{12} vs. $\tan\beta$ parameter space consistent with perturbativity for various m_H values (see in-figure color code in lower-left corner). Also shown are the narrow regions for which BR$(h \to AA) < 0.3$, assuming h is the SM-like Higgs at 125 GeV with a total decay width of 4.07 MeV, for the indicated values of m_A shown in the upper-right corner. The figure applies to both the Type I and Type II 2HDM. The perturbatively acceptable region also extends to $m_{12}^2 < 0$, but this region is not plotted since Eq. (5.114) would give large $|g_{hAA}|$ and, therefore, large BR$(h \to AA)$ if m_{12}^2 were negative.

Deviating from the strict SM limit, there is also another parameter region that gives small $|g_{hAA}|$ through a cancellation between the first and second terms in Eq. (5.113) (or, equivalently, between the m_{12}^2 and non-m_{12}^2 terms in this equation). This can be achieved when $\sin(\beta + \alpha)$ is close to one and allows also for larger m_{12}^2. As described in [180], $\sin(\beta + \alpha) \sim 1$ can be consistent with the h being SM-like so long as $\tan\beta$ is not too small. In particular, one finds in this limit

$$C_V = \sin(\beta - \alpha) \to \frac{\tan^2\beta - 1}{\tan^2\beta + 1}, \tag{5.115}$$

where C_V is the magnitude of the hVV coupling relative to the SM value. One obtains $C_V \gtrsim 0.95$ once $\tan\beta \gtrsim 6$, i.e. sufficiently close to unity for consistency with Higgs data from the LHC. Note, however, that one cannot actually use exactly $\sin(\beta + \alpha) = 1$. This is because if both $\sin(\beta - \alpha) \to 1$ and $\sin(\beta + \alpha) \to 1$, then $\beta \to \pi/2$ and $\alpha \to 0$, for which g_{hAA} becomes too large. Indeed, in the limit of $\sin(\beta + \alpha) = 1$, we obtain

$$g_{hAA} = \frac{2m_A^2 - m_h^2}{v} \cos 2\beta, \tag{5.116}$$

which is too large given that $\cos 2\beta \sim -1$ for $\tan\beta \gtrsim 6$.
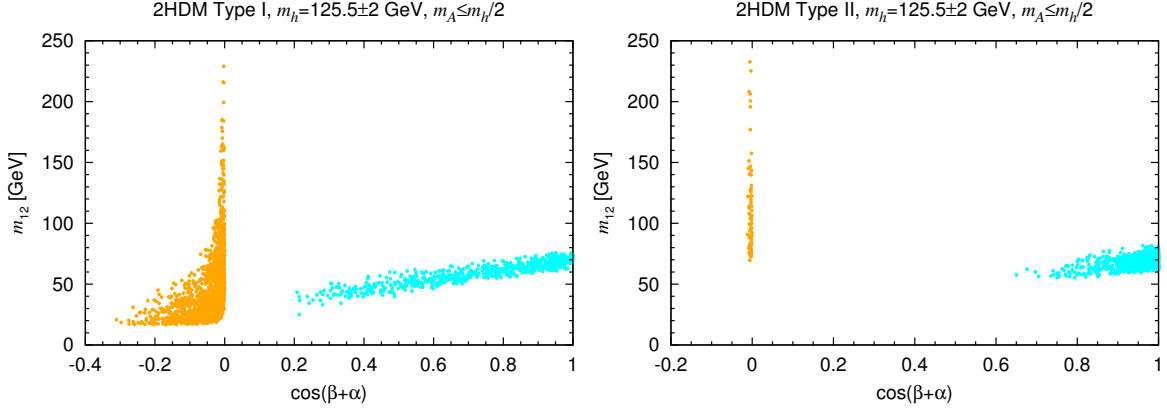
Figure 5.33. Phenomenologically viable points with $m_A \leq m_h/2$ in the m_{12} vs. $\cos(\beta + \alpha)$ plane, for 2HDM Type I (left) and Type II (right). The cyan points have $\sin(\beta-\alpha) \sim 1$, $\cos(\beta - \alpha) > 0$ and modest m_{12}, as for the $\sin(\beta - \alpha) = 1$ allowed region seen in Fig. 5.32, while the orange points have $\sin(\beta + \alpha) \sim 1$, small $\cos(\beta + \alpha) < 0$ and $\tan\beta > 5$.
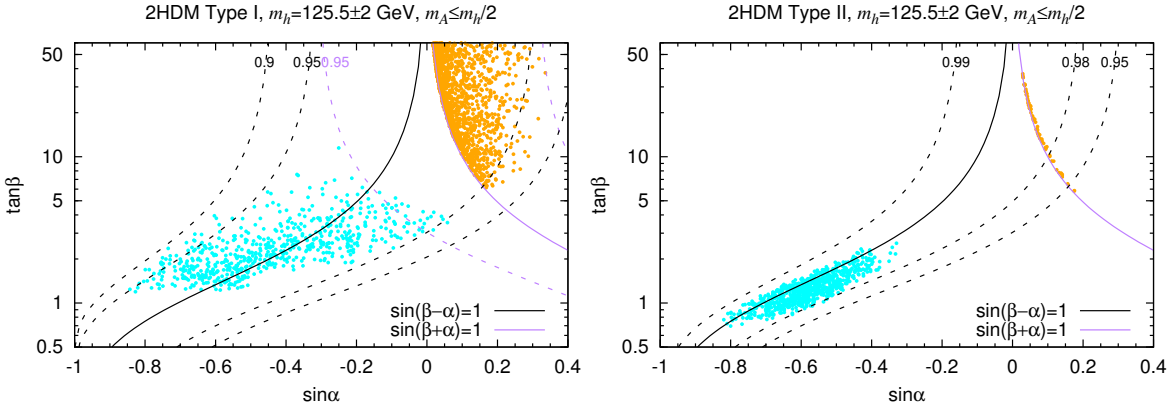
Figure 5.34. Same as Fig. 5.33 but in the $\tan\beta$ vs. $\sin\alpha$ plane. The solid black and purple lines indicate $\sin(\beta - \alpha) = 1$ and $\sin(\beta + \alpha) = 1$, respectively. The dashed black (purple) lines are iso-contours of values of $\sin(\beta - \alpha)$ $(\sin(\beta + \alpha))$ as indicated on the plots.

An overall view of the allowed low-m_A points in m_{12} vs. $\cos(\beta + \alpha)$ space for the Type I and Type II 2HDMs is provided by Fig. 5.33, and in the $\tan\beta$ vs. $\sin\alpha$ plane in Fig. 5.34. The cyan points have $\sin(\beta - \alpha) \sim 1$, $\cos(\beta + \alpha) > 0$ and modest m_{12}, as for the $\sin(\beta-\alpha) = 1$ allowed region seen in Fig. 5.32, while the orange points are those with $\sin(\beta + \alpha) \sim 1$, small $\cos(\beta + \alpha) < 0$, $\tan\beta > 5$ and $m_{12} > 0$. (The opposite case with $m_{12} < 0$ and $\cos(\beta + \alpha) > 0$ could also lead to the necessary cancellations in Eq. (5.113) but turns out to be excluded by the 125 GeV Higgs signal constraints.) In Fig. 5.34,
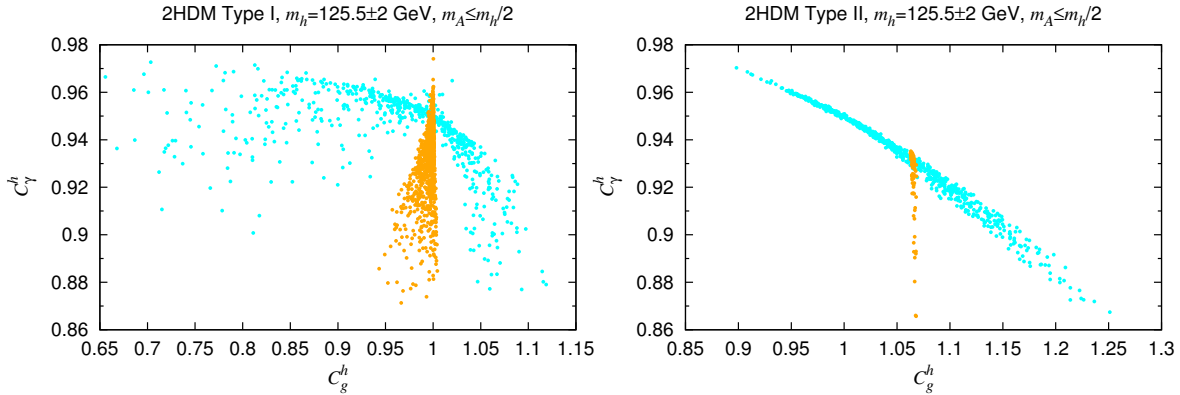
Figure 5.35. As Fig. 5.33 but for C_γ^h vs. C_g^h.

points to the right of the $\sin(\beta + \alpha) = 1$ curve have $\cos(\beta + \alpha) < 0$ and those to the left have $\cos(\beta + \alpha) > 0$. The requirement of small g_{hAA} (coupled with $m_{12} > 0$) thus creates a very sharp boundary between acceptable vs. non-acceptable parameter points. One should also note that the $\sin(\beta + \alpha) \sim 1$ points mostly (entirely) have $\sin\alpha > 0$ for Type I (Type II). Consequently, in the Type II model the orange points correspond to the "wrong-sign" Yukawa coupling $C_D^h \sim -1$ [196], whereas the cyan points have $C_D^h > 0$.

Having understood the constraints on this scenario, we now pursue the implications for LHC phenomenology. In Fig. 5.35 we plot the reduced couplings (relative to their SM values) of h to gluons and to photons, C_g^h vs. C_γ^h. The suppressed values of C_γ^h come from the negative contribution of the charged Higgs to the $h\gamma\gamma$ one-loop coupling. In the limit of $\sin(\beta - \alpha) = 1$,

$$g_{hH^\pm H^\pm} = g_{hAA} - (\lambda_5 - \lambda_4)v = g_{hAA} - 2(m_{H^\pm}^2 - m_A^2)/v. \qquad (5.117)$$

The first term, g_{hAA}, has to be small as discussed above and the second term is always negative because $m_{H^\pm} \gtrsim 90$ GeV (300 GeV) in Type I (Type II).

To illustrate the impact on observables, we plot in Fig. 5.36 the signal strengths μ (relative to the SM) for $gg \to h \to VV$ ($V = W, Z$) versus $gg \to h \to \gamma\gamma$, denoted as $\mu_{gg}^h(ZZ)$ vs. $\mu_{gg}^h(\gamma\gamma)$. Our first observation is that $\mu_{gg}^h(\gamma\gamma)$ is suppressed for all points in Type I as well as for the orange points in Type II. The deviations from the SM predictions of unity are of course consistent with current data, since this was a requirement of the scan, but it is obvious that future higher precision measurements will strongly constrain
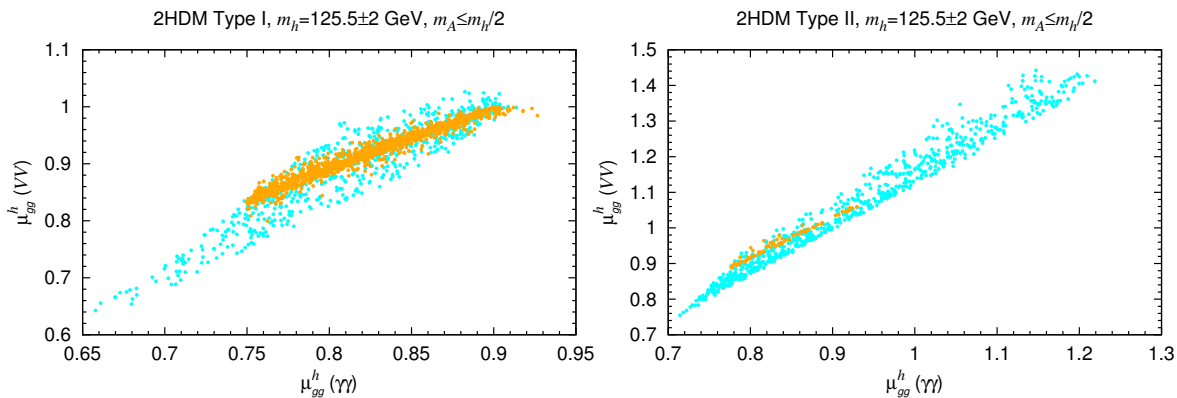
Figure 5.36. Signal strengths $\mu_{gg}^h(ZZ)$ vs. $\mu_{gg}^h(\gamma\gamma)$ for the Type I and Type II models. The orange points are, as for previous plots, the points with $\sin(\beta + \alpha) \sim 1$.

these scenarios. Remarkably — and in contrast to the case when $m_A > m_h/2$ — it is impossible to simultaneously achieve $\mu_{gg}^h(\gamma\gamma) = 1$ and $\mu_{gg}^h(VV) = 1$ in either Type I or Type II when $m_A \leq m_h/2$. (See Fig. 2 of [8] for comparison with the general case.) Thus, this scenario will be excluded should the Higgs observations converge sufficiently close to the SM expectations.

Figure 5.37 shows $\mathrm{BR}(h \to AA)$ vs. signal strength $\mu_{gg}^h(\gamma\gamma)$. From the left plot we can directly see that in Type I a precise measurement of this signal strength gives an upper bound on the allowed $h \to AA$ branching ratio. If $\mu_{gg}^h(\gamma\gamma)$ is measured to be within 10% of unity, this means $\mathrm{BR}(h \to AA) \lesssim 0.01$. Conversely, a measurement of $\mu_{gg}^h(\gamma\gamma) \simeq 1$ combined with detection of $h \to AA$ decays implies that the Type II model is strongly preferred and that the wrong-sign Yukawa solution is excluded.

Let us now turn to the question of the size of the cross sections for A production with decays to the potentially observable $\tau\tau$ and $\mu\mu$ final states. Figure 5.38 shows the gg fusion and $b\bar{b}$ associated production cross sections at $\sqrt{s} = 8$ TeV times $\mathrm{BR}(A \to \tau\tau)$. As can be seen, the $A \to \tau\tau$ signal can have quite substantial cross sections over the whole mass range considered. The cross sections for the $A \to \mu\mu$ signal have exactly the same shape but are about a factor of 100 lower. For reference, naive estimates suggest that, before cuts and efficiencies, for the existing 8 TeV dataset with integrated luminosity of $L \simeq 20$ fb^{-1}, a cross section of order 10 pb $(200,000$ events$)$ should be observable in the $\tau\tau$ final state while 0.1 pb $(2000$ events$)$ should be observable in the $\mu\mu$ final state,
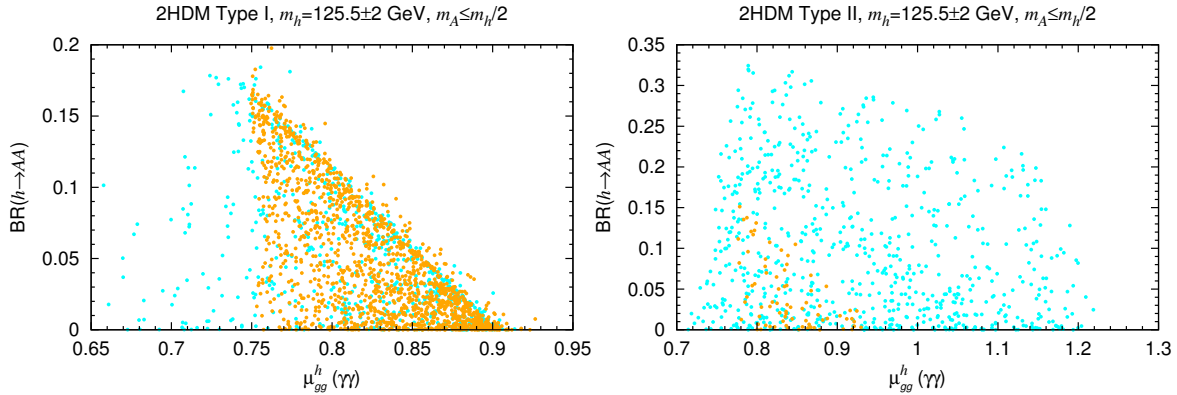
Figure 5.37. $\text{BR}(h \to AA)$ vs. $\mu_{gg}^h(\gamma\gamma)$ for the Type I and Type II models.

especially in the case of $b\bar{b}$ associated production by using modest p_T b-tagging. From Fig. 5.38, we observe that these levels are reached in the case of Type II for essentially the entire $m_A \leq m_h/2$ region in the case of gg fusion and for the orange points in the case of $b\bar{b}$ associated production.[43] Indeed, the cross sections for the orange points are really very large and should produce readily observable peaks. In the case of the Type I 2HDM, many of the cyan points have gg fusion cross sections at the probably observable 10 pb (0.1 pb) level in the $\tau\tau$ ($\mu\mu$) final states, but the orange points have cross sections that are almost certainly too small for detection in the run-1 data set.

Analyses by ATLAS and CMS for such signals at low m_A in the $\tau\tau$ channel have significant background from the Z peak. As a result, limits are currently only available for $m_A \gtrsim m_Z$. We are unaware of any public results for the $\mu\mu$ final state in the low mass region, but the excellent mass resolution in this channel should make separation from the Z peak straightforward.

Finally, we note that running at higher energies will not straightforwardly improve the sensitivity to the low m_A region, as the cross sections at 13–14 TeV are barely a factor 2 larger than those at 8 TeV. Therefore, one will need to accumulate more statistics via higher total integrated luminosity.

---

[43]Recall from Fig. 5.34 that the orange points can have high $\tan\beta$ while the cyan points have quite modest $\tan\beta$ values. This implies that the $b\bar{b}$ coupling in the Type I (Type II) model is suppressed (enhanced). As a result, the orange points have the smallest (largest) cross sections in the case of Type I (Type II).
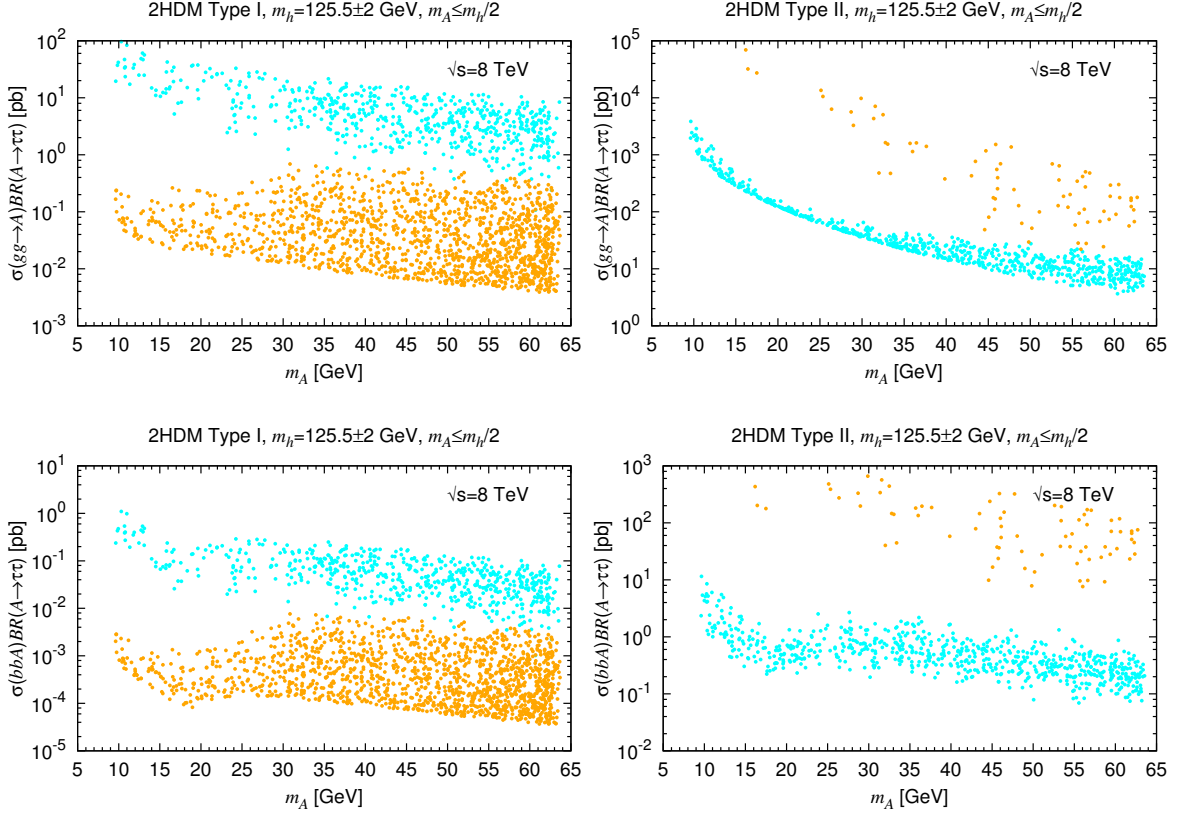
Figure 5.38. Cross sections at $\sqrt{s} = 8$ TeV for light A production from gg fusion (top row) and $b\bar{b}$ associated production (bottom row) in the $\tau\tau$ final state. The cross sections for the $\mu\mu$ final state have exactly the same form but are two orders of magnitude lower. Same colour scheme as in the previous figures.

5.7.2 Light (pseudo) scalar A or h in the $H125$ scenario

We first note that for $m_H \sim 125$ GeV in the Type II model, B-physics constraints require $m_A \gtrsim 200$ GeV. We therefore only consider the case of $m_h < m_H/2$ for Type II. In contrast, in the Type I model either m_A or m_h can be $< m_H/2$, but LEP limits imply that not both can be light simultaneously. This latter follows from the fact that the HVV coupling and the ZhA coupling are both proportional to $\cos(\beta - \alpha)$. Thus, for a SM-like H, *i.e.* $|\cos(\beta - \alpha)| \sim 1$ as required by signal strengths measurements, the ZhA coupling is near maximal and therefore the $Z^* \to hA$ cross section at LEP is too large, barring phase-space suppression.

In practice we can therefore consider the $H \to AA$ and $H \to hh$ cases independently of one another. With this in mind, we turn to the conditions for achieving small trilinear

162

couplings in order to evade too large $\text{BR}(H \to AA)$ or $\text{BR}(H \to hh)$. Analogous to Eq. (5.113) we find

$$g_{HAA} = \frac{1}{2v} \left[\left(2m_A^2 - m_H^2\right) \frac{\sin(\alpha - 3\beta)}{\sin 2\beta} + \left(8m_{12}^2 - \sin 2\beta \left(2m_A^2 + 3m_H^2\right)\right) \frac{\sin(\beta + \alpha)}{\sin^2 2\beta} \right]$$
(5.118)

and

$$g_{Hhh} = -\frac{1}{v} \cos(\beta - \alpha) \left[\frac{2m_{12}^2}{\sin 2\beta} + \left(2m_h^2 + m_H^2 - \frac{6m_{12}^2}{\sin 2\beta}\right) \frac{\sin 2\alpha}{\sin 2\beta} \right] .$$
(5.119)

As mentioned, for the H to be SM-like, we should have $|\cos(\beta - \alpha)|$ close to unity. One class of scenarios is easily understood by taking the strict limit of $|\cos(\beta - \alpha)| = 1$, yielding

$$g_{HXX} = -\frac{2m_X^2 + m_H^2 - 2\hat{m}_{12}^2}{v} , \qquad X = h, A .$$
(5.120)

Analogous to the $h125$ case, $\hat{m}_{12}^2 = m_{12}^2 \sec\beta \csc\beta$ should be small and positive to achieve small enough $|g_{HXX}|$. The interplay of the requirements of perturbativity and of small $|g_{HXX}|$ is illustrated in Fig. 5.39. We see that for $m_h \leq 60$ GeV, small $\tan\beta$ below about 2 is required. (Note also that if both h and A were light, they should be very close in mass to suppress $\text{BR}(H \to hh, AA)$; this follows from the fact that the bands of $\text{BR}(H \to XX) < 0.3$ are valid for both $X = h$ and $X = A$.) For $0.5\,m_H < m_h < m_H$, i.e. if only A is light, there is a bit more freedom and $\tan\beta$ can go up to 10–15, tightly related however with m_{12} for any given value of m_A. Figure 5.39 gives a somewhat idealized picture because the signal strength measurements at 125 GeV only require $C_V \gtrsim 0.9$, and constraints from the oblique parameters STU actually forbid $|\cos(\beta - \alpha)|$ being exactly 1; nonetheless Fig. 5.39 serves as useful guidance for the parameter scan.

As in the $h125$ case, sufficiently small $|g_{HXX}|$ can also be achieved by resorting to cancellations between the various terms in Eq. (5.118) or Eq. (5.119). In the $H125$ case, the $|\cos(\beta - \alpha)| = 1$ component shown in Eq. (5.120) is positive for larger m_{12} values than those shown in Fig. 5.39 and this component can be cancelled by the remaining term(s) for $\cos(\beta + \alpha) \sim 1$.

Putting everything together, including also the experimental constraints, we end up with the situation shown in Fig. 5.40. The top row shows allowed points in the m_{12} vs.
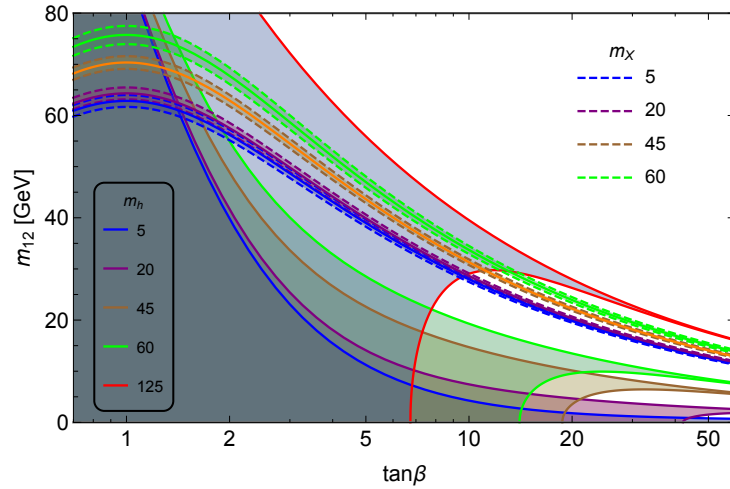
Figure 5.39. Constraints in the m_{12} vs. $\tan\beta$ plane for the $H125$ case with $|\cos(\beta - \alpha)| = 1$. The shaded regions are those allowed by perturbativity for m_h values indicated in the lower-left corner of the plot. The narrow strips between the dashed lines have $\mathrm{BR}(H \to XX) < 0.3$ for $m_A < m_H/2$ or $m_h < m_H/2$, respectively (the regions are the same for the two cases) with the colour code for the $X = h$ or A masses given in the upper-right corner of the plot. The solid line in the middle of the dashed ones shows $g_{HXX} = 0$.

$\tan\beta$ plane (analogous to Fig. 5.39); the bottom row displays these same allowed points in the $\tan\beta$ vs. $\sin\alpha$ plane. As explained at the beginning of this section, in Type I either h or A can be light (but not both) while in Type II only h can be light but not A. To distinguish these two cases, points with $m_A < m_H/2$ are shown in red and points with $m_h < m_H/2$ in blue. Considering first the top row of plots we see that, in agreement with Fig. 5.39, there is a small allowed region with $m_h < m_H/2$ at $m_{12} \simeq 60$–80 GeV and $\tan\beta \lesssim 2$. This region occurs for both Type I and Type II, although it is more constrained in Type I (because of combined SUP+STU constraints). In Type I there is moreover a diagonal strip of allowed points with $m_A < m_H/2$ at $\tan\beta \simeq 2 - 12$, as expected from Fig. 5.39. The points below this strip are mostly $\cos(\beta + \alpha) \sim 1$ points for which cancellations occur, cf. the lower-left plot of Fig. 5.40; they can have $m_A < m_H/2$ or $m_h < m_H/2$. Note that no such points survive in Type II. Last, but not least, it is worth noting that, in contrast to the $h125$ case, in the $H125$ case there are no allowed points with "wrong sign" Yukawa couplings, *i.e.* points for which the couplings of the H to vector bosons and to bottom quarks have opposite signs.

164
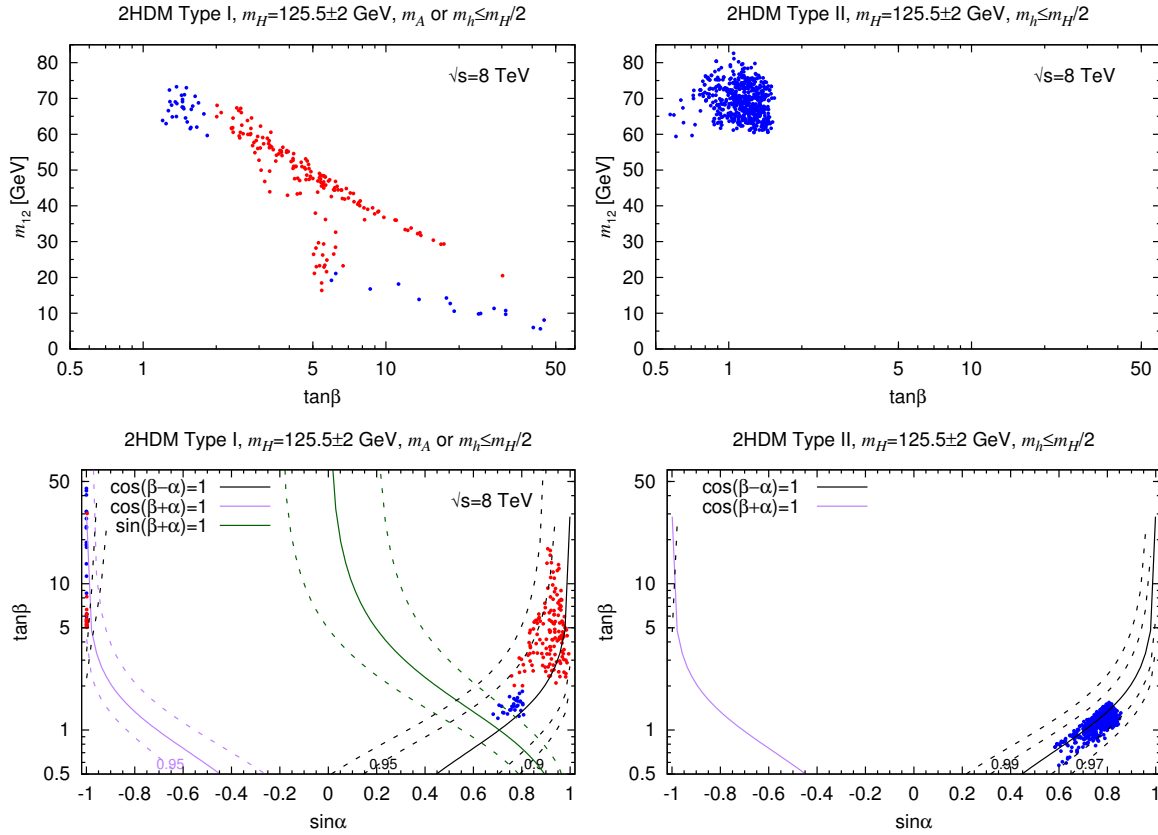
Figure 5.40. Phenomenologically viable scan points for the H125 scenario in the Type I (left) and Type II (right) models. The upper row shows the projection onto the m_{12} vs. $\tan\beta$ plane for comparison with Fig. 5.39. The lower row shows the $\tan\beta$ vs. $\sin\alpha$ plane, including contours of constant $\cos(\beta \pm \alpha)$ and $\sin(\beta + \alpha)$. In all four plots, the red points have $m_A \leq m_H/2$ while the blue points have $m_h \leq m_H/2$. Note that there are no red points for Type II; moreover, there are no $\cos(\beta + \alpha) \sim 1$ points in Type II that pass all constraints.

In Fig. 5.41, we take a closer look at the allowed points in the m_h vs. m_A plane for Type I. We see that indeed no points survive in the region where both m_h and m_A are below $m_H/2$. As m_h increases, some low m_A points appear, but these correspond to either $m_A \lesssim 12$ GeV for which there are no published limits at large m_h on $e^+e^- \to Z^* \to hA$ or to $m_A \gtrsim 40-50$ GeV and $m_h \gtrsim 90$ GeV $i.e.$ sufficiently close to LEP threshold as to escape limits on the hA final state by virtue of suppressed cross section. In the gap from about 15 GeV to about 40 GeV, LEP limits are strong enough to eliminate all points. It is also worth noting that the cyan points with $\sin\alpha > 0$ and the orange points with $\sin\alpha \sim -1$ occupy rather distinct parts of the m_h vs. m_A plane. In particular, if a light
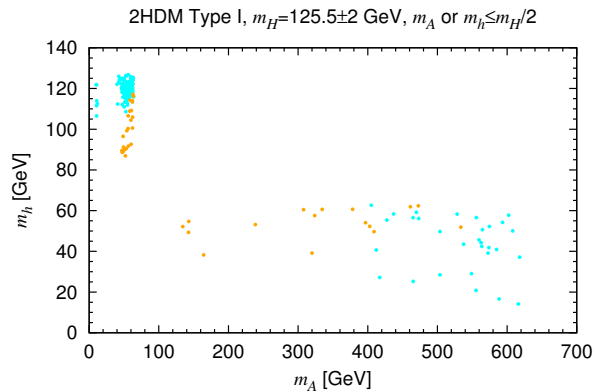
Figure 5.41. Allowed $H125$ points for the Type I model in the m_h vs. m_A plane. The cyan points have $\sin\alpha > 0$, while the orange points have $\sin\alpha \sim -1$, cf. the bottom-left plot in Fig. 5.40.

scalar with $m_h < 60$ GeV plus a pseudoscalar with $m_A < 400$ GeV were discovered, this would fix $\sin\alpha \sim -1$ in Type I.

Let us now explore the phenomenological consequences of the $H125$ scenario for the LHC. To this end, we first show in Fig. 5.42 the relation between the signal strengths for the high-resolution channels $gg \to H \to VV$ ($VV = WW^{(*)}, ZZ^{(*)}$) denoted as $\mu^H_{gg}(ZZ)$ and $gg \to H \to \gamma\gamma$ denoted as $\mu^H_{gg}(\gamma\gamma)$. As in the $h125$ case, quite substantial deviations from the SM values of unity are possible. With the increased precision expected at run-2, the Higgs measurements at the LHC should be sensitive to such deviations. Moreover, also as in the $h125$ case, the exact SM case $\mu^H_{gg}(\gamma\gamma) = \mu^H_{gg}(ZZ) = 1$ cannot be obtained in the $H125$ scenarios with light h or A. Though not shown here, this tension with SM-like signal strengths is also apparent in the $\mu^H_{\mathrm{VBF}}(\gamma\gamma)$ vs. $\mu^H_{gg}(\gamma\gamma)$ plane. Should the signal strength measurements for either of these pairs converge to values that lie within 10% of their SM values the $H125$ scenarios with m_h or m_A below $m_H/2$ will be excluded.[44] For completeness we show in Fig. 5.43 also BR($H \to XX$), $X = h$ or A, versus $\mu^H_{gg}(\gamma\gamma)$. Despite the existing run-1 constraints, the branching ratios can be sizeable and it may thus be interesting to look for these decays.

The most important issue is whether or not the existing 8 TeV, $L = 20$ fb^{-1} data set could be sensitive to this scenario by looking for the light h or A in the $\tau\tau$ or $\mu\mu$

[44]Comparing with Fig. 7 of [8] we see that this tension with SM-like signal strengths is much less in the general $H125$ case with heavier h, A.
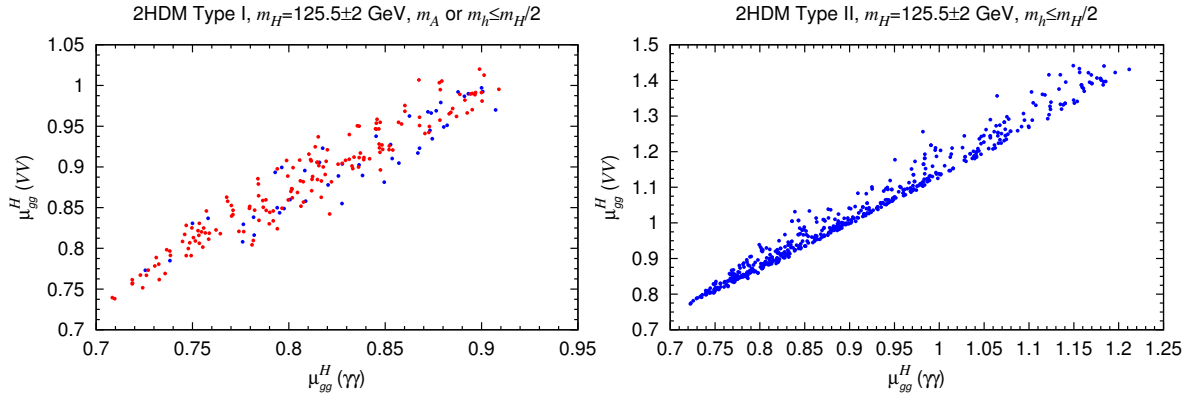
Figure 5.42. Signal strengths $\mu_{gg}^H(ZZ)$ vs. $\mu_{gg}^H(\gamma\gamma)$ for the Type I and Type II models. Points with $m_A \leq m_H/2$ are shown in red and points with $m_h \leq m_H/2$ in blue.
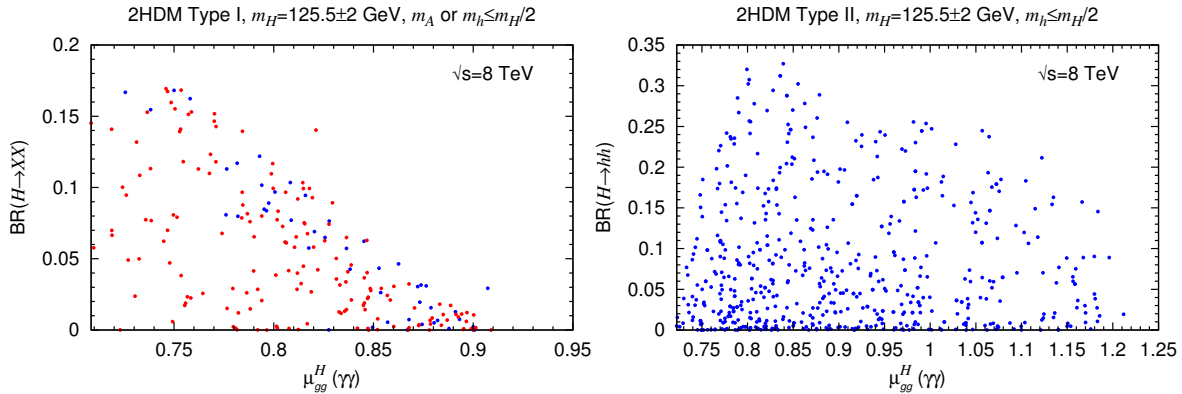
Figure 5.43. Branching ratios of $H \to XX$ ($X = h, A$) decays vs. $\mu_{gg}^H(\gamma\gamma)$ for the Type I and Type II models. Points with $m_A \leq m_H/2$ are shown in red and points with $m_h \leq m_H/2$ in blue.

final states. The relevant plots are given in Fig. 5.44. Since $\tan\beta$ cannot be large in the Type II model (see Fig. 5.40) and there is no $\tan\beta$ enhancement of the $b\bar{b}$ coupling in the Type I model, it is mostly gg fusion that's relevant. $\sigma(gg \to X) \times \mathrm{BR}(X \to \tau\tau)$ exceeds the required 10 pb (or 0.1 pb for decays into $\mu\mu$) in particular for the light h case, $X = h$. Light pseudoscalars (possible only in Type I) have smaller cross sections and will be harder to detect. Concretely, only for gg fusion with $A \to \tau\tau$ and $m_A \lesssim 12$ GeV does one obtain a cross section as large as 10 pb in the $\tau\tau$ channel, though for $m_A > 40$ GeV cross sections are still between 1 pb and 10 pb.
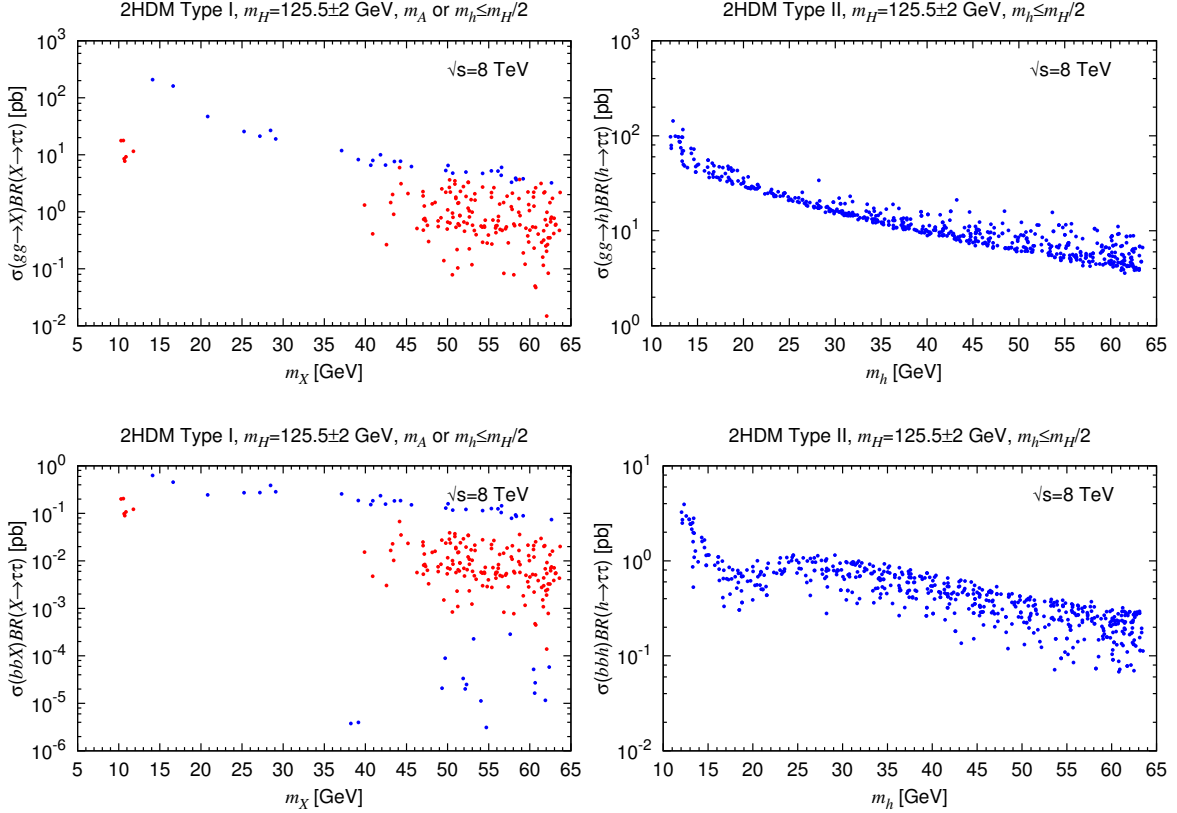
Figure 5.44. For the $H125$ case, we give 8 TeV cross sections for light $X = h, A$ production from gg fusion (upper row) and $b\bar{b}$ associated production (lower row) in the $\tau\tau$ final state. The blue points are for $X = h$, the red points for $X = A$.

5.8 Exploration of nearly degenerate h and H around 125 GeV

Finally, we consider the case where both m_h and m_H are around 125 GeV, while allowing $m_{H^\pm}$ and m_A to vary freely. Should two Higgs bosons have small mass difference ΔM, current 2σ sensitivity is such that if $\Delta M < 4$ GeV then they will appear to be degenerate regardless of the relative size of their contributions [197]. As ΔM increases, the peaks will only appear to be degenerate if the signal fraction of the smaller signal decreases. Since the transition is very rapid, we approximate by considering two peaks to be degenerate whenever $\Delta M < 4$ GeV.

Technically, when considering cases where more than one Higgs boson has mass of ~ 125 GeV [2], we sum the signal strength μ (defined in Eq. (3.2)) for different Higgs bosons of interest. This is justified by the fact that we always choose masses that are

Figure 5.45. We display the relative contribution of the h to the total $h + H$ signal in the $\gamma\gamma$ final state for Type I and Type II models.

separated by at least 100 MeV — in this case interference effects are negligible (given that the Higgs widths are substantially smaller than 100 MeV in the range of Higgs masses we consider).

Following a similar search strategy and procedure of analysis, we find that, relative to the cases where only the h or only the H was required to have mass of 125 GeV, the allowed region in the $s_{\beta-\alpha}$ vs. $\tan\beta$ plane is glossy the overlap of the ones which are surviving in when only $m_h = 125$ GeV or $m_H = 125$ GeV was required. This can be distinctly seen in the upper-row plots of Fig. 5.45, in which we also display the relative contribution of the h to the total $h+H$ signal in the $\gamma\gamma$ final state for Type I and Type II models. Given that the h and H couple to VV with factors of $\sin(\beta - \alpha)$ and $\cos(\beta - \alpha)$, respectively, it is not surprising that the h dominates the signal when $\cos(\beta - \alpha)$ is small whereas H is dominant when $\cos(\beta - \alpha)$ is large. In the case of Type I, essentially all values of of $\cos(\beta - \alpha)$ are possible, but in Type II $\cos(\beta - \alpha)$ can be either large or
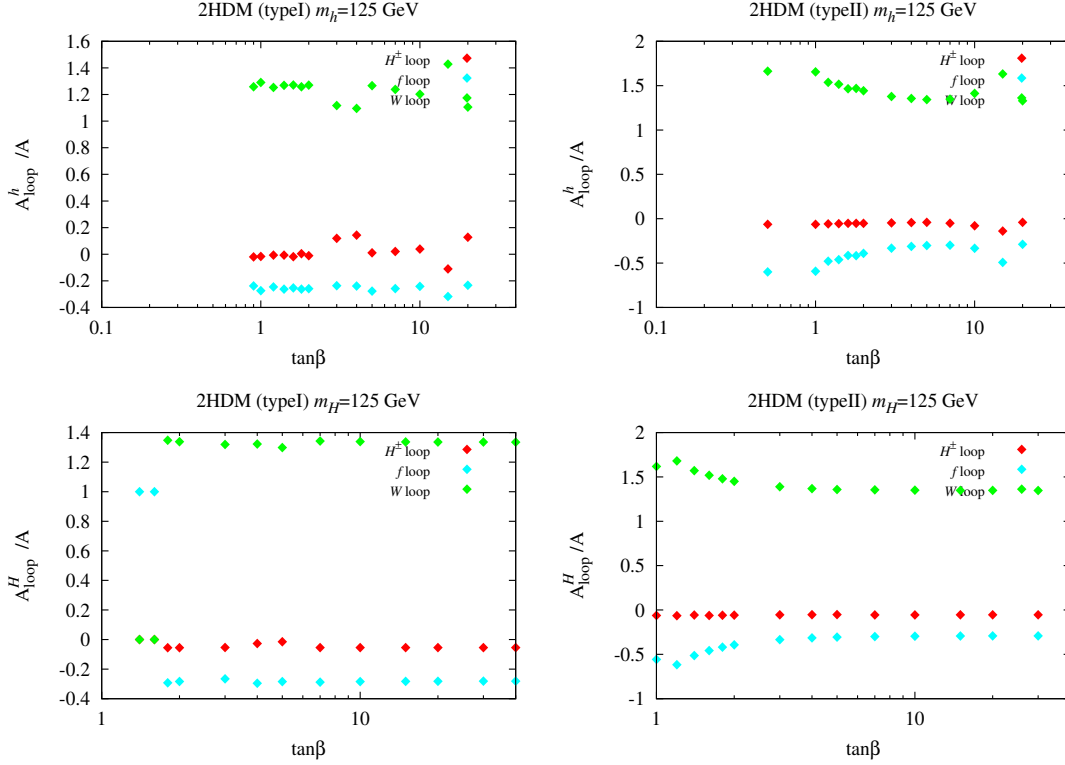
Figure 5.46. For the most interesting scenarios we show imaginary part of charged Higgs contributions to the $\gamma\gamma$ amplitude normalized to the imaginary part of the sum of all (fermions, W^+W^-, H^+H^-) contributions as a function of $\tan\beta$ after imposing all constraints. The parameters adopted correspond to maximal $R_{gg}^{h_i}(\gamma\gamma)$ (or an appropriate sum for degenerate cases).

small in magnitude, but not between for negative $\cos(\beta - \alpha)$. This means the comparable contribution from two Higgs bosons which are nearly close in mass is not possible. And this effect seems to be mainly due to the $\gamma\gamma$ final state not being well-fit in between. The multi-branch structure occurring in the $s_{\beta-\alpha}$ vs. $\tan\beta$ plane for Type II is clearly playing a crucial role.

5.9 Charged Higgs contribution to the di-photon decay

As discussed earlier and in [198], the charged Higgs contribution in the 2HDM to the $\gamma\gamma$ coupling loops is sometimes relevant. To verify this, we isolate the fermionic loop, W loop and $H^\pm$ loop contributions normalized to the total amplitude for the cases of both $h125$ and $H125$ that are intensively studied in this chapter. The left panel of Fig. 5.46 shows that the relative charged Higgs contribution may contribute as much as

the dominant (top quark) fermionic loop, but that the dominant loop is the W loop.

This should be contrasted with the Type II case which is illustrated in the right-hand plots of Fig. 5.46. One finds that the charged Higgs contributions are small when SUP constraints are imposed. In fact, the charged Higgs amplitude is strongly reduced by the requirement that the quartic couplings not violate the perturbativity condition when SUP constraints are imposed. This is partially due to the absence of a light charged Higgs in Type II that is eliminated by the B-physics constraints. However, the charged Higgs contribution cannot be rudely ignored and nondecoupling effects are inevitably of importance.

5.10 Summary

The Higgs data from the LHC run-1 clearly favor a fairly SM-like Higgs boson with mass of about 125.5 GeV. Motivated by this analysis, in this section we focused on CP-conserving 2HDMs of Type I and Type II, working under the hypothesis that one of the two scalar Higgs bosons (or both if they are degenerate in mass) is identified as the observed 125 GeV state and conclude that there are consistent descriptions of the LHC Higgs signal in the context of Type I and Type II 2HDMs. Indeed, the vector boson pair coupling of the 125 GeV state must be quite close to the SM Higgs coupling. In this case, the $W^\pm$ and Z gauge bosons dominantly acquire their masses from only one Higgs doublet of the Higgs basis. Moreover, the coupling of that CP-even Higgs boson to the gauge bosons tends towards the SM value, $C_V \to 1$. While this is automatically the case in the decoupling limit when the extra non-SM Higgs states are very heavy, such an alignment can also occur when the extra Higgs states are light, below about 600 GeV. We specifically investigated the phenomenological consequences of alignment without decoupling and contrasted them to the decoupling case.

Along the way, we clarified the important role played by constraints deriving from requirements of perturbativity in reducing the otherwise huge parameter space of the 2HDMs. We also delineated the (fortunately) rather limited impact of removing points that suffer from a large amount of feed down from heavier Higgs bosons decaying either

directly or via chain decay to a final state containing the 125 GeV state.

In the alignment limit without decoupling, despite C_V^h being very close to 1, the fermionic couplings of the 125 GeV Higgs can deviate substantially from the SM values. Concretely, C_U^h can deviate as much as about 10% (20%) from unity in Type I (Type II), and C_D^h as much as 30% in Type II. While C_U^h rather quickly approaches 1 with increasing m_H and/or $\cos(\beta - \alpha) \to 0$, the approach of the bottom Yukawa coupling to its SM value in the alignment limit is delayed in Type II, with $C_D^h \approx 0.70$–1.15 even for $|\cos(\beta - \alpha)| \sim 10^{-2}$. Large values of $C_D^h > 1$ are associated with light H, A. Moreover, for 230 GeV $\lesssim m_H \lesssim 665$ GeV and $m_A \lesssim 650$ GeV, there is an allowed region with $C_D^h \approx -1 \pm 0.2$; this "opposite-sign" solution can be tested decisively at run-2. The trilinear hhh coupling can also exhibit large deviations. Large values of $C_{hhh} > 1$ (up to $C_{hhh} \approx 1.7$ in Type I and up to $C_{hhh} \approx 1.5$ in Type II) can be achieved in the non-decoupling regime $m_H \lesssim 600$ GeV, for $|c_{\beta-\alpha}|$ of the order of 0.1, whereas for heavier m_H, C_{hhh} is always suppressed as compared to its SM prediction. The suppression can be about 50% for m_H of ~ 1 TeV and much larger for lighter m_H.

For the ratios $\mu_X^h(Y)$ of the $X \to h \to Y$ signal rates relative to the SM prediction, we found distinct correlations of these signal strengths in both Type I and Type II that depend on whether the additional Higgs states are decoupled or not. In fact, in the regime of alignment without decoupling, there are characteristic combinations of the $\mu_X^h(Y)$ signal strengths that cannot be mimicked by the decoupling limit. However, it is of course also possible that all signal strengths converge to 1 even though the additional Higgs states are very light.

A decisive test of the alignment without decoupling scenario would of course be the observation of the additional Higgs states of the 2HDM in the mass range below about 600 GeV. We delineated the many possibilities that for $\sqrt{s} = 14$ TeV could allow for observation of the H and A in a variety of modes, including not just the ZZ (for H only), $\tau\tau$ and $t\bar{t}$ final states, but also $\mu\mu$ and $\gamma\gamma$. While there are no guarantees in the case of the Type I model, in the Type II model there is always a definite lower bound on the $gg \to A, H \to \tau\tau$ cross sections at the LHC at any given m_A. For low $\tan\beta \sim 1$, this

lower bound is still of order 0.1 fb for $m_A \sim 500$ GeV, a level that we deem likely to be observable at the LHC during run-2. For high $\tan \beta$, the lower bound is roughly two orders of magnitude higher and only falls below the 0.1 fb level for $m_{A,H} \gtrsim 1.2$ TeV, which is already in the decoupling region. Moreover, while in Type I gluon-gluon fusion is always dominant for H or A production, in Type II both $b\bar{b}$ associated production and gluon-gluon fusion modes are in principle important since either can be dominant in different regions of the parameter space.

Higgs-to-Higgs decays of the non-SM-like states ($A \to ZH$, $H \to ZA$, $H \to AA$) also open intriguing possibilities for testing the regime of alignment without decoupling, with cross sections often in the range of 1–10 pb (although they can also be quite suppressed). Particularly promising are $gg \to H \to ZA$ and $gg \to H \to AA$ in Type II for light pseudoscalars below about 100 GeV; for such a light A, m_H can be at most ~ 650 GeV, and $\sigma \times$ BR values for these channels typically range from 10 fb to 10 pb.

In the $m_H \sim 125.5$ GeV case, the A can also be detected in these same modes (except ZZ). In addition, there is good probability for viable signals for the lighter h. In particular, the $V^* \to Vh$ with $h \to b\bar{b}$ channel might yield a detectable signal for at least a fraction of the points surviving the 95% C.L. limits on the H signal at 125.5 GeV.

Besides the cross section estimation, we have also ascertained expectations for the other Higgs bosons H, $H^\pm$ and A in the case that it is the h that gives the SM-like signal. An important general conclusion is that even if the 125.5 GeV signal rates converge to very SM-like values, the 2HDMs predict ample opportunity for detecting the other Higgs bosons. Still, it is also true that in the case of $m_h \sim 125.5$ GeV in the decoupling limit of very large $m_A \sim m_H \sim m_{H^\pm}$ detection of even one of the other Higgs bosons at LHC14 would not be possible. However, the case of $m_H \sim 125.5$ GeV is different. Because the maximum m_A is limited, having the h, A and $H^\pm$ all escape detection is very unlikely in Type II 2HDM. However, in Type I if $m_A \in [200, 300]$ GeV and $\tan \beta$ is large, then the A will not be detectable and h detection will be very marginal. Particularly, nondecoupling of the charged-Higgs loop contribution to the $h\gamma\gamma$ or $H\gamma\gamma$ coupling plays an important role once rates are required to be within $\pm 5\%$ of the SM predictions. The

result is elimination of all but a tiny fraction of the $m_H \sim 125.5$ GeV Type I scenarios and *all* of the $m_H \sim 125.5$ GeV Type II scenarios as well as *all* of the wrong-sign Yukawa Type II scenarios in the $m_h \sim 125.5$ GeV case.

In addition, we notice some special points with low $m_A < 100$ GeV that escape all LEP and (so far) LHC limits and yet have quite substantial $gg \to A$ and bbA production cross sections. It is interesting to probe these scenarios, and particularly we studied an extreme scenario in which the A or h has mass below one-half that of the observed 125 GeV SM-like Higgs state, when the latter is identified with either the lighter CP-even h or heavier CP-even H. It turns out that this is a region which LEP limits do not constrain at all in the $h125$ case or only partially constrain in the $H125$ case. The conditions and associated parameter choices for obtaining viable scenarios that have a small enough decay branching ratios of the ~ 125 GeV Higgs boson into a pair of lighter Higgs states were discussed in detail. Regarding LHC phenomenology, we found that in this scenario the signal strengths of the ~ 125 GeV Higgs boson cannot all be SM-like. Should the signal strength measurements in the high-resolution $\gamma\gamma$ and VV channels converge to their SM values to within 10% or better, then these scenarios will be excluded. Moreover, in the $h125$ case, surprisingly large gg fusion and $b\bar{b}$ associated production cross sections are possible for a light pseudoscalar in the 10–60 GeV mass range. In fact, the CMS collaboration has begun performing the analysis to search for a light pseudoscalar particle with masses below about 60 GeV in the $\tau\tau$ and $\mu\mu$ final states using the existing 8 TeV data from run-1 of the LHC.

In short, it is possible that the observed 125 GeV Higgs boson appears SM-like due to the alignment limit of a multi-doublet Higgs sector. The alignment limit does not necessarily imply that the additional Higgs states of the model are heavy. Indeed, they can be light and non-decoupled and thus lead to exciting new effects to be probed at run-2 of the LHC. If such a light Higgs is detected then models such as the MSSM will be eliminated and a strong preference in favour of, *e.g.*, a general 2HDM or the NMSSM will arise. Further, affirming the scenario in which there is a very light pseudoscalar present may provide an opportunity to account for the excess of the anomalous magnetic moment

of muon, $(g-2)_\mu$ beyond the SM. This is derived from a known fact two-loop Barr-Zee type diagrams to the anomalous magnetic moment of muon, $(g-2)_\mu$, could dominate over the one-loop contribution in the presence of a light Higgs boson. Therefore, we intend to reexamine the computation and analyze $(g-2)_\mu$ in the context of the general 2HDMs.

BSM alternative II: Supersymmetry and NMSSM

"Supersymmetry is the surprising idea, or hypothesis, that at the deepest level, for the ultimate or final theory, the laws of nature do not change if fermions are transformed into bosons and vice versa."

— *Gordon Kane*

One of the major issues for the SM is the fact that quantum corrections, $\delta\mu^2$, to the Higgs boson mass-squared parameter are enormous, potentially of order the square of the Planck mass. A very fine-tuned cancellation between the tree-level μ^2 and the quantum correction $\delta\mu^2$ is needed if the Higgs boson is to have a mass below the TeV scale. One possible solution to this problem is supersymmetry (SUSY), a hypothetical symmetry, very different from those we have so far encountered, which relates bosons to fermions. Quantum corrections due to bosons enter with a sign opposite to those due fermions, making possible a cancellation between their divergences when the masses and couplings of all of the high energy particles are related to one another, leaving a $\delta\mu^2$ that is of order

of the square of SUSY breaking scale [22].

Supersymmetric new physics is widely considered to be the most attractive solution to the above-described fine-tuning problem at energies well above the electroweak scale. The first realistic supersymmetric version of the SM was proposed in 1981 by adding a superpartner for each of the standard model particle types, leading to what is called the minimal supersymmetric standard model (MSSM). While the lightest CP-even Higgs h in this minimal model is bounded, its mass can be as high as about 130 GeV after including radiative corrections, which depend on various sparticle masses and mixings that enter the h self-energy calculation. However, the MSSM suffers from the known "μ problem" as this dimensional parameter must be directly introduced and is not associated with any obvious scale (e.g. the SUSY-breaking scale).

In order to solve this famous problem, many possible extensions to the MSSM has been proposed in the last few decades. One possible solution is to replace the μ term in the MSSM superpotential with a coupling of the Higgs doublets to a new gauge singlet field S, which is called the next-to-minimal supersymmetric standard model (NMSSM) [199, 200]. In the NMSSM "μ" is linked to the vacuum expectation value (VEV) of the singlet Higgs field, generating a value close to the SUSY-breaking scale. Alternative generalizations of the MSSM – known as the minimal non-minimal supersymmetric SM (MNSSM), new minimally-extended supersymmetric SM or nearly-minimal supersymmetric SM (nMSSM) or with additional $U(1)'$ gauge symmetries – exist [201], but these will not be considered here, nor the case of explicit CP violation [202–206].

Before turning to the NMSSM, I present a brief introduction to the MSSM and a simple comparison between the MSSM and the general 2HDM. Following this, I will review some theoretical aspects of the NMSSM including the radiative corrections to the Higgs masses. In the present chapter I confine myself to the NMSSM with a scale invariant superpotential. After classifying possible variants of the simplest NMSSM within specific assumptions regarding the origin of supersymmetry breaking (such as minimal SUGRA), extensive discussions of both the current phenomenology and the future collider tests in various Higgs scenarios are given. Of course, I cannot cover all details of all results that

have been obtained within the NMSSM up to now. Due to the organization of the thesis, the discussion on the lightest neutralino dark matter will be postponed to Chapter 8.

6.1 Why supersymmetry and a brief introduction to the MSSM

Supersymmetry (SUSY) is a generalization of the space-time symmetries of quantum field theory that transforms fermions into bosons and vice versa, Theories based on supersymmetry have widely been considered as the theoretically most appealing extension of the SM. They are consistent with the approximate unification of the gauge coupling constants at the GUT scale and provide a way to cancel the quadratic divergences in the Higgs sector hence alleviating the hierarchy between the GUT and the electroweak (EW) scale. In a theory with unbroken supersymmetry, for every type of fermion there exists a corresponding type of boson with the same mass and internal quantum numbers, and vice-versa. Since we have not yet observed any of the "spartner" partners of the SM particles, SUSY is apparently spontaneously broken. Furthermore, in SUSY theories the breaking of electroweak symmetry is naturally induced at the EW scale, and the lightest supersymmetric particle can be neutral, weakly interacting and absolutely stable, providing therefore a natural solution for the dark matter problem.

The Minimal Supersymmetric Standard Model (MSSM) constitutes, hence its name, the minimal supersymmetric extension of the SM. The number of SUSY generators is $N = 1$, the smallest possible value. In order to keep anomaly cancellation, contrary to the SM a second Higgs doublet is needed [136]. All SM multiplets, including the two Higgs doublets, are extended to supersymmetric multiplets, resulting in scalar partners for quarks and leptons ("squarks" and "sleptons") and fermionic partners for the SM gauge boson and the Higgs bosons ("gauginos", "higgsinos" and "gluinos"). Altogether, the MSSM possesses 124 independent parameters (of which 19 arise from the SM and 105 are genuinely new parameters of the supersymmetric extension of the SM) [207, 208].

Upon EWSB, the neutral components of two Higgs doublets H_u^0 and H_d^0 acquire VEVs, v_u and v_d respectively, and the Higgs mechanism proceed as in the SM except that now one

starts with eight degrees of freedom, corresponding to the two complex doublets.[1] Three degrees of freedom are absorbed in making the $W^\pm$ and the Z^0 massive. The W mass is chosen to be: $M_W^2 = g^2(v_u^2 + v_d^2)/4 = g^2 v^2/4$, and this fixes the normalization of v_u and v_d, leaving only two independent parameters to describe the entire MSSM Higgs sector. The remaining five degrees of freedom are physical and correspond to two neutral CP-even scalars h and H, a neutral CP-odd pseudoscalar A and a pair of charged scalars $H^\pm$. At the tree-level the MSSM Higgs sector can be described by two independent parameters (besides the SM parameters), naturally chosen as the mass of the CP-odd Higgs boson, M_A, and $\tan\beta = v_u/v_d$, the ratio of the two VEVs. Details will be presented in the next section. With these two inputs, the tree level masses of the scalar and pseudoscalar Higgs satisfy the following relations:

$$m_{H^\pm}^2 = m_A^2 + M_W^2 \ , \tag{6.1}$$

$$m_{H,h}^2 = \frac{1}{2}\left(m_A^2 + M_Z^2 \pm ((m_A^2 + M_Z^2)^2 - 4M_Z^2 m_A^2 \cos^2 2\beta)^{1/2}\right) \ , \tag{6.2}$$

Eq. (6.2) leads to the famous tree level upper bound on the mass of the lightest CP-even Higgs h:

$$m_h^2 \leq M_Z^2 \cos 2\beta \leq M_Z^2 \ , \tag{6.3}$$

While in the SM the Higgs mass is essentially a free parameter (and should simply be smaller than about 1 TeV), the mass of the lightest CP-even MSSM Higgs is bounded. There are, however, large one-loop corrections to the Higgs mass-squared dominated by loops of heavy top quarks and top squarks, Including the leading two-loop corrections proportional to y_t^2, the square of the top-quark Yukawa coupling. Applying RGE techniques to resum the leading orders of logarithms, the upper bound on the light neutral scalar in Eq. (6.3) is modified as follows:

$$m_h^2 \approx M_Z^2 \cos 2\beta + \Delta m_h^2 \leq M_Z^2 + \frac{3g^2 m_t^2}{8\pi^2 M_W^2}\left[\log\left(\frac{M_S^2}{m_t^2}\right) + \frac{X_t^2}{M_S^2}\left(1 - \frac{X_t^2}{12M_S^2}\right)\right] \ , \tag{6.4}$$

where Δm_h accounts for the radiative loop correction and $M_S^2 = (M_{\tilde{t}_1}^2 + M_{\tilde{t}_2}^2)/2$ is the average of the squares of the two top-squark masses, m_t is the running top-quark mass

---

[1] We follow the common notation used in the supersymmetric models, where the hatted field $\hat{\Phi}$ denotes a chiral superfield and Φ^0 its scalar component. The inner product of mathematical algorithm generates the $SU(2)$-invariant scalar product such that $\hat{H}_u \cdot \hat{H}_d = H_u^+ H_d^- - H_u^0 H_d^0$.
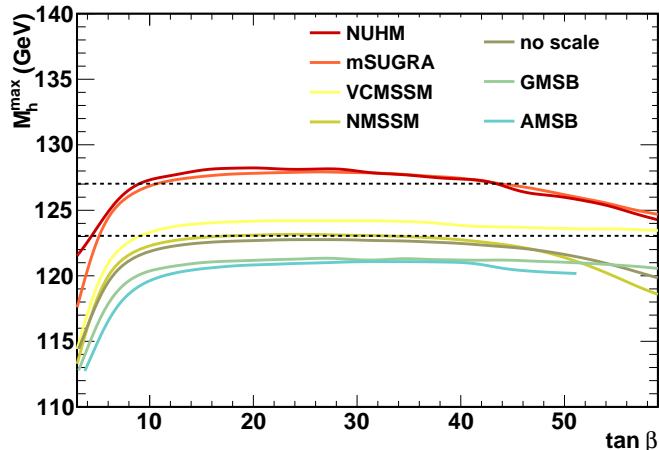
Figure 6.1. The maximal value of the h mass as a function of $\tan\beta$ in the various constrained MSSM models. The NMSSM refers to the constrained NMSSM.

(to account for the leading two-loop QCD corrections), and X_t is the top-squark mixing parameter defined by the top-squark mass matrix. Eq. (6.4) implies that parameter choices within the MSSM are possible that allow one to describe a Higgs boson with a mass in the 125 GeV range if certain combinations of the stop masses, stop mixings, $\tan\beta$ and the parameter M_A (essentially the heavy Higgs masses) are large enough [209–218]. Varying the basic SUSY parameters of the various models, one can determine the maximal m_h value as a function of $\tan\beta$ [212]. This is illustrated in Fig. 6.1. In all cases, the maximal m_h value is obtained for $\tan\beta \approx 20$. At such a large $\tan\beta$, we require $\Delta m_h \approx 85$ GeV which means that a very substantial loop contribution, nearly as large as the tree-level mass, is needed to raise the Higgs boson mass to 125 GeV. The rather complicated parameter dependence has been studied in [219] where it was shown that, with "maximal stop mixing", the lightest stop mass must be $m_{\tilde{t}_1} \gtrsim 500$ GeV (with the second stop mass considerably larger) in the MSSM in order to achieve a 125 GeV Higgs boson. Such a heavy stop typically implies a tuning at least of order 1% in the MSSM [219], depending on the parameter choices and the definition of fine-tuning [220–230].

Last, the MSSM superpotential $W^{(d)}$ contains, in addition to the Yukawa terms of mass dimension $d = 3$, the bilinear coupling $W^{(2)}_{\mathrm{MSSM}} = \mu \hat{H}_u \cdot \hat{H}_d$ of the two Higgs doublet superfields. The parameter μ has positive mass dimension, but since it is introduced directly in the supersymmetric theory it is not associated with any obvious scale (e.g. the

SUSY breaking scale). This leaves only $\mu = 0$ or M_{GUT} as natural choices, both of which are phenomenologically impossible. An acceptable phenomenology requires μ close to the scale of electroweak symmetry breaking: $\mu \sim \mu_{\mathrm{EW}} < M_{\mathrm{SUSY}}$, where M_{SUSY} is the scale of supersymmetry breaking. This is known as the 'μ problem' of the MSSM. To solve this problem, one can replace $W_{\mathrm{MSSM}}^{(2)}$ with a coupling of the Higgs doublets to a gauge singlet superfield $\hat{S}$, which is called the next-to-MSSM (NMSSM). In the NMSSM the μ parameter is generated dynamically from soft terms via the vacuum expectation value of S and thus is of the same order as the SUSY breaking scale. Another improvement of the NMSSM is to reduce the required amount of fine-tuning compared to the MSSM [231].

6.2 MSSM versus 2HDM [2]

Before turning to the core part of the NMSSM, I would like to compare the MSSM with a general two-Higgs-doublet (2HDM), which has been extensively discussed in Chapter 5. As a result of SUSY constraints, the pattern of the Higgs boson masses and couplings in the MSSM is rather special or more constrained. In other words, there will a smaller number of free parameters in the MSSM. Here I just sketch a brief summary of the main differences and highlight the unique features of the MSSM Higgs sector. For more details one can look up the Refs. [44, 145, 146]

As already shown in Section 5.1.1, the four Higgs masses m_h, m_H, m_A and $m_{H^\pm}$ as well as the mixing angles α and β constitute free parameters in the physical basis of a general 2HDM. In addition, as one can see from Eq. (5.25), the parameter Λ_5 in the HHG basis cannot be fixed by the masses and the mixing angles, unless one imposes a strict $\Phi_2 \to -\Phi_2$ symmetry resulting in $\Lambda_5 = 0$. This is a mere reflection of the fact that the model originally had seven inputs, $\tan\beta$ being also a free parameter in the case of a soft violation of $\mathbb{Z}_2$. On the contrary, SUSY imposes strong constraints on the parameter space of the MSSM Higgs sector in such a way that parameters are related each other by the gauge couplings and this results in only two free parameters. Taking $\tan\beta$ and Λ_1 as the free inputs, one has

---

[2]This section is adapted from Section 1.2.5 of a comprehensive review [158].

$$\Lambda_2 = \Lambda_1 , \tag{6.5}$$

$$\Lambda_3 = \frac{1}{8}(g_1^2 + g_2^2) - \Lambda_1 , \tag{6.6}$$

$$\Lambda_4 = -\frac{1}{2}g_1^2 + 2\Lambda_1 , \tag{6.7}$$

$$\Lambda_5 = \Lambda_6 = 2\Lambda_1 - \frac{1}{2}(g_1^2 + g_2^2) \equiv \frac{M_A^2}{v^2} \tag{6.8}$$

This demonstrates that with one input λ_1 all other λ's appearing in the Higgs sector potential will be determined. Traditionally, the MSSM Higgs sector at the tree-level is described by two parameters (besides the SM parameters), commonly chosen as the mass of the CP-odd Higgs boson, $m_A \simeq M_A$, and $\tan\beta$.

In analogy to the 2HDM, the Higgs couplings to gauge bosons in the MSSM are also suppressed by the familiar factors $\cos(\beta - \alpha)$ for the H and $\sin(\beta - \alpha)$ for the h; however, here, the parameter α is no longer free. Since the Higgs sector of the SUSY model is two-doublet in nature, the general sum rule

$$\sum_i \left(C_V^{h_i}\right)^2 = 1 \tag{6.9}$$

again applies. That is, the sum of the squares of the couplings of all the CP-even Higgs bosons (assuming no CP violation in the Higgs potential) to gauge bosons is simply the SM result.

The interaction of the Higgs bosons with fermions depends on the Yukawa structure. SUSY eliminates the possibility of Type I and permits the Type II models only [160, 161], in which the field H_d generates the masses of down–type quarks and leptons while H_u does the same for up–type quarks. Thus, the pattern of the MSSM Higgs couplings would be just like in the Type II 2HDM, see details in Table 5.4. In addition, the couplings among Higgs bosons may have different behavior as compared to a general 2HDM. For instance, the couplings $\lambda_{hH^+H^-}$ and $\lambda_{HH^+H^-}$, contrary to the 2HDM case, never diverge in the limit of very heavy $H^\pm$ bosons due to the fact that the decoupling limit is automatic in the MSSM [39, 232].
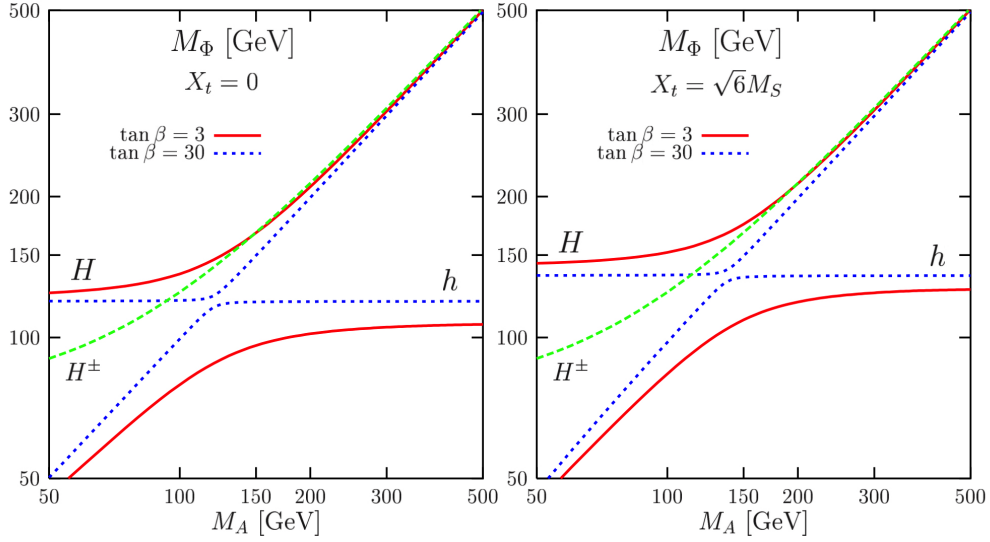
Figure 6.2. The masses of the MSSM Higgs bosons as a function of M_A for two values $t_\beta = 3$ and 30, in the no mixing (left) and maximal mixing (right) scenarios with $M_S = 2$ TeV and all the other SUSY parameters set to 1 TeV. The full set of radiative corrections is included with $m_t = 178$ GeV, $m_b = 4.88$ GeV and $\alpha_s(M_Z) = 0.1172$.

In fact, this difference originates from another remarkable feature of the MSSM, namely that the masses of $H, A, H^\pm$ Higgs bosons must all be strongly degenerate when any one of them is large. Only the mass of the lightest CP-even scalar can remain small. In contrast, such degeneracy need not always hold in the general 2HDM, as we have discussed. For illustration, we display the radiatively corrected masses of the neutral CP–even and the charged Higgs bosons in Fig. 6.2 as a function of M_A for the two values $\tan\beta = 3$ and 30. The full set of radiative corrections has been included and the "no–mixing" scenario with $X_t = 0$ (left) and "maximal mixing" scenario with $X_t = \sqrt{6}M_S$ (right) have been assumed. The SUSY scale has been set to $M_S = 2$ TeV and the other SUSY parameters except for A_t to 1 TeV.

As can be seen, the value of $m_h = 125$ GeV, that is the mass of the state observed at the LHC, can be easily obtained for large M_A values in the maximal mixing scenario as long as $\tan\beta$ is not too small, whereas it appears almost impossible to reach this level in mass for no stop mixing. Also for large M_A values, the A, H and $H^\pm$ bosons (the mass of the latter being almost independent of the stop mixing and the value of $\tan\beta$) become degenerate in mass. In the opposite case, i.e. for a light pseudoscalar Higgs boson, $M_A \lesssim m_h^{\text{max}}$, it is m_h which is very close to M_A, and the mass difference is particularly

small for large $\tan \beta$ values. In this case, H may play a role as the 125 GeV state as its mass could be as low as about 120 GeV in the no mixing scenario for low values of $M_A \lesssim 120$ GeV, and moderate values of $\tan \beta \simeq 10 - 30$. Such a possibility has also been extensively studied in [211, 233–237] and lately were ruled out [238] by applying the constraints from flavour physics, mainly the radiative decay $b \rightarrow s\gamma$. As a final note, I would recommend a recent short review [239] regarding the phenomenology for the MSSM after the Higgs discovery.

6.3   The next-to-minimal supersymmetric SM (NMSSM)

Since the Higgs boson discovery at the LHC, the NMSSM has gained a renewed attraction in view of its positive features as compared to the widely studied MSSM. Firstly, the NMSSM naturally solves in an elegant way the so–called μ problem [240] of the MSSM: to have an acceptable phenomenology, a value in the vicinity of the electroweak or SUSY breaking scale is needed for the supersymmetric Higgs mass parameter μ; this is automatically achieved in the NMSSM, since the μ-parameter is dynamically generated when the singlet Higgs field acquires a vacuum expectation value of the order of the SUSY breaking scale, leading to a fundamental Lagrangian that contains no dimensional parameters apart from the soft SUSY breaking terms. Secondly, as compared to the MSSM, the NMSSM can induce a richer phenomenology in the Higgs and neutralino sectors, both in collider and dark matter (DM) experiments: on the one hand, heavier Higgs states can decay into lighter ones with sizable rates [241–260] and, on the other hand, a new possibility appears for achieving the correct cosmological relic density [261–265] through the so-called "singlino", i.e. the fifth degree of freedom in the neutralino sector, which can have exceptionally weak couplings to SM particles. Thirdly, the NMSSM needs somewhat less fine tuning [248, 249, 266] (although some fine tuning is still required [267]): the upper limit on the mass of the lightest CP–even Higgs particle is larger than in the MSSM, and therefore more SUSY parameter space is consistent with a SM-like Higgs having mass as high as 125.5 GeV. Of course, there are more potential decay modes of an NMSSM Higgs of mass 125.5 GeV. The fact that current data implies that these decay modes cannot

have large branching ratio places constraints on the model parameter space. Nonetheless, in the end a SM-like Higgs boson of mass 125.5 GeV with very SM-like properties is achieved with less fine-tuning than in the MSSM case.

6.3.1 Higgs superpotential of the scale invariant NMSSM

The scale invariant (or $\mathbb{Z}_{\not3}$ invariant) superpotential of the NMSSM is given, in terms of (hatted) superfields, by

$$\mathcal{W} = y_t\,\widehat{Q}\,\widehat{H}_u\,\widehat{t}^c_R - y_b\,\widehat{Q}\,\widehat{H}_d\,\widehat{b}^c_R - y_\tau\,\widehat{L}\,\widehat{H}_d\,\widehat{\tau}^c_R + \lambda\,\widehat{S}\,\widehat{H}_u\,\widehat{H}_d + \frac{\kappa}{3}\,\widehat{S}^3 \,, \qquad (6.10)$$

where H_u, H_d and S represent the complex scalar Higgs fields, with v_u, v_d and s their vacuum expectation values. Tilded letters will denote the scalar components of quark and lepton superfields. For simplicity, only the third generation (s)fermions have been included (with possible neutrino Yukawa couplings having been set to zero) and $\widehat{Q}, \widehat{L}$ stand for the (t,b) and (τ, ν_τ) SU(2) doublet superfields. The three first terms in eq. (6.10) are the usual generalization of the Yukawa interactions, while the second to last term involving the singlet superfield $\widehat{S}$ acts as the substitute for the $\mu\widehat{H}_u\widehat{H}_d$ term in the MSSM superpotential: a non-vanishing value s of the scalar component of $\widehat{S}$ at the minimum of the Higgs potential generates an effective μ term

$$\mu_{\text{eff}} \equiv \lambda\langle S\rangle = \lambda\,s \,. \qquad (6.11)$$

The soft SUSY breaking terms consist of mass terms for the gaugino, Higgs and sfermion fields (for the latter, we will use the notation of the third generation; a sum over the three generations is implicitly assumed) which, in terms of the fields corresponding to the complex scalar components of the superfields, are given by

$$
\begin{aligned}
-\mathcal{L}_{\frac{1}{2}} &= \frac{1}{2}\left[M_1\tilde{B}\tilde{B} + M_2\sum_{a=1}^{3}\tilde{W}^a\tilde{W}_a + M_3\sum_{a=1}^{8}\tilde{G}^a\tilde{G}_a\right] + \text{h.c.} \,, \qquad &(6.12)\\
-\mathcal{L}_0 &= m_{H_u}^2|H_u|^2 + m_{H_d}^2|H_d|^2 + m_S^2|S|^2 \\
&\quad + m_Q^2|\tilde{Q}^2| + m_{\tilde t}^2|\tilde{t}_R^2| + m_{\tilde b}^2|\tilde{b}_R^2| + m_L^2|\tilde{L}^2| + m_\tau^2|\tilde{\tau}_R^2| \,, \qquad &(6.13)
\end{aligned}
$$

as well as trilinear interactions between the sfermion and the Higgs fields, including the

singlet field

$$
\begin{aligned}
-\mathcal{L}_{\text{tril}} =\ & \Big(h_t A_t\, \tilde{Q}\, H_u\, \tilde{t}_R^c - h_b A_b\, \tilde{Q}\, H_d\, \tilde{b}_R^c - h_\tau A_\tau\, \tilde{L}\, H_d\, \tilde{\tau}_R^c \\
& + \lambda A_\lambda\, H_u\, H_d\, S + \frac{1}{3}\kappa A_\kappa\, S^3 \Big) + \text{h.c.} \ .
\end{aligned}
\tag{6.14}
$$

All parameters in the above Lagrangian, including mass parameters for the gauginos $M_{1,2,3}$, sfermions $m_{\tilde{f}_{L,R}}$, Higgs fields $m_{H_{u,d}}$ and trilinear interactions A_f as in the MSSM, supplemented by an additional scalar mass m_S, two trilinear couplings A_λ and A_κ and two dimensionless parameters λ and κ for the singlet field, depend on the energy scale via the corresponding RG equations, so that the dominant radiative corrections involving large logarithms must be accounted for.

It is also clear that, in the limit $\lambda \to 0$ with finite μ_{eff}, the NMSSM turns into the MSSM with a decoupled singlet sector. Nonetheless, the phenomenology of the NMSSM for $\lambda \to 0$ could still differ somewhat from the MSSM in the case where the lightest SUSY particle (LSP), a possible dark matter candidate, is the singlino and hence gives the possibility of a long lived next-to-lightest SUSY particle [268, 269]. In cases where the LSP is singlino-like there will be significant modifications of all sparticle decay cascades as compared to the MSSM. We will not consider this situation here and delay the discussion to Chapter 8 .

From the SUSY gauge interactions, the F- and the soft SUSY breaking terms one obtains the Higgs potential:

$$
\begin{aligned}
V_{\text{Higgs}} =\ & \Big| \lambda \left(H_u^+ H_d^- - H_u^0 H_d^0 \right) + \kappa S^2 \Big|^2 \\
& + \left(m_{H_u}^2 + |\mu + \lambda S|^2 \right) \left(\left| H_u^0 \right|^2 + \left| H_u^+ \right|^2 \right) \\
& + \left(m_{H_d}^2 + |\mu + \lambda S|^2 \right) \left(\left| H_d^0 \right|^2 + \left| H_d^- \right|^2 \right) \\
& + \frac{g_1^2 + g_2^2}{8} \left(\left| H_u^0 \right|^2 + \left| H_u^+ \right|^2 - \left| H_d^0 \right|^2 - \left| H_d^- \right|^2 \right)^2 \\
& + \frac{g_2^2}{2} \left| H_u^+ H_d^{0*} + H_u^0 H_d^{-*} \right|^2 \\
& + m_S^2 |S|^2 + \left(\lambda A_\lambda \left(H_u^+ H_d^- - H_u^0 H_d^0 \right) S + \frac{1}{3}\kappa A_\kappa\, S^3 + \text{h.c.} \right)
\end{aligned}
\tag{6.15}
$$

where g_1 and g_2 denote the $U(1)_Y$ and $SU(2)$ gauge couplings, respectively.

In an unconstrained NMSSM with non-universal soft terms at the GUT scale, it is possible to use the extremization conditions for the scalar potential to replace the three mass-squared parameters for m_{H_u}, m_{H_d} and m_S appearing in V_{soft} by the three VEVs, v_u, v_d and s:

$$v_u \left(m_{H_u}^2 + \mu_{\text{eff}}^2 + \lambda^2 v_d^2 + \frac{g_1^2 + g_2^2}{4}(v_u^2 - v_d^2) \right) - v_d \mu_{\text{eff}}(A_\lambda + \kappa s) = 0 \qquad (6.16)$$

$$v_d \left(m_{H_d}^2 + \mu_{\text{eff}}^2 + \lambda^2 v_u^2 - \frac{g_1^2 + g_2^2}{4}(v_u^2 - v_d^2) \right) - v_u \mu_{\text{eff}}(A_\lambda + \kappa s) = 0 \qquad (6.17)$$

$$s \left(m_S^2 + \kappa A_\kappa s + 2\kappa^2 s^2 + \lambda^2(v_u^2 + v_d^2) - 2\lambda\kappa v_u v_d \right) - \lambda v_u v_d A_\lambda = 0 \qquad (6.18)$$

Thus, in contrast to the MSSM (where one has only two free parameters at the tree level), the Higgs sector of the NMSSM is described by six parameters, apart from gauge and quark/lepton Yukawa couplings: [3]

$$\lambda \, , \; \kappa \, , \; A_\lambda \, , \; A_\kappa, \; \tan \beta = v_u/v_d \text{ and } \mu_{\text{eff}} = \lambda s; \qquad (6.19)$$

Because of a larger number of both superpotential and soft SUSY breaking parameters than in the MSSM, there are more options for selecting unified boundary conditions at the GUT scale. For instance, in the most constrained version of the NMSSM that will be defined shortly in Section 6.4.1, a universal value for the soft SUSY breaking gaugino, sfermion and Higgs masses (other than the singlet mass parameter m_S) as well as universal trilinear couplings are assumed at the grand-unification (GUT) scale M_{GUT} in the form:

$$M_1 = M_2 = M_3 \equiv M_{1/2} \,,$$

$$(m_{H_u} = m_{H_d} =)m_Q = m_t = m_b = m_L = m_\tau \equiv m_0 \,,$$

$$A_t = A_b = A_\tau (= A_\lambda = A_\kappa) \equiv A_0 \,. \qquad (6.20)$$

Once imposed, the Higgs and sparticle sectors of the NMSSM depend on the few parameters $M_{1/2}, m_0, A_0$. [200, 270]. In practice, one integrates the RG equations for all soft

---

[3]In fact $\tan \beta$ is an output as the top quark Yukawa coupling y_t is an input. This becomes very difficult to obtain the correct value for the top quark mass m_t or, given m_t, y_t can only be obtained once $\tan \beta$ is known. Since y_t is very important for the radiative corrections and the RG evolution, it would be much more convenient to allow for $\tan \beta$ as an input parameter, which permits to determine y_t at the weak scale from the beginning in terms of m_t.

terms from M_{GUT} down to the SUSY scale M_{SUSY}. Of course, one can make less restrictive assumptions on the Higgs sector soft terms at the GUT scale [271].

On the other hand, the values of $\tan\beta$ and λ[4] are imposed at, respectively, the weak scale (defined by M_Z) and the SUSY scale M_{SUSY}, the latter defined by the order of magnitude of the soft SUSY-breaking terms. Further, the parameters κ, the soft singlet mass m_S^2 as well as the vev $|s|$ (or $|\mu_{\mathrm{eff}}| \equiv \lambda|s|$) are determined at low energy scale, M_{SUSY}, through the three minimization equations of the scalar potential with respect to v_u, v_d and s.

Obviously, the soft singlet mass squared m_S^2 at M_{GUT} will not coincide with m_0^2 in general (for a recent analysis allowing for a non-universal singlet mass term, see Ref. [272]). However, one can confine oneself to regions in parameter space where the difference between m_S^2 and m_0^2 is negligibly small. This condition leaves us with an effective 4-dimensional parameter space, consistent with the considerations above. In practice, we determine $\tan\beta$ by the requirement that m_S^2 at M_{GUT} should be close to m_0^2.[5]

6.3.2 Higgs mass spectrum

The singlet superfield $\widehat{S}$ contains a neutral CP-even and a neutral CP-odd scalar, as well as a neutralino. All these states mix with the corresponding components of the $\widehat{H}_u$ and $\widehat{H}_d$ superfields, increasing the rank of the CP-even, CP-odd and neutralino mass matrices by one as compared to the MSSM. As a result, the presence of S in the NMSSM implies an extended Higgs sector (3 neutral CP-even and 2 neutral CP-odd states) and an extended neutralino sector (5 neutralinos including the singlino) which will be fully analyzed in Chapter 8. This extended Higgs sector includes light CP-odd or CP-even states that can lead to important Higgs-to-Higgs decays and Higgs production in sparticle decay cascades.

- *CP-odd Higgs states*

---

[4]One can choose sign conventions such that the parameters λ and $\tan\beta$ are positive, while the parameters κ, A_λ, A_κ and μ_{eff} can have both signs. (With the convention $\lambda > 0$, κ typically turns out to be positive as well, and of $\mathcal{O}(\lambda/10)$; the sign of s or μ_{eff} can still be chosen at will.)

[5]The empirical result shows that the condition $|m_S^2(M_{\mathrm{GUT}}) - m_0^2| < (5\ \mathrm{GeV})^2$ typically requires to tune the fourth decimal of $\tan\beta$. This however should not be interpreted as a fine-tuning, since m_S^2 should be considered as an input parameter, whereas $\tan\beta$ is determined by the minimization of the effective potential.

Let us begin our analysis with the simple mass-squared matrix of the CP-odd Higgs states. The presentation of the Higgs mass matrices at tree-level is simplified by defining an effective doublet mass M_A as

$$M_A^2 \equiv \frac{\lambda s}{\sin \beta \cos \beta} \Big(A_\lambda + \kappa s \Big). \tag{6.21}$$

Although this quantity is equivalent to tree-level mass of the (only physical) CP-odd Higgs A in the MSSM, in general it does not correspond to the mass of any physical Higgs boson in the NMSSM. Eliminating the massless Goldstone boson G eaten by the Z, the remaining 2×2 mass matrix for the pseudoscalars can be written in the basis $(A, \mathfrak{Im}S)$, where $A = \cos \beta \mathfrak{Im}H_u + \sin \beta \mathfrak{Im}H_d$ is the doublet component. In this basis, it is given by

$$\mathcal{M}_A^2 =$$
$$\begin{pmatrix} M_A^2 & \frac{v}{s} \left(M_A^2 \cos \beta \sin \beta - 3\lambda \kappa s^2 \right) \\ \frac{v}{s} \left(M_A^2 \cos \beta \sin \beta - 3\lambda \kappa s^2 \right) & \frac{v^2 \cos \beta \sin \beta}{s^2} \left(M_A^2 \cos \beta \sin \beta + 3\lambda \kappa s^2 \right) - 3\kappa A_\kappa s \end{pmatrix}$$

The pseudoscalar masses are diagonalized by a simple rotation with an angle θ_A such that

$$\begin{pmatrix} a_1 \\ a_2 \end{pmatrix} = \begin{pmatrix} \cos \theta_A & \sin \theta_A \\ -\sin \theta_A & \cos \theta_A \end{pmatrix} \begin{pmatrix} A \\ \mathfrak{Im}S \end{pmatrix}, \tag{6.22}$$

where an explicit relation for the mixing angle is determined by the requirement that the off-diagonal elements of the mass matrix $\mathcal{M}_A^2$ are vanishing.

$$\cos \theta_A = \frac{\mathcal{M}_{A,12}^2}{\sqrt{\mathcal{M}_{A,12}^4 + \left(m_{A_1}^2 - \mathcal{M}_{A,11}^2 \right)^2}}. \tag{6.23}$$

The analytical forms for the mass of pseudoscalar Higgs eigenstates, a_1, a_2 are obtainable but are too complicated to write out here.

- *CP-even Higgs states*

Next we come to the CP-even sector.

To describe the mixing in the CP-even Higgs sector, one needs to convert the weak basis $S^{\text{weak}} = (\mathfrak{Re}H_u, \mathfrak{Re}H_d, \mathfrak{Re}S)$ to the mass eigenstates h_i by introducing a full 3×3

unitary matrix $\mathcal{S}$. We use the parametrization

$$\mathcal{S} = \begin{pmatrix} c_{12}c_{13} & s_{12}c_{13} & s_{13} \\ -s_{12}c_{23} - c_{12}s_{13}s_{23} & c_{12}c_{23} - s_{12}s_{13}s_{23} & c_{13}s_{23} \\ -c_{12}c_{23}s_{13} + s_{12}s_{23} & -c_{12}s_{23} - s_{12}s_{13}c_{23} & c_{13}c_{23} \end{pmatrix}, \tag{6.24}$$

with $c_{ij} = \cos\theta_{ij}$ and $s_{ij} = \sin\theta_{ij}$.[6] In fact, the realization of this transformation is decomposed into two successive steps, which can be sketched as

$$\begin{pmatrix} \mathfrak{Re}\, H_u \\ \mathfrak{Re}\, H_d \\ \mathfrak{Re}\, S \end{pmatrix} \xrightarrow{V(\beta)} \begin{pmatrix} h_V \\ H_V \\ S \end{pmatrix} \xrightarrow{U(\theta_P)} \begin{pmatrix} h_1 \\ h_2 \\ h_3 \end{pmatrix} \tag{6.25}$$

We label the resulting CP-even mass eigenstates in order of increasing mass. Both V and U are unitary matrices. The neutral Higgs sector of the NMSSM has three CP-even Higgs bosons: **I am not sure what your convention for CP is? Is it CP or *CP*?**

$$\begin{aligned} h_V &= \sqrt{2}\left((\mathrm{Re}H_d^0 - v\cos\beta)\cos\beta + (\mathrm{Re}H_u^0 - v\sin\beta)\sin\beta\right), \\ H_V &= \sqrt{2}\left((\mathrm{Re}H_d^0 - v\cos\beta)\sin\beta - (\mathrm{Re}H_u^0 - v\sin\beta)\cos\beta\right), \\ S &= \sqrt{2}\left(\mathrm{Re}S - \langle S\rangle\right), \end{aligned} \tag{6.26}$$

where $\langle H_u^0\rangle = v\sin\beta$ and $\langle H_d^0\rangle = v\cos\beta$. Among them, h_V behaves exactly like the SM Higgs boson if it does not mix with the others. and the 3×3 orthogonal matrix U may be obtained by diagonalizing $\mathcal{M}_h^2$.

For brevity, we do not give the entries of the CP-even mass matrix $\mathcal{M}_S$ in the weak basis here. They can be found for example in [200]. The squared-mass matrix for the CP-even scalars in the intermediate basis (h_V, H_V, S), is given by

$$\mathcal{M}_P^2 = v^2 \begin{pmatrix} r + \dfrac{M_Z^2}{v^2} & r\cot 2\beta & \lambda^2\dfrac{s}{v} - R \\[2ex] r\cot 2\beta & -r + \dfrac{\lambda\kappa s^2 + 2m_\lambda s}{v^2\sin 2\beta} & -R\cot 2\beta \\[2ex] \lambda^2\dfrac{s}{v} - R & -R\cot 2\beta & \dfrac{s}{v^2}\left(2\kappa^2 s - m_\kappa\right) + \dfrac{m_\lambda}{2s}\sin 2\beta \end{pmatrix} \tag{6.27}$$

---

[6]This corresponds to a mixing in the MSSM limit which takes the form $\theta_{12} \to -\alpha$, $\cos\theta_{13} \to 1$, and $\cos\theta_{23} \to 1$.

where we have defined

$$r \equiv \left(\frac{\lambda^2}{2} - \frac{M_Z^2}{v^2} \right) \sin^2 2\beta \ , \tag{6.28}$$

and

$$R \equiv \frac{1}{v} \left(\lambda \kappa s + m_\lambda \right) \sin 2\beta \ . \tag{6.29}$$

The tree-level value of m_{H_1} is no longer limited from above by $m_h^2 \leq m_Z^2 \cos^2 2\beta$ (as is the case in the MSSM). Instead the modified limit [273]

$$m_{h_1}^2 \leq m_Z^2 \cos^2 2\beta + \frac{\lambda^2 m_W^2}{g^2} \sin^2 2\beta \tag{6.30}$$

applies. The SM-like Higgs boson generally appears as a mixture of CP-even Higgs states:

$$h_1 = c_{\theta_1} c_{\theta_2} h_V - s_{\theta 1} H_V - c_{\theta_1} s_{\theta_2} S, \tag{6.31}$$

Here $s_\theta = \sin \theta$ and $c_\theta = \cos \theta$, for $-\pi/2 < \theta_i \leq \pi/2$ $(i = 1, 2, 3)$ being the mixing angles in the orthogonal matrix diagonalizing $\mathcal{M}_P^2$ (see eq. (6.27)). There are also two other mass eigenstates, h_2 and h_3 with mass m_{h_2} and m_{h_3}, respectively.

- *Charged Higgs states*

Finally, the tree-level mass of the physical charged Higgs boson is given by

$$m_{H^\pm}^2 = M_A^2 + m_W^2 - \lambda^2 v^2, \tag{6.32}$$

where M_A^2 is given by Equation (6.21). For a fixed doublet mass, the term $-\lambda^2 v^2$ reduces the charged Higgs mass compared to its MSSM value.

All in all, all eigenvalues of $\mathcal{M}_h^2$ and $\mathcal{M}_A^2$ have to be positive, and $m_{H^\pm}^2 > 0$. The whole discussion so far concerned the Higgs masses at tree-level. Like in the MSSM, the tree-level relations may be subject to sizeable higher order corrections [274, 275]. The Higgs mass corrections taken into account in our numerical analysis are discussed further in the next section. As a final point, let us discuss the MSSM limit. This is obtained by taking simultaneously $\lambda \to 0$ and $\kappa \to 0$, keeping the ratio κ/λ constant, thus decoupling the singlet from interacting with the Higgs doublets. A finite $|\mu| > 0$ in this limit (as required to get massive charginos) is achieved by taking $v_s \to \infty$. The remaining dimensionful parameters are held constant. This illustrates the possibility to

consider a class of models with a continuous transition from the MSSM to the NMSSM. Finally, we note the interesting fact that even if all influence on Higgs physics vanishes the LSP may be singlino-like, giving a possibly long-lived (or even charged) NLSP which could lead to modified collider phenomenology even in the decoupling limit [276].

6.3.3 Radiative corrections to the Higgs masses

The Higgs mass matrices in Eq. (6.27), and notably the upper bound (6.30) on the mass of the lightest CP-even Higgs scalar, have been derived from the tree level potential (6.15), where all quartic terms are determined by supersymmetry through the superpotential and (electroweak) supersymmetric gauge interactions. Thistreatment would be justified only if the scale of supersymmetry breaking M_{SUSY} would be of order the Higgs vevs (or M_Z), which, however, is obviously not the case.

Like the MSSM, for the case of $M_{\mathrm{SUSY}} > M_Z$ quantum corrections arise and are dominantly contributed from top quark/squark loops, leading to an increase of the upper bound (6.30) on the mass of the lightest CP-even Higgs scalar. The resulting upper bound on the lightest CP-even Higgs mass in the NMSSM has been studied in the leading log approximation in [277–285]. Full one-loop calculations of the corresponding upper bound involving top/bottom quark/squark loops have been carried out in [286–296]. (Analyses at large values of $\tan\beta$ have been performed in [297–299], and upper bounds for more general supersymmetric Higgs sectors have been considered in [300–302].)

An approximate formula for the mass M_{SM} of the SM-like Higgs scalar in the NMSSM in the limit $\kappa s \gg |A_\kappa|, |A_\lambda|$ (corresponding to a heavy singlet-like scalar), including the dominant top/stop radiative corrections, is given by

$$
\begin{aligned}
M_{\mathrm{SM}}^2 \;\simeq\; & M_Z^2 \cos^2 2\beta + \lambda^2 v^2 \sin^2 2\beta - \frac{\lambda^2}{\kappa^2} v^2 (\lambda - \kappa \sin 2\beta)^2 \\
& + \frac{3 m_t^4}{4\pi^2 v^2} \left(\ln\left(\frac{m_T^2}{m_t^2} \right) + \frac{A_t^2}{m_T^2} \left(1 - \frac{A_t^2}{12 m_T^2} \right) \right)
\end{aligned}
\tag{6.33}
$$

where v and $\tan\beta$ are defined in Section 6.1, the soft SUSY breaking stop masses are assumed to satisfy $m_T^2 \sim m_{Q_3}^2 \gg m_t^2$, A_t is the stop trilinear coupling assumed to satisfy $|A_t| \gg m_t, \mu_{\mathrm{eff}}$; the terms $\sim \lambda^2$ are specific to the NMSSM, and the last term in the first line originates from the mixing with the singlet-like scalar.

In order to maximize M_{SM} in the NMSSM, λ should be as large as possible, and $\tan\beta$ should be small in order to avoid a suppression from $\sin^2 2\beta$. (However, λ is bounded from above by $\lambda \lesssim 0.7 - 0.8$ if one requires the absence of a Landau singularity below the GUT scale.) On the other hand, the negative contribution from the mixing with the singlet-like scalar should vanish; without neglecting A_λ, the relevant mixing term is proportional to $(\lambda - \sin 2\beta(\kappa + A_\lambda/(2s)))^2$ [303]. If this expression is not small, a larger value of λ can even generate a decrease of the mass of the Higgs scalar with SM-like couplings to the Z boson in the NMSSM.

At present, additional known radiative corrections to the Higgs mass matrices in the NMSSM include MSSM-like electroweak together with the NMSSM-specific Higgs one-loop contributions [274, 304] and dominant two-loop terms [274, 305–308]. Taking these loop corrections into account, and requiring perturbative running Yukawa couplings h_t, λ and κ below the GUT scale, the upper bound on the lightest CP-even Higgs mass has been studied in [303] as a function of $\tan\beta$ and for different values of m_t in the NMSSM, and compared to the MSSM with the result shown in Fig. 6.3. (In Fig. 6.3, the upper bound is denoted as m_{max}.) The squark mass terms (and hence M_{SUSY}) have been chosen as 1 TeV; the upper bound would still increase slowly (logarithmically) with M_{SUSY}. In order to maximize the one-loop top/bottom (s)quark contributions to the lightest CP-even Higgs mass for these squark masses, the trilinear soft couplings are chosen as $A_t = A_b = 2.5$ TeV. The threshold effects depend somewhat on the gaugino masses, which are $M_1 = 150$ GeV, $M_2 = 300$ GeV and $M_3 = 1$ TeV (These values are chosen to be consistent with those that originate from a universal $M_{1/2}$ at the GUT scale.); the remaining parameters λ, κ, A_λ, A_κ and μ_{eff} of the $\mathbb{Z}_3$-invariant NMSSM have been chosen such that the upper bound is maximised, without encountering Landau singularities (which requires κ as small as possible) nor violating other constraints such as an unstable potential, which forbids $\kappa \to 0$.

In the NMSSM, the second term $\sim \sin^2 2\beta$ in the tree level expression (6.33) dominates the first one for sufficiently large λ, and accordingly m_{max} is maximal for low values of $\tan\beta$. On the other hand, the absence of a Landau singularity for λ below the GUT
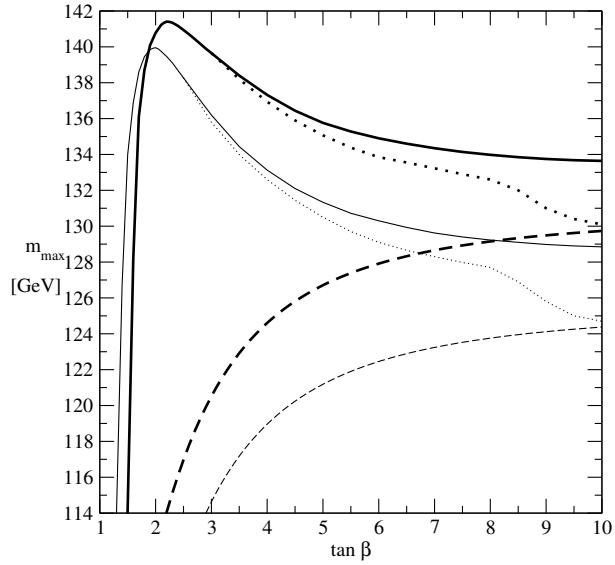
Figure 6.3. Upper bound on the lightest Higgs mass in the NMSSM as a function of $\tan\beta$ for $m_t = 178$ GeV (M_A arbitrary: thick full line, $M_A = 1$ TeV: thick dotted line) and $m_t = 171.4$ GeV (thin full line: M_A arbitrary, thick dotted line: $M_A = 1$ TeV) and in the MSSM (with $M_A = 1$ TeV) for $m_t = 178$ GeV (thick dashed line) and $m_t = 171.4$ GeV (thin dashed line). Squark and gluino masses are 1 TeV and $A_t = A_b = 2.5$ TeV. (From [303].)

scale implies a decrease of the maximally allowed value of λ at M_{SUSY} with increasing h_t, i.e. with increasing m_t and decreasing $\tan\beta$. (At large $\tan\beta$, arbitrary variations of the NMSSM parameters λ, κ, A_λ, A_κ and μ_{eff} can imply a mass M_A of the MSSM-like CP-odd scalar far above 1 TeV. For comparison with the MSSM, $m_{\max}$ in the NMSSM with $M_A \leq 1$ TeV is depicted as dotted lines in Fig. 6.3.) Numerically, for $m_t = 171.4$ GeV, $m_{\max}$ in the NMSSM (thin full line in Fig. 6.3) is 140 GeV, and assumed for $\tan\beta = 2$, $\lambda = 0.70$ and $\kappa = 0.05$, whereas for $m_t = 178$ GeV (thick full line in Fig. 6.3), $m_{\max}$ increases just to 141.5 GeV for $\tan\beta = 2.2$, $\lambda = 0.68$ and $\kappa = 0.07$.

It must be emphasized, however, that the observation of a Higgs boson in standard search channels with a mass ~ 125 GeV would *neither* rule out any BSM models *nor* favor the NMSSM. **[JG: Not clear to me that this is a true statement.]**

6.3.4 Two possible scenarios to achieve a SM-like Higgs

The masses of the CP-even scalars can be understood in a better way by considering what happens when the singlet is added to the MSSM spectrum. In analogy to the 2HDM
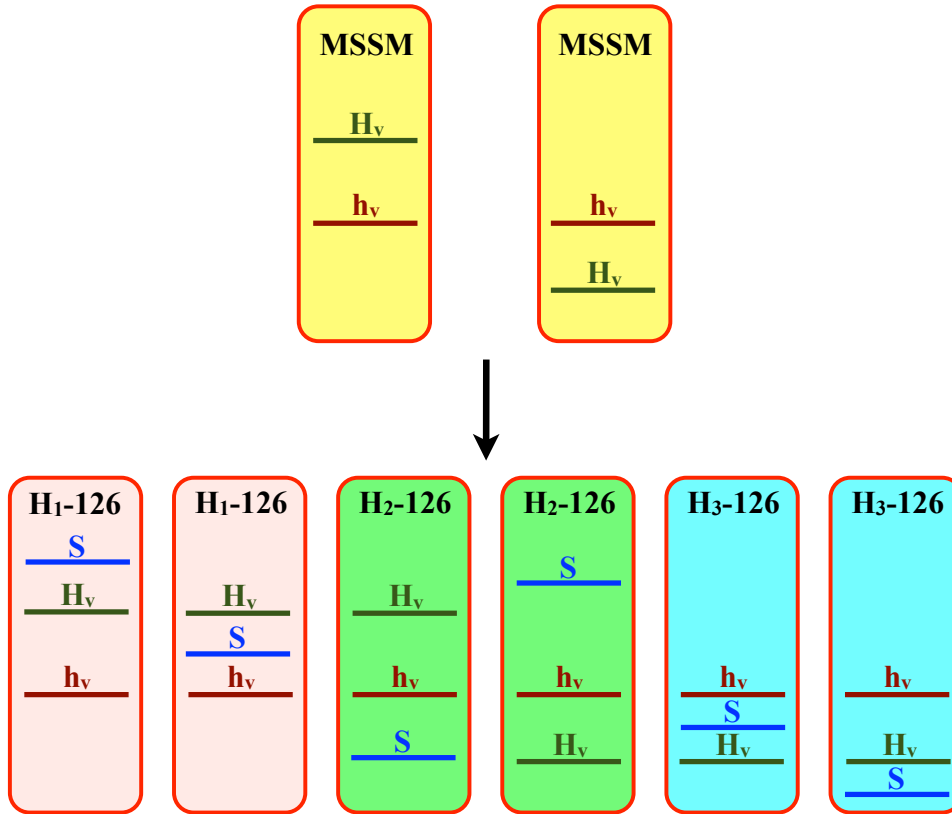
Figure 6.4. Illustration of the effect of adding the singlet to the MSSM CP-even Higgs boson spectrum before mixing. *Source: taken from [309].*

as we have studied in Chapter 5, the SM-like Higgs of the MSSM can be either the lighter eigenstate or the heavier eigenstate, as illustrated in the top row of Fig. 6.4. After adding the singlet scalar, the two panels of the MSSM give rise to six possible scenarios in the NMSSM. This is depicted in the lower row of Fig. 6.4 from Ref. [309]. In reality, the mass eigenstates are admixtures of the gauge interaction eigenstates, and thus cannot be labelled as simply as in Fig. 6.4. Nevertheless, these graphs give us an intuitive picture of the result of adding the singlet field of the NMSSM. We shall use h^0 for the SM-like mass state,[7] *i.e.* the one with the largest projection onto h_V; H^0 for the state corresponding to the "heavy" CP-even Higgs boson of the MSSM, *i.e.* the one with the largest projection onto H_V; and S^0 for the state corresponding to the additional singlet of the NMSSM, *i.e.* the one with the largest projection onto S.

---

[7]Whenever there is no confusion, we shall use an alternative labelling of the Higgs boson mass eigenstates, in analogy to the MSSM.

- h_1 *is SM-like Higgs*

As can be readily seen from (6.27), in the limit of large s, the SM-like Higgs boson h^0 is identified with the lightest mass eigenstate h_1.

- h_2 *is SM-like Higgs*

In contrast to the above case, for small values of s, h^0 can also be h_2 or even h_3, depending on the other parameters. Of course, accomplishing the latter possibility is certainly a big challenge.

6.4 Methodology and constraints

6.4.1 The constrained versions of the NMSSM

Various versions of the NMSSM have been studied, differing with respect to how universality among the SUSY soft-breaking parameters is imposed at the GUT scale. In the most constrained version, dubbed VC-NMSSM [270, 310], *all* soft terms are assumed to be universal at the GUT scale just as in the CMSSM. The VC-NMSSM has as many free parameters as the CMSSM: the parameters μ and B are replaced by λ and κ. With κ being determined by M_Z, one is left with

$$\text{VC} - \text{NMSSM}: \qquad m_{1/2},\ m_0,\ A_0,\ \lambda,\ \text{sign}(\mu)\ . \tag{6.34}$$

Phenomenological constraints imply that m_0 and λ are small [270, 310]; with A_0 being determined by the DM relic density, one is left with $m_{1/2}$ as the only essential free parameter (as a function of which also $\tan\beta$ is determined [270, 310]).

In the cNMSSM on the other hand one allows m_S to differ from m_0 [311], in which case the free parameters are

$$\text{cNMSSM}: \qquad m_{1/2},\ m_0,\ A_0,\ \lambda,\ \tan\beta,\ \text{sign}(\mu)\ . \tag{6.35}$$

In this chapter we limit ourselves in the context of constrained versions of the NMSSM with semi-universal GUT scale boundary conditions. The three models we shall consider are distinguished in terms of GUT scale parameters as follows:

I) the constrained NMSSM (CNMSSM) in which we adopt universal m_0, $m_{1/2}$, $A_0 = A_{t,b,\tau}$ values but require $A_\lambda = A_\kappa = 0$ (rather than $A_0 = A_{t,b,\tau} = A_\lambda = A_\kappa$ as in the

cNMSSM), as motivated by the $U(1)_R$ symmetry limit of the NMSSM.

Even more relaxed boundary conditions in the Higgs sector have been considered. Leaving A_κ, A_λ and m_S as free parameters and allowing as well non-universality for the Higgs soft masses squared leads to a very much broader range of possible phenomenologies as compared to the cNMSSM. For example, it is easy to find fully consistent scenarios with a singlino-like LSP *and* light neutral Higgs bosons. Once κ is determined by M_Z and m_S by $\tan\beta$, the parameter space of the semi-constrained scNMSSM can be taken as [271]

$$\text{scNMSSM}: \quad \lambda, \ m_{1/2}, \ m_0, \ m_{H_u}, \ m_{H_d}, \ A_0, \ A_\kappa, \ A_\lambda, \ \tan\beta, \ \text{sign}(\mu) \ . \quad (6.36)$$

We further split this type into two versions in the consideration. They are:

II) the non-universal Higgs mass (NUHM) relaxation of model **I** in which m_{H_u} and m_{H_d} are chosen independently of m_0, but still with $A_\lambda = A_\kappa = 0$, and

III) universal m_0, $m_{1/2}$, A_0 with NUHM relaxation and general A_λ and A_κ.

6.4.2 Tools

For the numerical analysis, we use NMSSMTools [247, 312, 313] version 3.2.0 to calculate the spectra of the Higgs and SUSY particles in the NMSSM in terms of the soft SUSY breaking terms at M_{GUT} (except for the parameter m_S^2), $\tan\beta$ at the weak scale (defined by M_Z) and λ at the SUSY scale M_{SUSY}. This program has improved convergence of RGEs in the case of large Yukawa couplings and thus allows us to explore parameter regions that were left uncharted in [1].

As discussed in Chapter 3, the main production/decay channels relevant for current LHC data are gluon fusion (gg) and vector boson fusion (VBF) with Higgs decay to $\gamma\gamma$ or $ZZ^* \to 4\ell$. The LHC also probes $W, Z+$Higgs with Higgs decay to $b\bar{b}$, a channel for which Tevatron data is relevant, and $WW \to$Higgs with Higgs$\to \tau^+\tau^-$. For the purposeof illustrating the consistency of our results with the experimental measurements, we employ the signal strength R as the ratio of the gg or VBF induced Higgs cross section times the Higgs branching ratio to a given final state X, relative to the corresponding value for the

SM Higgs boson.[8] Specifically, for the individual Higgs of the NMSSM we compute:

$$R_{gg}^{h_i}(X) \;\equiv\; \frac{\Gamma(h_i \to gg)\,\mathrm{BR}(h_i \to X)}{\Gamma(H_{\mathrm{SM}} \to gg)\,\mathrm{BR}(H_{\mathrm{SM}} \to X)}, \tag{6.37}$$

$$R_{\mathrm{VBF}}^{h_i}(X) \;\equiv\; \frac{\Gamma(h_i \to VV)\,\mathrm{BR}(h_i \to X)}{\Gamma(H_{\mathrm{SM}} \to VV)\,\mathrm{BR}(H_{\mathrm{SM}} \to X)}, \tag{6.38}$$

where h_i is the ith NMSSM scalar Higgs, and H_{SM} is the SM Higgs boson, taking $m_{H_{\mathrm{SM}}} = m_{h_i}$.

The ratio is computed in a self-consistent manner (that is, treating radiative corrections for the SM Higgs boson in the same manner as for the NMSSM Higgs bosons) using an appropriate additional routine for the SM Higgs added to the NMHDECAY component of the NMSSMTools package. To compute the SM denominator, we proceed as follows.[9] NMHDECAY computes couplings for each h_i defined by $C_Y^{h_i} \equiv g_{h_i Y}/g_{H_{\mathrm{SM}} Y}$, where $Y = gg, VV, b\bar{b}, \tau^+\tau^-, \gamma\gamma, \ldots$, as well as $\Gamma_{\mathrm{tot}}^{h_i}$ and $\mathrm{BR}(h_i \to Y)$ for all Y. From these results we obtain the partial widths $\Gamma^{h_i}(Y) = \Gamma_{\mathrm{tot}}^{h_i}\mathrm{BR}(h_i \to Y)$. We next compute $\Gamma^{H_{\mathrm{SM}}}(Y) = \Gamma^{h_i}(Y)/[C_Y^{h_i}]^2$ and $\Gamma_{\mathrm{tot}}^{H_{\mathrm{SM}}} = \sum_Y \Gamma^{H_{\mathrm{SM}}}(Y)$ and thence $\mathrm{BR}(H_{\mathrm{SM}} \to Y) = \Gamma^{H_{\mathrm{SM}}}(Y)/\Gamma_{\mathrm{tot}}^{H_{\mathrm{SM}}}$. We then have all the information needed to compute R^{h_i} for some given final state X.

Note that in the context of any two-Higgs-doublet plus singlets model, not all the R^{h_i} are independent. For example, $R_{VH}^{h_i}(X) = R_{VBF}^{h_i}(X)$, $R_Y^{h_i}(\tau\tau) = R_Y^{h_i}(bb)$ [10] and $R_Y^{h_i}(ZZ) = R_Y^{h_i}(WW)$. A complete independent set of R^{h_i}'s can be taken to be (with $h = h_1$ or $h = h_2$)

$$R_{gg}^h(WW), \quad R_{gg}^h(bb), \quad R_{gg}^h(\gamma\gamma), \quad R_{VBF}^h(WW), \quad R_{VBF}^h(bb), \quad R_{VBF}^h(\gamma\gamma). \tag{6.39}$$

---

[8] In this and next chapters the the signal strength ratio previously labeled as μ in Eq. (3.2) (and used frequently in the previous chapters) is instead called R.

[9] Ideally, the same radiative corrections would be present in NMHDECAY as are present in HDE-CAY [60] and we could then employ HDECAY results for the SM Higgs denominator. But, this is not the case at present, with HDECAY yielding, e.g., larger gg production rates. However, we note that since we compute the ratios of NMSSM rates to SM rates using the C_Y couplings, as discussed below, the computed ratios will be quite insensitive to the precise radiative corrections employed.

[10] This equality is altered by radiative corrections at large $\tan\beta$; however, these are small in our scenarios all of which have small to moderate $\tan\beta$ values.

6.4.3 **Constraints**

The precise constraints imposed are the following. Our 'basic constraints' will be to require that an NMSSM parameter choice be such as to give a proper RGE solution, have no Landau pole, have a neutralino as the lightest SUSY particle (LSP) and obey Higgs and SUSY mass limits as implemented in NMSSMTools-3.2.0 (Higgs mass limits are from LEP, TEVATRON, and early LHC data; SUSY mass limits are essentially from LEP.) As we will see, the gluino and squark masses that result from imposing the 'basic constraints' and requiring a Higgs signal consistent with observations are so high that current LHC data do not imply further constraints on SUSY masses.

Regarding B physics, the constraints considered are those on $\mathrm{BR}(B_s \to X_s\gamma)$, ΔM_s, ΔM_d, $\mathrm{BR}(B_s \to \mu^+\mu^-)$, $\mathrm{BR}(B^+ \to \tau^+\nu_\tau)$ and $\mathrm{BR}(B \to X_s\mu^+\mu^-)$ at 2σ as encoded in NMSSMTools-3.2.0, except that we updated the bounds on rare B decays to $3.04 < \mathrm{BR}(B_s \to X_s\gamma) \times 10^4 < 4.06$ and $\mathrm{BR}(B \to \mu^+\mu^-) < 4.5 \times 10^{-9}$; theoretical uncertainties in B-physics observables are taken into account as implemented in NMSSMTools-3.2.0. These combined constraints we term the 'B-physics contraints'.

Regarding a_μ, we require that the extra NMSSM contribution, δa_μ, falls into the window defined in NMSSMTools of $8.77 \times 10^{-10} < \delta a_\mu < 4.61 \times 10^{-9}$ expanded to $5.77 \times 10^{-10} < \delta a_\mu < 4.91 \times 10^{-9}$ after allowing for a 1σ theoretical error in the NMSSM calculation of $\pm 3 \times 10^{-10}$. In fact, points that fail to fall into the above δa_μ window always do so by virtue of δa_μ being too small.

Regarding dark matter constraints, we declare that the relic density Ωh^2 is consistent with WMAP data provided $0.094 < \Omega h^2 < 0.136$ [314], which is the 'WMAP window' defined in NMSSMTools-3.2.0 after including theoretical and experimental systematic uncertainties. We will also consider the implications of relaxing this constraint to simply $\Omega h^2 < 0.136$ so as to allow for scenarios in which the relic density arises at least in part from some other source.

The points in the following scatter plots are primarily obtained through random scans covering the following parameter ranges of the three types of models defined in Section 6.4.1, which correspond to an expanded version of those considered in [315]:

$0 \leq m_0 \leq 3000$; $100 \leq m_{1/2} \leq 3000$; $1 \leq \tan\beta \leq 40$; $-6000 \leq A_0 \leq 6000$; $0.1 \leq \lambda \leq 0.7$; $0.05 \leq \kappa \leq 0.5$; $-1000 \leq A_\lambda \leq 1000$; $-1000 \leq A_\kappa \leq 1000$; $100 \leq \mu_{\text{eff}} \leq 500$, and focusing on NMSSM parameter choices such that either $m_{h_1} \in [123, 128]$ GeV and/or $m_{h_2} \in [123, 128]$ GeV. In addition, we performed Markov Chain Monte Carlo (MCMC) scans to zero in better on points with $m_{h_j} \sim 125$ GeV that observe all constraints. For this purpose, we defined a $\chi^2(m_{h_j}) = (m_{h_j} - 125)^2/(1.5)^2$. The B-physics constraints were also implemented using a χ^2 approach with the 1σ errors from theory and experiment (as implemented in NMSSMTools) combined in quadrature. The global likelihood was then computed as $L_{\text{tot}} = \prod_i L_i$ with $L_i = e^{-\chi_i^2/2}$ for two-sided constraints and $L_i = 1/(1 + e^{(x_i - x_i^{\text{exp}})}/(0.01 x_i^{\text{exp}}))$ when x_i^{exp} is a 95% CL upper limit. The a_μ and Ωh^2 constraints were either implemented a-posteriori using the 2σ window approach of NMSSMTools, or also included in the global likelihood. Since CMSSM-like boundary conditions with $A_\lambda = A_\kappa = 0$ did not generate points anywhere near the interesting region, we have only performed this kind of scan for cases **II** and **III**. This allowed us to find additional "perfect" and "almost perfect" points for models **II** and **III** with $m_{h_1} \gtrsim 123$ GeV.

Thus, a "perfect" point will be one for which all constraints are satisfied including requiring that δa_μ is in the above defined window and Ωh^2 is in the WMAP window. In addition, in some cases (where specified) we impose bounds on the spin-independent LSP–proton scattering cross section implied by the neutralino-mass-dependent Xenon100 bound [316]. (For points with $\Omega h^2 < 0.094$, we rescale these bounds by a factor of $0.11/\Omega h^2$.)

6.5 LHC run-1 phenomenology

The possibility of describing the LHC observations in the context of the MSSM has been explored in numerous papers, including [210, 212–218, 317]. A general conclusion seems to be that if all the constraints noted above, including a_μ and Ωh^2, are imposed rigorously, then the MSSM—especially a constrained version such as the CMSSM—is hard pressed to yield a fairly SM-like light Higgs boson at 125 GeV. This is somewhat alleviated when the a_μ constraint is dropped [210, 317]. Overall, however, large mixing

and large SUSY masses are needed to achieve $m_h \sim 125$ GeV. There has also been some exploration in the context of the NMSSM [218, 219, 318], showing that for completely general parameters there is less tension between a light Higgs with mass ~ 125 GeV and a lighter SUSY mass spectrum.

In this section, we explore the ability or lack thereof of the constrained versions of the NMSSM defined in Section 6.4.1 to describe the observation of the 125 GeV Higgs while remaining consistent with all relevant constraints, including those from LEP and TEVATRON searches, B-physics, the muon anomalous magnetic moment, $a_\mu \equiv (g - 2)_\mu/2$, and the relic density of dark matter, Ωh^2, The demands of which in each category are described in details in Section 6.4.3. To achieve this goal, we perform extensive scan over the parameter spaces of the model considered.

6.5.1 Realization of a SM-like 125 GeV Higgs

Overall speaking, we find that only in models **II** and **III** is it possible for a "perfect" point to have a light scalar Higgs in the mass range $123 - 128$ GeV as consistent with the hints from the recent LHC Higgs searches. The largest m_{h_1} achieved for perfect points is about 125 GeV. Comparing with [210], the tension between obtaining an ideal or nearly ideal δa_μ while predicting a SM-like light Higgs near 125 GeV appears to be somewhat less in NUHM variants of the NMSSM than in those of the MSSM.

To facilitate the discussion, let us make an overall explanation for the color coding of the plots shown in this section.

- grey squares pass the 'basic' constraints but fail B-physics constraints (such points are rare);

- green squares pass the basic constraints *and* satisfy B-physics constraints;

- blue plusses ($+$) observe B-physics constraints as above and in addition have $\Omega h^2 <$ 0.136, thereby allowing for other contributions to the dark matter density (a fraction of order 20% of these points have $0.094 < \Omega h^2 < 0.136$) but they do not necessarily have acceptable δa_μ;

- magenta crosses ($\times$) have satisfactory δa_μ as well as satisfying B-physics constraints, but arbitrary Ωh^2;
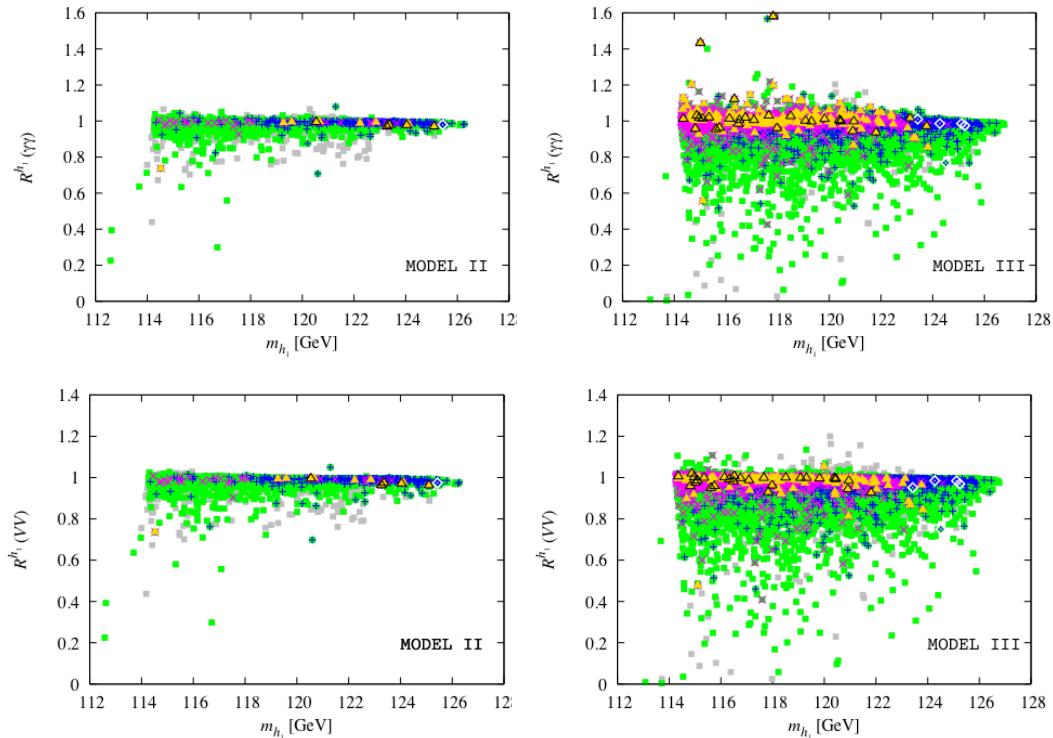
Figure 6.5. Scatter plots of $R^{h_1}(\gamma\gamma)$ (top row) and $R^{h_1}(VV = ZZ, WW)$ (lower row) versus m_{h_1} for boundary condition cases **II** and **III**. We hide the plot for case **I** in which $m_{h_1} < 123$ GeV once the $\Omega h^2 < 0.136$ is fulfilled. See text for symbol/color notations.

- golden triangle points pass all the same constraints as the magenta points and in addition have $\Omega h^2 < 0.136$;

- open black/grey[11] triangles are perfect, completely allowed points in the sense that they pass all the constraints listed earlier, including $5.77 \times 10^{-10} < \delta a_\mu < 4.91 \times 10^{-9}$ and $0.094 < \Omega h^2 < 0.136$;

- open white diamonds are points with $m_{h_1} \geq 123$ GeV that pass basic constraints, B-physics constraints and predict $0.094 < \Omega h^2 < 0.136$ but have $4.27 \times 10^{-10} < \delta a_\mu < 5.77 \times 10^{-10}$, that is we allow an excursion of half the 1σ theoretical systematic uncertainty below the earlier defined window. We will call these "almost perfect" points.

We begin by presenting the crucial plots of Fig. 6.5 in which we illustrate two most

---

[11]For perfect points, we will use black triangles if $m_{h_1} \geq 123$ GeV and grey triangles if $m_{h_1} < 123$ GeV in plots where m_{h_1} does not label the x axis.

precisely measured signal strengths $R^{h_1}(\gamma\gamma)$ and $R^{h_1}(VV)$ (the ratio being the same for $VV = WW$ and $VV = ZZ$) as a function of m_{h_1} for cases **II** and **III**. Clearly, one can observe there are ample points present that pass all constraints (the open black triangles) with $m_{h_1} \sim 124-125$ GeV. These points typically have the predicted rates, both $R^{h_1}(\gamma\gamma)$ and $R^{h_1}(VV)$, simultaneously of order $\lesssim 1$. It implies that the h_1 will be very SM-like for parameter choices yielding consistency with all constraints and yielding m_{h_1} close to 125 GeV. This can be seen in more detail in terms of its couplings and branching ratios from the sample point tables presented later. Indeed, our scans did not find parameter choices for which $R^{h_1}(\gamma\gamma)$ was significantly larger than 1 for $m_{h_1} = 123 - 128$ GeV, as hinted at by early ATLAS data. Thus, now that the combined ATLAS and CMS data are centered about $R^{h_1}(\gamma\gamma) \sim 1$, it would seem that models **II** and **III** are fully viable. Should future data return to showing a $\gamma\gamma$ rate in excess of the SM prediction, then it will be necessary to go beyond the constrained versions of the NMSSM considered here (cf. [318]). We again emphasize that a Higgs mass close to the current ~ 125 GeV measured value is very consistent with the predictions of the constrained models for parameter choices such that all constraints, including δa_μ and Ωh^2, are satisfied. Also, many additional points with $m_{h_1} \sim 125$ GeV emerge if we relax only slightly the δa_μ constraint. (The white diamonds show points for cases for which $4.27 \times 10^{-10} < \delta a_\mu < 5.77 \times 10^{-10}$ having $m_{h_1} \geq 123$ GeV.)

In passing, we note that should the Higgs hints disappear and a low-mass SM-like Higgs be excluded then it is of interest to know if $BR(h_1 \to a_1 a_1)$ can be large for m_{h_1} in the $\lesssim 130$ GeV range. It turns out that, although large $BR(h_1 \to a_1 a_1)$ is possible while satisfying basic and B-physics constraints, once additional constraints are imposed, $BR(h_1 \to a_1 a_1) \lesssim 0.2$ for all three model cases being considered. Small $BR(h_1 \to a_1 a_1)$ is expected [252] (see also [242]) when the a_1 is very singlet, as is the case in our scenarios once all constraints are imposed. So, in these models a light Higgs has nowhere to hide.

Given that the LHC data is currently consistent with a rather SM-like Higgs in the vicinity of $m_{h_1} \sim 125$ GeV (rather than one with an enhanced $\gamma\gamma$ rate), it is of interest to know the nature of the parameter choices that yield the perfect, black triangle and
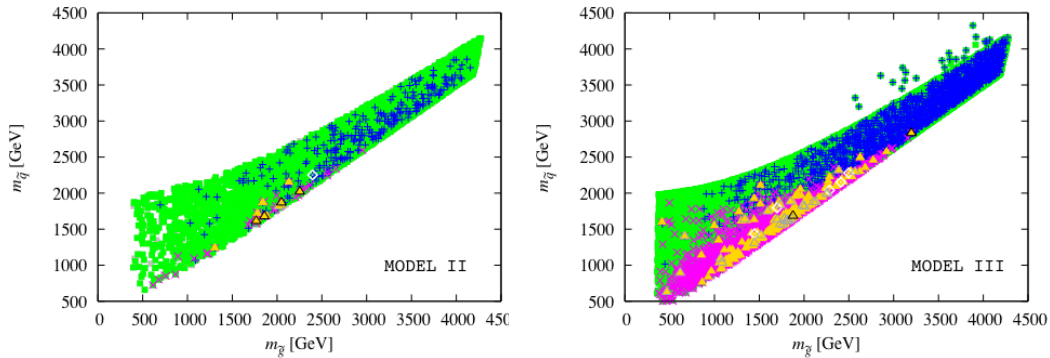
Figure 6.6. Scatter plots of squark versus gluino masses for models **II** and **III**. Here we use black (grey) open triangles for perfect points with $m_{h_1} \geq 123$ GeV ($m_{h_1} < 123$ GeV). See text for remaining symbol/color notations.

almost perfect white diamond points with $m_{h_1} \sim 125$ GeV and what the other experimental signatures of these points are. We therefore present a brief summary of the most interesting features. First, one must ask if such points are consistent with current LHC limits on SUSY particles, in particular squarks and gluinos. To this end, Fig. 6.6 shows the distribution of squark and gluino masses for the various kinds of points for models **II** and **III**. Interestingly, all the perfect, black triangle and almost perfect, white diamond points with $m_{h_1} \gtrsim 123$ GeV have squark and gluino masses sufficiently above 1 TeV that they have not yet been probed by current LHC results. (Note that since we are considering models with universal m_0 and $m_{1/2}$ for squarks and gauginos, analyses in the context of the CMSSM apply.) It is quite intriguing that the regions of parameter space that are consistent with a Higgs of mass close to 125 GeV automatically evade the current limits from LHC SUSY searches.

In order to further detail the parameters and some relevant features of perfect and almost perfect points we present in Tables 6.1–6.3 seven exemplary points with $m_{h_1} \gtrsim$ 124 GeV from models **II** and **III**. Some useful observations include the following:

- Because of the way we initiated our model **III** MCMC scans, restricting $|A_{\lambda,\kappa}| \leq$ 1 TeV, most of the tabulated model **III** points have quite modest A_λ and A_κ. However, a completely random scan finds almost perfect points with quite large A_λ and A_κ values as exemplified by tabulated point #7. The fact that the general scan over A_λ and A_κ did not find any perfect points with $m_{h_1} \gtrsim 124$ GeV, whereas such

Table 6.1. Input parameters for the exemplary points. We give $\tan\beta(m_Z)$ and GUT scale parameters, with masses in GeV and masses-squared in GeV^2. Starred points are the perfect points satisfying all constraints, including $\delta a_\mu > 5.77 \times 10^{-10}$ and $0.094 < \Omega h^2 < 0.136$. Unstarred points are the almost perfect points that have $4.27 \times 10^{-10} < \delta a_\mu < 5.77 \times 10^{-10}$ and $0.094 < \Omega h^2 < 0.136$.

	Model II			Model III			
Pt. #	1*	2*	3	4*	5	6	7
$\tan\beta(m_Z)$	17.9	17.8	21.4	15.1	26.2	17.9	24.2
λ	0.078	0.0096	0.023	0.084	0.028	0.027	0.064
κ	0.079	0.011	0.037	0.158	-0.045	0.020	0.343
$m_{1/2}$	923	1026	1087	842	738	1104	1143
m_0	447	297	809	244	1038	252	582
A_0	-1948	-2236	-2399	-1755	-2447	-2403	-2306
A_λ	0	0	0	-251	-385	-86.8	-2910
A_κ	0	0	0	-920	883	-199	-5292
$m_{H_d}^2$	$(2942)^2$	$(3365)^2$	$(4361)^2$	$(2481)^2$	$(935)^2$	$(3202)^2$	$(3253)^2$
$m_{H_u}^2$	$(1774)^2$	$(1922)^2$	$(2089)^2$	$(1612)^2$	$(1998)^2$	$(2073)^2$	$(2127)^2$

points were fairly quickly found using the MCMC technique, suggests that such points are quite fine-tuned in the general scan sense. See Table 6.1 for specifics.

- In Table 6.2, we display various details regarding the Higgs bosons for each of our exemplary points. As already noted, for the perfect and almost perfect points the h_1 is very SM-like when $m_{h_1} \gtrsim 123$ GeV. Thus, to repeat, our exemplary points listed above are very consistent with the Higgs measurements after the full data analysis of LHC run-1.

- The 7 points all have $m_{\tilde{g}}$ and $m_{\tilde{q}}$ above 1.5 TeV and in some cases above 2 TeV. Detection of the superparticles might become possible using data from the ongoing LHC 13 TeV run-2. Only the $\tilde{t}_1$ is seen to have a mass distinctly below 1 TeV for the tabulated points. Still, for all the points $m_{\tilde{t}_1}$ is substantial, ranging from ~ 500 GeV to above 1 TeV. For such masses, detection of the $\tilde{t}_1$ as an entity separate from the other squarks and the gluino will be quite difficult and, again, will only become

Table 6.2. Upper section: Higgs masses. Middle section: reduced h_1 couplings to up- and down-type quarks, $V = W, Z$ bosons, photons, and gluons. Bottom section: total width in GeV, decay branching ratios, $R^{h_1}(\gamma\gamma)$ and $R^{h_1}(VV)$ of the lightest CP-even Higgs for the seven exemplary points.

	Model II			Model III			
Pt. #	1*	2*	3	4*	5	6	7
m_{h_1}	124.0	125.1	125.4	123.8	124.5	125.2	125.1
m_{h_2}	797	1011	1514	1089	430	663	302
m_{a_1}	66.5	9.83	3.07	1317	430	352	302
C_u	0.999	0.999	0.999	0.999	0.999	0.999	0.999
C_d	1.002	1.002	1.001	1.003	1.139	1.002	1.002
C_V	0.999	0.999	0.999	0.999	0.999	0.999	0.999
$C_{\gamma\gamma}$	1.003	1.004	1.004	1.004	1.012	1.003	1.001
C_{gg}	0.987	0.982	0.988	0.984	0.950	0.986	0.994
$\Gamma_{\text{tot}}(h_1)$ [GeV]	0.0037	0.0039	0.0039	0.0037	0.0046	0.0039	0.0039
$\text{BR}(h_1 \to \gamma\gamma)$	0.0024	0.0024	0.0024	0.0024	0.002	0.0024	0.0024
$\text{BR}(h_1 \to gg)$	0.056	0.055	0.056	0.056	0.043	0.055	0.056
$\text{BR}(h_1 \to b\bar{b})$	0.638	0.622	0.616	0.643	0.680	0.619	0.621
$\text{BR}(h_1 \to WW)$	0.184	0.201	0.207	0.180	0.159	0.203	0.201
$\text{BR}(h_1 \to ZZ)$	0.0195	0.022	0.023	0.019	0.017	0.022	0.022
$R^{h_1}(\gamma\gamma)$	0.977	0.970	0.980	0.980	0.971	0.768	0.975
$R^{h_1}(ZZ, WW)$	0.971	0.962	0.974	0.974	0.964	0.750	0.969

possible with data from run-2.

- The effective superpotential μ-term, μ_{eff}, is small for all the exemplary points. This is interesting in that it suggests that electroweak fine-tuning will be modest in size.

For completeness, we have run separate scans for the case of the cNMSSM of [270, 310] with completely universal $m_0 = 0$ and $A_0 \equiv A_t = A_b = A_\tau = A_\lambda = A_\kappa$ (which is in fact a limiting case of our model **III**). Here, one can have a singlino LSP. This requires small $\lambda < 10^{-2}$. Correct relic density is achieved via co-annihilation with $\tilde{\tau}_R$ for the

Table 6.3. μ_{eff} and sparticle masses at the SUSY scale in GeV. $m_{\tilde{q}}$ is the average squark mass of the first two generations.

		Model II			Model III		
Pt. #	1*	2*	3	4*	5	6	7
μ_{eff}	400	447	472	368	421	472	477
$m_{\tilde{g}}$	2048	2253	2397	1876	1699	2410	2497
$m_{\tilde{q}}$	1867	2020	2252	1685	1797	2151	2280
$m_{\tilde{b}_1}$	1462	1563	1715	1335	1217	1664	1754
$m_{\tilde{t}_1}$	727	691	775	658	498	784	1018
$m_{\tilde{e}_L}$	648	581	878	520	1716	653	856
$m_{\tilde{e}_R}$	771	785	1244	581	997	727	905
$m_{\tilde{\tau}_1}$	535	416	642	433	784	443	458
$m_{\tilde{\chi}_1^+}$	398	446	472	364	408	471	478
$m_{\tilde{\chi}_1^0}$	363	410	438	328	307	440	452

rather definite choice of $A_0 \sim -\frac{1}{4}M_{1/2}$. For small enough $m_{1/2}$, the h_1 is dominantly singlet, while the h_2 is SM-like. For larger $m_{1/2}$, the h_1 is SM-like, and the h_2 is mostly singlet. The cross-over where h_1 and h_2 are highly mixed occurs roughly in the range of $m_{1/2} = 500 - 600$ GeV, depending on λ. Overall, we find that the h_1 can attain a mass of at most ~ 121 GeV in this scenario in the limit of large $m_{1/2}$.[12] The h_2, on the other hand, can have a mass in the $123 - 128$ GeV range for not too large $m_{1/2}$. For $\lambda = 10^{-2}$, this happens in the region of the cross-over where $R^{h_2}(\gamma\gamma)$ is of order $0.5 - 0.6$. Squark and gluino masses are around $1.2 - 1.3$ TeV in this case, and hence highly pressed by LHC exclusion limits. For smaller λ, an h_2 with mass near 125 GeV is always singlet-like and its signal strength in the $\gamma\gamma$ and VV channels is very much suppressed relative to the prediction for the SM Higgs, in apparent contradiction to the ATLAS and CMS results.

---

[12]A similar conclusion was reached in [212] based on a mSUGRA scenario with $m_0 \approx 0$ and $A_0 \approx -\frac{1}{4}M_{1/2}$, which approximately corresponds to the cNMSSM case with the singlet Higgs superfield decoupling from the rest of the spectrum; a maximum h^0 mass of 123.5 GeV was found in this case.

6.5.2 Single 125 GeV Higgs scenarios

As has been shown in the last section, an enhanced rate in the di-photon channel for the 125 GeV Higgs seems to be difficult to achieve in the NMSSM, while remaining consistent with all relevant constraints, including those from LEP and TEVATRON searches, B-physics, the muon anomalous magnetic moment, $a_\mu \equiv (g-2)_\mu/2$, and the relic density of dark matter, Ωh^2, when parameters are semi-unified at the GUT scale. However, such enhancements relative to the SM could be possible if large values of the superpotential coupling λ are employed and the a_μ constraint is greatly relaxed [315]. (See [318] for the first discussion of an enhanced $\gamma\gamma$ rate at large λ in the NMSSM with parameters defined at the weak scale.)

In this section we pursue the case of generally large λ and uncover a number of interesting scenarios with strikingly different phenomenological patterns. Hence, our scans have included ones specifically focusing on $\lambda \geq 0.3$ in addition to those encompassing the entire allowed range of the extensive scans defined in Section 6.4.3. In the figures shown in the following, we only display points which pass the basic constraints, satisfy B-physics constraints, have $\Omega h^2 < 0.136$, obey the XENON100 limit on the LSP scattering cross-section off protons *and* have one of the Higgses in the desired mass range: 123 GeV < m_{h_1} < 128 GeV and/or 123 GeV < m_{h_2} < 128 GeV. Then we color-code the points according to their $h_1 \to \gamma\gamma$ or $h_2 \to \gamma\gamma$ rate and according to whether or not Ωh^2 falls within the WMAP window. So for each 123 GeV < m_{h_i} < 128 GeV, $i = 1, 2$ the point legend is as follows:

- light blue points have $0.5 < R_{gg}^{h_i}(\gamma\gamma) \leq 1$ and $\Omega h^2 < 0.136$;

- cyan squares have an enhanced $\gamma\gamma$ signal rate of $1 < R_{gg}^{h_i}(\gamma\gamma) < 1.2$ and $\Omega h^2 < 0.094$, *i.e.* below the WMAP window;

- blue triangles have a much enhanced $\gamma\gamma$ signal rate of $R_{gg}^{h_i}(\gamma\gamma) > 1.2$ and $\Omega h^2 < 0.094$;

- salmon-colored squares and red triangles are the same as the cyan squares and blue triangles, respectively, but in addition have $0.094 < \Omega h^2 < 0.136$ meaning the LSP
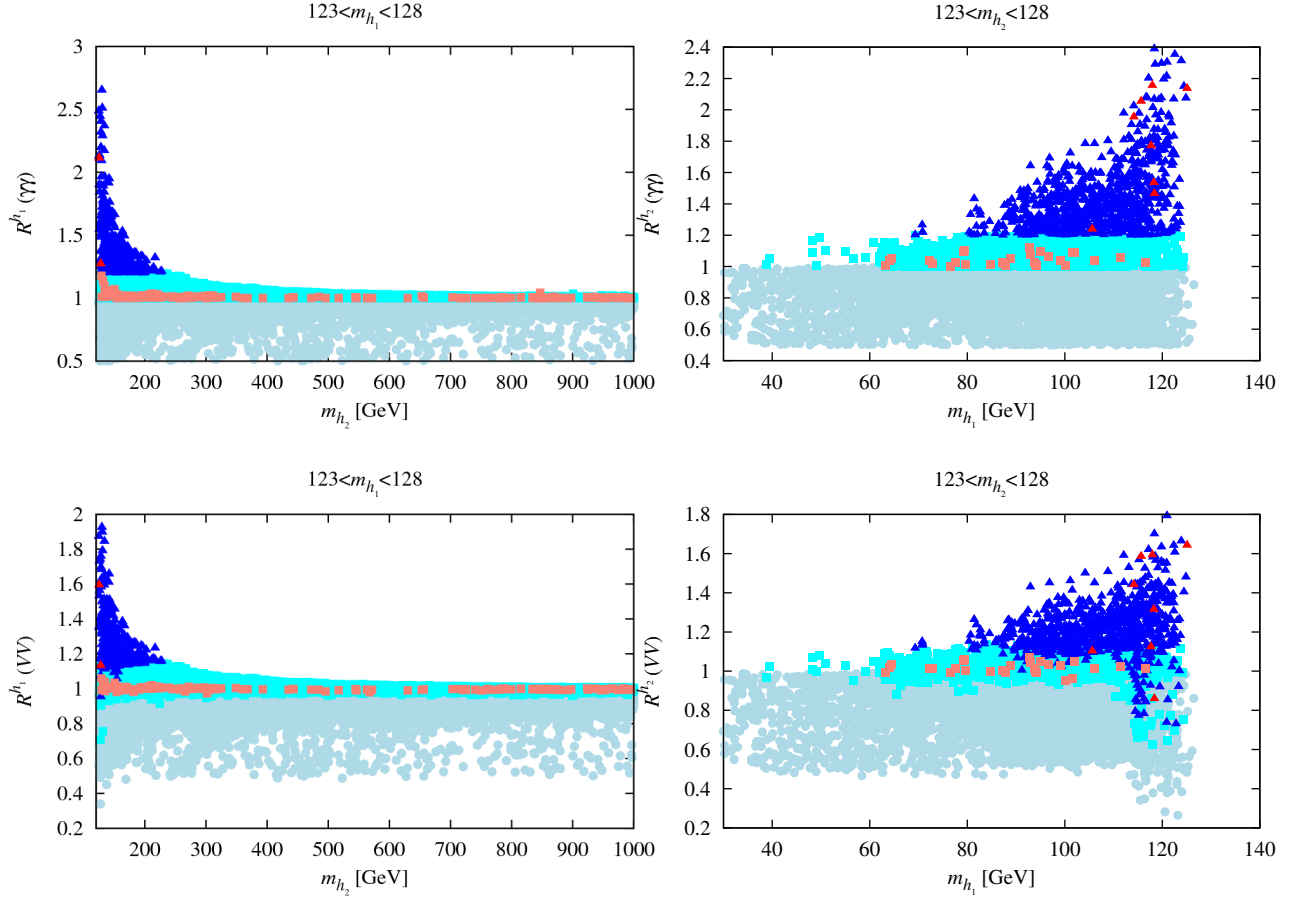
Figure 6.7. Signal strengths for a Higgs in the $123 - 128$ GeV mass range. On the left: $R_{gg}^{h_1}(\gamma\gamma)$ and $R_{gg}^{h_1}(VV)$ as a function of m_{h_2} for $m_{h_1} \in [123 - 128]$ GeV; on the right: $R_{gg}^{h_2}(\gamma\gamma)$ and $R_{gg}^{h_2}(VV)$ as a function of m_{h_1} for $m_{h_2} \in [123 - 128]$ GeV.

constitutes all of the dark matter;

- green points are chosen without regard to their $R_{gg}(\gamma\gamma)$ value but are required to have $0.094 < \Omega h^2 < 0.136$ and $\delta a_\mu > 4.27 \times 10^{-10}$, that is we allow an excursion of half the 1σ theoretical systematic uncertainty below the earlier defined window — there are no points with $\delta a_\mu > 5.77 \times 10^{-10}$ satisfying all the other criteria within the $\lambda > 0.1$

In Fig. 6.7 we show results for $R_{gg}^{h_1}(X)$ with $m_{h_1} \in [123, 128]$ GeV as a function of m_{h_2} and for $R_{gg}^{h_2}(X)$ with $m_{h_2} \in [123, 128]$ GeV as a function of m_{h_1} for $X = \gamma\gamma, VV$. We observe that one can have either the h_1 or the h_2 in the $[123, 128]$ GeV mass window with enhanced rates for the $X = \gamma\gamma$ and $X = VV$ channels from gluon fusion, most
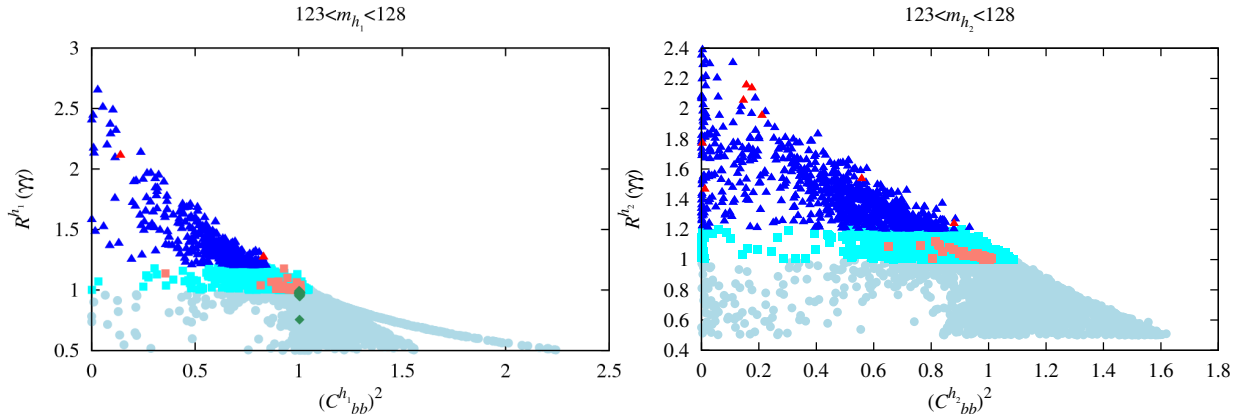
Figure 6.8. Left: $R^{h_1}_{gg}(\gamma\gamma)$ vs. $(C^{h_1}_{b\bar{b}})^2$. Right: $R^{h_2}_{gg}(\gamma\gamma)$ vs. $(C^{h_2}_{b\bar{b}})^2$.

particularly in the region where the "other" Higgs (*i.e.* the h_2 for $m_{h_1} \in [123, 128]$ GeV and the h_1 when $m_{h_2} \in [123, 128]$ GeV) has mass just above or below this window. Most interestingly, this is also the region where Ωh^2 can lie in the WMAP range, as indicated by the red triangles. The underlying reason that one obtains enhanced $\gamma\gamma$ and VV rates is that the partial width for the Higgs to decay to $b\bar{b}$ is suppressed as a result of small coupling, $C_{b\bar{b}}$, to the $b\bar{b}$ state. This correlation is completely clear from the plots of Fig. 6.8.

In the NMSSM, Higgs decays to a pair of Higgs bosons are possible, especially $h_1 \to a_1 a_1$ and $h_2 \to a_1 a_1$. Not surprisingly, $\mathrm{BR}(h_{1,2} \to a_1 a_1)$ is small for all $R^{h_{1,2}}_{gg}(\gamma\gamma) > 1$ points in the $123 < m_{h_{1,2}} < 128$ GeV mass windows, respectively. However, the $a_1 a_1$ decays of the "other" Higgs could be interesting as an avenue for discovering them. In particular, for $123 < m_{h_1} < 128$ GeV one finds $\mathrm{BR}(h_2 \to a_1 a_1)$ can be large for the blue-triangle points but not the red-triangle points, see Fig. 6.9.

The required values of λ and κ for an enhanced $\gamma\gamma$ rate for either the h_1 or h_2 are illustrated in Fig. 6.10. It appears a general tendency for $R^{h_1,h_2}_{gg}(\gamma\gamma)$ to increase with λ and large κ as well as large λ values are typically required for red-circle points. We also see that a 125 GeV Higgs state with enhanced $\gamma\gamma$ signal rate is easily obtained for large λ and small $\tan\beta$ [318] (see also [2, 315]), whereas smallish λ can yield points with SM-like $\gamma\gamma$ rates for a large range of $\tan\beta$.

An interesting question is the nature of the stop sector for the scenarios of interest.
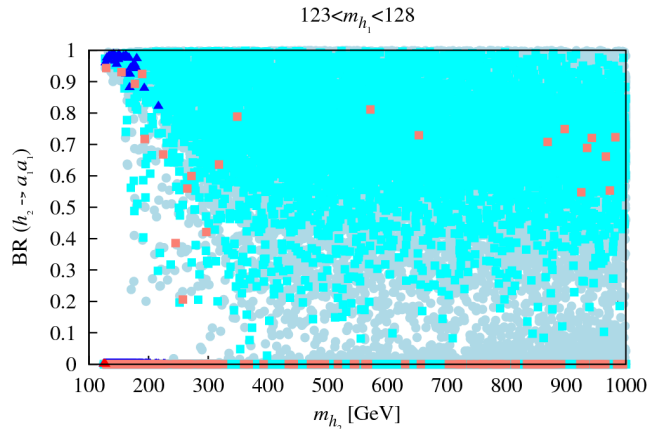
Figure 6.9. Branching ratio of $h_2 \to a_1 a_1$ decays when $m_{h_1} \in [123, 128]$ GeV. The $h_1 \to a_1 a_1$ rate is negligibly small in this case, as are the $h_{1,2} \to a_1 a_1$ rates when $m_{h_2} \in [123, 128]$ GeV.

In Fig. 6.11 we plot the ratio $X_t/(m_{\tilde{t}_1} m_{\tilde{t}_2})^{1/2}$, where $X_t = A_t + \mu \cot \beta$ is the standard stop-mixing parameter, as function of $(m_{\tilde{t}_1} m_{\tilde{t}_2})^{1/2}$. We observe that in order to achieve Higgs masses in the ~ 125 GeV region large stop mixing is required if $(m_{\tilde{t}_1} m_{\tilde{t}_2})^{1/2}$ is modest in size, whereas for very large $(m_{\tilde{t}_1} m_{\tilde{t}_2})^{1/2}$ the stop mixing must be smaller to obtain such a Higgs amss.

Implications of these enhanced $\gamma\gamma$ rate scenarios for other observables are also quite interesting. First, let us observe from Fig. 6.12 that these scenarios have squark and gluino masses that are above about 1.25 TeV ranging up to as high as 6 TeV (where our scanning more or less ended). However, for the red circle points with Ωh^2 in the WMAP window one finds $m_{\tilde{q}} \lesssim 3$ TeV and $m_{\tilde{g}} \lesssim 2$ TeV. Fig. 6.13 displays $R_{gg}^{h_1}(\gamma\gamma)$ and $R_{gg}^{h_2}(\gamma\gamma)$ vs. $m_{\tilde{t}_1}$. We observe a very large range for possible $m_{\tilde{t}_1}$ values if only $\Omega h^2 < 0.136$ is required, whereas all points with $0.96 < \Omega h^2 < 0.136$ (the WMAP window) have $m_{\tilde{t}_1} < 1.5$ TeV with $m_{\tilde{t}_1} \in [0.5, 1]$ TeV preferred, with $m_{\tilde{t}_1} < 800$ GeV needed for the largest possible $\gamma\gamma$ rates. This preference for accessible $m_{\tilde{t}_1}$ for enhanced $\gamma\gamma$ rates with Ωh^2 in the WMAP window is a recurring theme in NMSSM scans.

6.5.3 Degenerate 125 GeV Higgs scenarios

As can be seen from Fig. 6.7, an enhancement of a rare final state such as $\gamma\gamma$ arises when the h_1 and h_2 are sufficiently close in mass that one Higgs, h_i, "steals" (through
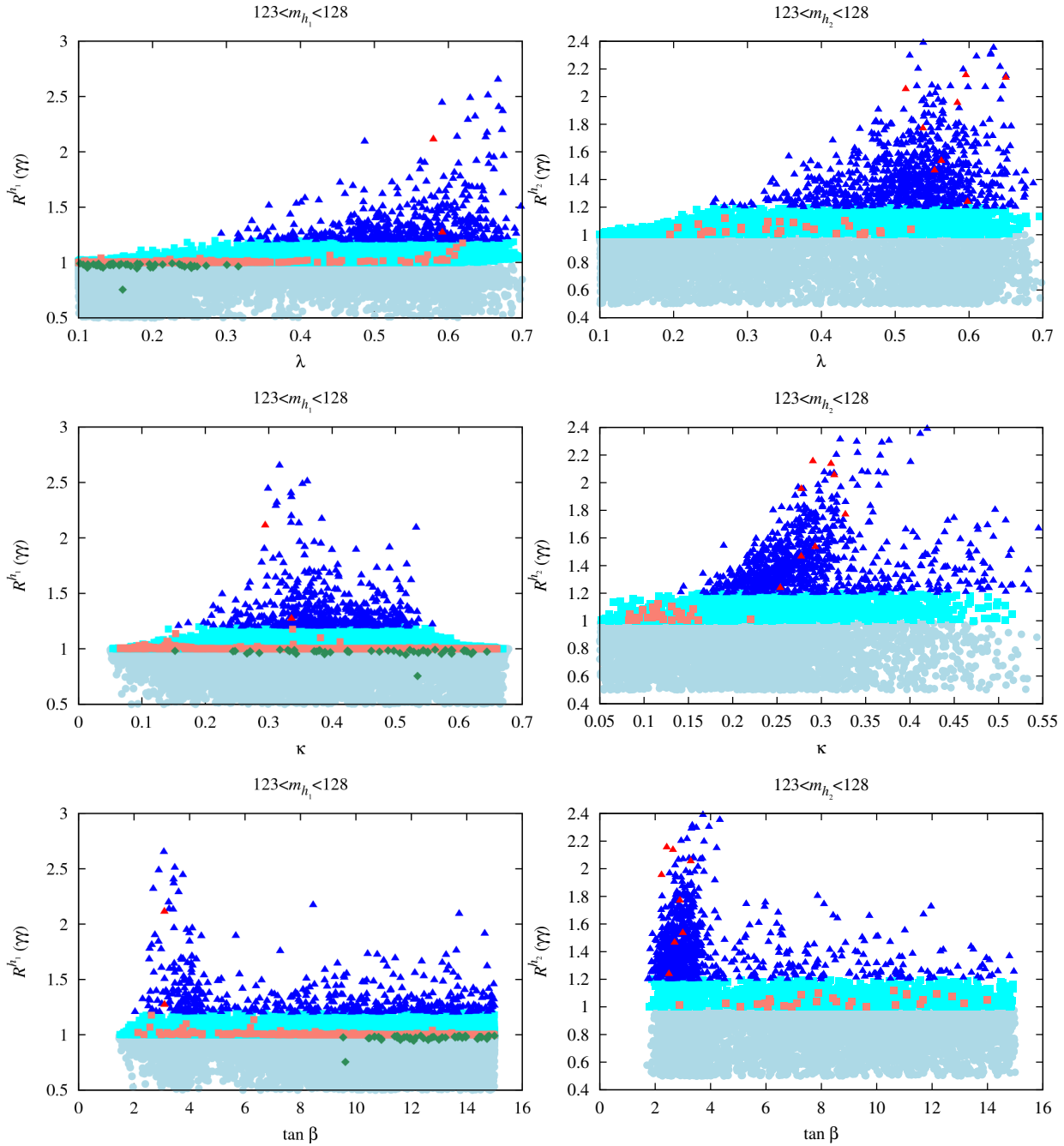
Figure 6.10. $R_{gg}^{h_1,h_2}(\gamma\gamma)$ versus λ (top row), versus κ (middle row), and versus $\tan\beta$ (bottom row).

mixing) some of the $b\bar{b}$ width of the other Higgs, h_j. When this happens it is generically the case that the gg and $\gamma\gamma$ partial widths of the h_j are much less affected and so $BR(h_j \to \gamma\gamma)$ is significantly enhanced, $b\bar{b}$ being the dominant contribution to the total width. In this
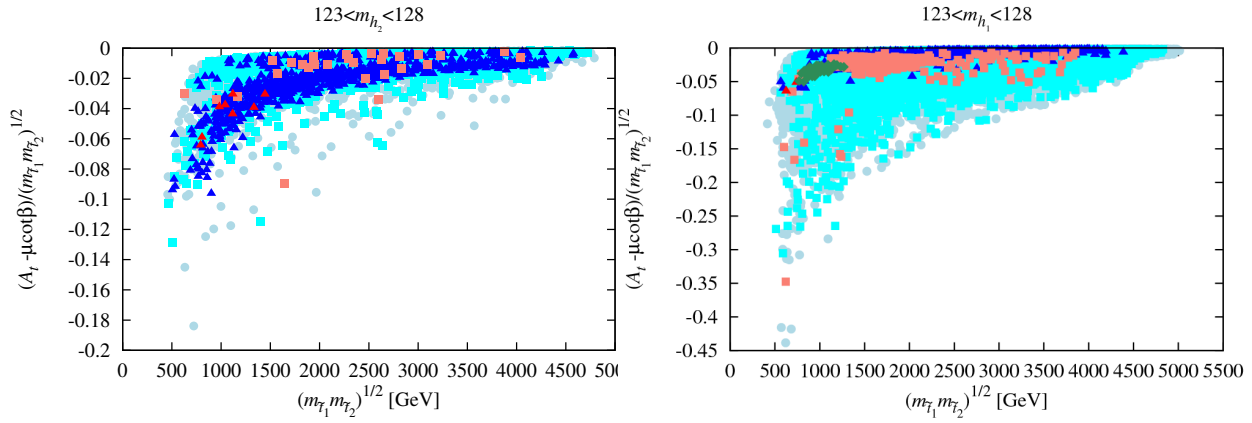
Figure 6.11. We plot $X_t/(m_{\tilde{t}_1}m_{\tilde{t}_2})^{1/2}$ as a function of $(m_{\tilde{t}_1}m_{\tilde{t}_2})^{1/2}$ for the $m_{h_1} \in [123-128]$ GeV and $m_{h_2} \in [123-128]$ GeV scenarios.

case, a second mechanism for large $\gamma\gamma$ rates emerges — namely both h_1 and h_2 contribute significantly and their summed rate is enhanced even though their individual rates are more or less at, or even somewhat below, the SM level. Enhanced $\gamma\gamma$ signals in the NMSSM context have also been considered in [319–321], the latter two noting the possible importance of light stau loop or light chargino loop, respectively, contributions to the $\gamma\gamma$ coupling of a ~ 126 GeV Higgs boson. In our semi-unified GUT scale parameter approach, these are never significant.

In this subsection we pursue the case of generally large λ, a range for which it is known [315, 318] that some enhancement, relative to the SM, of the Higgs signal in the
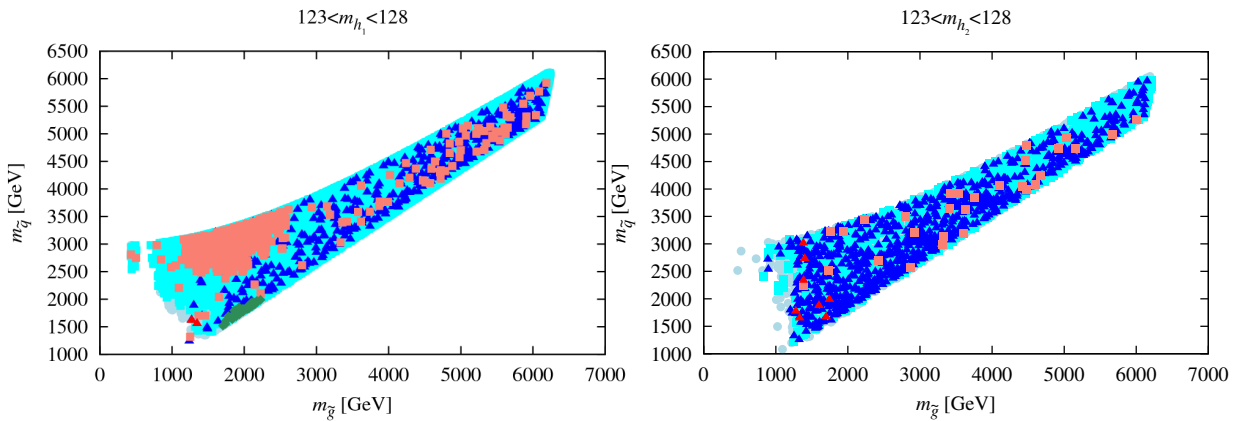
Figure 6.12. $m_{\tilde{q}}$ versus $m_{\tilde{g}}$ for the points plotted in previous figures.
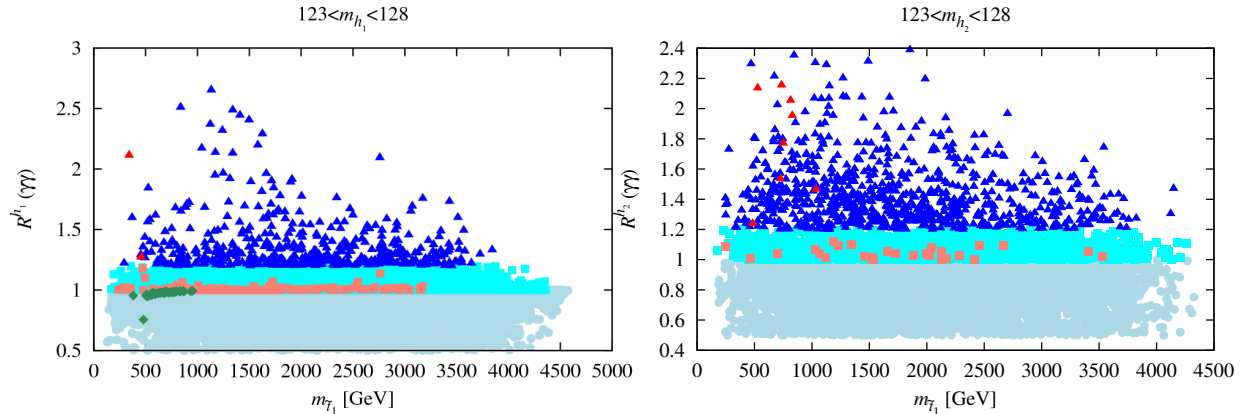
Figure 6.13. Left: $R_{gg}^{h_1}(\gamma\gamma)$ vs. $m_{\tilde{t}_1}$. Right: $R_{gg}^{h_2}(\gamma\gamma)$ vs. $m_{\tilde{t}_1}$.

$\gamma\gamma$ final state is possible, and uncover a particularly interesting set of scenarios in which the two lightest CP-even Higgs bosons, h_1 and h_2, both lie in the 123–128 GeV mass window. Should the $\gamma\gamma$ rate prove to be enhanced when run-2 results are included in the precision Higgs fits, scenarios in which the h_1 and h_2 are approximately degenerate take on special interest in that an enhanced $\gamma\gamma$ rate at ~ 125 GeV could arise as a result of the h_1 and h_2 rates summing together, even if the individual rates are not full SM-like strength (or enhanced). However, it should be stressed that even if all rates turn out to be SM-like, scenarios with $m_{h_1} \sim m_{h_2}$ remain of considerable interest.

We note that these scenarios do not provide an explanation for δa_μ. In fact, given the previously defined constraints and focusing on $\lambda \geq 0.1$, δa_μ is always too small, being at most $\sim 2 \times 10^{-10}$, while the desired range would be $5.77 \times 10^{-10} < \delta a_\mu < 4.91 \times 10^{-9}$ (including a theoretical uncertainty of $\pm 3 \times 10^{-10}$). Demanding δa_μ large enough to fall into the above window, or even come close to doing so, appears from our scans to date to only be possible if $\lambda < 0.1$ [1], for which the Higgs signal in the $\gamma\gamma$ and VV^* ($V = W, Z$) final states for Higgs in the 123–128 GeV window is very SM-like. In this work we neglect the a_μ constraint from now on, and we are therefore implicitly assuming that the observed discrepancy in a_μ comes, at least in part, from a source other than the NMSSM.

For the cases studied, where there are two nearly degenerate Higgs bosons, we define the effective Higgs mass in given production and final decay channels Y and X, respec-

tively, as

$$m_h^Y(X) \equiv \frac{R_Y^{h_1}(X)m_{h_1} + R_Y^{h_2}(X)m_{h_2}}{R_Y^{h_1}(X) + R_Y^{h_2}(X)} \tag{6.40}$$

and then combine the signals for individual Higgs defined in Eqs. (6.37) and (6.38) to obtain the net signal for the effective Higgs, h.

$$R_Y^h(X) = R_Y^{h_1}(X) + R_Y^{h_2}(X). \tag{6.41}$$

Of course, the extent to which it is appropriate to combine the rates from the h_1 and h_2 depends upon the degree of degeneracy and the experimental resolution. For the latter, we assume $\sigma_{\rm res} \sim 1.5$ GeV [322].[13] It should be noted that the widths of the h_1 and h_2 are of the same order of magnitude as the width of a 125 GeV SM Higgs boson, *i.e.* they are very much smaller than this resolution.

In the figures shown in the following, we only display points which pass the basic constraints, satisfy B-physics constraints, have $\Omega h^2 < 0.136$, obey the XENON100 limit on the LSP scattering cross-section off protons *and* have *both* h_1 and h_2 in the desired mass range: 123 GeV $< m_{h_1}, m_{h_2} <$ 128 GeV.

In Fig. 6.14, we display $R_{gg}^{h_2}(\gamma\gamma)$ versus $R_{gg}^{h_1}(\gamma\gamma)$ with points color coded according to $m_{h_2} - m_{h_1}$. The circular points have $\Omega h^2 < 0.094$, while diamond points have $0.094 \leq \Omega h^2 \leq 0.136$ (*i.e.* within the WMAP window). We observe a large number of points for which $m_{h_1}, m_{h_2} \in [123, 128]$ GeV and many are such that $R_{gg}^{h_1}(\gamma\gamma) + R_{gg}^{h_2}(\gamma\gamma) > 1$. A few such points have Ωh^2 in the WMAP window. However, the majority of the points with $R_{gg}^{h_1}(\gamma\gamma) + R_{gg}^{h_2}(\gamma\gamma) > 1$ have Ωh^2 below the WMAP window (implying that the current observations suggesting $R_{gg}^{h_1}(\gamma\gamma) + R_{gg}^{h_2}(\gamma\gamma) \sim 1$ are more consistent within the context of the model) and for many points the $\gamma\gamma$ signal is shared between the h_1 and the h_2.

Based on these results, we will now combine the h_1 and h_2 signals as described above and present plots coded according to the following legend. First, we note that circular (diamond) points have $\Omega h^2 < 0.094$ ($0.094 \leq \Omega h^2 \leq 0.136$). We then color the points according to:

---

[13]The values for $\sigma_{\rm res}$ quoted in this paper range from 1.39–1.84 GeV to 2.76–3.19 GeV, the better resolutions being for the case where both photons are in the barrel and the worse resolutions for when one or both photons are in the endcap. We anticipate that the more recent analyses have achieved substantially better mass resolutions, but details are not yet available.
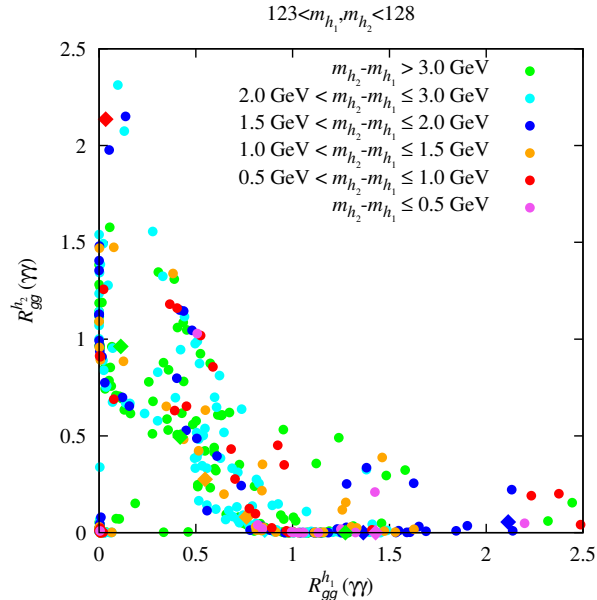
Figure 6.14. Correlation of $gg \to (h_1, h_2) \to \gamma\gamma$ signal strengths when both h_1 and h_2 lie in the 123–128 GeV mass range. The circular points have $\Omega h^2 < 0.094$, while diamond points have $0.094 \leq \Omega h^2 \leq 0.136$. Points are color coded according to $m_{h_2} - m_{h_1}$ as indicated on the figure.

- red for $m_{h_2} - m_{h_1} \leq 1$ GeV;

- blue for $1 \text{ GeV} < m_{h_2} - m_{h_1} \leq 2$ GeV;

- green for $2 \text{ GeV} < m_{h_2} - m_{h_1} \leq 3$ GeV.

For current statistics and $\sigma_{\text{res}} \gtrsim 1.5$ GeV we estimate that the h_1 and h_2 signals will not be seen separately for $m_{h_2} - m_{h_1} \leq 2$ GeV.

In the first three plots of Fig. 6.15 we show results for $R_{gg}^h(X)$ with $m_h^{gg}(X) \in$ [123, 128] GeV, where $m_h^{gg}(X)$ is defined in Eq. (6.40), for $X = \gamma\gamma, VV, b\bar{b}$. Enhanced $\gamma\gamma$ and VV rates from gluon fusion are very common. The bottom-right plot shows that enhancement of Wh production with $h \to b\bar{b}$ is rather limited; indeed the maximal value of $R_{\text{VBF}}^h(b\bar{b}) = R_{W^* \to Wh}^h(b\bar{b})$ is of order 1.2, a value that falls short of the best fit value suggested by the old Tevatron analysis [323], but is entirely consistent with the current average value found by CMS and ATLAS. (check and give reference)

In Fig. 6.16, we display in the left-hand plot the strong correlation between $R_{gg}^h(\gamma\gamma)$ and $R_{gg}^h(VV)$. Note that if $R_{gg}^h(\gamma\gamma) \sim 1$, as suggested by current experimental results,
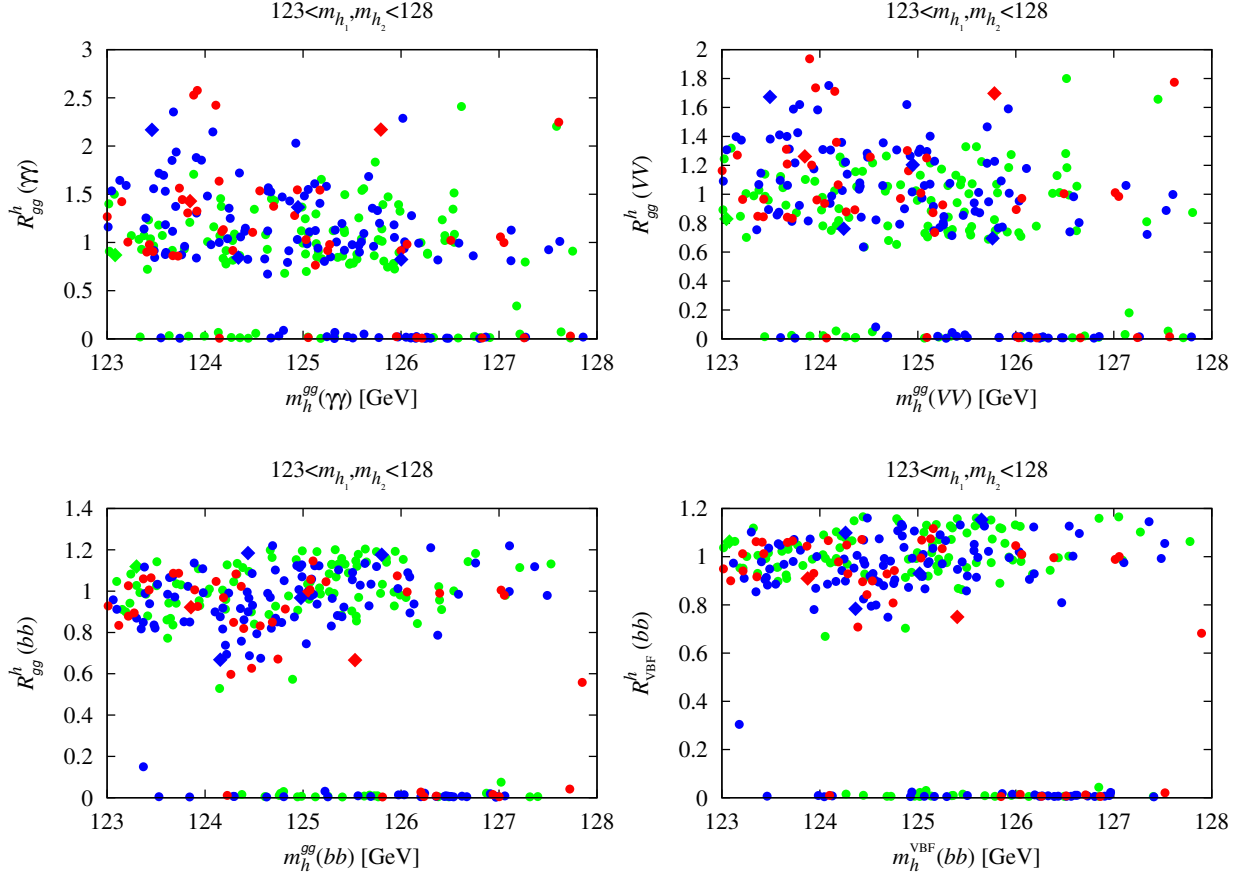
Figure 6.15. $R_{gg}^h(X)$ for $X = \gamma\gamma, VV, b\bar{b}$, and $R_{\text{VBF}}^h(b\bar{b})$ versus the appropriate effective Higgs mass m_h as defined in Eq. (6.40). For application to the Tevatron, note that $R_{\text{VBF}}^h(b\bar{b}) = R_{W^* \to Wh}^h(b\bar{b})$. The color code here and in the following figures is green for points with $2 \text{ GeV} < m_{h_2} - m_{h_1} \leq 3 \text{ GeV}$, blue for $1 \text{ GeV} < m_{h_2} - m_{h_1} \leq 2 \text{ GeV}$, and red for $m_{h_2} - m_{h_1} \leq 1 \text{ GeV}$.

then in this model also $R_{gg}^h(VV) \gtrsim 1$. The right-hand plot shows the (anti) correlation between $R_{gg}^h(\gamma\gamma)$ and $R_{W^* \to Wh}^h(b\bar{b}) = R_{\text{VBF}}^h(b\bar{b})$. In general, the larger $R_{gg}^h(\gamma\gamma)$ is, the smaller the value of $R_{W^* \to Wh}^h(b\bar{b})$. However, this latter plot shows that there *are* parameter choices for which both the $\gamma\gamma$ rate at the LHC and the $W^* \to Wh(\to b\bar{b})$ rate at the LHC can be enhanced relative to the SM as a result of there being contributions to these rates from both the h_1 and h_2. It is often the case that one of the h_1 or h_2 dominates $R_{gg}^h(\gamma\gamma)$ while the other dominates $R_{W^* \to Wh}^h(b\bar{b})$. However, a significant number of the points are such that either the $\gamma\gamma$ or the $b\bar{b}$ signal receives substantial contributions from both the h_1 and the h_2 (as seen, for example, in Fig. 6.14 for the $\gamma\gamma$ final state) while the other
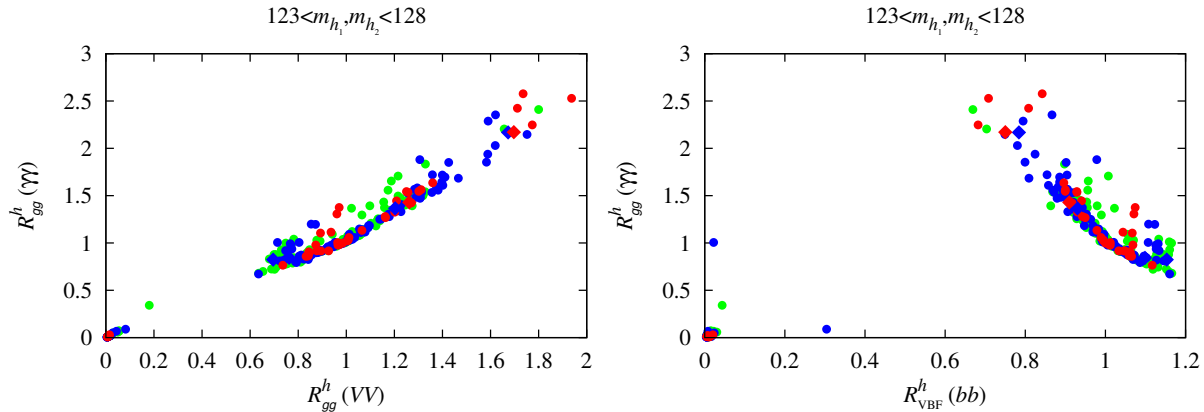
Figure 6.16. Left: correlation between the gluon fusion induced $\gamma\gamma$ and VV rates relative to the SM. Right: correlation between the gluon fusion induced $\gamma\gamma$ rate and the WW fusion induced $b\bar{b}$ rates relative to the SM; the relative rate for $W^* \to Wh$ with $h \to b\bar{b}$ (relevant for the Tevatron) is equal to the latter.

final state is dominated by just one of the two Higgses. We did not find points where the $\gamma\gamma$ and $b\bar{b}$ final states *both* receive substantial contributions from *both* the h_1 and h_2.

As noted above, there is a strong correlation between $R_{gg}^h(\gamma\gamma)$ and $R_{gg}^h(VV)$ described approximately by $R_{gg}^h(\gamma\gamma) \gtrsim R_{gg}^h(VV)$. Thus, it is not surprising that the m_h values for the gluon fusion induced $\gamma\gamma$ and VV final states are also strongly correlated — in fact, they differ by no more than a fraction of a GeV and are most often much closer, see the left plot of Fig. 6.17. The right plot of Fig. 6.17 illustrates one of the primary mechanisms behind enhanced rates, namely that large net $\gamma\gamma$ branching ratio is achieved by reducing the average total width by reducing the average $b\bar{b}$ coupling strength.

The dependence of $R_{gg}^h(\gamma\gamma)$ on λ, κ, $\tan\beta$ and μ_{eff} is illustrated in Fig. 6.18. We observe that the largest $R_{gg}^h(\gamma\gamma)$ values arise at large λ, moderate κ, small $\tan\beta < 5$ (but note that $R_{gg}^h(\gamma\gamma) > 1.5$ is possible even for $\tan\beta = 15$) and small $\mu_{\text{eff}} < 150$ GeV.

Such low values of μ_{eff} are very favorable in point of view of fine tuning, in particular if stops are also light. Indeed a good fraction of our points with degenerate h_1, h_2 and $R(\gamma\gamma) > 1$ features light stops with $m_{\tilde{t}_1} \in [300, 700]$ GeV and $M_{\text{SUSY}} = \sqrt{m_{\tilde{t}_1} m_{\tilde{t}_2}} \lesssim 1$ TeV. The stop mixing is typically, but not necessarily, large in these cases, $(A_t - \mu_{\text{eff}} \cot\beta)/M_{\text{SUSY}} \approx 1.5$–2. Fig. 6.19 explores the nature of the stop sector. From the left plot we see that enhanced $\gamma\gamma$ signals (and also VV signals) are possible for a large
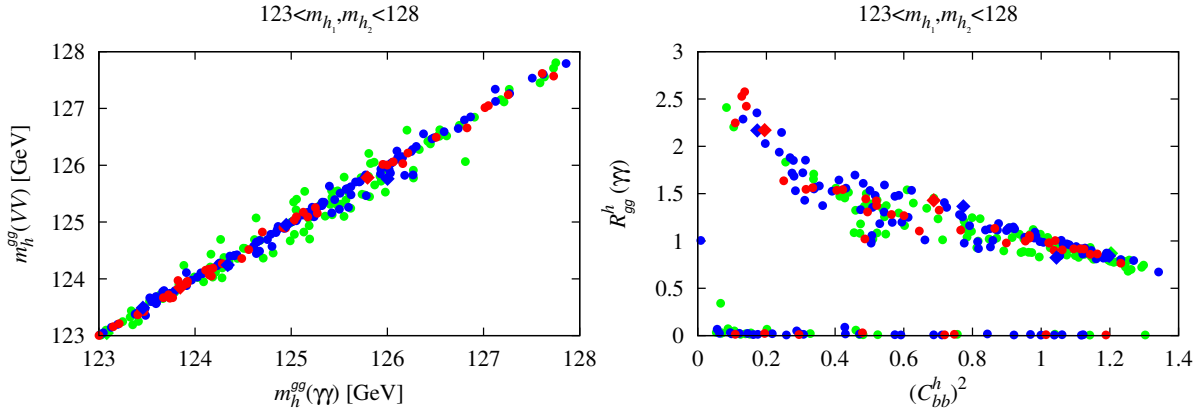
Figure 6.17. Left: effective Higgs masses obtained from different channels: $m_h^{gg}(\gamma\gamma)$ versus $m_h^{gg}(VV)$. Right: $\gamma\gamma$ signal strength $R_{gg}^h(\gamma\gamma)$ versus effective coupling to $b\bar{b}$ quarks $(C_{b\bar{b}}^h)^2$. Here, $C_{b\bar{b}}^{h\,2} \equiv \left[R_{gg}^{h_1}(\gamma\gamma)C_{b\bar{b}}^{h_1\,2} + R_{gg}^{h_2}(\gamma\gamma)C_{b\bar{b}}^{h_2\,2} \right] / \left[R_{gg}^{h_1}(\gamma\gamma) + R_{gg}^{h_2}(\gamma\gamma) \right]$.
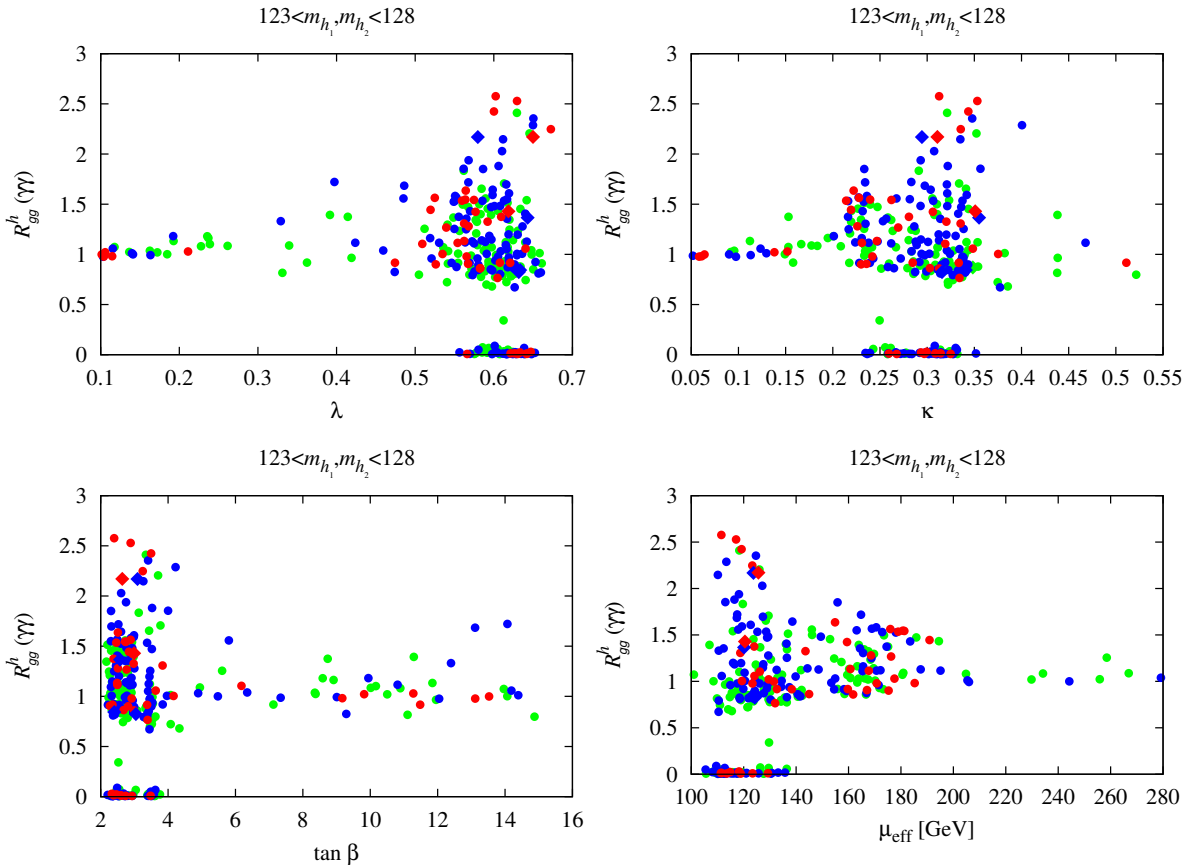
Figure 6.18. Dependence of $R_{gg}^h(\gamma\gamma)$ on λ, κ, $\tan\beta$ and μ_{eff}.
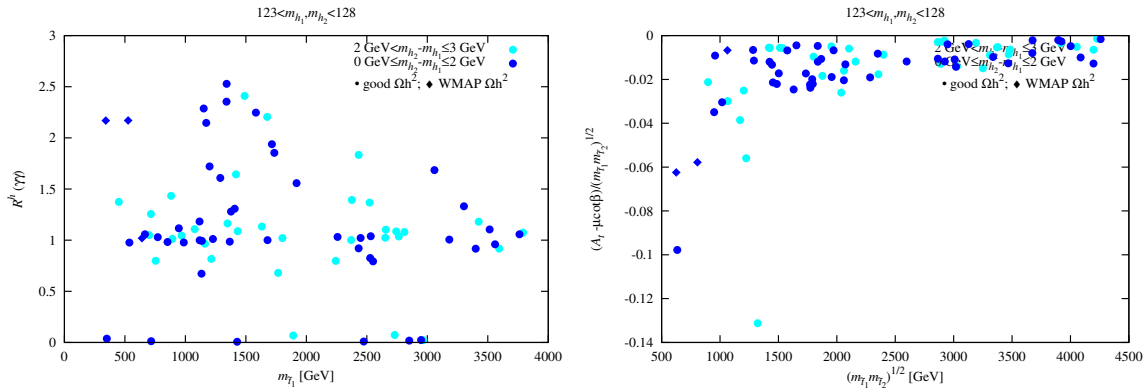
Figure 6.19. Left: $R^h_{gg}(\gamma\gamma)$ vs. $m_{\tilde{t}_1}$. Right: Stop mixing parameter $A_t - \mu_{\text{eff}} \cot \beta$ divided by rms stop mass $\sqrt{m_{\tilde{t}_1} m_{\tilde{t}_2}}$ vs $\sqrt{m_{\tilde{t}_1} m_{\tilde{t}_2}}$.

range of $m_{\tilde{t}_1}$, but that points in the WMAP window always have $m_{\tilde{t}_1} < 700$ GeV. This preference for accessible $m_{\tilde{t}_1}$ for enhanced $\gamma\gamma$ rates with Ωh^2 in the WMAP window is a recurring theme in NMSSM scans. From the right plot, we see that the stop mixing parameter $A_t - \mu_{\text{eff}} \cot \beta$ is always relatively small compared to the root-mean-square stop mass $\sqrt{m_{\tilde{t}_1} m_{\tilde{t}_2}}$. The latter typically has a large value, but not for the points lying in the WMAP window. Given the small μ_{eff} (see above) and the small $\sqrt{m_{\tilde{t}_1} m_{\tilde{t}_2}}$, fine tuning will be relatively small for the WMAP window points.

Implications of the enhanced $\gamma\gamma$ rate scenarios for other observables are also quite interesting. First, let us observe from Fig. 6.20 that these scenarios have squark and gluino masses that are above about 1.25 TeV ranging up to as high as 6 TeV (where our scanning more or less ended).

The value of $R^h_{gg}(\gamma\gamma)$ as a function of the masses of the other Higgs bosons is illustrated in Fig. 6.21. We see that values above 1.7 are associated with masses for the a_2, h_3 and $H^\pm$ of order $\lesssim 500$ GeV and for the a_1 of order $70 \lesssim m_{a_1} \lesssim 150$ GeV. (Note that $m_{a_2} \simeq m_{h_3} \simeq m_{H^\pm}$.) While modest in size, detectability of these states at such masses requires further study. One interesting point is that although $m_{a_1} \sim 125$ GeV is common for points with $R^h_{gg}(\gamma\gamma) > 1$, the contribution of the a_1 to the $\gamma\gamma$ signal is always small, typically $R^{a_1}_{gg}(\gamma\gamma) \lesssim 0.01$ (due to the fact that the a_1 is always largely singlet for these and, indeed, all $R^h_{gg}(\gamma\gamma) > 1$ points).

221
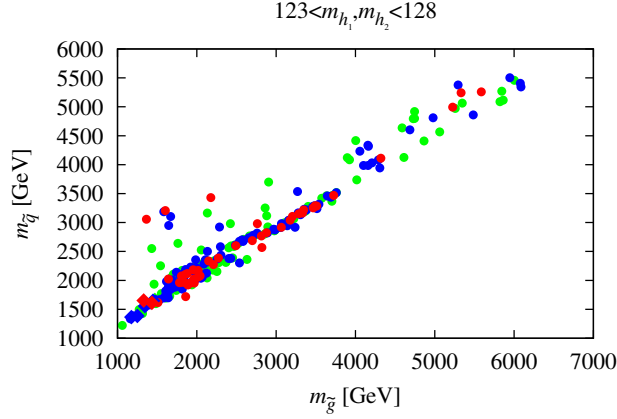
Figure 6.20. Average light-flavor squark mass, $m_{\tilde{q}}$, versus gluino mass, $m_{\tilde{g}}$, for the points plotted in the previous figures.
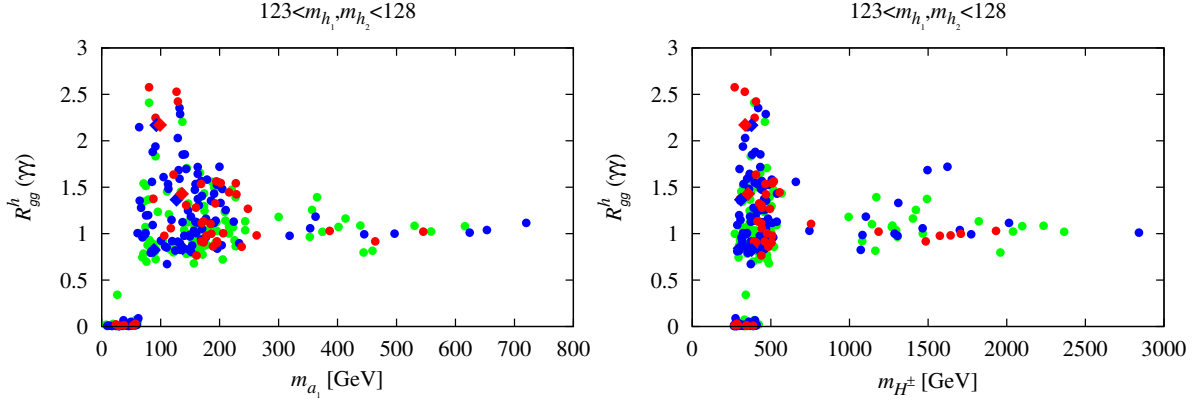
Figure 6.21. $R_{gg}^h(\gamma\gamma)$ versus the masses of m_{a_1} and $m_{H^\pm}$ (note that $m_{H^\pm} \simeq m_{a_2} \simeq m_{h_3}$).

Regarding the GUT-scale parameters associated with the points plotted in previous figures, we note that points with $R_{gg}^h(\gamma\gamma) > 1.3$ have $m_0 \in [0.65, 3]$ TeV, $m_{1/2} \in [0.5, 3]$ TeV, $A_0 \in [-4.2, -0.8]$ TeV, $A_\kappa \in [-500, +450]$ GeV, $A_\lambda \in [-750, +550]$ GeV, $m_S(\text{GUT}) \in [1.2, 4.2]$ TeV, $m_{H_u}(\text{GUT}) \in [1.7, 17]$ TeV, $m_{H_d}(\text{GUT}) \in [\sim 0, 4.2]$ TeV, $\lambda \in [0.33, 0.67]$, $\kappa \in [0.22, 0.36]$, and $\tan\beta \in [2, 14]$.

We have already noted that it is not possible to find scenarios of this degenerate/enhanced type while predicting a value of δa_μ consistent with that needed to explain the current discrepancy. In Fig. 6.22, we plot $R_{gg}^h(\gamma\gamma)$ and $R_{gg}^h(VV)$ as a function of δa_μ. We observe that the very largest value of δa_μ achieved is of order 1.8×10^{-10} and, further, the

WMAP-window points with large R have $\delta a_\mu < 6 \times 10^{-11}$.

Figure 6.22. $R^h_{gg}(\gamma\gamma)$ and $R^h_{gg}(VV)$ as a function of δa_μ.

Finally, we would like to mention that the WMAP-window points with large $R^h_{gg}(\gamma\gamma, VV)$ have $\delta a_\mu < 6 \times 10^{-11}$. It is only for $R^h_{gg}(\gamma\gamma, VV) \sim 1$ that one reaches the maximum value found in the scans of $\delta a_\mu \sim 1.8 \times 10^{-10}$. This is still significantly below the range $\delta a_\mu > 5.77 \times 10^{-10}$ needed to explain the anomalous magnetic moment anomaly. Thus, δa_μ somewhat disfavours the scenarios discussed above and, at the very least, favors those with SM-like $\gamma\gamma, VV$ rates.

6.5.4 Multiple Higgs scenarios

One of the most significant features of the current data is the absence of a statistically significant enhancement in the $\gamma\gamma$ final state for both gluon fusion (gg) and vector boson fusion (VBF) production. In contrast, enhancement is not atypical of models with multiple Higgs bosons in which the $b\bar{b}$ partial width of the observed h is reduced through mixing with a second (not yet observed at the LHC) Higgs boson, h', thereby enhancing the $\gamma\gamma$ branching ratio of the h [2, 315, 318, 320, 324, 325]. Thus, we devote this section to a discussion of multiple Higgs models that either do or do not have such enhancement.

Along this direction, a particularly interesting question is whether one could simultaneously explain the LHC signal and the small ($\sim 2\sigma$) LEP excess in $e^+e^- \to Zb\bar{b}$ in the vicinity of $M_{b\bar{b}} \sim 98$ GeV [326, 327] using the h' with $m_{h'} \sim 98$ GeV. Let us recall that the LEP excess is clearly inconsistent with a SM-like Higgs boson at this mass, being only about $10 - 20\%$ of the rate predicted for the $H_{\rm SM}$. Consistency with such a result for the
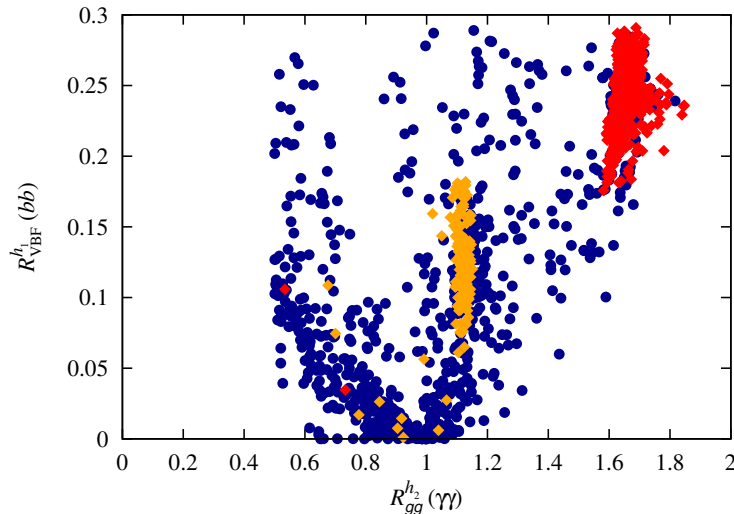
Figure 6.23. Signal strengths (relative to SM) $R^{h_1}_{VBF}(bb)$ versus $R^{h_2}_{gg}(\gamma\gamma)$ for $m_{h_1} \in$ [96, 100] GeV and $m_{h_2} \in [123, 128]$ GeV. In this and all subsequent plots, points with $\Omega h^2 < 0.094$ are represented by blue circles and points with $\Omega h^2 \in [0.094, 0.136]$ (the "WMAP window") are represented by red/orange diamonds.

h' is natural if the h' couples at a substantially reduced level to ZZ, which, in turn, is automatic if the h has SM-like ZZ coupling, as required by the observed LHC signals.

In the following we demonstrate that the two lightest CP-even Higgs bosons[14], h_1 and h_2, of the NMSSM could have properties such that the h_1 fits the LEP excess at ~ 98 GeV while the h_2 is reasonably consistent with the Higgs-like LHC signals at $\sim$ 125 GeV, including in particular either a larger-than-SM signal or a SM-like signal in the $\gamma\gamma$ channel. For simplicity we will refer to this NMSSM scenario as the "98 + 125 GeV Higgs scenarios" from now on. To achieve this goal the h_1 and h_2 must have $m_{h_1} \sim 98$ GeV and $m_{h_2} \sim 125$ GeV, respectively, with the h_1 being largely singlet and the h_2 being primarily doublet (mainly H_u for the scenarios we consider). In addition to the CP-even states, there are also two CP-odd states, a_1 and a_2, and a charged Higgs boson, $H^{\pm}$. Verification of the presence of the three CP-even Higgs bosons and/or two CP-odd Higgs bosons would establish a Higgs field structure that goes beyond the two-doublet structure of the MSSM.

- *Signal rates for the h_1 and h_2 states*

We first display in Fig. 6.23 the crucial plot that shows $R^{h_1}_{VBF}(bb)$ versus $R^{h_2}_{gg}(\gamma\gamma)$

---

[14]We assume the absence of CP-violating phases in the Higgs sector.

when $m_{h_1} \in [96, 100]$ GeV and $m_{h_2} \in [123, 128]$ GeV are imposed in addition to the above mentioned experimental constraints.[15] (In this and all subsequent plots, points with $\Omega h^2 < 0.094$ are represented by blue circles and points with $\Omega h^2 \in [0.094, 0.136]$ (the "WMAP window") are represented by red and orange diamonds. These two colors are associated with different LSP masses as will be discussed below.) Note that $R^{h_1}_{VBF}(bb)$ values are required to be smaller than 0.3 by virtue of the fact that the LEP constraint on the $e^+e^- \to Zb\bar{b}$ channel with $M_{b\bar{b}} \sim 98$ GeV is included in the NMSSMTools program. Those points with $R^{h_1}_{VBF}(bb)$ between about 0.1 and 0.25 would provide the best fit to the LEP excess. (We note again that $R^{h_1}_{VBF}(bb)$ is equivalent to $R^{h_1}_{Vh_1}(bb)$ as relevant for LEP.) The large portion of such points having $R^{h_2}_{gg}(\gamma\gamma)$ significantly larger than one are, of course, disfavored by current LHC run-1 data. In all the remaining plots we will impose the additional requirements: $R^{h_2}_{gg}(\gamma\gamma) \gtrsim 1$ and $0.1 \leq R^{h_1}_{VBF}(bb) \leq 0.25$. To repeat, the $R^{h_2}_{gg}(\gamma\gamma) \gtrsim 1$ requirement is such as to focus on points that could be consistent (within errors) with either an enhanced $\gamma\gamma$ Higgs signal at the LHC or a SM-like signal. The $0.1 \leq R^{h_1}_{VBF}(bb) \leq 0.25$ window is designed to reproduce the small excess seen in LEP data at $M_{b\bar{b}} \sim 98$ GeV in the $Zb\bar{b}$ final state.

In Fig. 6.24, we plot (upper row) $R^{h_1}_{gg}(\gamma\gamma)$ vs. $R^{h_2}_{gg}(\gamma\gamma)$ and $R^{h_1}_{VBF}(\gamma\gamma)$ vs. $R^{h_2}_{VBF}(\gamma\gamma)$ and (lower row) $R^{h_1}_{gg}(bb)$ vs. $R^{h_2}_{gg}(bb)$ and $R^{h_1}_{VBF}(bb)$ vs. $R^{h_2}_{VBF}(bb)$. In these and all subsequent plots, we only show points that satisfy all the basic constraints specified earlier and that also satisfy $m_{h_1} \in [96, 100]$ GeV, $m_{h_2} \in [123, 128]$ GeV, $R^{h_2}_{gg}(\gamma\gamma) \geq 1$ and $R^{h_1}_{VBF}(bb) \in [0.1, 0.25]$. The upper plots show that the h_2 can easily have either an enhanced or a SM-like $\gamma\gamma$ signal for both gg and VBF production whereas the $\gamma\gamma$ signal arising from the h_1 for both production mechanisms is quite small and unlikely to be observable. Note the two different $R^{h_2}_{gg}(\gamma\gamma)$ regions for which Ωh^2 lies in the WMAP window, one with $R^{h_2}_{gg}(\gamma\gamma) \sim 1.6$ (region A, red diamonds) and the other with $R^{h_2}_{gg}(\gamma\gamma) \sim 1.1$ (region B, orange diamonds). Only the latter region is consistent with current run-1 Higgs data. As we will show later, region A corresponds to $m_{\tilde{\chi}^0_1} \sim 77$ GeV and $m_{\tilde{t}_1}$ between 197 GeV and 1 TeV, while the region B corresponds to $m_{\tilde{\chi}^0_1} > 93$ GeV and $m_{\tilde{t}_1} > 1.8$ TeV. These

---

[15]Here the Higgs mass windows are designed to allow for theoretical errors in the computation of the Higgs masses.
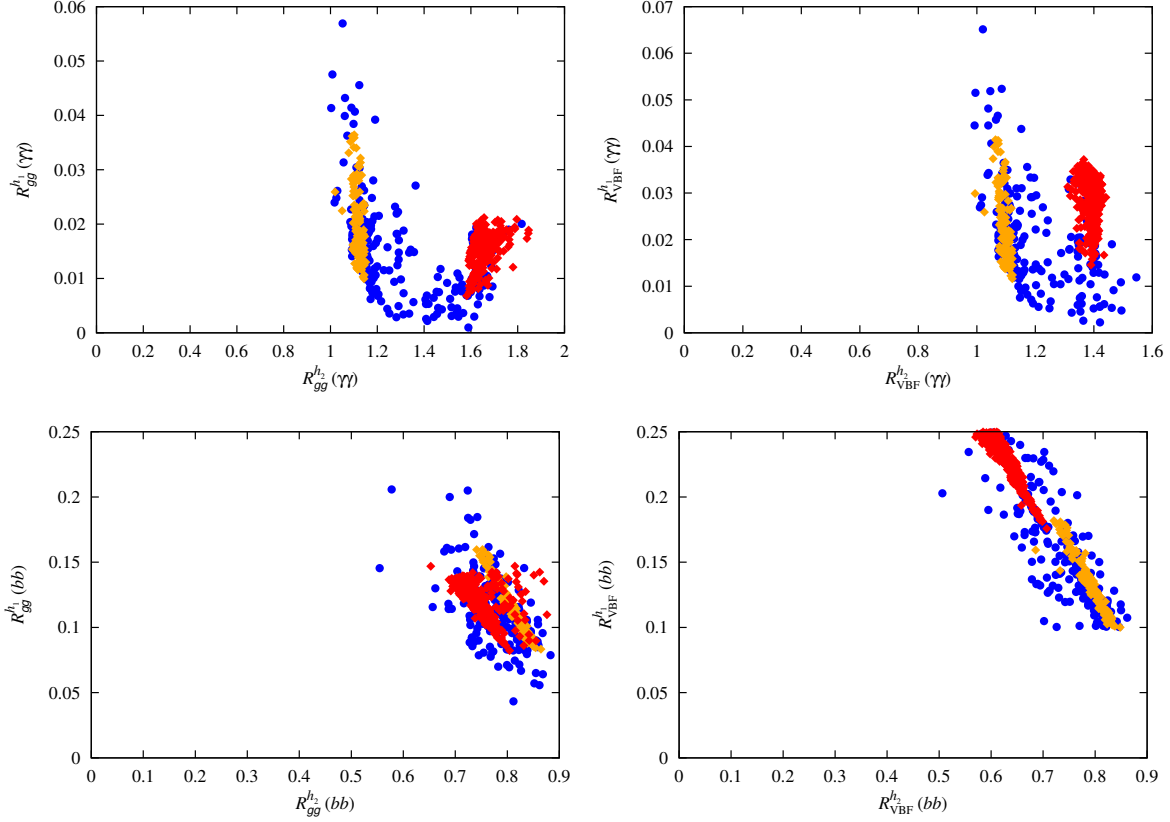
Figure 6.24.   For the h_1 and h_2, we plot (top) $R_{gg}^h(\gamma\gamma)$ and $R_{VBF}^h(\gamma\gamma)$ and (bottom) $R_{gg}^h(bb)$ and $R_{VBF}^h(bb)$ for NMSSM scenarios consistent with the LEP and LHC Higgs excesses.   More specifically, in this and all subsequent plots we only show points that satisfy all the basic constraints specified in the text and that also satisfy $m_{h_1} \in [96, 100]$ GeV, $m_{h_2} \in [123, 128]$ GeV, $R_{gg}^{h_2}(\gamma\gamma) \geq 1$ and $R_{VBF}^{h_1}(bb) \in [0.1, 0.25]$. These we have termed the "98 + 125 GeV Higgs scenarios". Regarding the WMAP-window points, we refer to the red diamonds as "region A" and to the orange ones as "region B".

same two regions will emerge in many subsequent figures. If $R_{gg}^{h_2}(\gamma\gamma)$ ends up converging to a large value (SM-like value), then masses for all strongly interacting SUSY particles would be close to (far above) current limits if the present $98 + 125$ GeV LEP-LHC Higgs scenario applies.

The bottom row of the figure focuses on the $b\bar{b}$ final state. We observe the reduced $R_{gg}^{h_2}(bb)$ and $R_{VBF}^{h_2}(bb)$ values that are associated with reduced $b\bar{b}$ width (relative to the SM) needed to have enhanced $R_{gg}^{h_2}(\gamma\gamma)$ and $R_{VBF}^{h_2}(\gamma\gamma)$. Meanwhile, the $R_{gg}^{h_1}(bb)$ and $R_{VBF}^{h_1}(bb)$ values are such that the h_1 could not yet have been seen at the Tevatron or LHC. Sensitivity to $R_{gg}^{h_1}(bb)$ ($R_{VBF}^{h_1}(bb)$) values from 0.05 to 0.2 (0.1 to 0.25) will be needed
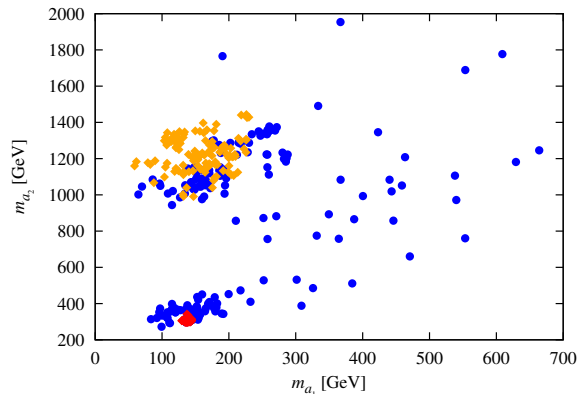
Figure 6.25. Scatter plot of m_{a_2} versus m_{a_1} for the 98+125 GeV scenario; note that $m_{a_2} \simeq m_{h_3} \simeq m_{H^\pm}$. Note that in this figure there is a dense region, located at $(m_{a_1}, m_{a_2}) \sim (130, 330)$ GeV, of strongly overlapping red diamond points. These are the points associated with the low-$m_{\widetilde{\chi}_1^0}$ WMAP-window region of parameter space. Corresponding dense regions appear in Figs. 6.26, 6.27 and 6.29.

at the LHC. This compares to expected sensitivities after the $\sqrt{s} = 8$ TeV run in these channels to R values of at best 0.8.[16] Statistically, a factor of 4 to 10 improvement requires integrated luminosity of order 16 to 100 times the current $L = 10$ fb^{-1}. Such large L values will eventually be reached during the ongoing 13 TeV LHC run-2 , although we should note that the luminosity required to probe this signal at 13 TeV could be lower than indicated by this simple estimate as the sensitivity to the Higgs signal improves at higher energies.

- *Other NMSSM particles and parameters*

It is also very interesting to consider expectations for the other NMSSM particles in these scenarios. For this purpose, we present a series of plots. Figure 6.25 displays the pseudoscalar masses in the m_{a_1}–m_{a_2} plane. We do not plot m_{h_3} nor $m_{H^\pm}$ since their masses are such that $m_{h_3} \simeq m_{H^\pm} \simeq m_{a_2}$ for the scenarios considered. We note that small m_{a_1} is typical of the WMAP-window points. We discuss discovery prospects for the a_1 later in the paper. The masses of some crucial SUSY particles are displayed in Fig. 6.26. We observe the typically low values of $m_{\widetilde{\chi}_1^0}$ and $m_{\widetilde{\chi}_1^\pm}$, the possibility of $m_{\tilde{t}_1}$ as small as 197 GeV, the mostly modest values of the mixing parameter $(A_t - \mu \cot\beta)/\sqrt{m_{\tilde{t}_1}m_{\tilde{t}_2}}$, and the fact that the predicted $m_{\tilde{q}}$ and $m_{\tilde{g}}$ are beyond current experimental limits, although

---

[16]Here, we have used Fig. 12 of [68] extrapolated to a Higgs mass near 98 GeV and assumed $L = 20$ fb^{-1} each for ATLAS and CMS.
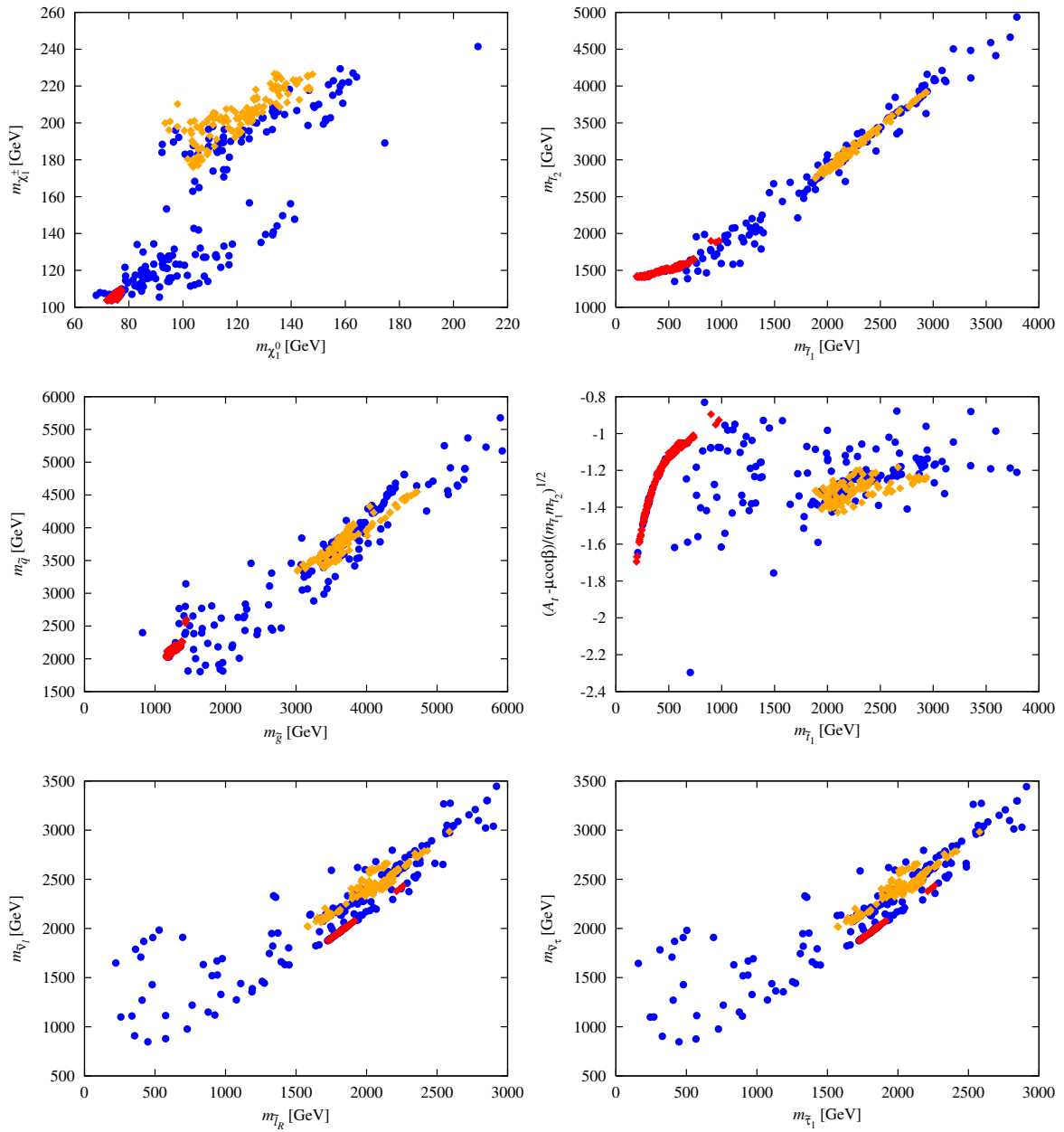
Figure 6.26. Plots showing $m_{\widetilde{\chi}_1^0}$, $m_{\widetilde{\chi}_1^\pm}$, $m_{\widetilde{t}_1}$, $m_{\widetilde{t}_2}$, $m_{\widetilde{q}}$, $m_{\widetilde{g}}$, and the mixing parameter $(A_t - \mu \cot \beta)/\sqrt{m_{\widetilde{t}_1} m_{\widetilde{t}_2}}$. Also shown are $m_{\widetilde{\ell}_R}$, $m_{\widetilde{\nu}_\ell}$, $m_{\widetilde{\tau}_1}$ and $m_{\widetilde{\nu}_\tau}$, where $\ell = e, \mu$.

the lowest values (as found in particular in region A) may soon be probed. Note that $m_{\widetilde{g}}$ can be below $m_{\widetilde{\ell}_R}$ (as common in constrained models when m_0 is large) for some points, including the points in region A. Low values of $m_{\widetilde{\chi}_1^0}$ are typical for the scan points, but more particular to this model are the rather low values of $m_{\widetilde{\chi}_1^\pm}$. ATLAS and CMS are currently performing analyses that could in principle be sensitive to the $m_{\widetilde{\chi}_1^\pm}$ values

predicted in this model. For some points, $m_{\widetilde{\chi}_1^\pm} - m_{\widetilde{\chi}_1^0}$ can be rather small, implying some difficulty in isolating the leptons or jets associated with $\widetilde{\chi}_1^\pm \to \widetilde{\chi}_1^0 + X$ decays. However, it should be noted that for the WMAP-window points $m_{\widetilde{\chi}_1^\pm} - m_{\widetilde{\chi}_1^0}$ is typically quite substantial, at least 35 GeV for the low-$m_{\widetilde{\chi}_1^0}$ points, so that for these points the above difficulty would not arise. Of particular interest is the very large range of $m_{\tilde{t}_1}$ that arises in the $98 + 125$ GeV LEP-LHC Higgs scenarios. For lighter values of $m_{\tilde{t}_1}$, as typical of the WMAP-window points in region A, the $\tilde{t}_1$ always decays via $\tilde{t}_1 \to \widetilde{\chi}_1^+ b$ or $\tilde{t}_1 \to \widetilde{\chi}_1^0 t$, the latter being absent when $m_{\tilde{t}_1} < m_{\widetilde{\chi}_1^0} + m_t$. At high $m_{\tilde{t}_1}$, these same channels are present but also $\tilde{t}_1 \to \widetilde{\chi}_{2,3,4,5}^0 t$ can be important, which channels being present depending upon whether $m_{\tilde{t}_1} - m_{\chi_{2,3,4,5}^0} - m_t > 0$ or not.

It is interesting to survey the GUT scale parameters that lead to the scenarios of interest. Relevant plots are shown in Fig. 6.27. No particular regions of these parameters appear to be singled out aside from some preference for negative values of A_0. These plots show clearly that scenarios A and B correspond to distinct regions in the parameter space. Note however that the density of red points in these plots is purely due to our scan procedures which have some focus on region A.

6.6 Test at future colliders

A critical issue is what other observations would either confirm or rule out the $98 + 125$ GeV LEP-LHC Higgs scenarios. We first discuss possibilities at the LHC and then turn to future colliders, including a future e^+e^- collider, a possible $\gamma\gamma$ collider and a future $\mu^+\mu^-$ collider.

6.6.1 Direct Higgs production and decay at the LHC

We have already noted in the discussion of Fig. 6.24 that gg and VBF production of the h_1 with $h_1 \to b\bar{b}$ provide event rates that might eventually be observable at the LHC once much higher integrated luminosity is attained. Other possibilities include production and decay of the a_1, a_2, and h_3. Decay branching ratios and LHC cross sections in the gg fusion mode for a_1, a_2 and h_3 are shown in Fig. 6.28. Since the a_1 is dominantly singlet in nature, its production rates at the LHC are rather small. The largest $\sigma BR(X)$ values are
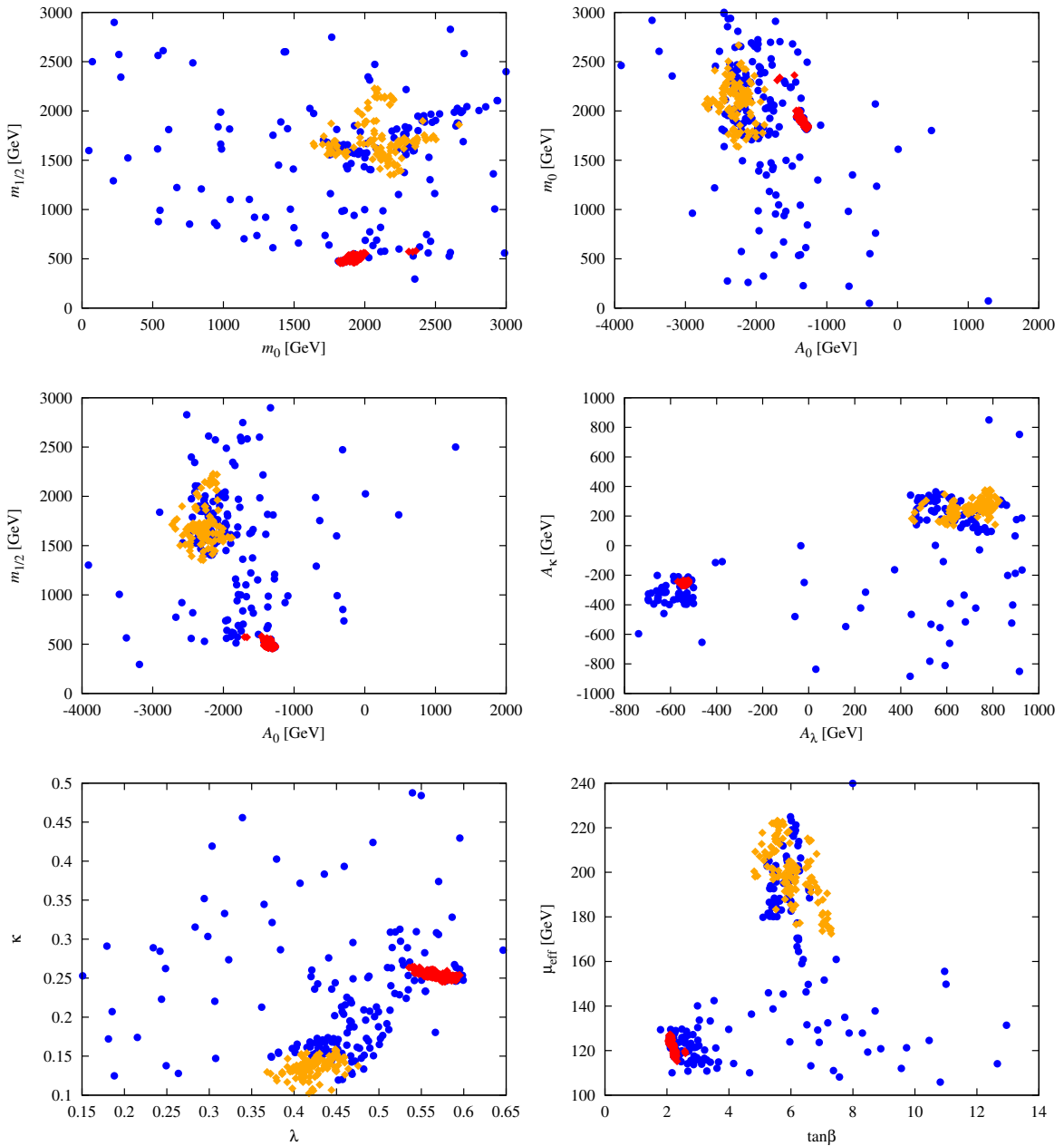
Figure 6.27. GUT scale and SUSY scale parameters leading to the $98 + 125$ GeV LEP-LHC Higgs scenarios.

in the $X = b\bar{b}$ final state, but this final state will have huge backgrounds. When allowed, $\sigma\mathrm{BR}(X)$ for $X = \widetilde{\chi}_1^0\widetilde{\chi}_1^0$ can be significant, but observation of this invisible final state would require a jet or photon tag that would further decrease the cross section. The a_2 is dominantly doublet and provides better discovery prospects. If $m_{a_2} > 2m_t$, the $t\bar{t}$ final state has $\sigma(gg \to a_2)\mathrm{BR}(a_2 \to t\bar{t}) > 0.01$ pb for $m_{a_2} < 550$ GeV, implying > 200 events

Figure 6.28. Branching ratios and LHC cross sections in the gg fusion mode (at $\sqrt{s} = 8$ TeV) for a_1, a_2 and h_3

231
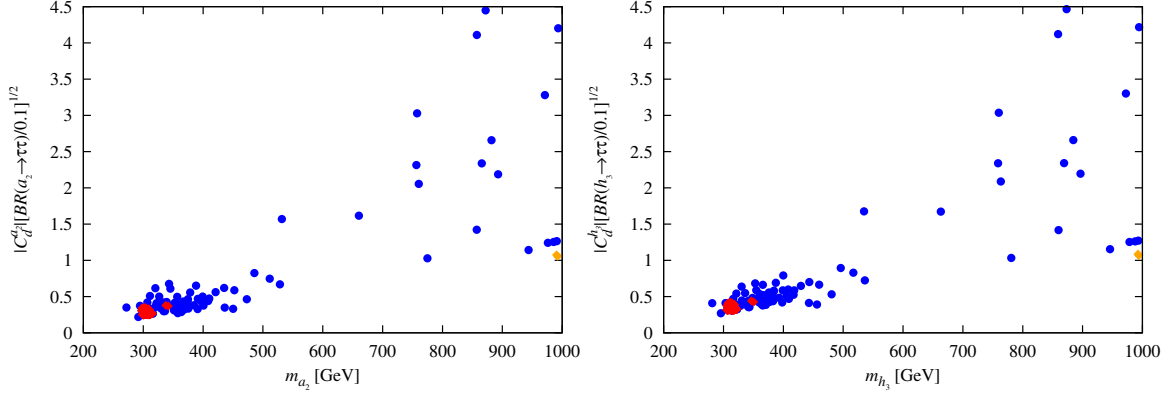
Figure 6.29. $C_d^{a_2,h_3}(\text{eff})$, see Eq. (6.42), vs. m_{a_2} and m_{h_3} for $gg \to a_2, h_3 \to \tau^+\tau^-$.

for $L = 20$ fb^{-1}. A study is needed to determine if this would be observable in the presence of the $t\bar{t}$ continuum background. No doubt, efficient b tagging and reconstruction of the $t\bar{t}$ invariant mass in, say, the single lepton final state would be needed. For $m_{a_2} < 2m_t$, the $X = a_1 h_2$ final state with both a_1 and h_2 decaying to $b\bar{b}$ might be visible above backgrounds. However, a dedicated study of this particular decay mode is still lacking. Similar remarks apply in the case of the h_3 where the possibly visible final states are $t\bar{t}$ for $m_{h_3} > 2m_t$ and $h_1 h_2$ for $m_{h_3} < 2m_t$. For both the a_2 and h_3, $\sigma\text{BR}(X)$ is substantial for $X = \tilde{\chi}_1^0 \tilde{\chi}_1^0$, but to isolate this invisible final state would require an additional photon or jet tag which would reduce the cross section from the level shown.

A final possible detection mode is $gg \to a_2, h_3 \to \tau^+\tau^-$. For this case we plot in Fig. 6.29 the effective down-quark coupling, $C_d^{a_2,h_3}(\text{eff})$ vs. m_{a_2} and m_{h_3}, where we define

$$C_d^{a_2,h_3}(\text{eff}) = |C_d^{a_2,h_3}| \left[\frac{\text{BR}(a_2, h_3 \to \tau^+\tau^-)}{0.1} \right]^{1/2} \tag{6.42}$$

and where 0.1 is a reference value of $\text{BR}(H, A \to \tau^+\tau^-)$ implicit in the MSSM limit plots discussed below. Noting that $m_{a_2} \simeq m_{h_3}$ and the fact that the two plots are nearly identical shows that we may sum the a_2 and h_3 signals together in the same manner as the H and A signals are summed together in the case of the analogous plot of $\tan\beta$ vs. $m_A \simeq m_H$ in the case of the MSSM. Limits from CMS 4.6 fb^{-1} data [328] are of order $C_d^{a_2,h_3}(\text{eff}) \lesssim 7 - 8$ for $m_{a_2} \simeq m_{h_3} \in [150, 220]$ GeV rising rapidly to reach ~ 50 at degenerate mass of order 500 GeV. A dedicated study is needed to determine the
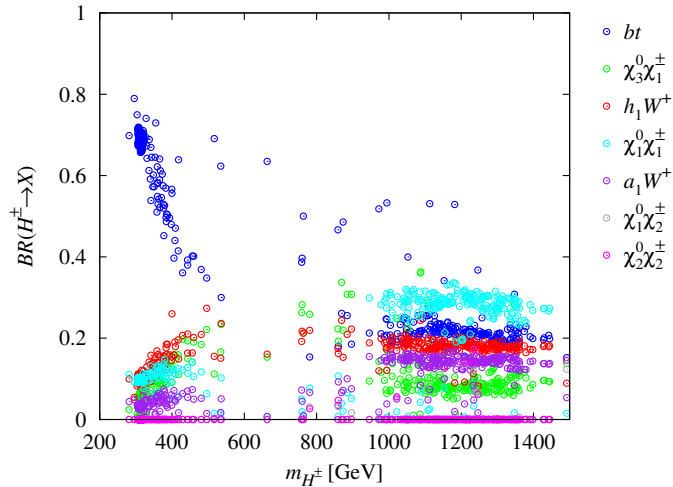
Figure 6.30. Decay branching ratios of the charged Higgs bosons.

precise luminosity for which LHC detection or meaningful limits will become possible for $C_d^{a_2,h_3}(\text{eff}) \lesssim 1$ (as relevant for $m_{a_2}, m_{h_3} < 550$ GeV). Even though Higgs cross sections from gg fusion increase, relative to $\sqrt{s} = 8$ TeV, for $\sqrt{s} = 13$ TeV quite high luminosity will be needed. Currently, for example, the CMS limit from 10 fb^{-1} of data at $m_{a_2} \simeq m_{h_3} \sim 300$ GeV is of order 18, and this amplitude level limit will only improve statistically by $1/L^{1/4}$. Even accounting for the $\sqrt{s} = 13$ TeV cross section increase, very significant improvements in the sensitivity of this analysis will be needed.

The branching ratios for the $H^{\pm}$ are plotted in Fig. 6.30. Prospects for its discovery at masses for which $H^+ H^-$ production has substantial cross section appear to be promising in the bt final state provided reconstruction of the bt mass is possible with good efficiency and one or more b tags are sufficient to reject SM background. Also very interesting would be detection of $H^{\pm} \to h_1 W^{\pm}$ in the $h_1 \to b\bar{b}$ final state using mass reconstruction for the $b\bar{b}$ and a leptonic trigger from the $W^{\pm}$ to reject backgrounds. This channel could prove especially essential in order to detect the $m_{h_1} \sim 98$ GeV Higgs at the LHC and verify the $98 + 125$ GeV Higgs scenario.
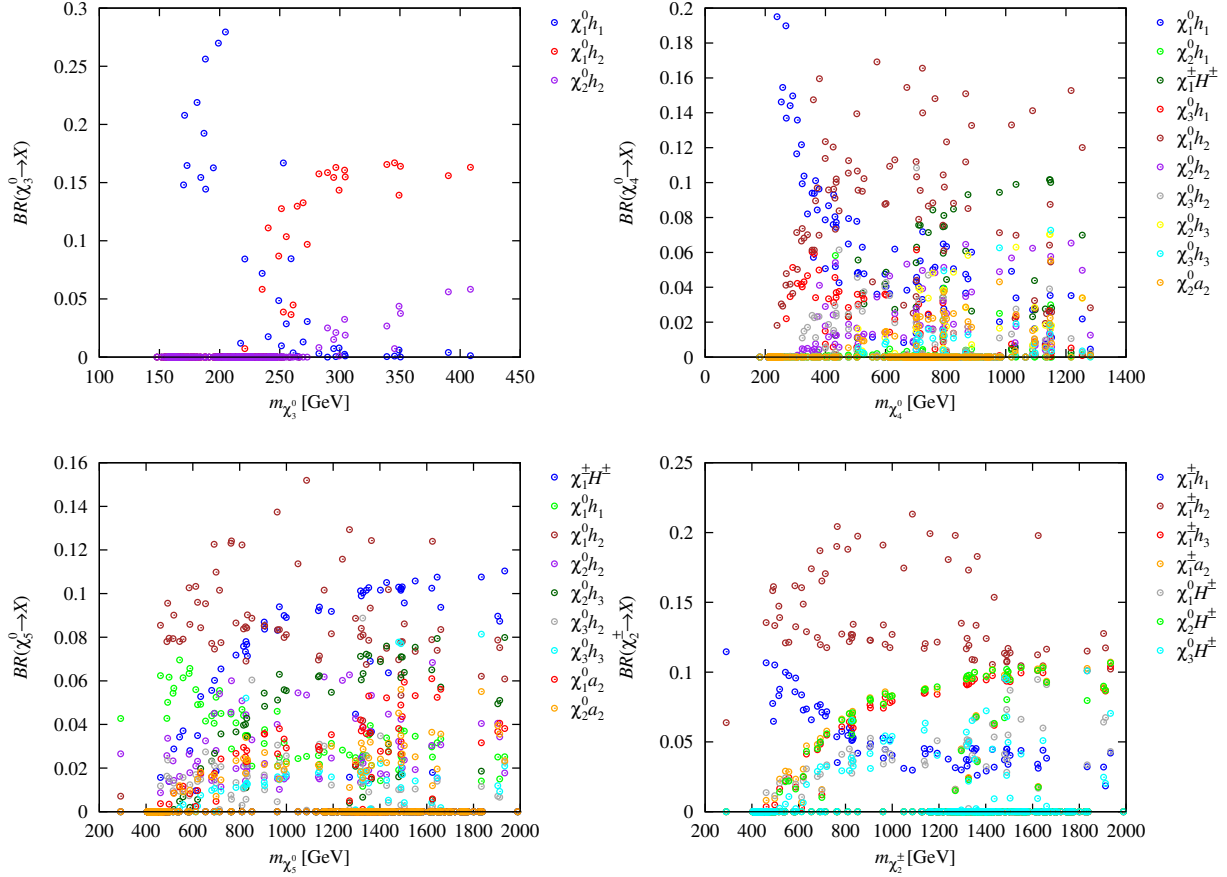
Figure 6.31. Branching ratios for neutralino and chargino decays into final states containing a Higgs boson for the $98 + 125$ GeV LEP-LHC Higgs scenarios.

6.6.2 Higgses from neutralino decays

Given that cascades from gluinos/squarks will have low event rate as a result of the large $m_{\tilde{g}}$ and $m_{\tilde{q}}$ masses predicted and the rather low $\tilde{\chi}_1^{\pm}$ and $\tilde{\chi}_1^0$ masses typical of the NMSSM scenarios we discuss, prospects for detecting chargino pair production and neutralino+chargino production would appear to be better, although one is faced with cross sections that are electroweak in size. Of particular interest is whether some of the Higgs bosons can be detected via ino-pair production. To assess the possibilities, we present in Fig. 6.31 the branching ratios for the decay of the neutralinos and charginos to lighter inos plus a Higgs boson. A brief summary of the results shown is in order. First, decays to the a_1 are not shown since they have very low branching ratios due to the singlet nature

234

of the a_1. The only decay with branching ratio to the a_2 above 0.1 is $\widetilde{\chi}_2^\pm \to \widetilde{\chi}_1^\pm a_2$ with $m_{\widetilde{\chi}_2^\pm} \gtrsim 1.4$ TeV (beyond LHC reach via electroweak production). In contrast, prospects for the all important h_1 are quite good, with $\mathrm{BR}(\widetilde{\chi}_3^0, \widetilde{\chi}_4^0 \to \widetilde{\chi}_1^0 h_1)$ and $\mathrm{BR}(\widetilde{\chi}_2^\pm \to \widetilde{\chi}_1^\pm h_1)$ being quite substantial (*i.e.* > 0.1) at lower values of $m_{\widetilde{\chi}_3^0}, m_{\widetilde{\chi}_4^0}$ and $m_{\widetilde{\chi}_2^\pm}$, respectively. Decays of $\widetilde{\chi}_3^0, \widetilde{\chi}_4^0, \widetilde{\chi}_5^0$ to $\widetilde{\chi}_1^0 h_2$ all have $\mathrm{BR} > 0.1$ once $m_{\widetilde{\chi}_3^0}, m_{\widetilde{\chi}_4^0}, m_{\widetilde{\chi}_5^0}$ are $\gtrsim 250, 400, 500$ GeV, respectively. Similarly, $\mathrm{BR}(\widetilde{\chi}_2^\pm \to \widetilde{\chi}_1^\pm h_2) > 0.1$ for $m_{\widetilde{\chi}_2^\pm} \gtrsim 500$ GeV. Since the charged Higgs has $m_{H^\pm} > 300$ GeV, decays to it, although present for the $\widetilde{\chi}_4^0$, $\widetilde{\chi}_5^0$ and $\widetilde{\chi}_2^\pm$, do not have $\mathrm{BR} > 0.1$ until $m_{\widetilde{\chi}_4^0}, m_{\widetilde{\chi}_5^0}, m_{\widetilde{\chi}_2^\pm} \gtrsim 1.1, 1.3, 1.3$ TeV, respectively.

6.6.3 Linear collider and photon collider tests

An e^+e^- collider would be the ideal machine to produce the additional Higgs states and resolve the scenario. Production cross sections for the various Higgs final states are shown in Fig. 6.32 for the three illustrative scenarios specified in Table 6.4 taken from our NMSSM scans. The first plot is for a WMAP-window scenario with $m_{\widetilde{\chi}_1^0} \sim 76$ GeV and light Higgs bosons. The third plot is for the point in region B with smallest m_{h_3}, for which $m_{a_2}, m_{h_3}, m_{H^\pm}$ are all around 1 TeV. The second plot is for a sample scenario with Higgs masses that are intermediate, as only possible if Ωh^2 lies below the WMAP window. With an integrated luminosity of 1000 fb^{-1}, substantial event rates for many Z+Higgs and Higgs pair final states are predicted. Of course, Zh_1 and Zh_2 production have the largest cross sections and lowest thresholds. The next lowest thresholds are for $a_1 h_1$

Table 6.4. Higgs masses and LSP mass in GeV for the three scenarios for which we plot e^+e^- cross sections in Fig. 6.32. Also given are Ωh^2, the singlino and Higgsino percentages and $R_{gg}^{h_2}(\gamma\gamma)$. Scenarios I) and III) have Ωh^2 in the WMAP window, with I) being typical of the low-$m_{\widetilde{\chi}_1^0}$ scenarios and III) being that with smallest m_{h_3} in the large-$m_{\widetilde{\chi}_1^0}$ group of points in the WMAP window. Scenario II) is chosen to have m_{a_2} and m_{h_3} intermediate between those for scenario I) and III), a region for which Ωh^2 is substantially below 0.1.

Scenario	m_{h_1}	m_{h_2}	m_{h_3}	m_{a_1}	m_{a_2}	$m_{H^\pm}$	$m_{\widetilde{\chi}_1^0}$	Ωh^2	LSP singlino	LSP Higgsino	$R_{gg}^{h_2}(\gamma\gamma)$
I	99	124	311	140	302	295	76	0.099	18%	75%	1.62
II	97	124	481	217	473	466	92	0.026	20%	74 %	1.53
III	99	126	993	147	991	989	115	0.099	75%	25%	1.14
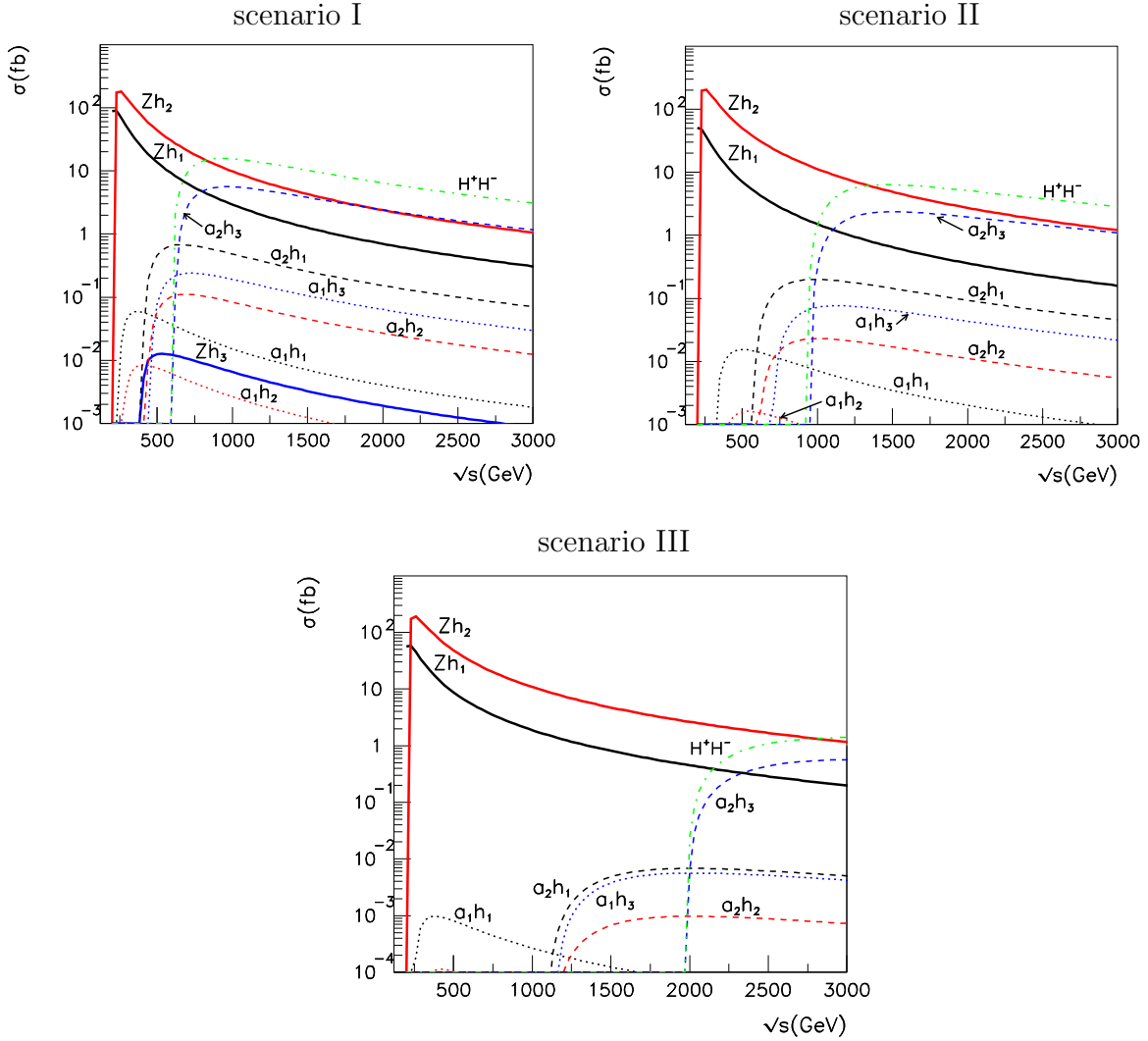
Figure 6.32. Cross sections for Higgs production at an e^+e^- collider, as functions of the center-of-mass energy $\sqrt{s}$, for three illustrative mass spectra as tabulated in Table 6.4.

production, but the cross sections are quite small, $< 0.1, 0.01, 0.001$ fb, respectively. The a_1h_2 cross sections are even smaller. Next in line are a_1h_3, a_2h_1 and a_2h_2, with a_2h_1 having thresholds $> 400, 600, 1190$ GeV for scenarios I), II) and III), respectively, as well as having the largest cross section, peaking at $\sigma > 0.7, 0.2, 0.007$ fb for the three respective scenarios. Production of a_2h_3 and H^+H^- have thresholds $> 620, 950, 2000$ GeV, respectively, but have much larger cross sections, that for H^+H^- being $> 16.6, 6.3, 1.4$ fb at the peak, for the three respective scenarios.

In the e^+e^- collider case, it would be easy to isolate signals in many final states. For

example, in the case of Higgs pairs, final states such as $(t\bar{t})(t\bar{t})$, $(\widetilde{\chi}_1^0\widetilde{\chi}_1^0)(t\bar{t})$ and so forth could be readily identified above background. Observation of the $(\widetilde{\chi}_1^0\widetilde{\chi}_1^0)(\widetilde{\chi}_1^0\widetilde{\chi}_1^0)$ final states would require a photon tag and would thus suffer from a reduced cross section. Associated Z+Higgs, with Higgs decaying to $t\bar{t}$ or $\widetilde{\chi}_1^0\widetilde{\chi}_1^0$ would be even more readily observed.

Another future collider that would become possible if an e^+e^- (or e^-e^-) collider is built is a $\gamma\gamma$ collider where the γ's are obtained by backscattering of laser photons off the energetic e's. For a recent summary see [329] and references therein. A huge range of energies is possible for such a $\gamma\gamma$ collider, ranging from low to high center of mass energies depending upon the center of mass energy of the underlying electron collider. A $\gamma\gamma$ collider based on e^-e^- collisions can even be considered as a stand-alone machine that could be built before an e^+e^- collider, especially if high $\sqrt{s}_{\gamma\gamma}$ is not needed. Typically, the largest $\sqrt{s}_{\gamma\gamma}$ that is possible with large instantaneous $\gamma\gamma$ luminosity is of order $0.8\sqrt{s}_{e^+e^-}$. That $\gamma\gamma \rightarrow$Higgs is an effective way to study a SM Higgs boson has been well established [330–332]. For low Higgs masses, the required electron collider could have energy of order $m_{\text{Higgs}}/0.8$.

In the present context, it is of interest to assess the extent to which a $\gamma\gamma$ collider would be able to study the neutral NMSSM Higgs bosons. This is determined by the ratio of the $\gamma\gamma$ coupling squared of the given Higgs boson to that of the SM Higgs. In Fig. 6.33 we present plots of $(C_{\gamma\gamma}^h)^2$ as a function of m_h for $h = h_1, h_2, h_3, a_1, a_2$ for masses below 1 TeV. The fairly SM-like h_2 at ~ 125 GeV can be studied easily at such a collider since its $\gamma\gamma$ coupling is close to SM strength. For example, at an e^-e^- collider with the optimal $E_{ee} = 206$ GeV, a 125 GeV SM Higgs has a cross section of 200 fb. After two years of operation, equivalent to $L = 500$ fb^{-1}, one can measure the $b\bar{b}, W^+W^-, \gamma\gamma$ partial widths with accuracies of $\Delta\Gamma(b\bar{b}, W^+W^-, \gamma\gamma)/\Gamma(b\bar{b}, W^+W^-, \gamma\gamma) \sim 0.015, 0.04, 0.06$, respectively [331] (see also [330, 332]).

Even though the h_1 and a_1 are largely singlet, both have $\gamma\gamma$ couplings-squared that are often of order $0.1\times$SM and above (at the same mass). In part, this is because even singlets couple to $\gamma\gamma$ through a Higgsino-like chargino loop using the singlet-Higgsino-Higgsino coupling that arises from the $\lambda\widehat{S}\widehat{H}_u\widehat{H}_d$ term in the superpotential. Indeed, this

237
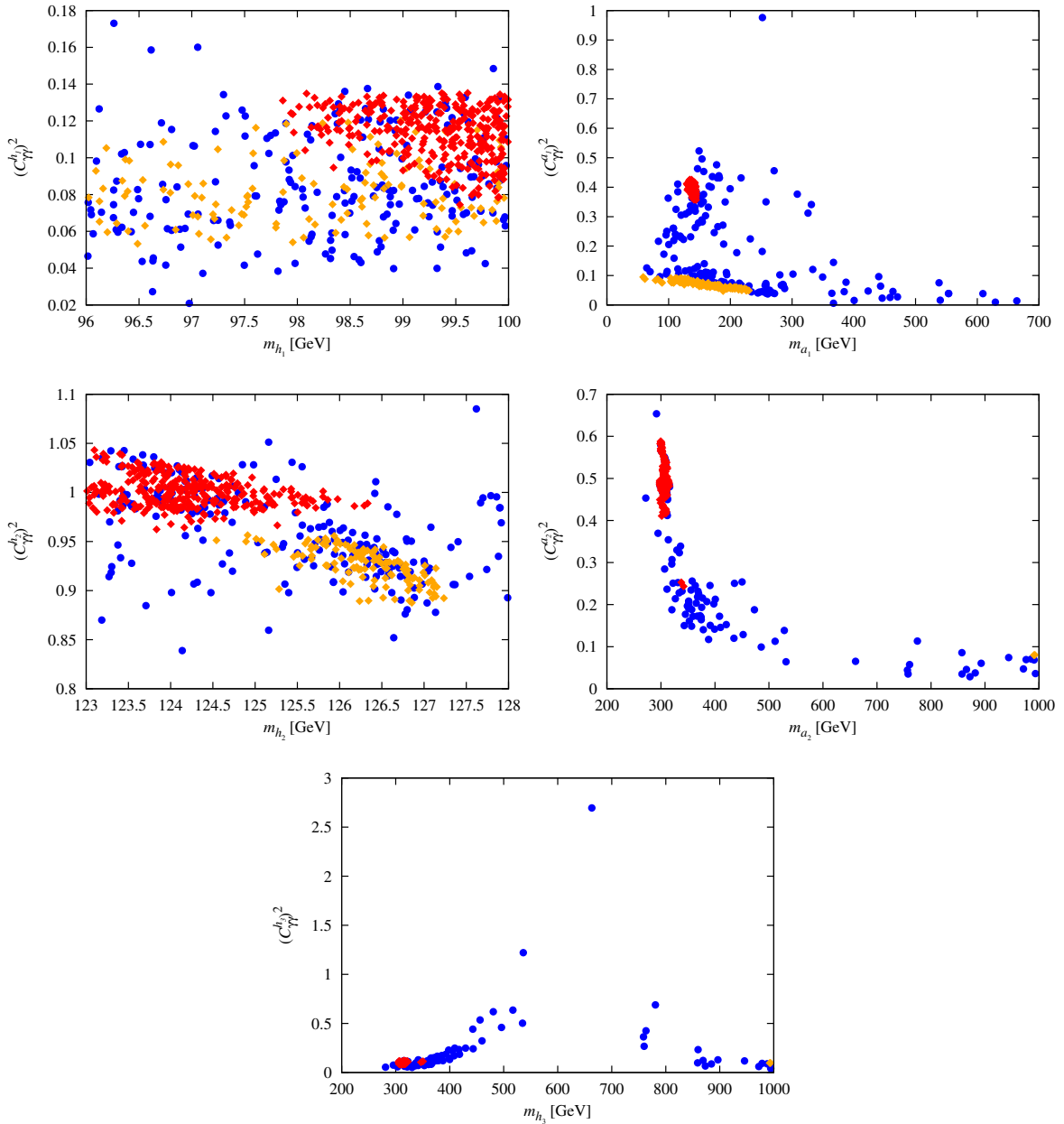
Figure 6.33. $(C_{\gamma\gamma}^h)^2$ as a function of m_h for $h = h_1, h_2, h_3, a_1, a_2$.

coupling becomes stronger as λ is increased. Of course, it is important to note that the modest values of μ_{eff} (see Fig. 6.27) that characterize many of our scenarios imply that the lightest chargino is largely Higgsino-like and has low mass (see Fig. 8.20), for which the Higgsino-chargino loop is less suppressed. Even for $\gamma\gamma$ coupling-squared of order $0.1\times$SM, with sufficient integrated luminosity observation of the h_1 and a_1 would

be possible. For example, for suitably chosen E_{ee}, the above SM Higgs rates multiplied by 0.1 would roughly apply for $m_{h_1} \sim 98$ GeV or $m_{a_1} < 300$ GeV, from which it is clear that the $b\bar{b}$ final state would be easily observable with $L = 500$ fb^{-1} and one could measure the partial width with an accuracy of order 5%. Even the h_3 and a_2 would be observable for $m_{a_2} < 500$ GeV, again assuming appropriately optimal E_{ee} for the given m_{h_3} or m_{a_2} and $L = 500$ fb^{-1}.

This raises the question of whether or not a $\gamma\gamma$ collider with adjustable (as is straightforward) $\sqrt{s}_{\gamma\gamma}$ in the 98 GeV range would be a good next step for high energy physics. It would have the advantage of allowing important detailed studies of the h_2 (or any SM-like Higgs boson with mass of 125 GeV) while testing for the presence of the h_1. With adjustable $\sqrt{s}_{\gamma\gamma}$ and $L \geq 500$ fb^{-1}, the h_3, a_1, a_2, or any other light Higgs boson with significant (even if somewhat suppressed) $\gamma\gamma$ coupling, would be observable as well.

6.6.4 Muon collider test

A muon-collider with $\sqrt{s}$ close to the Higgs mass in question would be a particularly ideal machine to study any Higgs boson with $\mu^+\mu^-$ coupling that is not too different from that of a SM Higgs boson of similar mass. Thus, in Fig. 6.34 we present plots of $(C^h_{\mu^+\mu^-})^2$ as a function of m_h for $h = h_1, h_2, h_3, a_1$, that for the a_2 being essentially identical to the $h = h_3$ case. We see that prospects are really quite good for the h_1 as well as the h_2. In addition, the WMAP-window a_1 points, all of which lie at relatively low mass, can be probed as well. As for the h_3 (and the a_2), the low-$m_{\tilde{\chi}^0_1}$ region points with low m_{h_3} ($\simeq m_{a_2}$) have nicely enhanced $(C^{h_3}_{\mu^+\mu^-})^2$ ($\simeq (C^{a_2}_{\mu^+\mu^-})^2$). A muon collider would be ideal for probing such scenarios. Additional experimental evidence for this $98+125$ GeV Higgs scenario from other machines would provide strong motivation for the muon collider.

6.7 Summary

We find that the fully constrained version of the NMSSM is not able to yield a Higgs boson consistent with the current hints from LHC data for a fairly SM-like Higgs with mass ~ 125 GeV, once all experimental constraints are imposed including acceptable a_μ and Ωh^2 in the WMAP window. However, by relaxing the CNMSSM to allow for non-universal
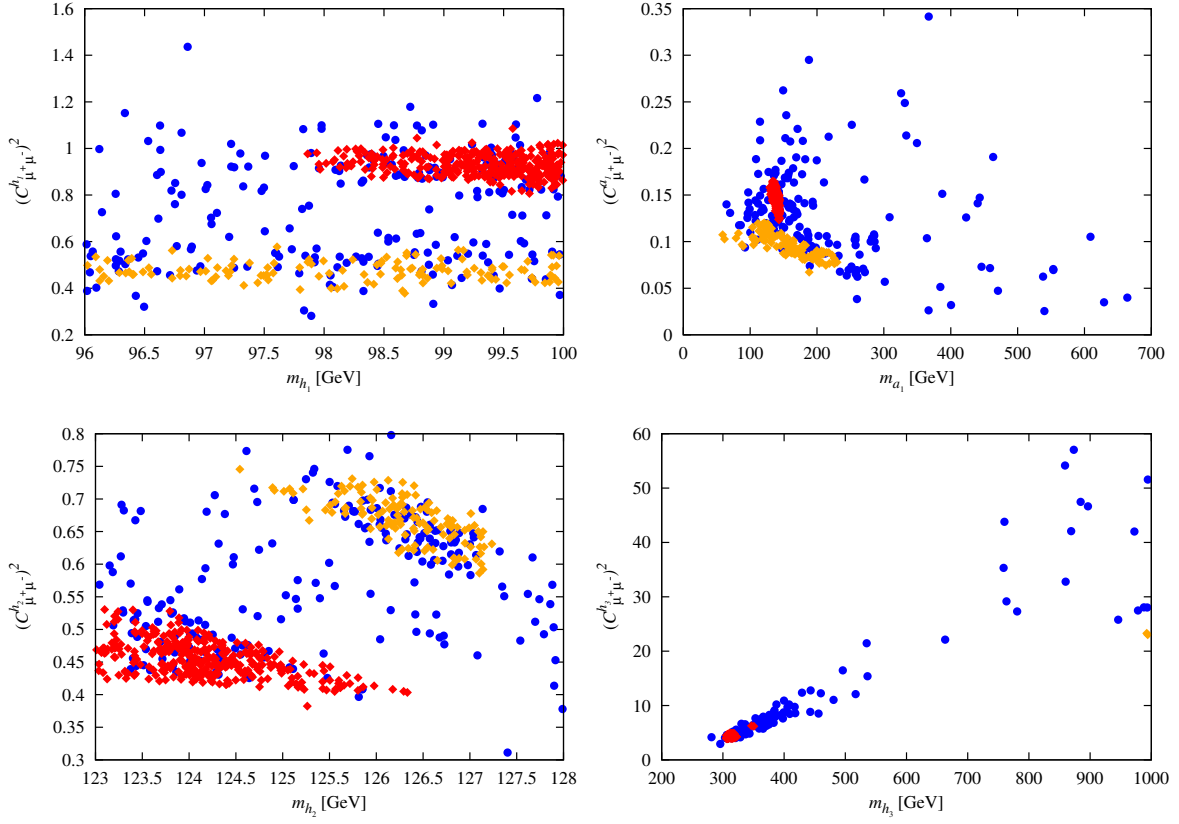
Figure 6.34. Reduced $\mu^+\mu^-$ couplings squared for h_1, h_2, h_3, a_1.

Higgs soft-masses-squared (NUHM scenarios), it is possible to obtain quite perfect points in parameter space satisfying all constraints with $m_{h_1} \sim 125$ GeV even if the attractive $U(1)_R$ symmetry limit of $A_\lambda = A_\kappa = 0$ is imposed at the GUT scale and certainly if general A_λ and A_κ values are allowed. We observe a mild tension between the a_μ constraint and obtaining $m_{h_1} \sim 125$ GeV; just slightly relaxing the a_μ requirement makes it much easier to find viable points with $m_{h_1} \sim 125$ GeV, thus opening up interesting regions of parameter space. We also note that our scanning suggests that relatively small A_λ, A_κ values are preferred for (almost) perfect points. Masses of SUSY particles for perfect/almost perfect points are such that direct detection of SUSY will have to await the data from the ongoing 13 TeV run-2 at the LHC. However, the predicted $\widetilde{\chi}_1^0$ masses and associated spin-independent cross sections suggest that direct detection of the $\widetilde{\chi}_1^0$ will be possible with the next round of upgrades to the direct detection experiments.

We have also identified a set of interesting NMSSM scenarios in which the two lightest CP-even Higgs bosons are closely degenerate and lie in the 123–128 GeV mass window. Large rates (relative to $gg \to H_{\mathrm{SM}} \to \gamma\gamma$ or $gg \to H_{\mathrm{SM}} \to ZZ^* \to 4\ell$) for $gg \to h_{1,2} \to \gamma\gamma$ and $gg \to h_{1,2} \to ZZ^* \to 4\ell$ are possible, sometimes because one of the rates is large but also sometimes because the rates are comparable and their sum is large. This suggests that, especially if enhanced rates continue to be observed in these channels, it will be important for the experimental community to be on the lookout for mass peaks in $m_{\gamma\gamma}$ and $m_{4\ell}$ that are broader than expected purely on the basis of the experimental mass resolution. In addition, the apparent mass in the $\gamma\gamma$ final state might differ slightly from the apparent mass in the 4ℓ final state. Significant statistics will be required to resolve such features.

In addition, we have demostrated the possibility that both the LEP excess in the $b\bar{b}$ final state at $M_{b\bar{b}} \sim 98$ GeV and the LHC Higgs-like signal at ~ 125 GeV with an enhanced rate in the two-photon final state can be explained in the context of the NMSSM. The NMSSM scenarios of this type (98 + 125 GeV LEP-LHC) have many attractive features. First, we particularly emphasized the fact that the h_1 could eventually be observed at the LHC in $gg, \mathrm{VBF} \to h_1 \to b\bar{b}$. We urge the ATLAS and CMS collaborations to give attention to this possibility. Second, there are important implications for the other Higgs bosons and for supersymmetric particles. If we focus only on the subset of these scenarios that have relic density in the WMAP window, then there are two separate regions of NMSSM parameter space that emerge. One region (A) is characterized by enhanced $\gamma\gamma$ rates for the 125 GeV Higgs, small $m_{\widetilde{\chi}_1^0} \sim 75$ GeV and low masses for many of the Higgs bosons and superpartners, including $m_{\tilde{t}_1}$ as low as 197 GeV. The second region (B) is characterized SM-like rates for the 125 GeV Higgs as well as by larger $m_{\widetilde{\chi}_1^0} \in [93, 150]$ GeV and much larger mass scales for the heavier Higgs bosons and supersymmetric particles. For this latter region, one finds $m_{a_1} \in [100, 200]$ GeV, $m_{\widetilde{\chi}_1^\pm} \in [170, 230]$ GeV, $m_{a_2} \simeq m_{h_3} \simeq m_{H^\pm} \in [1, 1.4]$ TeV, $m_{\tilde{t}_1} \in [1.9, 2.8]$ TeV, $m_{\tilde{q}}, m_{\tilde{g}} \in [3, 5]$ TeV and $\tan\beta \in [5, 7]$. Clearly this latter region leaves little hope for LHC detection of the colored particles and experimental probes would need to focus on the gauginos and lighter Higgs bosons. It is

further associated with rather modest values for the enhancement of the 125 GeV Higgs signal in the $\gamma\gamma$ channel. Information related to the prospects for Higgs and superparticle detection for the two regions (A) and (B) at an e^+e^-, $\gamma\gamma$ or $\mu^+\mu^-$ collider are summarized.

Diagnostic Tool: One or two Higgs bosons at 125 GeV?

A possibly very crucial issue is how to determine whether or not there are two (or more) Higgs bosons versus just one contributing to the Higgs signals at 125 GeV. One possibility, requiring high statistics given the experimental resolution (of order $\gtrsim$ 1.5 GeV), is that the mass peaks in the $\gamma\gamma$ and 4ℓ final states would display a structure of two overlapping peaks. However, for many of the degenerate scenarios explored in the NMSSM it turns out that the $\gamma\gamma$ and 4ℓ final states are dominated by only one of the degenerate Higgses, and the other one would show up primarily in $b\bar{b}$ and/or $\tau\tau$ final states. Unfortunately, mass resolutions in these latter channels are very poor and detection of a two peak structure using invariant mass distributions would appear to be very difficult. A direct probe of this kind of degeneracy using the full complement of final states is clearly highly desirable.

In this section, we will develop diagnostic tools that would reveal the presence of two Higgs bosons even if they are extremely close in mass. We illustrate our technique using the NMSSM scenarios generated for [2] (for which the NMSSM parameter ranges and all constraints are discussed in detail in the previous chapter) in which the two lightest CP-even Higgs bosons, h_1 and h_2, both lie in the 123–128 GeV mass window.

The diagnostic tools we suggest are however fully general and can be employed for any model/scenario with degenerate Higgs-like states; to exemplify we comment via footnotes regarding differences and similarities relative to the brane model studied in [333] in which a Higgs and the radion mix to form two mass eigenstates, $h_1 = h$, $h_2 = \phi$ (or vice versa) with $m_h \sim m_\phi$.

7.1 Search technique: double-μ ratio

The main production channels (denoted by Y) relevant for current LHC data are $gg \to H$ fusion ($Y = gg$) and vector boson fusion (Y=VBF), where VBF stands for the sum of the $WW \to H$ and $ZZ \to H$ vector boson fusion processes. Here, H stands for a generic Higgs boson. Higgs decay channels (denoted by X) include the high resolution $X = \gamma\gamma$ and $X = ZZ^* \to 4\ell$ final states, *i.e.* $H \to \gamma\gamma$ and $H \to ZZ^* \to 4\ell$, and the poor mass resolution $X = b\bar{b}$ and $X = \tau^+\tau^-$ channels. The most crucial production/decay channels at the LHC are $gg, \text{VBF} \to H \to \gamma\gamma, 4\ell$. The LHC also probes $V^* \to VH$ ($V = W$ or Z) with $H \to b\bar{b}$, channels for which Tevatron data is relevant, and VBF $\to H$ with $H \to \tau^+\tau^-$. Let us employ the notation h_i for the ith scalar Higgs, H_{SM} for the SM Higgs boson and $C_S^{h_i} = g_{Sh_i}/g_{SH_{\text{SM}}}$ is the ratio of the Sh_i coupling to the SH_{SM} coupling, where $S = \gamma\gamma, gg, WW, ZZ, bb, \tau^+\tau^-$ are the cases of interest. The ratio of the gg or VBF induced h_i cross section times $\text{BR}(h_i \to X)$, relative to the corresponding value for the SM Higgs boson, takes the form

$$R_{gg}^{h_i}(X) = (C_{gg}^{h_i})^2 \, \frac{\text{BR}(h_i \to X)}{\text{BR}(H_{\text{SM}} \to X)}, \quad R_{VBF}^{h_i}(X) = (C_{WW}^{h_i})^2 \, \frac{\text{BR}(h_i \to X)}{\text{BR}(H_{\text{SM}} \to X)}, \quad (7.1)$$

where the latter result assumes the custodial symmetry relation $C_{WW}^{h_i} = C_{ZZ}^{h_i}$ as applies in any doublets+singlets model; this latter also implies $R_{VBF}^{h_i}(X) = R_{V^* \to VH}^{h_i}(X)$ and, for either $Y = gg$ or $Y =$VBF, $R_Y^{h_i}(WW) = R_Y^{h_i}(ZZ)$. However, if custodial symmetry is broken there are many more independent R^{h_i}'s.[1]

As noted above, in this section we consider the case where there are two nearly degenerate Higgs bosons for which we must combine their signals. The net signal and the

---

[1]For example, in the Higgs-radion mixing model, $R_{V^* \to VH}^{h_i}(X) \neq R_{\text{VBF}}^{h_i}(X)$, $R_{gg}^{h_i}(WW) \neq R_{gg}^{h_i}(ZZ)$, *etc.*

effective Higgs mass, respectively, for given production and final decay channels Y and X, respectively, are computed as

$$R_Y^h(X) = R_Y^{h_1}(X) + R_Y^{h_2}(X), \quad m_h^Y(X) \equiv \frac{R_Y^{h_1}(X)m_{h_1} + R_Y^{h_2}(X)m_{h_2}}{R_Y^{h_1}(X) + R_Y^{h_2}(X)}. \tag{7.2}$$

Of course, the extent to which it is appropriate to combine the rates from the h_1 and h_2 depends upon the degree of degeneracy and the experimental resolution, estimated to be of order $\sigma_{\mathrm{res}} \sim 1.5$ GeV [322]. It should be noted that the widths of the h_1 and h_2 are of the same order of magnitude as the width of a 125 GeV SM Higgs boson (a few MeV), *i.e.* very much smaller than this resolution.[2]

As already noted in earlier sections, in the context of any doublets plus singlets model not all the R^{h_i}'s are independent; the relations among the R^{h_i}'s were noted in these earlier sections. In supersymmetric two-doublet plus singlets models we have in addition $R_Y^{h_i}(\tau\tau) = R_Y^{h_i}(bb)$. A complete independent set of R^h's can be taken to be:[3]

$$R_{gg}^h(WW), \quad R_{gg}^h(bb), \quad R_{gg}^h(\gamma\gamma), \quad R_{VBF}^h(WW), \quad R_{VBF}^h(bb), \quad R_{VBF}^h(\gamma\gamma). \tag{7.3}$$

Let us now look in more detail at a given $R_Y^h(X)$. It takes the form

$$R_Y^h(X) = \sum_{i=1,2} \frac{(C_Y^{h_i})^2 (C_X^{h_i})^2}{C_\Gamma^{h_i}} \tag{7.4}$$

where $C_X^{h_i}$ for $X = \gamma\gamma, WW, ZZ, \ldots$ is the ratio of the $h_i X$ to $H_{\mathrm{SM}}X$ coupling, as defined above Eq. (7.1), and $C_\Gamma^{h_i}$ is the ratio of the total width of the h_i to the SM Higgs total width. The diagnostic tools that we propose to reveal the existence of a second, quasi-degenerate (but non-interfering in the small width approximation) Higgs state are the double ratios:

$$\mathrm{I}): \; \frac{R_{VBF}^h(\gamma\gamma)/R_{gg}^h(\gamma\gamma)}{R_{VBF}^h(bb)/R_{gg}^h(bb)}, \quad \mathrm{II}): \; \frac{R_{VBF}^h(\gamma\gamma)/R_{gg}^h(\gamma\gamma)}{R_{VBF}^h(WW)/R_{gg}^h(WW)}, \quad \mathrm{III}): \; \frac{R_{VBF}^h(WW)/R_{gg}^h(WW)}{R_{VBF}^h(bb)/R_{gg}^h(bb)}, \tag{7.5}$$

---

[2] Note that this is not an assumption. The fact that a SM-like Higgs signal in the $\gamma\gamma$ and ZZ modes is even *visible* at the LHC tells us that the widths of any contributing Higgs boson must be very small, at most of order a few MeV as for the SM Higgs. Interference effects are negligible in this case unless one has extreme degeneracy of the two states. Our NMSSM scan points generally have $m_{h_2} - m_{h_1} > 50$ MeV for which interference effects are at most a fraction of a percent.

[3] In other models, more (or fewer) R^h's could be independent and more (or fewer) double ratios compared to those defined below could be useful/independent. In the Higgs-radion mixing model custodial symmetry is violated, leading to *more* independent R^h's. For example, $R_{gg}^h(WW) \neq R_{gg}(ZZ)$ and $R_{VH}^h(X) \neq R_{VBF}^h(X)$.

each of which should be unity if only a single Higgs boson is present but, due to the non-factorizing nature of the sum in Eq. (7.4), are generally expected to deviate from 1 if two (or more) Higgs bosons are contributing to the net h signals. This occurs because the h_1 and h_2 will in general have different relative production rates in the VBF and gg fusion channels for one or more final states. One can check that in a doublets+singlets model all other double ratios that are equal to unity for single Higgs exchange are not independent of the above three. Of course, the above three double ratios are not all independent. Which will be most useful depends upon the precision with which the R^h's for different initial/final states can be measured. For example, measurements of R^h for the bb final state may continue to be somewhat imprecise and it is then double ratio II) that might prove most discriminating. Or, it could be that one of the double ratios deviates from unity by a much larger amount than the others, in which case it might be most discriminating even if the R^h's involved are not measured with great precision.

7.2 Application to models

To explore how powerful these double ratios are in practice, we turn to the NMSSM scenarios with semi-unified GUT scale soft-SUSY-breaking sampled in [2] (and detailed earlier) and Higgs-radion mixing in the RS model (see Ref. [333] for a recent analysis).

7.2.1 General Higgs-multiplet sample: NMSSM

These scenarios obey all experimental constraints (including $\Omega h^2 < 0.136$ and 2011 XENON100 limits on the spin-independent scattering cross section) except that the SUSY contribution to the anomalous magnetic moment of the muon, δa_μ, is too small to explain the discrepancy between the observed value a_μ and that predicted by the SM. For a full discussion of the kind of NMSSM model employed see also [1, 315].

In Fig. 7.1, we plot the numerator versus the denominator of the double ratios I) and II), III) being very like I) due to the correlation between the $R_{gg}^h(\gamma\gamma)$ and $R_{gg}^h(WW)$ values discussed in [2]. We observe that any one of these double ratios will often, but not always, deviate from unity (the diagonal dashed line in the figure). The probability of such deviation increases dramatically if we require $R_{gg}^h(\gamma\gamma) > 1$, see the solid (vs.
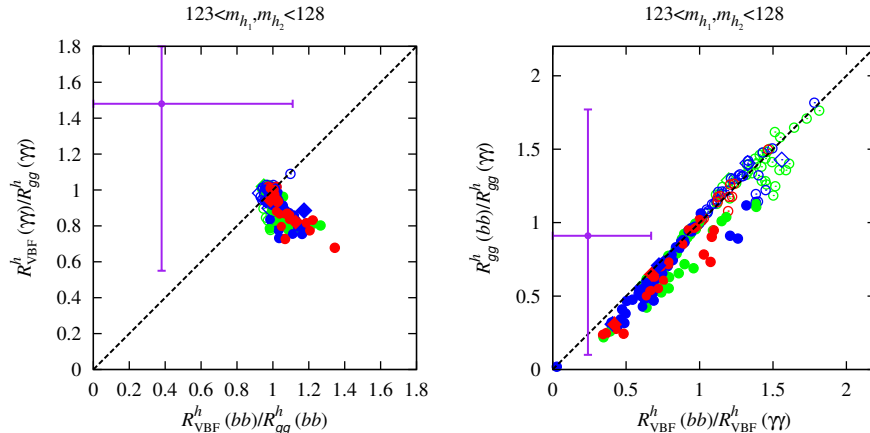
Figure 7.1. Comparisons of pairs of event rate ratios that should be equal if only a single Higgs boson is present. The color code is green for points with $2 \text{ GeV} < m_{h_2} - m_{h_1} \leq 3 \text{ GeV}$, blue for $1 \text{ GeV} < m_{h_2} - m_{h_1} \leq 2 \text{ GeV}$, and red for $m_{h_2} - m_{h_1} \leq 1 \text{ GeV}$. Large diamond points have Ωh^2 in the WMAP window of $[0.094, 0.136]$, while circular points have $\Omega h^2 < 0.094$. Solid points are those with $R_{gg}^h(\gamma\gamma) > 1$ and open symbols have $R_{gg}^h(\gamma\gamma) \leq 1$. Current experimental values for the ratios from CMS data along with their 1σ error bars are also shown.

open) symbols of Fig. 7.1. This is further elucidated in Fig. 7.2 where we display the double ratios I) and II) as functions of $R_{gg}^h(\gamma\gamma)$ (left plots). For the NMSSM, it seems that the double ratio I) provides the greatest discrimination between degenerate vs. non-degenerate scenarios with values very substantially different from unity (the dashed line) for the majority of the degenerate NMSSM scenarios explored in [2] that have enhanced $\gamma\gamma$ rates. Note in particular that I), being sensitive to the $b\bar{b}$ final state, singles out degenerate Higgs scenarios even when one or the other of h_1 or h_2 dominates the $gg \rightarrow \gamma\gamma$ rate, see the top right plot of Fig. 7.2. In comparison, double ratio II) is most useful for scenarios with $R_{gg}^h(\gamma\gamma) \sim 1$, as illustrated by the bottom left plot of Fig. 7.2. Thus, as illustrated by the bottom right plot of Fig. 7.2, the greatest discriminating power is clearly obtained by measuring both double ratios. In fact, a close examination reveals that there are no points for which *both* double ratios are exactly 1! Of course, experimental errors may lead to a region containing a certain number of points in which both double ratios are merely consistent with 1 within the errors.

7.2.2 Randall-Sundrum model with Higgs-radion mixing

We have quantitatively evaluated the diagnostic power of the double ratios of Eq. (7.5) in the Higgs-radion mixing model and again find that they deviate by substantial, often large amounts relative to unity. In addition, there are other double ratios (see footnote 3) that also have similar discriminating power as well as the ability to detect the custodial symmetry violation implicit in the Higgs-radion mixing model.

7.3 Summary: the implication of LHC data

A natural question is what does current LHC data say about these various double ratios? The central values and 1σ error bars[4] for the numerator and denominator of double ratios I) and II) obtained from CMS data [334] are also shown in Fig. 7.1. Obviously, current statistics are inadequate to discriminate whether or not the double ratios deviate from unity. For a $\sqrt{s} = 14$ TeV run with $L = 100$ fb^{-1} (300 fb^{-1}) of accumulated luminosity the SM Higgs cross sections at the relevant energies imply that the number of Higgs events will be about a factor of 25 (77) larger than the number produced for $L \sim 5$ fb^{-1} at $\sqrt{s} = 7$ TeV plus $L \sim 6$ fb^{-1} at $\sqrt{s} = 8$ TeV (as used in computing the error bars shown in Fig. 7.1). Using statistical scaling only that means the error bars plotted in Fig. 7.1 should be reduced by roughly a factor of 5 (9), levels that could indeed reveal a deviation from unity, or at least remove some model points if no deviation within that error is seen. Of course improvements in the experimental analyses may further increase the sensitivity. We thus conclude that our diagnostic tools will ultimately prove viable and perhaps crucial for determining if the ~ 125 GeV Higgs signal is really only due to a single Higgs-like resonance or if two resonances are contributing, the latter having significant probability in model contexts if enhanced $\gamma\gamma$ rates are indeed confirmed at higher statistics.

To summarize, we have emphasized the possibility that a $\gamma\gamma$ Higgs-like signal that is either significantly enhanced relative to the SM or SM-like could arise as a result of there

---

[4] For the ratio R_i/R_j, we use $\sigma^{\mathrm{upp,low}} = \frac{R_i}{R_j} \sqrt{(\sigma_i^{\mathrm{upp,low}}/R_i)^2 + (\sigma_j^{\mathrm{upp,low}}/R_j)^2}$ to calculate its combined asymmetric 1σ error bar, where $\sigma_i^{\mathrm{upp/low}}$ is the upper/lower 1σ error for the individual R_i.
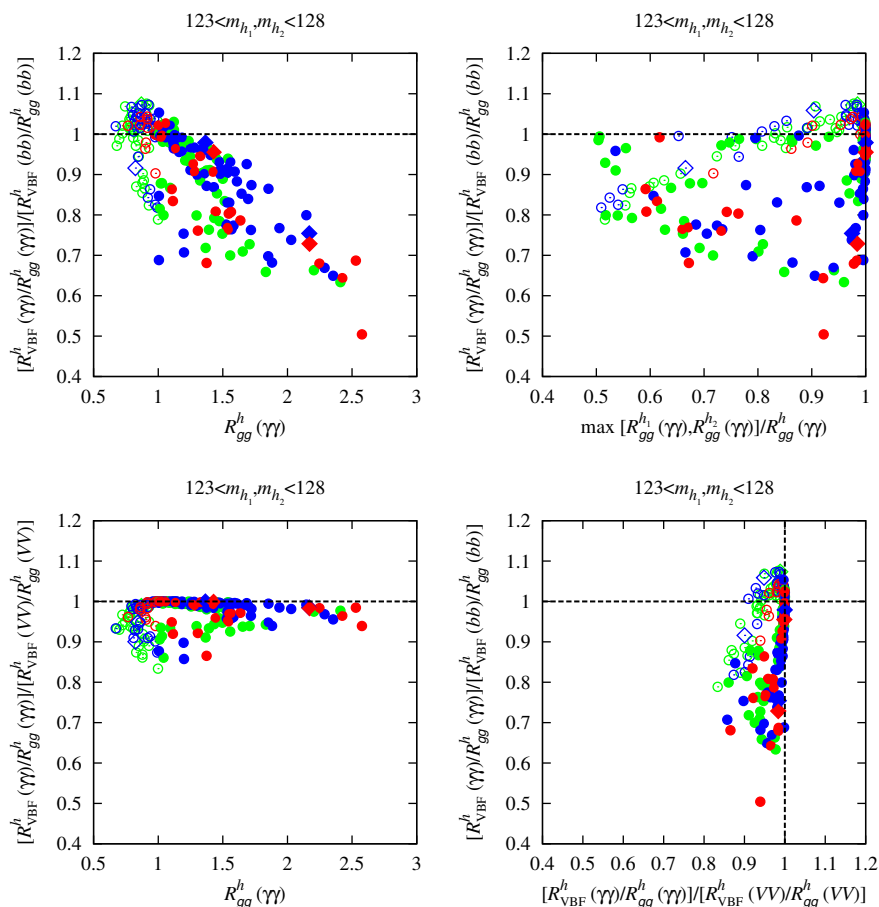
Figure 7.2. Double ratios I) and II) of Eq. (7.5) as functions of $R_{gg}^h(\gamma\gamma)$ (on the left). On the right we show (top) double ratio I) vs. $\max\left[R_{gg}^{h_1}(\gamma\gamma), R_{gg}^{h_2}(\gamma\gamma)\right]/R_{gg}^h(\gamma\gamma)$ and (bottom) double ratio I) vs. double ratio II) for the points displayed in Fig. 7.1. Colors and symbols are the same as in Fig. 7.1.

being two fairly degenerate Higgs bosons near 125 GeV. This situation arises in several model contexts in which the degeneracy can be such that separate mass peaks could not be observed in even the high-resolution $\gamma\gamma$ and $ZZ \to 4\ell$ final states. We have shown that deviations from unity of certain double ratios of event rates have strong potential for revealing the presence of two (or more) nearly degenerate Higgs bosons within the 125 GeV LHC signal. Such deviations arise when both the quasi-degenerate Higgses contribute significantly to at least one production/decay channel. We have employed the NMSSM as a prototype model to illustrate the discriminating power of these double ratios in the case of a doublets-plus-singlets Higgs model. We have also noted that the

diagnostic power of the double ratios discussed in this letter is at least as great in the brane model with Higgs-radion mixing and, in addition, there are more double ratios that can be defined as a result of the sometimes substantial violation of custodial symmetry in the latter type of model. Of course, substantial statistics will be required to reveal the deviations from unity that would signal a degenerate scenario.

PART III

Linking Higgs to Dark Matter

CHAPTER 8

Another puzzle — dark matter

"Dark matter study is becoming more and more complicated. However, maybe we are approaching the correct picture step by step."

— *Yun Jiang*

The existence of dark matter (DM) is one of the strongest indications that there must be physics beyond the SM of particle physics. Thus, among the issues to address in the BSM, one of the most outstanding is the inclusion of additional particle(s) that comprise the DM. It is not directly visible to telescopes but makes up a sizable fraction of the energy density of the Universe [335]. As of today the constitution of DM remains unknown. The absence of electromagnetic and strong interactions makes it experimentally 'dark', however, interactions at the weak scale might be possible. To mitigate the hierarchy problem, the idea that the DM could have a mass of the order of the electroweak scale is well-motivated although the mass scale of DM is also not yet known. In which, a particularly attractive paradigm is the weakly- interacting-massive-particle (WIMP) which can

produce a thermal relic density consistent with the current observations. Under protection of an additional symmetry, many particles which are neutral, cold (i.e. non-relativistic), and stable (or have half-lifes longer than the age of the Universe) predicted from the Higgs doublet fields in a variety of BSM theories could be viable DM candidates. Such excellent examples of WIMPs include the most prominent being the lightest neutralino in supersymmetric theories (for example in Ref. [336]), the Higgs-portal DM in the scalar singlet extensions of the SM (see the minimal models in Refs. [337, 338]) and the lightest Kaliza-Klein particle (LKP) in theories with extra-dimensions [339].

In this chapter I am going to address the first two scenarios in the NMSSM (see details in Chapter 6) and 2HDMS contexts together with a decent description of the models. Throughout the discussion I focus on the one-component DM scenario in which the WIMP is a single particle that emerges as part of an extended scalar sector of the electroweak theory. Another ingredient taken into account in our considerations is the role of isospin-violating effect that could dramatically change the analysis of dark matter direct detection. Given this, I provide an in-depth examination of this possibility in the generic Higgs-portal DM model.

8.1   Useful messages from DM detection experiments

As perhaps the most compelling window to new physics beyond the SM, DM has been searched for in various ways over many decades. Numerous indirect observations at astronomical and cosmological scales point to the presence of a new form of matter in the Universe, which only interacts significantly via gravity. The most famous observational evidence is the rotation profiles of galaxies, the dynamics of galaxy clusters, the separation of dark and light matter in galaxy clusters, and the interpretation of the cosmic microwave background (CMB). Recently the Planck satellite mission [335] has published new and precise measurements of the CMB, which are in full agreement with the predictions of the ΛCDM model, describing a cosmos dominated by dark energy and cold dark matter (CDM).

In addition, a number of collaborations have been devoted to working on the direct

detection of DM. They typically translate the event rate against recoil energy in the detector into the limit on the spin-independent cross section for the DM scattering off a proton $\sigma_{\mathrm{DM}-p}^{\mathrm{SI}}$ as a function of WIMP mass, resulting an important constraint on the WIMP scenario. Existing results and projected sensitivities for the spin-independent WIMP-nucleon interactions as a function of the WIMP mass are summarized in Fig. 8.1.The strongest of those limits is currently a result of the LUX Collaboration [87] and the superCDMS [340], where the LUX limit is strongest for DM masses above about 6 GeV while the SuperCDMS limit is strongest for masses below this. [1] In particular, the lower energy threshold of LUX allows a significant improvement in constraints at small WIMP mass, *i.e.* below 15 GeV where positive signals are reported by other collaborations looking for DM-nucleon scattering. For example, the CDMS II Collaboration found a signal that can be interpreted as a scattering of a WIMP with mass of $\sim 8.6\,\mathrm{GeV}$ and cross-section of $\sigma^{\mathrm{SI}} \sim 1.9 \times 10^{-41}\,\mathrm{cm}^2$ [85, 341]. Presence of other positive hints (DAMA [342], CoGeNT [343], and CRESST-II [79]) supports the findings of CDMS II. They are overall statistically compatible with each other, despite that they do not fully overlap at face value. Roughly, their results suggest WIMP mass in the range roughly from $7 - 40$ GeV and $\sigma_{\mathrm{DM}-p}^{\mathrm{SI}}$ of order $10^{-42} - 10^{-40}\mathrm{cm}^2$. However, given the null XENON 100/LUX results the situation is rather unclear.

However, it is worthwhile to note that there are several standard assumptions hidden in the translation that might not be correct. For instance, one assumes a DM halo in the vicinity of Earth and the truncated Maxwell-Boltzmann velocity distribution below the escape velocity borrowing from Standard Halo Model. It is also supposed that the DM elastically scatters with a short range contact interaction via a 'heavy mediator', that is zero-momentum transfer. More important, it is somehow of with prejudice that DM is assumed to have the equal coupling with neutron and proton, that is to say the ratio $f_n/f_p = 1$. Since many recent data hints are only marginally consistent with typical WIMP models, it is thus not clear whether these assumptions are really desirable. It is intriguing to notice that in contrast to DAMA, CoGeNT and CRESST-II, most CDMS II

---

[1]We note that the XENON 100 limit [81] is roughly about one order of magnitude weaker than the LUX limit in the overall WIMP mass region and, thus, we do not reference it in our discussions.
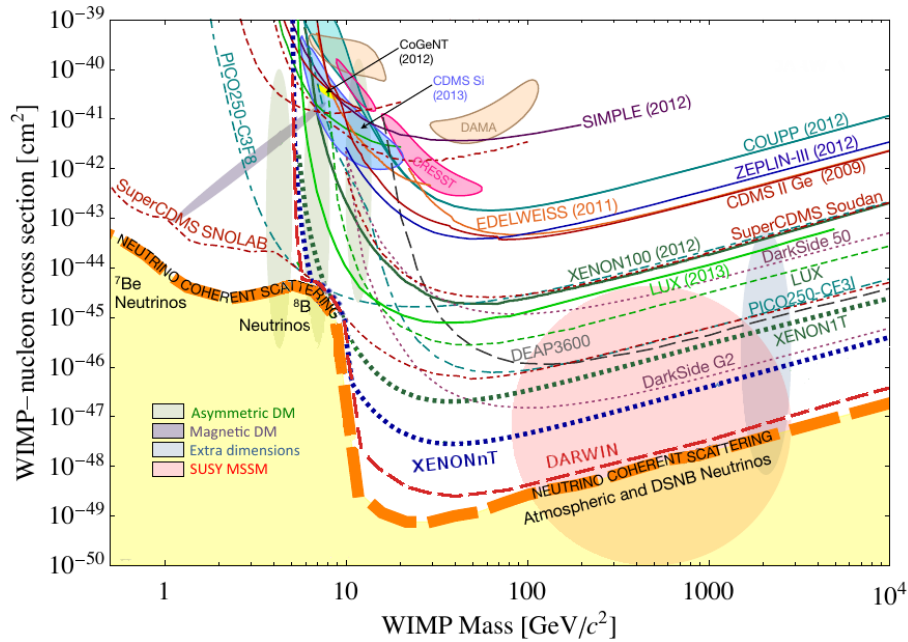
Figure 8.1. Summary for spin-independent WIMP-nucleon scattering results. Selective existing limits from XENON100 [81], and LUX [87], along with projections for LUX [87], XENON1T [344], XENONnT (similar sensitivity as the LZ project [345]) are shown. Experiments based on the mK cryogenic technique such as SuperCDMS [340] have access to lower WIMP masses. Figure selected from [346].

region escapes the XENON 100 exclusion limit (but not for LUX) if the WIMP interactions with nucleons are allowed to violate isospin symmetry [347–349]. In the aftermath of LUX one is trying to include large and nucleus-dependent corrections at the next-to-leading order (NLO) in the chiral expression [350].

8.2   Scalar dark matter from Higgs portal

In the minimal extension of the SM, a scalar singlet is introduced and couples to the SM exclusively through $\lambda_s S^2 H^\dagger H$ interaction. This physical state of this singlet could be a DM as its decays is prevented by imposing a new $\mathbb{Z}_2$ symmetry. Such scenario was originally proposed in [337, 338] and has been thoroughly studied in details in [351, 352] after the Higgs discovery at the LHC. For a light ($\lesssim 60$ GeV) scalar DM of this model, one requires relatively large value of the portal coupling λ_s to acquire the proper relic abundance. As a result, this minimal model suffers from two mortal diseases: Higgs boson invisible decay branching ratio $BR(h \to SS)$ is nearly 100% and the cross-section

for DM scattering off a nucleon is too large, exceeding the exclusion upper limit provided by LUX collaboration [87].

To cure both two issues, it appears that a second Higgs doublet is needed [11]. The main idea is that if a second Higgs boson is present and interacts with the singlet DM, then the 125 GeV Higgs could be SM-like with a very small portal coupling to S (and therefore a small invisible branching ratio) while still producing a proper relic abundance, as the yet non-observed Higgs boson could be responsible for interactions with DM, with a relatively strong coupling to S even if the singlet DM S is very light (for instance the case of $m_S < 50$ GeV).

An economical example to accomplish this idea is to impose an extra $\mathbb{Z}'_2$ symmetry on the second doublet, as a result one of the neutral components in this doublet would be a stable particle and could be play a role of DM. Such model in the literature is known as the inert doublet model (IDM) [353] and its phenomenology associated with Higgs boson and DM has been analyzed in earlier literatures [354–358]. This model was also received recent attentions in the aspects of the electroweak phase transition [359] and LHC searches [360]. Instead, we propose another solution and extend the two-Higgs-doublet model (2HDM) by adding a real gauge-singlet scalar, inheriting the Yukawa structure of the 2HDM. We term this extended model "2HDMS" [2] [11], which has been studied earlier in [361–369] and also discussed in the frameworks of scale invariance [370]. We introduce an extra $\mathbb{Z}'_2$ symmetry under which S is the only odd field. Provided S does not acquire a vacuum expectation value (VEV), it is stable and thereby a possible DM candidate. The 2HDMS then contains three CP-even states, h and H ($m_h \leq m_H$) from the 2HDM sector and S, a CP-odd state, A, and a charged Higgs pair, $H^\pm$. The 2HDM context allows for increased flexibility for DM predictions as compared to adding an S to the one-doublet SM in that either h or H can be identified with the observed SM-like CP-even state at ~ 125.5 GeV while the other CP-even state and the A and $H^\pm$ can provide additional channels for early-universe annihilation. Further, both of the CP-even states contribute to DM scattering and annihilation.

---

[2]This model was referred to as the 2HDM Darkon model (2HDMD) in some earlier literature.

257

As has been extensively studied in Chapter 5, either of two CP-even Higgs bosons originated from the Higgs sector of 2HDM in the extended 2HDMS could be identified as the 125 GeV state which was observed at the LHC and provide a consistent description of all LHC observed signal strengths. However, these two scenarios are qualitatively distinctive as far as the experimental constraints on DM are concerned. Due to the length limitation we shall only consider the case of $m_h \sim 125.5$ GeV. In Section 8.2.1, we discuss the general features of 2HDMS and derive the theoretical constraints on the singlet parameters resulting from imposing perturbativity, stability, unitarity and correct electroweak symmetry breaking. In Section 8.2.2 we discuss the properties of the singlet scalar DM and elaborate on the methodology of constraining the full 2HDMS parameter space using various experimental observations and limits when the 2HDM sector of the model is restricted to fit existing LHC data. In Section 8.2.4 we will present the results of our 2HDMS parameter space scan. There, we show that the combined LUX and SuperCDMS DM limits can only be satisfied for $m_S \gtrsim 55$ GeV. However, we do explore the extent to which IVDM scenarios arise in the 2HDMS case and how they come close to allowing the CDMS II signal to be consistent with the LUX limit.

8.2.1 2HDM plus singlet models description

Our first goal is to offer a complete description for the 2HDMS model which contains two Higgs doublets H_1, H_2 with an equal $U(1)_Y$ charge $Y = 1$ and a real scalar singlet S, that is neutral under the SM gauge group. To have a possible DM candidate, we introduce a $\mathbb{Z}'_2$ symmetry under which $S \to -S$ (other fields are taken to be even under $\mathbb{Z}'_2$) and demand that the scalar field S does not acquire a vacuum expectation value (VEV), which thereby makes it stable. Hence, the $\mathbb{Z}'_2$ symmetric and gauge-invariant 2HDMS scalar potential of our choice is:

$$
\begin{aligned}
V(H_1, H_2, S) =\ & m_1^2 H_1^\dagger H_1 + m_2^2 H_2^\dagger H_2 - \left[m_{12}^2 H_1^\dagger H_2 + h.c. \right] \\
& + \frac{\lambda_1}{2}(H_1^\dagger H_1)^2 + \frac{\lambda_2}{2}(H_2^\dagger H_2)^2 + \lambda_3(H_1^\dagger H_1)(H_2^\dagger H_2) + \lambda_4|H_1^\dagger H_2|^2 \\
& + \left[\frac{\lambda_5}{2}(H_1^\dagger H_2)^2 + \lambda_6(H_1^\dagger H_1)(H_1^\dagger H_2) + \lambda_7(H_2^\dagger H_2)(H_1^\dagger H_2) + h.c. \right] \\
& + \frac{1}{2}m_0^2 S^2 + \frac{1}{4!}\lambda_S S^4 + \kappa_1 S^2(H_1^\dagger H_1) + \kappa_2 S^2(H_2^\dagger H_2) + S^2(\kappa_3 H_1^\dagger H_2 + h.c.)
\end{aligned}
\tag{8.1}
$$

which contains 20 (real) parameters. However, for simplicity we make several additional assumptions. We consider a model without explicit CP violation (*i.e.* all the λ coefficients of Eq. (8.1) are taken to be real) and we only consider parameter choices for which there is no spontaneous CP breaking. As a result, the Higgs VEVs are real. We also impose a primitive $\mathbb{Z}_2$ symmetry in the 2HDM under which $H_1 \to H_1, H_2 \to -H_2, S \to S$. This eliminates the λ_6, λ_7 and κ_3 couplings of Eq. (8.1). However, we do allow for $m_{12}^2 \neq 0$, corresponding to a soft breaking of $\mathbb{Z}_2$. The resulting potential takes the form

$$
\begin{aligned}
V(H_1, H_2, S) &= m_1^2 H_1^\dagger H_1 + m_2^2 H_2^\dagger H_2 - \left[m_{12}^2 H_1^\dagger H_2 + h.c. \right] + \frac{\lambda_1}{2}(H_1^\dagger H_1)^2 + \frac{\lambda_2}{2}(H_2^\dagger H_2)^2 \\
&+ \lambda_3(H_1^\dagger H_1)(H_2^\dagger H_2) + \lambda_4 |H_1^\dagger H_2|^2 + \left[\frac{\lambda_5}{2}(H_1^\dagger H_2)^2 + h.c. \right] \\
&+ \frac{1}{2}m_0^2 S^2 + \frac{1}{4!}\lambda_S S^4 + \kappa_1 S^2(H_1^\dagger H_1) + \kappa_2 S^2(H_2^\dagger H_2)
\end{aligned}
\tag{8.2}
$$

The next stage is to convert from the Lagrangian basis to the mass eigenstate basis. Despite the presence of the $S^2 H_1^\dagger H_1$ and $S^2 H_2^\dagger H_2$ interactions that allow 2HDMS for increased flexibility for DM predictions (in comparison to the minimal singlet extension), the analysis of the 2HDM sector can be performed independently of the S and the usual mass matrices for the 2HDM, see [39], are not changed due to the fact that the extra field S does not acquire a VEV. [3] However, the fields H_1 and H_2 do contribute to the S^2 mass term when they develop VEVs, $H_{1,2} \to v_{1,2}$.

In terms of the mass eigenstates, the S-dependent part of the scalar potential, after electroweak symmetry breaking, has the form:

$$
-V_S = -\frac{1}{2}m_S^2 S^2 - \lambda_h v h S^2 - \lambda_H v H S^2 - S^2(\lambda_{HH} HH + \lambda_{hH} hH + \lambda_{hh} hh + \lambda_{AA} AA + \lambda_{H^+H^-} H^+ H^-)
\tag{8.3}
$$

where the physical S particle mass and the DM-Higgs trilinear couplings are

$$
\begin{aligned}
m_S^2 &= m_0^2 + (\kappa_1 \cos^2\beta + \kappa_2 \sin^2\beta)v^2 & (8.4) \\
\lambda_h &= -\kappa_1 \sin\alpha \cos\beta + \kappa_2 \cos\alpha \sin\beta & (8.5) \\
\lambda_H &= \kappa_1 \cos\alpha \cos\beta + \kappa_2 \sin\alpha \sin\beta \,. & (8.6)
\end{aligned}
$$

---

[3]If S acquires a VEV spontaneously, as considered in [369], the S mixes with the doublet Higgs and cannot be dark matter.

While m_0, κ_1 and κ_2 constitute a complete set of extra (as compared to the 2HDM) free parameters for the scalar sector of the 2HDMS Lagrangian, in practice it is more convenient to employ the DM mass m_S and the couplings λ_h and λ_H as the new independent set of free parameters associated with the S sector, together with the DM self-interaction λ_S. In the alignment limit of $\sin(\beta - \alpha) = 1$, for which the h has exactly SM-like couplings to VV and $f\overline{f}$, the portal couplings among them reduce to

$$\lambda_h = \kappa_1 \cos^2 \beta + \kappa_2 \sin^2 \beta \,, \tag{8.7}$$

$$\lambda_H = (\kappa_1 - \kappa_2) \sin \beta \cos \beta \,. \tag{8.8}$$

We also emphasize that although there is no ASS term in V_S due to CP, the CP-odd Higgs boson A still plays a role in determining the DM relic density through the creation/annihilation process $SS \longleftrightarrow AA$. We will discuss this issue in Section 8.2.2.

The quadrilinear couplings $\lambda_{HH}, \lambda_{hH}, \lambda_{hh}, \lambda_{AA}, \lambda_{H^+H^-}$ can also be expressed in terms of the κ_1, κ_2, α and β parameters:

$$\lambda_{AA} = \tfrac{1}{2}\lambda_{H^+H^-} = \tfrac{1}{2}(\kappa_1 \sin^2 \beta + \kappa_2 \cos^2 \beta)$$

$$\lambda_{hh} = \tfrac{1}{2}(\kappa_2 \cos^2 \alpha + \kappa_1 \sin^2 \alpha)\,, \quad \lambda_{HH} = \tfrac{1}{2}(\kappa_1 \cos^2 \alpha + \kappa_2 \sin^2 \alpha)\,, \tag{8.9}$$

$$\lambda_{hH} = \tfrac{1}{2}(\kappa_2 - \kappa_1) \sin 2\alpha \,.$$

We note that the above Lagrangian-level trilinear and quadrilinear couplings convert to Feynman rules according to:

$$g_{hSS,HSS} = -2\lambda_{h,H} v, \quad g_{hhSS,HHSS} = -4\lambda_{hh,HH}, \tag{8.10}$$

$$g_{hHSS} = -2\lambda_{hH}, \qquad g_{AASS} = g_{H^+H^-SS} = -4\lambda_{AA}\,. \tag{8.11}$$

The fermionic couplings in the 2HDMS depend upon the behavior of the fermionic fields under $\mathbb{Z}_2$ and $\mathbb{Z}'_2$. We assume that the fermions are even under $\mathbb{Z}'_2$ so that the S has no tri-linear coupling to $f\overline{f}$ [4]. Fermionic couplings to H_1 and H_2 inherit the structure of the 2HDM and still depend on the $\mathbb{Z}_2$ signs for fermions. We choose these so as to

---

[4]We do not consider here the possibility of coupling the singlet to the Majorana mass term for right-handed neutrinos, $s\nu^T_{Ri} C \nu_{Rj}$ for $i \neq j$. In fact such couplings are allowed if ν_{Ri} carry $\mathbb{Z}'_2$ charge, see [371].

forbid flavour-changing Yukawa couplings for the neutral Higgs bosons, resulting in the couplings listed in Table 5.4 for the models of Type I and Type II.

In the following we shall, in sequence, derive the theoretical constraints on the singlet parameters coming from the requirements on perturbativity, stability, unitarity and correct electroweak symmetry breaking.

- *Perturbativity (P)*

All quartic Feynman rules associated with the mass eigenstates $h, H, A, H^{\pm}, S$ are required to satisfy the standard perturbativity constraint, *i.e.* their absolute values must be $\leq 4\pi$. As regards the sector involving the S field, the quartic couplings of interest are those in which S^2 multiplies two 2HDM fields and the S^4 term. One can show that the quartic Feynman rules connecting S^2 to two neutral 2HDM fields, summarized above, are guaranteed to be smaller than 4π in absolute value if $|\kappa_1|, |\kappa_2| \leq 4\pi$ is imposed. However, these maximum values are only allowed for $\alpha = \pm\pi/4$. The Feynman rule for S^4 interactions being λ_S means that we must also impose $0 < \lambda_S \leq 4\pi$, the lower bound being that required for stability.

- *Vacuum Stability (S)*

We require that the vacuum is stable at tree level, which means that the potential in (8.2) has to be bounded from below. As already noted this requires first of all that $\lambda_S > 0$. Given this, the necessary and sufficient conditions for stability [5] consist of the standard ones in the 2HDM for the case that both κ_1 and κ_2 are positive.

$$\lambda_1, \lambda_2, \lambda_S > 0, \quad \lambda_3 + \lambda_4 - |\lambda_5| > -\sqrt{\lambda_1\lambda_2}, \quad \lambda_3 > -\sqrt{\lambda_1\lambda_2} \tag{8.12}$$

Whereas, for $\kappa_1 < 0$ and/or $\kappa_2 < 0$, vacuum stability depends on the value of the S self-interaction coupling λ_S and has to be guaranteed by satisfying the additional conditions.

$$\kappa_1 > -\sqrt{\tfrac{1}{12}\lambda_S\lambda_1}, \quad \kappa_2 > -\sqrt{\tfrac{1}{12}\lambda_S\lambda_2}, \tag{8.13}$$

$$-2\kappa_1\kappa_2 + \tfrac{1}{6}\lambda_S\lambda_3 > -\sqrt{4\left(\tfrac{1}{12}\lambda_S\lambda_1 - \kappa_1^2\right)\left(\tfrac{1}{12}\lambda_S\lambda_2 - \kappa_2^2\right)}, \tag{8.14}$$

$$-2\kappa_1\kappa_2 + \tfrac{1}{6}\lambda_S(\lambda_3 + \lambda_4 - |\lambda_5|) > -\sqrt{4\left(\tfrac{1}{12}\lambda_S\lambda_1 - \kappa_1^2\right)\left(\tfrac{1}{12}\lambda_S\lambda_2 - \kappa_2^2\right)}. \tag{8.15}$$

---

[5]The full derivation can be found in Appendix A of Ref. [11].

- *S-Matrix unitarity (U)*

In addition, there are constraints deriving from unitarity that are closely correlated with the constraints from perturbativity. Indeed, the dominant non-vanishing contributions to amplitudes for two-body scattering at high energy come from the processes mediated by quartic couplings. Therefore, the unitarity constraint for $J = 0$ partial waves, $|a_0| \leq 1/2$, reduces to a constraint on these quartic couplings. Concretely, this demands the largest eigenvalue of the full multi-state scattering matrix to be less than the upper limit. [6]

$$max\{|a_{1,2,3}|\}, |f_+|, |e_1|, |p_1|, 2\kappa_1, 2\kappa_2 \leq 8\pi \tag{8.16}$$

for which the solutions obtained in the Higgs basis of the 2HDM, that was defined in Section 5.1.1, are

$$
\begin{aligned}
f_+ &= 2\Lambda_3 - \Lambda_4 + \frac{5}{2}\Lambda_5 - \frac{1}{2}\Lambda_6 \\
e_1 &= 2\Lambda_3 - \Lambda_4 - \frac{1}{2}\Lambda_5 + \frac{5}{2}\Lambda_6 \\
p_1 &= 2(\Lambda_3 + \Lambda_4) - \frac{1}{2}\Lambda_5 - \frac{1}{2}\Lambda_6
\end{aligned}
\tag{8.17}
$$

and the $a_{1,2,3}$ are the roots of the cubic polynomial equation

$$x^3 - 12\left(\tilde{\Lambda}^+_{321} + \frac{1}{24}\lambda_S\right)x^2 + \left[36\overline{\Lambda}_{123} + (2\Lambda_3 - \tilde{\Lambda}^+_{456})(10\Lambda_3 + \tilde{\Lambda}^+_{456}) + 6\lambda_S\tilde{\Lambda}^+_{321} - 4(\kappa_1^2 + \kappa_2^2)\right]x$$

$$- 18\lambda_S\overline{\Lambda}_{123} - \frac{1}{2}\lambda_S(2\Lambda_3 - \tilde{\Lambda}^+_{456})(10\Lambda_3 + \tilde{\Lambda}^+_{456}) + 24(\kappa_1^2\Lambda^+_{23} + \kappa_2^2\Lambda^+_{13}) - 8\kappa_1\kappa_2(4\Lambda_3 + \tilde{\Lambda}^+_{456}) = 0$$

where $\tilde{\Lambda}^+_{ijk} = \Lambda_i + \frac{\Lambda_j + \Lambda_k}{2}$ and $\overline{\Lambda}_{ijk} = \Lambda_i\Lambda_j + \Lambda_i\Lambda_k + \Lambda_j\Lambda_k$.

- *Electroweak Symmetry Breaking (EW)*

In order to ensure a stable DM particle S, one has to require $\langle S \rangle = 0$ at the global minimum of the scalar potential, Eq. (8.2). In practice, we traverse all the minima of Eq. (8.2) numerically and then eliminate the points for which the global minimum is not at $\langle S \rangle = 0, \langle H_1 \rangle \neq 0, \langle H_2 \rangle \neq 0$.

In combination, one can find the allowed regions in the (κ_1, κ_2) parameter space after sequentially imposing the various constraints discussed above, and map them into the λ_h

---

[6]In Appendix B of Ref. [11], we describe in more detail the unitarity bounds and give explicit formulae for the scattering matrix of two-body processes in the scalar sector of the 2HDMS model.
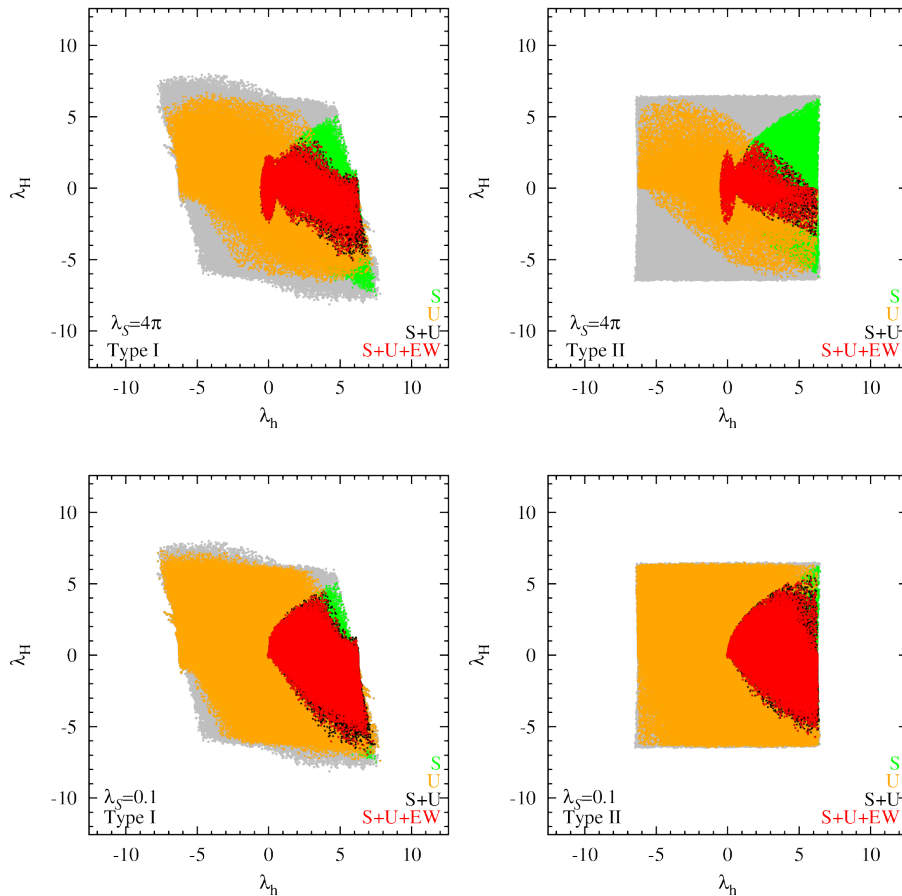
Figure 8.2. The plot shows the impact of the perturbativity (P), vacuum stability (S), unitarity (U) and electroweak symmetry breaking (EW) global minimum bounds discussed in Sec. 8.2.1 on the (λ_h, λ_H) plane. At the first level, the grey points are those which satisfy P — all subsequent point layers obey P. Note that $|\kappa_1|, |\kappa_2| \leq 4\pi$ contains the perturbative region. Subsequent point layers were plotted in the following order: points after the stability bound, S (green), points after the unitarity bound, U (orange), points after the stability and unitarity bounds, S+U (black), points after the stability, unitarity and EW bounds, S+U+EW (red). The value of the λ_S parameter was set to 4π (0.1) in the upper (lower) plots. In this figure, no restriction on m_S is imposed.

vs. λ_H parameter space for the consideration of phenomenology study. This is displayed in Fig. 8.2. In this figure, no restriction on m_S is imposed. In fact, the P+S+U+EW constraints are much more restrictive for $m_S < m_h/2$. This is illustrated in Fig. 8.3. In particular, note that the maximum value of λ_H that is allowed is of order 3 in magnitude, at large λ_S, and is very tiny for small λ_S. As a result, very large values of m_H cannot result in sufficient annihilation through the H pole diagram when $m_S < m_h/2$ given that
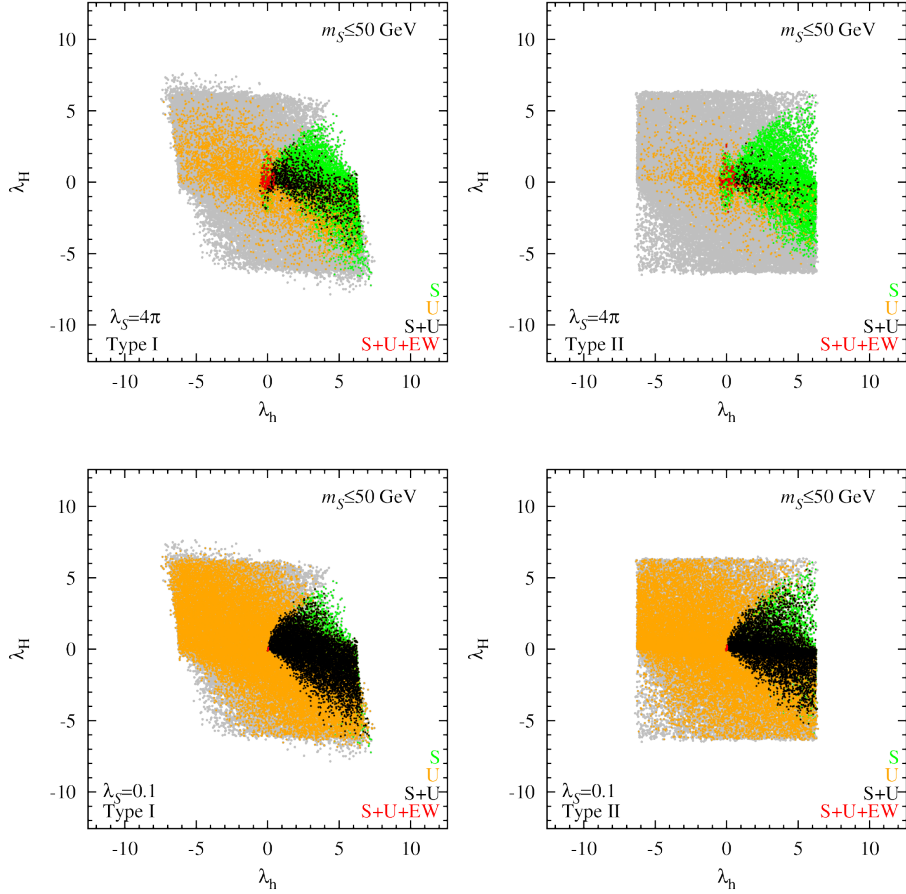
Figure 8.3. Bounds in the (λ_h, λ_H) plane associated with the sequential constraints as described in the caption for Fig. 8.2 for parameter choices yielding $m_S \leq 50$ GeV. We observe that EW is an especially strong constraint in this mass region.

the h pole diagram is suppressed because λ_h must be very small in order to avoid too large BR($h \to SS$).

Of course, P+S+U+EW are only the most basic constraints. In the following sections, we will show that once Ωh^2 is required to agree with observations, then $|\lambda_h|$ and $|\lambda_H|$ are restricted to values $\lesssim 0.2$ and $\lesssim 2.5$, respectively. When $m_S < m_h/2$, BR($h \to SS$) ≤ 0.1 further constrains $|\lambda_h|$ to values $\lesssim 0.01$.

Demanding perturbativity, tree level vacuum stability, and tree level unitarity for the overall 2HDMS potential and properly choosing the electroweak vacuum[7], it turns out

---

[7]The presence of an extra singlet would significantly change the behaviour of the potential and thus the theoretical constraints such as perturbativity, tree level vacuum stability and tree level unitarity needs a re-examination based on the 2HDM. A dedicate illustration and full derivation for these conditions can be found in Ref. [11].

that the maximum value of the DM coupling with the non-SM Higgs, λ_H (if h is SM-like with $m_h \sim 125$ GeV) or λ_h (if H is the SM-like one), is $\mathcal{O}(1)$ in magnitude, at large λ_S, whereas it is very tiny for small λ_S. [8] As a result, one finds that very large values of m_H cannot result in sufficient annihilation for a light DM mass ($m_S < m_h/2$) through the H-mediator diagram given that the h-mediator diagram is suppressed.

8.2.2 Experimental constraints on 2HDMS

Before starting our analysis of the model, we would like to summarize the experiments that impact the extra singlet S particle.

- *Dark matter relic abundance*

In the 2HDMS, the S particle provides the only candidate for DM and thus should comprise the total relic abundance of the early Universe. To a good approximation, the relic density is given by

$$\Omega_S \simeq 1.07 \times 10^9 \frac{x_f}{\sqrt{g_*}\, M_{\mathrm{Pl}} \langle \sigma_{\mathrm{ann}} v_{\mathrm{rel}} \rangle} \ \mathrm{GeV}^{-1} \tag{8.18}$$

where $x_f = m_S/T_f \simeq 20$ is the typical freeze-out temperature of a WIMP [372], M_{Pl} is the Planck mass, g_* is number of relativistic degrees of freedom, $\langle \sigma v \rangle$ is the thermally averaged cross section for SS annihilation into the SM particles (*i.e.* leptons and quarks , $f\bar{f}$, and gauge bosons, W^+W^-, ZZ, denoted collectively as $X\overline{X}$) and into Higgs bosons (hh, hH, HH, AA, H^+H^-). The Feynman diagrams for all the processes are shown in Fig. 8.4. First, the process of annihilation into the SM particles is mediated by an s-channel h or H only. Following [362] (see also [367], which however has small numerical factor errors), we find

$$\langle \sigma_{SS \to X\overline{X}} v_{\mathrm{rel}} \rangle = \sum_{\mathcal{H}=h,H} \left| \frac{g_{\mathcal{H}SS} C_X^{\mathcal{H}}}{4m_S^2 - m_{\mathcal{H}}^2 + i\Gamma_{\mathcal{H}} m_{\mathcal{H}}} \right|^2 \frac{\Gamma_{\mathrm{SM}}(\mathcal{H}^* \to X\overline{X})}{2m_S} \tag{8.19}$$

where $C_X^{\mathcal{H}}$ is the coupling of $\mathcal{H}$ to $X\overline{X}$ relative to the coupling of the SM Higgs boson to $X\overline{X}$ and $\Gamma_{\mathrm{SM}}(\mathcal{H}^* \to X\overline{X})$ stands for the SM partial width in the $X\overline{X}$ final state calculated at invariant mass $\sqrt{s} = 2m_S$. (Note: for $X = Z$, then $\overline{X} = Z$ also. In this

---

[8]For the purpose of generating as many points as possible, we maximize the parameter $\lambda_S = 4\pi$ in the numerical analysis.
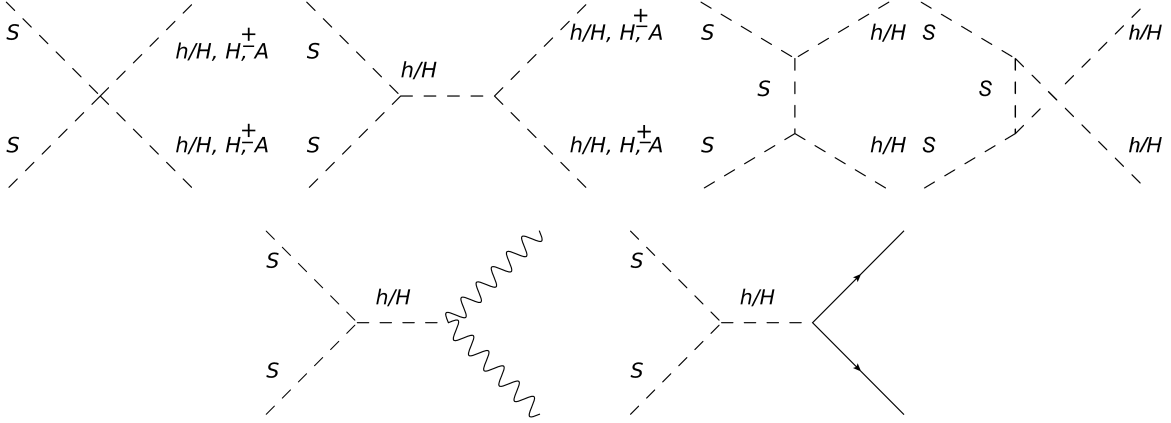
Figure 8.4. Singlet annihilation diagrams relevant for the relic density calculation.

case, $\Gamma(\mathcal{H}^* \to X\overline{X})$ must include the $1/2!$ for identical particles in the final state.) In this equation, the total width, $\Gamma_{\mathcal{H}}$, must include the width for $\mathcal{H} \to SS$ and any partial width modifications relative to the SM width for the various SM channels (in particular, the enhancement of $\Gamma(H \to b\bar{b})$ at large $\tan\beta$ in the Type II case.)

Second, there are all the channels containing Higgs pairs. For the $(H_i H_i) = (AA)$ or $(H^+ H^-)$ final states, the relevant diagrams are the first two diagrams in the upper row of the figure, which include not only s-channel h or H exchange but also a four-point contact self-coupling. For final states containing CP-even Higgs pairs, $(H_i H_j) = (hh), (HH), (hH)$, there are contributions from t- and u-channel S exchange (the last two diagrams with different topologies in the top row of Fig. 8.4) in addition to the s-channel h or H exchange diagrams and the four-point contact self-coupling. A formula that applies to all these different cases is most easily given in terms of the Feynman rules for the various relevant vertices: the quartic Feynman rules were given earlier in Eq. (8.11) and the trilinear coupling $g_{\mathcal{H}hH}$ Feynman rule can be found in Appendix F of [39]. We find

$$
\langle \sigma_{SS \to H_i H_j} v_{\text{rel}} \rangle = \frac{\beta(m_{H_i}, m_{H_j})}{32(1+\delta_{ij})\pi m_S^2} \bigg| g_{H_i H_j SS} + \sum_{\mathcal{H}=h,H} \frac{g_{\mathcal{H}SS} g_{\mathcal{H}H_i H_j}}{4m_S^2 - m_{\mathcal{H}}^2 + i\Gamma_{\mathcal{H}} m_{\mathcal{H}}}
$$
$$
+ 2\delta_{CP} \frac{g_{H_i SS} g_{H_j SS}}{\frac{1}{2}(m_{H_i}^2 + m_{H_j}^2) - 2m_S^2} \bigg|^2 ,
\tag{8.20}
$$

where

$$
\delta_{CP} = \begin{cases} 0 & H_i H_j = AA, H^+ H^- \\ 1 & H_i H_j = hh, HH, hH \end{cases}
\tag{8.21}
$$

and

$$\beta(m_{H_i}, m_{H_j}) = \left(1 - \frac{m_{H_i}^2 + m_{H_j}^2}{2m_S^2} + \frac{(m_{H_i}^2 - m_{H_j}^2)^2}{16m_S^4}\right)^{1/2}. \qquad (8.22)$$

Note that some final states will typically be kinematically closed. In particular, for $m_S < m_h$ only the $f\bar{f}$ ($f \neq t$), VV and, possibly, AA channels will be allowed.

In order to illustrate results of the scan over singlet parameter space, in Figs. 8.5 and 8.6 we show Ωh^2 as a function of m_S for representative 2HDM points when scanning over the remaining singlet parameters. The 2HDM parameters for these four points are given in Table 8.1. For the first case, Fig. 8.5, the 2HDM parameters are such that low m_S is eliminated when correct EWSB is imposed in addition to stability and unitarity. In the second case, Fig. 8.6, a large range of m_S values is consistent with EWSB and the observed $\Omega h^2 \sim 0.1$. Note that for the case of Fig. 8.6, m_H is relatively small. This means that relatively modest values of $|\lambda_H|$ provide adequate annihilation for achieving the observed Ωh^2. In contrast, in the case of Fig. 8.5 relatively large values of m_H were employed. As a result, quite large values of $|\lambda_H|$ would be needed for sufficient annihilation. However, as shown in Fig. 8.3, in the region of $m_S \leq 50$ GeV P+S+U+EW (especially the latter) require $|\lambda_H| \lesssim 3$, a value that is insufficient, implying that no points satisfying P+S+U+EW (*i.e.* red points) are found in this region. In addition, at low m_S values, it is possible that BR($h \to SS$) is not below the 68% C.L. upper limit of ~ 0.1 required by fitting of the h properties to the LHC data — see next subsection. The figures show the impact of the additional requirement of BR($h \to SS$) ≤ 0.1.

Table 8.1. 2HDM parameters for the plots of Figs. 8.5 and 8.6. Masses in GeV; m_{12}^2 in GeV^2.

BMP #	$\tan\beta$	$\sin\alpha$	m_{12}^2	m_h	m_H	m_A	$m_{H^\pm}$	λ_1	λ_2	λ_3	λ_4	λ_5
I-1	1.586	-0.587	5621	123.71	534.25	645.13	549.25	5.98	1.683	3.203	-1.032	-4.81
II-1	0.969	-0.721	1.251×10^5	127.96	678.98	600.36	563.18	3.463	4.046	-0.997	-0.389	-1.816
I-2	1.346	-0.663	-2236	126.49	168.01	560.92	556.94	1.199	0.59	10.101	-5.12	-5.267
II-2	2.092	-0.4096	-1.264×10^4	125.89	137.86	451.33	398.76	3.984	0.454	5.732	-2.422	-3.896

In both Fig. 8.5 and Fig. 8.6, one can see a sharp dip in Ωh^2 at $m_S \simeq 63$ GeV which arises from on-shell h exchange, as well as a sudden drop in Ωh^2 near 80/90 GeV due to the WW and ZZ final states becoming available in the SS annihilation (the relic abundance is inversely proportional to the annihilation cross section). A similar threshold appears
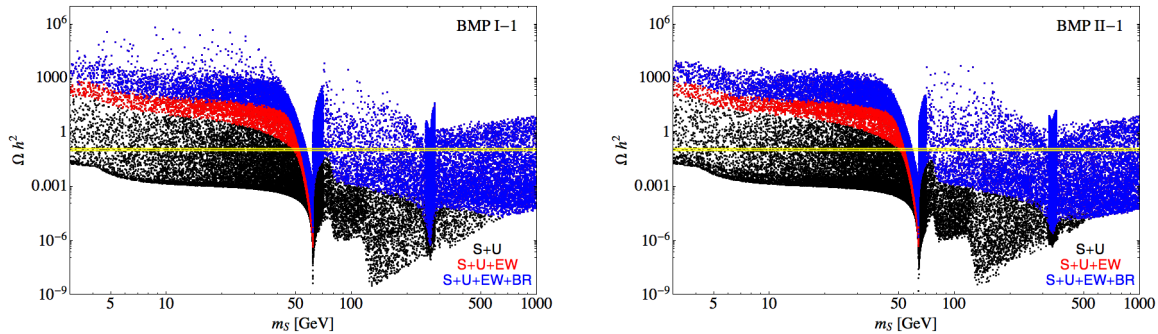
Figure 8.5. Results for the relic abundance Ωh^2 as a function of m_S coming from a scan over the singlet parameter space for a fixed 2HDM point. The sample 2HDM parameters employed are given in Table 8.1. All points satisfy perturbativity as defined earlier. Black points satisfy the stability and unitarity conditions, red points satisfy also the EWSB conditions. Blue points satisfy S+U+EW *and* have BR($h \to SS$) ≤ 0.1. The yellow band is the recent $\pm 3\sigma$ Planck window $\Omega h^2 = 0.1187 \pm 0.0017$ at 68% CL [373]. We emphasize that the LUX and other limits on DM detection are not yet imposed in these plots.
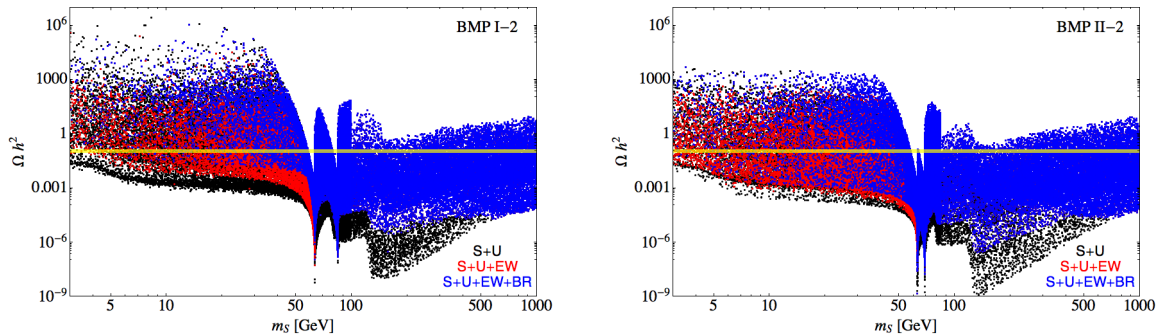
Figure 8.6. As for Fig. 8.5, but for different 2HDM points, see the last two points of Table 8.1, chosen so that a large fraction of the low m_S values pass all constraints other than limits on DM detection.

around $m_S \sim m_t$. One can also observe sharp dips in Ωh^2, corresponding to s-channel exchange of the heavy scalar H, at $m_S \simeq m_H/2 \sim 265$ GeV and 340 GeV for Type I and Type II, respectively, for Fig. 8.5 and at $m_S \sim 85$ GeV and 68 GeV in the case of Fig. 8.6.

- *Higgs invisible/unseen decays*

In addition to decays into SM particles, the CP-even Higgs bosons h and H of the 2HDMS have a number of possible invisible and/or "unseen" decays. By "unseen" we mean decay modes that contain visible particles, but that the experimental analyses have not explored and/or are not yet able to place useful limits on. In the 2HDMS, the interaction of Higgs with S would apparently constitute the invisible decay into SS state

and the potentially important unseen decay modes are $h \to AA$ and $H \to AA, hh$. As demonstrated in Section 5.7, one is always able to find a parameter space in which the 125 GeV Higgs has sufficiently small branching ratio into possible light Higgs bosons. Thus, here our concern is only the $h, H \to SS$ decay widths, which are given by:

$$\Gamma(h_i \to SS) = \frac{1}{2\pi} \frac{g_{h_i SS}^2}{m_{h_i}} \sqrt{1 - \frac{4m_S^2}{m_{h_i}^2}} \tag{8.23}$$

where $i = 1, 2$ denotes h, H and the dimensional Feynman-rule couplings $g_{h_i SS}$ are given in Eq. (8.11). In what follows, it will be most convenient to discuss results in the space of the dimensionless λ_H vs. λ_h parameters, where $g_{h_i SS} = -2\lambda_{h_i} v$. In general, such decay (when kinematically open) dominates the decay of the Higgs at 125 GeV and would significantly disturb the fit of the 125 GeV Higgs to the LHC data. In fact, the constraints on such an invisible decay are quite strong: $BR(h \to SS) \leq 10\%$ at 68% C.L. [170]. We illustrate an example of h being SM-like state at 125 GeV in Fig. 8.7 presenting points in the (λ_h, λ_H) plane, coloured with respect to the resulting $BR(h \to SS)$. It shows the bound $BR(h \to SS) \leq 10\%$ is violated for most $m_S < 55$ GeV points in the full 2HDMS parameter space leaving only a small number of points with $\lambda_h \ll 1$ for which $BR(h \to SS) \leq 0.1$. This means the constraint of small branching ratio for invisible decay plays a major role in eliminating much parameter space for the low-mass DM scenarios. For simplicity, one can switch off the interaction of the 125 GeV Higgs with the S so that the presence of S will become irrelevant to the Higgs data, while the other CP-even Higgs and the A and $H^\pm$ can be used to provide additional channels for early-universe DM annihilation.

- *DM-nucleon scattering direct detection*

The rate at which DM-particles scattering off nuclei can be detected is directly related to the DM-nuclei scattering cross-section [336], which is given by:

$$\sigma_{\text{DM}-N} = \int_0^{4\mu_r^2 v^2} \frac{d\sigma(q=0)}{d|\mathbf{q}|^2} d|\mathbf{q}|^2 = \frac{4\mu_r^2}{\pi} f_p^2 \left[Z + \frac{f_n}{f_p}(A - Z) \right]^2 \tag{8.24}$$

where $\mathbf{q}$ is the momentum transfer, $\mu_r = (m_N m_S)/(m_N + m_S)$ and v is the relative velocity.
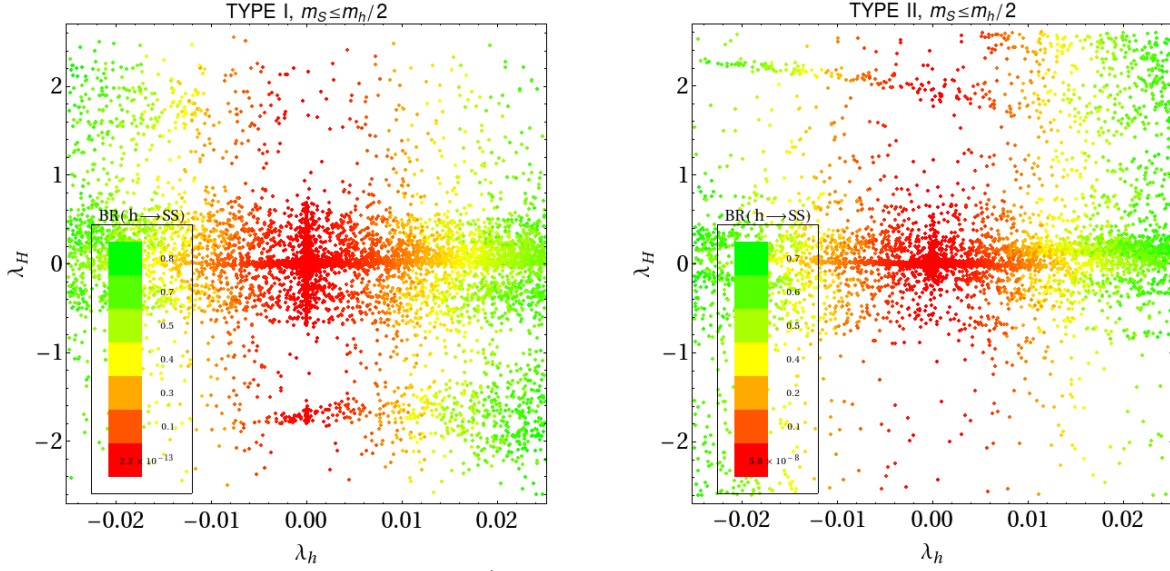
Figure 8.7. The couplings of h/H to SS after imposing the full set of constraints including Ωh^2 but not LUX and without the $\mathrm{BR}(h \to SS) \leq 0.1$ constraint. Coloring is according to $\mathrm{BR}(h \to SS)$: points with small BR are red, large BR points are green. The 2HDM points employed in this scan are the red points of Fig.1 in Ref. [11] that provide a fit the LHC/Tevatron signal strengths at 68% C.L.. A full scan over the singlet sector parameters is performed subject to the standard P+S+U+EW constraints.

The couplings of DM to the proton and neutron, f_p and f_n, can be expressed as

$$f_N = \frac{m_N}{2m_S} \left(\sum_{q=u,d,s} f_{Tq}^N \frac{\lambda_{SSqq}}{m_q} + \frac{2}{27} f_{TG}^N \sum_{q=c,b,t} \frac{\lambda_{SSqq}}{m_q} \right), \tag{8.25}$$

where m_N is the mass of the nucleon and f_{Tq}^N is the form factor of the nucleon (see Table 8.2) satisfying the relation

$$f_{TG}^N = 1 - \sum_{q=u,d,s} f_{Tq}^N, \quad (N = p, n). \tag{8.26}$$

and, in addition, λ_{SSqq} is the effective coupling of the DM particle S to a q-flavor quark component in the nucleon. In the 2HDMS, this interaction derives from t-channel exchange of the h and H, as illustrated in Fig. 8.8. Thus, in the limit of zero momentum transfer, the Higgs $h_i = h$ or H propagator reduces to $\frac{i}{-m_{h_i}^2}$ and we find

$$\lambda_{SSqq} = \sum_{h_i=h,H} \frac{g_{h_iSS}g_{h_iq\bar{q}}}{-m_{h_i}^2} = \left(\frac{2\lambda_h}{m_h^2} C_q^h + \frac{2\lambda_H}{m_H^2} C_q^H \right) m_q, \tag{8.27}$$

where we have used $g_{h_iq\bar{q}} = -i\frac{gm_q}{2m_W}C_q^{h_i}$ ($m_W = \frac{1}{2}gv$ in our convention) with the quark coupling factors $C_q^{h_i}$ for Type I and II models as listed in Table 5.4 and the Feynman rule

270
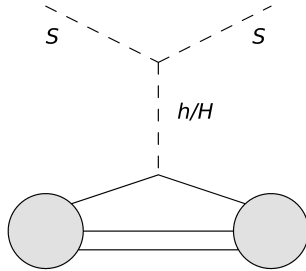
Figure 8.8. Feynman diagram for the scattering of DM off a nucleon.

Table 8.2. Form factors extracted from microOMEGAs 3.0.

q	u	d	s
f_{Tq}^{p}	0.0153	0.0191	0.0447
f_{Tq}^{n}	0.0110	0.0273	0.0447

$g_{h_i SS}$ expressions given in Eq. (8.11). In practice, direct detection rates in our calculation have been evaluated using microOMEGAs [374], including QCD NLO corrections.

8.2.3 Methodology and scan strategy

Instead of scanning over the full 2HDMS parameter space, for simplicity we used selected points from the 2HDM phenomenologically allowed points of [7] (labelled as "postLHC8-FDOK"), as outlined at the beginning of Section 8.2. For each phenomenologically viable 2HDM point, we perform a scan over the extra singlet parameters: $m_S, \lambda_h, \lambda_H$. We then check theoretical constraints for the 2HDMS model including perturbativity, stability, unitarity and proper electroweak symmetry breaking, as discussed in Section 8.2. Since the extra scalar S does not acquire a VEV, it does not mix with the other Higgs bosons h and H. As a result, the experimental constraints from electroweak precision tests (STU parameters), B physics, direct searches at LEP and also limits on the heavier Higgs bosons (H and possibly A) are barely influenced by the presence of the singlet scalar S. Therefore, the postLHC8-FDOK points in the 2HDM can be adopted as good starting points when expanding to the 2HDMS. As we have noted, the only caveat that arises is the need to take into account the possibility of $h \to SS$ decays when the scalar S

is light. Substantial $\text{BR}(h \to SS)$ will spoil the pure 2HDM fit performed in [7]. Including limits from the current Higgs invisible decay searches at the LHC one finds roughly that $\text{BR}(h \to SS) \leq 30\%(10\%)$ is required at $95\%(68\%)$ C.L. Therefore, as discussed earlier, we impose a cut of $BR(h \to SS) \leq 10\%$ for all points presented in the following context (except for a few situations as described later) in order to maintain the LHC signal fit and consistency with invisible decay limits. Finally, we use microOMEGAs [374] to calculate the relic abundance of the DM candidate S and require that the predicted Ωh^2 fall within the $\pm 3\sigma$ Planck window $\Omega_{\text{DM}}^{\text{exp}} = 0.1187 \pm 0.0017$ at 68% C.L. [373]. Hereafter, we refer to this set of constraints as the "preLUX" constraints.

Note that we adopt different scan strategies in the various regions of m_S so as to achieve a maximum density around the most interesting points that pass all theoretical and experimental constraints, depending on the status of the exotic decay $h \to SS$:

- low mass region $(1 - 55 \text{ GeV})$ where the decay is open and could be substantial without λ_h being very small;

- resonance region $(55 - 70 \text{ GeV})$ where m_S is not far from the h pole location. For $m_S < m_h/2$, one finds that, after imposing P+S+U+EW, λ_h is sufficiently limited that $\text{BR}(h \to SS) \leq 0.1$. In fact, in this region, the strongest constraint on λ_h comes from the need to avoid too much annihilation.

- high mass region $(70 - 1000 \text{ GeV})$ where the decay is absolutely closed.

The scans are also preformed in a different way for Type I and Type II models.

8.2.4 DM full mass analysis

For the points satisfying the "preLUX" constraints, we calculate the cross section for the scattering of the S off a nucleon and compare the predicted value $\overline{\sigma}_{\text{DM}-p}$ (after rescaling by Θ in the case of Type II) to the latest LUX limits for the DM-proton cross section, denoted $\sigma_{\text{DM}-p}^{\text{LUX}}$ (which are obtained assuming $f_n/f_p = 1$). If the points obey the condition $\overline{\sigma}_{\text{DM}-p} \leq \sigma_{\text{DM}-p}^{\text{LUX}}$, they are not excluded by the LUX limit. We are going to expand the analysis for DM phenomenology separately in Type I and Type II.

- *Type I analysis*
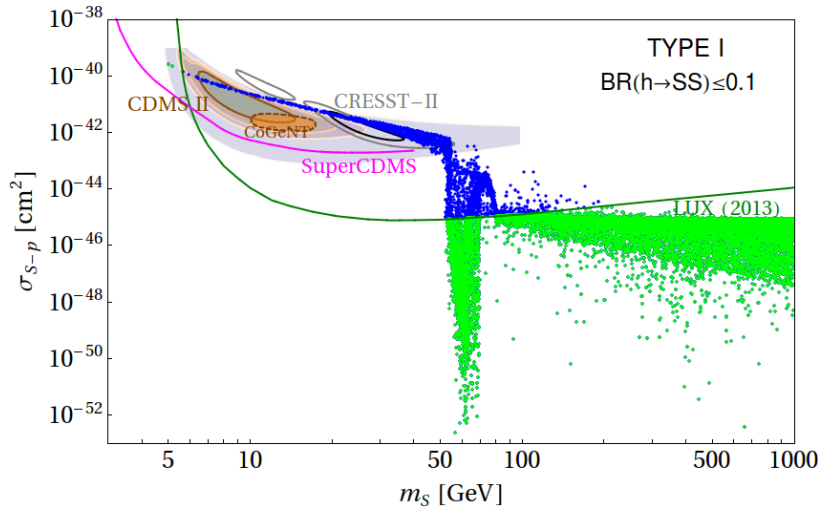
Figure 8.9. Cross section for DM-proton scattering for the Type I model. All points shown satisfy the full set of preLUX constraints, including $\mathrm{BR}(h \to SS) \leq 0.1$, while the green points satisfy in addition the LUX limits. The pink and green lines are the limits from SuperCDMS and LUX, respectively. Recall that for Type I, $f_n/f_p \sim 1$ and so no rescaling is required between target types. Also shown are contours corresponding to the CRESST-II, CoGeNT and CDMS II positive signal regions. In the case of CRESST-II, the darker black contour is at 68% C.L. and the lighter grey contours are at 95% C.L. In the case of CoGeNT (orange region) we show only the 90% C.L. contour. For CDMS II, we display contours (using various levels of grey) at 68%, 90%, 95% and 99% C.L.

As mentioned in Section 8.1, it is of particular importance to adopt the assumption that DM has equal coupling to the neutron and proton, that is to say the ratio $f_n/f_p = 1$. Indeed, this equality approximately holds in the Type I model because of the universal coupling structure with up-type and down-type quarks, see Table 5.4. In fact, $\frac{\lambda_{SSqq}}{m_q}$ is independent of quark-species and the common couplings $C_{U,D}^h$ and $C_{U,D}^H$ in the Type I model can be factored out and will then cancel out in the ratio. From eqs. (8.25) and (8.27), one can then derive the ratio of f_n/f_p in the Type I case:

$$\frac{f_n}{f_p} = \frac{m_n}{m_p} \frac{\sum_{q=u,d,s} f_{Tq}^n + \frac{2}{27} f_{TG}^n \sum_{q=c,b,t}}{\sum_{q=u,d,s} f_{Tq}^p + \frac{2}{27} f_{TG}^p \sum_{q=c,b,t}} \approx 1.01208 \tag{8.28}$$

This result implies that isospin-violating effects for DM-nucleon scattering are negligible for a Type I 2HDMS and that one can thus directly compare results of our calculations with all experimental bounds including the LUX and SuperCDMS upper limits and the CDMS II/CRESST positive signals.

In Fig. 8.9 we present the cross section versus m_S for the Type I model. Since $f_n/f_p \sim 1$

in the case of the Type I model, all experimental results can be displayed on the same plot. Points obeying the LUX limit are shown in green. Points that do not pass the LUX limit but do satisfy all preLUX conditions (including correct Ωh^2 and $\mathrm{BR}(h \to SS) \leq 0.1$) are shown in blue. Note that few green points at very low m_S that pass the LUX limit are excluded by the SuperCDMS limit. Note that the Type I predictions for $\overline{\sigma}_{\mathrm{DM}-p}$ agree pretty well with CDMS II/CRESST-II data, but, of course, disobey the LUX limit. The narrowness of the $\overline{\sigma}_{\mathrm{DM}-p}$ band at low m_S can be understood as follows. In this mass region, we know that $\lambda_h \simeq 0$, DM annihilation and scattering off nucleons are thus realized via H exchange in the s- and t-channels, respectively. Both processes are essentially controlled by the ratio λ_H/m_H^2. We observe that once the constraints of $BR(h \to SS) \leq 10\%$ and good Ωh^2 are both satisfied λ_h and λ_H are roughly fixed. As a result, the predicted value of σ_{S-p} as a function of m_S is constrained to a narrow band that happens to pass through the CDMS II/CRESST-II preferred regions. However, the CDMS II/CRESST-II regions are simply not consistent with the combination of LUX and SuperCDMS limits in the Type I model. Finally, once $m_S \gtrsim 55$ GeV essentially all of the points that are consistent with preLUX constraints also pass the LUX limit (SuperCDMS limits do not extend to masses $\gtrsim 40$ GeV).

- *Type II analysis*

We now turn to the Type II model. In contrast to Type I, the relation $f_n/f_p = 1$ is not always true in the Type II model due to the non-universal pattern of the Yukawa couplings for the Higgs. In order to compare the predicted cross-sections for DM-nucleon scattering with the results presented by the experimental groups, we define the nucleon-normalized cross section, $\overline{\sigma}_{\mathrm{DM}-p}$, following [347, 348]:

$$\overline{\sigma}_{\mathrm{DM}-p} = \sigma_{\mathrm{DM}-p} \, \Theta_X(f_n, f_p) \tag{8.29}$$

where $\sigma_{\mathrm{DM}-p}$ is the predicted DM-proton cross-section and the rescaling factor Θ_X is defined as

$$\Theta_X(f_n, f_p) \equiv \begin{cases} \left[\frac{Z}{A} + \frac{f_n}{f_p}\left(1 - \frac{Z}{A}\right)\right]^2, & \text{single isotope detector} \\[2mm] \frac{\sum_I \eta_I \mu_{A_I}^2 [Z + f_n/f_p(A_I - Z)]^2}{\sum_I \eta_I \mu_{A_I}^2 A_I^2}, & \text{multiple isotope detector} \end{cases} \tag{8.30}$$

where I runs over all isotopes present in the detector X and η_I is the relative abundance of the I'th isotope. Note that if $f_n/f_p = 1$, then $\Theta_X(f_n, f_p) = 1$. However, when $f_n/f_p \neq 1$, $\Theta_X(f_n, f_p)$ will depend upon the isotope abundances and is therefore determined by the properties of the chemical elements used in the various detectors. It was pointed out in [348–350, 375] that the scattering amplitudes of DM with proton and neutron may interfere destructively in such a way as to achieve $f_n/f_p \sim -0.7$, the value for which the resulting LUX exclusion limits are not in strong conflict with the favored signal regions of the Silicon-based CDMS II experiment and the Germanium-based CoGeNT experiment. However, these positive signal regions are in direct conflict with the limits obtained by SuperCDMS [376, 377]. In any case, in order to interpret any given DM scattering result, it is necessary to compute f_n/f_p for each Type II parameter point. Further, f_n/f_p in general depends on the singlet sector parameters.

However, there is an interesting special case in which f_n/f_p depends only on the 2HDM parameters. Recalling that the positive CDMS II and CoGeNT signals are both at rather low $m_S \sim 6 - 12$ GeV and noting that $BR(h \to SS)$ will be large for such masses unless λ_h is very small, it is useful to give an approximation for f_n/f_p in the limit of $\lambda_h \to 0$, *i.e.* in the limit of ignoring the h term in Eq. (8.25). In this limit, the value of f_N depends only on the quark couplings of the H:

$$f_N = \frac{m_N}{2 m_S m_H^2} \left\{ \left[f_{Tu}^N + \frac{2}{27} \left(f_{TGc}^N + f_{TGt}^N \right) \right] C_u^H + \left(f_{Td}^N + f_{Ts}^N + \frac{2}{27} f_{TGb}^N \right) C_d^H \right\}, \quad (N = p, n).$$
$$(8.31)$$

In Fig. 8.10, we display the resulting f_n/f_p as a function of $\sin\alpha$ for the Type II points from [7] that give Higgs boson property fits at the 95% C.L. or better. There, we see a large range of f_n/f_p values, ranging from $+1.5$ to ~ -0.9. However, for the 68% C.L. Type II points that we include in our study, points with substantially negative f_n/f_p are rather sparse, with the most negative value associated with a single isolated point close to -0.7. This is just an accidental result given the scanning procedure/density employed in [7]. We will offer a dedicate study on how to achieve a negative value of f_n/f_p and extensively discuss the role of isospin-violating effect in the next section.

Adopting the parameters in [347] to calculate the rescaling factor Θ_{Xe} for the Xenon-
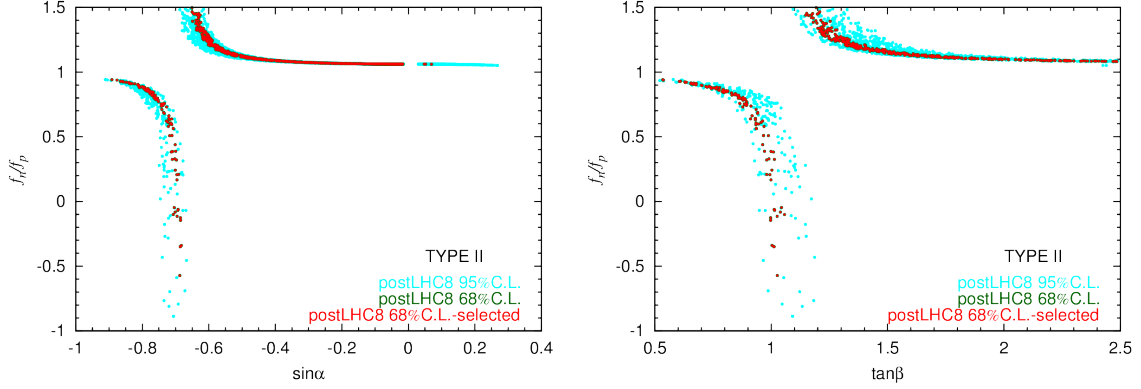
Figure 8.10. f_n/f_p in the limit of $\lambda_h = 0$ as a function of $\sin\alpha$ and $\tan\beta$ for the 68% C.L. Type II 2HDM scan points.
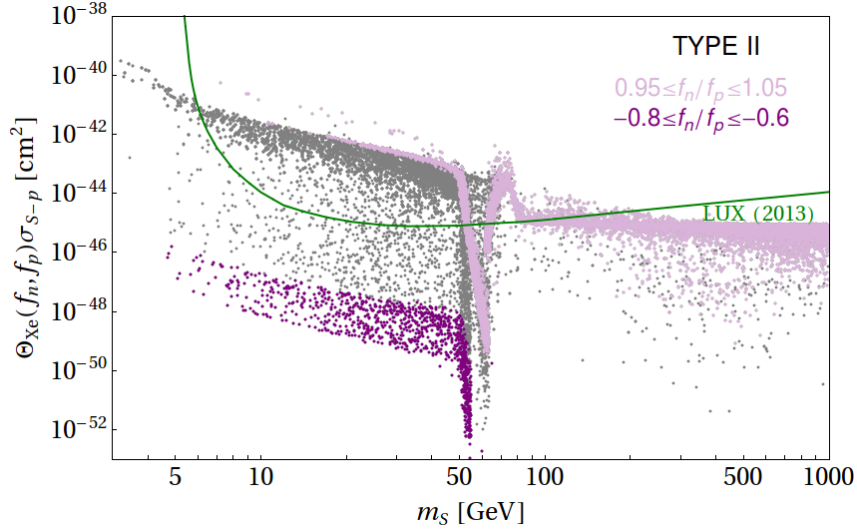
Figure 8.11. Cross section for DM-proton scattering for the Type II model rescaled by the function Θ_X defined in Eq. (8.30), where X = Xe for a Xenon-based detector. All points plotted satisfy the preLUX constraints *except* BR($h \rightarrow SS$) ≤ 0.1 (*i.e.* they satisfy the theoretical constraints for 2HDMS, 2HDM fitting at 68% C.L. and the constraint on Ωh^2). In the plot, for the light purple points the ratio f_n/f_p is within the range (0.95, 1.05). For the darker purple points $-0.8 \leq f_n/f_p \leq -0.6$.

based detectors, we present in Fig. 8.11 the overall picture for Type II in terms of the $\overline{\sigma}_{DM-p}$ cross sections. In the left plot, we impose all preLUX constraints (including Ωh^2 in the 3σ window) other than BR($h \rightarrow SS$) ≤ 0.1. Points with $f_n/f_p \sim 1$ (for which $\Theta_{Xe} \sim 1$) are singled out as are points with $f_n/f_p \sim -0.7$. To explore in more detail the level of inconsistency between the LUX and SuperCDMS limits and the positive signal regions for CDMS II and CoGeNT, we present Fig. 8.12 which focuses on the $m_S \leq 35$ GeV mass range. All plotted points obey the full set of preLUX constraints
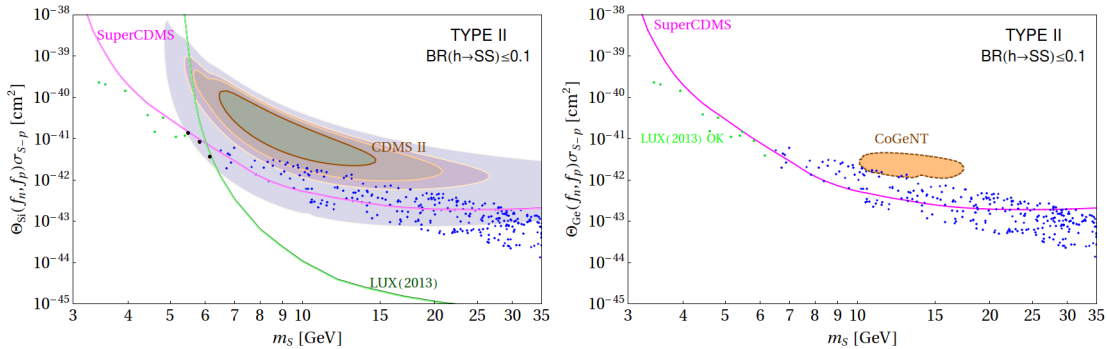
Figure 8.12. Cross section for DM - proton scattering for the Type II model rescaled by the function Θ_X defined in Eq. (8.30), where X = Si for a Silicon detector (CDMS II) on the left and X=Ge for the Germanium detector (CoGeNT) on the right. All points satisfy all the preLUX constraints (*i.e.* they satisfy the theoretical constraints for 2HDMS, 2HDM fitting at 68% C.L., BR($h \to SS$) ≤ 0.1 and the constraint on Ωh^2). The CDMS II contours shown are at 68%, 90%, 95% and 99% C.L. The CoGeNT contour is the 90% C.L. level contour. Light green points are allowed by LUX results. The larger black points are those allowed by both SuperCDMS and LUX and that also lie within the 99% C.L. CDMS II contour. The pink and light pink lines (almost degenerate) correspond to the SuperCDMS limit, after rescaling from the SuperCDMS Germanium target to the CDMS-II Silicon target using $f_n/f_p = 1.05$ and 1.25. Also shown by the dark green lines is the rescaled LUX limit, $\sigma_{\mathrm{Si}}^{\mathrm{LUX}} = \sigma^{\mathrm{LUX}}\Theta_{\mathrm{Si}}(f_n, f_p)/\Theta_{\mathrm{Xe}}(f_n, f_p)$, using the same two f_n/f_p values.

(including BR($h \to SS$) ≤ 0.1). For the left figure, we have rescaled the DM-proton scattering cross section predicted for a given point by the factor Θ_X, see Eq. (8.30), as computed for X = Si in order to compare to the positive signal region found by the CDMS II Silicon detector. We also display the relevant limits from the SuperCDMS experiment. These are f_n/f_p dependent. The two lines correspond to the SuperCDMS limit after rescaling from the SuperCDMS Germanium target to the CDMS-II Silicon target. We rescaled $\sigma_{\mathrm{Si}}^{\mathrm{SuperCDMS}} = \sigma^{\mathrm{SuperCDMS}}\Theta_{\mathrm{Si}}(f_n, f_p)/\Theta_{\mathrm{Ge}}(f_n, f_p)$ using $f_n/f_p = 1.05$ and 1.25 — the minimum and maximum values for the points plotted for $m_S \leq 35$ GeV. We see that for the predicted range of f_n/f_p the resulting rescaling is fairly minimal and those two limits are almost degenerate. Also shown by another two lines is the rescaled LUX limit, $\sigma_{\mathrm{Si}}^{\mathrm{LUX}} = \sigma^{\mathrm{LUX}}\Theta_{\mathrm{Si}}(f_n, f_p)/\Theta_{\mathrm{Xe}}(f_n, f_p)$, using the same two f_n/f_p values. From this plot, we observe that there are a few points (the large black points) with $m_S \sim 5.5 - 6.2$ GeV that lie below both the rescaled LUX limits and rescaled SuperCDMS limits. Further, although these points lie below the 2σ (95% C.L.) contour of the positive

277

Table 8.3. Summary of the properties of the 2HDM Type II points in Fig. 8.12 which make it possible to realize $m_S < 50$ GeV, after imposing the full set of preLUX constraints together with the LUX and SuperCDMS bounds. All masses are given in GeV units.

$\tan\beta$	$\sin\alpha$	m_H	m_A	$m_{H^\pm}$	m_{12}^2	$(m_S$ [GeV], $\log\Theta_{\mathrm{Xe}}(f_n, f_p)\sigma_{S-p}[\mathrm{cm}^2])$
2.092	-0.41	138	451	399	-12642	(3.44, -39.65); (3.56,-39.69); (3.95, -39.85)
3.121	-0.282	187	546	571	8943	(4.82, -40.50); (5.48, -40.83)
2.192	-0.394	209	488	503	7518	(5.40, -40.93)
1.728	-0.476	177	318	389	9382	(5.16, -40.97)
1.789	-0.461	198	420	430	-6594	(4.44,-40.43); (5.15, -40.96)
1.488	-0.528	157	553	576	-10094	(4.61, -40.83)
2.375	-0.363	259	260	339	15899	(5.83, -41.05)

signal region of CDMS II, they do fall within the 3σ (99% C.L.) contour. Thus, the 2HDMS Type II model allows consistency between the CDMS II signal region (at 99% C.L.) and the SuperCDMS and LUX limits for a small range of low m_S.

It is perhaps important to understand the points in Fig. 8.12 with low m_S that obey LUX *and* SuperCDMS constraints in the case of the Type II model. Their properties appear in Table 8.3. All have low $\tan\beta$, very modest m_H with $m_A, m_{H^\pm}$ somewhat larger (in the $300-600$ GeV range). It is worth recalling that for each 2HDM phenomenologically allowed point, the 2HDM parameters including $\tan\beta$, $\sin\alpha$, m_h, m_H, m_A, $m_{H^\pm}$ and m_{12} are fixed. We then randomly scan over the singlet sector parameters κ_1, κ_2 (or equivalently λ_h, λ_H) and m_S. Therefore, one can have many values of m_S and corresponding rescaled cross section (the pair of numbers appearing in the last column of Table IV) for each fixed 2HDM point whose parameters are listed in the first 6 columns.

For the right figure, we rescale $\sigma_{\mathrm{DM}-p}$ using Θ_X as computed for X=Ge in order to compare to the potential signal region for the CoGeNT Germanium detector. We find points consistent with all pre-LUX constraints within the CoGeNT 90% C.L. signal region for $m_S \sim 10 - 15$ GeV. However, the entire CoGeNT signal region is excluded by the SuperCDMS limit (no relative rescaling required since both are for a Germanium target)

and by the LUX limit as indicated by the point coloring (where these limits have been rescaled using the f_n/f_p value for a given point to determine whether or not the point is excluded).

8.2.5 Non-standard model-like Higgs detection

It is perhaps useful to summarize what Type I and II models predict with regard to the invisible decays of the heavier H and how this will impact possibilities for detecting the H in upcoming LHC runs. For $m_S \lesssim 55$ GeV, the BR$(h \to SS) \leq 0.1$ constraint required by a good h fit to the 125.5 GeV data implies that λ_h is small and this indirectly impacts BR$(H \to SS)$. Before imposing the LUX limits, we find that $BR(H \to SS)$ can have a number of semi-discrete values below 1, the discreteness being associated with particular 2HDM 68% C.L. points, but for the bulk of $m_S \lesssim 55$ GeV points one has BR$(H \to SS) \gtrsim 0.9$. Of course, we have seen above that once the LUX and SuperCDMS limits are imposed all the low-m_S points are eliminated in the Type I case, whereas in the Type II case a handful of points survive in the $m_S \leq 6$ GeV region. Once $m_S \gtrsim 55$ GeV, BR$(h \to SS)$ is automatically small or zero and constraints on λ_h in the singlet sector scan are greatly relaxed. As a result, BR$(H \to SS)$ can take on most any value for $m_S \lesssim 200$ GeV, declining to small values once $m_S \gtrsim 500$ GeV.

As regards H detection, we first note that since the HVV couplings are small (since the hVV coupling must be large for a good Higgs fit) the $Z + inv$ final state LHC data do not currently constrain BR$(H \to SS)$, and in future runs very high integrated luminosity would be needed to have any hope of seeing a signal in this channel. Further, if $H \to SS$ decays are dominant this would reduce the strength of the H signals in other production/decay modes, such as $gg \to H \to \tau\tau$, and thus decrease the prospects for H discovery as outlined in [7]. In such instances, experimental sensitivity to the H may have to rely on $gg \to H$ production with a jet or photon tag of the invisible $H \to SS$ final state.

8.2.6 **Summary**

To summarize up to this point, we have analyzed the 2HDMS models obtained by extending the Type I and Type II two-Higgs-doublet models to include a scalar gauge-singlet dark matter candidate, denoted S with mass m_S. We have discussed various theoretical and experimental constraints on the 2HDMS and how these constrain the additional (beyond the 2HDM) three parameters of the 2HDMS, m_S and the trilinear hSS and HSS couplings. We begin with the 2HDM fits of [7] for the case where it is the lighter h that is identified with the ~ 125.5 GeV state, in particular employing the 2HDM parameter space points for which the combined LHC/Tevatron signal strengths are fit within the 68% C.L. We then study the constraints on the singlet parameter space based on cosmological data, most particularly the observed Ωh^2 and the LUX and SuperCDMS limits on DM-nucleon scattering. If $m_S > 55$ GeV, 2HDMS parameter choices for which the 2HDMS is completely consistent with all the above data are plentiful in both the Type I and Type II models. For $m_S \leq 55$ GeV, requiring $\mathrm{BR}(h \to SS) \leq 0.1$ in order to avoid destroying the fit of the h to the LHC data makes it impossible (almost impossible) in the Type I (Type II) model to find parameter points that give correct Ωh^2 and satisfy both the LUX and SuperCDMS limits. Nonetheless, it is interesting to note that if we do not impose the LUX and SuperCDMS limits, for both model types $m_S < 50$ GeV-points with $\mathrm{BR}(h \to SS) \leq 0.1$ and correct Ωh^2 fall within one or more of the CDMS II, CRESST-II or CoGeNT signal regions.

An important issue in the 2HDMS context is whether or not there is a possibility of isospin violation, $f_n/f_p \neq 1$. In the case of the 2HDMS Type I model, $f_n/f_p \simeq 1$ is inevitable. This, implies that despite the fact that all points with correct Ωh^2 and $\mathrm{BR}(h \to SS) \leq 0.1$ have σ_{S-p} values falling within one or more of the CDMS II, CRESST-II or CoGeNT signal regions, they are simply inconsistent with the LUX and SuperCDMS limits.

In the case of the 2HDMS Type II model, a significant isospin violation in DM-nucleon scattering is possible, even reaching the value of $f_n/f_p \sim -0.7$ that would allow consistency of the LUX limit with the CDMS II signal region. However, at the low m_S

values corresponding to the signal region, we find that points with $f_n/f_p \sim -0.7$ either have an hSS coupling that is too large for $\mathrm{BR}(h \to SS) \leq 0.1$ or too small to give sufficient annihilation to achieve correct Ωh^2. (At low m_S, the H exchange contribution to SS annihilation is not sufficient, given upper bounds on the HSS coupling coming from perturbativity and unitarity.) Therefore, even though isospin violation might be present, the level of $f_n/f_p \sim -0.7$ cannot be made consistent with all phenomenological requirements. The SuperCDMS limit further constrains the picture. For the f_n/f_p values predicted by the 2HDMS once correct Ωh^2 and $\mathrm{BR}(h \to SS) \leq 0.1$ are imposed, the isospin violation is only a small effect in comparing the Germanium target SuperCDMS limit to the Silicon target CDMS II result. In the end, one does find a few $m_S \sim 5.5 - 6.2$ GeV-points that lie below both the SuperCDMS and LUX limits and, interestingly, also fall within (but are outside) the 99% C.L. (95% C.L.) CDMS II signal region. As typical for $m_S \leq 50$ GeV, these points are such that $\mathrm{BR}(H \to SS)$ is large, implying that jet- and/or photon-tagging will be needed for H detection.

8.3 The role of isospin-violating effect

As seen in the last section, the DM-nucleon cross section in the 2HDMS model with Type II Yukawa couplings can avoid the LUX exclusion bounds for low mass DM. This is absolutely impossible in the minimal singlet extension for a light DM being $6 - 50$ GeV. The key point is that the Higgs couplings to up- and down-type quark in the Type II models are no longer universal so that it can couple differently to protons and neutrons. This results in the violation of isospin symmetry. In particular, the opposite sign on the up- and down-type Yukawa couplings could induce a cancellation between flavor components of quarks in the amplitude of DM-proton and DM-neutron scattering, respectively. Such cancellation will effectively suppresses the cross section of DM scattering off a nucleus.

A particularly interesting question is whether or not one can have consistency between the CDMS II/CRESST-II preferred regions and the LUX limits through achieving the relation $f_n/f_p \sim -0.7$ as already noted. Therefore, in this section we study in particular the low dark matter mass region ($m_S \leq 50$ GeV) and aim at exploring the possibility of
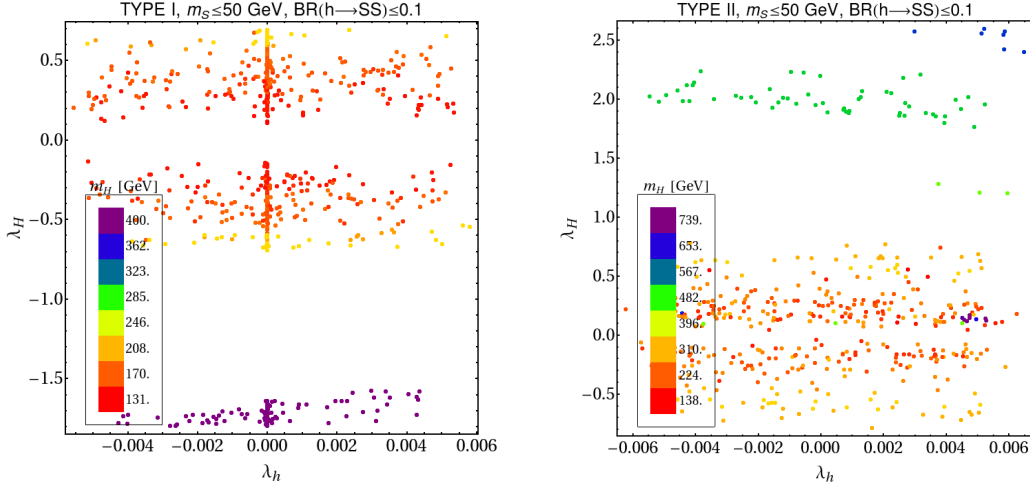
Figure 8.13. Couplings λ_h, λ_H allowed by the full set of preLUX constraints for the $m_S \leq 50$ GeV mass region. Points are temperatured according to m_H, with red points corresponding to the lowest H mass for which a solution was found.

using the isospin-violation mechanism to suppress direct detection signals in the context of 2HDMS model. We will discuss both $m_h \sim 125$ GeV and $m_H \sim 125$ GeV scenarios and the implications for DM observables within the model. Identifying the precise region in which a sufficiently large isospin-violating effect occurs is our first goal.

We have derived the analytical expression for f_n/f_p in terms of the Higgs couplings at quark level. Also, we construct a Higgs-portal DM model to realize the negative value of f_n/f_p, together with a precise relation of f_n/f_p with $\tan\beta$ in the exact alignment limit ($C_V = 1$) with a generic parameter w (which controls the s-channel mediator).

8.3.1 Low-mass dark matter in the 2HDMS

As we have already noted, in the low mass region $m_S < 50$ GeV, the exotic decay $h \to SS$ could have a large branching ratio. In contrast to the minimal singlet extension to the SM, in the 2HDMS one can keep BR($h \to SS$) small enough (≤ 0.1) to avoid destroying the fit of the h to the 125.5 GeV Higgs data if $\lambda_h \ll 1$. Nonetheless, correct Ωh^2 can be still accomplished because in this model the annihilation of DM is mediated not only by h but also by H (see Fig. 8.4). Therefore, the desired large cross section for SS annihilation is obtainable if λ_H is sufficiently large when λ_h is small. This trend was already apparent in Fig. 8.7. Here, we zero in on the $m_h \leq 50$ GeV region in Fig. 8.13,
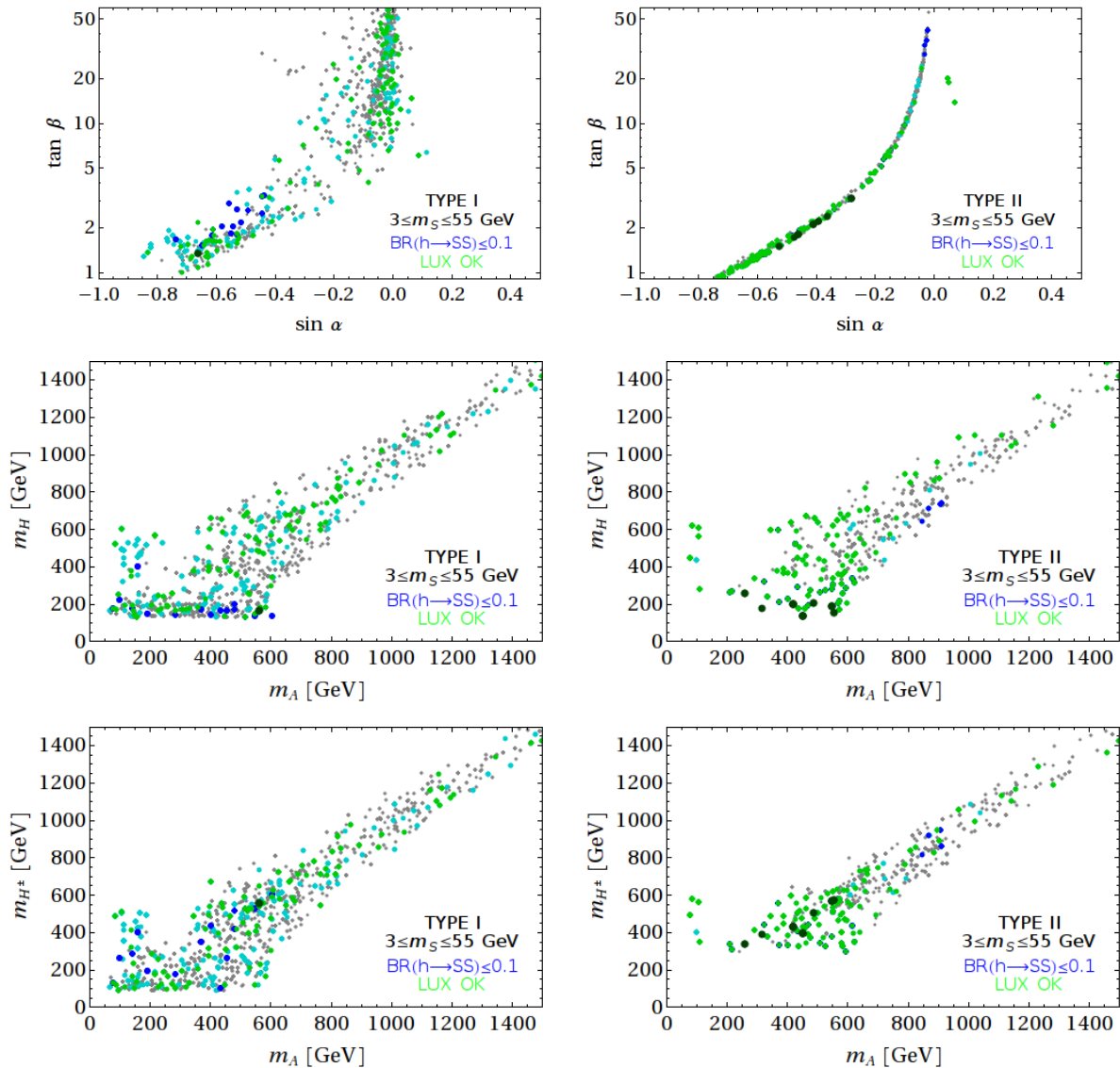
Figure 8.14. We show how the full set of preLUX constraints on the singlet sector affects the 2HDM parameter space that we used for the singlet sector scans. We have required $m_S \leq 55$ GeV. Gray points satisfy all preLUX constraints aside from BR($h \to SS$) ≤ 0.1. Cyan and blue points satisfy in addition BR($h \to SS$) ≤ 0.1, *i.e.* the full set of preLUX constraints. Cyan points have $50 < m_S \leq 55$ GeV while blue points have $m_S \leq 50$ GeV. The green and dark green points satisfy the LUX bound as well as the full set of preLUX constraints, with dark green showing the $m_S \leq 50$ GeV points.

where we have employed a special scan strategy designed to cover a large range of f_n/f_p and small λ_h.

As expected, the temperature plots show that, generally speaking, the larger m_H is the larger λ_H must be for correct relic density (the SS annihilation amplitude containing

the ratio λ_H/m_H^2). However, there is an exception in the case of the Type II model; at large $\tan\beta$ ($\gtrsim 25$) one can have sufficient annihilation even if λ_H/m_H^2 is not large since the $Hb\bar{b}$ coupling is highly enhanced, $C_D^H \propto \tan\beta$, see Eq. (8.19). We observe a smattering of such points in the (upper) $m_S \leq 50$ GeV Type II plot. For these points, the $SS \to b\bar{b}$ annihilation cross section is large enough to produce relic abundance within the experimental limit even though $|\lambda_H| < 0.2$ and $m_H > 500$ GeV.

We end this subsection with the plots of Fig. 8.14 showing the regions of the 2HDM parameter space with $m_S \leq 55$ GeV that remain after imposing the full set of preLUX constraints. The allowed regions are displayed in the $(\tan\beta, \sin\alpha)$, (m_H, m_A) and $(m_{H^\pm}, m_A)$ planes. Different colors are used to distinguish those points with $m_S \leq 50$ from those with $50 < m_S \leq 55$ GeV. Also shown are those points that in addition satisfy the LUX limit.

8.3.2 The mechanism of isospin-violation

We know that the DM-nucleon interaction is isospin-violating once the effective couplings of DM with a proton (f_p) and a neutron (f_n) are significantly different. This essentially demands that the Higgs has no common Yukawa couplings to up- and down-type quarks. Thus, we limit the discussion in the Type II model. Using the expression of $f_N(N = n, p)$ in Eq. (8.25), one can easily derive out the ratio, f_n/f_p, that is a parametrization of isospin-violation effect.

$$f_n/f_p = \frac{F_u^n \tilde{\lambda}_U + F_d^n \tilde{\lambda}_D}{F_u^p \tilde{\lambda}_U + F_d^p \tilde{\lambda}_D} \tag{8.32}$$

where $F_q^N(q = u, d)$ are the combined form factors (including the QCD NLO corrections),

$$F_u^N = f_{Tu}^N + \frac{2}{27}f_{TG}^N\left(1 + \frac{35}{36\pi}\alpha_S(m_c)\right) + \frac{2}{27}f_{TG}^N\left(1 + \frac{35}{36\pi}\alpha_S(m_t)\right) \tag{8.33}$$

$$F_d^N = f_{Td}^N + f_{Ts}^N + \frac{2}{27}f_{TG}^N\left(1 + \frac{35}{36\pi}\alpha_S(m_b)\right) \tag{8.34}$$

in which the α_S terms are scale-dependent and account for the QCD NLO corrections and the nucleon form factor has the relation defined as $f_{TG}^N = 1 - \sum_{q=u,d,s} f_{Tq}^N$, while the effective couplings are

$$\tilde{\lambda}_U = \sum_{\mathcal{H}} \frac{\lambda_{\mathcal{H}}}{m_{\mathcal{H}}^2} C_U^{\mathcal{H}}, \qquad \tilde{\lambda}_D = \sum_{\mathcal{H}} \frac{\lambda_{\mathcal{H}}}{m_{\mathcal{H}}^2} C_D^{\mathcal{H}}, \tag{8.35}$$
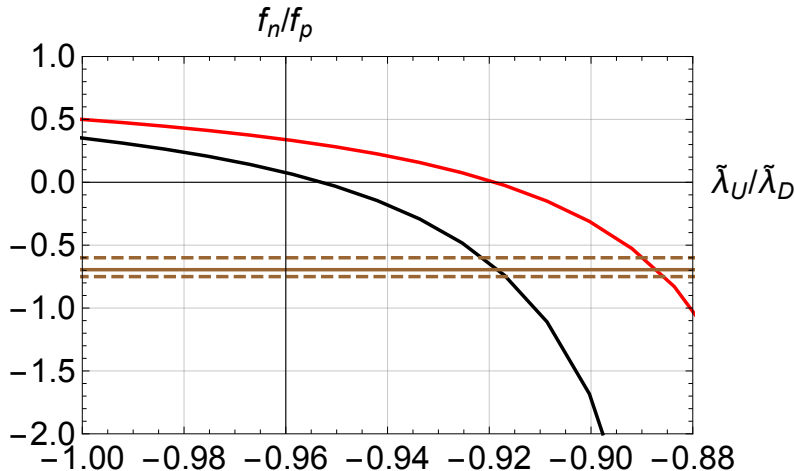
Figure 8.15. The correlation of isospin-violating effect f_n/f_p triggered by means of the relative Yukawa couplings. Both curves are plotted for the cases that include the QCD NLO correction (red) or not (black). In our analysis, the values of the hadron form factor are $f^n_{Tu} = 0.011, f^n_{Td} = 0.0273, f^n_{Ts} = 0.0447$ for neutron and $f^p_{Tu} = 0.0153, f^p_{Td} = 0.0191, f^p_{Ts} = 0.0447$ for proton.

where $\mathcal{H}$ represents all Higgs bosons participating into the t-channel exchange mediators and C_U and C_D denotes the Higgs couplings to up- and down-type quark, respectively, normalized to the SM value. Apparently, $f_n/f_p \simeq 1$ if the relation that $C_U = C_D$ is satisfied as that occurs in Type I model. Otherwise, we demonstrate in Fig. 8.15 the correlation of the ratio f_n/f_p that is triggered by means of the relative Yukawa couplings, It shows that, in a general Higgs portal DM model, a negative value of f_n/f_p could be realized at the quark level when the Higgs boson that participates the DM-nucleon interaction has *opposite* signs of the couplings with the up-type and down-type quarks, particularly within a narrow range on $\tilde{\lambda}_U/\tilde{\lambda}_D$ around -1 and that the value of f_n/f_p is very sensitive to the QCD correction. For instance, a typical value $f_n/f_p \simeq -0.7$ is attainable at $\tilde{\lambda}_U/\tilde{\lambda}_D \simeq -0.89$ and -0.92 when the QCD NLO correction is included or not, respectively.

8.3.3 Isospin-violating DM and direct detection

While the most interesting region of $f_n/f_p < 0$ allows for a substantial suppression of $\sigma^{\rm SI}$, possibly below experimental limits, it is an extremely difficult task to find solutions for f_n/f_p in the vicinity of -0.7 from a random or uniform scan. However, in fact it

is indeed possible to find analytically regions of $\tan\beta, \sin\alpha$ that implies desired f_n/f_p. Applying the pattern of Higgs-quark couplings C_U, C_D listed in Table 5.4 to the generic expression of f_n/f_p derived in Eq. (8.32) yields,

$$\tan\beta = -\frac{f_n/f_p F_u^p - \frac{m_n}{m_p}F_u^n}{f_n/f_p F_d^p - \frac{m_n}{m_p}F_d^n}\frac{w+\tan\alpha}{1-w\tan\alpha} \tag{8.36}$$

where the weight parameter is defined by $w = \frac{\lambda_h}{\lambda_H}\frac{m_H^2}{m_h^2}$. In our analysis one of the SM Higgs coupling to the DM λ_h or λ_H is vanishing to fully suppress the decay into SS, mathematically, $w \to 0$ for H-only mediator and $w \to \infty$ for h-only mediator.

Following this strategy, in Fig. 8.16 we plot $\tan\beta$ versus $\sin\alpha$ for various values of f_n/f_p. In addition we show (dashed lines) lines of constant $\sin(\beta-\alpha)$ and $\cos(\beta-\alpha)$ in left and right panels of the figure. It is most important to notice that the wanted value of $f_n/f_p \sim -0.7$ corresponds to a very narrow band (line) in $(\tan\beta, \sin\alpha)$ space and even small deviation off the proper line moves f_n/f_p quickly away from -0.7. This is why the scan over parameter space must be very focused in the close vicinity of the line of $f_n/f_p \sim -0.7$. Since the observed Higgs couples in a SM-like manner ($\sin(\beta-\alpha) \sim 1$ for $m_h \sim 125.5$ GeV and $\cos(\beta-\alpha) \sim 1$ for $m_H \sim 125.5$ GeV) therefore an extra relation between β and α must be satisfied and that implies relatively small region (a narrow band along $f_n/f_p \sim -0.7$ limited by largest $\sin\alpha$ ($\cos\alpha$) for H (h) mediation) that is of our interest. This leads to the final solution that the particularly interesting region of $f_n/f_p \sim -0.7$, occurs in the vicinity of ($\sin\alpha \sim \pm 0.7$, $\tan\beta \sim 1$) which corresponds to $\beta \sim \pi/4$ and $\alpha \sim \pm\pi/4$.

In the following we will discuss the implication of direct and indirect detection bounds for the 2HDMS parameter space and prospects for its experimental verification. For both the $m_h \sim 125$ GeV and $m_H \sim 125$ GeV cases, we display the expected cross sections for S scattering off nuclei in Xenon-based detectors on Fig. 8.17, together with current LUX results and Xenon 1T future projection. All points satisfy the DM abundance constraint. The points are coloured with respect to f_n/f_p. Note that, in accordance with expectations points for which the cross section is suppressed correspond to f_n/f_p approaching -0.7, it is particularly apparent in the cast that $m_A \geq m_h/2$, where the is no AA contamination in
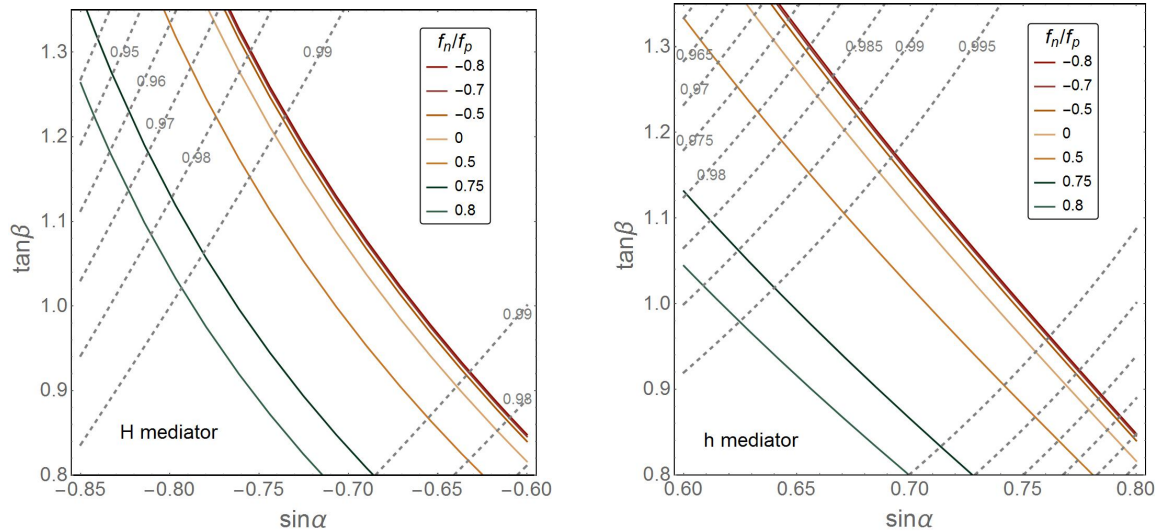
Figure 8.16. The left and right panes show contour plots (solid lines) of constant f_n/f_p in the $(\tan\beta, \sin\beta)$ space for the case $m_h \sim 125.5$ GeV (H is the mediator) and $m_H \sim 125.5$ GeV (h is the mediator), respectively. NLO QCD corrections are taken into account. The dashed lines are contours of constant $\sin(\beta - \alpha)$ and $\cos(\beta - \alpha)$ in left and right panels, respectively.

the DM annihilation final state. The conclusion from the plots is that the 2HDSM could easily be consistent both with the present LUX limits and also with the limits anticipated for Xenon 1T.

Therefore, we can conclude that, compared to simply adding a singlet to the SM, the 2HDMS can provide a consistent DM picture in the overall mass range for m_S from a few GeV to a few TeV. In particular, with the help of a cancelation between up and down type quarks that is possible for negative f_n/f_p, the DM-nucleon cross section in the low-mass region could be heavily suppressed so as to escape the current LUX bound and also the future projected bound. In turns, the exclusion bound would give the maximal allowed value of f_n/f_p.

8.4 Supersymmetric dark matter in the NMSSM

8.4.1 Neutralino sector and a possible DM candidate in the NMSSM

[JY: If time allowed, i attempt to add a few things on the theoretical structure of the neutralino sector and R-parity.]
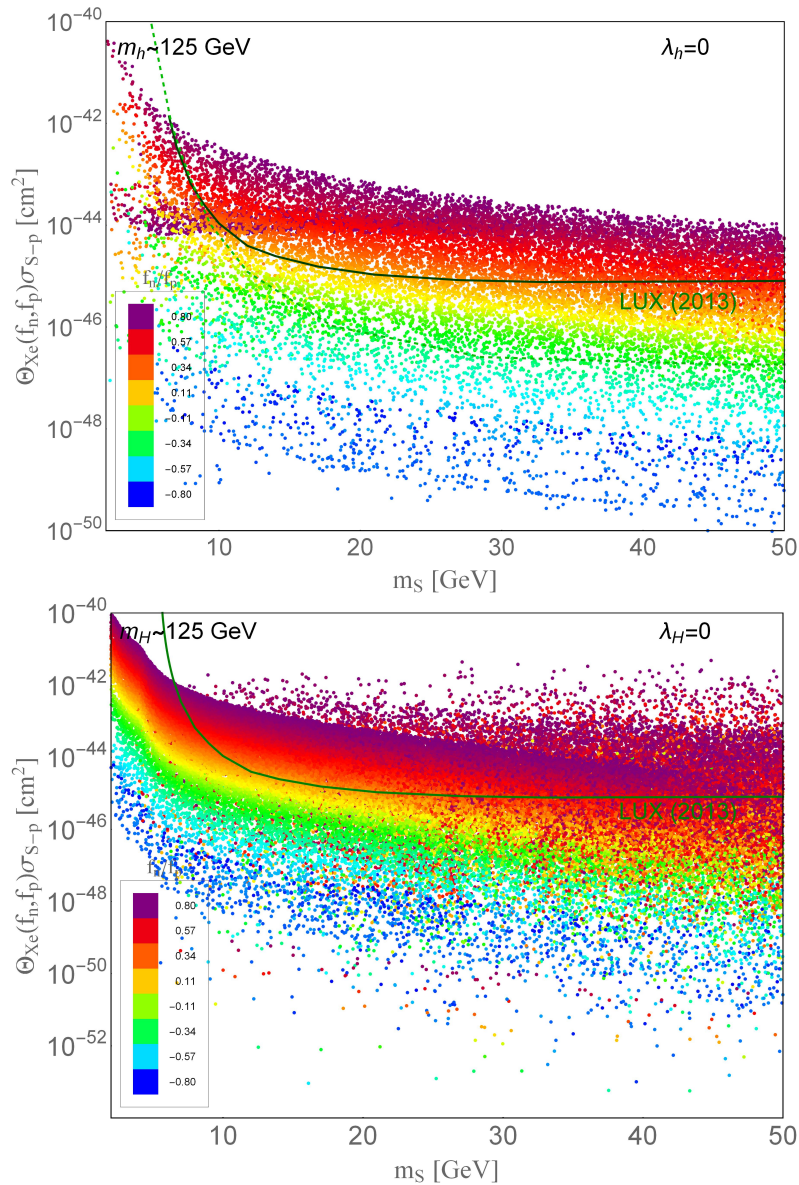
Figure 8.17. Prediction for the DM-proton cross section for Xenon-based detectors in the 2HDMS for the case that either h (upper row) or H (lower row) is identified as the SM-like Higgs boson at 125 GeV. The upper limits from DM direct detection imposed include the LUX bound [87] in dark green dashed line and the XENON 1T (2017) projections [344] in little dark-green boxes.

8.4.2 Properties of the LSP in various specific 125 GeV Higgs scenarios

In section 6.5, we explored using constrained versions of the NMSSM to fit the Higgs data. Given that a reasonable fit can be obtained, it is then of interest to consider whether or not the lightest neutralino obtained for points with an acceptable Higgs fit can provide

Table 8.4. LSP mass and its decomposition for the exemplary points listed in Tables 6.1-6.3. The LSP bino, wino, higgsino and singlino fractions are $f_{\tilde{B}} = N_{11}^2$, $f_{\tilde{W}} = N_{12}^2$, $f_{\tilde{H}} = N_{13}^2 + N_{14}^2$ and $f_{\tilde{S}} = N_{15}^2$, respectively, with N the neutralino mixing matrix.

	Model II			Model III			
Pt. #	1*	2*	3	4*	5	6	7
$m_{\tilde{\chi}_1^0}$	363	410	438	328	307	440	452
$f_{\tilde{B}}$	0.506	0.534	0.511	0.529	0.914	0.464	0.370
$f_{\tilde{W}}$	0.011	0.009	0.008	0.012	0.002	0.009	0.009
$f_{\tilde{H}}$	0.483	0.457	0.482	0.459	0.083	0.528	0.622
$f_{\tilde{S}}$	10^{-4}	10^{-6}	10^{-6}	10^{-4}	10^{-6}	10^{-4}	10^{-6}

a viable dark matter candidate.

To pursue this, we return to the perfect and almost perfect points presented in Tables 6.1 and 6.2 seven exemplary points with $m_{h_1} \simeq 125$ GeV from models II and III. The properties of LSP for these points, including the LSP compositions and main annihilation channels, are summarized in Tables 8.4.2 and 8.5. Clearly, the mass of the neutralino LSP, $\tilde{\chi}_1^0$, is rather similar, $m_{\tilde{\chi}_1^0} \approx 300 - 450$ GeV, for the different perfect and almost perfect points with $m_{h_1} \gtrsim 124$ GeV. For all but pt. #5, the $\tilde{\chi}_1^0$ is approximately an equal mixture of higgsino and bino. However, there is some variation in the primary annihilation mechanism, with $\tilde{\tau}_1 \tilde{\tau}_1$ and $\tilde{\chi}_1^0 \tilde{\chi}_1^0$ annihilation being the dominant channels except for pt. #2 for which $\tilde{\nu}_\tau \tilde{\nu}_\tau$ and $\tilde{\nu}_\tau \overline{\tilde{\nu}}_\tau$ annihilations are dominant. In the case of dominant $\tilde{\tau}_1 \tilde{\tau}_1$ annihilation, the bulk of the $\tilde{\chi}_1^0$'s come from those $\tilde{\tau}$'s that have not annihilated against one another or co-annihilated with a $\tilde{\chi}_1^0$. In addition, all the tabulated points yield a spin-independent direct detection cross section of order $(3.5 - 6) \times 10^{-8}$ pb. For the above $m_{\tilde{\chi}_1^0}$ values, current limits on σ^{SI} are somewhat below 10^{-8} pb.

Apart from analyzing the benchmark points, we generally study the properties of the LSP that have acceptable relic density $\Omega h^2 < 0.136$, including both those with an enhanced $\gamma\gamma$ rate and those with $R_{gg}^h(\gamma\gamma, VV) \gtrsim 1$. [9] For a rather low μ, the LSP is

---

[9]The original purpose of the scans employed was to look for points with enhanced $R_{gg}^h(\gamma\gamma, VV)$.

Table 8.5. δa_μ in units of 10^{-10}, LSP relic abundance, primary annihilation channels and spin-independent LSP scattering cross section off protons.

Pt. #	δa_μ	Ωh^2	Prim. Ann. Channels	$\sigma_{\rm SI}$ [pb]
1*	6.01	0.094	$\widetilde{\chi}_1^0\widetilde{\chi}_1^0 \to W^+W^-(31.5\%), ZZ(21.1\%)$	4.3×10^{-8}
2*	5.85	0.099	$\widetilde{\nu}_\tau\widetilde{\nu}_\tau \to \nu_\tau\nu_\tau(11.4\%), \widetilde{\nu}_\tau\overline{\widetilde{\nu}}_\tau \to W^+W^-(8.8\%)$	3.8×10^{-8}
3	4.48	0.114	$\widetilde{\chi}_1^0\widetilde{\chi}_1^0 \to W^+W^-(23.9\%), ZZ(17.1\%)$	3.7×10^{-8}
4*	6.87	0.097	$\widetilde{\chi}_1^0\widetilde{\chi}_1^0 \to W^+W^-(36.9\%), ZZ(23.5\%)$	4.5×10^{-8}
5	5.31	0.135	$\widetilde{\chi}_1^0\widetilde{\chi}_1^0 \to b\bar{b}(39.5\%), h_1a_1(20.3\%)$	5.8×10^{-8}
6	4.89	0.128	$\widetilde{\tau}_1\widetilde{\tau}_1 \to \tau\tau(17.4\%), \widetilde{\chi}_1^0\widetilde{\chi}_1^0 \to W^+W^-(14.8\%)$	4.0×10^{-8}
7	4.96	0.101	$\widetilde{\chi}_1^0\widetilde{\chi}_1^0 \to W^+W^-(17.7\%), ZZ(12.9\%)$	4.0×10^{-8}

nearly always wino-like and will have large annihilation cross section. In Fig. 8.18, we display the spin-independent cross section for LSP scattering on protons for the points collected in Section 6.5.2. As a reminder, the salmon-colored points are those that have $R_{gg}^h(\gamma\gamma, VV) \sim 1$ and a proper relic density within the WMAP window $0.094 < \Omega h^2 < 0.136$. (A more complete legend summary appears above Fig. 6.7.) Note the rather limited range of LSP masses that arise in the limited scan, roughly $m_{\widetilde{\chi}_1^0} \in [62, 113]$ GeV for $m_{h_1} \in [123 - 128]$ GeV and $m_{\widetilde{\chi}_1^0} \in [42, 120]$ GeV for $m_{h_2} \in [123 - 128]$ GeV, with $\sigma^{\rm SI}$ obeying the XENON100 bound for nearly all points (only a small fraction of the points) in the former (latter) case.

Furthermore, we would also like to mention some properties of the LSP for the case that the two CP-even Higgs bosons, h_1 and h_2, are close to 125 GeV in mass, a scenario that was extensively discussed in Section 6.5.3. As before, we display in the plots of Fig. 8.19 Ωh^2 and the spin-independent cross section for LSP scattering on protons, $\sigma^{\rm SI}$, for the points plotted in Section 6.5.3. As observed in Fig. 6.18, a large fraction of the points have small $\mu_{\rm eff}$ in which case the LSP is dominantly higgsino implying that Ωh^2 will be too low. Let us now focus on the (diamond) points with Ωh^2 in the WMAP window. [10]

Fortunately, at the same time the scans picked up points with $R_{gg}^h(\gamma\gamma, VV) \sim 1$, and it is these that are of greatest interest given current Run 1 Higgs data.

[10]Of course, since such points comprise only 1.6% of the total sample, it is very possible that they
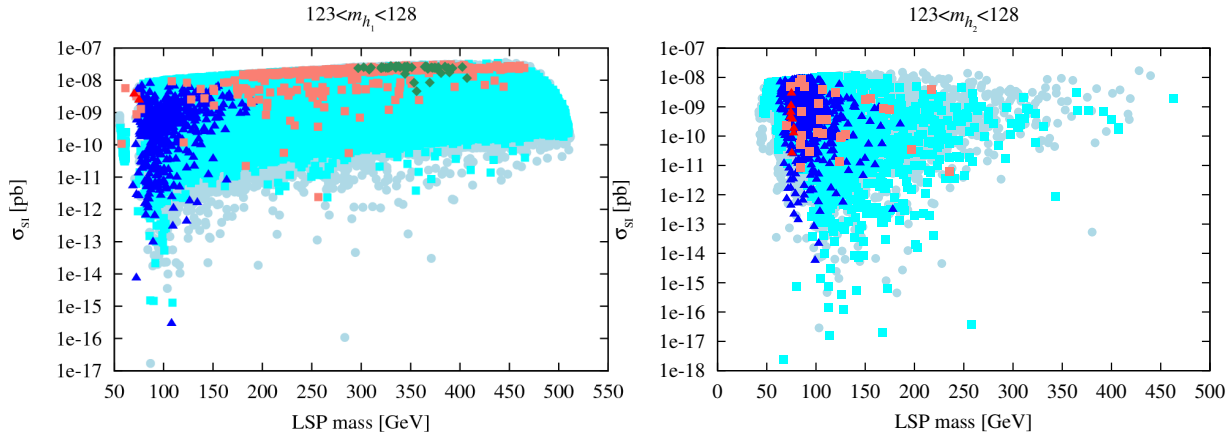
Figure 8.18. Spin-independent scattering cross section on protons versus LSP mass for the points collected in Section 6.5.2 for the cases of $m_{h_1} \in [123 - 128]$ GeV (left) and $m_{h_2} \in [123 - 128]$ GeV (right).

As seen from Fig. 6.15, about half of our WMAP-window points show enhanced rates, and are thus unable to fit the final run-1 Higgs data. Since this could change with run-2 data, we remind the reader about a few of their features. These WMAP-window points have a rather limited range of LSP masses, roughly $m_{\tilde{\chi}_1^0} \in [60, 80]$ GeV. They have large enough Ωh^2 since they are mixed higgsino–singlino, with a singlino component of the order of 20%, see the bottom-row plots of Fig. 8.19.

In another NMSSM scenario discussed in Section 6.5.4, we considered the possibility of explaining the run-1 Higgs data using the h_2 with $m_{h_2} \sim 125.5$ GeV as well as having an h_1 with $m_{h_1} \sim 98$ GeV that would explain the old LEP excess. We now briefly summarize DM implications for this scenario. The composition of the $\tilde{\chi}_1^0$ and the $\tilde{\chi}_1^\pm$ are crucial when it comes to the relic density of the $\tilde{\chi}_1^0$. **In what follows, we switch to the different color scheme, as described below, employed for the 98+125 scenarios. (I find it hard to make this switch without more material here. I cannot be sure that the text I have added is correct.)** For those points in the WMAP window in region A (red diamonds), **i.e. the region with enhanced $\gamma\gamma$ rates (check this)**, the $\tilde{\chi}_1^0$ can have a large Higgsino fraction since the $\tilde{\chi}_1^0 \tilde{\chi}_1^0 \to W^+ W^-$ annihilation mode (mainly via t-channel exchange of the light Higgsino-like — see second plot of Fig. 8.20 — chargino)

---

do not cover the full WMAP region and it is thus hard to be certain as to how well they exemplify the properties of a larger sample of such points.
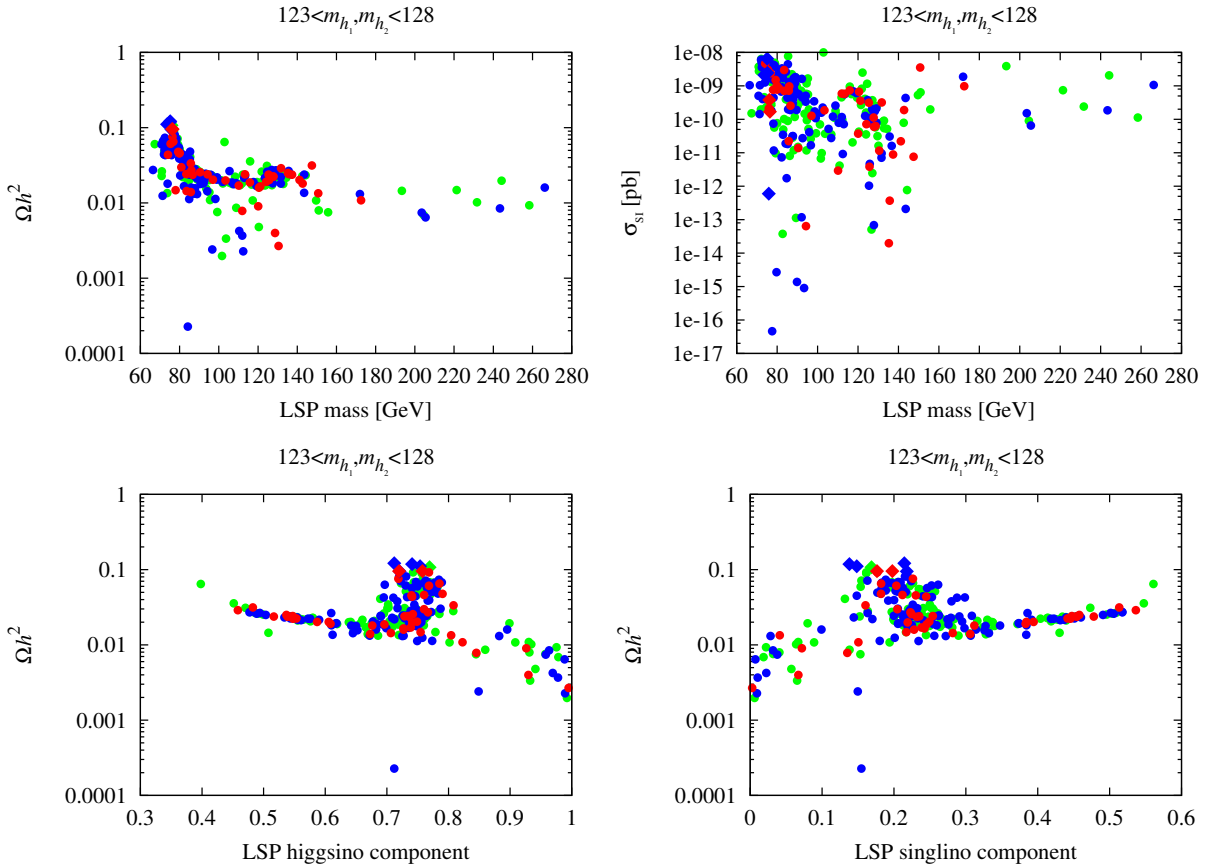
Figure 8.19. Top row: Ωh^2 and spin-independent cross section on protons versus LSP mass for the points plotted in previous figures. Bottom row: Ωh^2 versus LSP higgsino (left) and singlino (right) components.

is below threshold; the group of points with $m_{\widetilde{\chi}_1^0} > 93$ GeV (region B, orange diamonds **(the region with SM-like $\gamma\gamma$ rates)**) can lie in the WMAP window only if the $\widetilde{\chi}_1^0$ does not have a large Higgsino fraction. This division is clearly seen in Fig. 8.20. We note that to a reasonable approximation the singlino fraction of the $\widetilde{\chi}_1^0$ is given by 1 minus the Higgsino fraction plotted in the left-hand window of the figure.

DM properties for the surviving NMSSM parameter points are summarized in Fig. 8.21. Referring to the figure, we see a mixture of blue circle points (those with $\Omega h^2 < 0.094$) and red/orange diamond points (those with $0.094 \leq \Omega h^2 \leq 0.136$, *i.e.* in the WMAP window). The main mechanism at work to make Ωh^2 too small for many points is rapid $\widetilde{\chi}_1^0 \widetilde{\chi}_1^0$ annihilation to $W^+ W^-$ due to a substantial Higgsino component of the $\widetilde{\chi}_1^0$ (see third plot of Fig. 8.21). Indeed, the relic density of a Higgsino LSP is typically of order
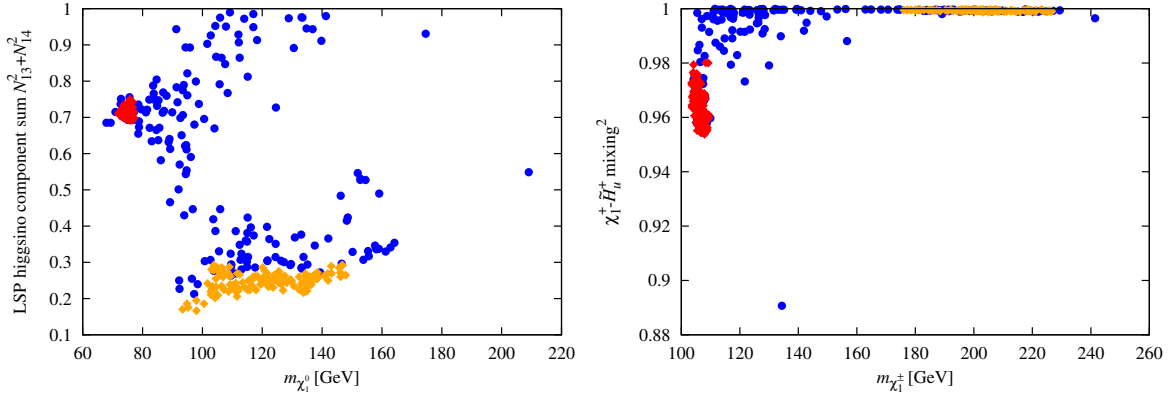
Figure 8.20. Neutralino and chargino compositions for the $98 + 125$ GeV LEP-LHC Higgs scenarios.
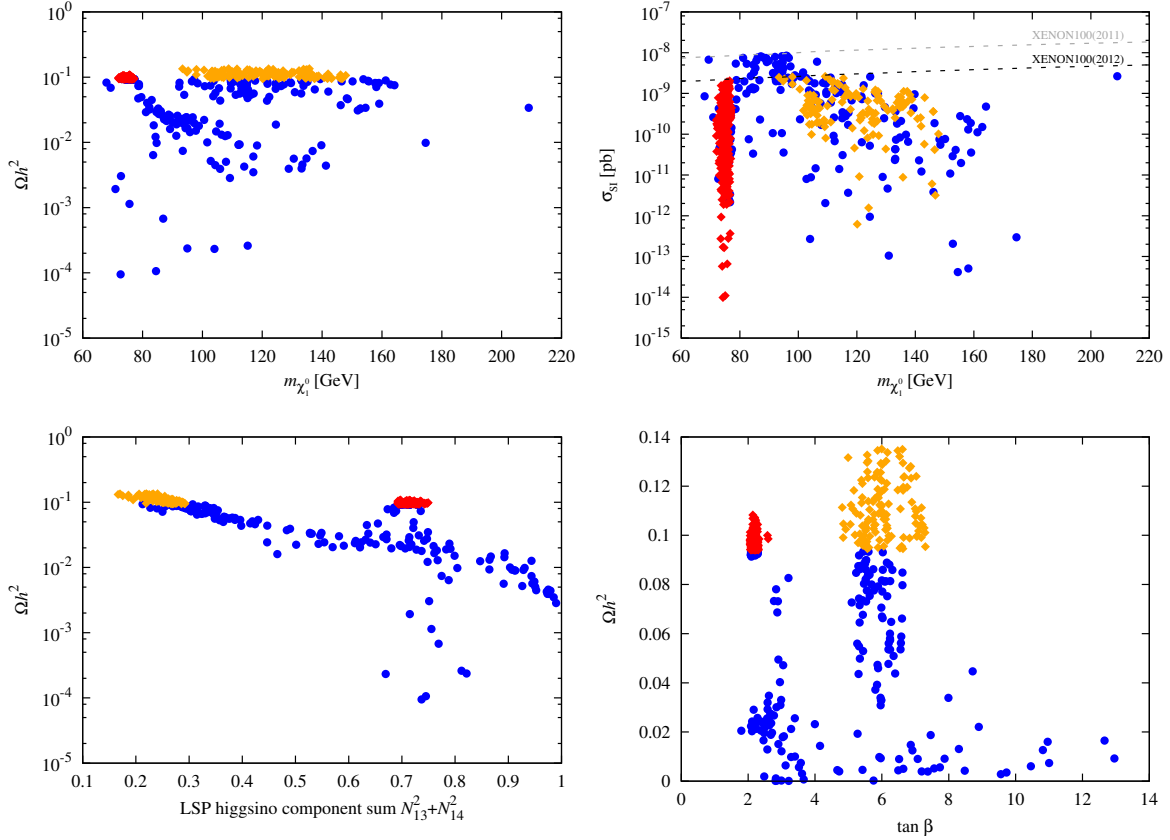
Figure 8.21. Dark matter properties for the $98 + 125$ GeV LEP-LHC Higgs scenarios.

$\Omega h^2 \approx 10^{-3} - 10^{-2}$. As the Higgsino component declines Ωh^2 increases and (except for the strongly overlapping points with $m_{\widetilde{\chi}_1^0} < m_W$, for which $\widetilde{\chi}_1^0 \widetilde{\chi}_1^0 \to W^+ W^-$ is below threshold) it is the points for which the LSP is dominantly singlino that have large enough Ωh^2

to fall in the WMAP window.

Also plotted in Fig. 8.21 is the spin-independent direct detection cross section, σ^{SI}, as a function of $m_{\widetilde{\chi}_1^0}$. First of all, we note that the 2012 XENON100 limits on σ^{SI} are obeyed by all the points that have Ωh^2 in the WMAP window, even though our scans only implemented the 2011 XENON100 limits — indeed only a modest number of the $\Omega h^2 < 0.094$ points are inconsistent with the 2012 limits. The σ^{SI} plot also shows that experiments probing the spin-independent cross section will reach sensitivities that will probe some of the σ^{SI} values that survive the 2012 XENON100 limits relatively soon, especially the $m_{\widetilde{\chi}_1^0} > 93$ GeV points that are in the WMAP window (region B). However, it is also noteworthy that the $m_{\widetilde{\chi}_1^0} \sim 75$ GeV points in region A can have very small σ^{SI}.

The fourth plot of Fig. 8.21 and fifth plot of Fig. 6.27 illustrate clearly the two categories of WMAP-window points. The first category (A) of points is that for which the $\widetilde{\chi}_1^0$ has low mass and large Higgsino component with $\tan\beta \in [2, 2.6]$ and $\lambda \in [0.53, 0.6]$; ; the second category (B) is that for which $m_{\widetilde{\chi}_1^0} > 93$ GeV, $\tan\beta \in [5, 7]$ and $\lambda \in [0.37, 0.48]$.

It is interesting to discuss whether or not any of the $98+125$ GeV Higgs scenario points are such as to describe the monochromatic signal at 130 GeV observed in the Fermi-LAT data [378]. We recall that the observation requires $\langle \sigma v \rangle (\widetilde{\chi}_1^0 \widetilde{\chi}_1^0 \to \gamma\gamma) \sim 10^{-27} \mathrm{cm}^3/\mathrm{sec}$ (this quoted value assumes standard dark matter density, $\rho \sim 0.3$).[11] The situation is illustrated in Fig. 8.22 where we plot $\langle \sigma v \rangle (\widetilde{\chi}_1^0 \widetilde{\chi}_1^0 \to a_1 \to \gamma\gamma)$ vs. Ωh^2 for just those points with $m_{\widetilde{\chi}_1^0} \in [125, 135]$ GeV. (It is the s-channel a_1 diagram that can give a large $\langle \sigma v \rangle$.) We observe that points with Ωh^2 in the WMAP window have values of $\langle \sigma v \rangle$ four orders of magnitude below that required to explain the excess. Those points with the largest $\langle \sigma v \rangle$ always have quite small Ωh^2 and hence ρ_{DM}. Incidentally, we have checked that all the points in our plots are fully consistent with the current bounds from the continuum γ spectrum as measured by Fermi-LAT [379, 380].

If the 130 GeV gamma ray line is confirmed, then the above questions will need to be explored more carefully. That a fully general NMSSM model (no GUT scale unifications)

---

[11]Here, and below, v is the very small velocity typical of dark matter in the current epoch, $v \sim 10^{-3}c$, as relevant for indirect detection of the $\widetilde{\chi}_1^0$ through $\widetilde{\chi}_1^0 \widetilde{\chi}_1^0$ annihilations. This, of course, differs from the velocity at the time of freeze out, which is substantially higher.
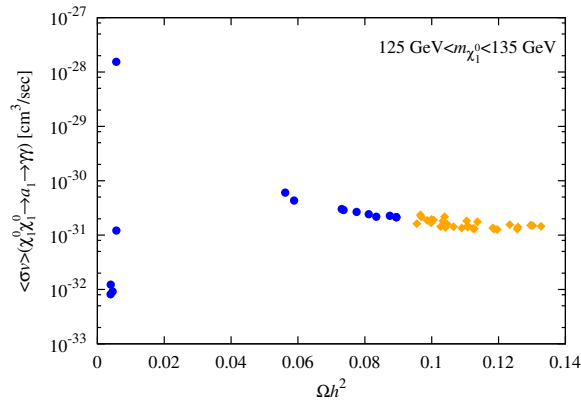
Figure 8.22. We plot $\langle\sigma v\rangle(\widetilde{\chi}_1^0\widetilde{\chi}_1^0 \to a_1 \to \gamma\gamma)$ vs. Ωh^2 for just those points with $m_{\widetilde{\chi}_1^0} \in [125, 135]$ GeV.

can be consistent simultaneously with the WMAP window, $\langle\sigma v\rangle(\widetilde{\chi}_1^0\widetilde{\chi}_1^0 \to a_1 \to \gamma\gamma) \sim 10^{-27}$cm^3/sec, a Higgs mass close to 125 GeV and 2011 XENON100 constraints was demonstrated in [381]. However, the value of m_{a_1} has to be carefully tuned and the 125 GeV Higgs couplings to all particles (including photons) must be within 5% of those for a SM Higgs boson of this mass, as consistent with the $\gamma\gamma$ LHC rates being roughly of SM size in this channel. Some general (non-NMSSM) theoretical discussions of the 130 GeV line in the context of DM appear in [382, 383].

8.5 Remark

The Higgs and DM sectors may be intimately connected. If this is true, then detecting the signs of one of sectors could shine light on still hidden elements of the other. Complementary to the searches at the LHC, programs of dark matter direct and indirect detection provide important information on understanding the nature of DM. In contrast to the effective theory approach, analyzing this information in a consistent framework requires a more model-dependent approach. Therefore, it is of great interest to explore some of the implications of recent developments in hunting for Higgs and detecting DM in the context of as simple a framework as possible.

PART IV

Future Outlook

CHAPTER 9

Outlook for future prospects

"Progress in Physics is to prove yourself wrong as soon as possible."

— *Richard Feynman*

There is no doubt that the discovery of a new particle with mass of about 125 GeV and properties that match very well those expected for a SM Higgs boson was a real triumph of LHC run-1. However, one has to keep in mind that the present precisions on the Higgs couplings are, roughly, of the order of tens of percent, so substantial deviations are still possible. (The analysis for combining the ATLAS and the CMS data from LHC run-1 is underway at the time of writing this thesis.) We are hoping that deviations from SM predictions will become apparent via future precision analyses of LHC run-2 data and provide clues to the nature of the ultimate BSM theory, since one believes that the SM is certainly not the ultimate theory of physics.

Rather than being the end of the story, this sensational discovery has launched the exploration of EWSB and, more importantly, brought the research in high energy frontier

into a new era. It potentially opened a window into BSM physics such as an extended Higgs sector, anomalous Higgs boson production mechanisms, or rare Higgs boson decay modes. On the other hand, precisely measuring the properties of the new particle is also urgent because it is critical in ascertaining whether the newly discovered particle is fully responsible for EWSB and whether there are potential deviations from SM predictions. One of the most important missions for the incoming LHC run-2 operation and other future collider programs (i.e., the international linear collider (ILC) [384] and the circular electron-positron collider (CEPC) [385], a project that is currently under discussion in China.) is to determine whether the observed state is in fact the SM Higgs boson, or whether it is just one SM-like degree of freedom of a non-minimal Higgs sector of a more fundamental theory. This can be done on the one hand by direct searches for additional Higgs bosons, and on the other hand by precision measurements of the couplings. Both ways have been extensively demonstrated in specific models in this volume. Nonetheless, in pursuing precise studies of the data, a truly model-independent approach, such as that based on effective field theory (EFT), can be of great value. This is because this powerful tool allows the data to be studied with minimal theoretical bias, without the need to know all the details of the high scale theory, and to deduce general implications for electroweak and TeV scale physics given whatever data is available.

In addition to likely representing a smoking gun for an extended Higgs sector and associating with dark matter, the discovery of a SM-like Higgs at the LHC could also have far-reaching implications for our understanding of how Nature works at its most fundamental level, including many cosmological puzzles (for instance, the baryon asymmetry present in the early universe and the origin of our Universe). Hence, it will also be a good idea to utilize the Higgs boson as a bridge to address a number of topical problems, ranging from BSM Higgs physics to dark matter and cosmology, allowing us to unravel the mysteries of our Universe. But, this represents a broad and ambitious research program in parallel with precise measurements of Higgs boson properties at the LHC and future electron-positron and/or proton-proton colliders. Complementary to the searches at the LHC, programs of dark matter direct and indirect detection provide important informa-

tion on understanding the nature of DM. In contrast to the effective theory approach, analyzing this information in a consistent framework requires a more model-dependent approach.

Finally, let us wait for the more exciting run-2 at the LHC. I anticipate that the full 14 TeV data could either discover new physics or result in increased constraints on particular well-motivated models and further reduce the errors/limits on the general EFT parameterization. And a variety of ongoing experiments aimed at detecting dark matter will either provide further limits or succeed in detecting dark matter. Either way, DM models will be constrained and/or eliminated, thereby providing guidance to ongoing theoretical work. As a young researcher, I am fortunate to be in the midst of an exciting time and will certainly work extremely hard to contribute to these research areas.

References

[1] J. F. Gunion, Y. Jiang, and S. Kraml, *The Constrained NMSSM and Higgs near 125 GeV*, Phys.Lett. **B710** (2012) 454–459, [arXiv:1201.0982].

[2] J. F. Gunion, Y. Jiang, and S. Kraml, *Could two NMSSM Higgs bosons be present near 125 GeV?*, Phys.Rev. **D86** (2012) 071702, [arXiv:1207.1545].

[3] J. F. Gunion, Y. Jiang, and S. Kraml, *Diagnosing Degenerate Higgs Bosons at 125 GeV*, Phys. Rev. Lett. **110** (2013), no. 5 051801, [arXiv:1208.1817].

[4] G. Belanger, U. Ellwanger, J. F. Gunion, Y. Jiang, and S. Kraml, *Two Higgs Bosons at the Tevatron and the LHC?*, arXiv:1208.4952.

[5] G. Belanger, U. Ellwanger, J. F. Gunion, Y. Jiang, S. Kraml, and J. H. Schwarz, *Higgs Bosons at 98 and 125 GeV at LEP and the LHC*, JHEP **01** (2013) 069, [arXiv:1210.1976].

[6] A. Drozd, B. Grzadkowski, J. F. Gunion, and Y. Jiang, *Two-Higgs-Doublet Models and Enhanced Rates for a 125 GeV Higgs*, JHEP **1305** (2013) 072, [arXiv:1211.3580].

[7] B. Dumont, J. F. Gunion, Y. Jiang, and S. Kraml, *Constraints on and future prospects for Two-Higgs-Doublet Models in light of the LHC Higgs signal*, Phys.Rev. **D90** (2014) 035021, [arXiv:1405.3584].

[8] B. Dumont, J. F. Gunion, Y. Jiang, and S. Kraml, *Addendum to "Constraints on and future prospects for Two-Higgs-Doublet Models in light of the LHC Higgs signal"*, arXiv:1409.4088.

[9] J. Bernon, J. F. Gunion, Y. Jiang, and S. Kraml, *Light Higgs bosons in Two-Higgs-Doublet Models*, arXiv:1412.3385.

[10] J. Bernon, J. F. Gunion, H. E. Haber, Y. Jiang, and S. Kraml, *Scrutinizing the Alignment Limit in Two-Higgs-Doublet Models. Part 1: $m_h = 125$ GeV*, arXiv:1507.0093.

[11] A. Drozd, B. Grzadkowski, J. F. Gunion, and Y. Jiang, *Extending two-Higgs-doublet models by a singlet scalar field - the Case for Dark Matter*, *JHEP* **1411** (2014) 105, [arXiv:1408.2106].

[12] A. Ahmed, B. Grzadkowski, J. F. Gunion, and Y. Jiang, *Higgs Dark Matter from a Warped Extra-Dimension – the truncated-inert-doublet model*, arXiv:1504.0370.

[13] F. Englert and R. Brout, *Broken Symmetry and the Mass of Gauge Vector Mesons*, *Phys.Rev.Lett.* **13** (1964) 321–323.

[14] P. W. Higgs, *Broken Symmetries and the Masses of Gauge Bosons*, *Phys.Rev.Lett.* **13** (1964) 508–509.

[15] G. Guralnik, C. Hagen, and T. Kibble, *Global Conservation Laws and Massless Particles*, *Phys.Rev.Lett.* **13** (1964) 585–587.

[16] S. Weinberg, *The Quantum theory of fields. Vol. 1: Foundations*, *Cambridge University Press* (1995) p.246.

[17] B. W. Lee, C. Quigg, and H. Thacker, *The Strength of Weak Interactions at Very High-Energies and the Higgs Boson Mass*, *Phys.Rev.Lett.* **38** (1977) 883–885.

[18] B. W. Lee, C. Quigg, and H. Thacker, *Weak Interactions at Very High-Energies: The Role of the Higgs Boson Mass*, *Phys.Rev.* **D16** (1977) 1519.

[19] W. J. Marciano, G. Valencia, and S. Willenbrock, *Renormalization Group Improved Unitarity Bounds on the Higgs Boson and Top Quark Masses*, *Phys.Rev.* **D40** (1989) 1725.

[20] T. Plehn, *Lectures on LHC Physics*, *Lect.Notes Phys.* **886** (2015).

[21] M. D. Schwartz, *Quantum Field Theory and the Standard Model.* Cambridge University Press, 2014.

[22] P. Langacker, *The standard model and beyond*, *CPC Press* (2010).

[23] L. Reina, *TASI 2004 lecture notes on Higgs boson physics*, hep-ph/0512377.

[24] L. Reina, *TASI 2011: lectures on Higgs-Boson Physics*, arXiv:1208.5504.

[25] A. Djouadi, *The Anatomy of electro-weak symmetry breaking. I: The Higgs boson in the standard model*, *Phys.Rept.* **457** (2008) 1–216, [hep-ph/0503172].

[26] J. Gunion, H. Haber, and J. Wudka, *Sum rules for Higgs bosons*, *Phys.Rev.* **D43** (1991) 904–912.

[27] N. Cabibbo, L. Maiani, G. Parisi, and R. Petronzio, *Bounds on the Fermions and Higgs Boson Masses in Grand Unified Theories*, Nucl.Phys. **B158** (1979) 295–305.

[28] R. A. Flores and M. Sher, *Upper Limits to Fermion Masses in the Glashow-Weinberg-Salam Model*, Phys.Rev. **D27** (1983) 1679.

[29] M. Lindner, *Implications of Triviality for the Standard Model*, Z.Phys. **C31** (1986) 295.

[30] B. Grzadkowski and M. Lindner, *Stability of Triviality Mass Bounds in the Standard Model*, Phys.Lett. **B178** (1986) 81.

[31] M. Sher, *Electroweak Higgs Potentials and Vacuum Stability*, Phys.Rept. **179** (1989) 273–418.

[32] J. Casas, J. Espinosa, and M. Quiros, *Improved Higgs mass stability bound in the standard model and implications for supersymmetry*, Phys.Lett. **B342** (1995) 171–179, [`hep-ph/9409458`].

[33] G. Altarelli and G. Isidori, *Lower limit on the Higgs mass in the standard model: An Update*, Phys.Lett. **B337** (1994) 141–144.

[34] J. Espinosa and M. Quiros, *Improved metastability bounds on the standard model Higgs mass*, Phys.Lett. **B353** (1995) 257–266, [`hep-ph/9504241`].

[35] T. Hambye and K. Riesselmann, *Matching conditions and Higgs mass upper bounds revisited*, Phys.Rev. **D55** (1997) 7255–7262, [`hep-ph/9610272`].

[36] **ALEPH, CDF, D0, DELPHI, L3, OPAL, SLD, LEP Electroweak Working Group, Tevatron Electroweak Working Group, SLD Electroweak and Heavy Flavour Groups** Collaboration, L. E. W. Group, *Precision Electroweak Measurements and Constraints on the Standard Model*, `arXiv:1012.2367`.

[37] M. Baak, M. Goebel, J. Haller, A. Hoecker, D. Kennedy, et al., *The Electroweak Fit of the Standard Model after the Discovery of a New Boson at the LHC*, Eur.Phys.J. **C72** (2012) 2205, [`arXiv:1209.2716`].

[38] **Gfitter Group** Collaboration, M. Baak et al., *The global electroweak fit at NNLO and prospects for the LHC and ILC*, Eur.Phys.J. **C74** (2014) 3046, [`arXiv:1407.3792`].

[39] J. F. Gunion and H. E. Haber, *The CP conserving two Higgs doublet model: The Approach to the decoupling limit*, Phys.Rev. **D67** (2003) 075019, [`hep-ph/0207010`].

[40] **ATLAS, CMS** Collaboration, G. Aad et al., *Combined Measurement of the Higgs Boson Mass in pp Collisions at $\sqrt{s} = 7$ and 8 TeV with the ATLAS and CMS Experiments*, Phys.Rev.Lett. **114** (2015) 191803, [`arXiv:1503.0758`].

[41] **ATLAS, CDF, CMS, D0** Collaboration, *First combination of Tevatron and LHC measurements of the top-quark mass*, arXiv:1403.4427.

[42] M. Spira, *QCD effects in Higgs physics*, *Fortsch.Phys.* **46** (1998) 203–284, [hep-ph/9705337].

[43] J. Gunion and H. E. Haber, *Higgs Bosons in Supersymmetric Models. 1.*, *Nucl.Phys.* **B272** (1986) 1.

[44] J. F. Gunion, H. E. Haber, G. L. Kane, and S. Dawson, *THE HIGGS HUNTER'S GUIDE*, *Front.Phys.* **80** (2000) 1–448.

[45] E. Braaten and J. Leveille, *Higgs Boson Decay and the Running Mass*, *Phys.Rev.* **D22** (1980) 715.

[46] N. Sakai, *Perturbative QCD Corrections to the Hadronic Decay Width of the Higgs Boson*, *Phys.Rev.* **D22** (1980) 2220.

[47] T. Inami and T. Kubota, *Renormalization Group Estimate of the Hadronic Decay Width of the Higgs Boson*, *Nucl.Phys.* **B179** (1981) 171.

[48] S. Gorishnii, A. Kataev, and S. Larin, *The Width of Higgs Boson Decay Into Hadrons: Three Loop Corrections of Strong Interactions*, *Sov.J.Nucl.Phys.* **40** (1984) 329–334.

[49] M. Drees and K.-i. Hikasa, *Heavy Quark Thresholds in Higgs Physics*, *Phys.Rev.* **D41** (1990) 1547.

[50] M. Drees and K.-i. Hikasa, *NOTE ON QCD CORRECTIONS TO HADRONIC HIGGS DECAY*, *Phys.Lett.* **B240** (1990) 455.

[51] S. Gorishnii, A. Kataev, S. Larin, and L. Surguladze, *Corrected Three Loop QCD Correction to the Correlator of the Quark Scalar Currents and γ (Tot) ($H^0 \to$ Hadrons)*, *Mod.Phys.Lett.* **A5** (1990) 2703–2712.

[52] S. Gorishnii, A. Kataev, S. Larin, and L. Surguladze, *Scheme dependence of the next to next-to-leading QCD corrections to Gamma(tot) (H0 —¿ hadrons) and the spurious QCD infrared fixed point*, *Phys.Rev.* **D43** (1991) 1633–1640.

[53] K. Chetyrkin, *Correlator of the quark scalar currents and Gamma(tot) (H —¿ hadrons) at O (alpha-s**3) in pQCD*, *Phys.Lett.* **B390** (1997) 309–317, [hep-ph/9608318].

[54] K. Chetyrkin and M. Steinhauser, *Complete QCD corrections of order O (alpha-s**3) to the hadronic Higgs decay*, *Phys.Lett.* **B408** (1997) 320–324, [hep-ph/9706462].

REFERENCES

[55] **LHC Higgs Cross Section Working Group** Collaboration, S. Heinemeyer et al., *Handbook of LHC Higgs Cross Sections: 3. Higgs Properties*, arXiv:1307.1347.

[56] J. F. Gunion, P. Kalyniak, M. Soldate, and P. Galison, *Hunting for the Intermediate Mass Higgs Boson in a Hadron Collider, Phys. Rev. Lett.* **54** (1985) 1226.

[57] J. F. Gunion, P. Kalyniak, M. Soldate, and P. Galison, *Searching for the Intermediate Mass Higgs Boson, Phys. Rev.* **D34** (1986) 101.

[58] M. Spira, A. Djouadi, D. Graudenz, and P. Zerwas, *Higgs boson production at the LHC, Nucl.Phys.* **B453** (1995) 17–82, [hep-ph/9504378].

[59] LHC Higgs Cross Section Working Group. https://twiki.cern.ch/twiki/bin/view/LHCPhysics/CrossSections.

[60] A. Djouadi, J. Kalinowski, and M. Spira, *HDECAY: A Program for Higgs boson decays in the standard model and its supersymmetric extension, Comput.Phys.Commun.* **108** (1998) 56–74, [hep-ph/9704448].

[61] S. Dittmaier, S. Dittmaier, C. Mariotti, G. Passarino, R. Tanaka, et al., *Handbook of LHC Higgs Cross Sections: 2. Differential Distributions*, arXiv:1201.3084.

[62] M. Farina, C. Grojean, F. Maltoni, E. Salvioni, and A. Thamm, *Lifting degeneracies in Higgs couplings using single top production in association with a Higgs boson, JHEP* **1305** (2013) 022, [arXiv:1211.3736].

[63] S. Dawson, A. Gritsan, H. Logan, J. Qian, C. Tully, et al., *Working Group Report: Higgs Boson*, arXiv:1310.8361.

[64] **ATLAS** Collaboration, G. Aad et al., *Measurements of the Higgs boson production and decay rates and coupling strengths using pp collision data at $\sqrt{s} = 7$ and 8 TeV in the ATLAS experiment*, arXiv:1507.0454.

[65] **ATLAS** Collaboration, G. Aad et al., *Measurements of Higgs boson production and couplings in diboson final states with the ATLAS detector at the LHC, Phys.Lett.* **B726** (2013) 88–119, [arXiv:1307.1427].

[66] **CMS** Collaboration, V. Khachatryan et al., *Observation of the diphoton decay of the Higgs boson and measurement of its properties, Eur.Phys.J.* **C74** (2014), no. 10 3076, [arXiv:1407.0558].

[67] **ATLAS** Collaboration, G. Aad et al., *Observation of a new particle in the search for the Standard Model Higgs boson with the ATLAS detector at the LHC, Phys.Lett.* **B716** (2012) 1–29, [arXiv:1207.7214].

[68] **CMS** Collaboration, S. Chatrchyan et al., *Observation of a new boson at a mass of 125 GeV with the CMS experiment at the LHC*, Phys.Lett. **B716** (2012) 30–61, [arXiv:1207.7235].

[69] **CMS** Collaboration, S. Chatrchyan et al., *Observation of a new boson with mass near 125 GeV in pp collisions at $\sqrt{s} = 7$ and 8 TeV*, JHEP **1306** (2013) 081, [arXiv:1303.4571].

[70] **ATLAS** Collaboration, G. Aad et al., *Measurement of Higgs boson production in the diphoton decay channel in pp collisions at center-of-mass energies of 7 and 8 TeV with the ATLAS detector*, Phys.Rev. **D90** (2014), no. 11 112015, [arXiv:1408.7084].

[71] **CMS** Collaboration, S. Chatrchyan et al., *Measurement of the properties of a Higgs boson in the four-lepton final state*, Phys.Rev. **D89** (2014), no. 9 092007, [arXiv:1312.5353].

[72] L. Landau, *On the angular momentum of a two-photon system*, Dokl.Akad.Nauk Ser.Fiz. **60** (1948) 207–209.

[73] C.-N. Yang, *Selection Rules for the Dematerialization of a Particle Into Two Photons*, Phys.Rev. **77** (1950) 242–245.

[74] **CMS** Collaboration, V. Khachatryan et al., *Constraints on the spin-parity and anomalous HVV couplings of the Higgs boson in proton collisions at 7 and 8 TeV*, arXiv:1411.3441.

[75] **ATLAS** Collaboration, G. Aad et al., *Evidence for the spin-0 nature of the Higgs boson using ATLAS data*, Phys.Lett. **B726** (2013) 120–144, [arXiv:1307.1432].

[76] T. A. collaboration, *Study of the spin and parity of the Higgs boson in HVV decays with the ATLAS detector*, .

[77] T. A. collaboration, *Measurements of the Higgs boson production and decay rates and coupling strengths using pp collision data at s = 7 and 8 TeV in the ATLAS experiment*, .

[78] **CMS** Collaboration, V. Khachatryan et al., *Precise determination of the mass of the Higgs boson and tests of compatibility of its couplings with the standard model predictions using proton collisions at 7 and 8 TeV*, Eur.Phys.J. **C75** (2015), no. 5 212, [arXiv:1412.8662].

[79] G. Angloher, M. Bauer, I. Bavykina, A. Bento, C. Bucci, et al., *Results from 730 kg days of the CRESST-II Dark Matter Search*, Eur.Phys.J. **C72** (2012) 1971, [arXiv:1109.0702].

[80] **XENON10** Collaboration, J. Angle et al., *A search for light dark matter in XENON10 data*, Phys.Rev.Lett. **107** (2011) 051301, [arXiv:1104.3088].

[81] **XENON100 Collaboration** Collaboration, E. Aprile et al., *Dark Matter Results from 225 Live Days of XENON100 Data, Phys.Rev.Lett.* **109** (2012) 181301, [arXiv:1207.5988].

[82] **DAMA** Collaboration, R. Bernabei et al., *First results from DAMA/LIBRA and the combined results with DAMA/NaI, Eur.Phys.J.* **C56** (2008) 333–355, [arXiv:0804.2741].

[83] C. Savage, G. Gelmini, P. Gondolo, and K. Freese, *Compatibility of DAMA/LIBRA dark matter detection with other searches, JCAP* **0904** (2009) 010, [arXiv:0808.3607].

[84] **CoGeNT** Collaboration, C. Aalseth et al., *CoGeNT: A Search for Low-Mass Dark Matter using p-type Point Contact Germanium Detectors, Phys.Rev.* **D88** (2013), no. 1 012002, [arXiv:1208.5737].

[85] **CDMS Collaboration** Collaboration, R. Agnese et al., *Silicon Detector Dark Matter Results from the Final Exposure of CDMS II, Phys.Rev.Lett.* **111** (2013) 251301, [arXiv:1304.4279].

[86] **COUPP** Collaboration, E. Behnke et al., *First Dark Matter Search Results from a 4-kg CF$_3$I Bubble Chamber Operated in a Deep Underground Site, Phys.Rev.* **D86** (2012), no. 5 052001, [arXiv:1204.3094].

[87] **LUX Collaboration** Collaboration, D. Akerib et al., *First results from the LUX dark matter experiment at the Sanford Underground Research Facility, Phys.Rev.Lett.* **112** (2014) 091303, [arXiv:1310.8214].

[88] P. J. Fox, J. Kopp, M. Lisanti, and N. Weiner, *A CoGeNT Modulation Analysis, Phys.Rev.* **D85** (2012) 036008, [arXiv:1107.0717].

[89] T. A. collaboration, *Search for an Invisibly Decaying Higgs Boson Produced via Vector Boson Fusion in pp Collisions at $\sqrt{s} = 8$ TeV using the ATLAS Detector at the LHC,* .

[90] **CMS** Collaboration, C. Collaboration, *Search for invisible decays of Higgs bosons in the vector boson fusion production mode,* .

[91] **ATLAS** Collaboration, G. Aad et al., *Search for neutral Higgs bosons of the minimal supersymmetric standard model in pp collisions at $\sqrt{s} = 8$ TeV with the ATLAS detector, JHEP* **1411** (2014) 056, [arXiv:1409.6064].

[92] **CMS** Collaboration, V. Khachatryan et al., *Search for neutral MSSM Higgs bosons decaying to a pair of tau leptons in pp collisions, JHEP* **1410** (2014) 160, [arXiv:1408.3316].

[93] **ATLAS** Collaboration, *Measurements of the properties of the Higgs-like boson in the four lepton decay channel with the ATLAS detector using 25 fb1 of proton-proton collision data,* .

[94] **CMS** Collaboration, C. Collaboration, *Search for a heavy Higgs boson in the H to ZZ to 2l2nu channel in pp collisions at sqrt(s)= 7 and 8 TeV,* .

[95] **CMS** Collaboration, C. Collaboration, *Search for extended Higgs sectors in the H to hh and A to Zh channels in sqrt(s) = 8 TeV pp collisions with multileptons and photons final states,* .

[96] **CMS** Collaboration, C. Collaboration, *Search for a pseudoscalar boson A decaying into a Z and an h boson in the llbb final state,* .

[97] **ATLAS** Collaboration, G. Aad et al., *Search for a CP-odd Higgs boson decaying to Zh in pp collisions at $\sqrt{s} = 8$ TeV with the ATLAS detector, Phys.Lett.* **B744** (2015) 163–183, [arXiv:1502.0447].

[98] H. Flacher, M. Goebel, J. Haller, A. Hocker, K. Monig, et al., *Revisiting the Global Electroweak Fit of the Standard Model and Beyond with Gfitter, Eur.Phys.J.* **C60** (2009) 543–583, [arXiv:0811.0009].

[99] M. Baak, M. Goebel, J. Haller, A. Hoecker, D. Ludwig, et al., *Updated Status of the Global Electroweak Fit and Constraints on New Physics, Eur.Phys.J.* **C72** (2012) 2003, [arXiv:1107.0975].

[100] **ALEPH, DELPHI, L3, OPAL, LEP Electroweak** Collaboration, S. Schael et al., *Electroweak Measurements in Electron-Positron Collisions at W-Boson-Pair Energies at LEP, Phys.Rept.* **532** (2013) 119–244, [arXiv:1302.3415].

[101] J. Erler, *The Mass of the Higgs Boson in the Standard Electroweak Model, Phys.Rev.* **D81** (2010) 051301, [arXiv:1002.1320].

[102] M. Ciuchini, E. Franco, S. Mishima, and L. Silvestrini, *Electroweak Precision Observables, New Physics and the Nature of a 126 GeV Higgs Boson, JHEP* **1308** (2013) 106, [arXiv:1306.4644].

[103] O. Eberhardt, G. Herbert, H. Lacker, A. Lenz, A. Menzel, et al., *Impact of a Higgs boson at a mass of 126 GeV on the standard model with three and four fermion generations, Phys.Rev.Lett.* **109** (2012) 241802, [arXiv:1209.1101].

[104] A. Freitas, *Higher-order electroweak corrections to the partial widths and branching ratios of the Z boson, JHEP* **1404** (2014) 070, [arXiv:1401.2447].

[105] **ALEPH, DELPHI, L3, OPAL, SLD, LEP Electroweak Working Group, SLD Electroweak Group, SLD Heavy Flavour Group** Collaboration, S. Schael et al., *Precision electroweak measurements on the Z resonance, Phys.Rept.* **427** (2006) 257–454, [hep-ex/0509008].

[106] **Particle Data Group** Collaboration, J. Beringer et al., *Review of Particle Physics (RPP), Phys.Rev.* **D86** (2012) 010001.

[107] M. Davier, A. Hoecker, B. Malaescu, and Z. Zhang, *Reevaluation of the Hadronic Contributions to the Muon g-2 and to alpha(MZ)*, *Eur.Phys.J.* **C71** (2011) 1515, [arXiv:1010.4180].

[108] **ATLAS** Collaboration, G. Aad et al., *Measurement of the Higgs boson mass from the $H \to \gamma\gamma$ and $H \to ZZ^* \to 4\ell$ channels with the ATLAS detector using 25 fb^{-1} of pp collision data*, *Phys.Rev.* **D90** (2014), no. 5 052004, [arXiv:1406.3827].

[109] **CMS** Collaboration, C. Collaboration, *Precise determination of the mass of the Higgs boson and studies of the compatibility of its couplings with the standard model*, .

[110] M. E. Peskin and T. Takeuchi, *A New constraint on a strongly interacting Higgs sector*, *Phys.Rev.Lett.* **65** (1990) 964–967.

[111] M. E. Peskin and T. Takeuchi, *Estimation of oblique electroweak corrections*, *Phys.Rev.* **D46** (1992) 381–409.

[112] J. Bernon, B. Dumont, and S. Kraml, *Status of Higgs couplings after run 1 of the LHC*, *Phys.Rev.* **D90** (2014), no. 7 071301, [arXiv:1409.1588].

[113] P. Ferreira, R. Santos, H. E. Haber, and J. P. Silva, *Mass-degenerate Higgs bosons at 125 GeV in the two-Higgs-doublet model*, *Phys.Rev.* **D87** (2013) 055009, [arXiv:1211.3131].

[114] C.-W. Chiang and K. Yagyu, *Implications of Higgs boson search data on the two-Higgs doublet models with a softly broken Z_2 symmetry*, *JHEP* **1307** (2013) 160, [arXiv:1303.0168].

[115] B. Grinstein and P. Uttayarat, *Carving Out Parameter Space in Type-II Two Higgs Doublets Model*, *JHEP* **1306** (2013) 094, [arXiv:1304.0028].

[116] B. Coleppa, F. Kling, and S. Su, *Constraining Type II 2HDM in Light of LHC Higgs Searches*, *JHEP* **1401** (2014) 161, [arXiv:1305.0002].

[117] O. Eberhardt, U. Nierste, and M. Wiebusch, *Status of the two-Higgs-doublet model of type II*, *JHEP* **1307** (2013) 118, [arXiv:1305.1649].

[118] S. Chang, S. K. Kang, J.-P. Lee, K. Y. Lee, S. C. Park, et al., *Two Higgs doublet models for the LHC Higgs boson data at $\sqrt{s} = 7$ and 8 TeV*, *JHEP* **1409** (2014) 101, [arXiv:1310.3374].

[119] K. Cheung, J. S. Lee, and P.-Y. Tseng, *Higgcision in the Two-Higgs Doublet Models*, *JHEP* **1401** (2014) 085, [arXiv:1310.3937].

[120] A. Celis, V. Ilisie, and A. Pich, *Towards a general analysis of LHC data within two-Higgs-doublet models*, *JHEP* **1312** (2013) 095, [arXiv:1310.7941].

[121] L. Wang and X.-F. Han, *Status of the aligned two-Higgs-doublet model confronted with the Higgs data*, *JHEP* **1404** (2014) 128, [`arXiv:1312.4759`].

[122] J. Baglio, O. Eberhardt, U. Nierste, and M. Wiebusch, *Benchmarks for Higgs Pair Production and Heavy Higgs Searches in the Two-Higgs-Doublet Model of Type II*, *Phys.Rev.* **D90** (2014) 015008, [`arXiv:1403.1264`].

[123] S. Inoue, M. J. Ramsey-Musolf, and Y. Zhang, *CPV Phenomenology of Flavor Conserving Two Higgs Doublet Models*, *Phys.Rev.* **D89** (2014) 115023, [`arXiv:1403.4257`].

[124] N. Craig, J. Galloway, and S. Thomas, *Searching for Signs of the Second Higgs Doublet*, `arXiv:1305.2424`.

[125] V. Barger, L. L. Everett, H. E. Logan, and G. Shaughnessy, *Scrutinizing the 125GeV Higgs boson in two Higgs doublet models at the LHC, ILC, and Muon Collider*, *Phys.Rev.* **D88** (2013) 115003, [`arXiv:1308.0052`].

[126] M. Carena, I. Low, N. R. Shah, and C. E. Wagner, *Impersonating the Standard Model Higgs Boson: Alignment without Decoupling*, *JHEP* **1404** (2014) 015, [`arXiv:1310.2248`].

[127] M. Carena, H. E. Haber, I. Low, N. R. Shah, and C. E. M. Wagner, *Complementarity between nonstandard Higgs boson searches and precision Higgs boson measurements in the MSSM*, *Phys.Rev.* **D91** (2015), no. 3 035003, [`arXiv:1410.4969`].

[128] C.-Y. Chen, S. Dawson, and M. Sher, *Heavy Higgs Searches and Constraints on Two Higgs Doublet Models*, *Phys.Rev.* **D88** (2013) 015018, [`arXiv:1305.1624`].

[129] S. Kanemura, H. Yokoya, and Y.-J. Zheng, *Complementarity in direct searches for additional Higgs bosons at the LHC and the International Linear Collider*, *Nucl.Phys.* **B886** (2014) 524–553, [`arXiv:1404.5835`].

[130] L. Wang and X.-F. Han, *Study of the heavy CP-even Higgs with mass 125 GeV in two-Higgs-doublet models at the LHC and ILC*, *JHEP* **1411** (2014) 085, [`arXiv:1404.7437`].

[131] G. Dorsch, S. Huber, and J. No, *A strong electroweak phase transition in the 2HDM after LHC8*, *JHEP* **1310** (2013) 029, [`arXiv:1305.6610`].

[132] J. Shu and Y. Zhang, *Impact of a CP Violating Higgs Sector: From LHC to Baryogenesis*, *Phys.Rev.Lett.* **111** (2013) 091801, [`arXiv:1304.0773`].

[133] M. Ahmadvand, *Baryogenesis within the two-Higgs-doublet model in the Electroweak scale*, *Int.J.Mod.Phys.* **A29** (2014) 1450090, [`arXiv:1308.3767`].

[134] G. Dorsch, S. Huber, K. Mimasu, and J. No, *Echoes of the Electroweak Phase Transition: Discovering a second Higgs doublet through $A_0 \to ZH_0$*, Phys.Rev.Lett. **113** (2014), no. 21 211802, [arXiv:1405.5537].

[135] G. Branco, P. Ferreira, L. Lavoura, M. Rebelo, M. Sher, et al., *Theory and phenomenology of two-Higgs-doublet models*, Phys.Rept. **516** (2012) 1–102, [arXiv:1106.0034].

[136] S. L. Glashow and S. Weinberg, *Natural Conservation Laws for Neutral Currents*, Phys.Rev. **D15** (1977) 1958.

[137] E. A. Paschos, *Diagonal Neutral Currents*, Phys. Rev. **D15** (1977) 1966.

[138] U. Haisch, *$\bar{B} \to X_s\gamma$: Standard Model and Beyond*, arXiv:0805.2141.

[139] F. Mahmoudi and O. Stal, *Flavor constraints on the two-Higgs-doublet model with general Yukawa couplings*, Phys.Rev. **D81** (2010) 035016, [arXiv:0907.1791].

[140] R. S. Gupta and J. D. Wells, *Next Generation Higgs Bosons: Theory, Constraints and Discovery Prospects at the Large Hadron Collider*, Phys.Rev. **D81** (2010) 055012, [arXiv:0912.0267].

[141] M. Jung, A. Pich, and P. Tuzon, *Charged-Higgs phenomenology in the Aligned two-Higgs-doublet model*, JHEP **1011** (2010) 003, [arXiv:1006.0470].

[142] A. Barroso, P. M. Ferreira, and R. Santos, *Charge and CP symmetry breaking in two Higgs doublet models*, Phys. Lett. **B632** (2006) 684–687, [hep-ph/0507224].

[143] I. P. Ivanov, *Minkowski space structure of the Higgs potential in 2HDM*, Phys. Rev. **D75** (2007) 035001, [hep-ph/0609018]. [Erratum: Phys. Rev.D76,039902(2007)].

[144] H. Georgi, *A Model of Soft CP Violation*, Hadronic J. **1** (1978) 155.

[145] I. F. Ginzburg, M. Krawczyk, and P. Osland, *Two Higgs doublet models with CP violation*, hep-ph/0211371.

[146] S. Kanemura, Y. Okada, E. Senaha, and C.-P. Yuan, *Higgs coupling constants as a probe of new physics*, Phys.Rev. **D70** (2004) 115002, [hep-ph/0408364].

[147] J. Gunion and H. Haber, *Errata for Higgs bosons in supersymmetric models: 1, 2 and 3*, hep-ph/9301205.

[148] F. Boudjema and A. Semenov, *Measurements of the SUSY Higgs selfcouplings and the reconstruction of the Higgs potential*, Phys.Rev. **D66** (2002) 095007, [hep-ph/0201219].

[149] M. Dubinin and A. Semenov, *Triple and quartic interactions of Higgs bosons in the general two Higgs doublet model*, hep-ph/9812246.

[150] R. Santos, S. Oliveira, and A. Barroso, *Mass terms in two Higgs doublet models*, hep-ph/0112202.

[151] S. Davidson and H. E. Haber, *Basis-independent methods for the two-Higgs-doublet model, Phys.Rev.* **D72** (2005) 035004, [hep-ph/0504050].

[152] G. C. Branco, L. Lavoura, and J. P. Silva, *CP Violation, Int.Ser.Monogr.Phys.* **103** (1999) 1–536.

[153] J. Gunion and H. E. Haber, *Higgs Bosons in Supersymmetric Models. 2. Implications for Phenomenology, Nucl.Phys.* **B278** (1986) 449.

[154] P. Zerwas, *e+ e- Collisions at 500-GeV: the Physics Potential. Proceedings, Workshop, Munich, Germany, February 4, 1991, Annecy, France, June 10-11, 1991, Hamburg, Germany, September 2-3, 1991*, .

[155] J. Grifols and A. Mendez, *The $WZH^{\pm}$ Coupling in $SU(2) \times U(1)$ Gauge Models, Phys.Rev.* **D22** (1980) 1725.

[156] A. Mendez and A. Pomarol, *One loop induced H^+W^+Z vertex in the minimal supersymmetry model, Nucl.Phys.* **B349** (1991) 369–380.

[157] G. Keller and D. Wyler, *The Couplings of Higgs Bosons to Two Vector Mesons in Multi Higgs Models, Nucl.Phys.* **B274** (1986) 410.

[158] A. Djouadi, *The Anatomy of electro-weak symmetry breaking. II. The Higgs bosons in the minimal supersymmetric model, Phys.Rept.* **459** (2008) 1–241, [hep-ph/0503173].

[159] M. Aoki, S. Kanemura, K. Tsumura, and K. Yagyu, *Models of Yukawa interaction in the two Higgs doublet model, and their collider phenomenology, Phys.Rev.* **D80** (2009) 015017, [arXiv:0902.4665].

[160] L. J. Hall and M. B. Wise, *FLAVOR CHANGING HIGGS - BOSON COUPLINGS, Nucl.Phys.* **B187** (1981) 397.

[161] J. F. Donoghue and L. F. Li, *Properties of Charged Higgs Bosons, Phys.Rev.* **D19** (1979) 945.

[162] H. Haber, G. L. Kane, and T. Sterling, *The Fermion Mass Scale and Possible Effects of Higgs Bosons on Experimental Observables, Nucl.Phys.* **B161** (1979) 493.

[163] D. Eriksson, J. Rathsman, and O. Stal, *2HDMC: Two-Higgs-doublet model calculator, Comput.Phys.Commun.* **181** (2010) 833–834.

[164] N. G. Deshpande and E. Ma, *Pattern of Symmetry Breaking with Two Higgs Doublets, Phys.Rev.* **D18** (1978) 2574.

[165] I. Ginzburg and I. Ivanov, *Tree-level unitarity constraints in the most general 2HDM*, *Phys.Rev.* **D72** (2005) 115010, [`hep-ph/0508020`].

[166] **OPAL** Collaboration, G. Abbiendi et al., *Decay mode independent searches for new scalar bosons with the OPAL detector at LEP*, *Eur.Phys.J.* **C27** (2003) 311–329, [`hep-ex/0206022`].

[167] **OPAL** Collaboration, G. Abbiendi et al., *Flavor independent h0A0 search and two Higgs doublet model interpretation of neutral Higgs boson searches at LEP*, *Eur.Phys.J.* **C40** (2005) 317–332, [`hep-ex/0408097`].

[168] S. M. Barr and A. Zee, *Electric Dipole Moment of the Electron and of the Neutron*, *Phys.Rev.Lett.* **65** (1990) 21–24.

[169] **Muon g-2** Collaboration, G. Bennett et al., *Measurement of the negative muon anomalous magnetic moment to 0.7 ppm*, *Phys.Rev.Lett.* **92** (2004) 161802, [`hep-ex/0401008`].

[170] G. Belanger, B. Dumont, U. Ellwanger, J. Gunion, and S. Kraml, *Global fit to Higgs signal strengths and couplings and implications for extended Higgs sectors*, *Phys.Rev.* **D88** (2013) 075008, [`arXiv:1306.2941`].

[171] F. Domingo, U. Ellwanger, E. Fullana, C. Hugonie, and M.-A. Sanchis-Lozano, *Radiative Upsilon decays and a light pseudoscalar Higgs in the NMSSM*, *JHEP* **01** (2009) 061, [`arXiv:0810.4736`].

[172] **CMS** Collaboration, S. Chatrchyan et al., *Search for a light pseudoscalar Higgs boson in the dimuon decay channel in pp collisions at $\sqrt{s} = 7$ TeV*, *Phys. Rev. Lett.* **109** (2012) 121801, [`arXiv:1206.6326`].

[173] "https://twiki.cern.ch/twiki/bin/view/CMSPublic/Hig13002TWiki#Limit_Plot."

[174] A. Korytov. private communication.

[175] **CMS** Collaboration, C. Collaboration, *Search for scalar resonances in the 200-500 GeV mass range decaying into a Z and a photon in pp collisions at sqrt(s)=8 TeV*, .

[176] **CMS** Collaboration, V. Khachatryan et al., *Search for resonant pair production of Higgs bosons decaying to two bottom quark-antiquark pairs in proton-proton collisions at 8 TeV*, `arXiv:1503.0411`.

[177] **CMS** Collaboration, C. Collaboration, *Search for H/A decaying into Z+A/H, with Z to ll and A/H to fermion pair*, .

[178] R. V. Harlander, S. Liebler, and H. Mantler, *SusHi: A program for the calculation of Higgs production in gluon fusion and bottom-quark annihilation in the Standard Model and the MSSM*, *Comput.Phys.Commun.* **184** (2013) 1605–1617, [`arXiv:1212.3249`].

[179] K. Arnold, M. Bahr, G. Bozzi, F. Campanario, C. Englert, et al., *VBFNLO: A Parton level Monte Carlo for processes with electroweak bosons*, *Comput.Phys.Commun.* **180** (2009) 1661–1670, [arXiv:0811.4559].

[180] P. Ferreira, J. F. Gunion, H. E. Haber, and R. Santos, *Probing wrong-sign Yukawa couplings at the LHC and a future linear collider*, *Phys.Rev.* **D89** (2014) 115003, [arXiv:1403.4736].

[181] A. Efrati and Y. Nir, *What if $\lambda_{hhh} \neq 3m_h^2/v$*, arXiv:1401.0935.

[182] V. F. Weisskopf, *On the Self-Energy and the Electromagnetic Field of the Electron*, *Phys. Rev.* **56** (1939) 72–85.

[183] G. Altarelli, *The Higgs: so simple yet so unnatural*, *Phys.Scripta* **T158** (2013) 014011, [arXiv:1308.0545].

[184] M. Carena, H. E. Haber, H. E. Logan, and S. Mrenna, *Distinguishing a MSSM Higgs boson from the SM Higgs boson at a linear collider*, *Phys. Rev.* **D65** (2002) 055005, [hep-ph/0106116]. [Erratum: Phys. Rev.D65,099902(2002)].

[185] P. M. Ferreira, H. E. Haber, and J. P. Silva, *Generalized CP symmetries and special regions of parameter space in the two-Higgs-doublet model*, *Phys. Rev.* **D79** (2009) 116004, [arXiv:0902.1537].

[186] G. 't Hooft, *Naturalness, chiral symmetry, and spontaneous chiral symmetry breaking*, *NATO Sci. Ser. B* **59** (1980) 135.

[187] M. Misiak, H. Asatrian, R. Boughezal, M. Czakon, T. Ewerth, et al., *Updated NNLO QCD predictions for the weak radiative B-meson decays*, *Phys.Rev.Lett.* **114** (2015), no. 22 221801, [arXiv:1503.0178].

[188] L.-F. Li, Y. Liu, and L. Wolfenstein, *Hidden Higgs Particles*, *Phys.Lett.* **B159** (1985) 45.

[189] D. Curtin, R. Essig, S. Gori, P. Jaiswal, A. Katz, et al., *Exotic decays of the 125 GeV Higgs boson*, *Phys.Rev.* **D90** (2014), no. 7 075004, [arXiv:1312.4992].

[190] M. Carena, S. Heinemeyer, O. Stl, C. Wagner, and G. Weiglein, *MSSM Higgs Boson Searches at the LHC: Benchmark Scenarios after the Discovery of a Higgs-like Particle*, *Eur.Phys.J.* **C73** (2013) 2552, [arXiv:1302.7033].

[191] D. G. Cerdeno, P. Ghosh, and C. B. Park, *Probing the two light Higgs scenario in the NMSSM with a low-mass pseudoscalar*, *JHEP* **1306** (2013) 031, [arXiv:1301.1325].

[192] J. Cao, F. Ding, C. Han, J. M. Yang, and J. Zhu, *A light Higgs scalar in the NMSSM confronted with the latest LHC Higgs data*, *JHEP* **1311** (2013) 018, [arXiv:1309.4939].

REFERENCES

[193] N.-E. Bomark, S. Moretti, S. Munir, and L. Roszkowski, *A light NMSSM pseudoscalar Higgs boson at the LHC redux*, arXiv:1409.8393.

[194] J. Huang, T. Liu, L.-T. Wang, and F. Yu, *Supersymmetric Exotic Decays of the 125 GeV Higgs Boson, Phys.Rev.Lett.* **112** (2014), no. 22 221803, [arXiv:1309.6633].

[195] J. F. Gunion, H. E. Haber, and T. Moroi, *Will at least one of the Higgs bosons of the next-to-minimal supersymmetric extension of the standard model be observable at LEP-2 or the LHC?, eConf* **C960625** (1996) LTH095, [hep-ph/9610337].

[196] P. Ferreira, R. Guedes, M. O. Sampaio, and R. Santos, *Wrong sign and symmetric limits and non-decoupling in 2HDMs, JHEP* **1412** (2014) 067, [arXiv:1409.6723].

[197] A. Korytov, "How well can we resolve two bosons with near degenerate masses? Presented at the Davis Higgs Workshop, April, 2013."

[198] W. Altmannshofer, S. Gori, and G. D. Kribs, *A Minimal Flavor Violating 2HDM at the LHC, Phys.Rev.* **D86** (2012) 115009, [arXiv:1210.2465].

[199] M. Drees, R. Godbole, and P. Roy, *Theory and phenomenology of sparticles: An account of four-dimensional N=1 supersymmetry in high energy physics*, .

[200] U. Ellwanger, C. Hugonie, and A. M. Teixeira, *The Next-to-Minimal Supersymmetric Standard Model, Phys.Rept.* **496** (2010) 1–77, [arXiv:0910.1785].

[201] D. A. Demir, G. L. Kane, and T. T. Wang, *The Minimal U(1)' extension of the MSSM, Phys. Rev.* **D72** (2005) 015012, [hep-ph/0503290].

[202] M. Matsuda and M. Tanimoto, *Explicit CP violation of the Higgs sector in the next-to-minimal supersymmetric standard model, Phys.Rev.* **D52** (1995) 3100–3107, [hep-ph/9504260].

[203] N. Haba, *Explicit CP violation in the Higgs sector of the next-to-minimal supersymmetric standard model, Prog.Theor.Phys.* **97** (1997) 301–310, [hep-ph/9608357].

[204] S. Ham, S. Oh, and D. Son, *Neutral Higgs sector of the next-to-minimal supersymmetric standard model with explicit CP violation, Phys.Rev.* **D65** (2002) 075004, [hep-ph/0110052].

[205] M. Boz, *The Higgs sector and electron electric dipole moment in next-to-minimal supersymmetry with explicit CP violation, Mod.Phys.Lett.* **A21** (2006) 243–264, [hep-ph/0511072].

[206] S. Ham, S. Kim, S. OH, and D. Son, *Higgs bosons of the NMSSM with explicit CP violation at the ILC, Phys.Rev.* **D76** (2007) 115013, [arXiv:0708.2755].

[207] H. E. Haber, *The Status of the minimal supersymmetric standard model and beyond*, *Nucl.Phys.Proc.Suppl.* **62** (1998) 469–484, [`hep-ph/9709450`].

[208] **MSSM Working Group** Collaboration, A. Djouadi et al., *The Minimal supersymmetric standard model: Group summary report*, `hep-ph/9901246`.

[209] I. Gogoladze, Q. Shafi, and C. S. Un, *Higgs Boson Mass from t-b-τ Yukawa Unification*, *JHEP* **1208** (2012) 028, [`arXiv:1112.2206`].

[210] H. Baer, V. Barger, and A. Mustafayev, *Implications of a 125 GeV Higgs scalar for LHC SUSY and neutralino dark matter searches*, *Phys.Rev.* **D85** (2012) 075010, [`arXiv:1112.3017`].

[211] S. Heinemeyer, O. Stal, and G. Weiglein, *Interpreting the LHC Higgs Search Results in the MSSM*, *Phys.Lett.* **B710** (2012) 201–206, [`arXiv:1112.3026`].

[212] A. Arbey, M. Battaglia, A. Djouadi, F. Mahmoudi, and J. Quevillon, *Implications of a 125 GeV Higgs for supersymmetric models*, *Phys.Lett.* **B708** (2012) 162–169, [`arXiv:1112.3028`].

[213] A. Arbey, M. Battaglia, and F. Mahmoudi, *Constraints on the MSSM from the Higgs Sector: A pMSSM Study of Higgs Searches, $B_s^0->\mu^+\mu^-$ and Dark Matter Direct Detection*, *Eur.Phys.J.* **C72** (2012) 1906, [`arXiv:1112.3032`].

[214] M. Carena, S. Gori, N. R. Shah, and C. E. Wagner, *A 125 GeV SM-like Higgs in the MSSM and the $\gamma\gamma$ rate*, *JHEP* **1203** (2012) 014, [`arXiv:1112.3336`].

[215] S. Akula, B. Altunkaynak, D. Feldman, P. Nath, and G. Peim, *Higgs Boson Mass Predictions in SUGRA Unification, Recent LHC-7 Results, and Dark Matter*, *Phys.Rev.* **D85** (2012) 075001, [`arXiv:1112.3645`].

[216] M. Kadastik, K. Kannike, A. Racioppi, and M. Raidal, *Implications of the 125 GeV Higgs boson for scalar dark matter and for the CMSSM phenomenology*, *JHEP* **1205** (2012) 061, [`arXiv:1112.3647`].

[217] J. Cao, Z. Heng, D. Li, and J. M. Yang, *Current experimental constraints on the lightest Higgs boson mass in the constrained MSSM*, *Phys.Lett.* **B710** (2012) 665–670, [`arXiv:1112.4391`].

[218] A. Arvanitaki and G. Villadoro, *A Non Standard Model Higgs at the LHC as a Sign of Naturalness*, *JHEP* **1202** (2012) 144, [`arXiv:1112.4835`].

[219] L. J. Hall, D. Pinner, and J. T. Ruderman, *A Natural SUSY Higgs Near 126 GeV*, *JHEP* **1204** (2012) 131, [`arXiv:1112.2703`].

[220] B. de Carlos and J. Casas, *One loop analysis of the electroweak breaking in supersymmetric models and the fine tuning problem*, *Phys.Lett.* **B309** (1993) 320–328, [`hep-ph/9303291`].

REFERENCES

[221] P. H. Chankowski, J. R. Ellis, and S. Pokorski, *The Fine tuning price of LEP*, *Phys.Lett.* **B423** (1998) 327–336, [hep-ph/9712234].

[222] R. Barbieri and A. Strumia, *About the fine tuning price of LEP*, *Phys.Lett.* **B433** (1998) 63–66, [hep-ph/9801353].

[223] G. L. Kane and S. King, *Naturalness implications of LEP results*, *Phys.Lett.* **B451** (1999) 113–122, [hep-ph/9810374].

[224] L. Giusti, A. Romanino, and A. Strumia, *Natural ranges of supersymmetric signals*, *Nucl.Phys.* **B550** (1999) 3–31, [hep-ph/9811386].

[225] Z. Chacko, Y. Nomura, and D. Tucker-Smith, *A Minimally fine-tuned supersymmetric standard model*, *Nucl.Phys.* **B725** (2005) 207–250, [hep-ph/0504095].

[226] R. Kitano and Y. Nomura, *A Solution to the supersymmetric fine-tuning problem within the MSSM*, *Phys.Lett.* **B631** (2005) 58–67, [hep-ph/0509039].

[227] P. Athron and D. Miller, *A New Measure of Fine Tuning*, *Phys.Rev.* **D76** (2007) 075010, [arXiv:0705.2241].

[228] S. Cassel, D. Ghilencea, and G. Ross, *Fine tuning as an indication of physics beyond the MSSM*, *Nucl.Phys.* **B825** (2010) 203–221, [arXiv:0903.1115].

[229] R. Barbieri and D. Pappadopulo, *S-particles at their naturalness limits*, *JHEP* **0910** (2009) 061, [arXiv:0906.4546].

[230] M. Asano, H. D. Kim, R. Kitano, and Y. Shimizu, *Natural Supersymmetry at the LHC*, *JHEP* **1012** (2010) 019, [arXiv:1010.0692].

[231] R. Dermisek, *Unusual Higgs or Supersymmetry from Natural Electroweak Symmetry Breaking*, *Mod.Phys.Lett.* **A24** (2009) 1631–1648, [arXiv:0907.0297].

[232] A. Dobado, M. J. Herrero, and S. Penaranda, *The Higgs sector of the MSSM in the decoupling limit*, *Eur.Phys.J.* **C17** (2000) 487–500, [hep-ph/0002134].

[233] N. D. Christensen, T. Han, and S. Su, *MSSM Higgs Bosons at The LHC*, *Phys. Rev.* **D85** (2012) 115018, [arXiv:1203.3207].

[234] M. Drees, *A Supersymmetric Explanation of the Excess of Higgs–Like Events at the LHC and at LEP*, *Phys. Rev.* **D86** (2012) 115018, [arXiv:1210.6507].

[235] P. Bechtle, S. Heinemeyer, O. Stal, T. Stefaniak, G. Weiglein, and L. Zeune, *MSSM Interpretations of the LHC Discovery: Light or Heavy Higgs?*, *Eur. Phys. J.* **C73** (2013), no. 4 2354, [arXiv:1211.1955].

[236] M. Carena, S. Heinemeyer, O. Stl, C. E. M. Wagner, and G. Weiglein, *MSSM Higgs Boson Searches at the LHC: Benchmark Scenarios after the Discovery of a Higgs-like Particle*, Eur. Phys. J. **C73** (2013), no. 9 2552, [arXiv:1302.7033].

[237] T. Han, T. Li, S. Su, and L.-T. Wang, *Non-Decoupling MSSM Higgs Sector and Light Superpartners*, JHEP **11** (2013) 053, [arXiv:1306.3229].

[238] G. Barenboim, C. Bosch, M. L. Lpez-Ibaez, and O. Vives, *Eviction of a 125 GeV "heavy"-Higgs from the MSSM*, JHEP **11** (2013) 051, [arXiv:1307.5973].

[239] A. Djouadi, *Implications of the Higgs discovery for the MSSM*, Eur. Phys. J. **C74** (2014) 2704, [arXiv:1311.0720].

[240] J. E. Kim and H. P. Nilles, *The mu Problem and the Strong CP Problem*, Phys.Lett. **B138** (1984) 150.

[241] B. A. Dobrescu, G. L. Landsberg, and K. T. Matchev, *Higgs boson decays to CP odd scalars at the Tevatron and beyond*, Phys.Rev. **D63** (2001) 075003, [hep-ph/0005308].

[242] B. A. Dobrescu and K. T. Matchev, *Light axion within the next-to-minimal supersymmetric standard model*, JHEP **0009** (2000) 031, [hep-ph/0008192].

[243] U. Ellwanger, J. F. Gunion, C. Hugonie, and S. Moretti, *Towards a no lose theorem for NMSSM Higgs discovery at the LHC*, hep-ph/0305109.

[244] U. Ellwanger, J. Gunion, C. Hugonie, and S. Moretti, *NMSSM Higgs discovery at the LHC*, hep-ph/0401228.

[245] **Higgs Working Group** Collaboration, K. Assamagan et al., *The Higgs working group: Summary report 2003*, hep-ph/0406152.

[246] **LHC/LC Study Group** Collaboration, G. Weiglein et al., *Physics interplay of the LHC and the ILC*, Phys.Rept. **426** (2006) 47–358, [hep-ph/0410364].

[247] U. Ellwanger, J. F. Gunion, and C. Hugonie, *NMHDECAY: A Fortran code for the Higgs masses, couplings and decay widths in the NMSSM*, JHEP **0502** (2005) 066, [hep-ph/0406215].

[248] R. Dermisek and J. F. Gunion, *Escaping the large fine tuning and little hierarchy problems in the next to minimal supersymmetric model and h —¿ aa decays*, Phys.Rev.Lett. **95** (2005) 041801, [hep-ph/0502105].

[249] R. Dermisek and J. F. Gunion, *The NMSSM Solution to the Fine-Tuning Problem, Precision Electroweak Constraints and the Largest LEP Higgs Event Excess*, Phys.Rev. **D76** (2007) 095006, [arXiv:0705.4387].

[250] U. Ellwanger, J. F. Gunion, and C. Hugonie, *Difficult scenarios for NMSSM Higgs discovery at the LHC*, JHEP **0507** (2005) 041, [hep-ph/0503203].

320

REFERENCES

[251] R. Dermisek and J. F. Gunion, *Consistency of LEP event excesses with an h —¿ aa decay scenario and low-fine-tuning NMSSM models*, Phys.Rev. **D73** (2006) 111701, [hep-ph/0510322].

[252] R. Dermisek and J. F. Gunion, *The NMSSM Close to the R-symmetry Limit and Naturalness in h —¿ aa Decays for m(a) ¡ 2m(b)*, Phys.Rev. **D75** (2007) 075019, [hep-ph/0611142].

[253] S. Chang, P. J. Fox, and N. Weiner, *Naturalness and Higgs decays in the MSSM with a singlet*, JHEP **0608** (2006) 068, [hep-ph/0511250].

[254] P. W. Graham, A. Pierce, and J. G. Wacker, *Four tau s at the Tevatron*, hep-ph/0605162.

[255] S. Moretti, S. Munir, and P. Poulose, *Another step towards a no-lose theorem for NMSSM Higgs discovery at the LHC*, Phys.Lett. **B644** (2007) 241–247, [hep-ph/0608233].

[256] C. Hugonie and S. Moretti, *Higgs sector of nonminimal supersymmetric models at future hadron colliders*, eConf **C010630** (2001) P108, [hep-ph/0110241].

[257] S. Chang, P. J. Fox, and N. Weiner, *Visible Cascade Higgs Decays to Four Photons at Hadron Colliders*, Phys.Rev.Lett. **98** (2007) 111802, [hep-ph/0608310].

[258] T. Stelzer, S. Wiesenfeldt, and S. Willenbrock, *Higgs at the Tevatron in Extended Supersymmetric Models*, Phys.Rev. **D75** (2007) 077701, [hep-ph/0611242].

[259] U. Aglietti, A. Belyaev, S. Berge, A. Blum, R. Bonciani, et al., *Tevatron for LHC report: Higgs*, hep-ph/0612172.

[260] K. Cheung, J. Song, and Q.-S. Yan, *Role of h —¿ eta eta in Intermediate-Mass Higgs Boson Searches at the Large Hadron Collider*, Phys.Rev.Lett. **99** (2007) 031801, [hep-ph/0703149].

[261] G. Belanger, F. Boudjema, C. Hugonie, A. Pukhov, and A. Semenov, *Relic density of dark matter in the NMSSM*, JCAP **0509** (2005) 001, [hep-ph/0505142].

[262] J. F. Gunion, D. Hooper, and B. McElrath, *Light neutralino dark matter in the NMSSM*, Phys.Rev. **D73** (2006) 015011, [hep-ph/0509024].

[263] D. Cerdeno, E. Gabrielli, D. Lopez-Fogliani, C. Munoz, and A. Teixeira, *Phenomenological viability of neutralino dark matter in the NMSSM*, JCAP **0706** (2007) 008, [hep-ph/0701271].

[264] V. Barger, P. Langacker, I. Lewis, M. McCaskey, G. Shaughnessy, et al., *Recoil Detection of the Lightest Neutralino in MSSM Singlet Extensions*, Phys.Rev. **D75** (2007) 115002, [hep-ph/0702036].

[265] C. Hugonie, G. Belanger, and A. Pukhov, *Dark matter in the constrained NMSSM*, *JCAP* **0711** (2007) 009, [`arXiv:0707.0628`].

[266] M. Bastero-Gil, C. Hugonie, S. King, D. Roy, and S. Vempati, *Does LEP prefer the NMSSM?*, *Phys.Lett.* **B489** (2000) 359–366, [`hep-ph/0006198`].

[267] P. C. Schuster and N. Toro, *Persistent fine-tuning in supersymmetry and the NMSSM*, `hep-ph/0512189`.

[268] V. Barger, P. Langacker, and G. Shaughnessy, *Neutralino signatures of the singlet extended MSSM*, *Phys.Lett.* **B644** (2007) 361–369, [`hep-ph/0609068`].

[269] V. Barger, P. Langacker, and G. Shaughnessy, *Collider Signatures of Singlet Extended Higgs Sectors*, *Phys.Rev.* **D75** (2007) 055013, [`hep-ph/0611239`].

[270] A. Djouadi, U. Ellwanger, and A. Teixeira, *The Constrained next-to-minimal supersymmetric standard model*, *Phys.Rev.Lett.* **101** (2008) 101802, [`arXiv:0803.0253`].

[271] J. F. Gunion, D. E. Lopez-Fogliani, L. Roszkowski, R. Ruiz de Austri, and T. A. Varley, *Next-to-Minimal Supersymmetric Model Higgs Scenarios for Partially Universal GUT Scale Boundary Conditions*, *Phys.Rev.* **D84** (2011) 055026, [`arXiv:1105.1195`].

[272] C. Balazs and D. Carter, *Discovery potential of the next-to-minimal supergravity motivated model*, *Phys.Rev.* **D78** (2008) 055001, [`arXiv:0808.0770`].

[273] M. Drees, *Supersymmetric Models with Extended Higgs Sector*, *Int.J.Mod.Phys.* **A4** (1989) 3635.

[274] G. Degrassi and P. Slavich, *On the radiative corrections to the neutral Higgs boson masses in the NMSSM*, *Nucl.Phys.* **B825** (2010) 119–150, [`arXiv:0907.4682`].

[275] F. Staub, W. Porod, and B. Herrmann, *The Electroweak sector of the NMSSM at the one-loop level*, *JHEP* **1010** (2010) 040, [`arXiv:1007.4049`].

[276] U. Ellwanger and C. Hugonie, *Neutralino cascades in the (M+1)SSM*, *Eur.Phys.J.* **C5** (1998) 723–737, [`hep-ph/9712300`].

[277] J. Espinosa and M. Quiros, *Two loop radiative corrections to the mass of the lightest Higgs boson in supersymmetric standard models*, *Phys.Lett.* **B266** (1991) 389–396.

[278] U. Ellwanger and M. Rausch de Traubenberg, *Natural range of Higgs masses in supersymmetry*, *Z.Phys.* **C53** (1992) 521–528.

[279] P. Binetruy and C. A. Savoy, *Higgs and top masses in a nonminimal supersymmetric theory*, *Phys.Lett.* **B277** (1992) 453–458.

REFERENCES

[280] J. Espinosa and M. Quiros, *On Higgs boson masses in nonminimal supersymmetric standard models*, *Phys.Lett.* **B279** (1992) 92–97.

[281] T. Moroi and Y. Okada, *Upper bound of the lightest neutral Higgs mass in extended supersymmetric Standard Models*, *Phys.Lett.* **B295** (1992) 73–78.

[282] U. Ellwanger and M. Lindner, *Constraints on new physics from the Higgs and top masses*, *Phys.Lett.* **B301** (1993) 365–371, [hep-ph/9211249].

[283] T. Elliott, S. King, and P. White, *Supersymmetric Higgs bosons at the limit*, *Phys.Lett.* **B305** (1993) 71–77, [hep-ph/9302202].

[284] M. A. Diaz, T. A. ter Veldhuis, and T. J. Weiler, *The Higgs mass as the discriminator of electroweak models*, *Phys.Rev.Lett.* **74** (1995) 2876–2879, [hep-ph/9408319].

[285] G. Asatrian and G. Egiian, *Higgs boson masses in supersymmetric theories*, *Mod.Phys.Lett.* **A10** (1995) 2943–2954, [hep-ph/9508263].

[286] U. Ellwanger, *Radiative corrections to the neutral Higgs spectrum in supersymmetry with a gauge singlet*, *Phys.Lett.* **B303** (1993) 271–276, [hep-ph/9302224].

[287] T. Elliott, S. King, and P. White, *Squark contributions to Higgs boson masses in the next-to-minimal supersymmetric standard model*, *Phys.Lett.* **B314** (1993) 56–63, [hep-ph/9305282].

[288] T. Elliott, S. King, and P. White, *Radiative corrections to Higgs boson masses in the next-to-minimal supersymmetric Standard Model*, *Phys.Rev.* **D49** (1994) 2435–2456, [hep-ph/9308309].

[289] P. Pandita, *Radiative corrections to the scalar Higgs masses in a nonminimal supersymmetric Standard Model*, *Z.Phys.* **C59** (1993) 575–584.

[290] P. Pandita, *One loop radiative corrections to the lightest Higgs scalar mass in nonminimal supersymmetric Standard Model*, *Phys.Lett.* **B318** (1993) 338–346.

[291] U. Ellwanger, M. Rausch de Traubenberg, and C. A. Savoy, *Higgs phenomenology of the supersymmetric model with a gauge singlet*, *Z.Phys.* **C67** (1995) 665–670, [hep-ph/9502206].

[292] S. King and P. White, *Resolving the constrained minimal and next-to-minimal supersymmetric standard models*, *Phys.Rev.* **D52** (1995) 4183–4216, [hep-ph/9505326].

[293] F. Franke and H. Fraas, *Mass bounds for the neutral Higgs bosons in the next-to-minimal supersymmetric standard model*, *Phys.Lett.* **B353** (1995) 234–242, [hep-ph/9504279].

[294] S. W. Ham, S. K. Oh, and B. R. Kim, *Absolute upper bound on the one loop corrected mass of S(1) in the NMSSM*, *J.Phys.* **G22** (1996) 1575–1584, [hep-ph/9604243].

[295] Y. Daikoku and D. Suematsu, *Radiative symmetry breaking and Higgs mass bound in the NMSSM*, *Prog.Theor.Phys.* **104** (2000) 827–833, [hep-ph/0003206].

[296] R. Nevzorov and M. Trusov, *Particle spectrum in the modified NMSSM in the strong Yukawa coupling limit*, *J.Exp.Theor.Phys.* **91** (2000) 1079–1097, [hep-ph/0106351].

[297] B. Ananthanarayan and P. Pandita, *The nonminimal supersymmetric standard model with tan Beta approximately = m(t) / m(b)*, *Phys.Lett.* **B353** (1995) 70–78, [hep-ph/9503323].

[298] B. Ananthanarayan and P. Pandita, *Particle spectrum in the nonminimal supersymmetric standard model with tan beta approximately = m(t) / m(b)*, *Phys.Lett.* **B371** (1996) 245–251, [hep-ph/9511415].

[299] B. Ananthanarayan and P. Pandita, *The Nonminimal supersymmetric standard model at large tan beta*, *Int.J.Mod.Phys.* **A12** (1997) 2321–2342, [hep-ph/9601372].

[300] G. L. Kane, C. F. Kolda, and J. D. Wells, *Calculable upper limit on the mass of the lightest Higgs boson in any perturbatively valid supersymmetric theory*, *Phys.Rev.Lett.* **70** (1993) 2686–2689, [hep-ph/9210242].

[301] J. Espinosa and M. Quiros, *Upper bounds on the lightest Higgs boson mass in general supersymmetric Standard Models*, *Phys.Lett.* **B302** (1993) 51–58, [hep-ph/9212305].

[302] J. R. Espinosa and M. Quiros, *Gauge unification and the supersymmetric light Higgs mass*, *Phys.Rev.Lett.* **81** (1998) 516–519, [hep-ph/9804235].

[303] U. Ellwanger and C. Hugonie, *The Upper bound on the lightest Higgs mass in the NMSSM revisited*, *Mod.Phys.Lett.* **A22** (2007) 1581–1590, [hep-ph/0612133].

[304] U. Ellwanger and C. Hugonie, *Yukawa induced radiative corrections to the lightest Higgs boson mass in the NMSSM*, *Phys.Lett.* **B623** (2005) 93–103, [hep-ph/0504269].

[305] M. A. Diaz, T. A. ter Veldhuis, and T. J. Weiler, *Updated: Higgs mass bounds separate models of electroweak symmetry breaking*, *Phys.Rev.* **D54** (1996) 5855–5865, [hep-ph/9512229].

[306] M. Masip, R. Munoz-Tapia, and A. Pomarol, *Limits on the mass of the lightest Higgs in supersymmetric models*, *Phys.Rev.* **D57** (1998) R5340, [hep-ph/9801437].

REFERENCES

[307] G. Yeghian, *Upper bound on the lightest Higgs mass in supersymmetric theories*, *Acta Phys.Slov.* **49** (199) 823, [`hep-ph/9904488`].

[308] U. Ellwanger and C. Hugonie, *Masses and couplings of the lightest Higgs bosons in the (M+1) SSM*, *Eur.Phys.J.* **C25** (2002) 297–305, [`hep-ph/9909260`].

[309] N. D. Christensen, T. Han, Z. Liu, and S. Su, *Low-Mass Higgs Bosons in the NMSSM and Their LHC Implications*, *JHEP* **1308** (2013) 019, [`arXiv:1303.2113`].

[310] A. Djouadi, U. Ellwanger, and A. Teixeira, *Phenomenology of the constrained NMSSM*, *JHEP* **0904** (2009) 031, [`arXiv:0811.2699`].

[311] D. E. Lopez-Fogliani, L. Roszkowski, R. R. de Austri, and T. A. Varley, *A Bayesian Analysis of the Constrained NMSSM*, *Phys.Rev.* **D80** (2009) 095013, [`arXiv:0906.4911`].

[312] U. Ellwanger and C. Hugonie, *NMHDECAY 2.0: An Updated program for sparticle masses, Higgs masses, couplings and decay widths in the NMSSM*, *Comput.Phys.Commun.* **175** (2006) 290–303, [`hep-ph/0508022`].

[313] "http://www.th.u-psud.fr/NMHDECAY/nmssmtools.htmlhttp://www.th.u-psud.fr/NMHDECAY/nmssmtools.html."

[314] **WMAP** Collaboration, E. Komatsu et al., *Seven-Year Wilkinson Microwave Anisotropy Probe (WMAP) Observations: Cosmological Interpretation*, *Astrophys. J. Suppl.* **192** (2011) 18, [`arXiv:1001.4538`].

[315] U. Ellwanger and C. Hugonie, *Higgs bosons near 125 GeV in the NMSSM with constraints at the GUT scale*, *Adv.High Energy Phys.* **2012** (2012) 625389, [`arXiv:1203.5048`].

[316] **XENON100** Collaboration, E. Aprile et al., *Dark Matter Results from 100 Live Days of XENON100 Data*, *Phys.Rev.Lett.* **107** (2011) 131302, [`arXiv:1104.2549`].

[317] O. Buchmueller, R. Cavanaugh, A. De Roeck, M. Dolan, J. Ellis, et al., *Higgs and Supersymmetry*, *Eur.Phys.J.* **C72** (2012) 2020, [`arXiv:1112.3564`].

[318] U. Ellwanger, *A Higgs boson near 125 GeV with enhanced di-photon signal in the NMSSM*, *JHEP* **1203** (2012) 044, [`arXiv:1112.3548`].

[319] D. A. Vasquez, G. Belanger, C. Boehm, J. Da Silva, P. Richardson, et al., *The 125 GeV Higgs in the NMSSM in light of LHC results and astrophysics constraints*, *Phys.Rev.* **D86** (2012) 035023, [`arXiv:1203.3446`].

[320] J.-J. Cao, Z.-X. Heng, J. M. Yang, Y.-M. Zhang, and J.-Y. Zhu, *A SM-like Higgs near 125 GeV in low energy SUSY: a comparative study for MSSM and NMSSM*, *JHEP* **1203** (2012) 086, [`arXiv:1202.5821`].

[321] S. King, M. Muhlleitner, and R. Nevzorov, *NMSSM Higgs Benchmarks Near 125 GeV*, *Nucl.Phys.* **B860** (2012) 207–244, [arXiv:1201.2671].

[322] **CMS** Collaboration, S. Chatrchyan et al., *Search for the standard model Higgs boson decaying into two photons in pp collisions at $\sqrt{s} = 7$ TeV*, *Phys.Lett.* **B710** (2012) 403–425, [arXiv:1202.1487].

[323] **Tevatron New Physics Higgs Working Group, CDF, D0** Collaboration, *Updated Combination of CDF and D0 Searches for Standard Model Higgs Boson Production with up to 10.0 fb^{-1} of Data*, arXiv:1207.0449.

[324] M. Carena, S. Heinemeyer, C. Wagner, and G. Weiglein, *Suggestions for benchmark scenarios for MSSM Higgs boson searches at hadron colliders*, *Eur.Phys.J.* **C26** (2003) 601–607, [hep-ph/0202167].

[325] J. Cao, Z. Heng, J. M. Yang, and J. Zhu, *Status of low energy SUSY models confronted with the LHC 125 GeV Higgs data*, *JHEP* **1210** (2012) 079, [arXiv:1207.3698].

[326] **ALEPH, DELPHI, L3, OPAL, LEP Working Group for Higgs Boson Searches** Collaboration, S. Schael et al., *Search for neutral MSSM Higgs bosons at LEP*, *Eur.Phys.J.* **C47** (2006) 547–587, [hep-ex/0602042].

[327] **LEP Working Group for Higgs boson searches, ALEPH, DELPHI, L3, OPAL** Collaboration, R. Barate et al., *Search for the standard model Higgs boson at LEP*, *Phys.Lett.* **B565** (2003) 61–75, [hep-ex/0306033].

[328] **CMS** Collaboration, S. Chatrchyan et al., *Search for neutral Higgs bosons decaying to τ pairs in pp collisions at $\sqrt{s} = 7$ TeV*, *Phys.Lett.* **B713** (2012) 68–90, [arXiv:1202.4083].

[329] J. Gronberg, *Photon Linear Collider Gamma-Gamma Summary*, arXiv:1203.0031.

[330] D. M. Asner, J. B. Gronberg, and J. F. Gunion, *Detecting and studying Higgs bosons at a photon-photon collider*, *Phys.Rev.* **D67** (2003) 035009, [hep-ph/0110320].

[331] M. M. Velasco, M. Schmitt, G. Barenboim, H. E. Logan, D. Atwood, et al., *Photon photon and electron photon colliders with energies below a TeV*, *eConf* **C010630** (2001) E3005, [hep-ex/0111055].

[332] D. Asner, S. J. Asztalos, A. De Roeck, S. Heinemeyer, J. Gronberg, et al., *Complementarity of a low-energy photon collider and LHC physics*, hep-ph/0308103.

[333] B. Grzadkowski, J. F. Gunion, and M. Toharia, *Higgs-Radion interpretation of the LHC data?*, *Phys.Lett.* **B712** (2012) 70–80, [arXiv:1202.5017].

[334] **CMS** Collaboration, C. Collaboration, *Observation of a new boson with a mass near 125 GeV*, .

[335] **Planck** Collaboration, R. Adam et al., *Planck 2015 results. I. Overview of products and scientific results*, arXiv:1502.0158.

[336] G. Jungman, M. Kamionkowski, and K. Griest, *Supersymmetric dark matter*, *Phys.Rept.* **267** (1996) 195–373, [hep-ph/9506380].

[337] J. McDonald, *Gauge singlet scalars as cold dark matter*, *Phys. Rev.* **D50** (1994) 3637–3649, [hep-ph/0702143].

[338] C. P. Burgess, M. Pospelov, and T. ter Veldhuis, *The Minimal model of nonbaryonic dark matter: A Singlet scalar*, *Nucl. Phys.* **B619** (2001) 709–728, [hep-ph/0011335].

[339] D. Hooper and S. Profumo, *Dark matter and collider phenomenology of universal extra dimensions*, *Phys. Rept.* **453** (2007) 29–115, [hep-ph/0701197].

[340] **SuperCDMS Collaboration** Collaboration, R. Agnese et al., *Search for Low-Mass WIMPs with SuperCDMS*, *Phys.Rev.Lett.* **112** (2014) 241302, [arXiv:1402.7137].

[341] **CDMS Collaboration** Collaboration, R. Agnese et al., *Silicon detector results from the first five-tower run of CDMS II*, *Phys.Rev.* **D88** (2013) 031104, [arXiv:1304.3706].

[342] R. Bernabei, P. Belli, F. Cappella, V. Caracciolo, S. Castellano, et al., *Final model independent result of DAMA/LIBRA-phase1*, *Eur.Phys.J.* **C73** (2013) 2648, [arXiv:1308.5109].

[343] **CoGeNT collaboration** Collaboration, C. Aalseth et al., *Results from a Search for Light-Mass Dark Matter with a P-type Point Contact Germanium Detector*, *Phys.Rev.Lett.* **106** (2011) 131301, [arXiv:1002.4703].

[344] **XENON1T** Collaboration, E. Aprile, *The XENON1T Dark Matter Search Experiment*, *Springer Proc. Phys.* **148** (2013) 93–96, [arXiv:1206.6288].

[345] D. C. Malling et al., *After LUX: The LZ Program*, arXiv:1110.0103.

[346] L. Baudis, *WIMP Dark Matter Direct-Detection Searches in Noble Gases*, *Phys. Dark Univ.* **4** (2014) 50–59, [arXiv:1408.4371].

[347] J. L. Feng, J. Kumar, D. Marfatia, and D. Sanford, *Isospin-Violating Dark Matter*, *Phys.Lett.* **B703** (2011) 124–127, [arXiv:1102.4331].

[348] J. L. Feng, J. Kumar, and D. Sanford, *Xenophobic Dark Matter*, *Phys.Rev.* **D88** (2013) 015021, [arXiv:1306.2315].

[349] E. Del Nobile, G. B. Gelmini, P. Gondolo, and J.-H. Huh, *Update on Light WIMP Limits: LUX, lite and Light*, *JCAP* **1403** (2014) 014, [arXiv:1311.4247].

[350] V. Cirigliano, M. L. Graesser, G. Ovanesyan, and I. M. Shoemaker, *Shining LUX on Isospin-Violating Dark Matter Beyond Leading Order*, arXiv:1311.5886.

[351] J. M. Cline, K. Kainulainen, P. Scott, and C. Weniger, *Update on scalar singlet dark matter*, *Phys. Rev.* **D88** (2013) 055025, [arXiv:1306.4710].

[352] A. Drozd, B. Grzadkowski, and J. Wudka, *Multi-Scalar-Singlet Extension of the Standard Model - the Case for Dark Matter and an Invisible Higgs Boson*, *JHEP* **1204** (2012) 006, [arXiv:1112.2582].

[353] L. Lopez Honorez, E. Nezri, J. F. Oliver, and M. H. G. Tytgat, *The Inert Doublet Model: An Archetype for Dark Matter*, *JCAP* **0702** (2007) 028, [hep-ph/0612275].

[354] B. Swiezewska and M. Krawczyk, *Diphoton rate in the inert doublet model with a 125 GeV Higgs boson*, *Phys. Rev.* **D88** (2013), no. 3 035019, [arXiv:1212.4100].

[355] A. Goudelis, B. Herrmann, and O. Stl, *Dark matter in the Inert Doublet Model after the discovery of a Higgs-like boson at the LHC*, *JHEP* **09** (2013) 106, [arXiv:1303.3010].

[356] C. Garcia-Cely and A. Ibarra, *Novel Gamma-ray Spectral Features in the Inert Doublet Model*, *JCAP* **1309** (2013) 025, [arXiv:1306.4681].

[357] A. Arhrib, Y.-L. S. Tsai, Q. Yuan, and T.-C. Yuan, *An Updated Analysis of Inert Higgs Doublet Model in light of the Recent Results from LUX, PLANCK, AMS-02 and LHC*, *JCAP* **1406** (2014) 030, [arXiv:1310.0358].

[358] K. P. Modak and D. Majumdar, *Confronting Galactic and Extragalactic γ-rays Observed by Fermi-lat With Annihilating Dark Matter in an Inert Higgs Doublet Model*, *Astrophys. J. Suppl.* **219** (2015), no. 2 37, [arXiv:1502.0568].

[359] N. Blinov, S. Profumo, and T. Stefaniak, *The Electroweak Phase Transition in the Inert Doublet Model*, *JCAP* **1507** (2015), no. 07 028, [arXiv:1504.0594].

[360] G. Belanger, B. Dumont, A. Goudelis, B. Herrmann, S. Kraml, and D. Sengupta, *Dilepton constraints in the Inert Doublet Model from Run 1 of the LHC*, *Phys. Rev.* **D91** (2015), no. 11 115011, [arXiv:1503.0736].

[361] X.-G. He, T. Li, X.-Q. Li, J. Tandean, and H.-C. Tsai, *Constraints on Scalar Dark Matter from Direct Experimental Searches*, *Phys.Rev.* **D79** (2009) 023521, [arXiv:0811.0658].

[362] B. Grzadkowski and P. Osland, *Tempered Two-Higgs-Doublet Model*, *Phys.Rev.* **D82** (2010) 125026, [arXiv:0910.4068].

REFERENCES

[363] M. Boucenna and S. Profumo, *Direct and Indirect Singlet Scalar Dark Matter Detection in the Lepton-Specific two-Higgs-doublet Model*, *Phys.Rev.* **D84** (2011) 055011, [arXiv:1106.3368].

[364] X.-G. He, B. Ren, and J. Tandean, *Hints of Standard Model Higgs Boson at the LHC and LIGHT Dark Matter Searches*, *Phys.Rev.* **D85** (2012) 093019, [arXiv:1112.6364].

[365] Y. Bai, V. Barger, L. L. Everett, and G. Shaughnessy, *Two-Higgs-doublet-portal dark-matter model: LHC data and Fermi-LAT 135 GeV line*, *Phys.Rev.* **D88** (2013) 015008, [arXiv:1212.5604].

[366] X.-G. He and J. Tandean, *Low-Mass Dark-Matter Hint from CDMS II, Higgs Boson at the LHC, and Darkon Models*, *Phys.Rev.* **D88** (2013) 013020, [arXiv:1304.6058].

[367] Y. Cai and T. Li, *Singlet Dark Matter in Type II Two Higgs Doublet Model*, *Phys.Rev.* **D88** (2013) 115004, [arXiv:1308.5346].

[368] L. Wang, *A simplified 2HDM with a scalar dark matter and the galactic center gamma-ray excess*, arXiv:1406.3598.

[369] C.-Y. Chen, M. Freid, and M. Sher, *The Next-to-Minimal Two Higgs Doublet Model*, *Phys.Rev.* **D89** (2014) 075009, [arXiv:1312.3949].

[370] J. Guo and Z. Kang, *Higgs Naturalness and Dark Matter Stability by Scale Invariance*, arXiv:1401.5609.

[371] B. Grzadkowski and J. Wudka, *Pragmatic approach to the little hierarchy problem: the case for Dark Matter and neutrino physics*, *Phys.Rev.Lett.* **103** (2009) 091802, [arXiv:0902.0628].

[372] E. W. Kolb and M. S. Turner, *The Early Universe*, *Front.Phys.* **69** (1990) 1–547.

[373] **Planck Collaboration** Collaboration, P. Ade et al., *Planck 2013 results. XVI. Cosmological parameters*, arXiv:1303.5076.

[374] G. Belanger, F. Boudjema, A. Pukhov, and A. Semenov, *microMEGAs_3: A program for calculating dark matter observables*, *Comput.Phys.Commun.* **185** (2014) 960–985, [arXiv:1305.0237].

[375] M. T. Frandsen, F. Kahlhoefer, C. McCabe, S. Sarkar, and K. Schmidt-Hoberg, *The unbearable LIGHTNESS of being: CDMS versus XENON*, *JCAP* **1307** (2013) 023, [arXiv:1304.6066].

[376] N. Chen, Q. Wang, W. Zhao, S.-T. Lin, Q. Yue, et al., *Exothermic isospin-violating dark matter after SuperCDMS and CDEX*, arXiv:1404.6043.

[377] G. B. Gelmini, A. Georgescu, and J.-H. Huh, *Direct Detection of Light "Ge-phobic" Exothermic Dark Matter*, arXiv:1404.7484.

[378] C. Weniger, *A Tentative Gamma-Ray Line from Dark Matter Annihilation at the Fermi Large Area Telescope*, *JCAP* **1208** (2012) 007, [arXiv:1204.2797].

[379] **Fermi-LAT** Collaboration, W. Atwood et al., *The Large Area Telescope on the Fermi Gamma-ray Space Telescope Mission*, *Astrophys.J.* **697** (2009) 1071–1102, [arXiv:0902.1089].

[380] T. Bringmann, X. Huang, A. Ibarra, S. Vogl, and C. Weniger, *Fermi LAT Search for Internal Bremsstrahlung Signatures from Dark Matter Annihilation*, *JCAP* **1207** (2012) 054, [arXiv:1203.1312].

[381] D. Das, U. Ellwanger, and P. Mitropoulos, *A 130 GeV photon line from dark matter annihilation in the NMSSM*, *JCAP* **1208** (2012) 003, [arXiv:1206.2639].

[382] Y. Bai and J. Shelton, *Gamma Lines without a Continuum: Thermal Models for the Fermi-LAT 130 GeV Gamma Line*, *JHEP* **1212** (2012) 056, [arXiv:1208.4100].

[383] T. Bringmann and C. Weniger, *Gamma Ray Signals from Dark Matter: Concepts, Status and Prospects*, *Phys.Dark Univ.* **1** (2012) 194–217, [arXiv:1208.5481].

[384] D. M. Asner et al., *ILC Higgs White Paper*, in *Community Summer Study 2013: Snowmass on the Mississippi (CSS2013) Minneapolis, MN, USA, July 29-August 6, 2013*, 2013. arXiv:1310.0763.

[385] "CEPC-SppC Preliminary Conceptual Design Report." http://cepc.ihep.ac.cn/preCDR/volume.html.